NASA
Technical
Paper
2478

October 1985

Effect of Aileron Deflections on the Aerodynamic Characteristics of a Semispan Model of a Subsonic Energy-Efficient Transport

Peter F. Jacobs

NASA

NASA
Technical
Paper
2478

1985

Effect of Aileron Deflections on the Aerodynamic Characteristics of a Semispan Model of a Subsonic Energy-Efficient Transport

Peter F. Jacobs

Langley Research Center
Hampton, Virginia

NASA
National Aeronautics
and Space Administration

Scientific and Technical
Information Branch

SUMMARY

An investigation was conducted in the Langley 8-Foot Transonic Pressure Tunnel to determine the effect of aileron deflections on the aerodynamic characteristics of a subsonic energy-efficient transport (EET) model. The semispan model had an aspect-ratio-10 supercritical wing and was configured with a conventionally located set of ailerons (i.e., a high-speed aileron located inboard and a low-speed aileron located outboard). Data for the model were taken over a Mach number (M_∞) range from 0.30 to 0.90 and an angle of attack range from approximately -2° to 10°. The Reynolds number was 2.5×10^6 per foot for $M_\infty = 0.30$ and 4.0×10^6 per foot for the other Mach numbers. Model force and moment data, aileron-effectiveness parameters, aileron hinge-moment data, chordwise pressure distributions, and spanwise load data are presented.

The data indicate positive aileron effectiveness for the inboard aileron (based on averaged, equal-magnitude, positive and negative deflections) for all test conditions except for deflections of ±2.5° at a Mach number of 0.90 and angles of attack from approximately 0° to 2°. Control reversal at these conditions may be caused by shock-induced flow separation on the wing and interference effects from the nacelle and pylon. The outboard aileron had positive aileron effectiveness at all test conditions. The effectiveness of both ailerons increased near $M_\infty = 0.82$, mainly because of the influence of negative aileron deflections on shock location and the chordwise extent of the upper surface pressure plateau. The effectiveness of the outboard aileron did not increase as much as that of the inboard aileron, since the wing loads were lower at the tip. The effectiveness of both ailerons decreased at about $M_\infty = 0.84$ because of shock-induced boundary layer separation over much of the wing. The extensive aft camber of this supercritical wing produced negative hinge moments for most deflections of the ailerons.

INTRODUCTION

As part of the National Aeronautics and Space Administration's Aircraft Energy Efficiency (ACEE) project, extensive theoretical studies and experimental wind tunnel investigations have produced a group of aerodynamically efficient jet transport wings. These wings have higher lift-drag ratios, thicker airfoil sections, less sweep, and higher aspect ratios than the wings on current wide-body jet transports. The performance characteristics of these configurations have been documented in references 1 to 3, and aileron-effectiveness data for a preliminary active-control configuration are presented in references 4 and 5.

Further tests of lateral controls on an energy-efficient transport configuration were undertaken for two reasons. First, data for a more conventionally sized and located set of ailerons than those used in references 4 and 5 were desired. Second, since aileron effectiveness is sensitive to Reynolds number, a model larger than the one used in references 4 and 5 was required to increase the test Reynolds number. Therefore, a semispan model twice the scale of one of the configurations (SCW-2C) in reference 1 was constructed for the present investigation. The model had a conventional set of ailerons (i.e., a high-speed aileron located inboard and a low-speed aileron located outboard). Model force and moment data, aileron-effectiveness parameters, aileron hinge-moment data, chordwise pressure distributions, and spanwise load data are presented in this report.

SYMBOLS

The longitudinal and lateral-directional aerodynamic characteristics presented in this report are referred to the stability and body axis systems, respectively. Force and moment data have been reduced to conventional coefficient form based on the trapezoidal planform of the semispan wing panel (extended to the fuselage centerline). All dimensional values are given in the U.S. Customary Units.

a_1, a_2 — ailerons 1 and 2 (fig. 3)

$b/2$ — wing semispan, 53.17 in.

C_D — drag coefficient, $\frac{\text{Drag}}{q_\infty S}$

C_{HM_1} — hinge-moment coefficient for aileron 1, $\frac{\text{Hinge moment}}{q_\infty S_{a_1} c_{a_1}}$

C_{HM_2} — hinge-moment coefficient for aileron 2, $\frac{\text{Hinge moment}}{q_\infty S_{a_2} c_{a_2}}$

C_L — lift coefficient, $\frac{\text{Lift}}{q_\infty S}$

C_{L_α} — lift-curve slope, per degree

C_l — rolling-moment coefficient, $\frac{\text{Rolling moment}}{q_\infty Sb/2}$

$C_{l_{\delta a}}$ — lateral aileron-effectiveness parameter, $\frac{C_l|_{\delta a} - C_l|_{0°}}{\delta a - 0°}$, per degree

C_m — pitching-moment coefficient, $\frac{\text{Pitching moment}}{q_\infty S\bar{c}}$

C_n — yawing-moment coefficient, $\frac{\text{Yawing moment}}{q_\infty Sb/2}$

C_n' — section normal-force coefficient obtained from integration of pressure measurements

$C_{n_{\delta a}}$ — directional aileron-effectiveness parameter, $\frac{C_n|_{\delta a} - C_n|_{0°}}{\delta a - 0°}$, per degree

C_p — pressure coefficient, $\frac{p - p_\infty}{q_\infty}$

c — local chord, in.

c_{a_1}	average chord of a_1, 3.28 in.
c_{a_2}	average chord of a_2, 1.87 in.
$\bar{c}$	mean geometric chord of reference wing panel, 11.48 in.
M_∞	free-stream Mach number
p	local static pressure, lb/ft^2
p_∞	free-stream static pressure, lb/ft^2
q_∞	free-stream dynamic pressure, lb/ft^2
R_N	Reynolds number, per foot
S	wing planform reference (trapezoidal) area, 3.992 ft^2
S_{a_1}	planform area of a_1, 0.141 ft^2
S_{a_2}	planform area of a_2, 0.124 ft^2
t	local maximum thickness of wing, in.
x	chordwise distance from wing leading edge, positive aft, in.
y	spanwise distance from model centerline, in.
z	vertical distance, positive up, in.
α	angle of attack, deg
$\delta a_1, \delta a_2$	deflection of ailerons 1 and 2, positive for trailing edge down, deg
ε	local wing incidence measured from fuselage waterline, positive for leading edge up, deg
η	semispan station, $y/(b/2)$

Abbreviations:

F.S.	fuselage station, in.
L.E.	leading edge
L.S.	lower surface
T.E.	trailing edge
U.S.	upper surface

EXPERIMENTAL APPARATUS AND PROCEDURES

Test Facility

This investigation was conducted in the Langley 8-Foot Transonic Pressure Tunnel (ref. 6). This facility is a continuous-flow, single-return tunnel with a slotted test section. Tunnel controls allow independent variation of Mach number, density, stagnation temperature, and dew-point temperature. The test section is approximately 7.1 ft square (same cross-sectional area as that of a circle with an 8.0-ft diameter). The ceiling and floor are slotted axially and have an average openness ratio of 0.06. These features permit the test section Mach number to be changed continuously throughout the transonic speed range. The stagnation pressure in the tunnel can be varied from a minimum of 0.25 atm (1 atm = 2116 lb/ft^2) at all Mach numbers to a maximum of approximately 2.00 atm at Mach numbers less than 0.40. At transonic Mach numbers, the maximum stagnation pressure that can be obtained is approximately 1.5 atm.

Model Description

A photograph of the model in the Langley 8-Foot Transonic Pressure Tunnel is shown in figure 1. Drawings of the model are shown in figures 2 and 3.

Fuselage.- The fuselage for the semispan model used in this investigation was metric, had a maximum radius of 5.75 in., and was 108.61 in. long. Typical fuselage cross sections are shown in figure 4. The fineness ratio of this fuselage (9.44) is slightly higher than typical second-generation (wide-body) jet transports. The lower surface of the wing was faired into the fuselage to produce a relatively flat bottom that extended approximately 7 in. both ahead of the wing leading edge and aft of the wing trailing edge. The center section of the fuselage consisted of two fiberglass cover plates that surrounded the wing. The parting line for the cover plates extended horizontally fore of the leading edge and aft of the trailing edge of the wing root. A rubber seal between the wing and fuselage prevented airflow through the juncture. In order to prevent fouling, the fuselage was mounted approximately 0.2 in. away from the tunnel wall. A splitter plate was not used.

Wing.- A modified version of wing configuration SCW-2C from reference 1 was used in this investigation. The wing had 5° of dihedral and 30° of sweep at the quarter-chord. Based on the trapezoidal planform (extended to the fuselage centerline), the wing had a reference area (semispan) of 3.992 ft^2, an aspect ratio of 9.8, and a taper ratio of 0.397. The wing was designed for a cruise lift coefficient of 0.55 at a Mach number of 0.82.

The planform and airfoils of the original configuration were modified (ref. 2) from the wing root outboard to the trailing-edge break. Trailing-edge and leading-edge extensions were added to allow a substantial increase in the thickness of the wing root where the rear spar and landing-gear attachment would be located (see fig. 5). The wing trailing edge near the original planform break was also modified to correct local upper surface flow separation. To reduce the curvature of the wing upper surface at the trailing edge, the chord was shortened slightly. The planform of the trailing edge was altered from a simple break to an elliptical fairing of the outboard geometry into the new inboard trailing-edge extension. Twist and thickness distributions for the original and modified wings are shown in figure 6. Note that the twist remained the same for both wings, and although t/c for the modified wing was reduced inboard, the local wing thickness was greater than that of the original wing because of the increased chords inboard for the modified wing. Several airfoil sections from the modified wing are shown in figure 7 and measured coordinates are given in table I.

Ailerons.- The wing was equipped with a high-speed aileron inboard and a low-speed aileron outboard. The locations of the ailerons are shown in figure 3. The aileron chords were 25 percent of the local wing chord. The inboard and outboard ailerons could be deflected 0°, ±2.5°, ±7.5°, and ±12.5°. In addition, the outboard aileron could be deflected ±17.5°. The ailerons had a thin plastic wiper strip at the leading edge to prevent airflow through the wing-aileron gap.

Nacelle.- A flow-through, long-duct nacelle representative of an advanced energy-efficient engine was used throughout this investigation. The axis of the nacelle was canted inward 2° (leading edge of the nacelle toward the fuselage). Details of the nacelle are shown in figure 8. The centerline of the nacelle was located at $\eta = 0.400$.

Pylon.- A cambered pylon was used to attach the nacelle to the wing. Previous investigations with cambered and symmetrical pylons (ref. 2) have shown less installed drag with a cambered pylon. The pylon had an NACA 4412 airfoil section (upper surface was outboard) that was modified by local area rule shaping to reduce the installed drag at cruise conditions. A typical cross section of the pylon is shown in figure 9. The pylon for this investigation was developed in previous propulsion-integration tests of a similar configuration that did not have lateral-control surfaces. The pylon extended to the trailing edge of the wing and was located (spanwise) near the middle of the inboard aileron. To allow deflections of the inboard aileron, a section was cut out of the aft end of the pylon (fig. 8). For each deflection, plastic material was used to fill in all but a 0.06-in. gap in the pylon. The gap allowed hinge moments to be measured without fouling.

Transition Strips

Boundary layer transition strips were applied to the model wing, nacelle, and pylon. The strips were comprised of a 0.1-in. wide band of Carborundum grit set in a plastic adhesive. The grains were sized on the basis of reference 7.

Transition strips of No. 120 grit were located on the inside and outside of the nacelle 0.7 in. aft of the lip. Transition strips of No. 120 grit were also located on both sides of the pylon 0.5 in. aft of the leading edge. The transition strip patterns on the wing are shown in figure 10. The positions of the transition strips on the wing were determined from analyses of oil-flow photographs (ref. 8) of the baseline configuration near its drag-divergence Mach number and cruise lift coefficient. The aft transition strip locations on the wing were used to simulate a higher effective Reynolds number by producing a thinner boundary layer over the aft portion of the wing (ref. 9). The transition strips on the wing in the region of the nacelle were moved forward, since the influence of the nacelle caused the flow transition to occur naturally near the wing leading edge.

Measurements

Force and moment data on the wing and fuselage were obtained with a five-component electrical strain-gage balance. Side force was not measured. An accelerometer attached to the wing mounting block inside the fuselage was used to measure angle of attack. Chordwise static pressures were measured with pressure-scanning valves at seven semispan stations (fig. 3) of the wing. Chordwise locations of the pressure tubes are given in table II. Electrical strain gages were used to measure hinge moments for the inboard and outboard ailerons. Mass flow through the nacelle was not measured; therefore, no internal drag corrections were made.

Test Conditions

Data were taken at the test conditions presented in the following table:

M_∞	α, deg	R_N, per foot	q_∞, lb/ft^2
0.30	-2 to 10	2.5×10^6	176
.60	-2 to 10	4.0	528
.80	-2 to 7	4.0	660
.82	-2 to 7	4.0	671
.84	-2 to 7	4.0	683
.86	-2 to 7	4.0	693
.90	-2 to 7	4.0	714

Throughout the entire test, stagnation temperature was maintained at 120°F, and the air was dried until the dew point was sufficiently low to prevent condensation.

PRESENTATION OF RESULTS

A large quantity of force and pressure data were obtained for the many configurations of this investigation. The data are presented in the figures, as indicated in the following list and table:

Figure

Variation of lift-curve slope with Mach number for the baseline configuration. $C_L = 0.55$ 11

Variation of drag coefficient with Mach number for the baseline configuration. $C_L = 0.55$ 12

Configuration	Figure numbers presenting -								
	C_L vs. α	C_D vs. C_L	C_m vs. C_L	C_l, C_n vs. α	C_{HM_1}, C_{HM_2} vs. α	$C_{l_{\delta\alpha}}$, $C_{n_{\delta\alpha}}$ vs. α	$C_{l_{\delta\alpha}}$, $C_{n_{\delta\alpha}}$ vs. M_∞	C_p vs. x/c	$\frac{C'_n c}{\bar{c}}$ vs. η
Baseline ($\delta\alpha_1 = 0$, $\delta\alpha_2 = 0$)								13-19	
$\delta\alpha_1 = 0, \pm 2.5, \pm 7.5, \pm 12.5$	20	21	22	23	24	25	26	27-33	34-35
$\delta\alpha_2 = 0, \pm 2.5, \pm 7.5, \pm 12.5, \pm 17.5$	36	37	38	39	40	41	42	43-58	59-60

DISCUSSION OF RESULTS

The purpose of this investigation was to determine the effect of aileron deflections on the aerodynamic characteristics of a subsonic energy-efficient transport model. However, the use of a semispan model for this investigation precluded determination of aileron effectiveness in the conventional manner. Normally, aileron effectiveness is determined from simultaneous asymmetric aileron deflections on a full span model. For this investigation, aileron-effectiveness parameters ($C_{l_{\delta a}}$ and $C_{n_{\delta a}}$) for an individual positive or negative deflection on the semispan model were calculated from increments in C_l and C_n from the values for the baseline (undeflected) configuration. Therefore, aileron-effectiveness parameters for equal-magnitude, positive and negative deflections from this investigation must be averaged to simulate the results for a full span model with asymmetric aileron deflections. The aileron-effectiveness parameters presented herein were computed at discrete angles of attack. The increments in rolling- and yawing-moment coefficients used to compute aileron-effectiveness parameters at discrete angles of attack were determined from cubic spline fairings of the rolling- and yawing-moment data.

Baseline Configuration

The flow field around a high-aspect-ratio supercritical transport wing, like the one used in this investigation, changes dramatically with Mach number and angle of attack. Details of the flow field changes have been established since the early 1970's (ref. 10); however, since aileron effectiveness is related to changes in the flow field and the associated boundary layer (refs. 4 and 5), some reiteration of the details is considered necessary to this discussion.

Chordwise pressure distributions for this wing change significantly from subcritical to supercritical Mach numbers. For Mach numbers less than 0.70 (figs. 13 and 14), this wing has "peaky-type" upper surface pressure distributions across most of the span for positive angles of attack. Inboard of approximately $\eta = 0.25$, the wing sections are not typical supercritical airfoils. The airfoils on the inboard portion of the wing were modified by the addition of leading- and trailing-edge extensions (fig. 5) which reduced fuselage interference effects. These airfoils have reduced aft camber, reduced upper surface curvature, and the location of maximum t/c is farther forward than for airfoils outboard of $\eta = 0.25$. Those modifications all help keep the wing isobars swept at the side of the fuselage. Therefore, pressure distributions at $\eta = 0.122$ and $\eta = 0.247$ are not typical of the rest of the wing. For Mach numbers greater than 0.70 (figs. 15 to 19), this wing develops "plateau-type" upper surface pressure distributions on the outboard portion of the wing at positive angles of attack. This local region of supersonic flow terminates in a weak shock wave at lift coefficients near the design value, $C_L = 0.55$. Note that figures 15 to 19 have been plotted with a different scale factor for C_p from that used in figures 13 and 14. The plateau region develops very rapidly with increasing angle of attack, resulting in a nonlinear lift-curve slope. The chordwise extent of the plateau region increases with Mach number until the onset of trailing-edge separation. A comparison of the data at $M_\infty = 0.82$ for $\alpha = 4°$ and $5°$ (figs. 16(d) and 16(e)) at $\eta = 0.500$ shows that trailing-edge separation occurs at $\alpha = 5°$ and forces the shock wave forward approximately $0.05x/c$. Normally the chordwise extent of the plateau region at cruise lift coefficients varies from about 40 to 60 percent of the chord. The variation of lift-curve slope with Mach number (fig. 11) illustrates the increase in lift-curve slope near the design cruise Mach number.

The influence of the nacelle and pylon on the wing pressures is greater at supercritical Mach numbers than at subcritical Mach numbers. The nacelle, which extends aft of the wing leading edge approximately 30 percent of the chord, forms a three-sided converging-diverging channel with the pylon and wing lower surface. Acceleration of the flow through this channel results in more negative pressure coefficients near the leading edge of the wing lower surface than would be expected for a wing without a nacelle and pylon. The local area rule shaping on the pylon (fig. 9) was developed to prevent a shock wave in the throat of the converging-diverging channel at the design cruise conditions, $M_\infty = 0.82$ and $C_L = 0.55$. This lift coefficient corresponds to an angle of attack of approximately 2.75°. Wing pressure data at $M_\infty = 0.82$ and $\alpha = 3°$ (fig. 16(c)) indicate that the shaping was successful in preventing a strong shock from forming near the pylon ($\eta = 0.375$). However, at lower angles of attack (figs. 16(a) and 16(b)), a shock wave is present. The influence of the nacelle also affects the wing upper surface pressures at $\eta = 0.375$. The wing exhibits more of a peaky-type pressure distribution in this area (fig. 16(c)). As previously mentioned, the transition strips in the vicinity of the nacelle were located forward, since flow transition would occur near the leading edge naturally.

For Mach numbers greater than 0.84, the baseline configuration develops trailing-edge separation over much of the span. The separation starts near the portion of the wing with the highest section loads (near a_1) and spreads inboard and outboard from there (figs. 18 and 19). The separation moves forward with increasing angle of attack until it reaches the shock wave.

The variation of drag coefficient with Mach number for $C_L = 0.55$ (fig. 12) indicates a drag-divergence Mach number of 0.825 for this configuration (based on a slope of 0.1). Unpublished data from the Langley 8-Foot Transonic Pressure Tunnel for a full span model with the same wing, but without nacelles, pylons, and ailerons, indicate a drag-divergence Mach number of 0.832. Thus, blockage effects were not large for the semispan model used in this investigation, even though the wing area was twice the wing area for the full span model. A significant amount of drag creep (fig. 12) may be attributable to the flow around and through the nacelle and to interference between the nacelle and wing.

Deflections of Aileron 1

Longitudinal aerodynamic characteristics and wing loads.- The general changes with Mach number in the flow field over this wing with a_1 deflected are reflected in the lift and pitching-moment data (figs. 20 and 22). For subcritical Mach numbers, the chordwise pressure distributions are peaky throughout the positive angle of attack range and the lift curves remain linear up to stall (figs. 20(a) and 20(b)). For supercritical Mach numbers ($M_\infty > 0.7$), the rapid increase in the upper surface supersonic pressure plateau region with angle of attack results in a nonlinear lift curve. The lift-curve slope increases at the angle of attack corresponding to the onset of the pressure plateau region (figs. 20(c) to 20(g)). In general, positive a_1 deflections increased lift coefficient and negative a_1 decreased lift coefficient, as would be expected.

Details of the effect of a_1 deflections on wing loads are shown in the chordwise and spanwise pressure data (figs. 27 to 35). Pressures for most aileron deflections were measured only at the cruise Mach number, $M_\infty = 0.82$, and at $M_\infty = 0.90$, which is near the dive speed for this configuration. At the cruise Mach number, chordwise pressure data (figs. 27 to 31) indicate the influence of a_1 deflections on the wing flow field. Negative a_1 deflections (figs. 27 and 28) strongly influence the upper surface wing pressures. The shock wave which terminates the plateau region on the wing moves forward and the pressure coefficient level of the plateau becomes less negative in the vicinity of a_1 ($\eta = 0.300$ to 0.425). The spanwise load distributions (fig. 34) indicate that in addition to a strong localized effect near a_1, negative deflections cause a major loss of lift across the entire span of the wing. For positive a_1 deflections (figs. 29 to 31), the wing lower surface loads increase slightly over the aft portion of the wing. For a_1 deflections greater than 2.5°, increased upper surface trailing-edge separation occurs and spreads inboard and outboard of a_1. The trailing-edge separation acts like a negative a_1 deflection, in that the plateau is prevented from moving aft and less lift gain is realized than if the flow were completely attached. As expected, the spanwise load distributions (fig. 34) show that equal positive and negative a_1 deflections produce changes in wing loading that are not equal in magnitude (i.e., negative deflections of a_1 are more effective than positive deflections of a_1).

For $M_\infty = 0.90$, chordwise pressure distributions (figs. 32 and 33) indicate trailing-edge separation over much of the wing and most of a_1 for $\delta a_1 = \pm 7.5°$. The large amount of separation results in less influence of a_1 deflections on the wing loading (fig. 35) than was shown at $M_\infty = 0.82$ (fig. 34).

It should be noted that the wing loading inboard of the pylon was slightly higher for the baseline configuration than for some of the configurations with a_1 deflections (figs. 34 and 35) and all of the configurations with a_2 deflections (figs. 59 and 60). This anomaly may have been caused by some outward flexing of the fuselage cover plate at the upper surface wing-fuselage juncture; this flexing broke a portion of the seal between the wing and fuselage and allowed some flow through the gap. Repairs were made after the initial series of runs of the baseline configuration to prevent further cover plate flexing. The anomaly is best illustrated by comparing the chordwise pressure distributions for the baseline configuration and an a_2 deflection configuration (e.g., $\delta a_2 = 2.5°$). Pressure data for the baseline configuration (fig. 16(c)) indicate slightly reduced upper surface loading next to the fuselage ($\eta = 0.122$) at approximately $x/c = 0.4$ and better trailing-edge pressure recovery inboard of the pylon than is shown for the $\delta a_2 = 2.5°$ configuration (fig. 47(c)). The better pressure recovery results in slightly higher upper surface wing loading in the region near the fuselage outboard to the pylon.

The effect of a_1 deflections on pitching-moment data is shown in figure 22. Since the center of pressure of the wing moves aft with the formation of the plateau region, this configuration becomes more stable as Mach number increases. The increments in pitching-moment coefficient with a_1 deflection are generally consistent with an aileron mounted aft of the moment reference center.

Rolling-moment and yawing-moment characteristics.- As would be expected for a semispan model, the rolling-moment data for deflections of a_1 (fig. 23) exhibit variations with Mach number similar to those of the lift data. It also should be noted from figure 23 that the wing-flow-field changes with Mach number have an impact on the yawing-moment data. For subcritical Mach numbers, the leading-edge pressure peaks on the wing at moderate angles of attack (figs. 13 and 14) create enough leading-edge suction to result in negative yawing-moment coefficients. For supercritical Mach numbers, the center of pressure on the wing moves aft and leading-edge suction decreases (figs. 15 to 19). Therefore, the yawing-moment coefficients tend to remain positive throughout the angle of attack range. The effects of individual deflections of a_1 on yawing-moment data are small.

Hinge-moment characteristics.- Measured hinge-moment coefficients for both ailerons are presented in figure 24 for deflections of a_1. Data for a_1 are not available for $\delta a_1 = 0°$; however, these data would be expected to fall between the data for $\delta a_1 = -2.5°$ and $\delta a_1 = 2.5°$. The extensive aft camber of this supercritical wing creates a considerable positive load on the lower surface of the ailerons, even for negative deflections. The hinge moments that result from this aft camber are negative for most of the Mach number and angle of attack test ranges (i.e., a negative hinge moment tends to rotate the trailing edge of the aileron up). The hinge-moment coefficients for a_1 are reasonably linear with angle of attack for $\alpha > 0°$. However, the rate of change of C_{HM_1} with angle of attack becomes much more negative for $M_\infty > 0.82$, because the extent of upper surface separation on a_1 increases rapidly with angle of attack (figs. 32 and 33) and thereby increases the a_1 loading. The effect of deflections of a_1 on the hinge-moment coefficients of a_2 are small.

Aileron effectiveness.- As was shown in references 4 and 5, aileron effectiveness depends on the transition location and growth rate of the boundary layer. The thicker boundary layers on the aft portion of a wing that result from a forward movement of the wing transition strips reduce aileron effectiveness and may be considered an effective reduction in the aileron deflection.

The transition strips over most of the wing of the present investigation were located rearward specifically to simulate a higher effective Reynolds number at cruise Mach numbers (fig. 10). However, the actual boundary layer transition location varied as a result of the previously mentioned changes in chordwise pressure distributions with Mach number for this supercritical wing. The adverse pressure gradient associated with the upper surface pressure peak for subcritical Mach numbers (figs. 13 and 14) causes transition to occur near the wing leading edge instead of at the aft transition strip; therefore, the boundary layer over the aft portion of the wing is thicker. For Mach numbers with supercritical flow (figs. 15 to 19), natural transition (clean wing) on the upper surface would occur at the shock wave which terminates the plateau region. The shock wave moves aft with increasing Mach number, resulting in relatively thin boundary layers (higher effective Reynolds number). At the design cruise Mach number ($M_\infty = 0.82$), the shock wave is located at approximately 40 to 60 percent of the wing chord. The transition strips for this investigation were located ahead of the shock to prevent the formation of a laminar separation bubble at the base of the shock and also to provide a repeatable transition point.

The relatively thin boundary layers associated with the aft movement of the transition point at cruise Mach numbers resulted in greater inboard aileron effectiveness for the configurations of references 4 and 5. It should be noted that the configurations of references 4 and 5 did not have wing-mounted nacelles, while the configuration of this investigation had a nacelle located at $\eta = 0.40$. The transition strips in the vicinity of this nacelle were moved forward (fig. 10), since the wing pressures remained somewhat peaky even at cruise Mach numbers (fig. 16(c)) and flow transition tended to occur near the leading edge naturally. Since a_1 is located downstream of both the nacelle and the forward-transition section of the wing, the effectiveness of a_1 (based on averaged, equal-magnitude, positive and negative deflection data) at cruise conditions did not increase as much (fig. 26) as the inboard aileron effectiveness of references 4 and 5. Nevertheless, near cruise conditions, the data of figures 25 and 26 indicate an increase in lateral control effectiveness for averaged deflection data, which is mainly due to the influence of negative a_1 deflections on both the shock location and the chordwise extent of the upper surface plateau. Aileron effectiveness decreases at about $M_\infty = 0.84$ because of shock-induced boundary layer separation over much of the wing. A small amount of adverse yaw (positive $C_{n_{\delta a}}$) is shown for averaged asymmetric deflections of a_1.

Certain individual a_1 deflections appear to exhibit control reversal (positive $C_{l_{\delta a}}$) for some combinations of Mach number and angle of attack (figs. 25 and 26). For $M_\infty > 0.80$, control reversal is shown for $\delta a_1 = 2.5°$. However, this apparent control reversal is a consequence of the higher inboard loads for the baseline configuration, which, as described previously, were due to a broken seal; probably, no control reversal exists at these conditions. Control reversal for individual deflections is indicated for positive a_1 deflections at $M_\infty = 0.86$ and for all a_1 deflections at $M_\infty = 0.90$. For these conditions, control reversal may be caused by shock-induced flow separation on the wing and interference effects from the nacelle and pylon. Control reversal is also indicated for $\delta a_1 = -2.5°$ at $M_\infty = 0.30$ and $\alpha < 1°$. This anomaly is not understood and is difficult to explain in the absence of wing pressure distributions at these conditions.

Despite any apparent control reversal for individual aileron deflections, when data for equal-magnitude, positive and negative a_1 deflections are averaged (to simulate a full span configuration with asymmetric control deflection), control reversal generally does not occur. The only actual instance of a_1 control reversal occurs for $\delta a_1 = \pm 2.5°$ at $M_\infty = 0.90$ and $0° < \alpha < 2°$.

Deflections of Aileron 2

Most currently flying transport aircraft have their outboard ailerons locked out at high subsonic speeds; however, future transport aircraft may use outboard ailerons for gust load alleviation. For this reason, a full range of outboard aileron deflections was tested on this model over the same Mach number range as the inboard aileron, from $M_\infty = 0.30$ to 0.90. Again, pressures were measured only at the cruise Mach number, $M_\infty = 0.82$, and at $M_\infty = 0.90$.

Longitudinal aerodynamic characteristics and wing loads.- The lift and pitching-moment data for deflections of a_2 (figs. 36 and 38) also reflect the changes in the wing flow field with Mach number that were discussed for deflections of a_1. Chordwise pressures at the cruise Mach number indicate variations with deflections of a_2 (figs. 43 to 50) similar to those shown for deflections of a_1. However the outboard portion of the wing is not loaded as highly, and the pressures on a_2 are not influenced strongly by the nacelle and pylon. Also, spanwise load data for this model indicate that changes in the wing loading (at a given angle of attack) due to deflections of a_1 (figs. 34 and 35) extend across most of the span, whereas changes in wing loading due to deflections of a_2 (figs. 59 and 60) are not significant inboard of $\eta = 0.69$. Therefore, individual deflections of a_2 produce smaller increments in lift than comparable deflections of a_1. Pressure data at $M_\infty = 0.82$ for positive a_2 deflections equal to or greater than 12.5° (figs. 49 and 50) indicate upper surface trailing-edge separation in the vicinity of a_2 ($\eta = 0.792$ to 0.972) for all positive angles of attack. A similar effect was shown for a_1 at a much lower deflection angle. This difference is caused by the lower wing loading near a_2, which is a function of twist (washout).

For $M_\infty = 0.90$, chordwise pressure distributions (figs. 51 to 58) indicate trailing-edge separation over much of the wing, which decreases the effectiveness of a_2. Deflections of a_2 again influence spanwise load distributions at

$M_\infty = 0.90$ (fig. 60) less than at $M_\infty = 0.82$ (fig. 59). Note that since a_2 is located farther aft of the moment reference center than a_1, a_2 deflections influence pitching moment (fig. 38) more than a_1 deflections do (fig. 22).

Rolling-moment and yawing-moment characteristics.- The rolling-moment and yawing-moment data for deflections of a_2 (fig. 39) exhibit very similar variations with Mach number and angle of attack as the data for deflections of a_1 (fig. 23). Note that for Mach numbers greater than 0.60, both the lift and rolling-moment data for $\delta a_2 = 2.5°$ appear to indicate aeroelastic deformation of the wing (i.e., less lift and a less negative rolling-moment coefficient at some angles of attack than for the baseline configuration). However, this effect is a consequence of the higher loads inboard for the baseline configuration, which, as discussed earlier, were due to a broken seal.

Hinge-moment characteristics.- The hinge-moment data for deflections of a_2 (fig. 40) indicate a fairly constant variation of C_{HM_2} with angle of attack for $M_\infty < 0.90$. For $M_\infty = 0.90$, however, the loading and hinge moments on a_2 increase significantly with angle of attack because of upper surface separation (especially for positive deflections). This change in hinge-moment characteristics for a_2 is delayed to a higher Mach number than was shown for a_1 (fig. 24), because a_2 is not loaded as highly as a_1.

The data for a_2 also indicate a more negative hinge-moment coefficient for $\delta a_2 = -2.5°$ than for the baseline configuration. A comparison of the chordwise pressures at $M_\infty = 0.82$ and $\alpha = 3°$ (figs. 16(c) and 43(c)) indicates that the upper surface pressures on the portion of a_2 that is ahead of the hinge line ($0.750 < x/c < 0.775$) are slightly less negative for $\delta a_2 = -2.5°$ than for $\delta a_2 = 0°$. The pressures on the rest of a_2 are nearly equal for both configurations. Thus, the slight loss of lift on the leading edge of a_2 for $\delta a_2 = -2.5°$ results in more negative hinge moments. The effect of deflections of a_2 on the hinge-moment coefficients of a_1 are small.

Aileron effectiveness.- The effectiveness of individual positive and negative deflections of a_2 is shown in figures 41 and 42. On the basis of averaged, positive and negative deflection data, the lateral control effectiveness of a_2 increases slightly with Mach number near $M_\infty = 0.82$ for small deflections ($\delta a_2 = \pm 2.5°$ and $\pm 7.5°$). For larger deflections, the effectiveness of a_2 remains nearly constant with Mach number. The effectiveness of a_2 for smaller deflections does not increase as much as the effectiveness of a_1 at cruise Mach numbers, since the wing loads are lower at the tip and the influence of a_2 deflections is felt over a smaller portion of the span. As was shown for a_1 (fig. 26), the effectiveness of a_2 decreases at about $M_\infty = 0.84$ because of shock-induced boundary layer separation over much of the wing. Again, a small amount of adverse yaw is shown for asymmetric aileron deflections.

Control reversal is indicated for certain individual a_2 deflections at Mach numbers of 0.30, 0.80, 0.84, and 0.90 (figs. 41 and 42). However, based on averaged asymmetric a_2 deflection data, control reversal does not occur over the range of conditions tested.

SUMMARY OF RESULTS

An investigation to determine the effect of aileron deflections on the aerodynamic characteristics of a subsonic energy-efficient transport model with an aspect-ratio-10 supercritical wing was conducted in the Langley 8-Foot Transonic Pressure Tunnel. Significant results of this investigation are summarized as follows:

1. On the basis of averaged, equal-magnitude, positive and negative deflection data for the inboard aileron (a_1) on this semispan model, positive aileron effectiveness was indicated for all test conditions except for a_1 deflections of ±2.5° at a Mach number (M_∞) of 0.90 and angles of attack from approximately 0° to 2°. Control reversal at these conditions may be caused by shock-induced flow separation on the wing and interference effects from the nacelle and pylon.

2. On the basis of averaged, equal-magnitude, positive and negative deflection data for the outboard aileron (a_2), positive aileron effectiveness was indicated for all test conditions.

3. The effectiveness of a_1 increased near $M_\infty = 0.82$, mainly because of the strong influence of negative a_1 deflections on shock location and the chordwise extent of the upper surface pressure plateau.

4. The effectiveness of a_2 increased only slightly near $M_\infty = 0.82$, since a_2 was not loaded as highly as a_1.

5. The effectiveness of both a_1 and a_2 decreased at about $M_\infty = 0.84$ because of shock-induced boundary layer separation over much of the wing.

6. The extensive aft camber of this supercritical wing resulted in negative hinge moments for most deflections of a_1 and a_2.

NASA Langley Research Center
Hampton, VA 23665
May 21, 1985

REFERENCES

1. Bartlett, Dennis W.: Wind-Tunnel Investigation of Several High Aspect-Ratio Supercritical Wing Configurations on a Wide-Body-Type Fuselage. NASA TM X-71996, 1977.

2. Bartlett, Dennis W.; and Patterson, James C., Jr.: NASA Supercritical-Wing Technology. NASA TM-78731, 1978.

3. Jacobs, Peter F.: Experimental Trim Drag Values and Flow-Field Measurements for a Wide-Body Transport Model With Conventional and Supercritical Wings. NASA TP-2071, 1982.

4. Jacobs, Peter F.: Aileron Effectiveness for a Subsonic Transport Model With a High-Aspect-Ratio Supercritical Wing. NASA TM-85674, 1983.

5. Anglin, Ernie L.; and Byrdsong, Thomas A.: Wing Flap-Type Control Effectiveness and Effects of Control Hinge Gap Seals for a Supercritical Wing. AIAA-82-0960, June 1982.

6. Schaefer, William T., Jr.: Characteristics of Major Active Wind Tunnels at the Langley Research Center. NASA TM X-1130, 1965.

7. Braslow, Albert L.; and Knox, Eugene C.: Simplified Method for Determination of Critical Height of Distributed Roughness Particles for Boundary-Layer Transition at Mach Numbers from 0 to 5. NACA TN 4363, 1958.

8. Loving, Donald L.; and Katzoff, Samuel: The Fluorescent-Oil Film Method and Other Techniques for Boundary-Layer Flow Visualization. NASA MEMO 3-17-59L, 1959.

9. Blackwell, James A., Jr.: Preliminary Study of Effects of Reynolds Number and Boundary-Layer Transition Location on Shock-Induced Separation. NASA TN D-5003, 1969.

10. Whitcomb, Richard T.: Review of NASA Supercritical Airfoils. ICAS Paper No. 74-10, Aug. 1974.

TABLE I.- WING AIRFOIL COORDINATES

(a) $\eta = 0.123$

x/c	z/c		x/c	z/c	
	U.S.	L.S.		U.S.	L.S.
0.000	0.0000	0.0000	0.496	0.0387	-0.0862
.002	.0112	-.0066	.506	.0374	-.0857
.005	.0160	-.0128	.516	.0361	-.0852
.010	.0214	-.0194	.526	.0347	-.0846
.020	.0286	-.0273	.536	.0333	-.0840
.030	.0337	-.0325	.546	.0319	-.0833
.040	.0374	-.0366	.556	.0306	-.0825
.050	.0406	-.0401	.566	.0292	-.0817
.060	.0436	-.0431	.576	.0278	-.0808
.069	.0461	-.0461	.586	.0264	-.0799
.079	.0484	-.0488	.595	.0250	-.0789
.089	.0503	-.0515	.605	.0236	-.0779
.099	.0520	-.0540	.615	.0222	-.0768
.109	.0535	-.0563	.625	.0208	-.0757
.119	.0547	-.0586	.635	.0193	-.0745
.129	.0559	-.0607	.645	.0179	-.0733
.139	.0569	-.0628	.655	.0165	-.0720
.149	.0577	-.0647	.665	.0151	-.0707
.159	.0584	-.0666	.675	.0137	-.0693
.169	.0591	-.0684	.685	.0123	-.0678
.179	.0596	-.0701	.695	.0109	-.0664
.189	.0600	-.0718	.705	.0095	-.0648
.198	.0603	-.0733	.715	.0081	-.0633
.208	.0605	-.0747	.725	.0067	-.0617
.218	.0607	-.0760	.734	.0052	-.0601
.228	.0607	-.0773	.744	.0038	-.0584
.238	.0607	-.0784	.754	.0024	-.0568
.248	.0606	-.0795	.764	.0009	-.0552
.258	.0605	-.0806	.774	-.0006	-.0535
.268	.0602	-.0815	.784	-.0020	-.0519
.278	.0599	-.0824	.794	-.0035	-.0503
.288	.0595	-.0832	.804	-.0051	-.0487
.298	.0591	-.0840	.814	-.0066	-.0473
.308	.0586	-.0846	.824	-.0081	-.0458
.318	.0579	-.0853	.834	-.0097	-.0445
.328	.0573	-.0859	.844	-.0112	-.0432
.337	.0565	-.0864	.854	-.0128	-.0421
.347	.0557	-.0868	.863	-.0144	-.0410
.357	.0549	-.0871	.873	-.0160	-.0401
.367	.0540	-.0875	.883	-.0176	-.0393
.377	.0530	-.0877	.893	-.0192	-.0387
.387	.0520	-.0879	.903	-.0209	-.0382
.397	.0510	-.0880	.913	-.0225	-.0380
.407	.0499	-.0881	.923	-.0242	-.0378
.417	.0487	-.0881	.933	-.0259	-.0379
.427	.0476	-.0881	.943	-.0276	-.0382
.437	.0464	-.0879	.953	-.0294	-.0385
.447	.0452	-.0878	.963	-.0311	-.0392
.457	.0439	-.0876	.973	-.0329	-.0401
.466	.0426	-.0873	.983	-.0347	-.0412
.476	.0414	-.0870	.992	-.0365	-.0426
.486	.0401	-.0866	1.000	-.0378	-.0439

TABLE I.- Continued

(b) η = 0.189

x/c	z/c U.S.	z/c L.S.	x/c	z/c U.S.	z/c L.S.
0.000	-0.0005	-0.0005	0.496	0.0409	-0.0781
.002	.0094	-.0104	.506	.0399	-.0775
.005	.0151	-.0158	.516	.0389	-.0769
.010	.0208	-.0215	.526	.0379	-.0763
.020	.0279	-.0285	.536	.0368	-.0755
.030	.0323	-.0333	.546	.0357	-.0747
.040	.0356	-.0371	.556	.0346	-.0739
.050	.0384	-.0403	.566	.0335	-.0730
.060	.0409	-.0433	.575	.0323	-.0721
.069	.0431	-.0460	.585	.0311	-.0711
.079	.0450	-.0487	.595	.0299	-.0701
.089	.0468	-.0512	.605	.0287	-.0690
.099	.0483	-.0536	.615	.0275	-.0678
.109	.0497	-.0558	.625	.0262	-.0666
.119	.0509	-.0579	.635	.0249	-.0654
.129	.0520	-.0599	.645	.0236	-.0641
.139	.0529	-.0618	.655	.0223	-.0628
.149	.0537	-.0636	.665	.0210	-.0615
.159	.0544	-.0653	.675	.0197	-.0601
.169	.0550	-.0669	.685	.0183	-.0587
.179	.0554	-.0684	.695	.0170	-.0572
.189	.0558	-.0698	.704	.0156	-.0558
.198	.0561	-.0711	.714	.0142	-.0543
.208	.0564	-.0724	.724	.0128	-.0528
.218	.0565	-.0735	.734	.0113	-.0512
.228	.0566	-.0746	.744	.0099	-.0497
.238	.0567	-.0756	.754	.0084	-.0481
.248	.0566	-.0764	.764	.0069	-.0466
.258	.0565	-.0773	.774	.0054	-.0450
.268	.0564	-.0781	.784	.0039	-.0435
.278	.0562	-.0788	.794	.0024	-.0420
.288	.0559	-.0794	.804	.0008	-.0406
.298	.0556	-.0799	.814	-.0008	-.0392
.308	.0552	-.0804	.824	-.0024	-.0379
.318	.0548	-.0808	.833	-.0040	-.0366
.327	.0543	-.0811	.843	-.0056	-.0355
.337	.0538	-.0814	.853	-.0072	-.0344
.347	.0533	-.0816	.863	-.0089	-.0334
.357	.0527	-.0817	.873	-.0106	-.0326
.367	.0520	-.0817	.883	-.0123	-.0319
.377	.0514	-.0817	.893	-.0140	-.0314
.387	.0506	-.0816	.903	-.0157	-.0311
.397	.0499	-.0816	.913	-.0174	-.0310
.407	.0491	-.0814	.923	-.0192	-.0311
.417	.0483	-.0812	.933	-.0210	-.0314
.427	.0475	-.0809	.943	-.0228	-.0319
.437	.0466	-.0807	.953	-.0247	-.0326
.446	.0457	-.0803	.962	-.0266	-.0335
.456	.0448	-.0800	.972	-.0284	-.0346
.466	.0439	-.0796	.982	-.0304	-.0360
.476	.0429	-.0792	.992	-.0323	-.0376
.486	.0419	-.0787	1.000	-.0338	-.0389

TABLE I.- Continued

(c) $\eta = 0.255$

x/c	z/c		x/c	z/c	
	U.S.	L.S.		U.S.	L.S.
0.000	-0.0014	-0.0014	0.500	0.0444	-0.0692
.002	.0082	-.0013	.510	.0436	-.0685
.005	.0135	-.0167	.520	.0428	-.0678
.010	.0193	-.0220	.530	.0420	-.0670
.020	.0264	-.0289	.540	.0411	-.0661
.030	.0309	-.0336	.550	.0402	-.0652
.040	.0341	-.0373	.560	.0393	-.0642
.050	.0367	-.0404	.570	.0383	-.0632
.060	.0389	-.0431	.580	.0373	-.0621
.070	.0410	-.0455	.590	.0363	-.0610
.080	.0427	-.0478	.600	.0352	-.0598
.090	.0443	-.0499	.610	.0341	-.0586
.100	.0456	-.0519	.620	.0330	-.0573
.110	.0467	-.0537	.630	.0319	-.0560
.120	.0477	-.0554	.640	.0307	-.0547
.130	.0486	-.0570	.650	.0295	-.0533
.140	.0493	-.0584	.660	.0283	-.0519
.150	.0500	-.0597	.670	.0270	-.0504
.160	.0505	-.0610	.680	.0258	-.0489
.170	.0511	-.0622	.690	.0245	-.0473
.180	.0515	-.0633	.700	.0233	-.0458
.190	.0519	-.0643	.710	.0219	-.0442
.200	.0522	-.0653	.720	.0206	-.0426
.210	.0525	-.0662	.730	.0192	-.0410
.220	.0528	-.0670	.740	.0178	-.0394
.230	.0529	-.0678	.750	.0164	-.0379
.240	.0531	-.0685	.760	.0150	-.0363
.250	.0531	-.0692	.770	.0135	-.0348
.260	.0532	-.0697	.780	.0121	-.0333
.270	.0532	-.0703	.790	.0106	-.0318
.280	.0531	-.0707	.800	.0091	-.0304
.290	.0531	-.0712	.810	.0075	-.0291
.300	.0530	-.0715	.820	.0059	-.0279
.310	.0529	-.0718	.830	.0043	-.0267
.320	.0528	-.0721	.840	.0028	-.0257
.330	.0526	-.0723	.850	.0011	-.0248
.340	.0524	-.0725	.860	-.0005	-.0240
.350	.0522	-.0726	.870	-.0022	-.0234
.360	.0519	-.0727	.880	-.0038	-.0229
.370	.0516	-.0727	.890	-.0055	-.0226
.380	.0512	-.0727	.900	-.0073	-.0225
.390	.0508	-.0727	.910	-.0090	-.0225
.400	.0504	-.0726	.920	-.0108	-.0227
.410	.0499	-.0724	.930	-.0125	-.0231
.420	.0494	-.0723	.940	-.0143	-.0236
.430	.0489	-.0721	.950	-.0161	-.0243
.440	.0484	-.0718	.960	-.0179	-.0253
.450	.0478	-.0715	.970	-.0197	-.0264
.460	.0472	-.0711	.980	-.0216	-.0277
.470	.0465	-.0708	.990	-.0234	-.0292
.480	.0458	-.0703	1.000	-.0253	-.0308
.490	.0451	-.0698			

TABLE I.- Continued

(d) η = 0.301

x/c	z/c		x/c	z/c	
	U.S.	L.S.		U.S.	L.S.
0.000	-0.0026	-0.0026	0.494	0.0476	-0.0681
.002	.0068	-.0120	.504	.0470	-.0674
.005	.0121	-.0171	.514	.0463	-.0667
.010	.0177	-.0223	.524	.0457	-.0658
.020	.0249	-.0290	.534	.0450	-.0649
.030	.0295	-.0337	.543	.0443	-.0640
.040	.0328	-.0374	.553	.0435	-.0629
.049	.0354	-.0405	.563	.0427	-.0618
.059	.0375	-.0432	.573	.0419	-.0606
.069	.0393	-.0455	.583	.0410	-.0593
.079	.0408	-.0476	.593	.0402	-.0579
.089	.0422	-.0496	.603	.0392	-.0565
.099	.0435	-.0514	.613	.0383	-.0551
.109	.0446	-.0531	.623	.0374	-.0536
.119	.0457	-.0547	.632	.0364	-.0521
.128	.0466	-.0562	.642	.0354	-.0505
.138	.0474	-.0576	.652	.0343	-.0488
.148	.0482	-.0589	.662	.0332	-.0472
.158	.0489	-.0601	.672	.0321	-.0455
.168	.0496	-.0612	.682	.0309	-.0437
.178	.0502	-.0622	.692	.0297	-.0420
.188	.0507	-.0631	.702	.0285	-.0402
.198	.0512	-.0640	.711	.0272	-.0385
.208	.0516	-.0648	.721	.0259	-.0367
.217	.0520	-.0656	.731	.0246	-.0350
.227	.0523	-.0662	.741	.0232	-.0333
.237	.0526	-.0668	.751	.0218	-.0317
.247	.0528	-.0674	.761	.0204	-.0301
.257	.0530	-.0679	.771	.0189	-.0285
.267	.0532	-.0685	.781	.0174	-.0270
.277	.0533	-.0689	.790	.0159	-.0256
.287	.0534	-.0694	.800	.0144	-.0242
.296	.0535	-.0697	.810	.0129	-.0229
.306	.0535	-.0700	.820	.0113	-.0218
.316	.0535	-.0703	.830	.0097	-.0207
.326	.0534	-.0706	.840	.0080	-.0198
.336	.0533	-.0708	.850	.0064	-.0190
.346	.0531	-.0710	.860	.0047	-.0183
.356	.0530	-.0712	.870	.0029	-.0178
.366	.0528	-.0713	.879	.0012	-.0174
.375	.0526	-.0713	.889	-.0006	-.0172
.385	.0523	-.0714	.899	-.0023	-.0171
.395	.0521	-.0713	.909	-.0041	-.0172
.405	.0518	-.0713	.919	-.0060	-.0175
.415	.0515	-.0712	.929	-.0078	-.0179
.425	.0511	-.0710	.939	-.0097	-.0186
.435	.0507	-.0708	.949	-.0115	-.0194
.445	.0502	-.0705	.958	-.0134	-.0204
.455	.0498	-.0701	.968	-.0154	-.0215
.464	.0493	-.0697	.978	-.0173	-.0229
.474	.0487	-.0693	.988	-.0193	-.0245
.484	.0482	-.0687	1.000	-.0218	-.0267

TABLE I.- Continued

(e) η = 0.377

x/c	z/c		x/c	z/c	
	U.S.	L.S.		U.S.	L.S.
0.000	-0.0048	-0.0048	0.490	0.0547	-0.0651
.002	.0045	-.0119	.500	.0544	-.0644
.005	.0094	-.0171	.510	.0540	-.0636
.010	.0148	-.0225	.520	.0535	-.0628
.020	.0217	-.0295	.540	.0526	-.0619
.030	.0265	-.0341	.550	.0521	-.0609
.040	.0299	-.0378	.560	.0515	-.0599
.050	.0328	-.0408	.570	.0509	-.0587
.060	.0351	-.0435	.580	.0503	-.0575
.070	.0372	-.0458	.590	.0497	-.0562
.080	.0389	-.0479	.600	.0490	-.0548
.090	.0406	-.0498	.610	.0483	-.0534
.100	.0420	-.0516	.620	.0475	-.0519
.110	.0433	-.0531	.630	.0468	-.0503
.120	.0446	-.0546	.640	.0460	-.0487
.130	.0457	-.0560	.650	.0451	-.0470
.140	.0468	-.0573	.660	.0443	-.0453
.150	.0478	-.0585	.670	.0434	-.0435
.160	.0487	-.0596	.680	.0425	-.0417
.170	.0496	-.0606	.690	.0415	-.0399
.180	.0504	-.0616	.700	.0405	-.0381
.190	.0512	-.0625	.710	.0395	-.0363
.200	.0518	-.0633	.720	.0384	-.0345
.210	.0525	-.0641	.730	.0373	-.0327
.220	.0530	-.0648	.740	.0361	-.0309
.230	.0536	-.0654	.750	.0349	-.0290
.240	.0541	-.0660	.760	.0337	-.0273
.250	.0545	-.0665	.770	.0324	-.0255
.260	.0549	-.0670	.780	.0311	-.0238
.270	.0553	-.0674	.790	.0297	-.0222
.280	.0556	-.0678	.800	.0283	-.0206
.290	.0559	-.0681	.810	.0269	-.0190
.300	.0562	-.0684	.820	.0254	-.0175
.310	.0564	-.0686	.830	.0239	-.0162
.320	.0566	-.0688	.840	.0223	-.0149
.330	.0567	-.0690	.850	.0207	-.0137
.340	.0568	-.0691	.860	.0191	-.0126
.350	.0569	-.0692	.870	.0173	-.0116
.360	.0569	-.0692	.880	.0156	-.0108
.370	.0569	-.0692	.890	.0138	-.0101
.380	.0569	-.0691	.900	.0120	-.0096
.390	.0569	-.0690	.910	.0101	-.0092
.400	.0568	-.0689	.920	.0082	-.0089
.410	.0567	-.0687	.930	.0062	-.0089
.420	.0566	-.0684	.940	.0042	-.0091
.430	.0564	-.0681	.950	.0021	-.0096
.440	.0562	-.0678	.960	-.0000	-.0102
.450	.0559	-.0673	.970	-.0022	-.0111
.460	.0557	-.0668	.980	-.0045	-.0122
.470	.0554	-.0663	.990	-.0068	-.0137
.480	.0551	-.0657	1.000	-.0092	-.0154

TABLE I.- Continued

(f) η = 0.426

x/c	z/c		x/c	z/c	
	U.S.	L.S.		U.S.	L.S.
0.000	-0.0035	-0.0035	0.500	0.0560	-0.0566
.002	.0040	-.0128	.510	.0557	-.0558
.005	.0087	-.0179	.520	.0555	-.0550
.010	.0136	-.0229	.530	.0552	-.0540
.020	.0203	-.0289	.540	.0549	-.0530
.030	.0248	-.0328	.550	.0545	-.0519
.040	.0282	-.0360	.560	.0542	-.0507
.050	.0310	-.0386	.570	.0538	-.0494
.060	.0333	-.0409	.580	.0533	-.0480
.070	.0353	-.0429	.589	.0528	-.0465
.080	.0371	-.0447	.599	.0523	-.0449
.090	.0386	-.0463	.609	.0518	-.0433
.100	.0401	-.0478	.619	.0512	-.0417
.110	.0414	-.0491	.629	.0506	-.0400
.120	.0426	-.0503	.639	.0499	-.0383
.130	.0438	-.0514	.649	.0492	-.0366
.140	.0449	-.0524	.659	.0485	-.0349
.150	.0459	-.0534	.669	.0478	-.0332
.160	.0468	-.0544	.679	.0470	-.0314
.170	.0477	-.0552	.689	.0462	-.0297
.180	.0485	-.0560	.699	.0453	-.0279
.190	.0493	-.0567	.709	.0444	-.0262
.200	.0501	-.0574	.719	.0435	-.0245
.210	.0507	-.0580	.729	.0425	-.0228
.220	.0514	-.0585	.739	.0415	-.0212
.230	.0520	-.0590	.749	.0405	-.0196
.240	.0525	-.0594	.759	.0394	-.0179
.250	.0530	-.0599	.769	.0382	-.0164
.260	.0535	-.0603	.779	.0370	-.0148
.270	.0539	-.0606	.789	.0358	-.0134
.280	.0543	-.0609	.799	.0344	-.0120
.290	.0547	-.0612	.809	.0331	-.0107
.300	.0550	-.0614	.819	.0316	-.0094
.310	.0553	-.0616	.829	.0301	-.0082
.320	.0556	-.0617	.839	.0286	-.0071
.330	.0558	-.0618	.849	.0270	-.0061
.340	.0561	-.0619	.859	.0253	-.0052
.350	.0563	-.0619	.869	.0236	-.0045
.360	.0564	-.0619	.879	.0218	-.0039
.370	.0566	-.0618	.889	.0199	-.0034
.380	.0567	-.0616	.899	.0179	-.0031
.390	.0568	-.0614	.909	.0159	-.0030
.400	.0568	-.0612	.919	.0138	-.0030
.410	.0568	-.0610	.929	.0117	-.0033
.420	.0569	-.0607	.939	.0094	-.0038
.430	.0569	-.0603	.949	.0071	-.0046
.440	.0568	-.0599	.959	.0047	-.0057
.450	.0568	-.0595	.969	.0022	-.0069
.460	.0567	-.0591	.979	-.0004	-.0085
.470	.0565	-.0586	.989	-.0030	-.0105
.480	.0564	-.0580	.999	-.0058	-.0127
.490	.0562	-.0573	1.000	-.0060	.0000

TABLE I.- Concluded

(g) η = 0.965

x/c	z/c		x/c	z/c	
	U.S.	L.S.		U.S.	L.S.
0.000	-0.0122	-0.0114	0.498	0.0508	-0.0511
.002	-.0040	-.0195	.508	.0508	-.0501
.005	.0004	-.0243	.518	.0507	-.0492
.010	.0047	-.0290	.528	.0507	-.0481
.020	.0101	-.0343	.538	.0505	-.0470
.030	.0140	-.0378	.548	.0504	-.0458
.040	.0170	-.0404	.558	.0502	-.0446
.050	.0195	-.0425	.568	.0500	-.0433
.060	.0217	-.0444	.578	.0498	-.0419
.069	.0237	-.0460	.588	.0496	-.0405
.079	.0256	-.0475	.598	.0493	-.0391
.089	.0272	-.0489	.608	.0490	-.0375
.099	.0288	-.0501	.618	.0486	-.0360
.109	.0303	-.0512	.628	.0483	-.0344
.119	.0316	-.0522	.638	.0479	-.0327
.129	.0329	-.0531	.648	.0474	-.0311
.139	.0342	-.0539	.658	.0470	-.0293
.149	.0353	-.0547	.668	.0465	-.0276
.159	.0363	-.0553	.678	.0459	-.0258
.169	.0373	-.0559	.688	.0454	-.0240
.179	.0383	-.0564	.698	.0448	-.0222
.189	.0392	-.0569	.708	.0441	-.0204
.199	.0401	-.0573	.718	.0435	-.0187
.209	.0409	-.0577	.728	.0427	-.0169
.218	.0417	-.0580	.738	.0420	-.0151
.228	.0424	-.0583	.748	.0412	-.0133
.238	.0431	-.0585	.758	.0403	-.0116
.248	.0438	-.0587	.768	.0395	-.0099
.258	.0444	-.0588	.778	.0385	-.0082
.268	.0450	-.0589	.789	.0376	-.0066
.278	.0455	-.0590	.799	.0365	-.0050
.288	.0461	-.0591	.809	.0355	-.0035
.298	.0466	-.0591	.819	.0343	-.0021
.308	.0470	-.0591	.829	.0331	-.0007
.318	.0475	-.0591	.839	.0319	.0005
.328	.0478	-.0590	.849	.0306	.0016
.338	.0482	-.0589	.859	.0293	.0026
.348	.0485	-.0587	.869	.0278	.0035
.358	.0489	-.0585	.879	.0263	.0043
.368	.0491	-.0583	.889	.0247	.0049
.378	.0494	-.0581	.899	.0231	.0053
.388	.0497	-.0578	.909	.0214	.0055
.398	.0499	-.0574	.919	.0196	.0055
.408	.0501	-.0570	.929	.0177	.0053
.418	.0503	-.0566	.939	.0157	.0049
.428	.0505	-.0561	.950	.0136	.0041
.438	.0506	-.0555	.960	.0113	.0031
.448	.0507	-.0549	.970	.0089	.0018
.458	.0508	-.0543	.980	.0064	.0000
.468	.0508	-.0535	.990	.0037	-.0020
.478	.0508	-.0528	1.000	.0009	-.0044
.488	.0509	-.0519			

TABLE II.- NOMINAL WING CHORDWISE PRESSURE-TUBE LOCATIONS

x/c	
U.S.	L.S.
0.025	0.025
.075	.075
.125	.125
.200	.200
.300	.300
.400	.400
.450	.500
.500	.600
.550	.700
.600	.800
.650	.840
.700	.880
.800	.920
.850	.980
.900	
.950	
1.000	

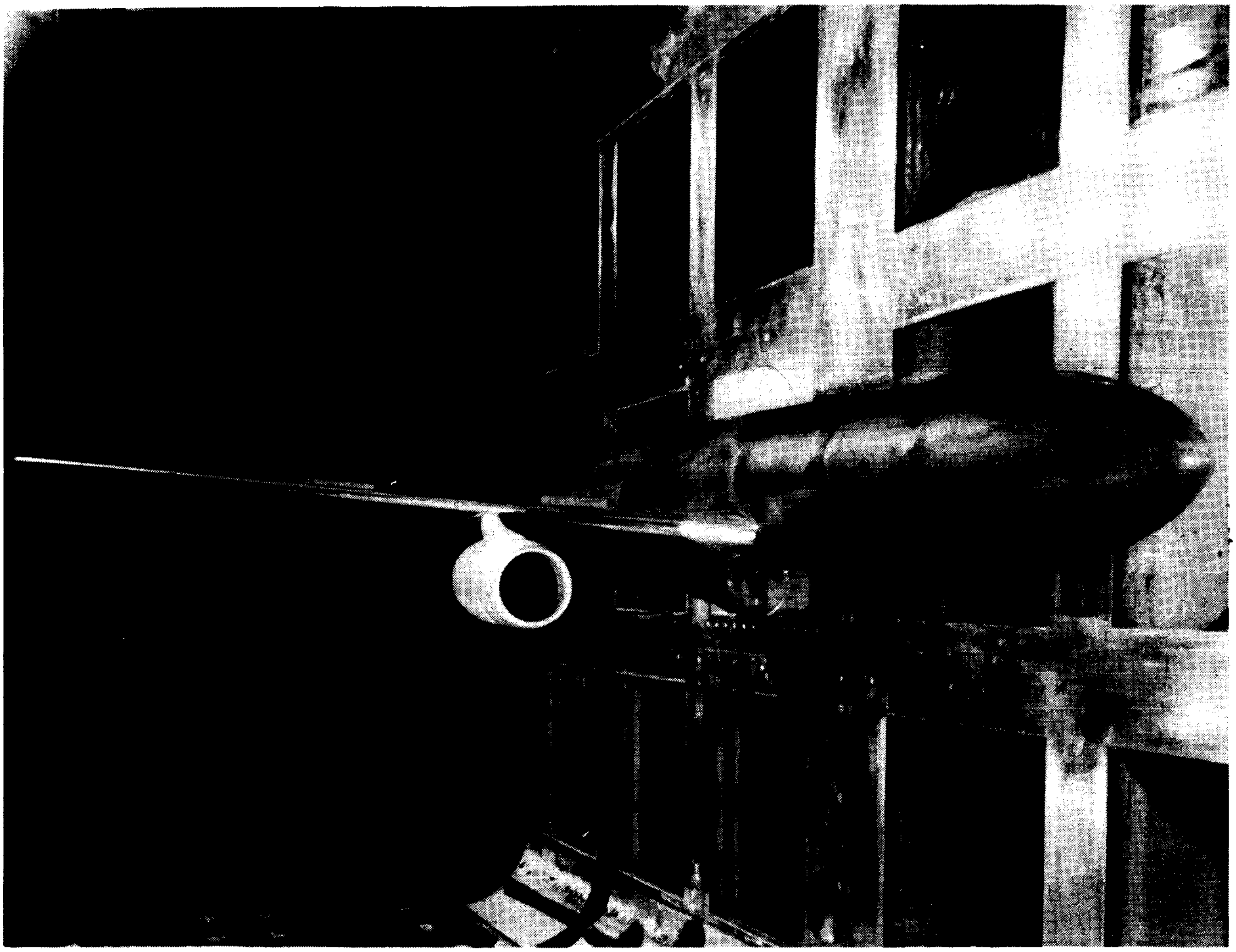

L-80-7973

Figure 1.- Semispan model in the Langley 8-Foot Transonic Pressure Tunnel.

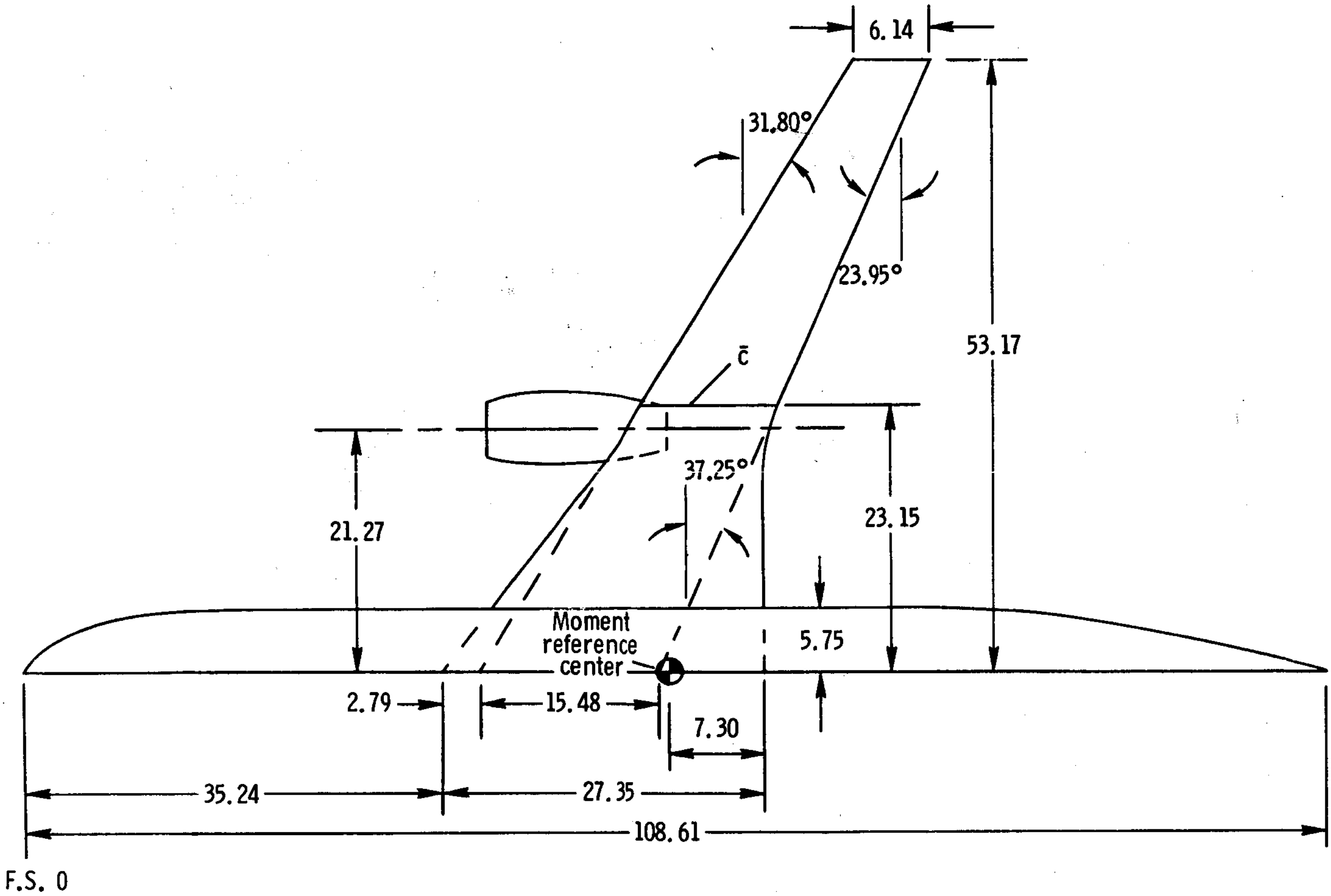

Figure 2.- Drawing of model. (Linear dimensions are in inches.)

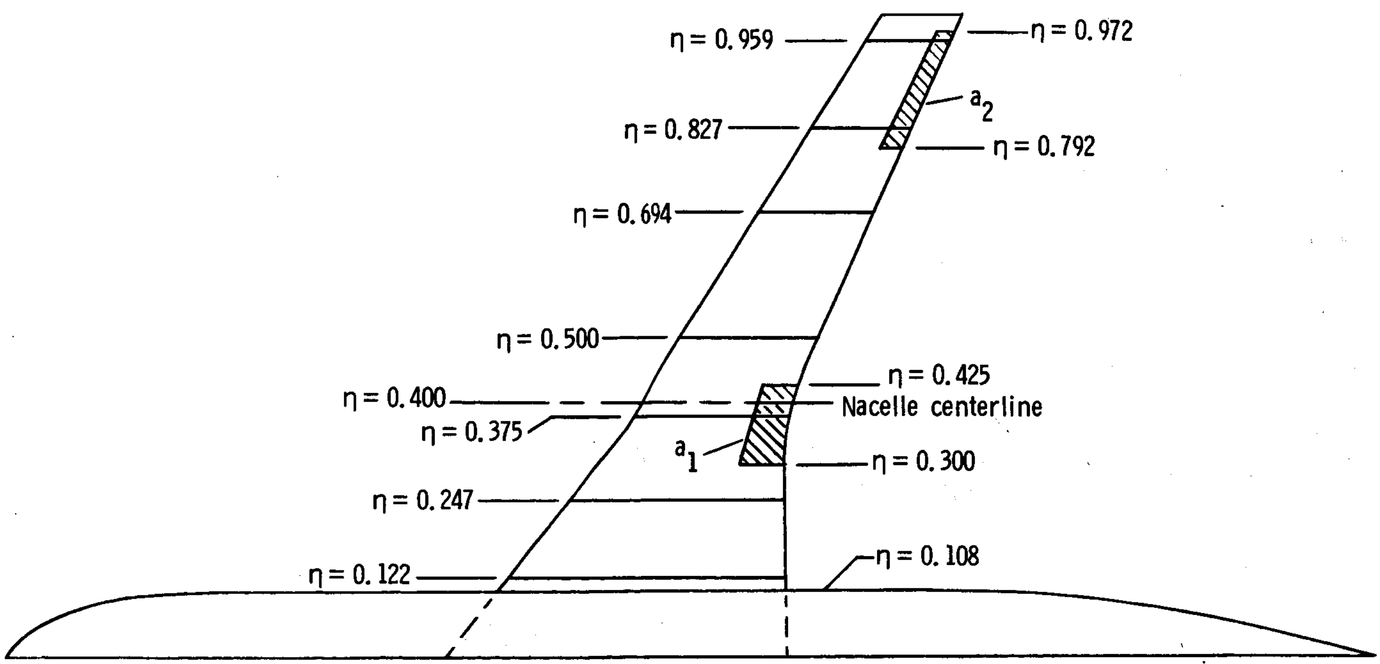

Figure 3.- Locations of ailerons and pressure orifice rows.

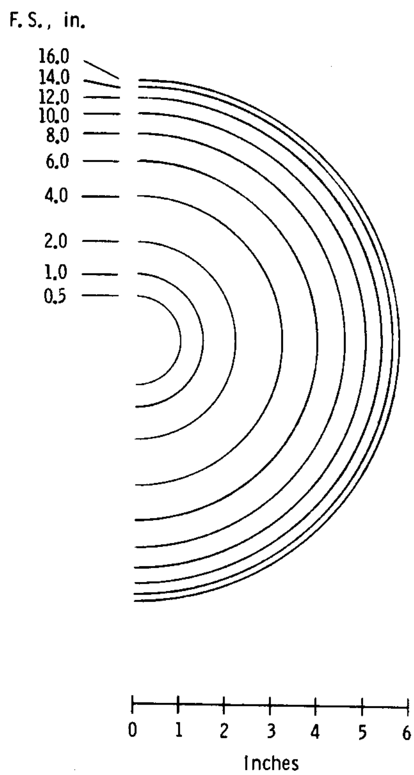

Figure 4.- Fuselage cross sections.

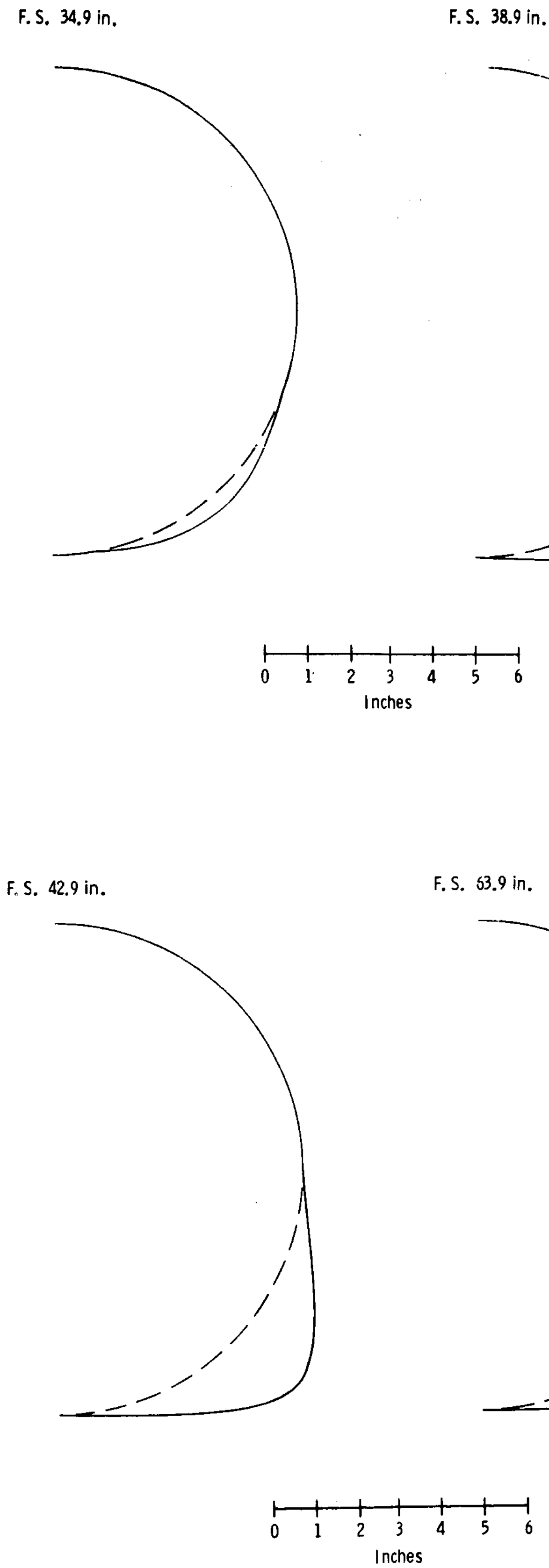

Figure 4.- Continued.

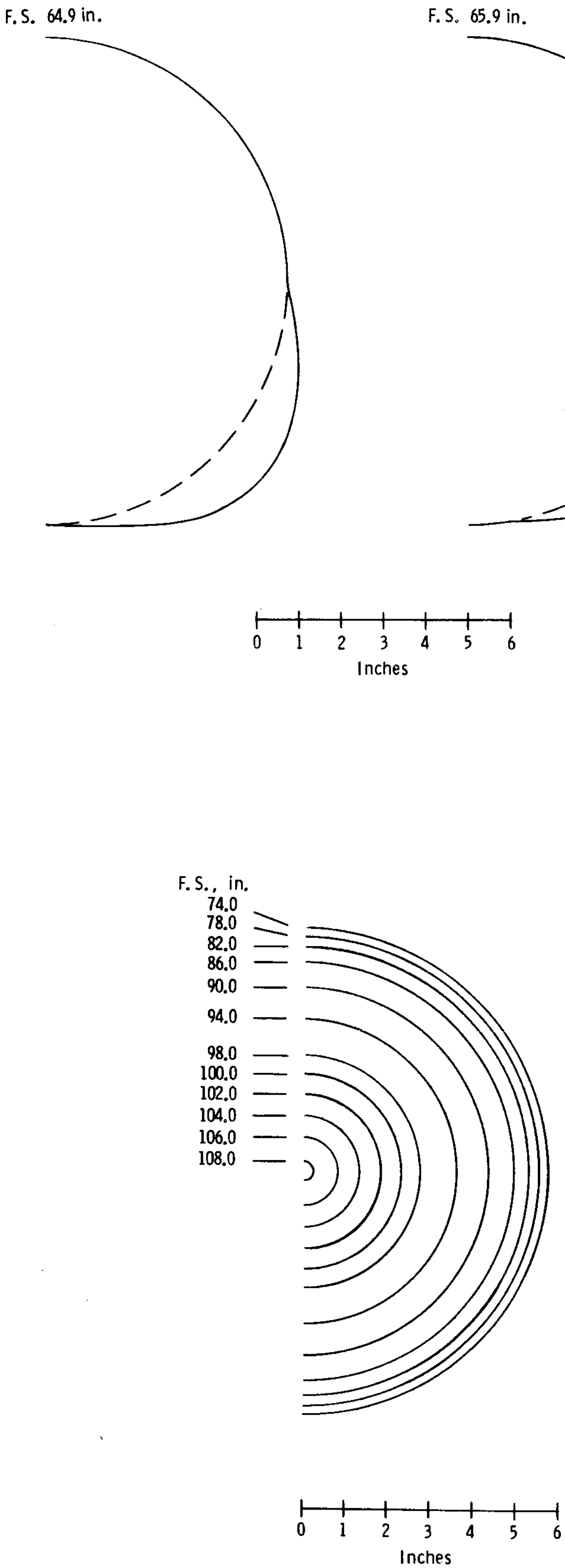

Figure 4.- Concluded.

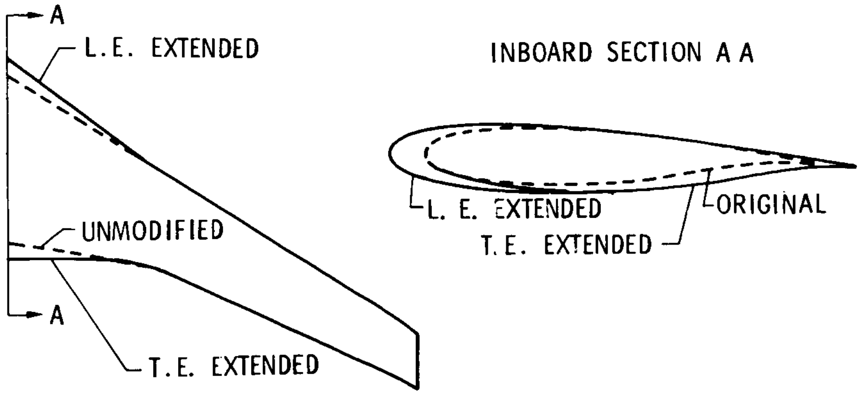

Figure 5.- Inboard wing modifications.

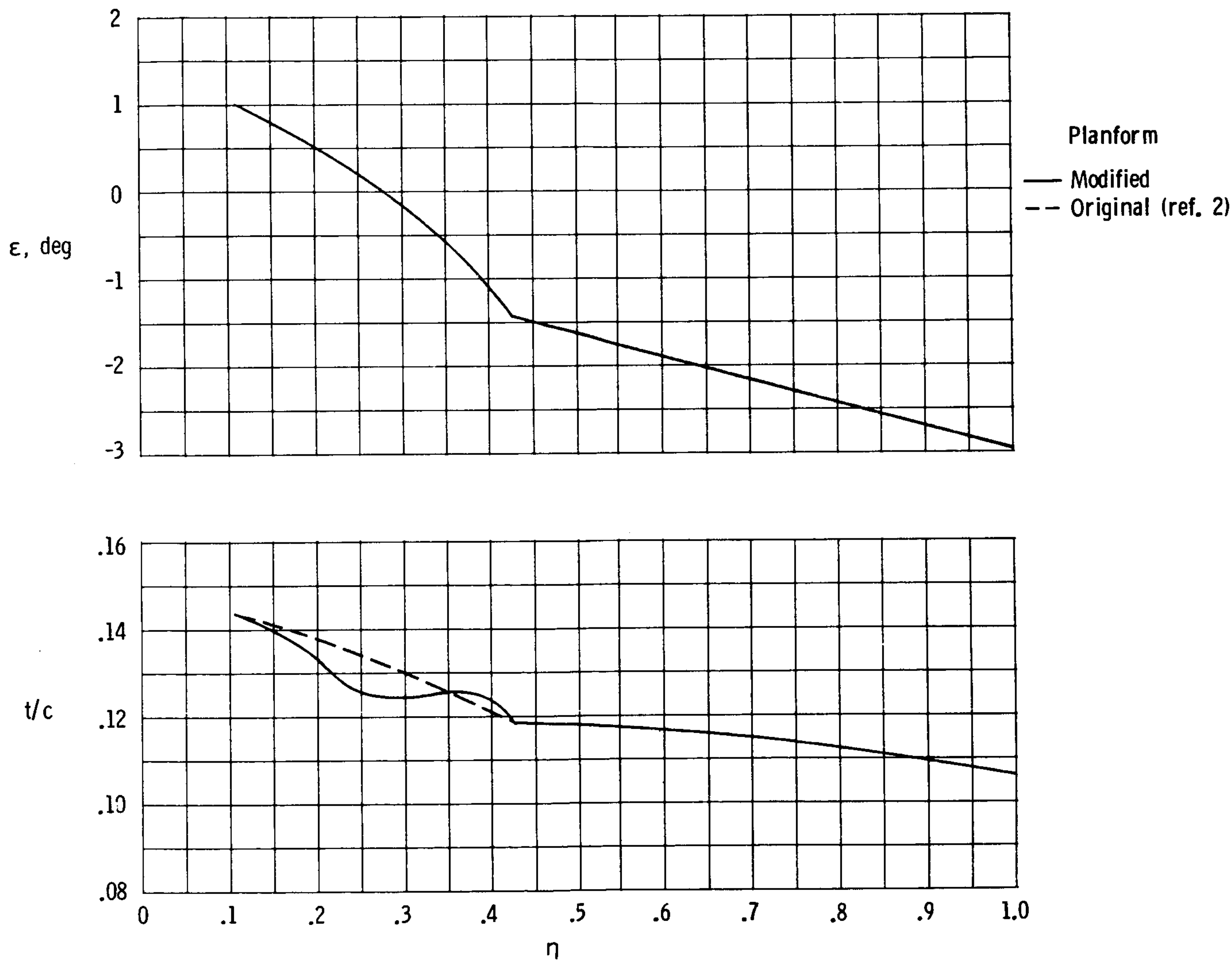

Figure 6.- Twist and thickness distributions.

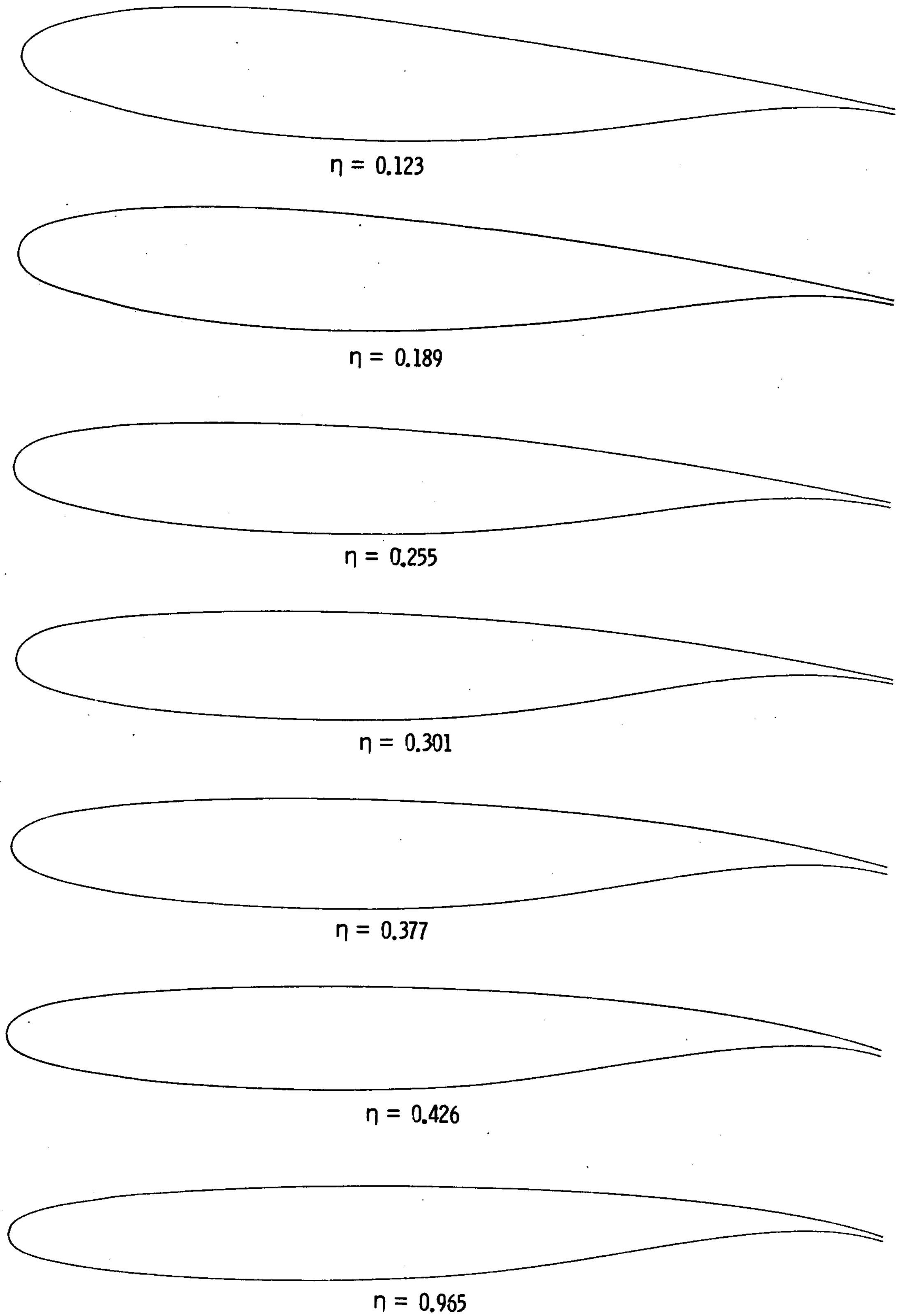

Figure 7.- Wing airfoil sections.

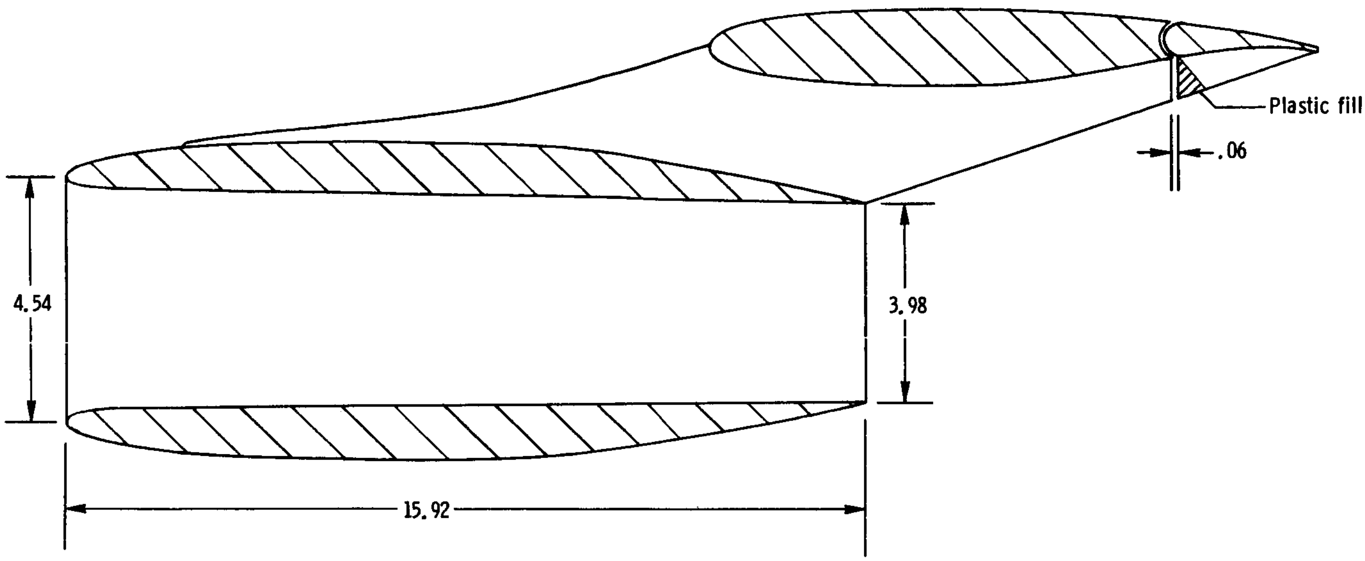

Figure 8.- Drawing of nacelle and pylon. (All dimensions are in inches.)

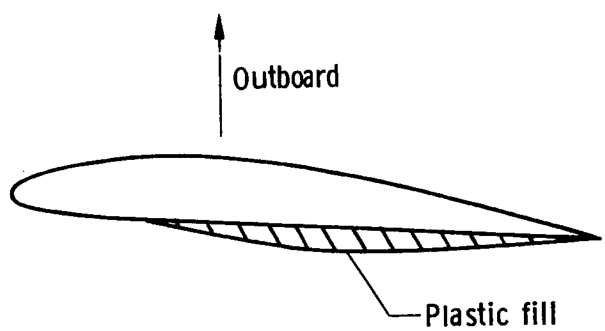

Figure 9.- Typical pylon cross section.

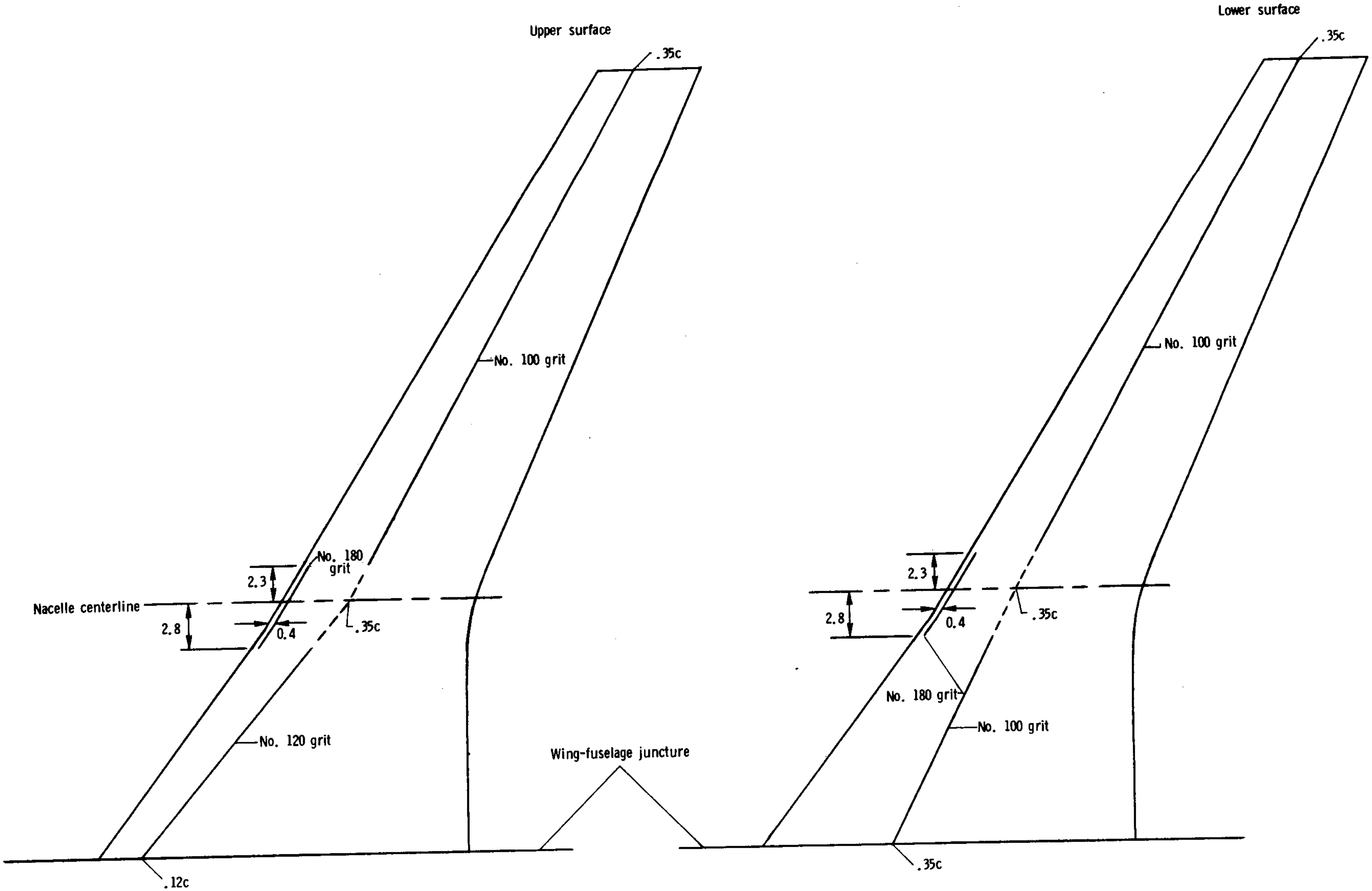

Figure 10.- Transition strip patterns. (All dimensions are in inches.)

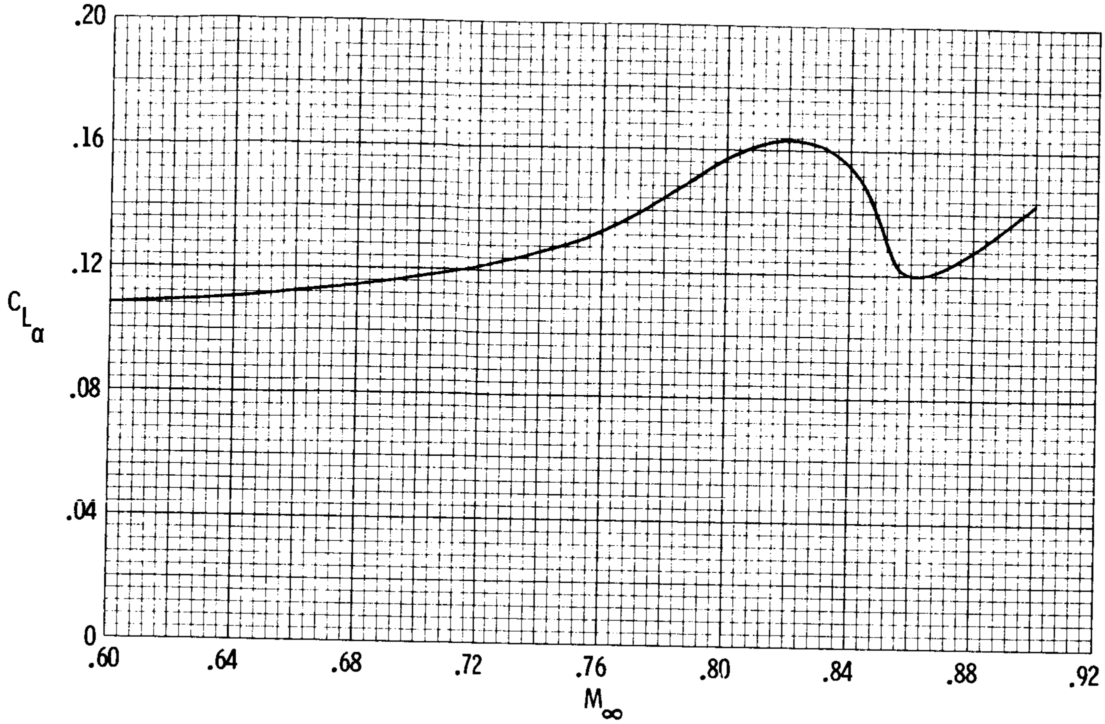

Figure 11.- Variation of lift-curve slope with Mach number for the baseline configuration. $C_L = 0.55$.

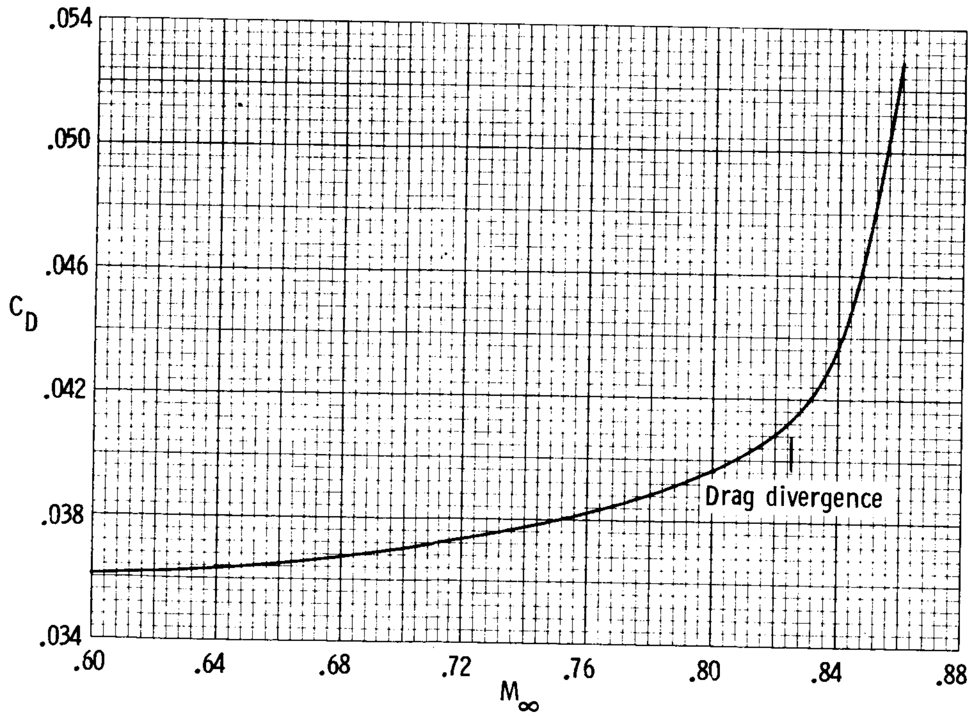

Figure 12.- Variation of drag coefficient with Mach number for the baseline configuration. $C_L = 0.55$.

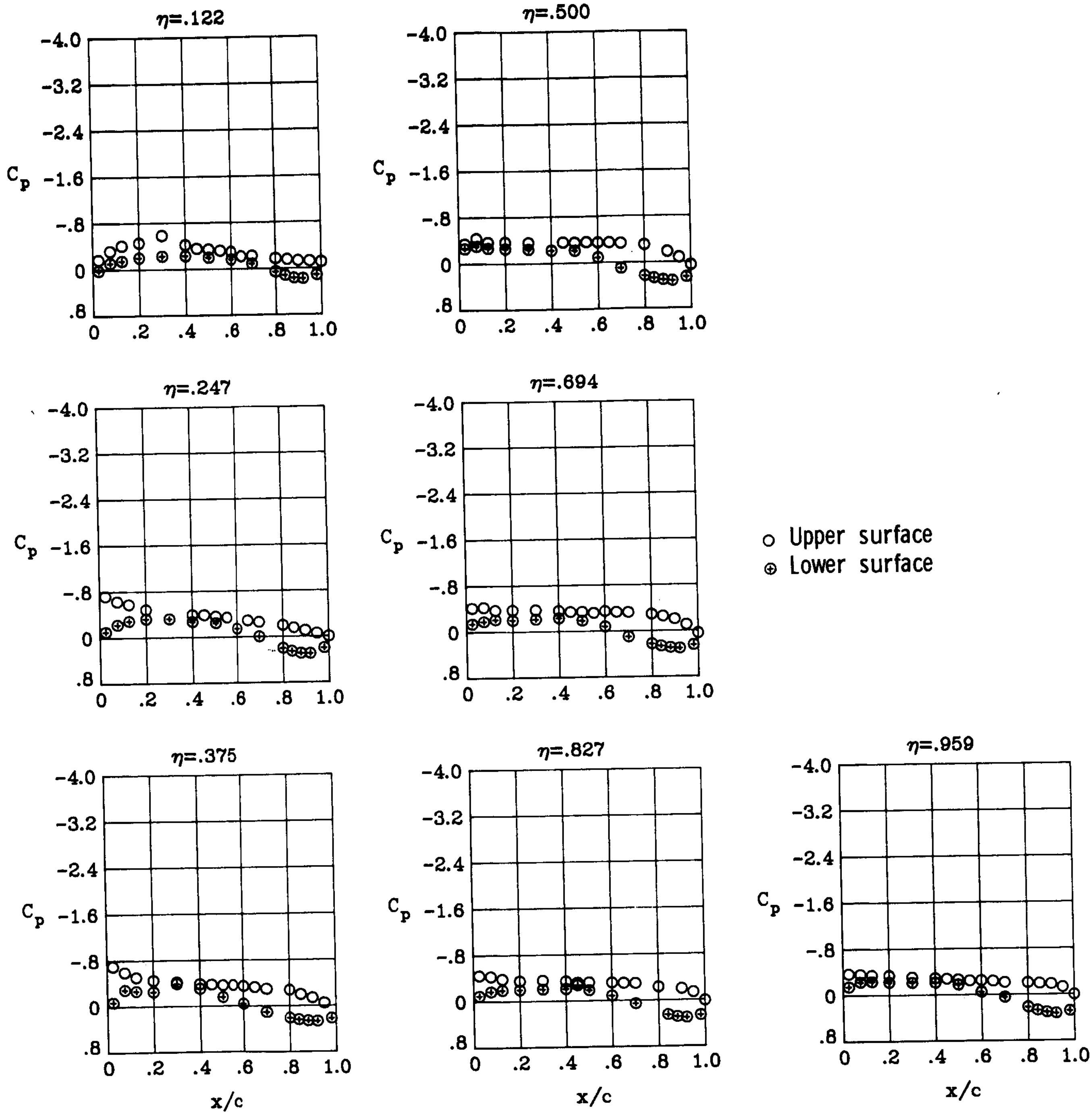

(a) $M_\infty = 0.30$; $\alpha = 1°$.

Figure 13.- Wing chordwise pressure distributions for the baseline configuration at $M_\infty = 0.30$.

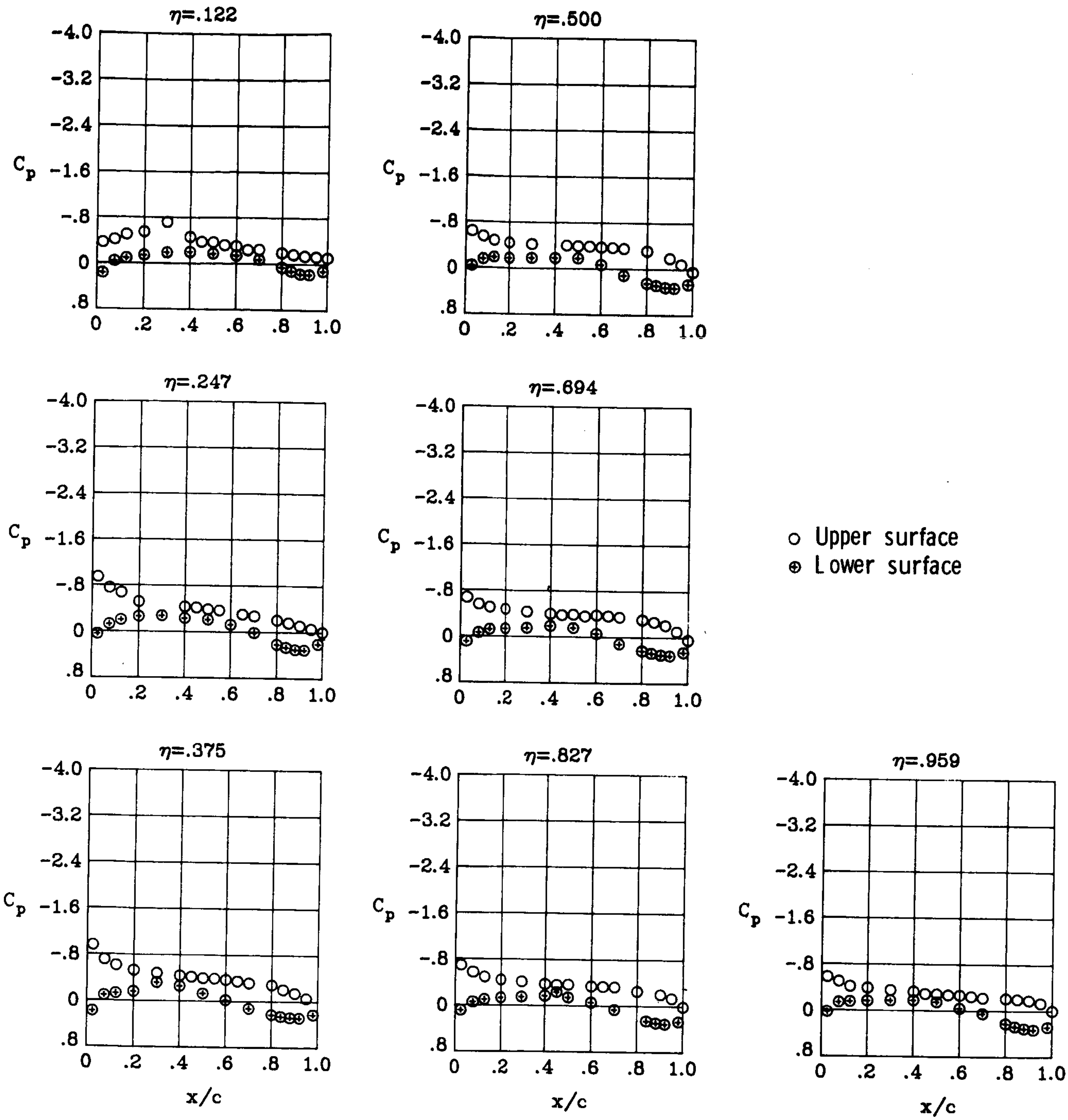

(b) $M_\infty = 0.30$; $\alpha = 2°$.

Figure 13.- Continued.

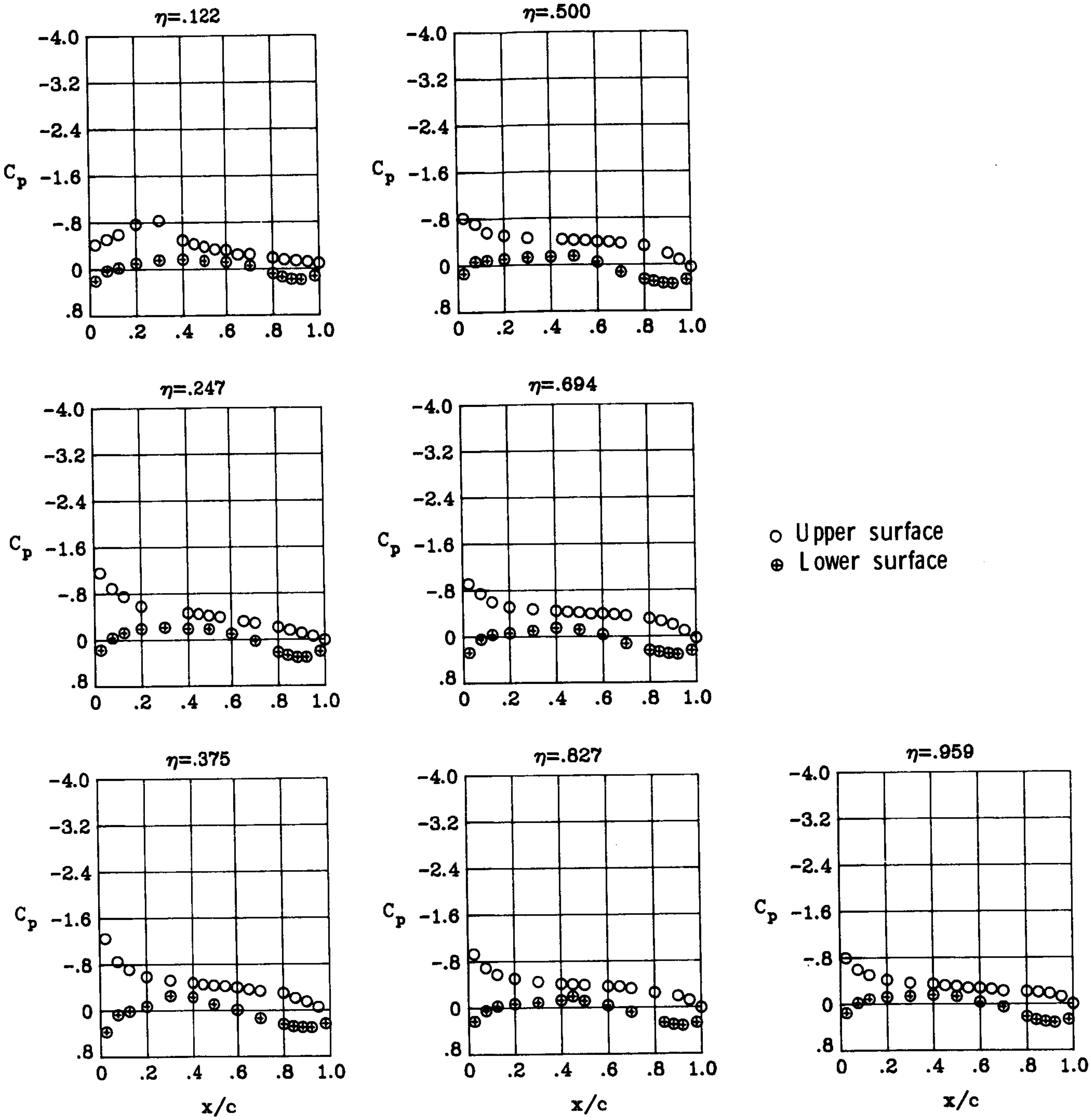

(c) $M_\infty = 0.30$; $\alpha = 3°$.

Figure 13.- Continued.

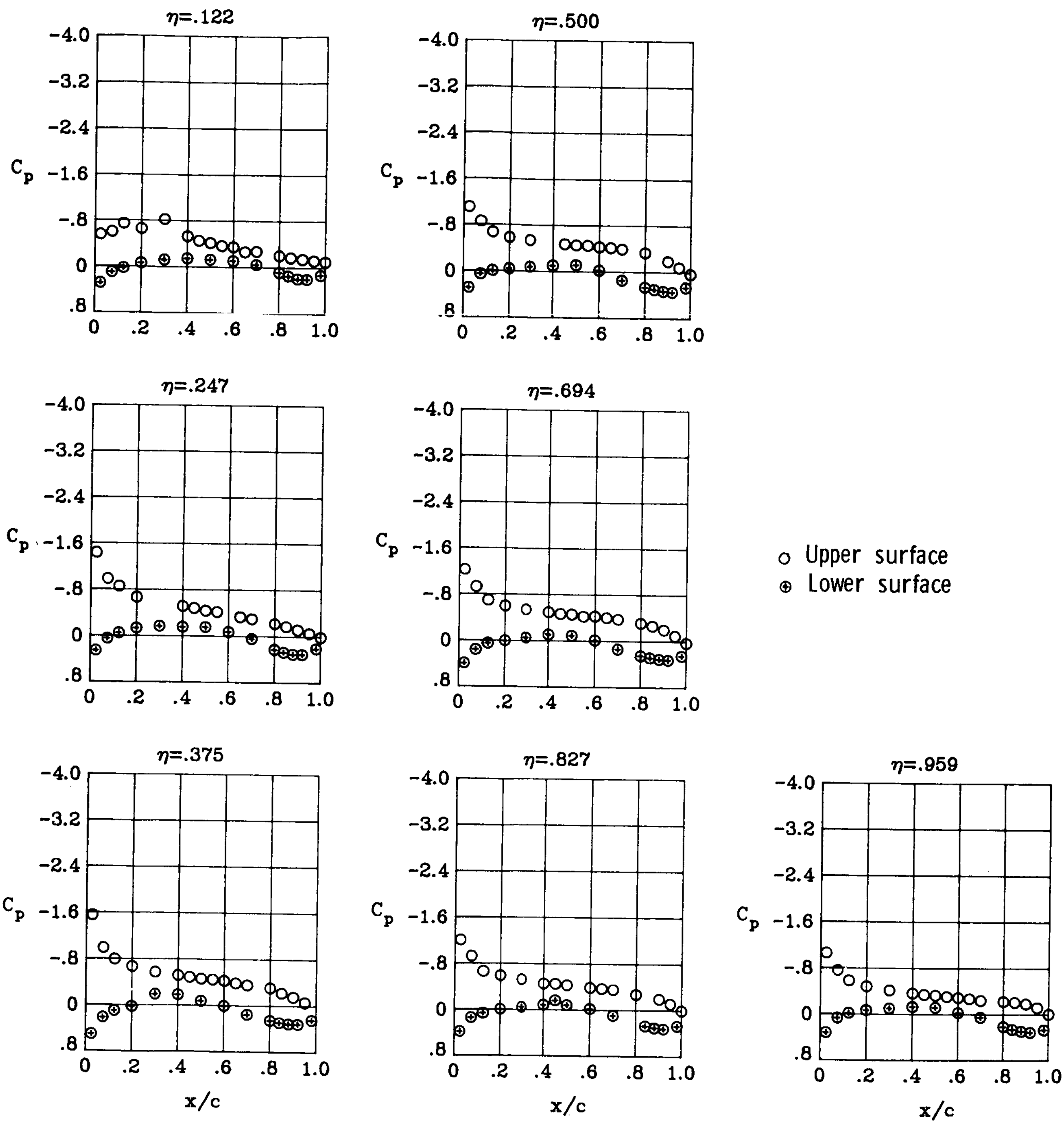

(d) $M_\infty = 0.30$; $\alpha = 4°$.

Figure 13.- Continued.

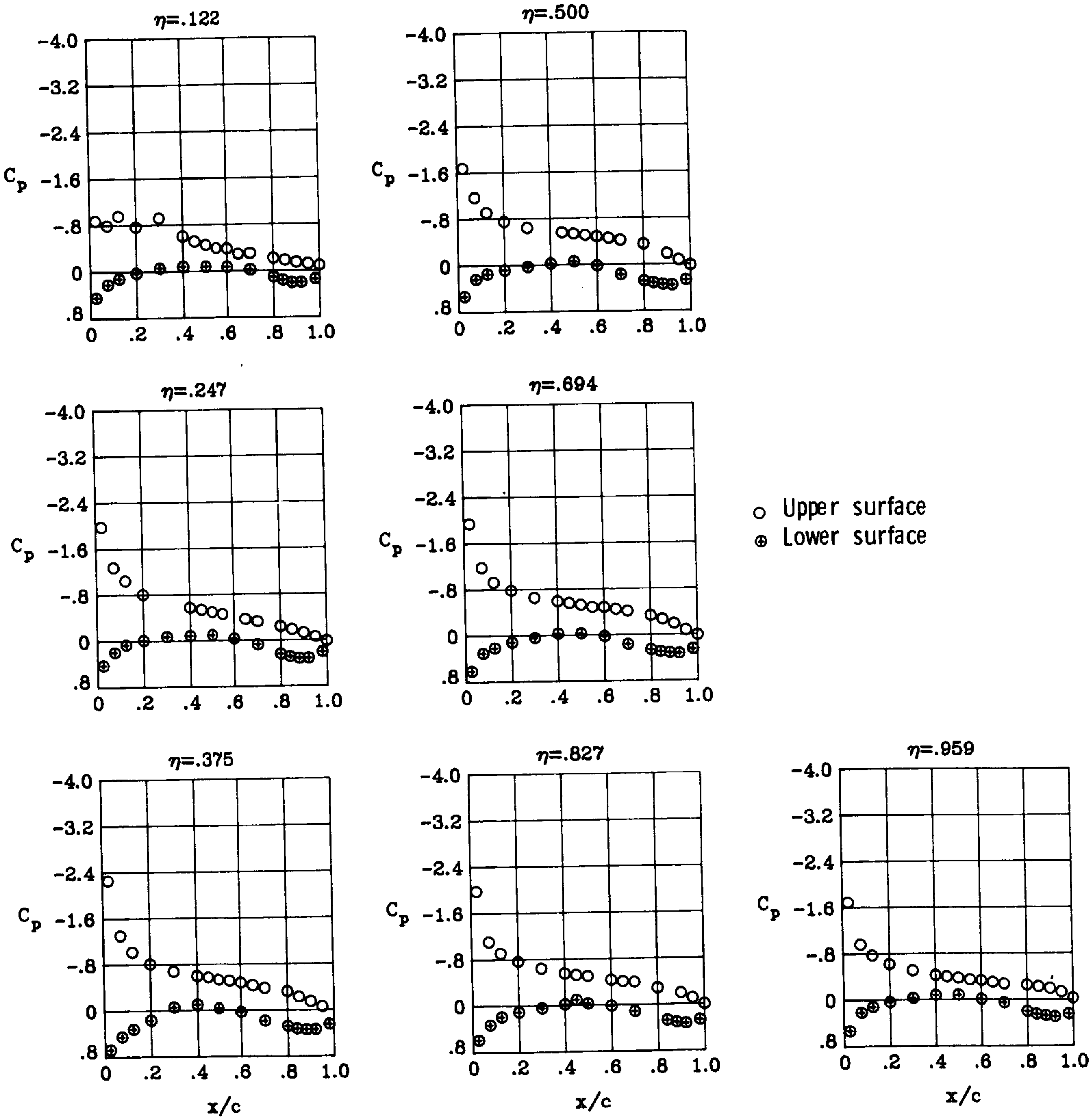

(e) $M_\infty = 0.30$; $\alpha = 6°$.

Figure 13.- Concluded.

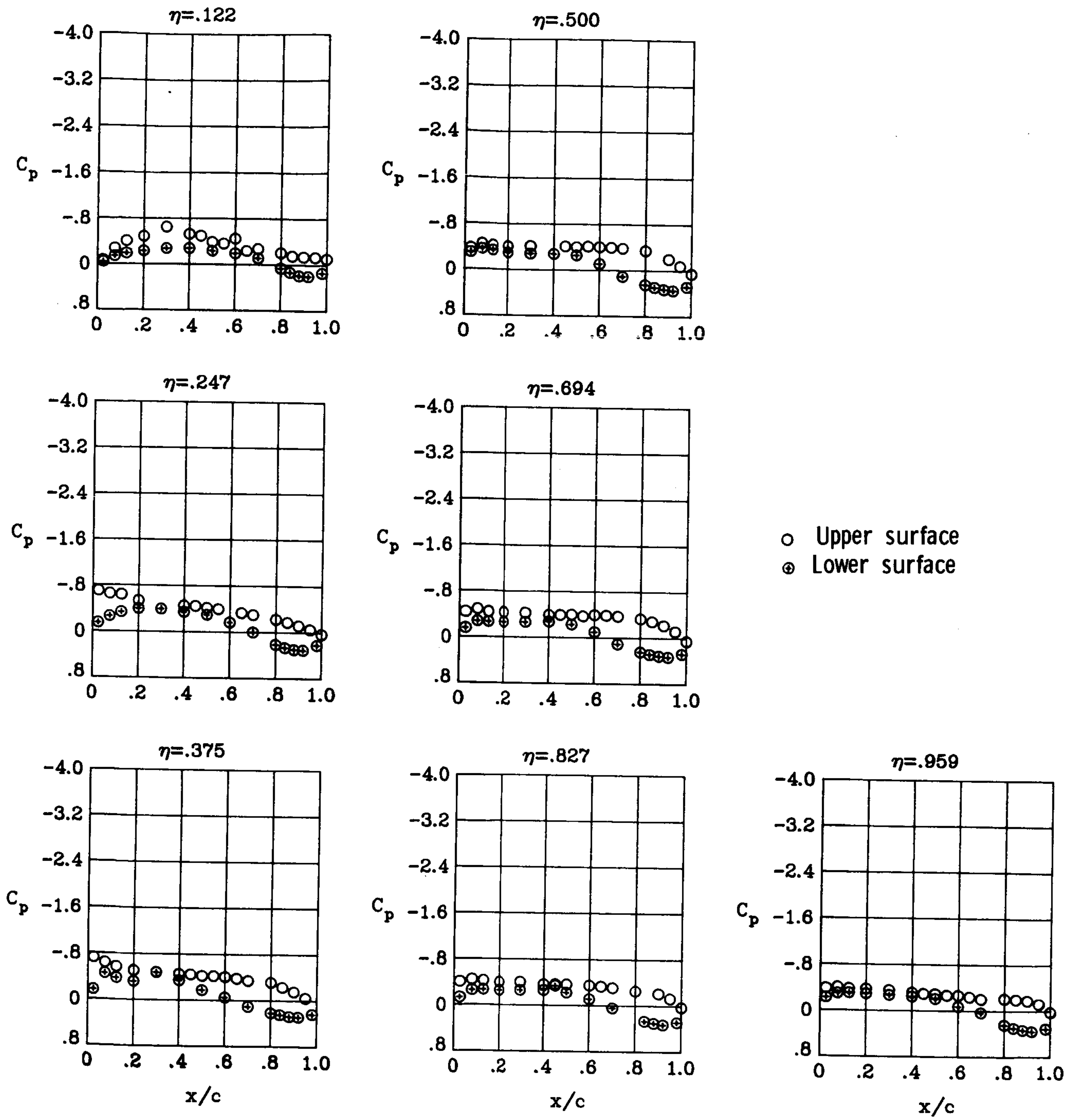

(a) $M_\infty = 0.60$; $\alpha = 1°$.

Figure 14.- Wing chordwise pressure distributions for the baseline configuration at $M_\infty = 0.60$.

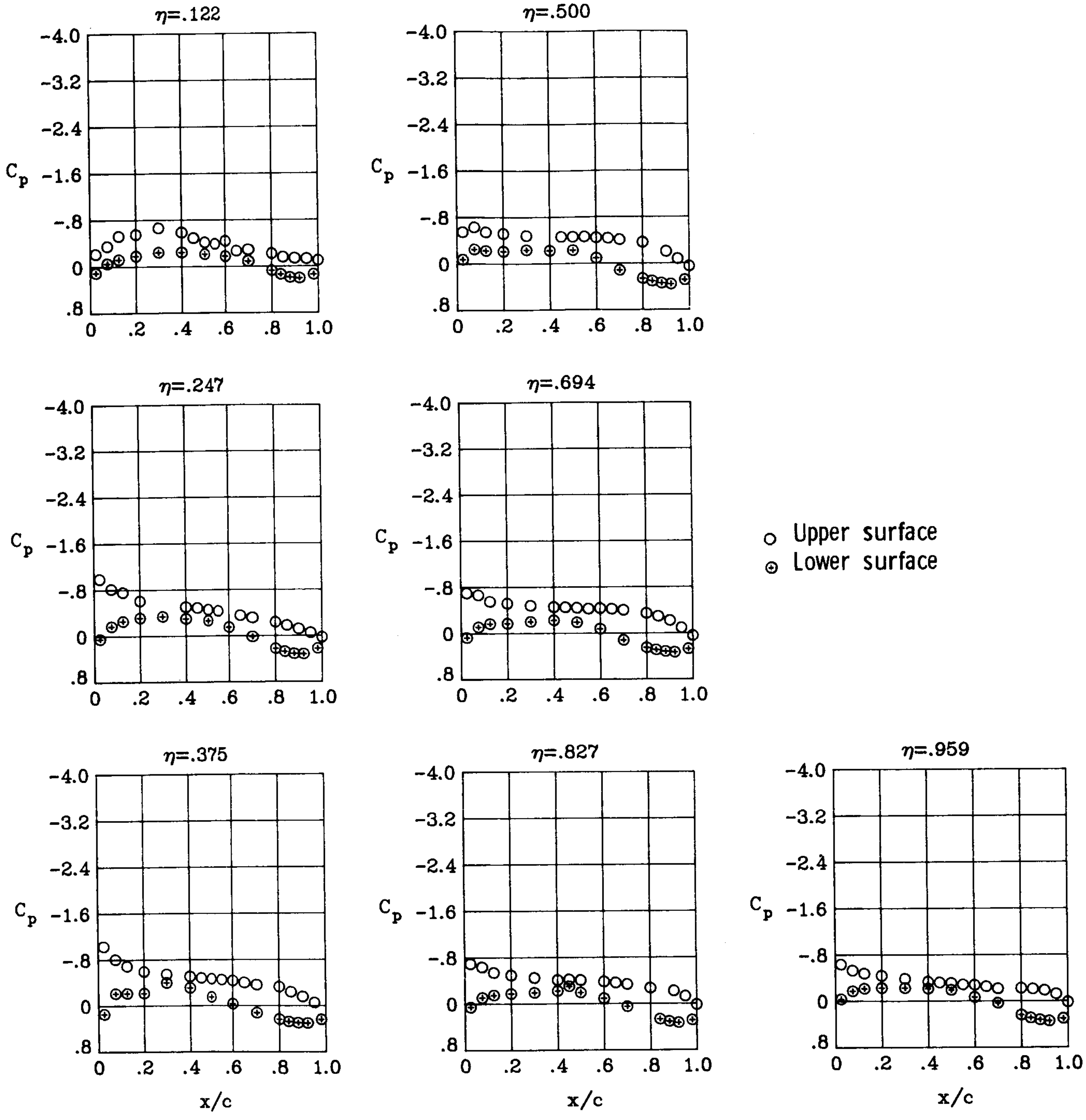

(b) $M_\infty = 0.60$; $\alpha = 2°$.

Figure 14.- Continued.

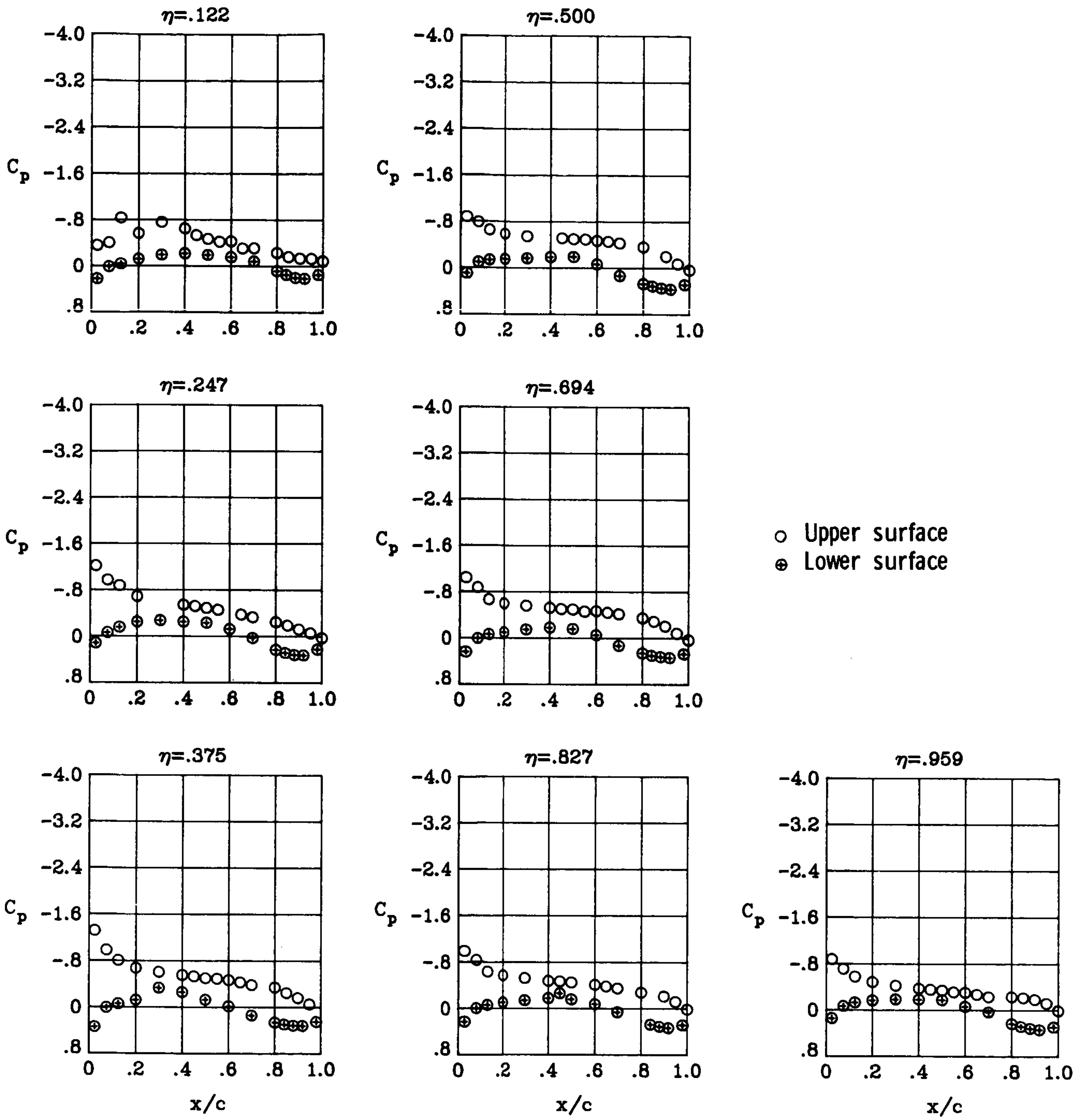

(c) $M_\infty = 0.60$; $\alpha = 3°$.

Figure 14.- Continued.

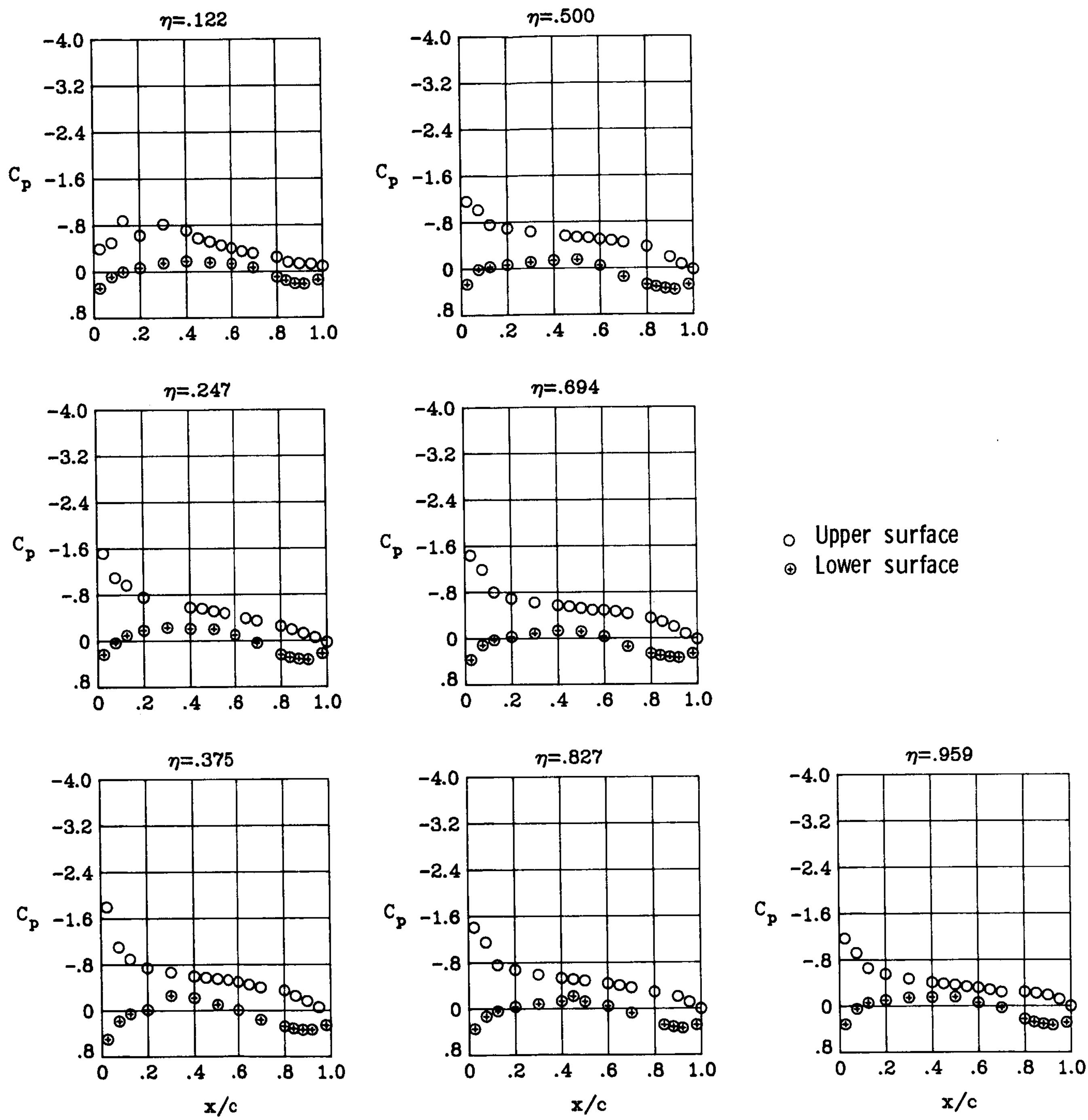

(d) $M_\infty = 0.60$; $\alpha = 4°$.

Figure 14.- Continued.

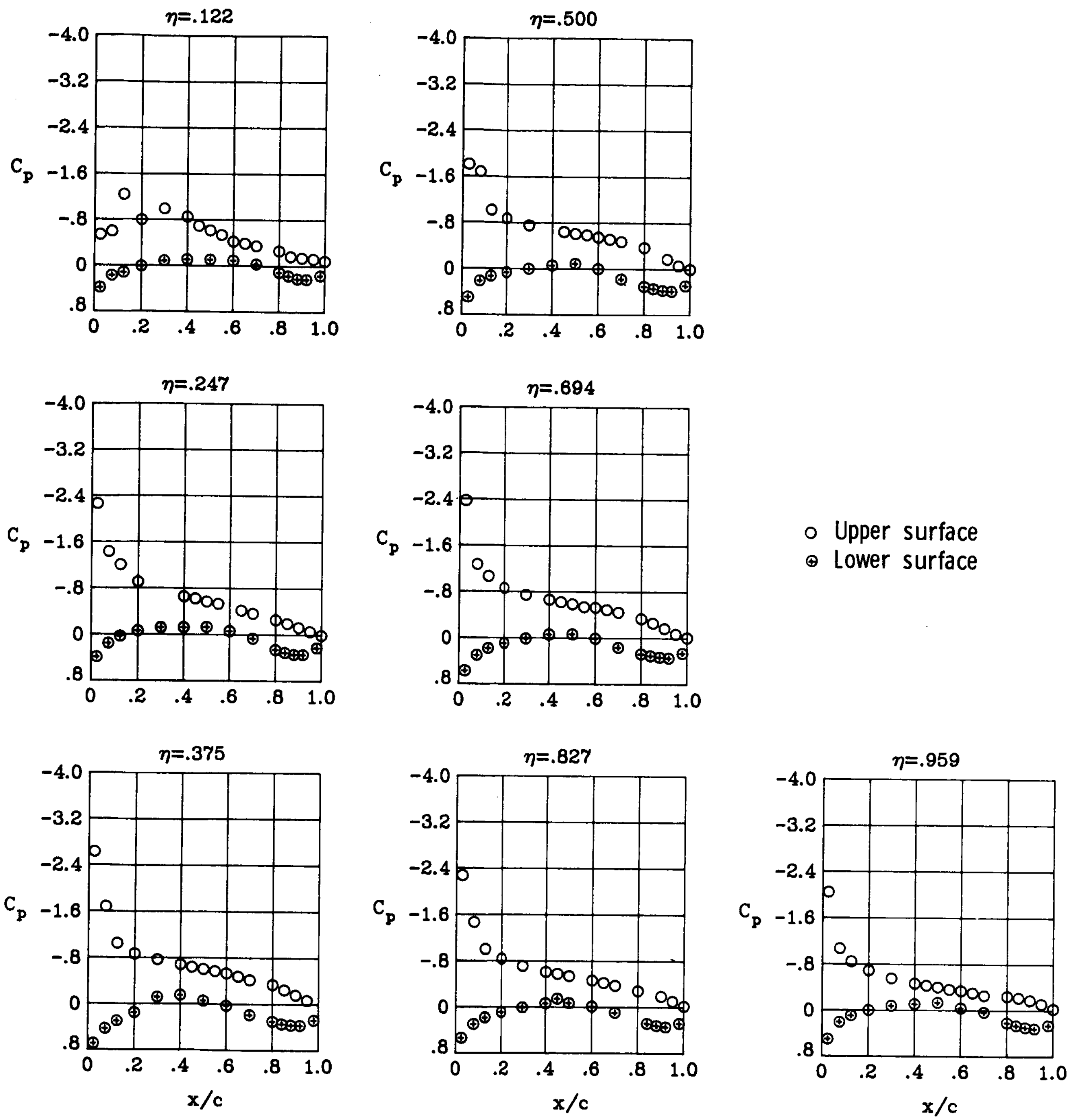

(e) $M_\infty = 0.60$; $\alpha = 6°$.

Figure 14.- Concluded.

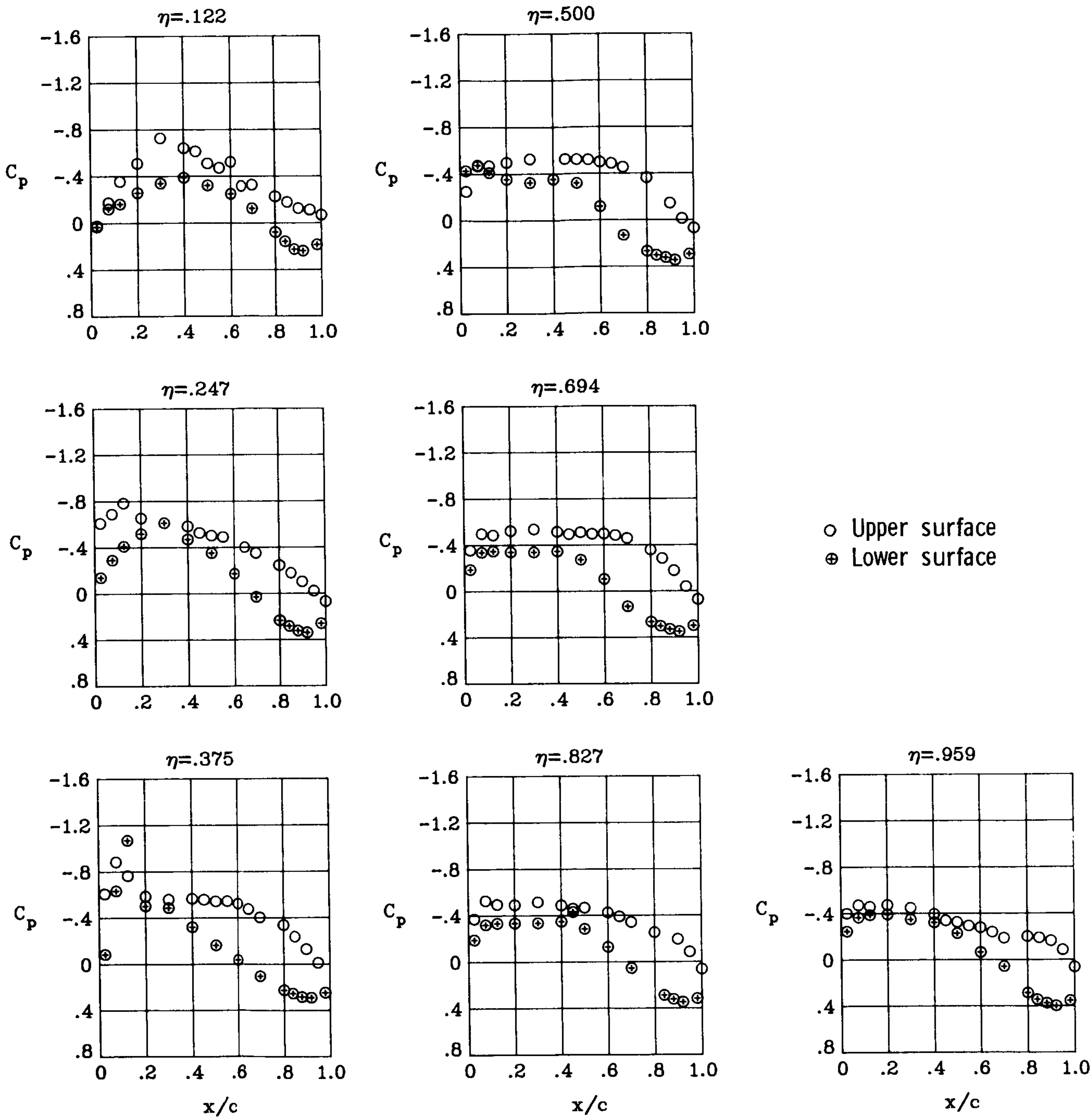

(a) $M_\infty = 0.80$; $\alpha = 1°$.

Figure 15.- Wing chordwise pressure distributions for the baseline configuration at $M_\infty = 0.80$.

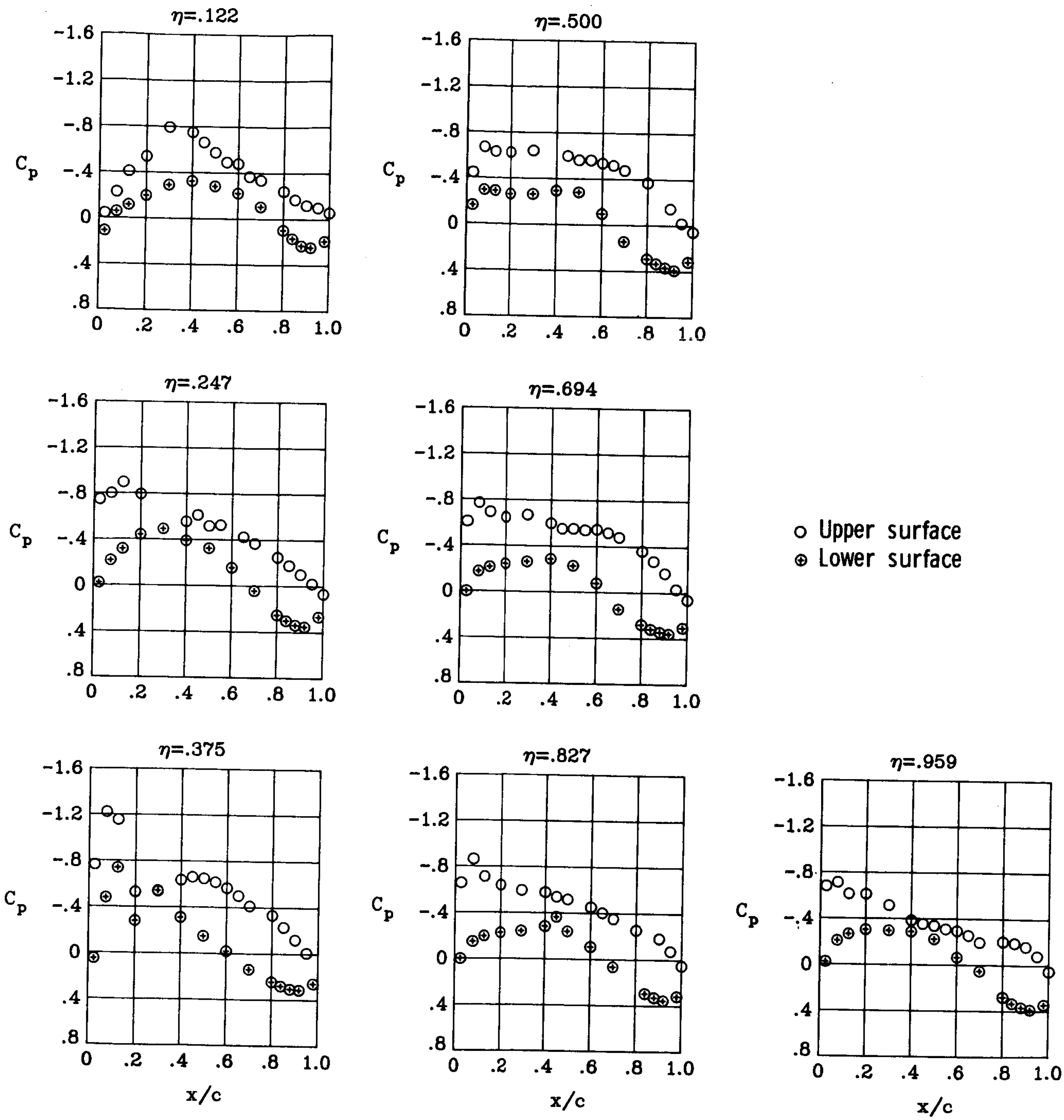

(b) $M_\infty = 0.80$; $\alpha = 2°$.

Figure 15.- Continued.

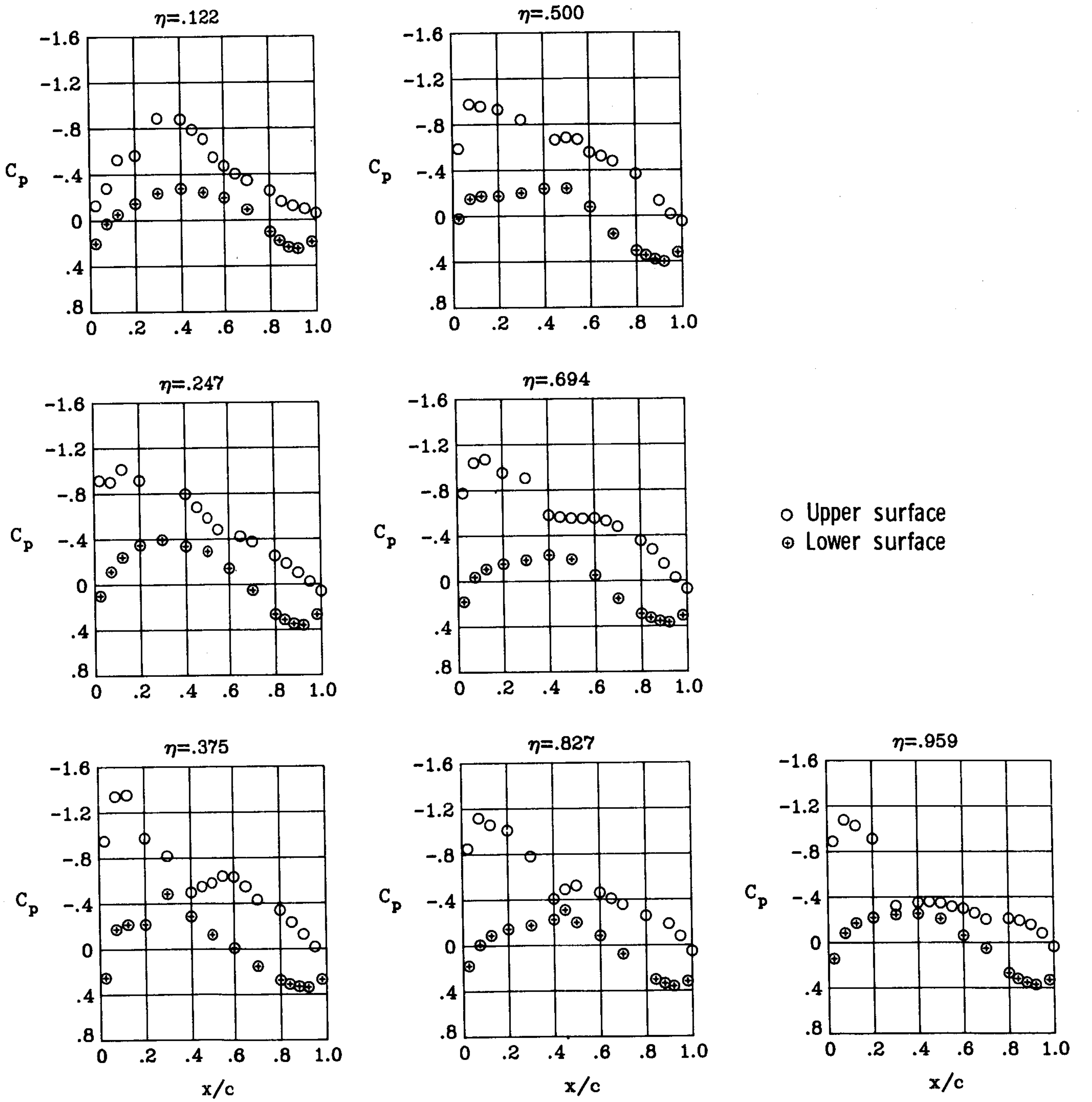

(c) M_∞ = 0.80; α = 3°.

Figure 15.- Continued.

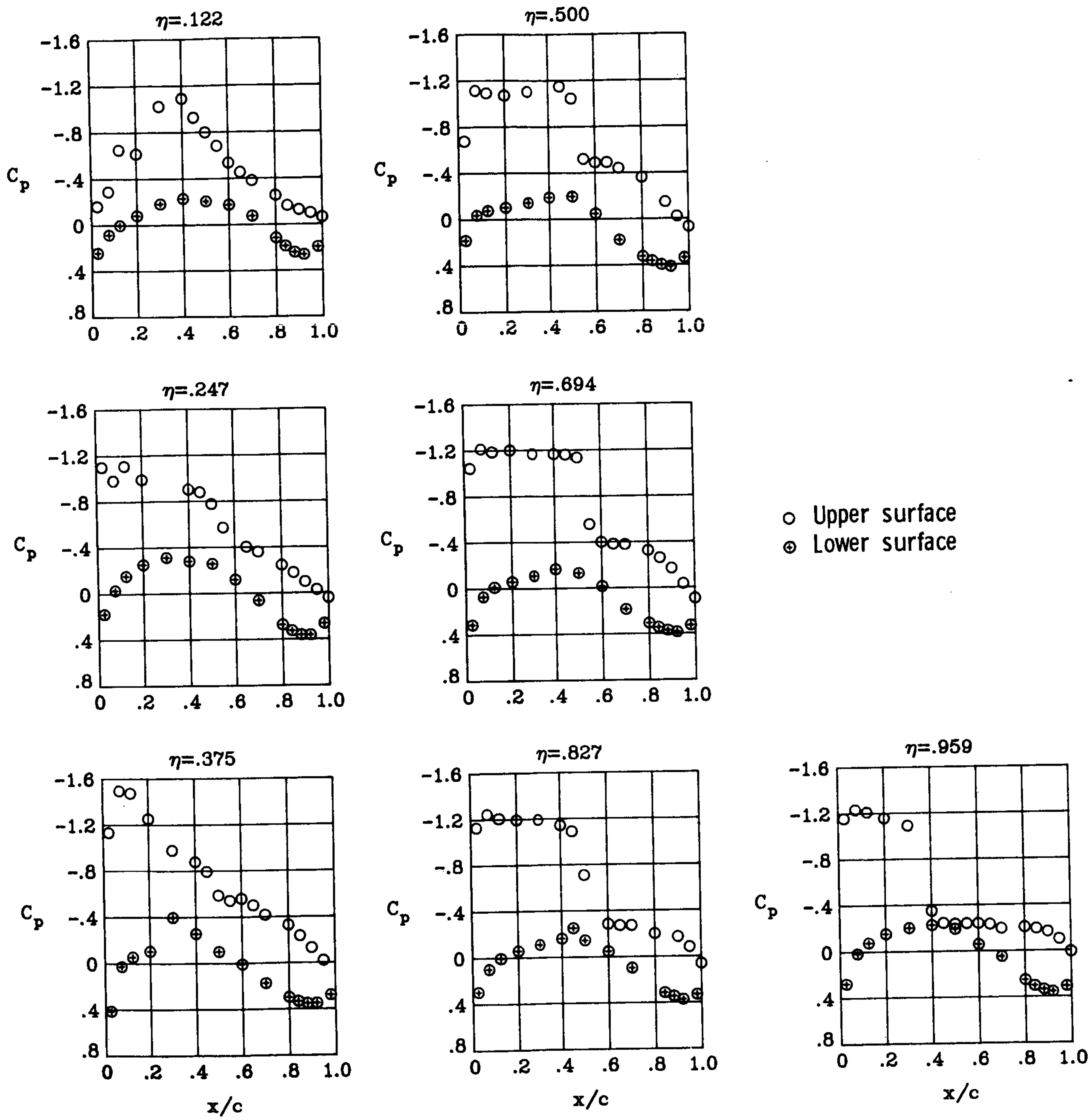

(d) $M_\infty = 0.80$; $\alpha = 4°$.

Figure 15.- Continued.

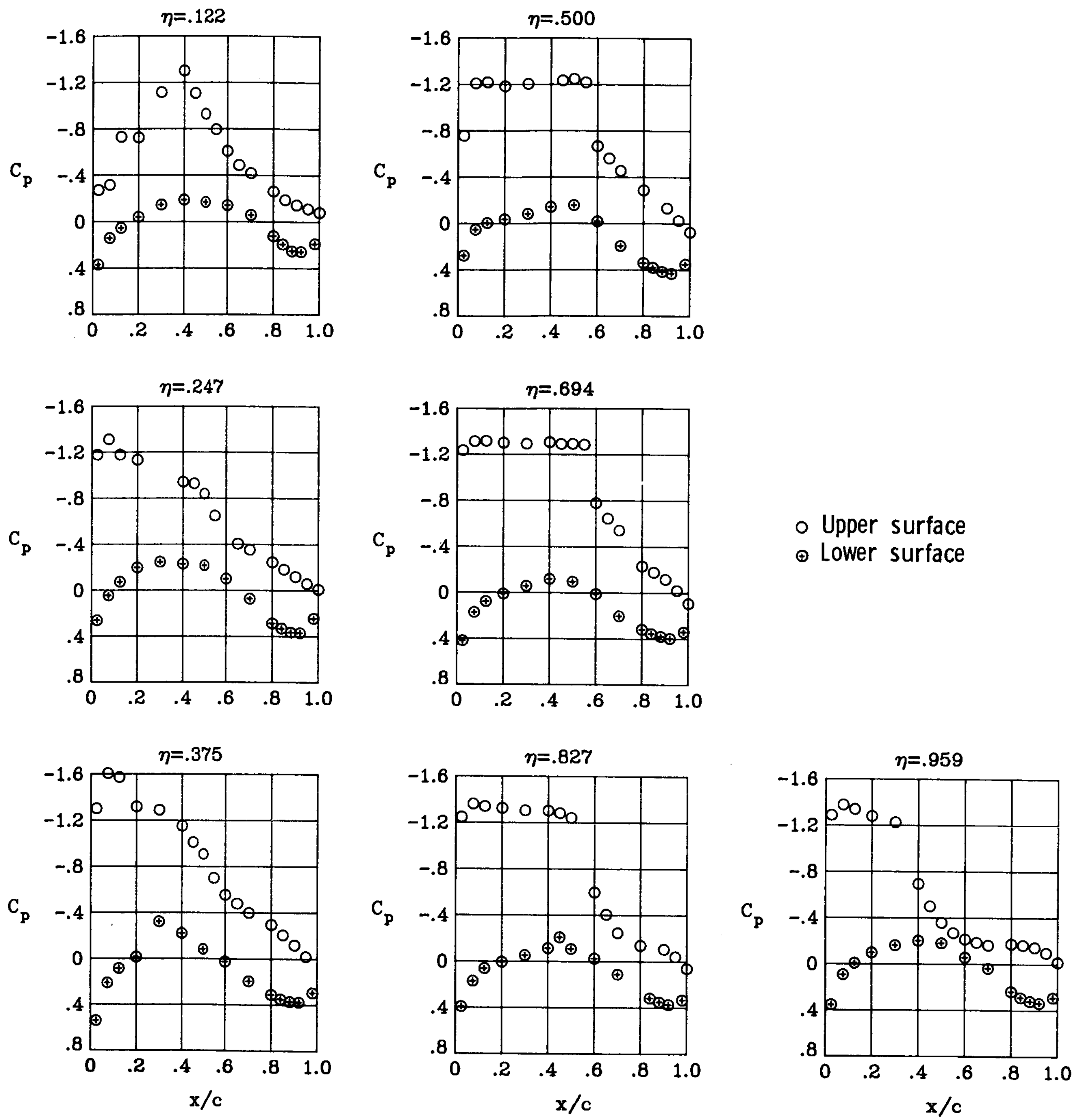

(e) $M_\infty = 0.80$; $\alpha = 5°$.

Figure 15.- Concluded.

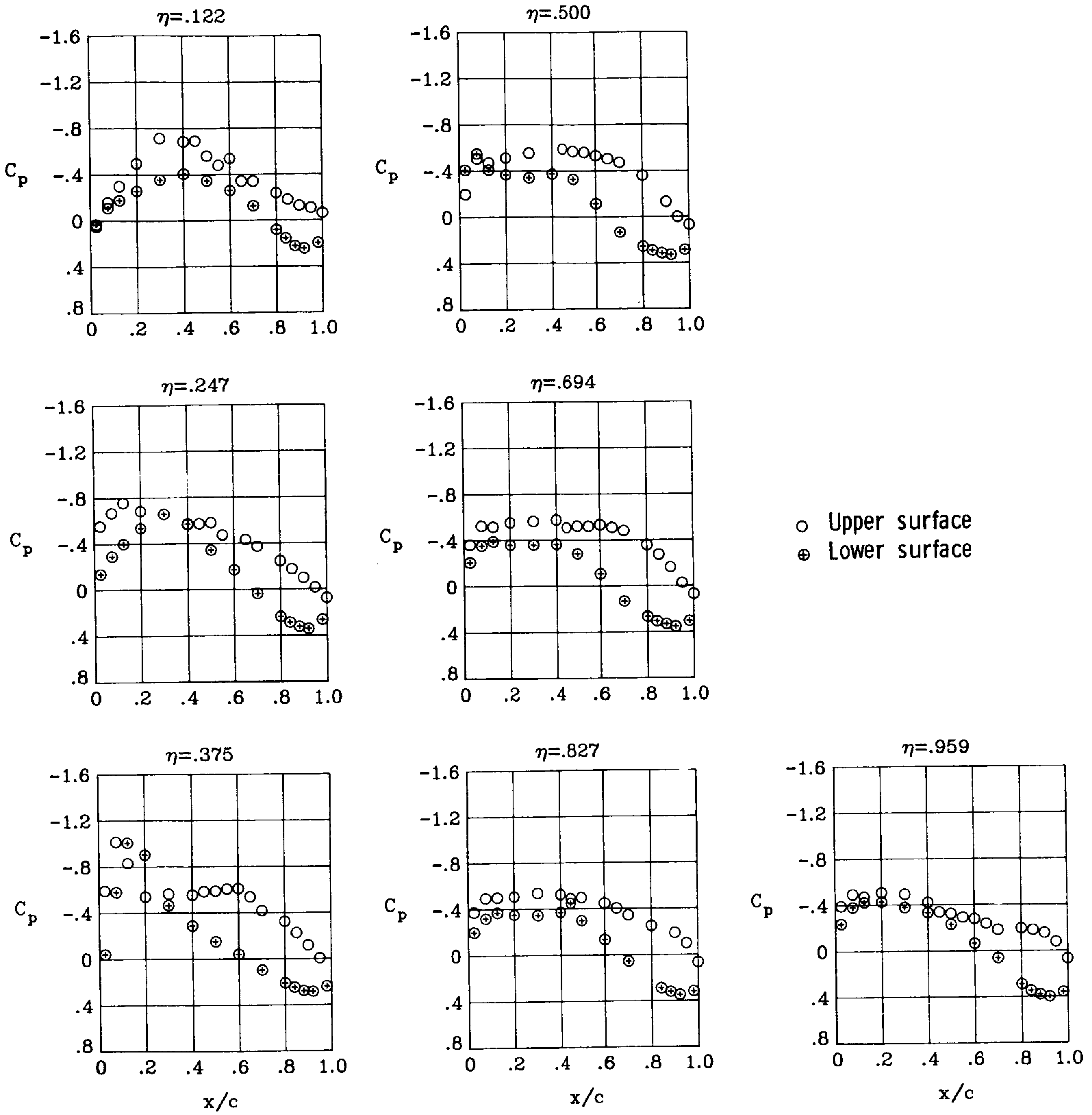

(a) $M_\infty = 0.82$; $\alpha = 1°$.

Figure 16.- Wing chordwise pressure distributions for the baseline configuration at $M_\infty = 0.82$.

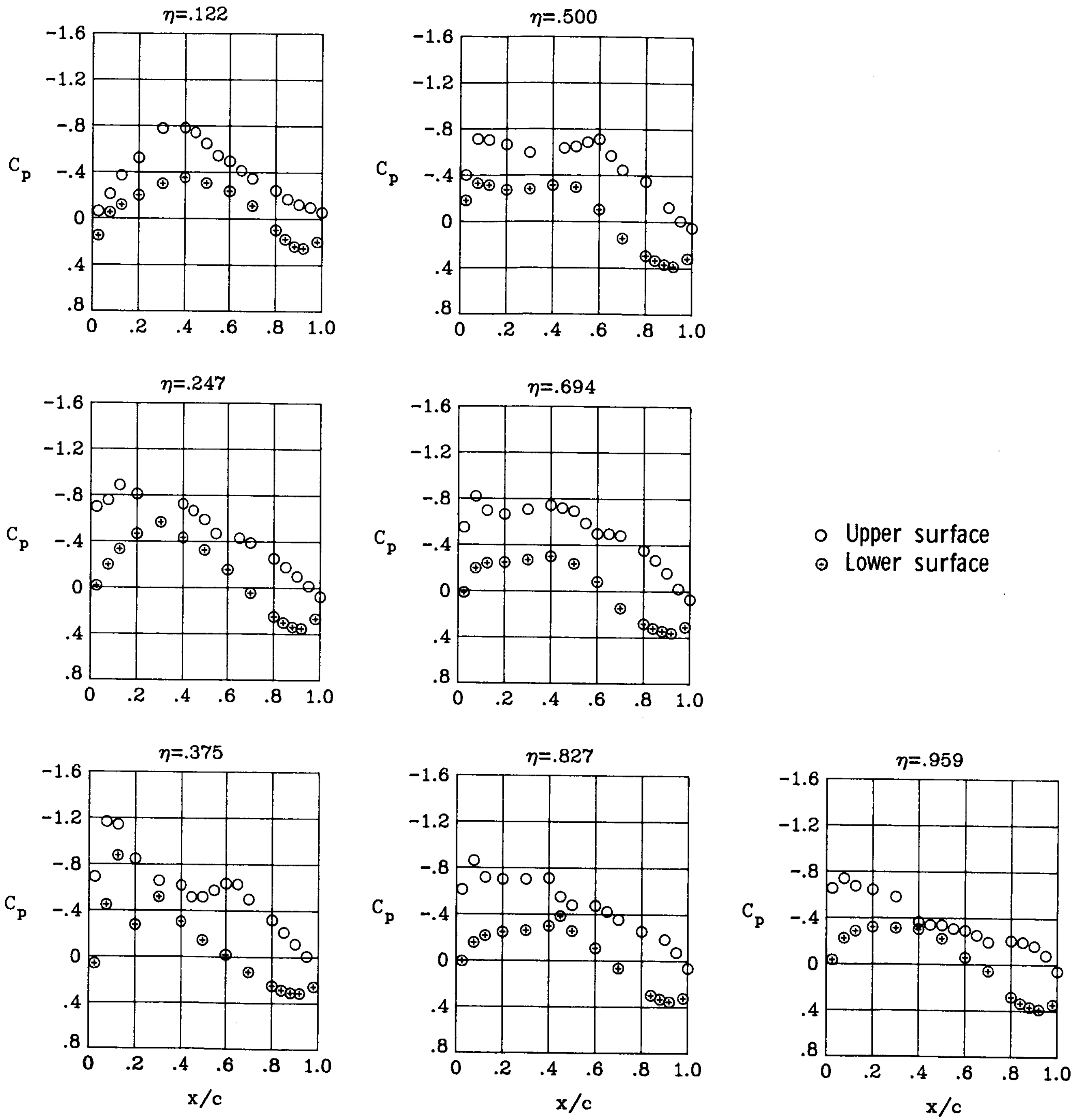

(b) $M_\infty = 0.82$; $\alpha = 2°$.

Figure 16.- Continued.

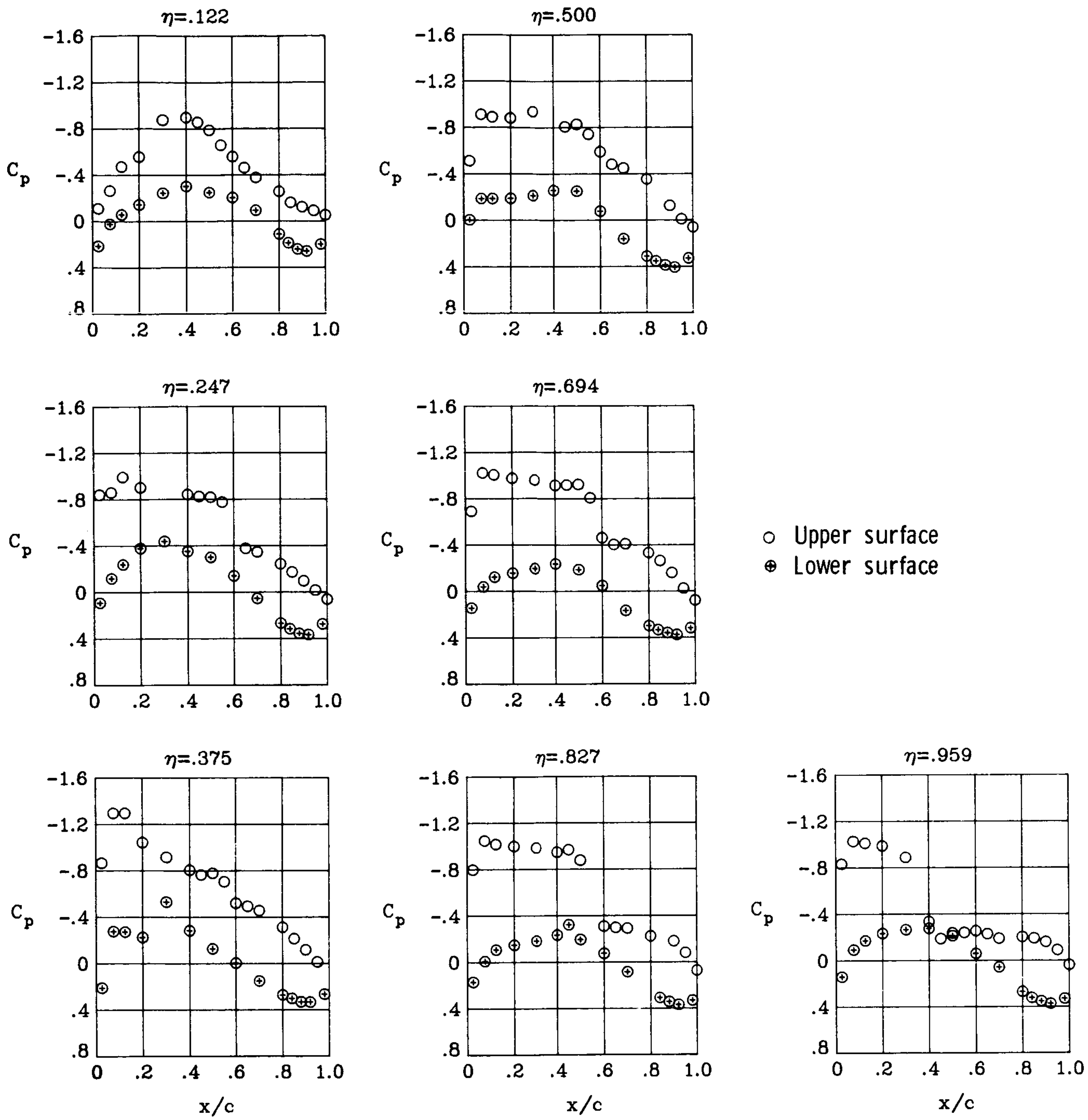

(c) $M_\infty = 0.82$; $\alpha = 3°$.

Figure 16.- Continued.

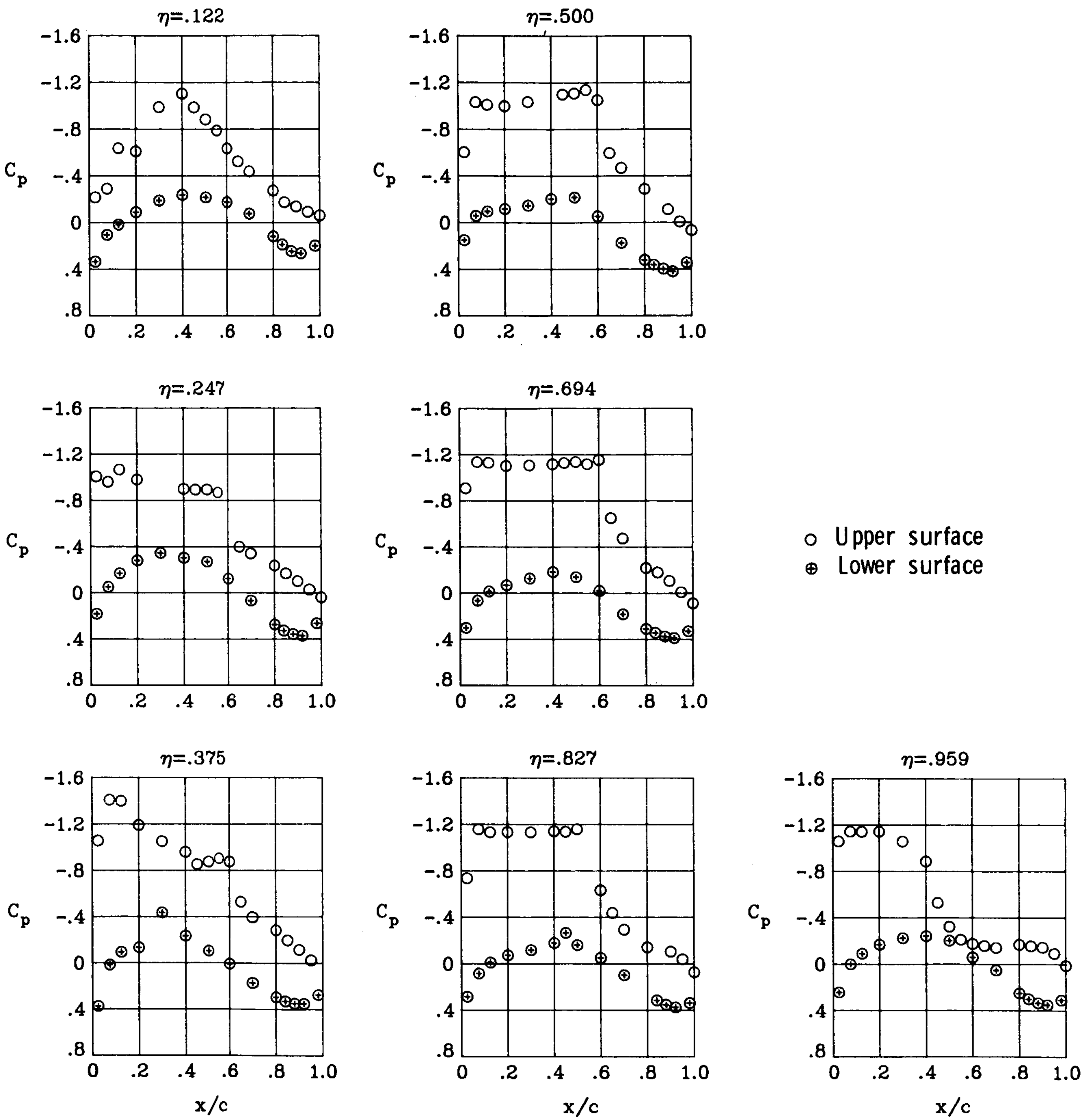

(d) $M_\infty = 0.82$; $\alpha = 4°$.

Figure 16.- Continued.

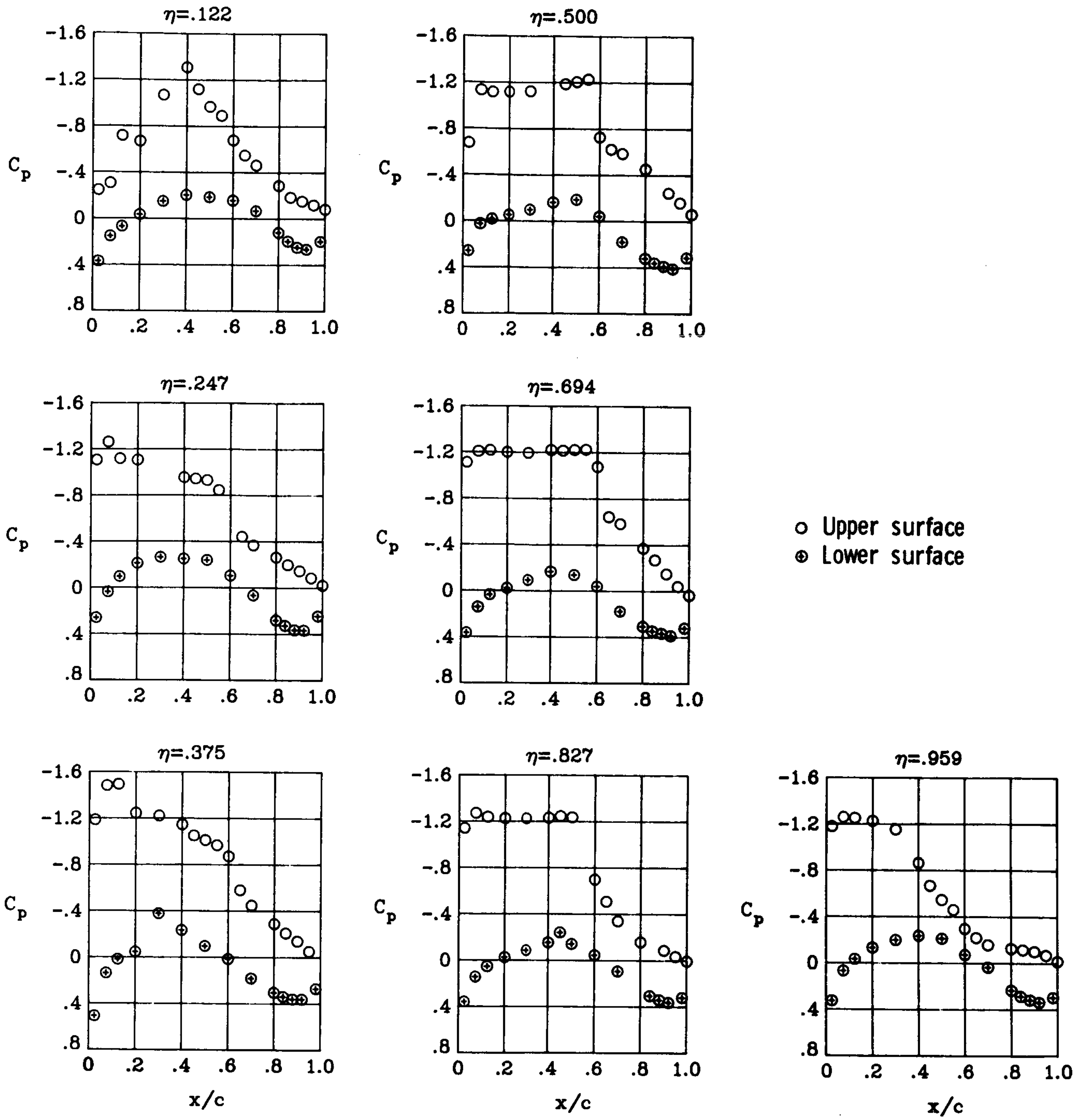

(e) $M_\infty = 0.82$; $\alpha = 5°$.

Figure 16.- Concluded.

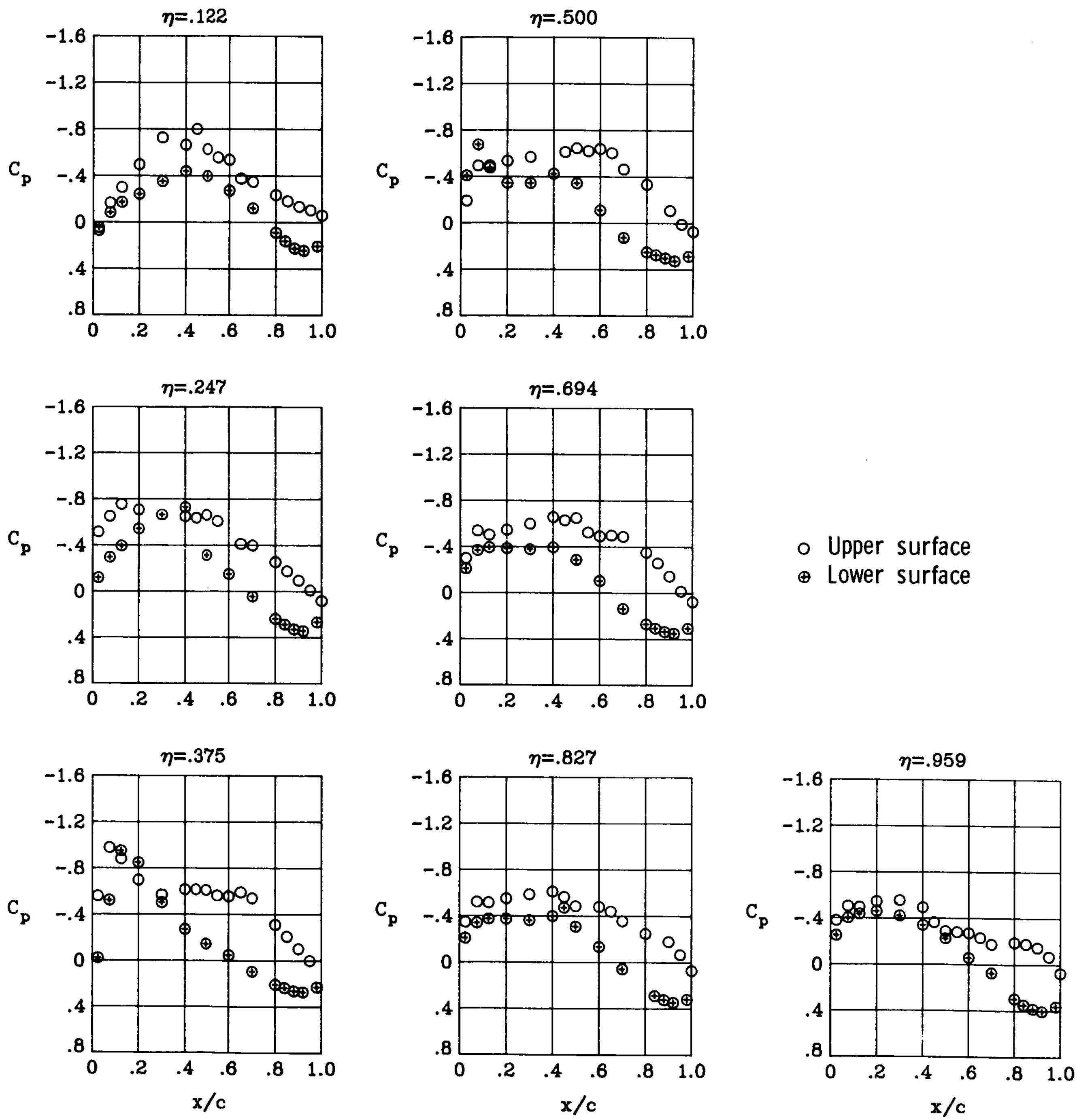

(a) $M_\infty = 0.84$; $\alpha = 1°$.

Figure 17.- Wing chordwise distributions for the baseline configuration at $M_\infty = 0.84$.

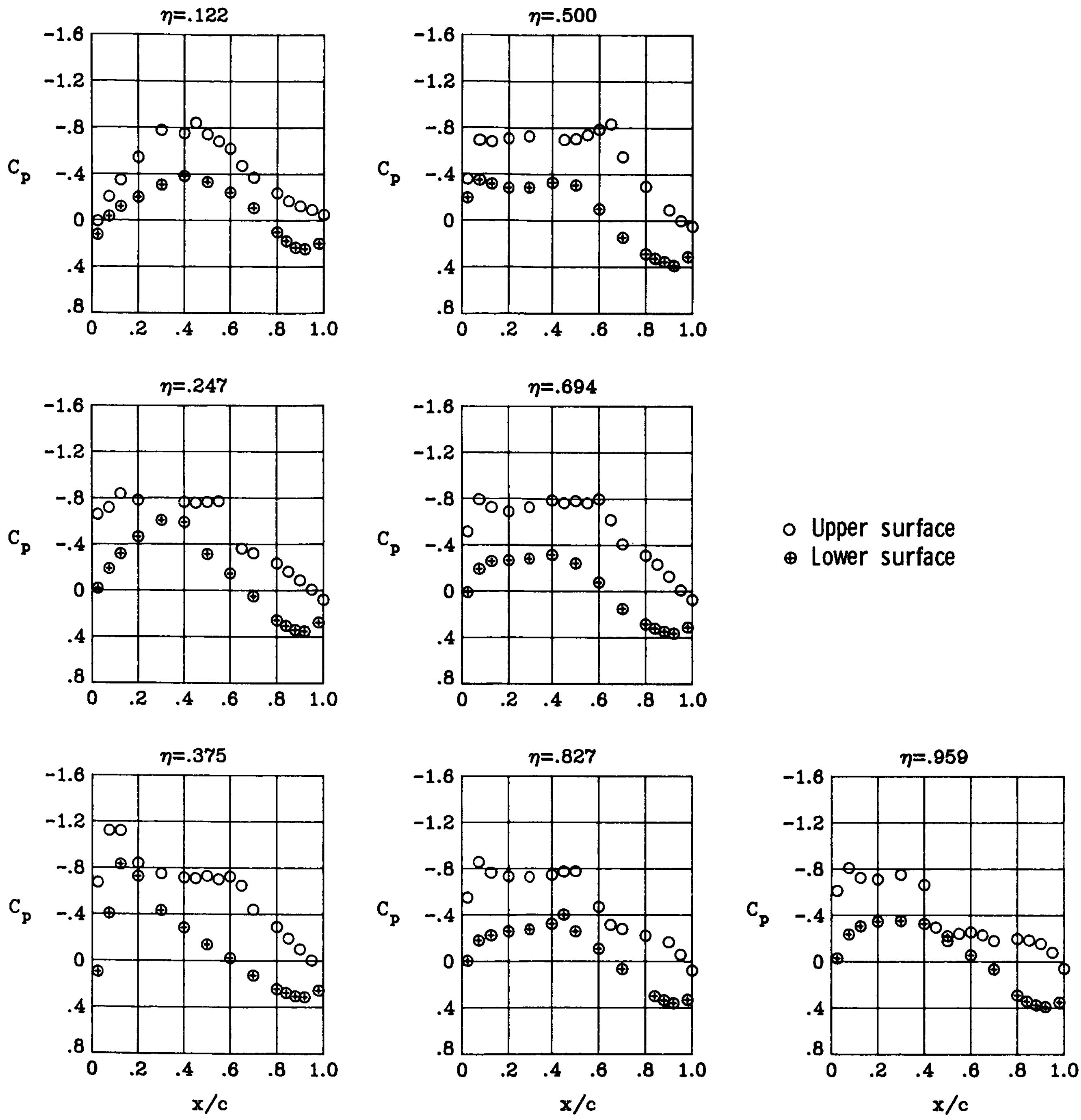

(b) $M_{\infty} = 0.84$; $\alpha = 2°$.

Figure 17.- Continued.

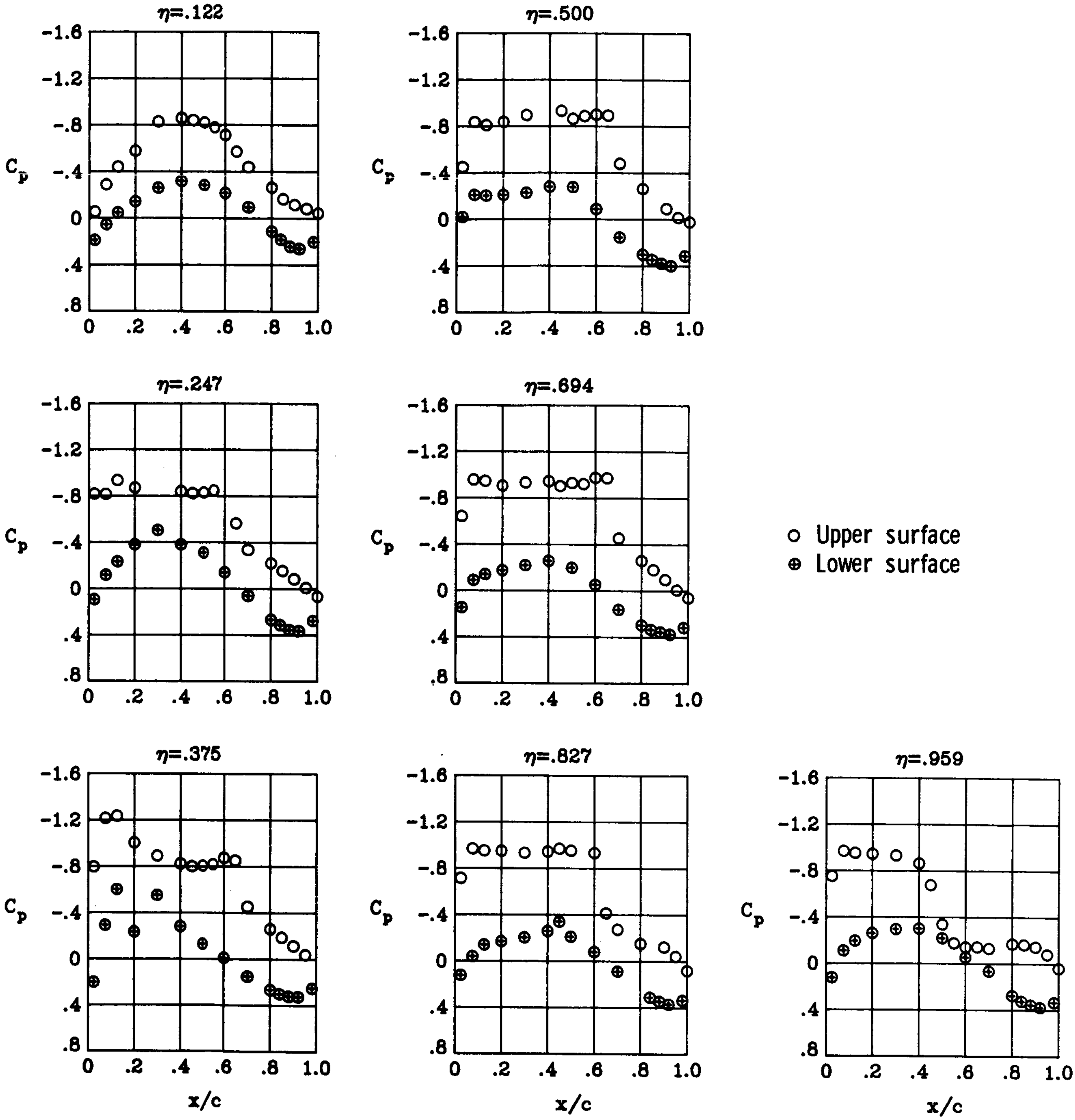

(c) $M_\infty = 0.84$; $\alpha = 3°$.

Figure 17.- Continued.

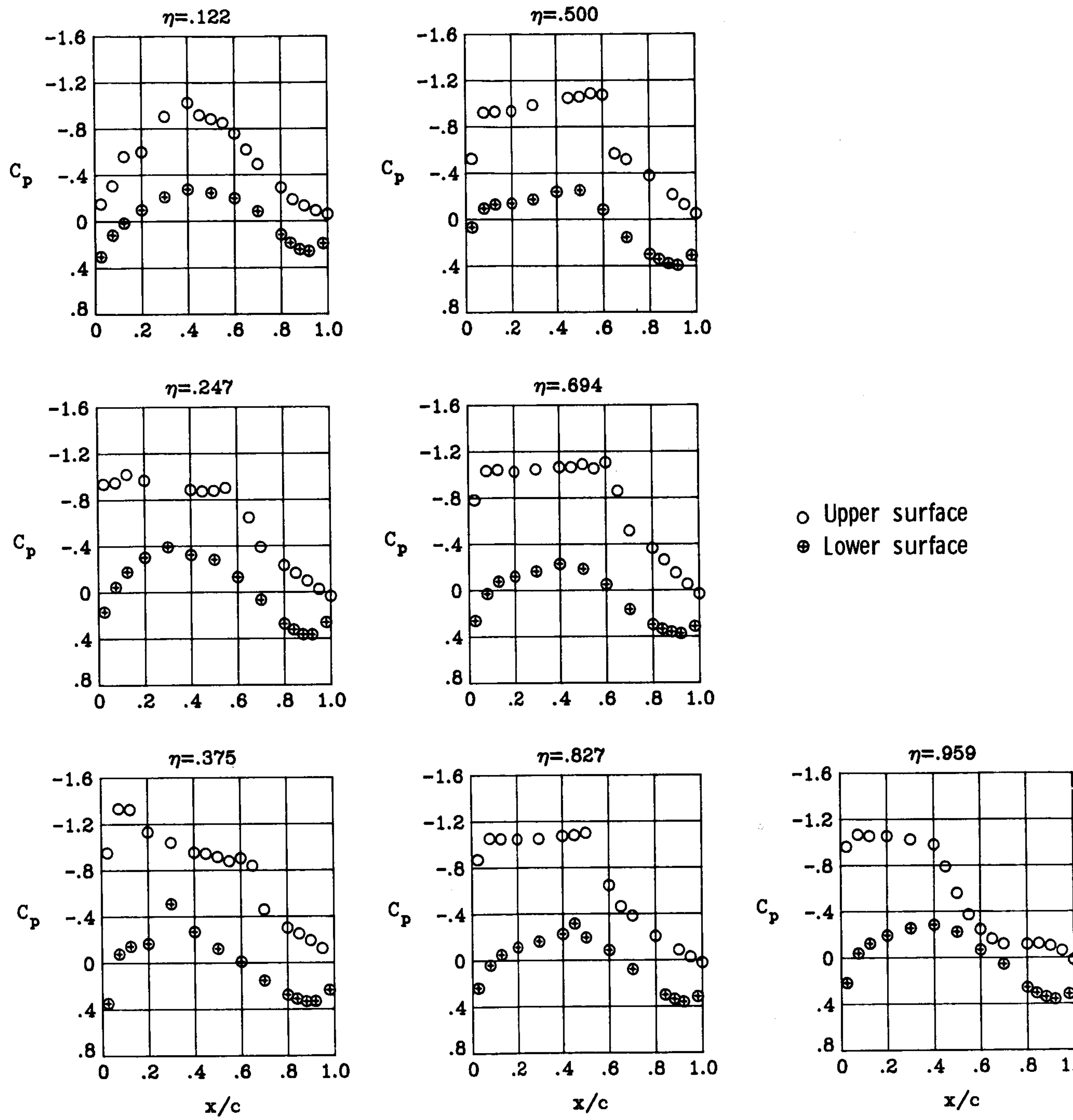

(d) $M_\infty = 0.84$; $\alpha = 4°$.

Figure 17.- Continued.

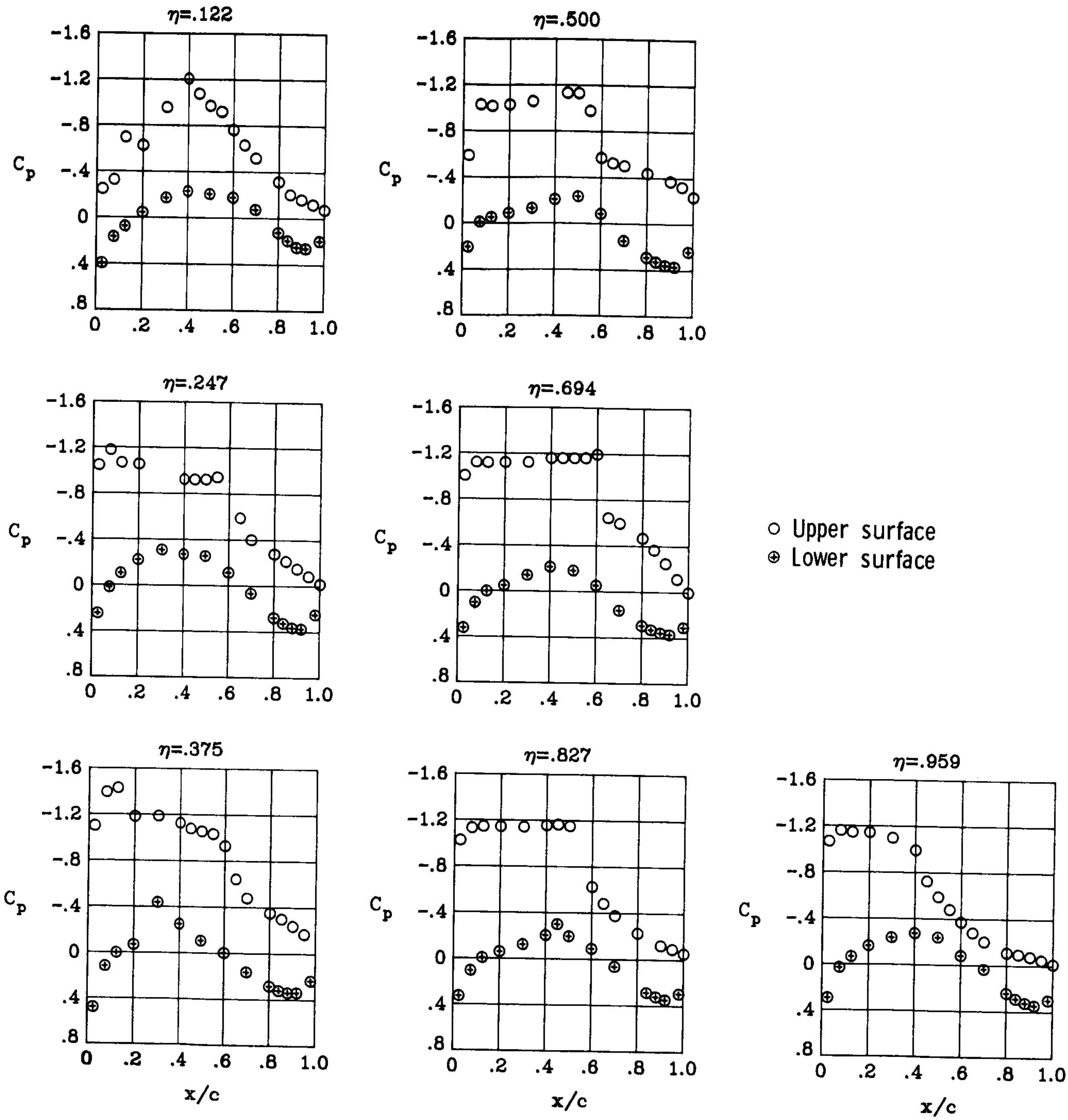

(e) $M_\infty = 0.84$; $\alpha = 5°$.

Figure 17.- Concluded.

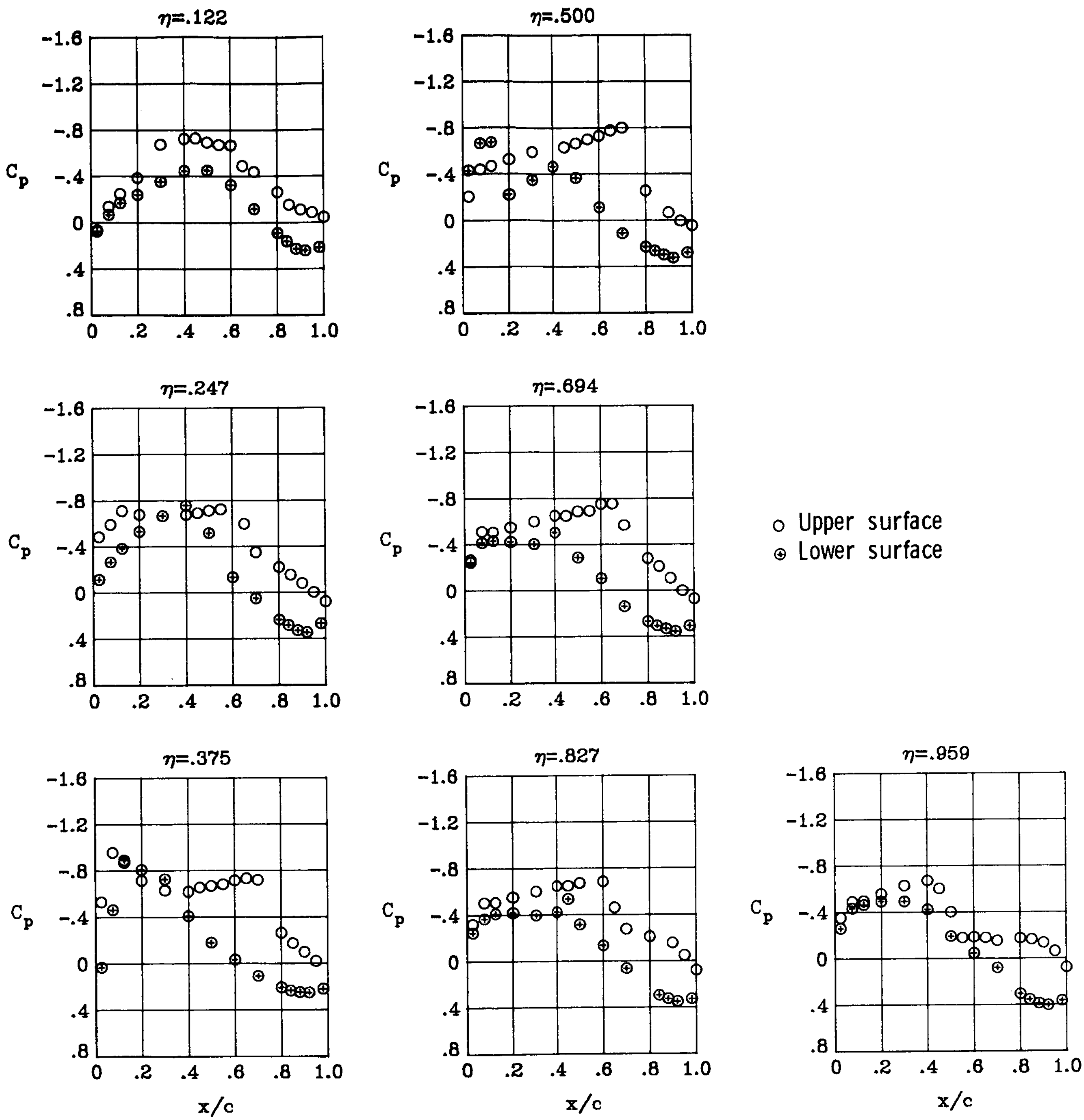

(a) $M_\infty = 0.86$; $\alpha = 1°$.

Figure 18.- Wing chordwise pressure distributions for the baseline configuration at $M_\infty = 0.86$.

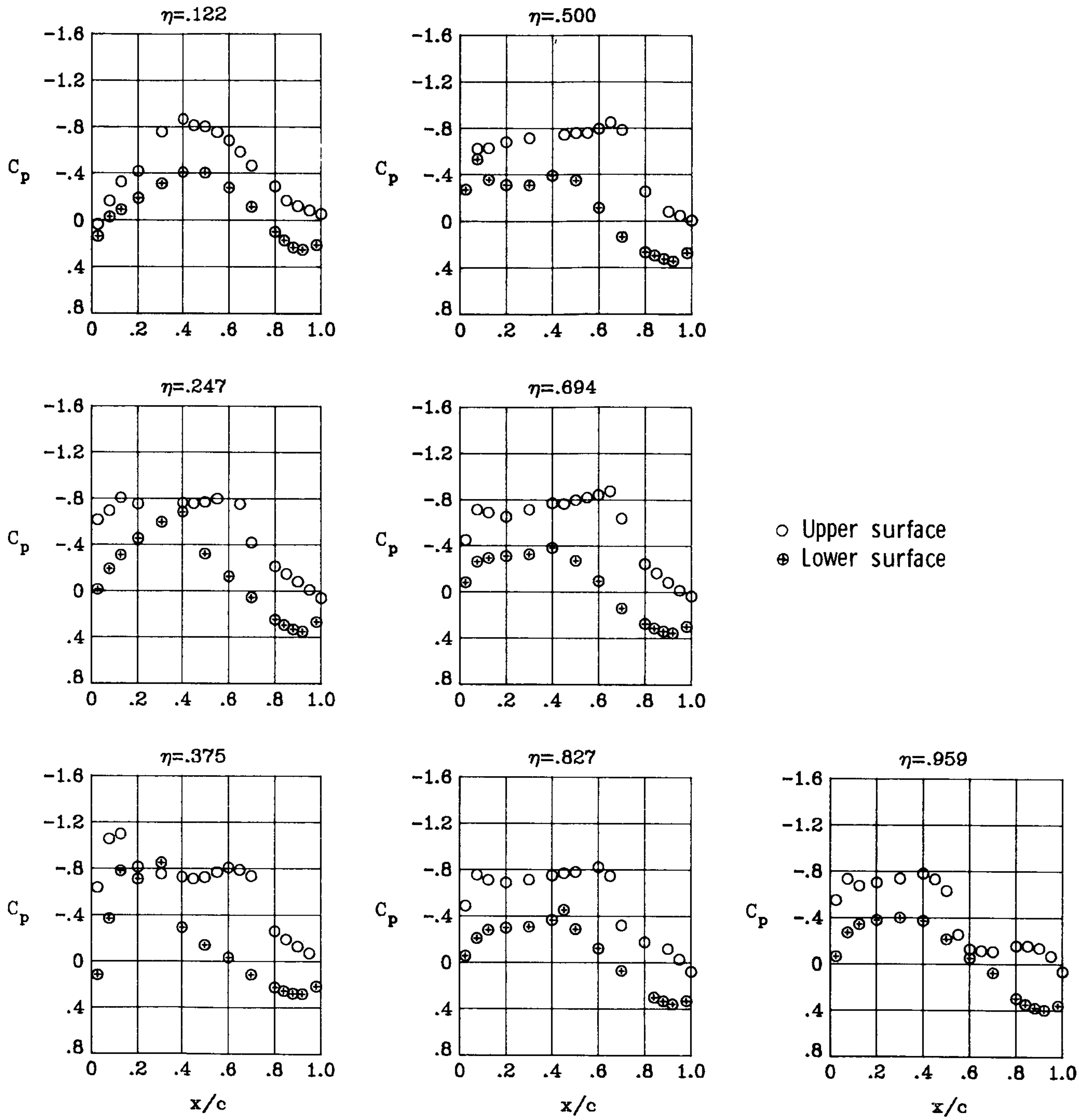

(b) $M_\infty = 0.86$; $\alpha = 2°$.

Figure 18.- Continued.

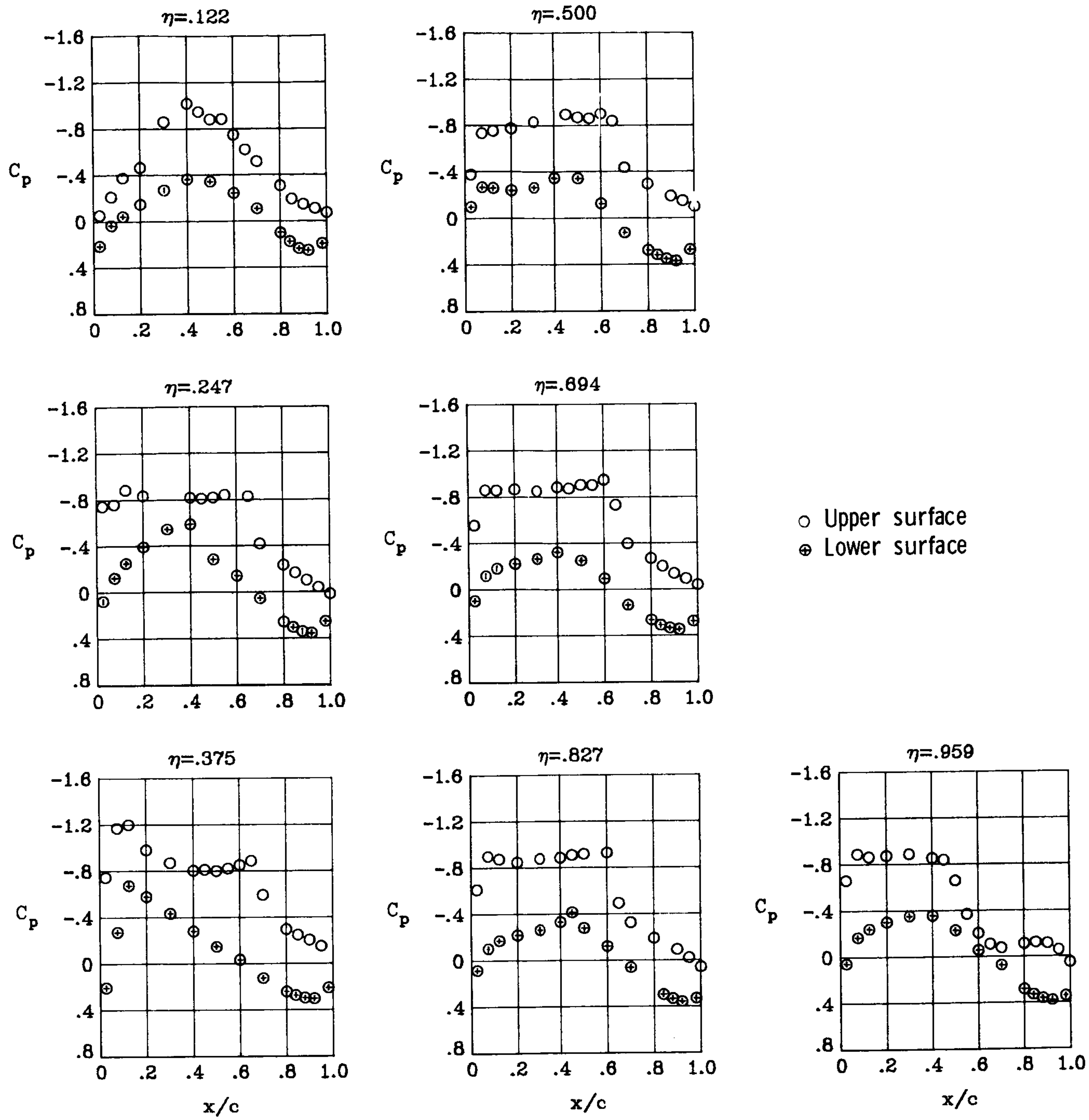

(c) $M_\infty = 0.86$; $\alpha = 3°$.

Figure 18.- Continued.

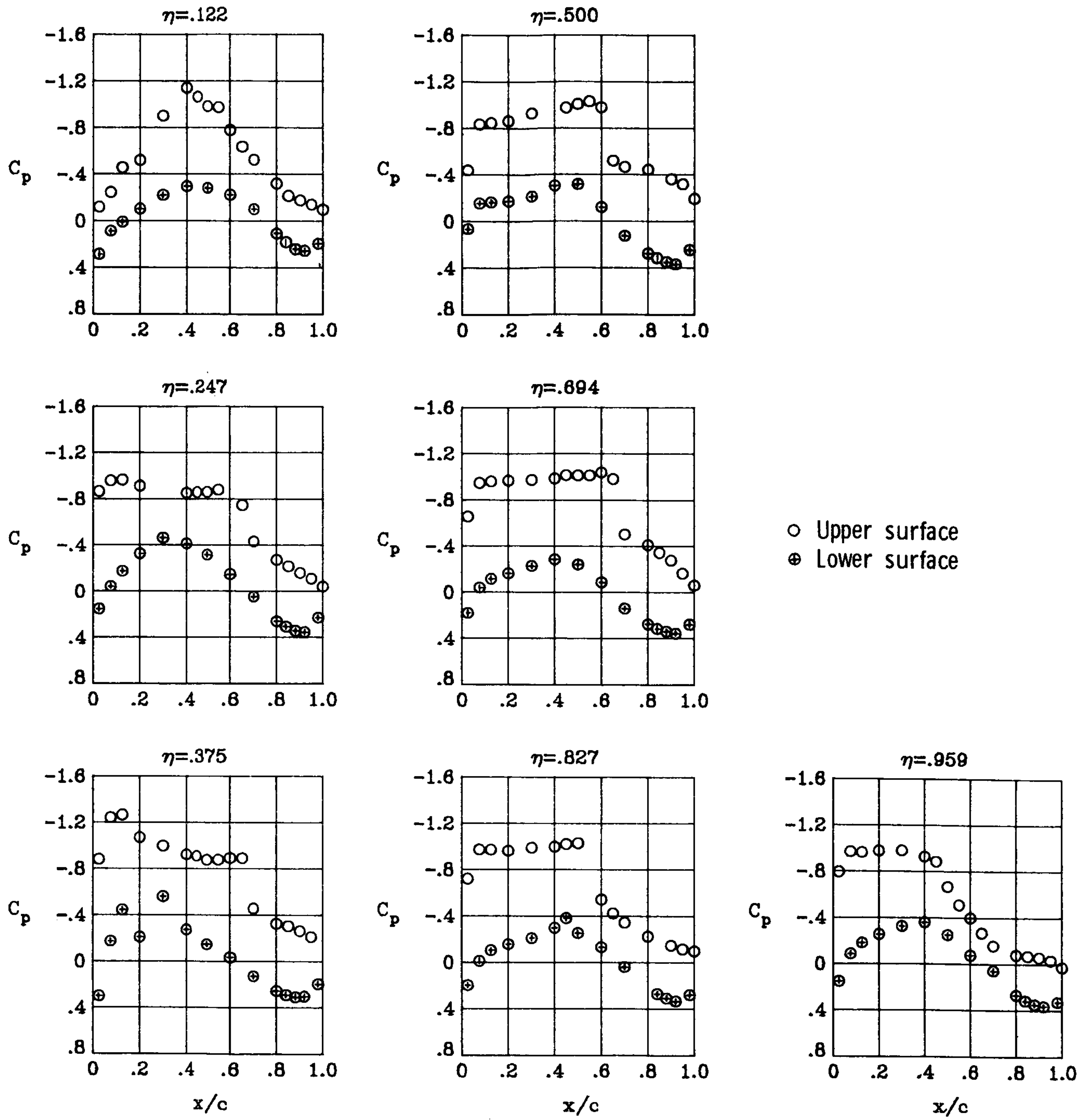

(d) M_∞ = 0.86; α = 4°.

Figure 18.- Continued.

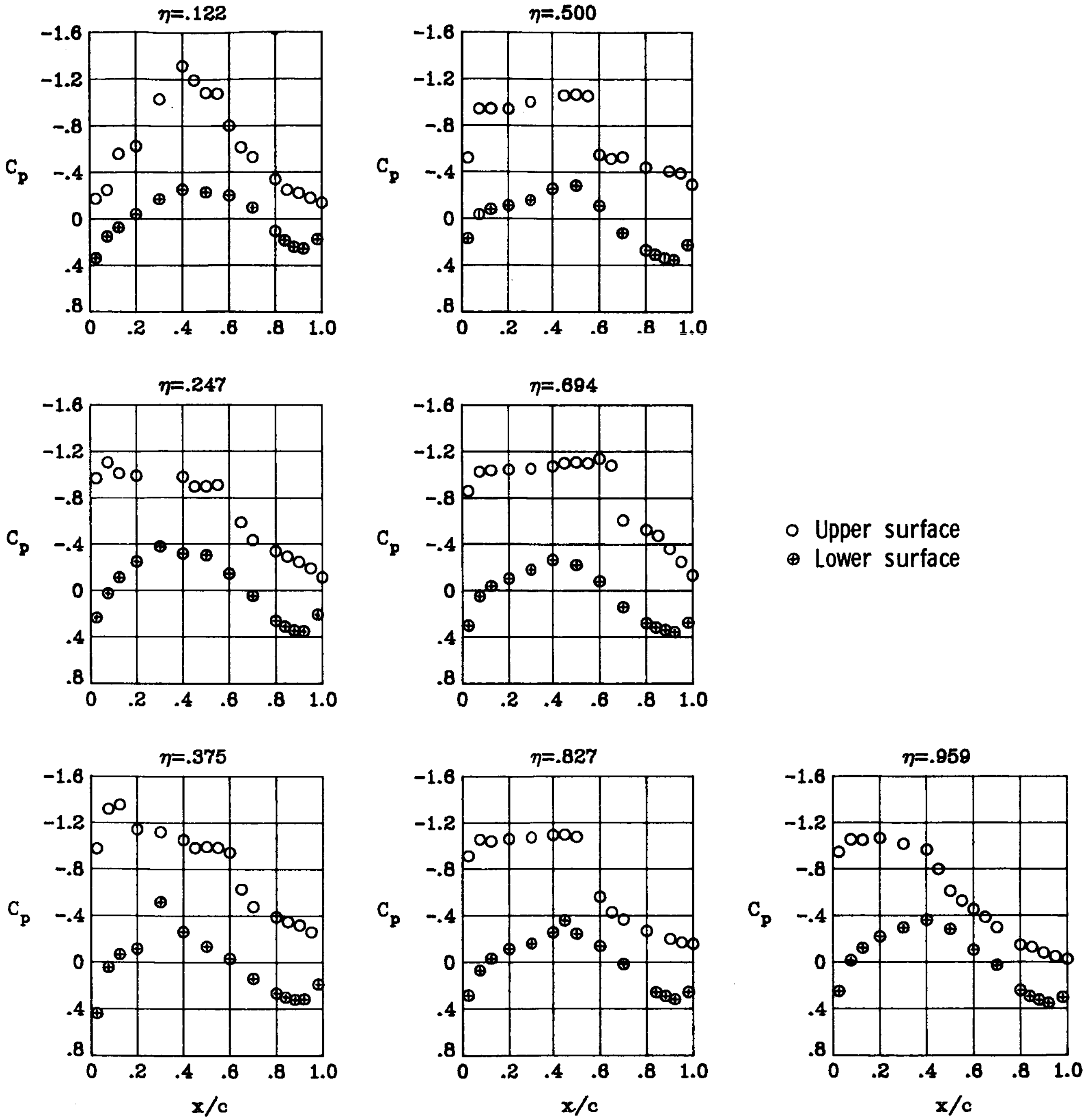

(e) $M_\infty = 0.86$; $\alpha = 5°$.

Figure 18.- Concluded.

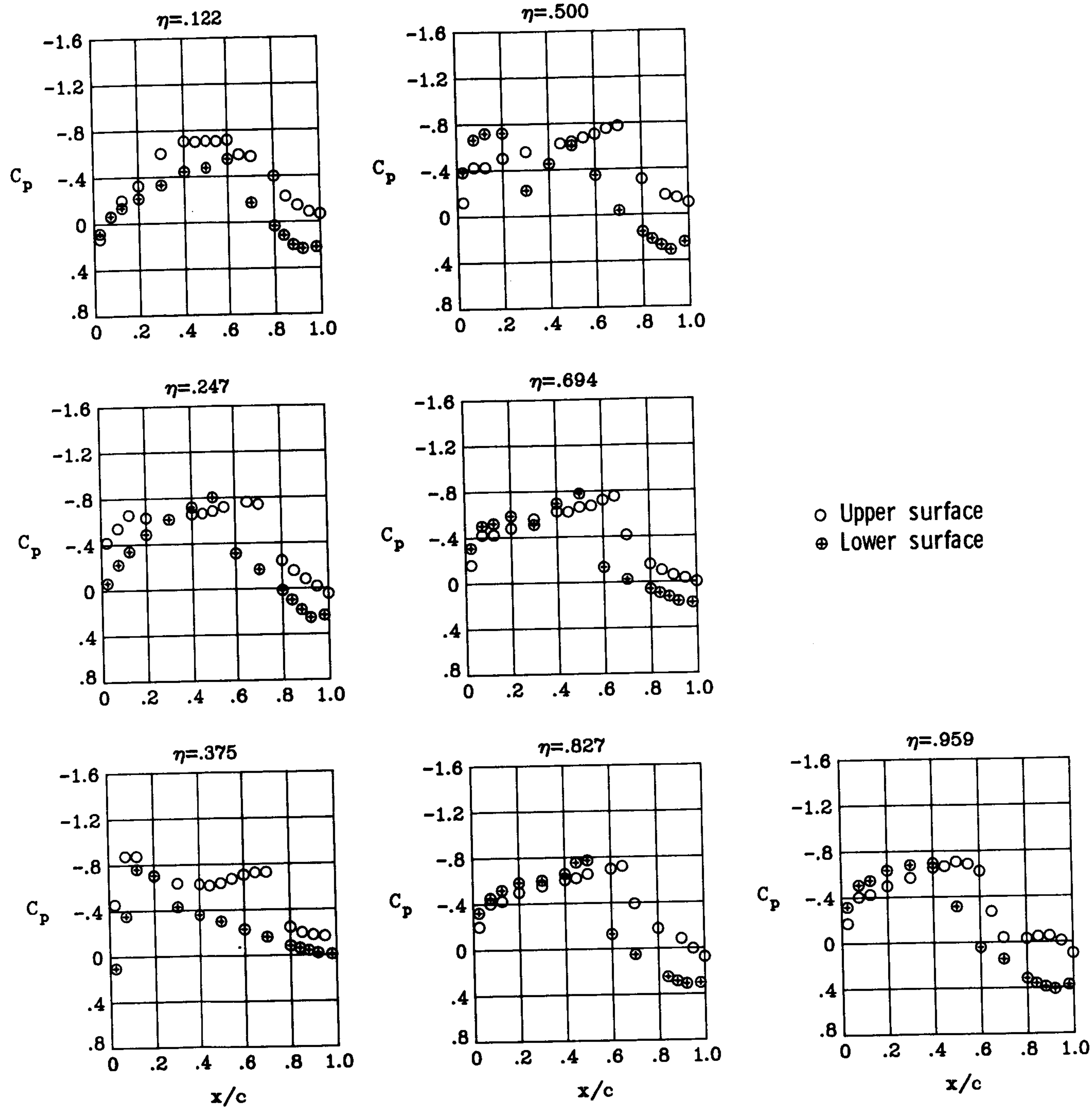

(a) $M_\infty = 0.90$; $\alpha = 1°$.

Figure 19.- Wing chordwise pressure distributions for the baseline configuration at $M_\infty = 0.90$.

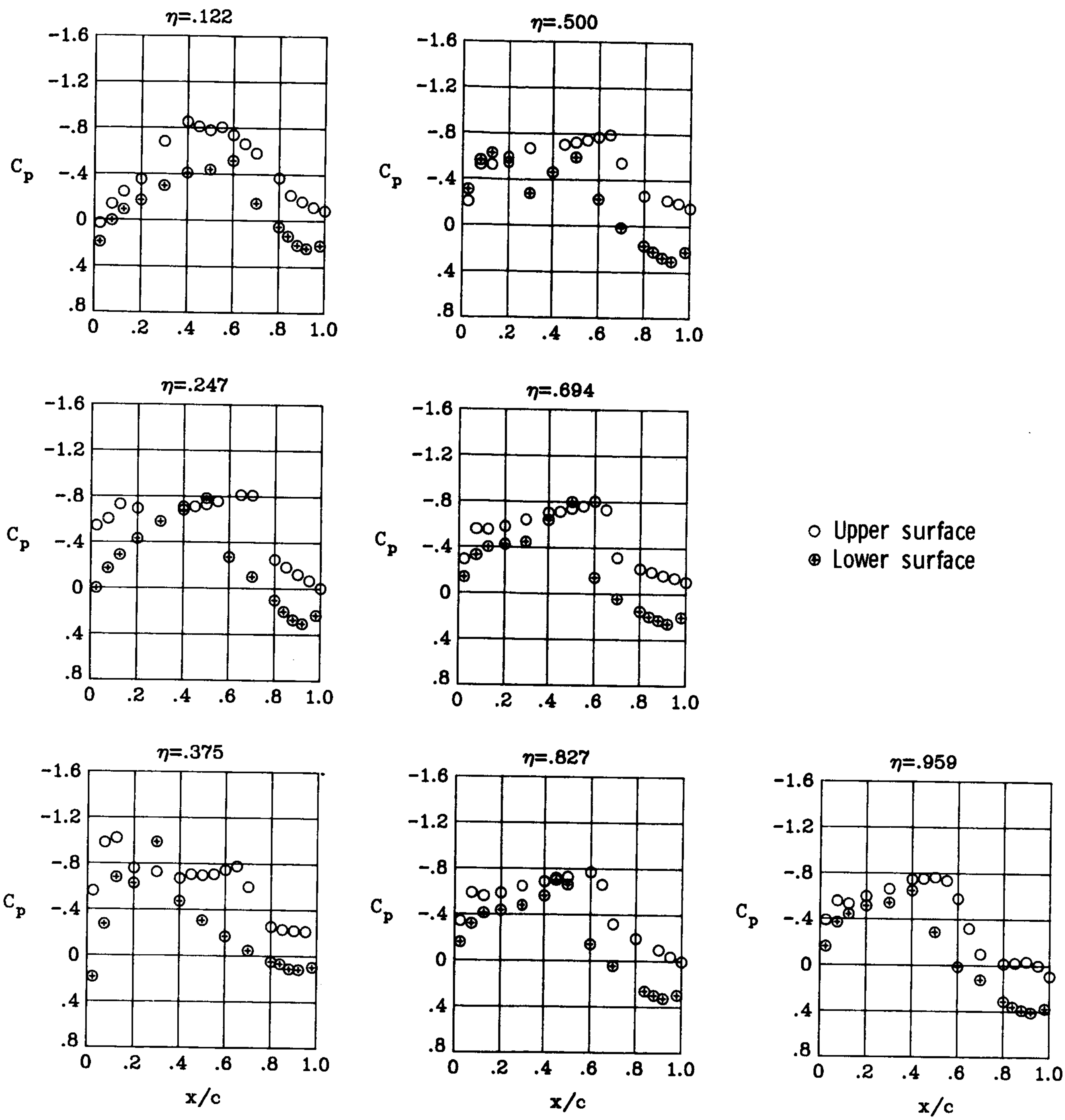

(b) $M_\infty = 0.90$; $\alpha = 2°$.

Figure 19.- Continued.

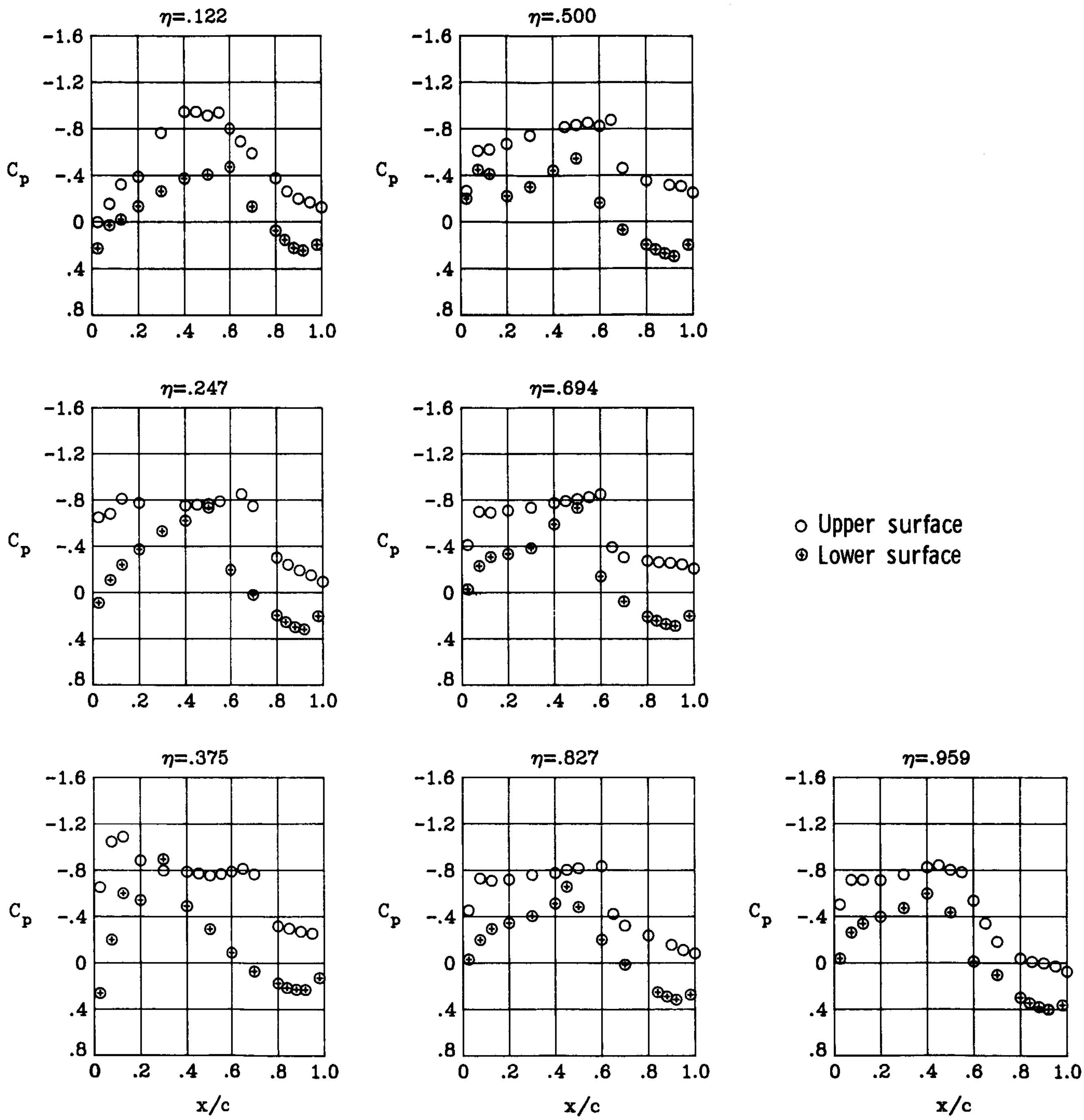

(c) $M_\infty = 0.90$; $\alpha = 3°$.

Figure 19.- Continued.

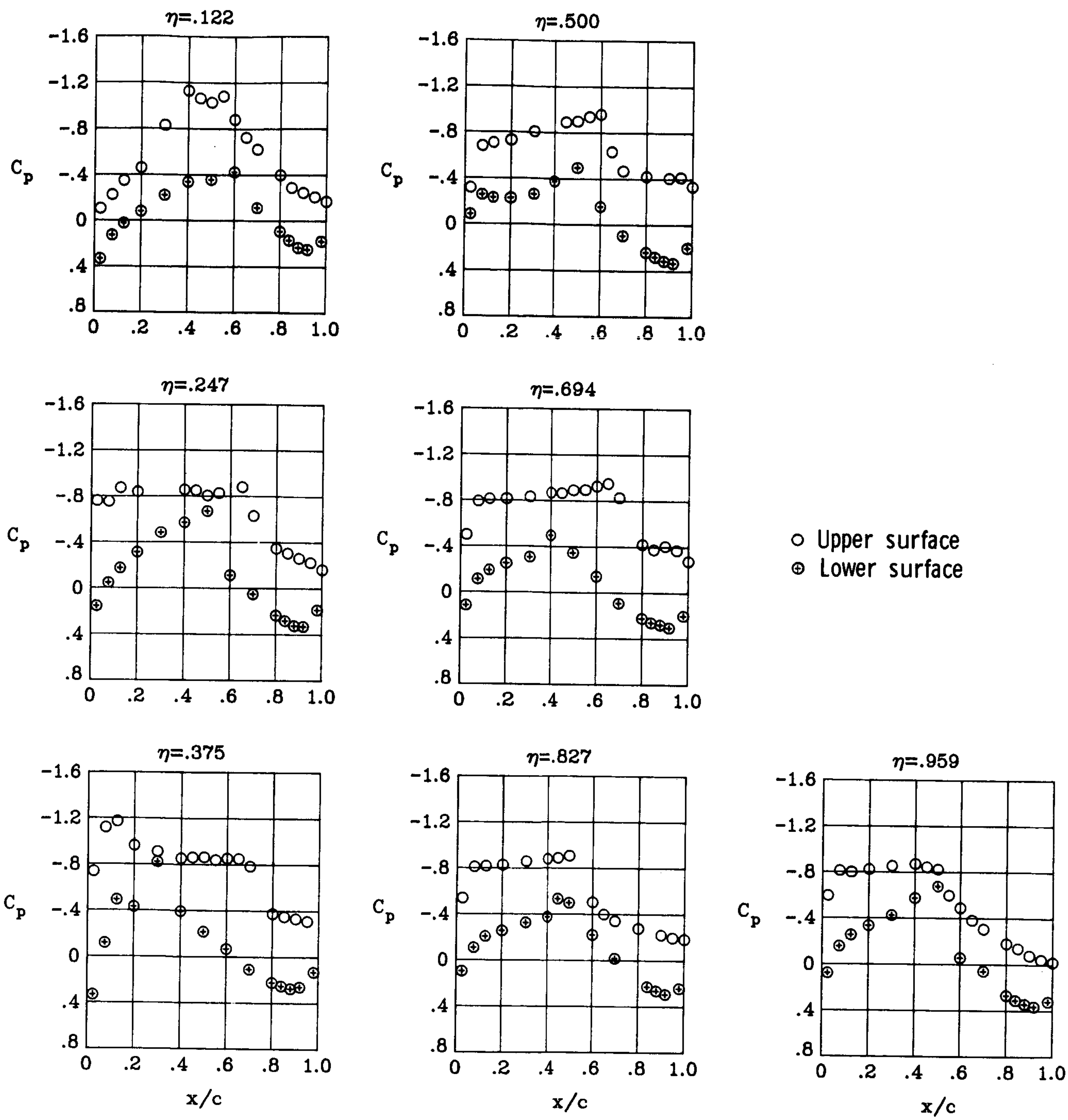

(d) $M_\infty = 0.90$; $\alpha = 4°$.

Figure 19.- Continued.

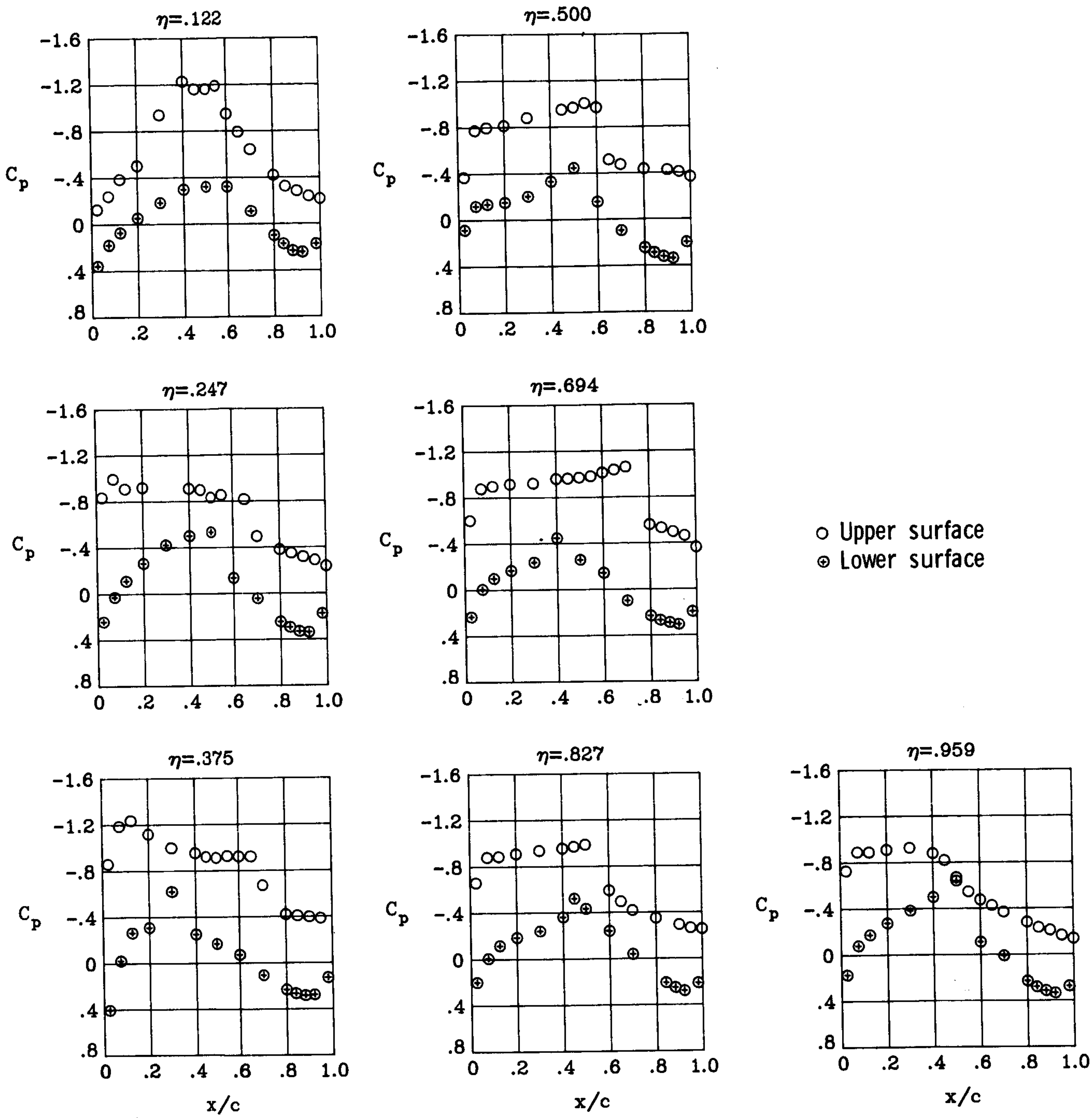

(e) $M_\infty = 0.90$; $\alpha = 5°$.

Figure 19.- Concluded.

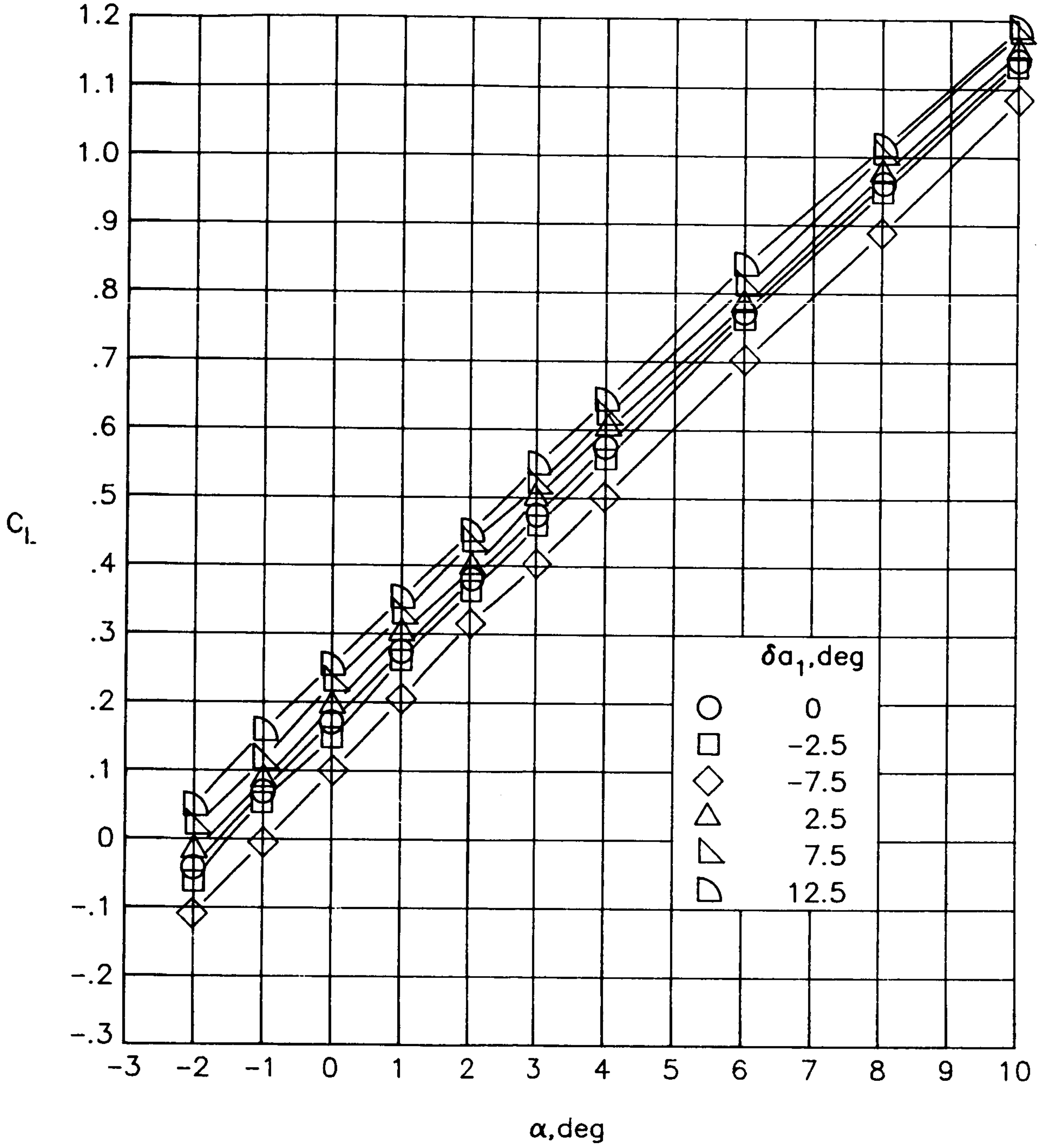

(a) $M_\infty = 0.30$.

Figure 20.- Variation of lift coefficient with angle of attack for deflections of a_1. $\delta a_2 = 0°$.

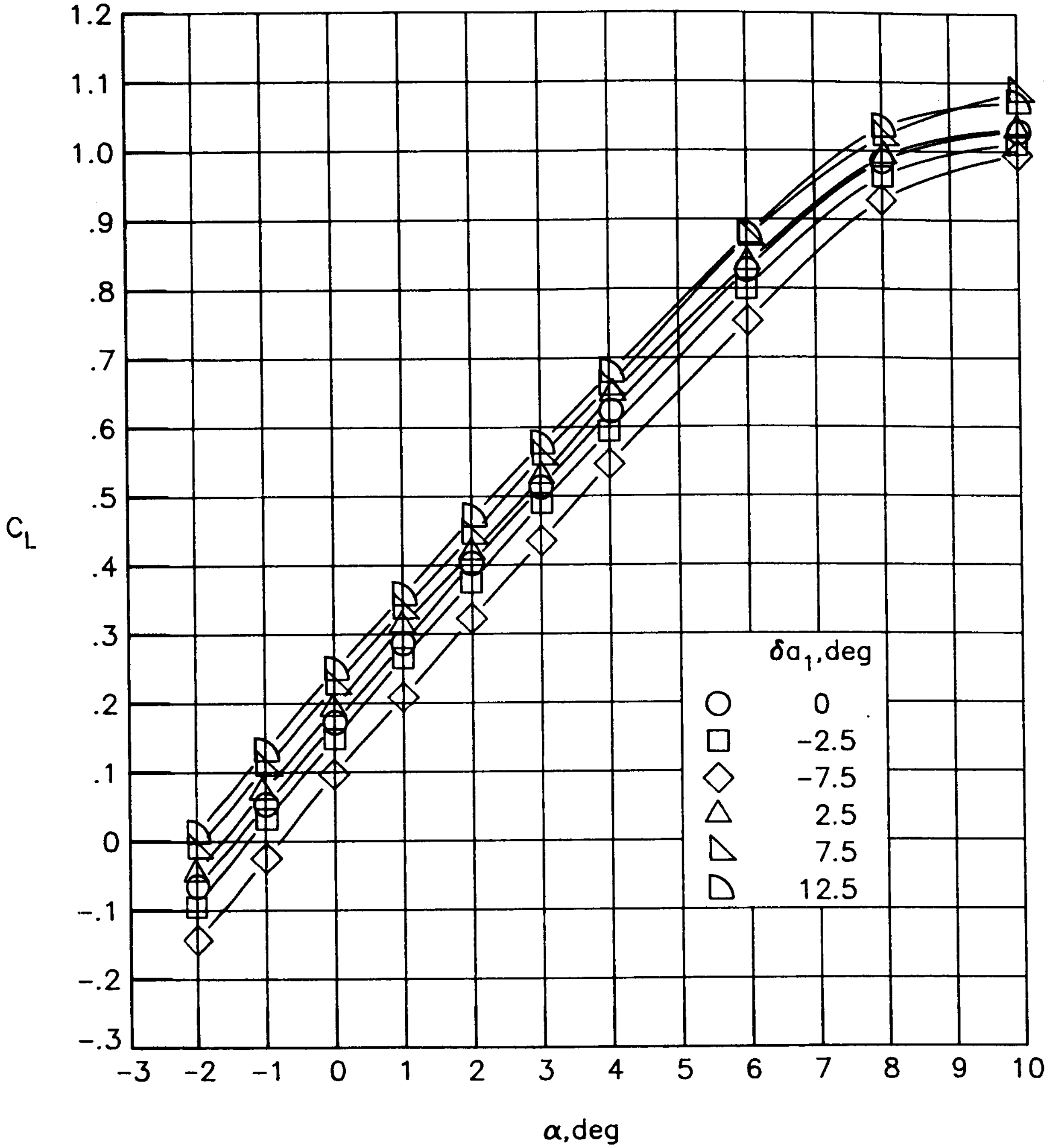

(b) $M_\infty = 0.60$.

Figure 20.- Continued.

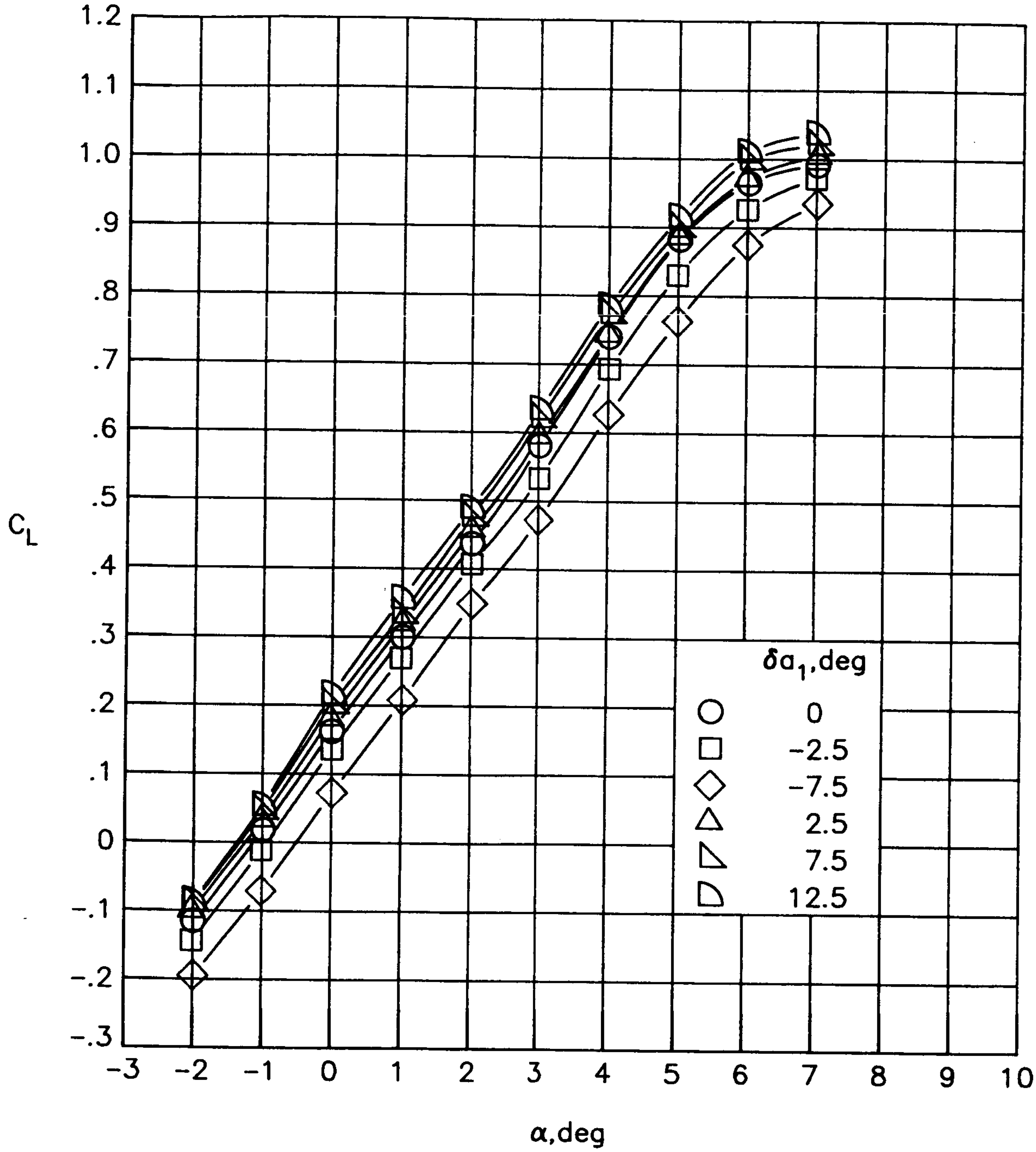

(c) M_∞ = 0.80.

Figure 20.- Continued.

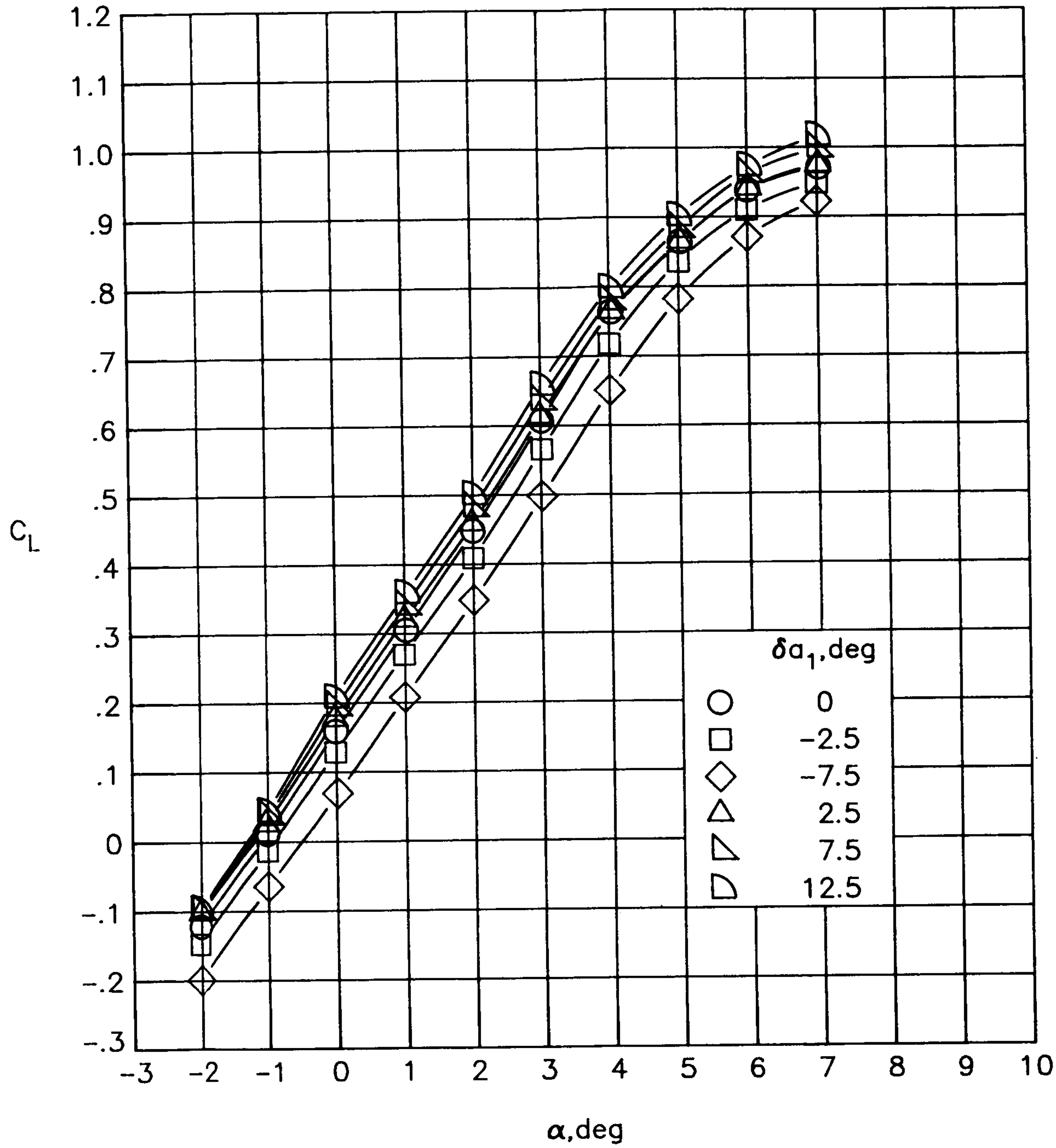

(d) $M_\infty = 0.82$.

Figure 20.- Continued.

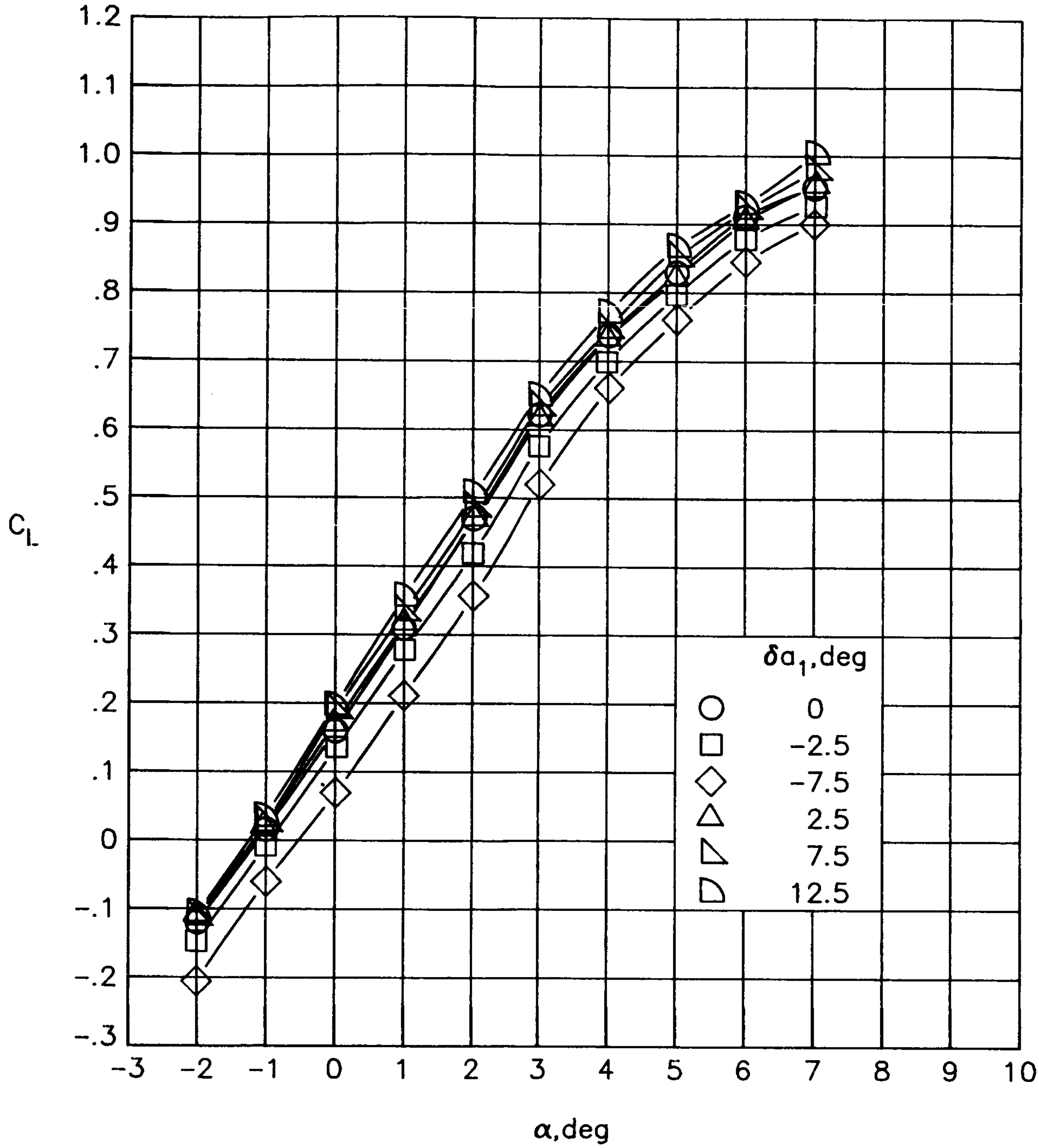

(e) $M_\infty = 0.84$.

Figure 20.- Continued.

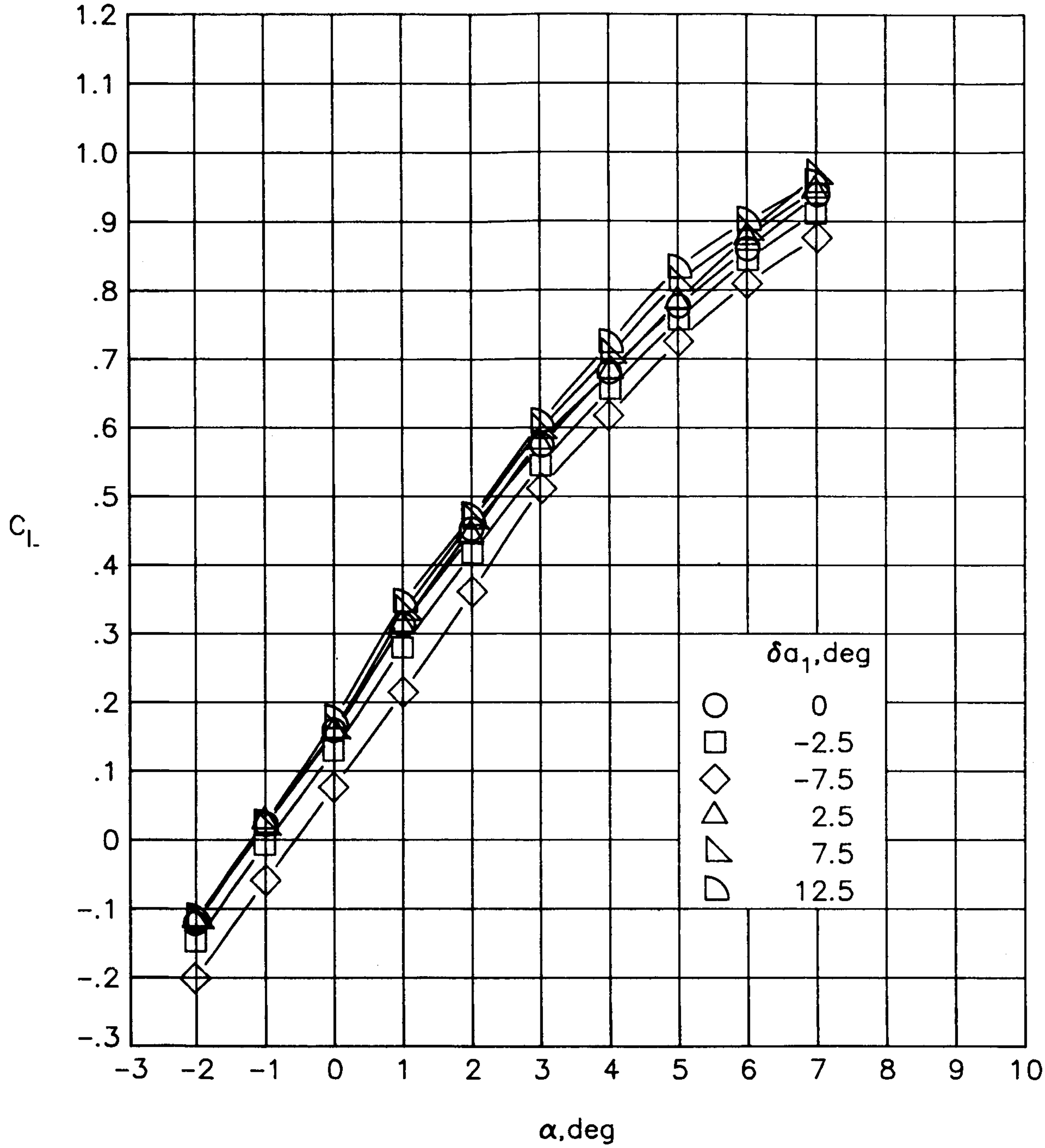

(f) $M_\infty = 0.86$.

Figure 20.- Continued.

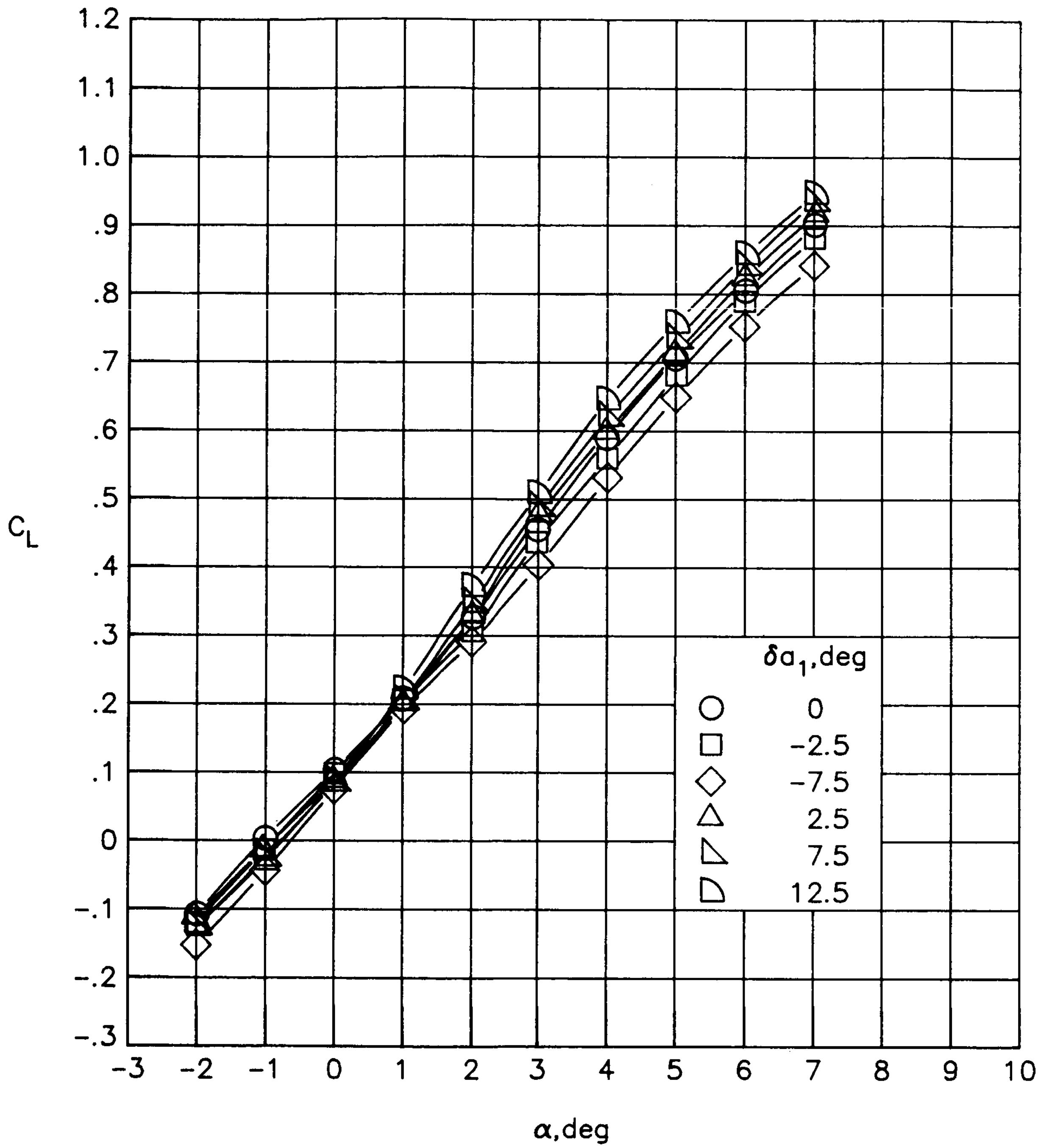

(g) $M_\infty = 0.90$.

Figure 20.- Concluded.

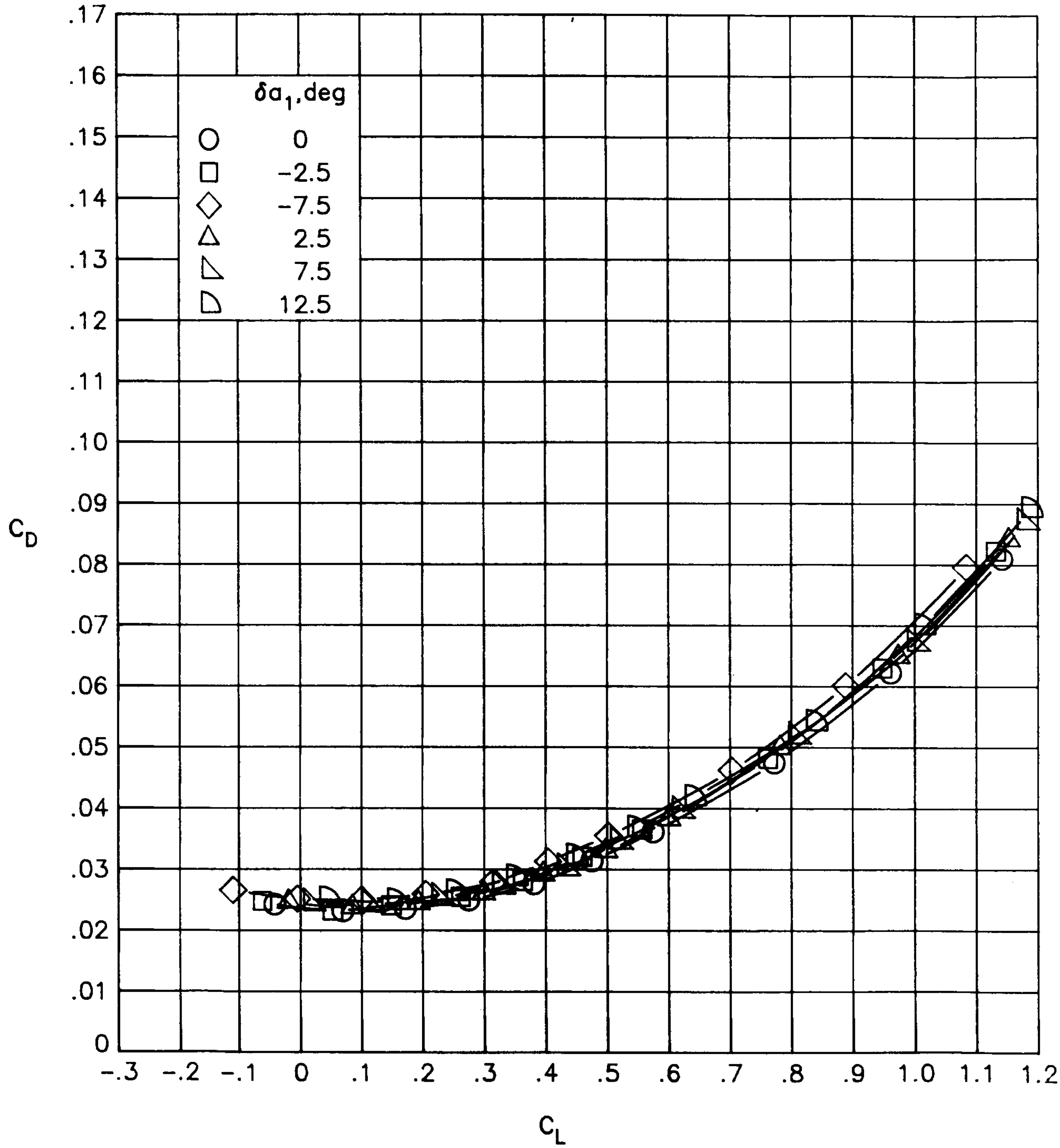

(a) $M_\infty = 0.30$.

Figure 21.- Variation of drag coefficient with lift coefficient for deflections of a_1. $\delta a_2 = 0°$.

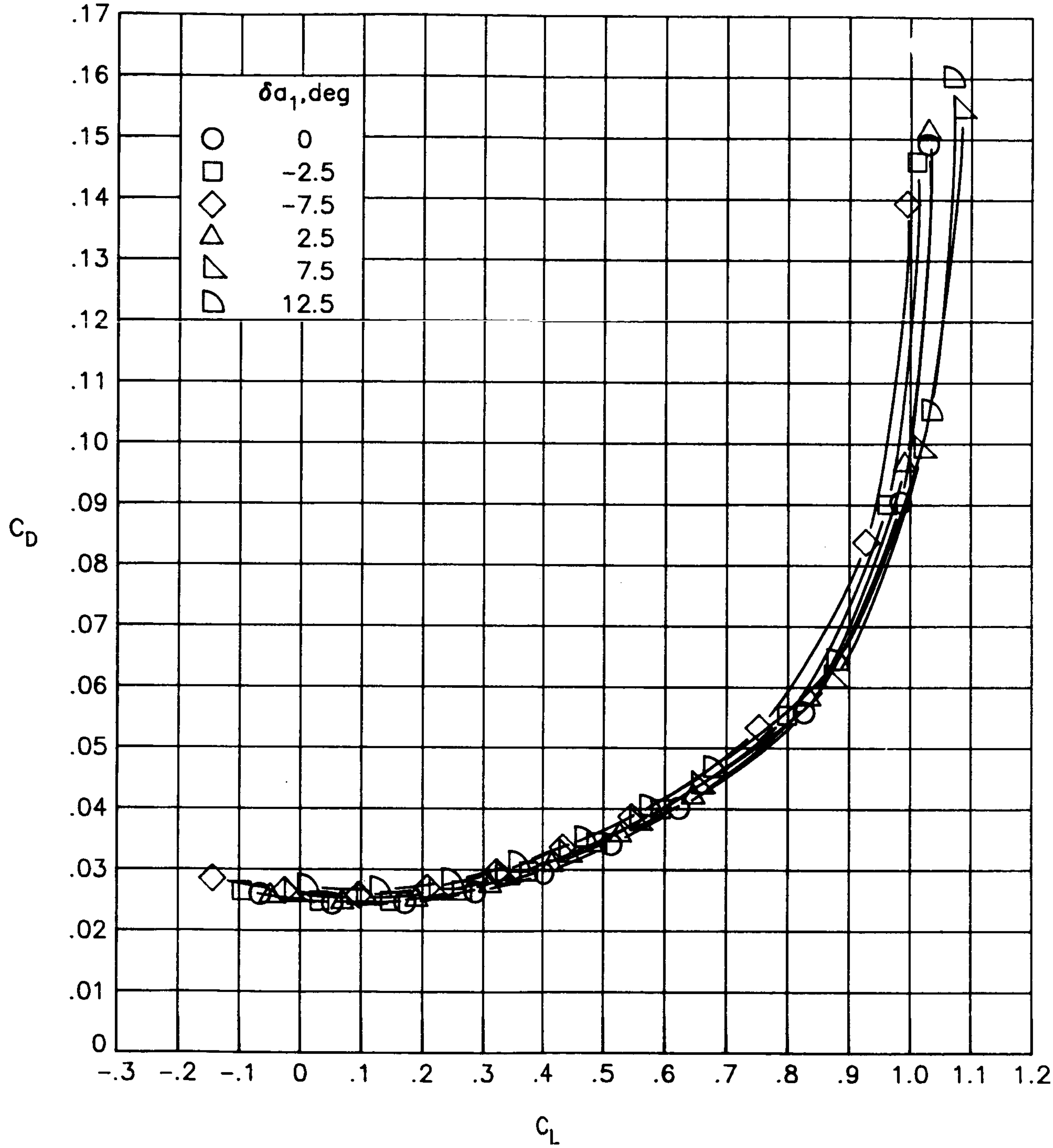

(b) $M_\infty = 0.60$.

Figure 21.- Continued.

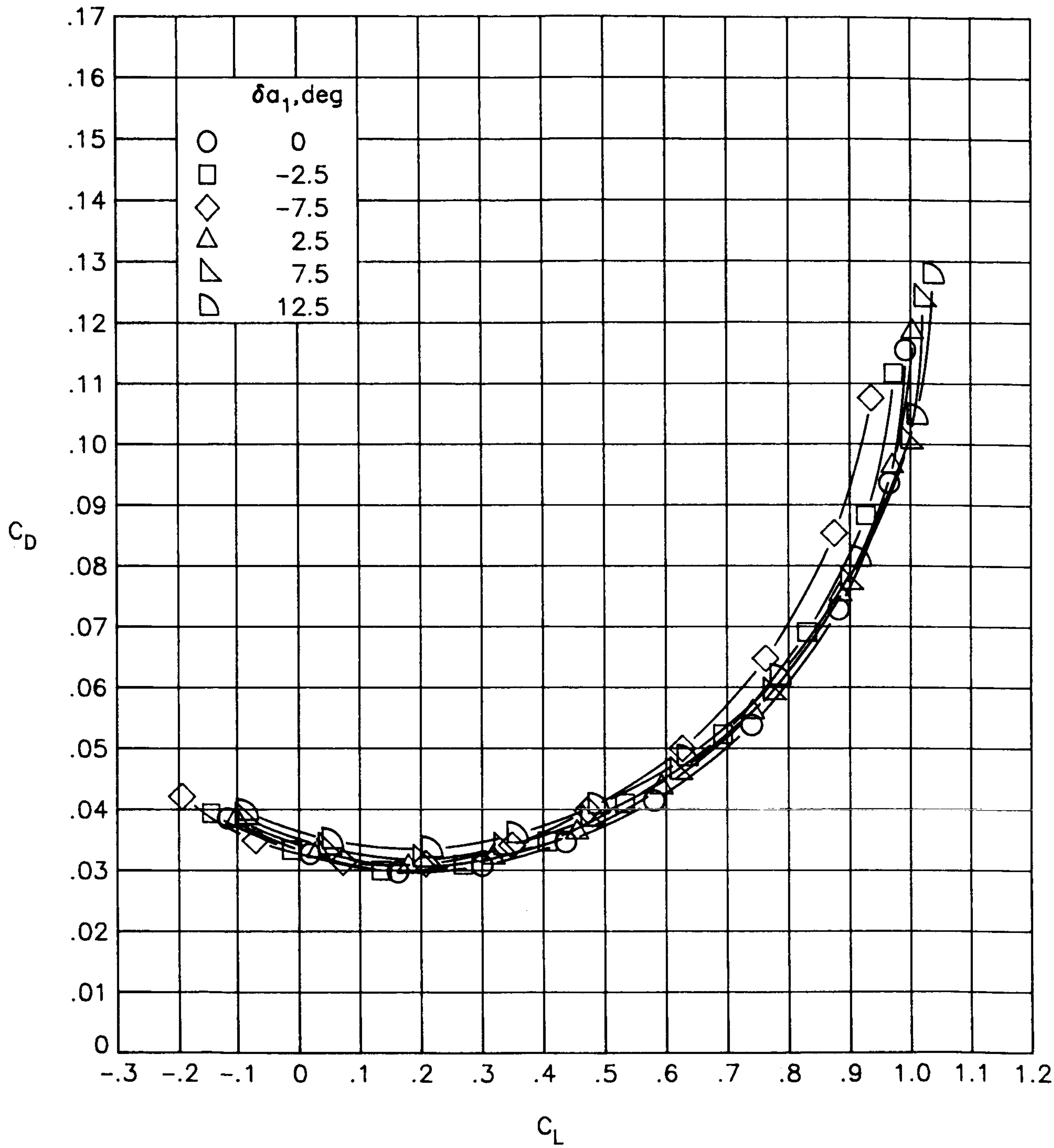

(c) $M_\infty = 0.80$.

Figure 21.- Continued.

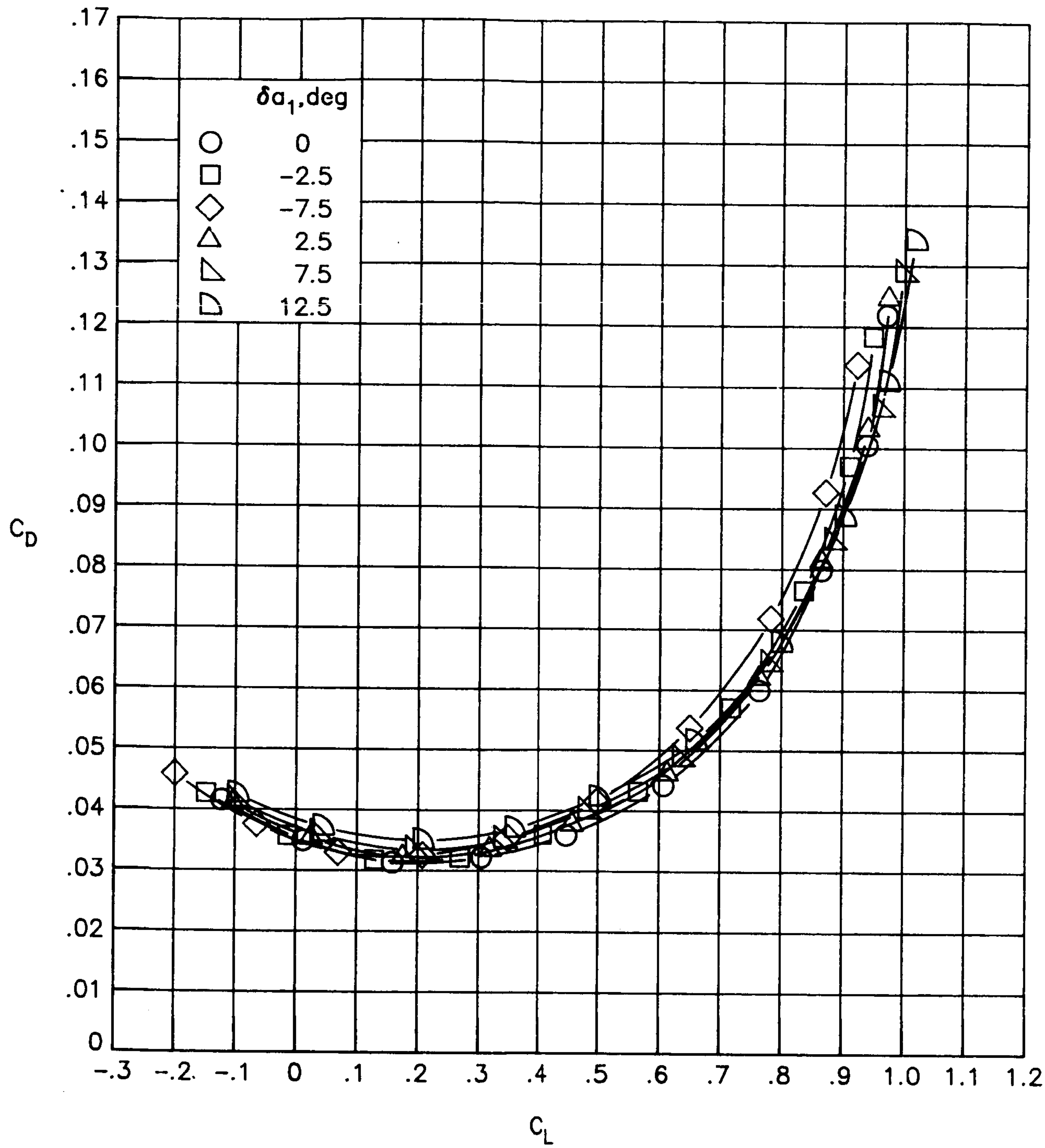

(d) $M_\infty = 0.82$.

Figure 21.- Continued.

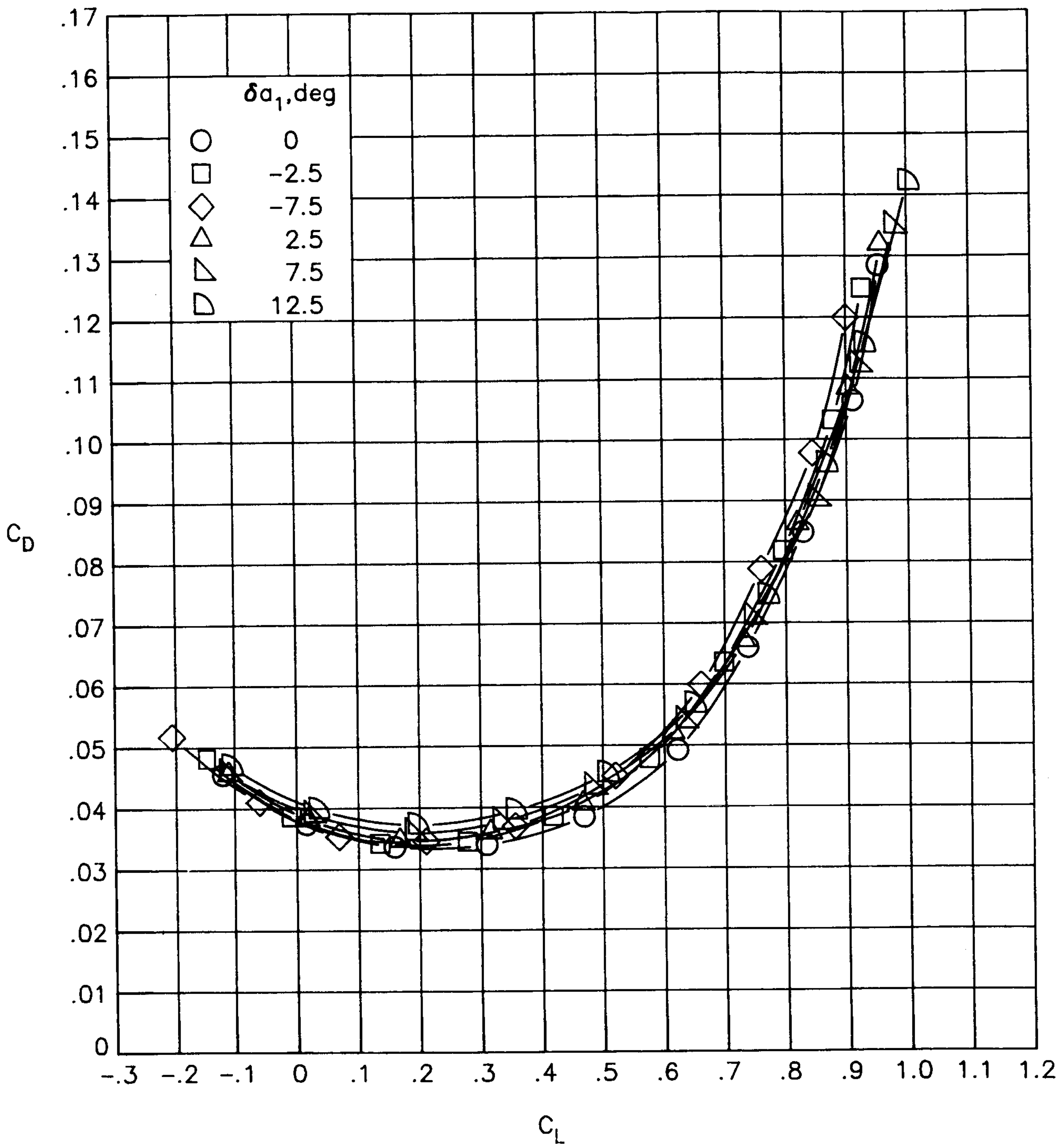

(e) $M_\infty = 0.84$.

Figure 21.- Continued.

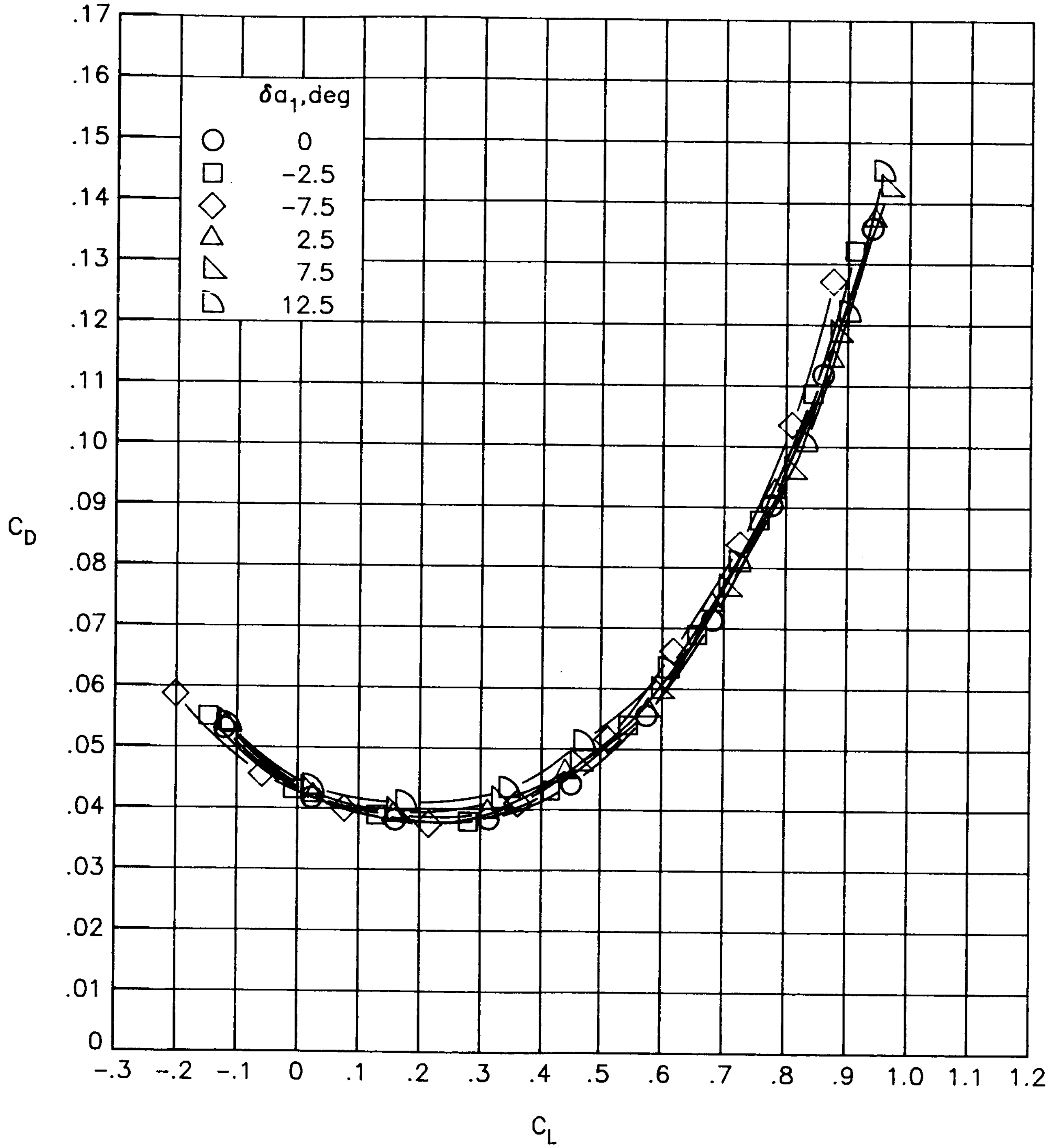

(f) $M_\infty = 0.86$.

Figure 21.- Continued.

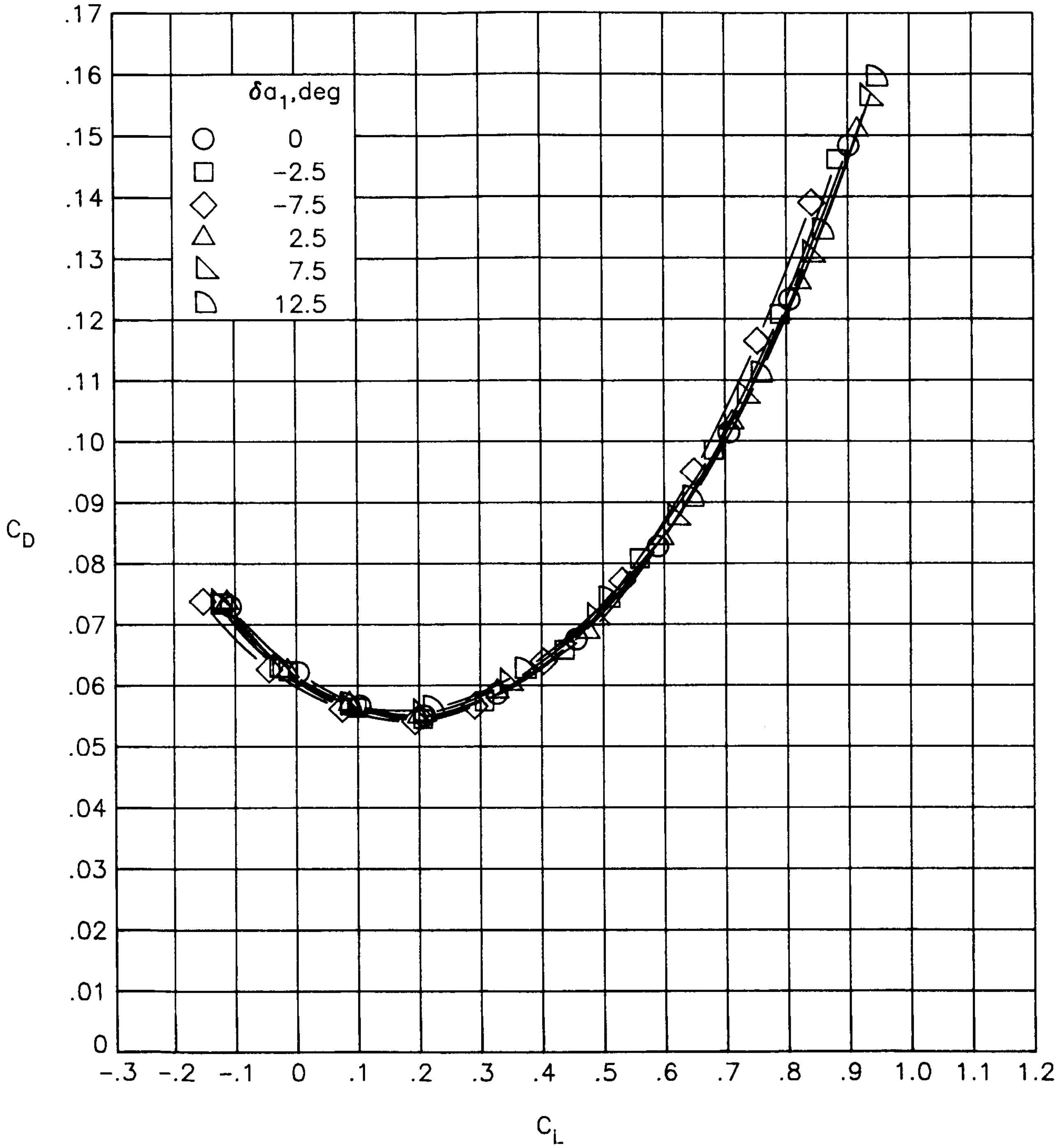

(g) $M_\infty = 0.90$.

Figure 21.- Concluded.

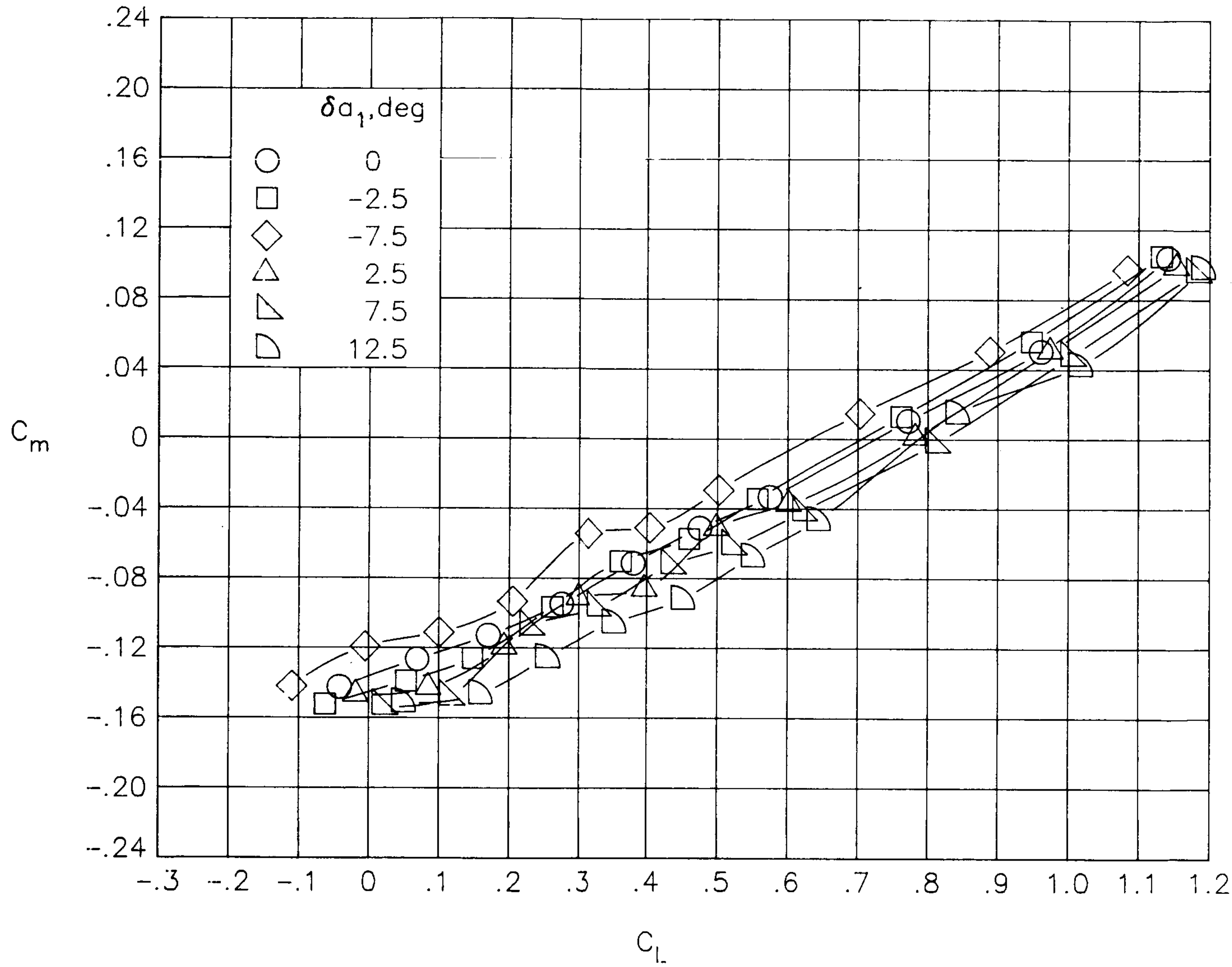

(a) $M_\infty = 0.30$.

Figure 22.- Variation of pitching-moment coefficient with lift coefficient. for deflections of a_1. $\delta a_2 = 0°$.

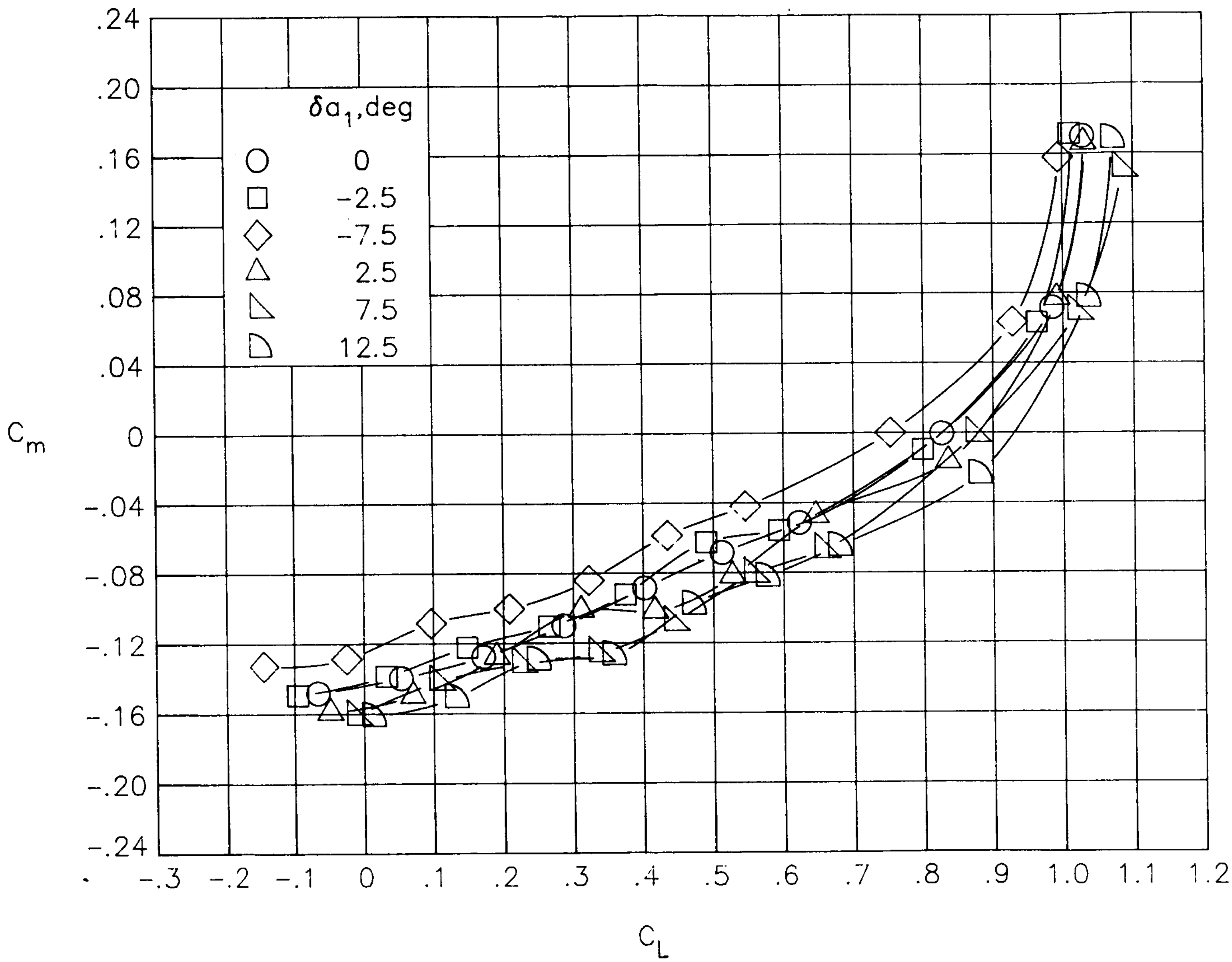

(b) M_∞ = 0.60.

Figure 22.- Continued.

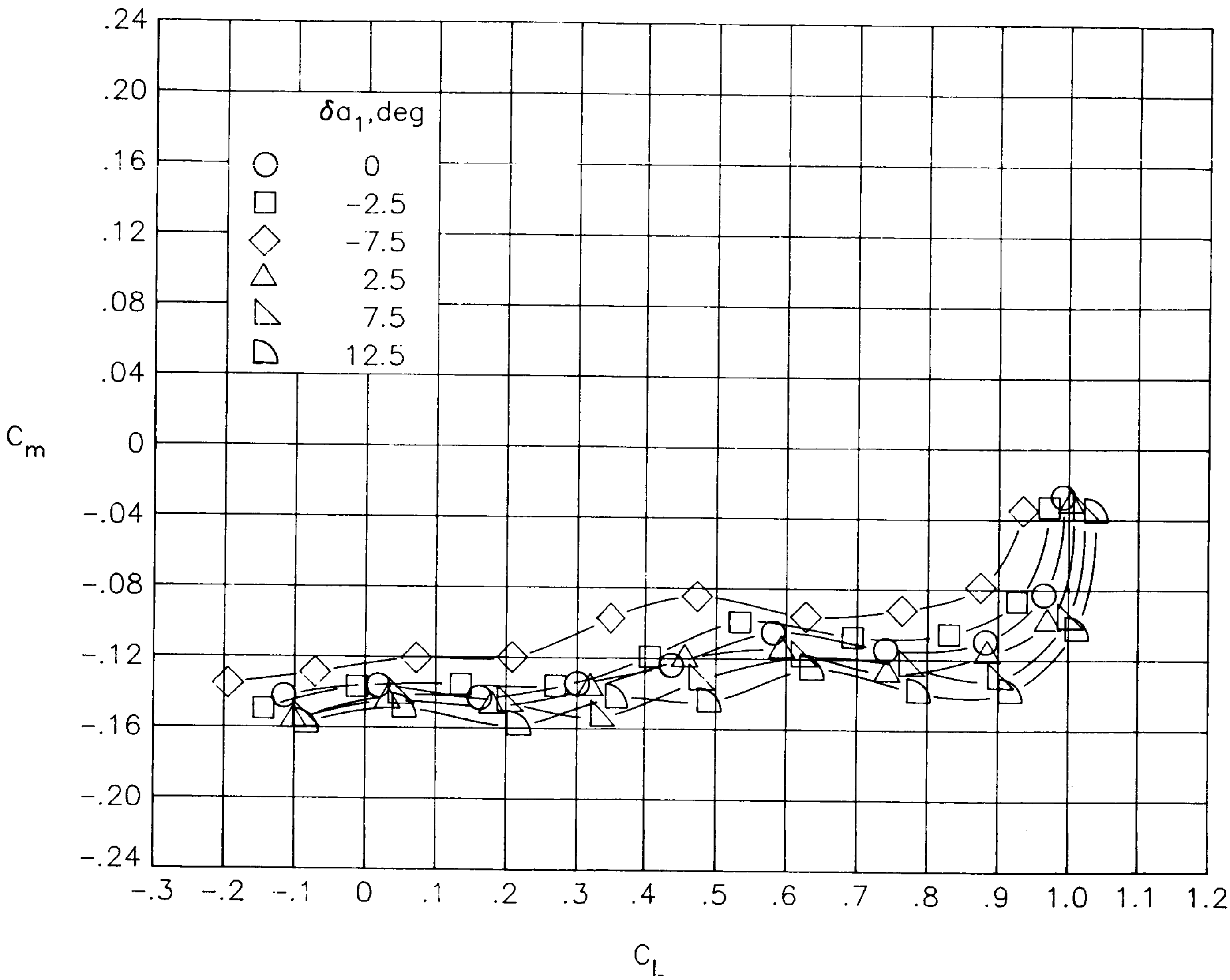

(c) M_∞ = 0.80.

Figure 22.- Continued.

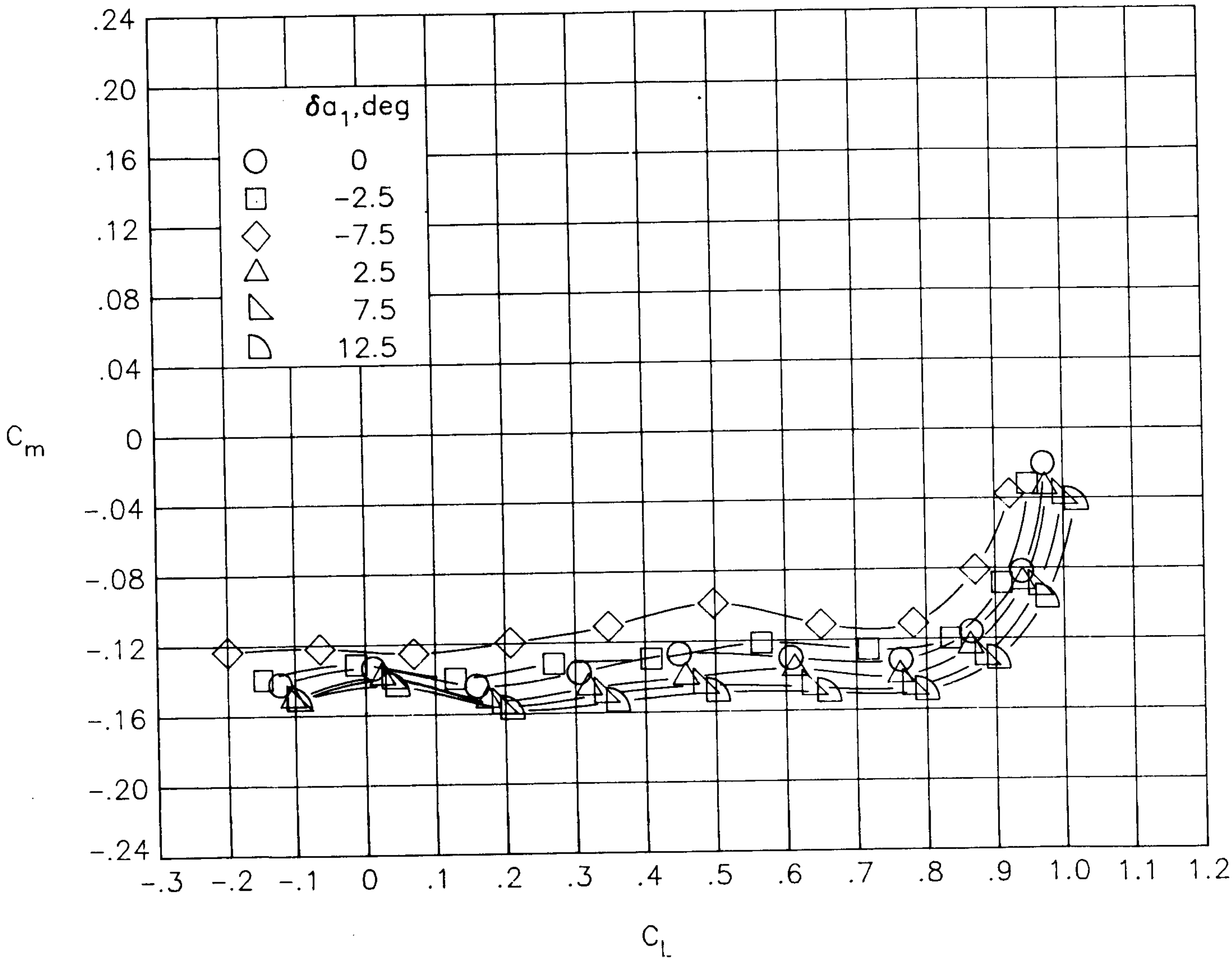

(d) $M_\infty = 0.82$.

Figure 22.- Continued.

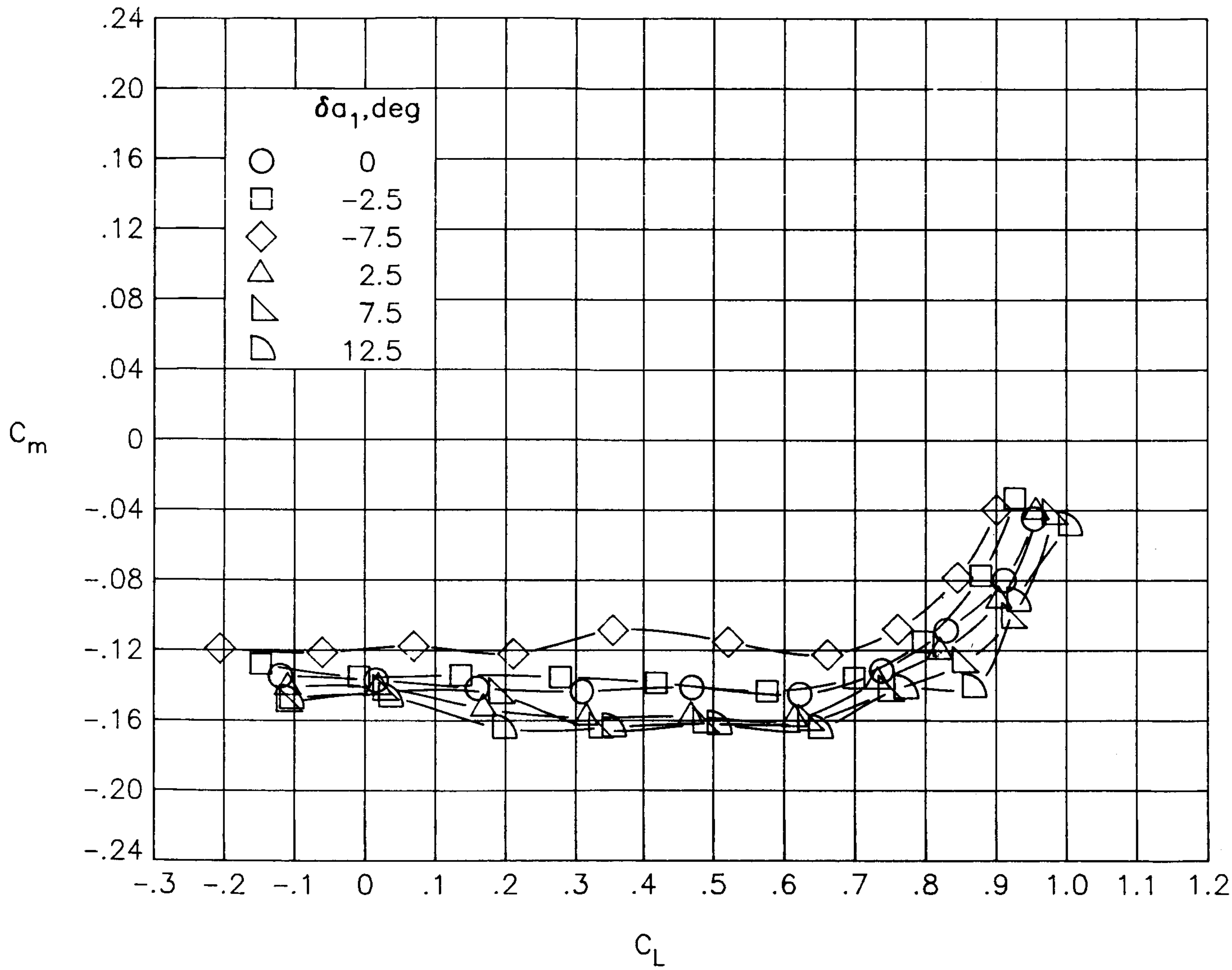

(e) $M_\infty = 0.84$.

Figure 22.- Continued.

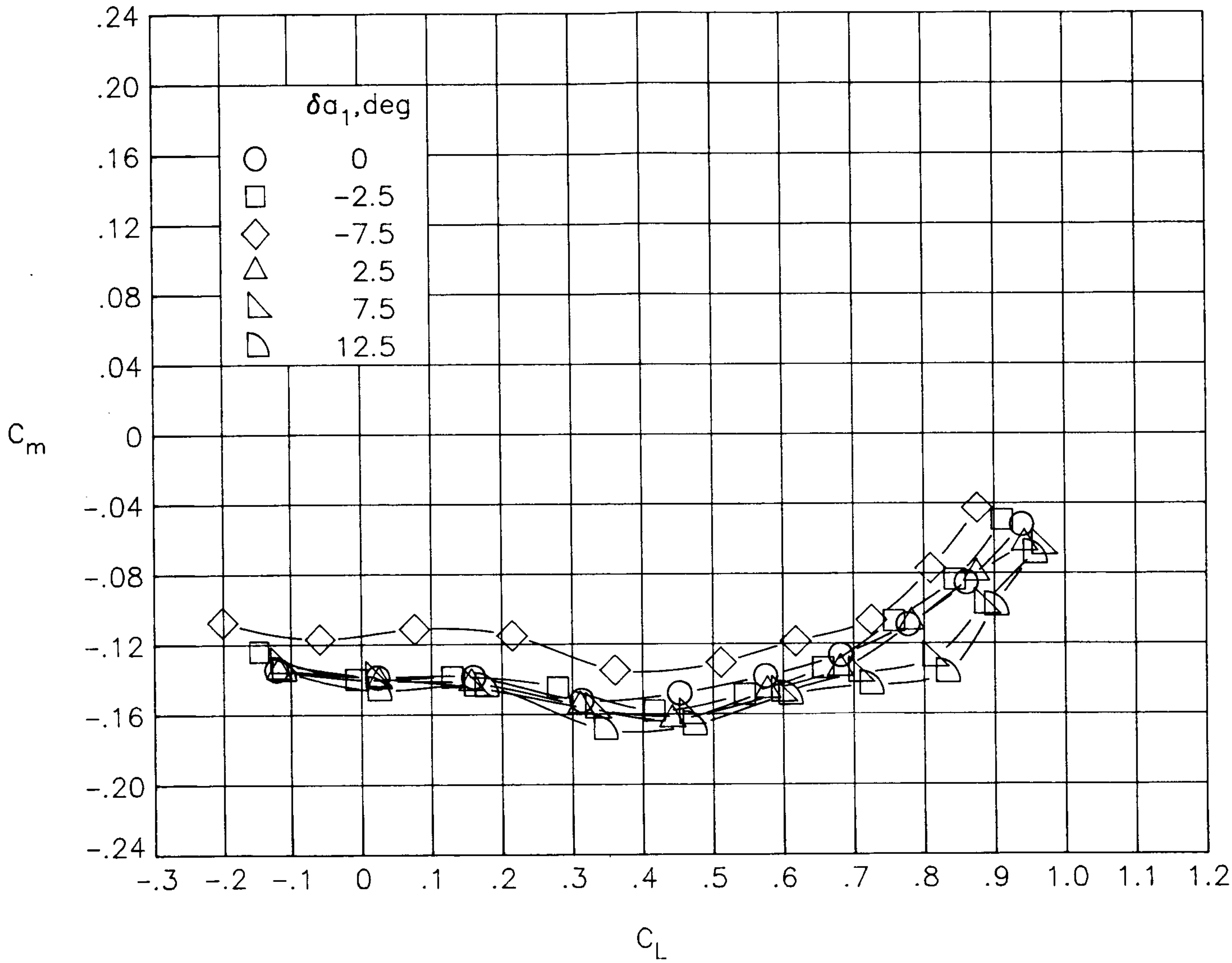

(f) $M_\infty = 0.86$.

Figure 22.- Continued.

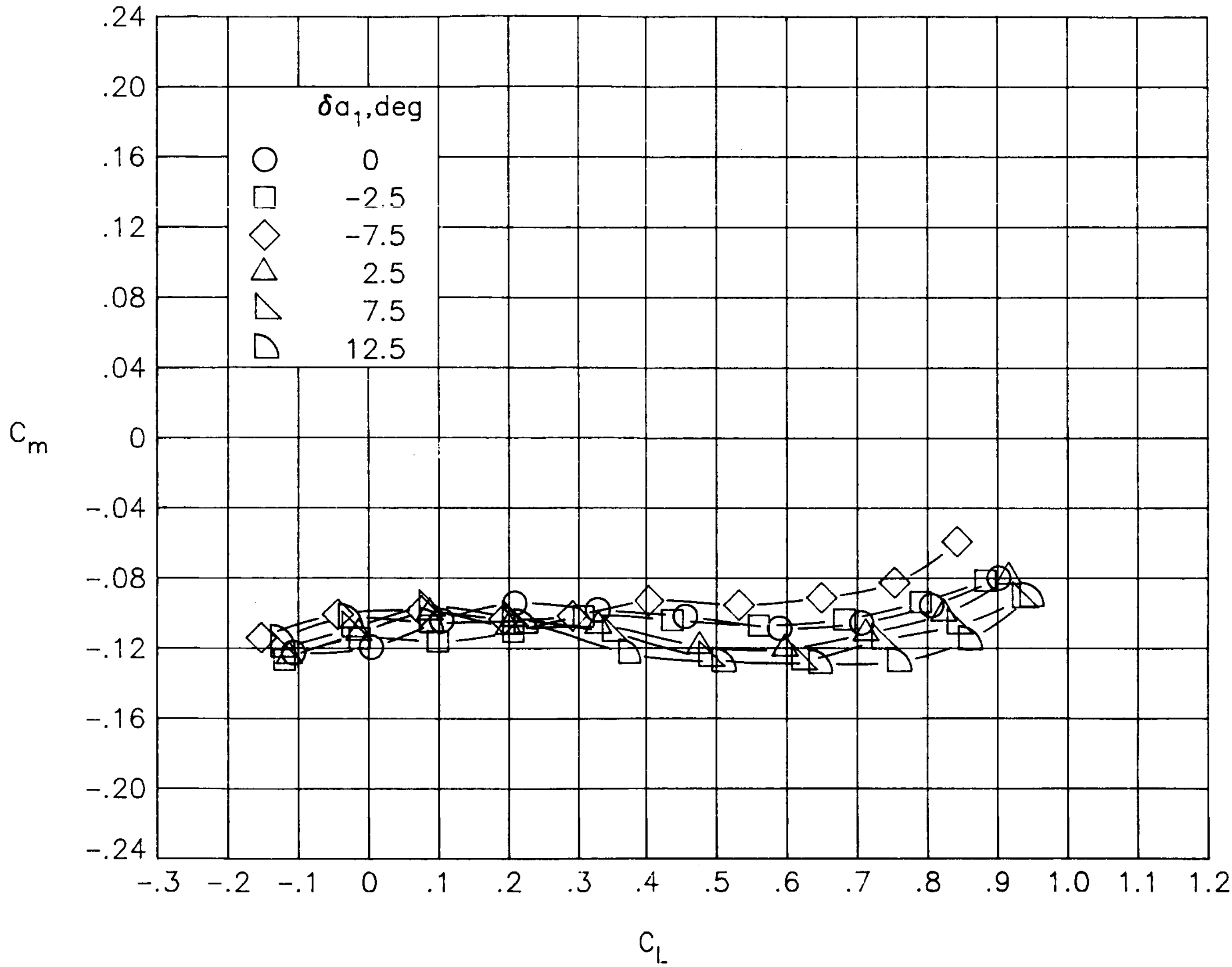

(g) $M_\infty = 0.90$.

Figure 22.- Concluded.

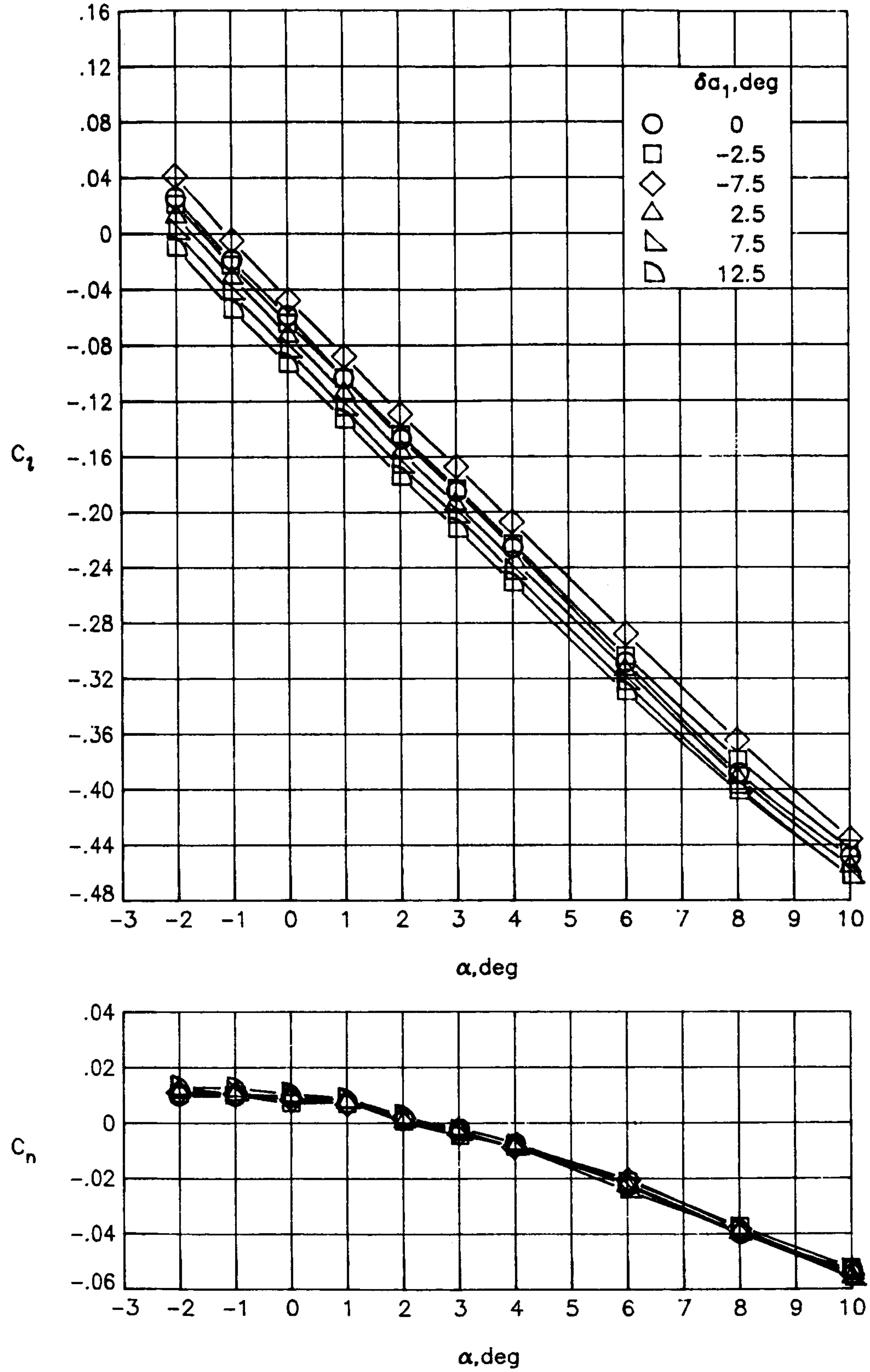

(a) $M_\infty = 0.30$.

Figure 23.- Variations of rolling-moment and yawing-moment coefficient with angle of attack for deflections of a_1. $\delta a_2 = 0°$.

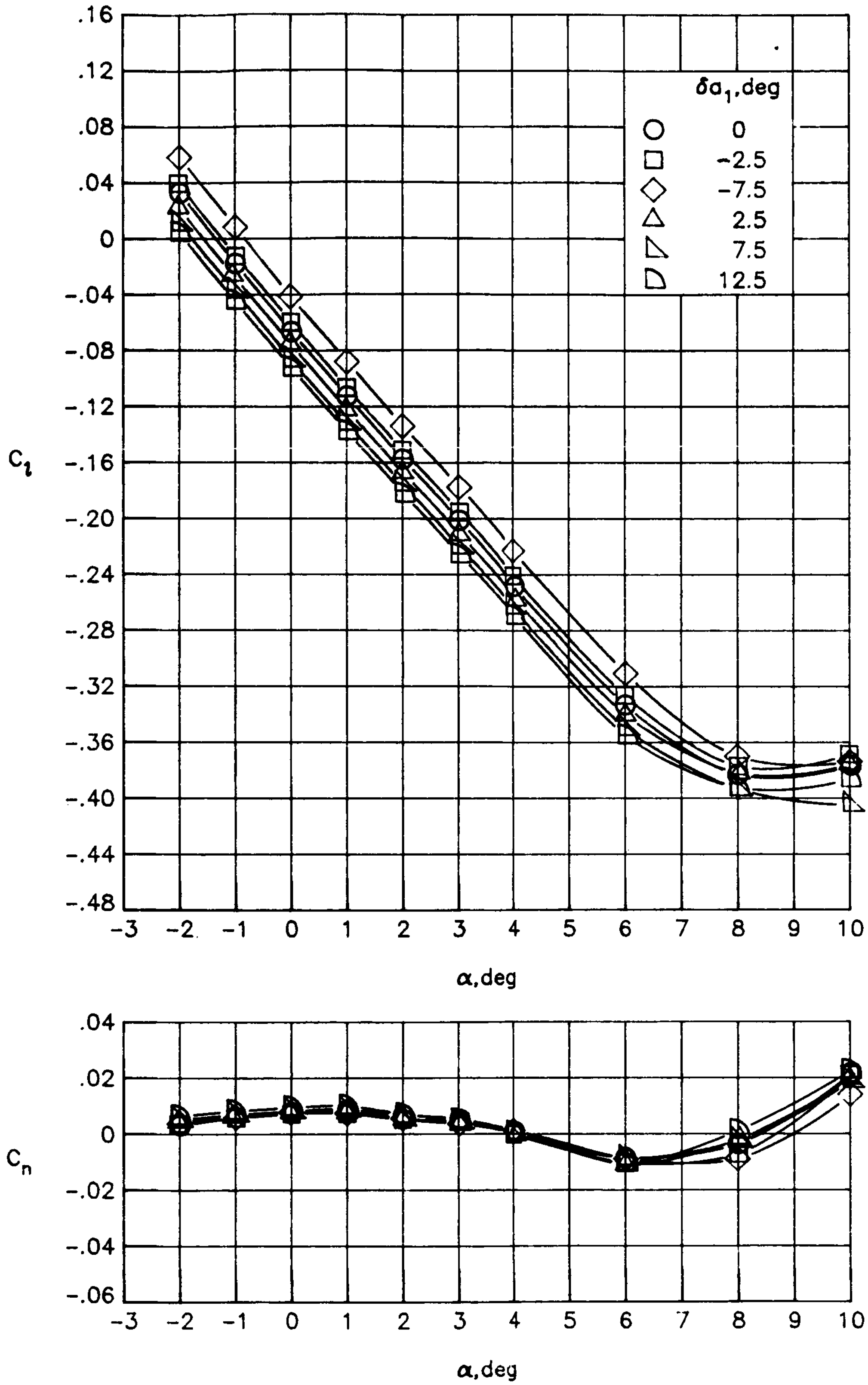

(b) $M_\infty = 0.60$.

Figure 23.- Continued.

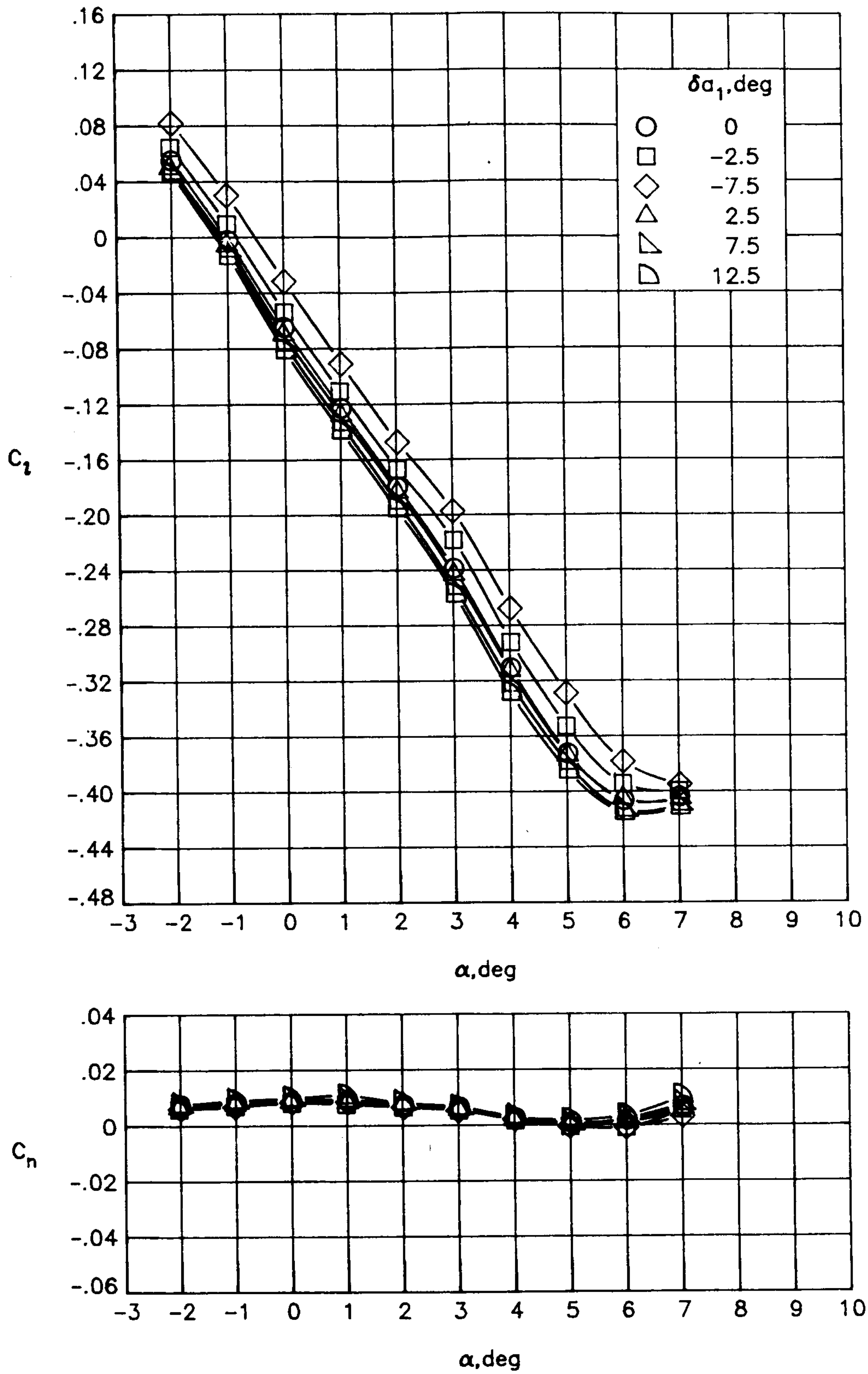

(c) $M_\infty = 0.80$.

Figure 23.- Continued.

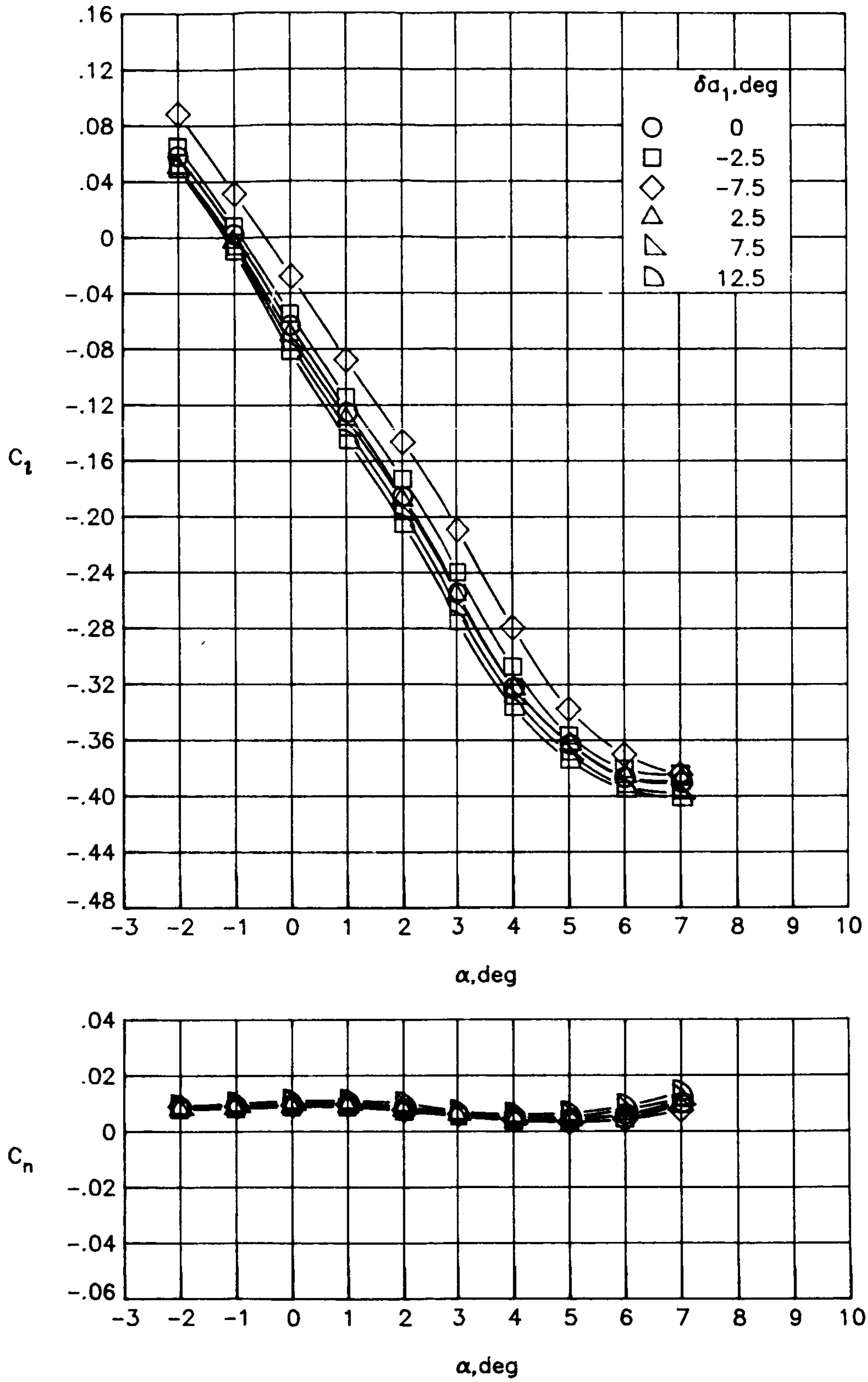

(d) $M_\infty = 0.82$.

Figure 23.- Continued.

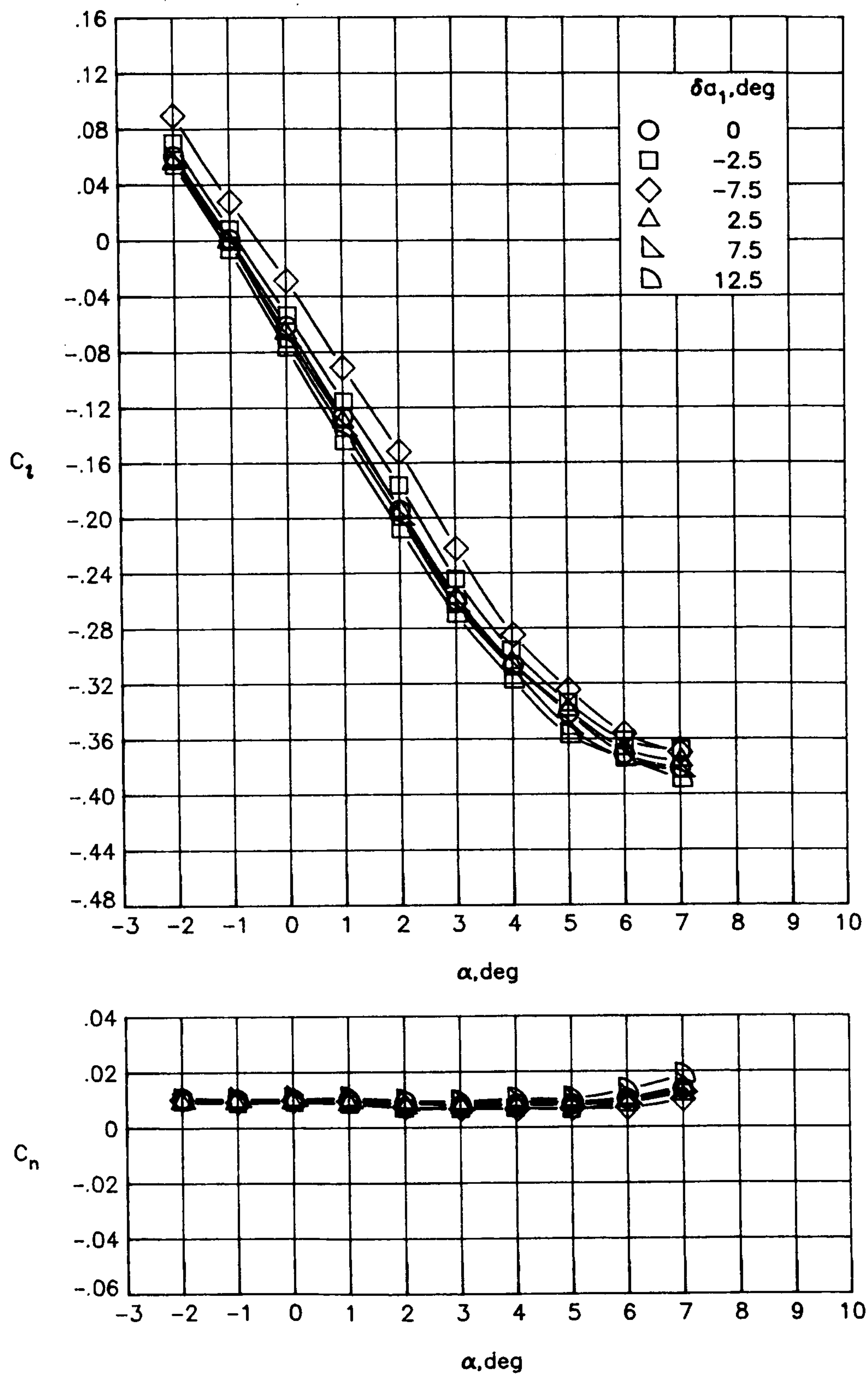

(e) $M_\infty = 0.84$.

Figure 23.- Continued.

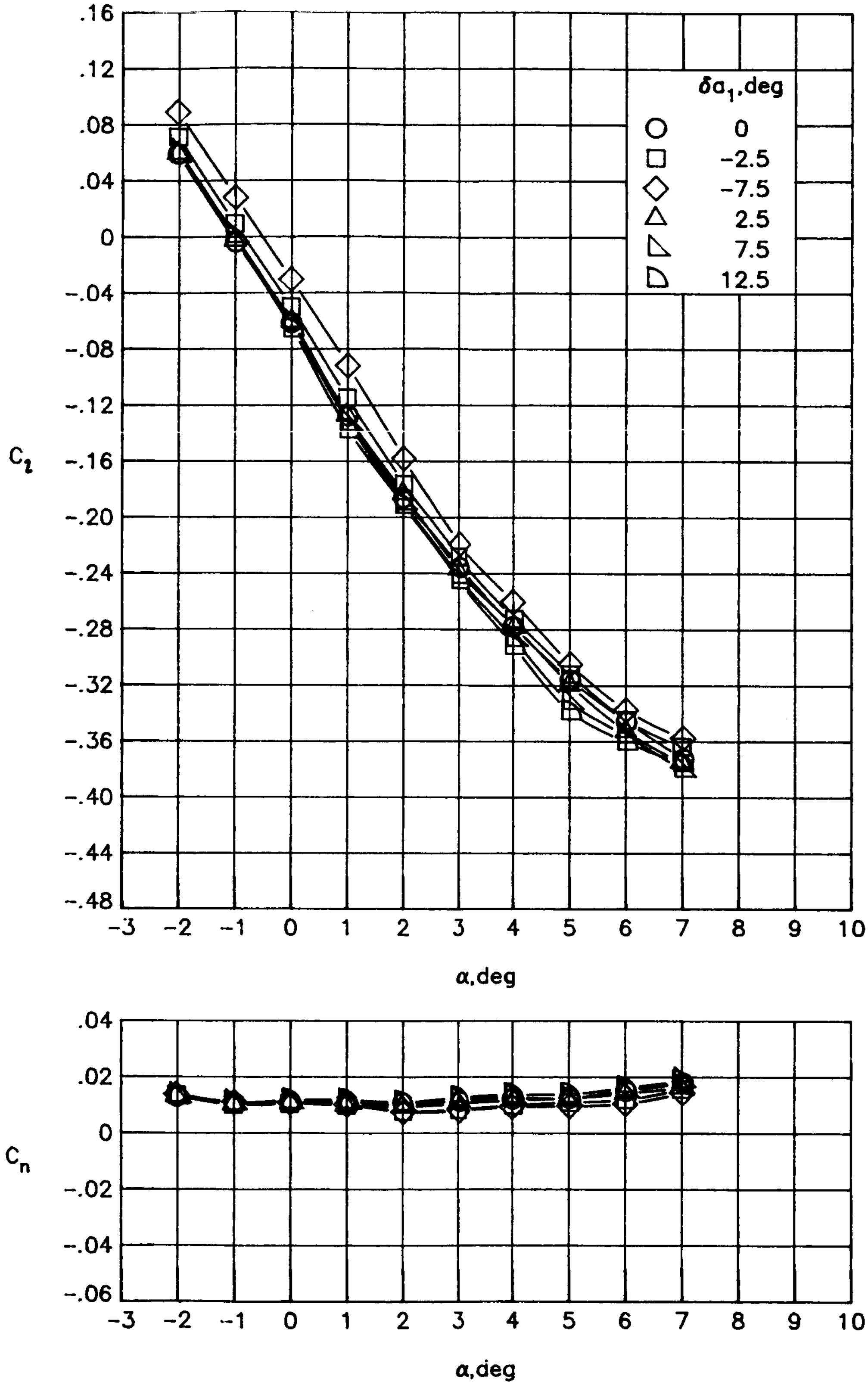

(f) $M_\infty = 0.86$.

Figure 23.- Continued.

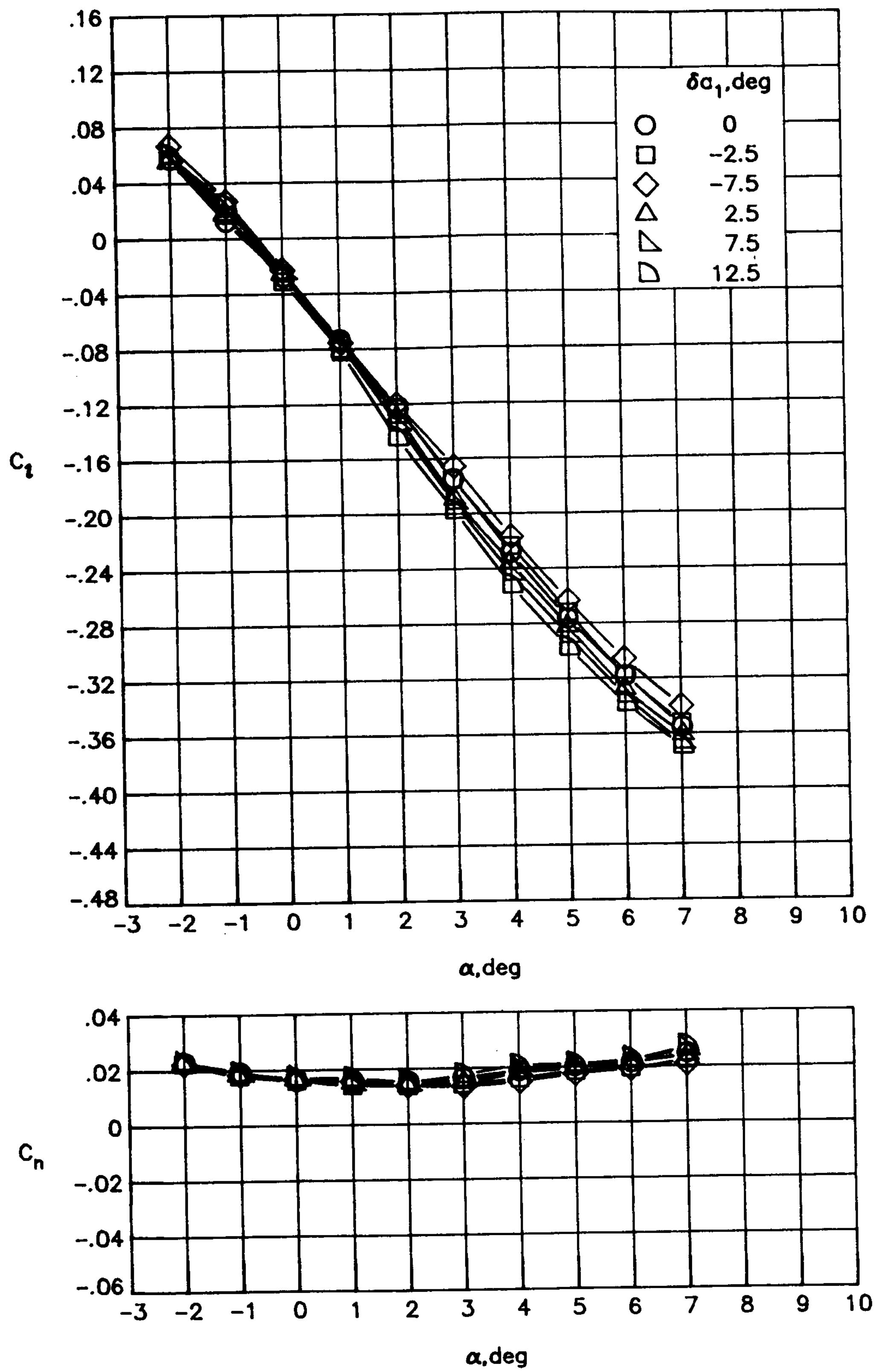

(g) $M_\infty = 0.90$.

Figure 23.- Concluded.

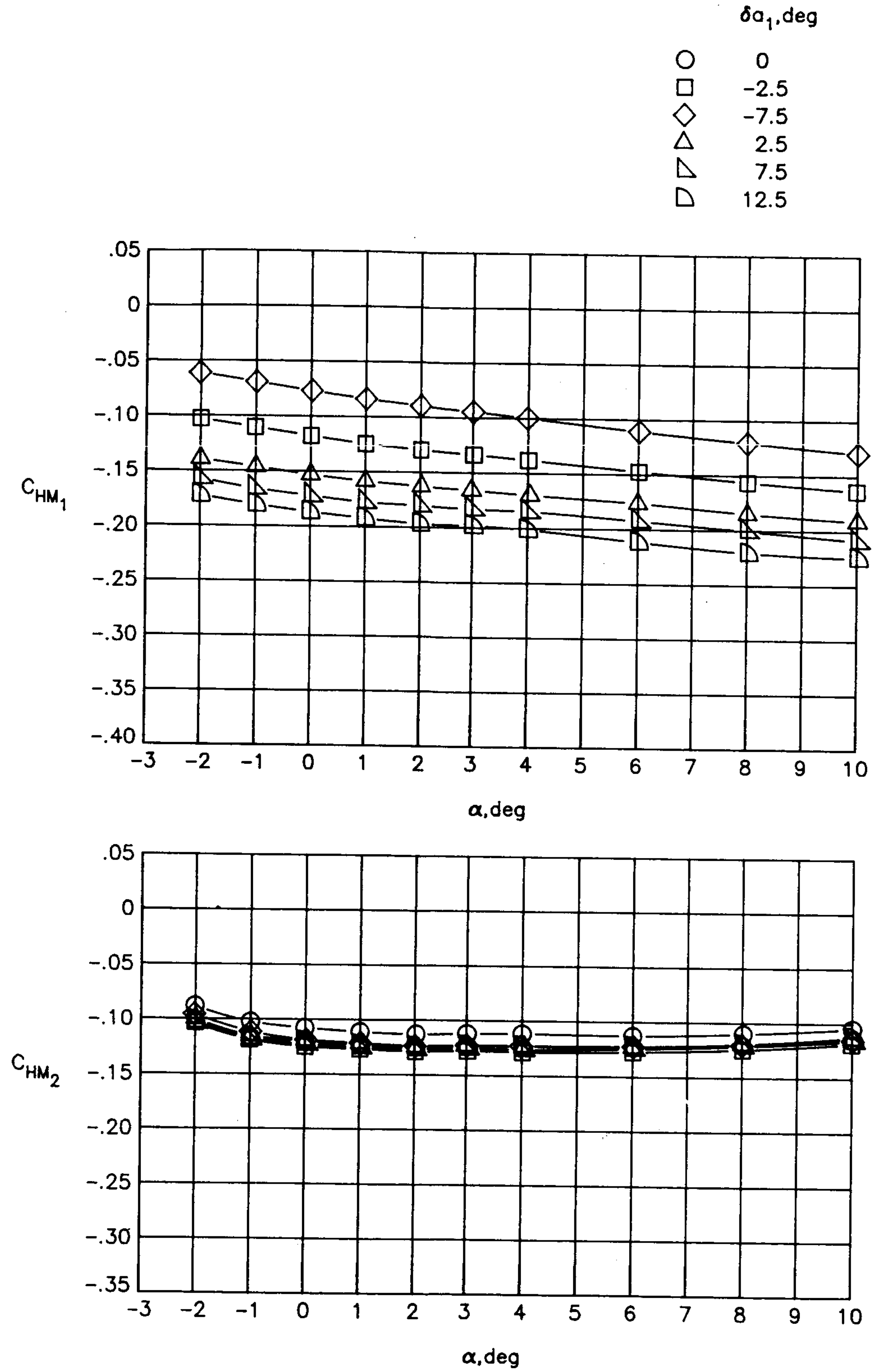

(a) $M_\infty = 0.30$.

Figure 24.- Variations of hinge-moment coefficients with angle of attack for deflections of a_1. $\delta a_2 = 0°$.

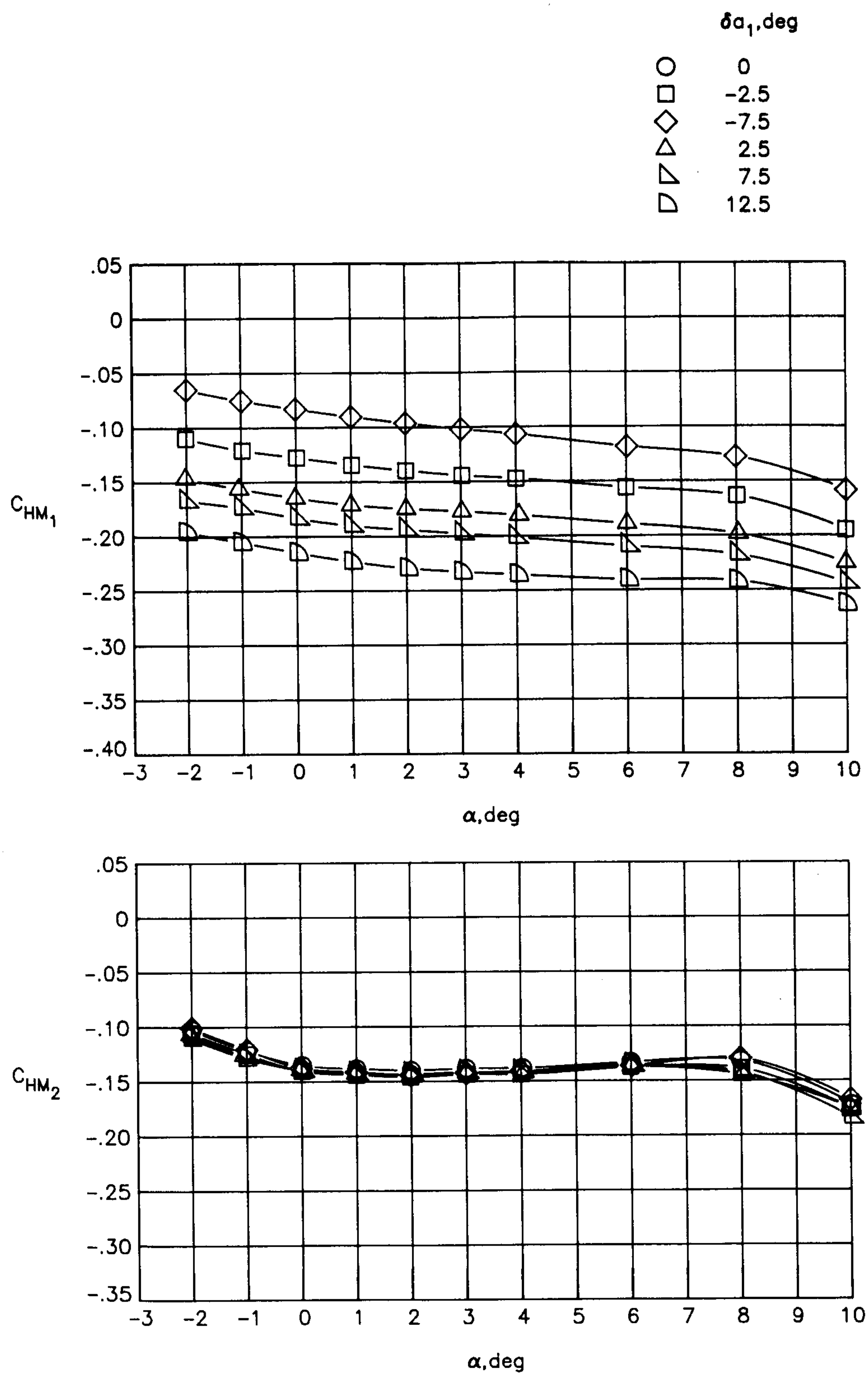

(b) M_{∞} = 0.60.

Figure 24.- Continued.

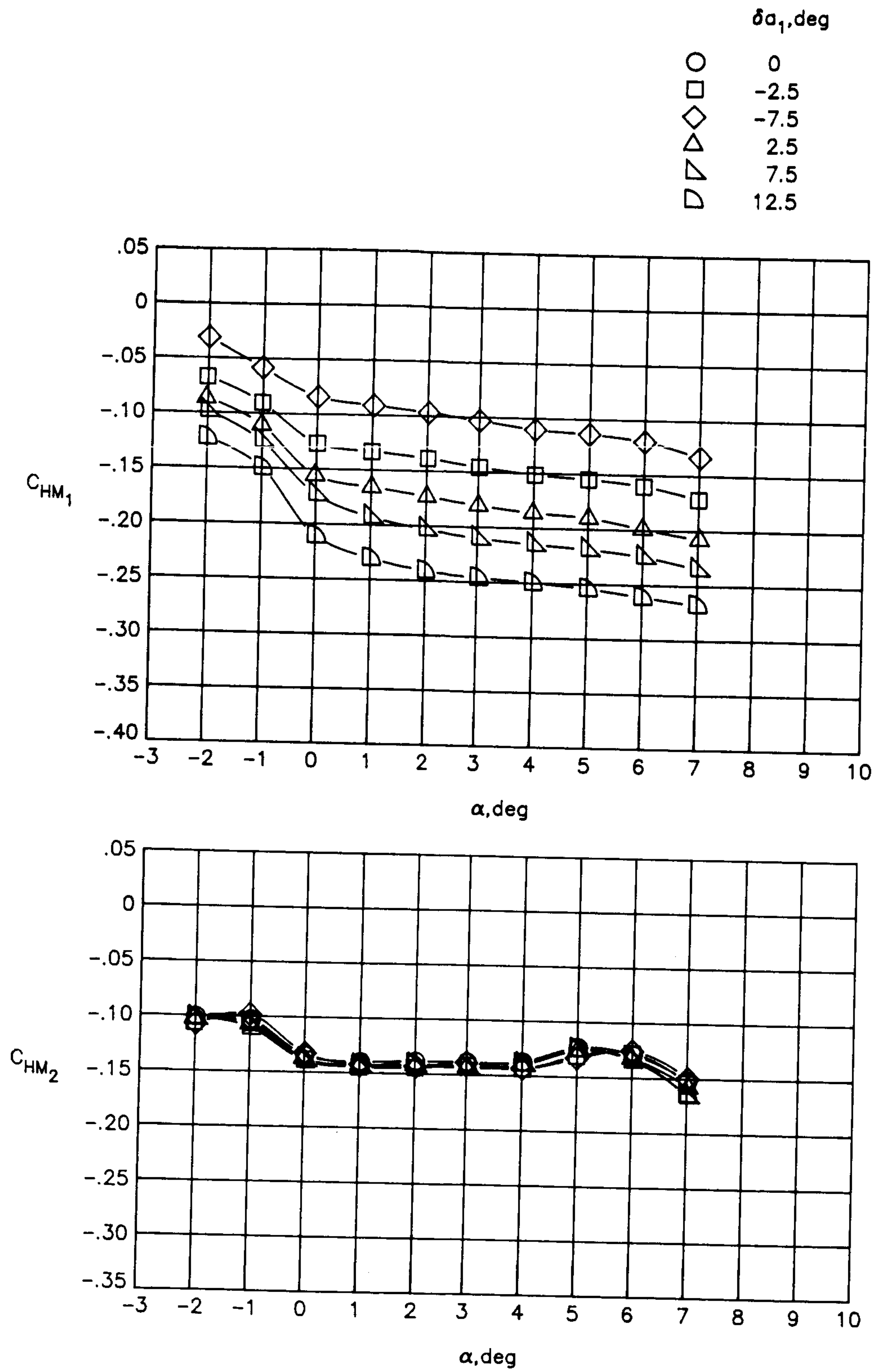

(c) $M_\infty = 0.80$.

Figure 24.- Continued.

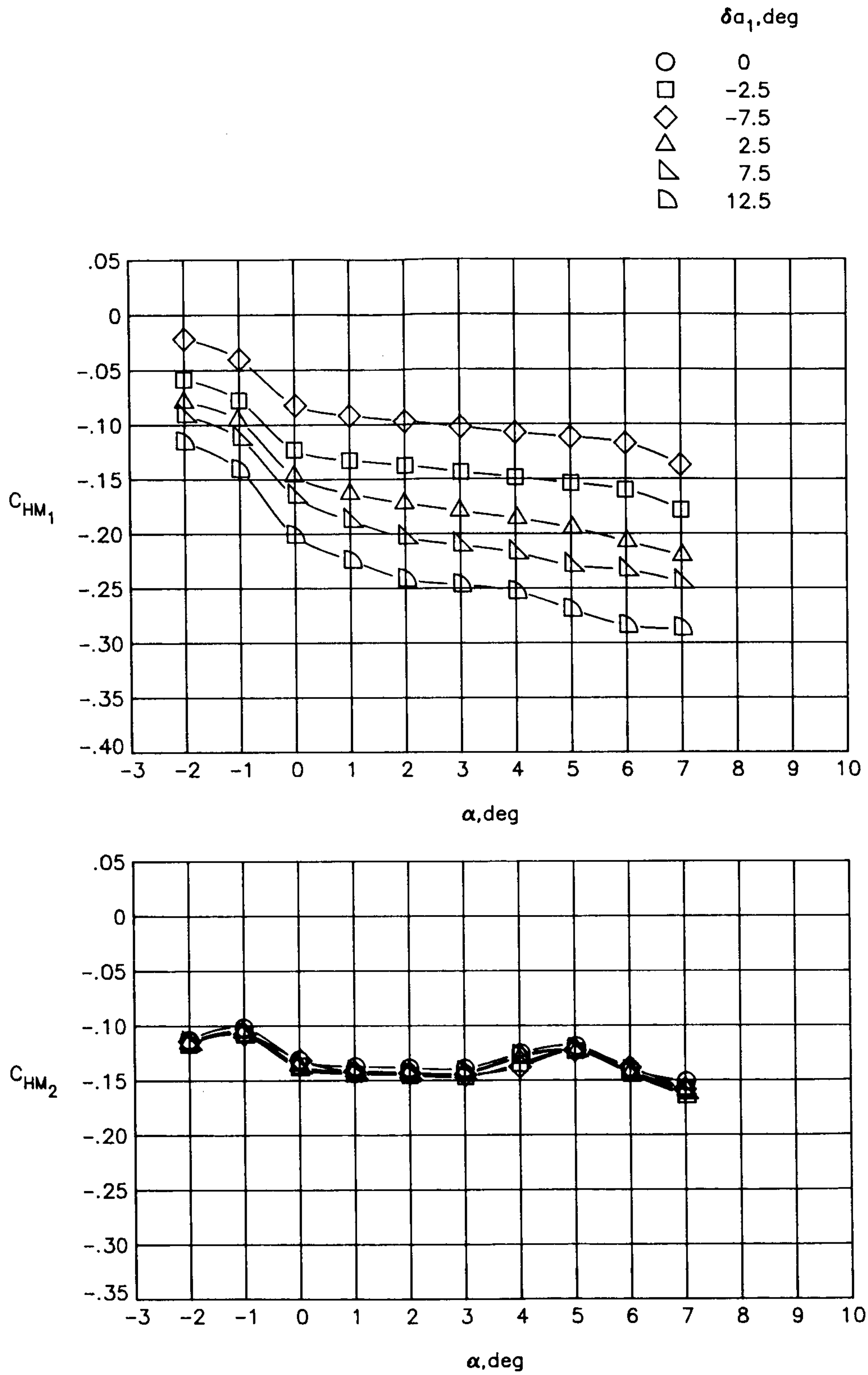

(d) $M_\infty = 0.82$.

Figure 24.- Continued.

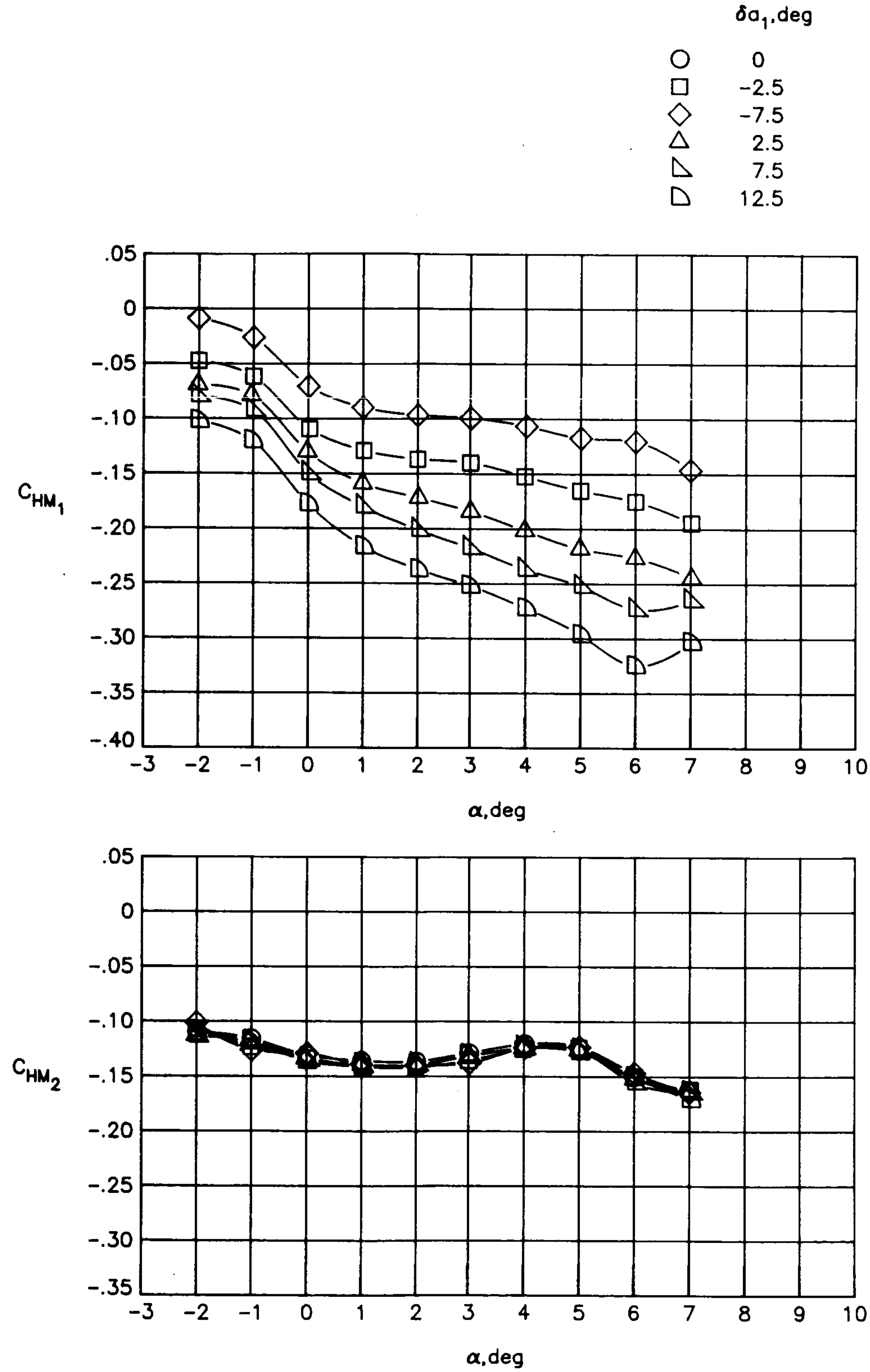

(e) $M_\infty = 0.84$.

Figure 24.- Continued.

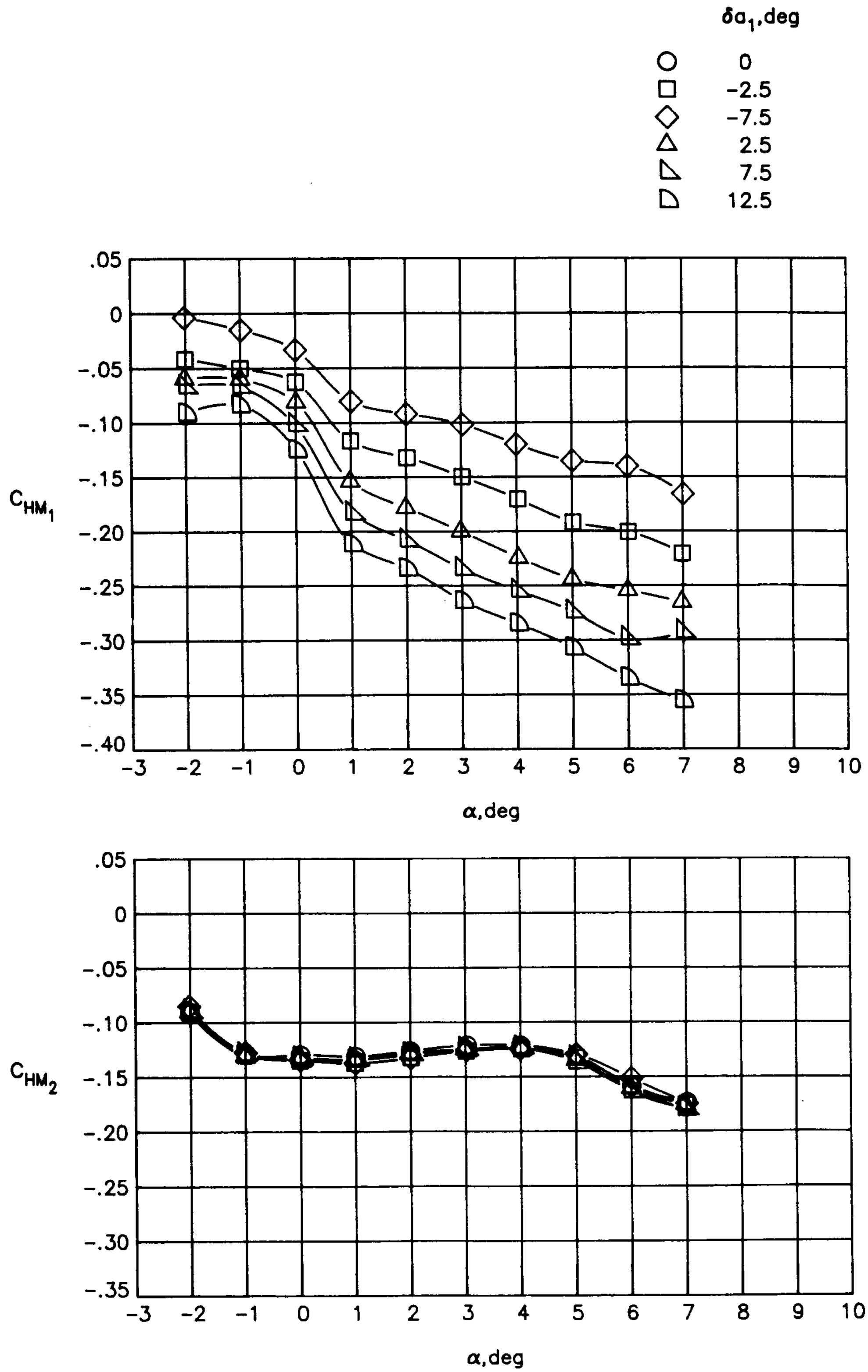

(f) $M_\infty = 0.86$.

Figure 24.- Continued.

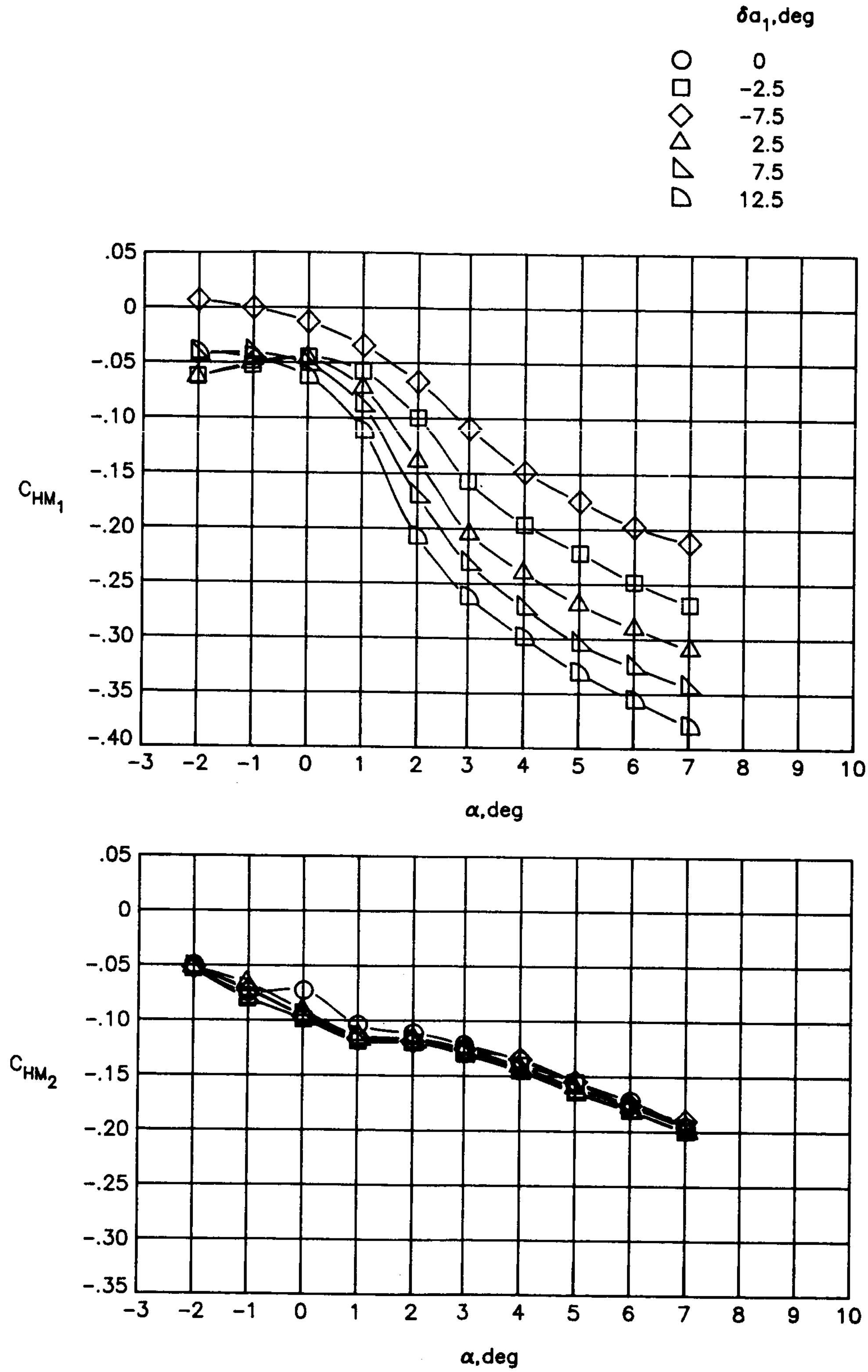

(g) M_{∞} = 0.90.

Figure 24.- Concluded.

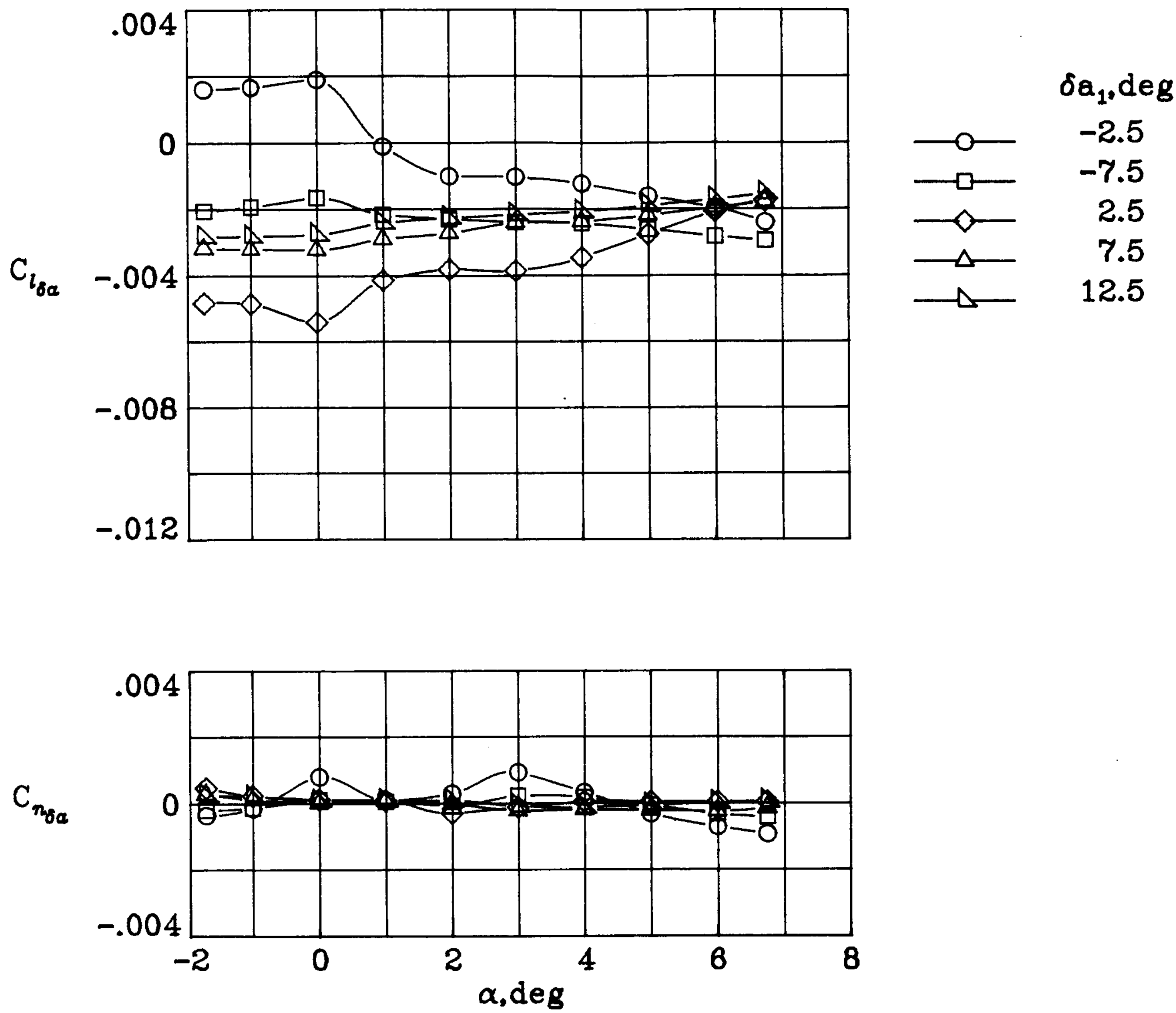

(a) $M_\infty = 0.30$.

Figure 25.- Variations of aileron-effectiveness parameters with angle of attack for deflections of a_1. $\delta a_2 = 0°$.

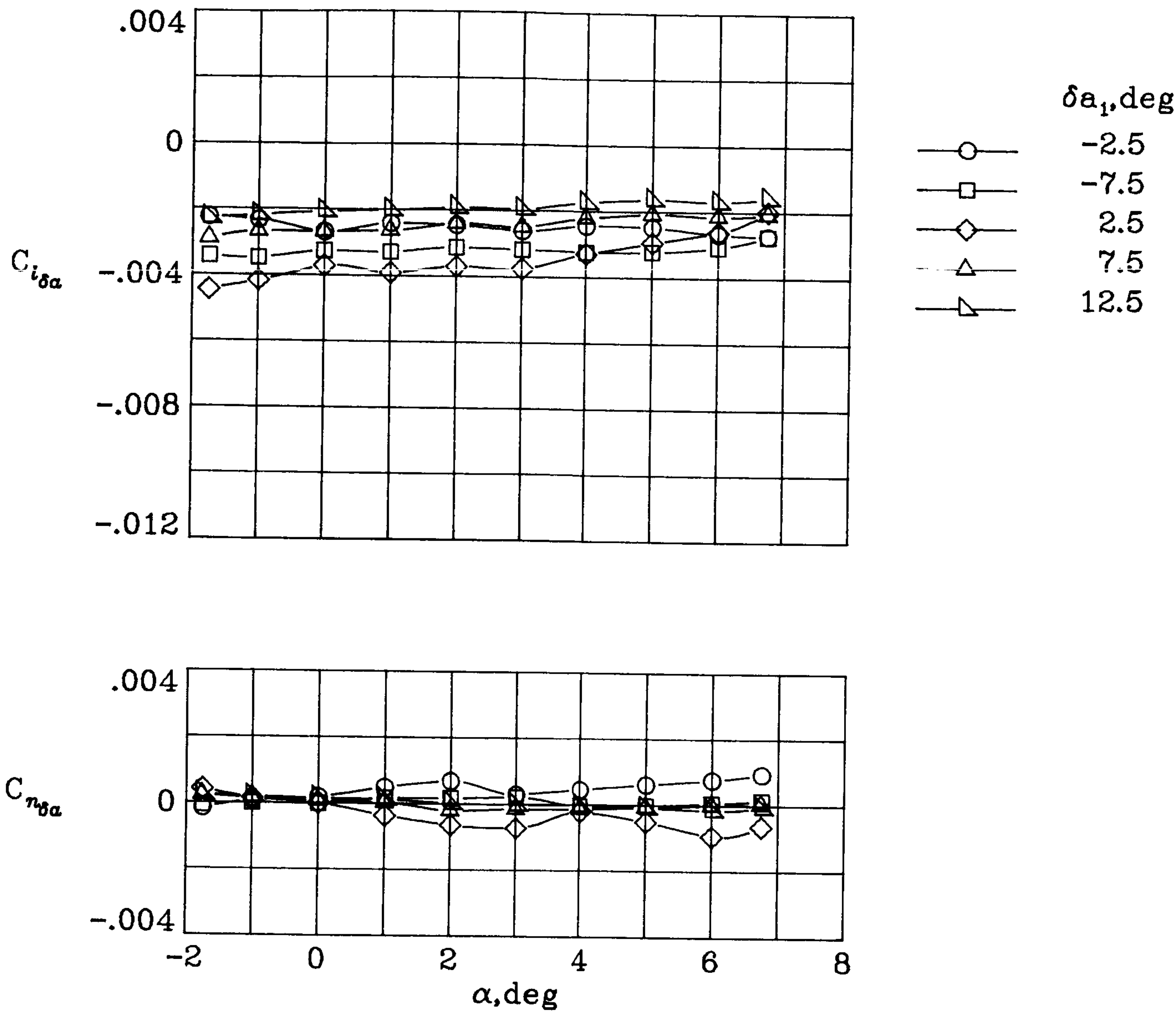

(b) $M_\infty = 0.60$.

Figure 25.- Continued.

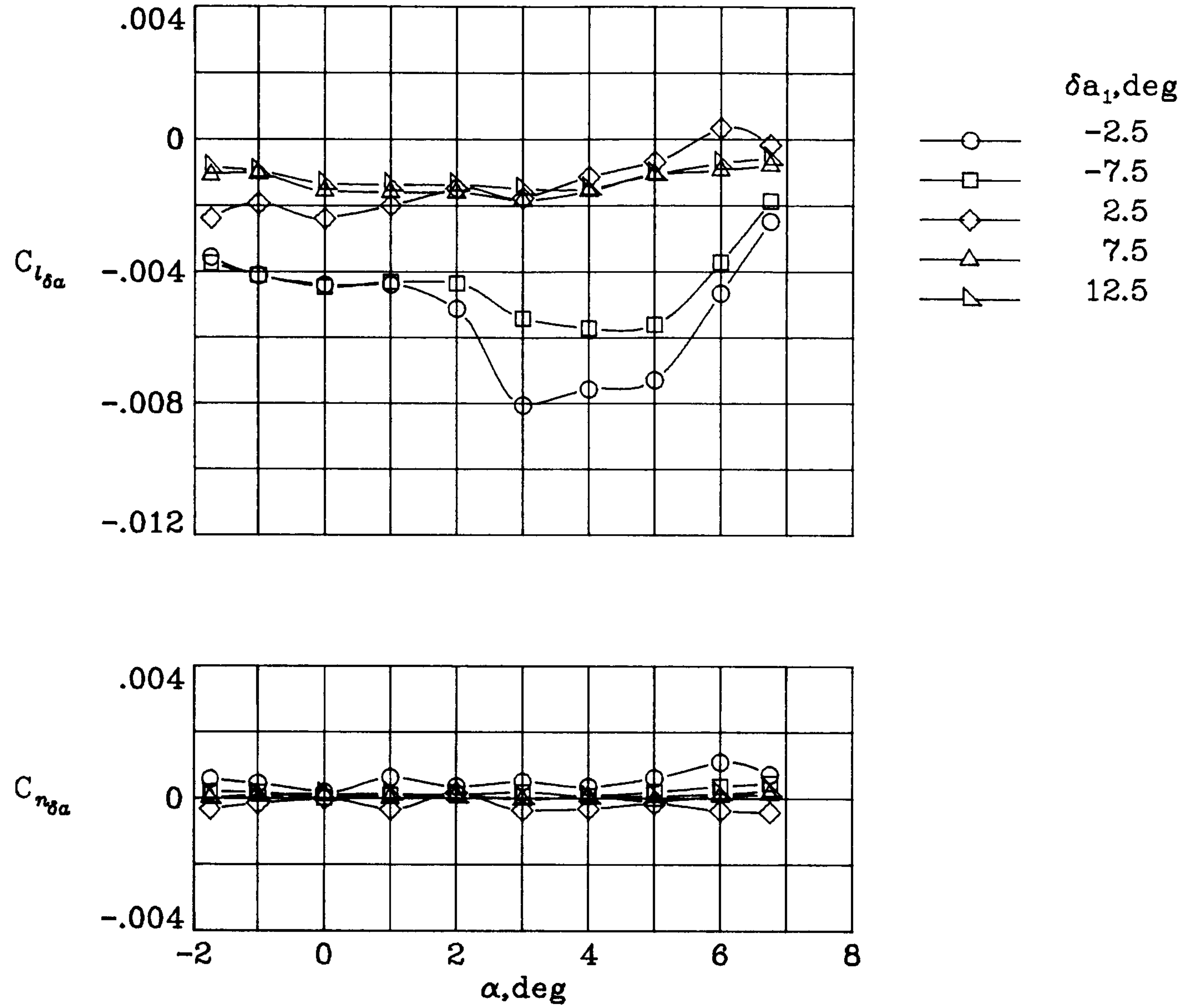

(c) M_∞ = 0.80.

Figure 25.- Continued.

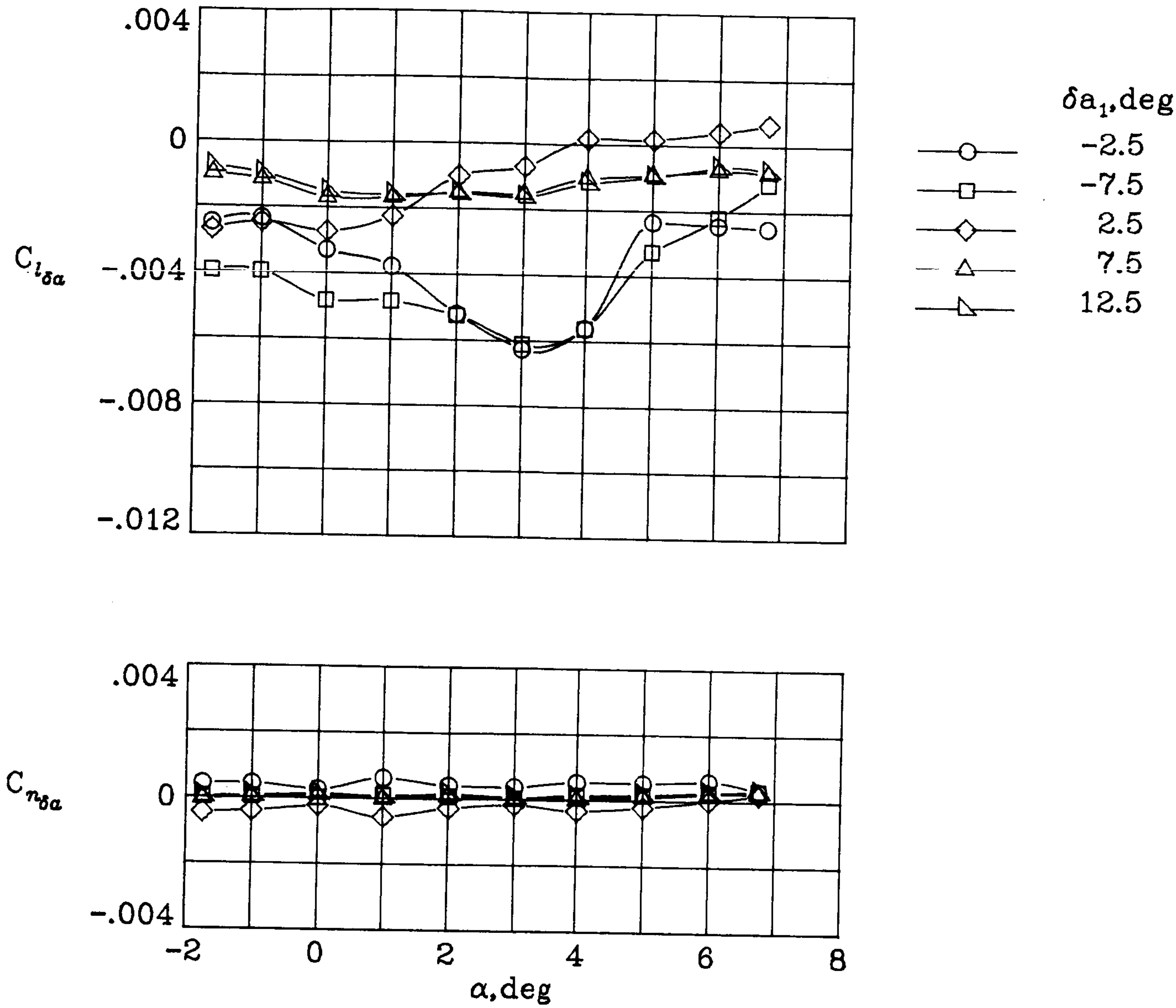

(d) $M_\infty = 0.82$.

Figure 25.- Continued.

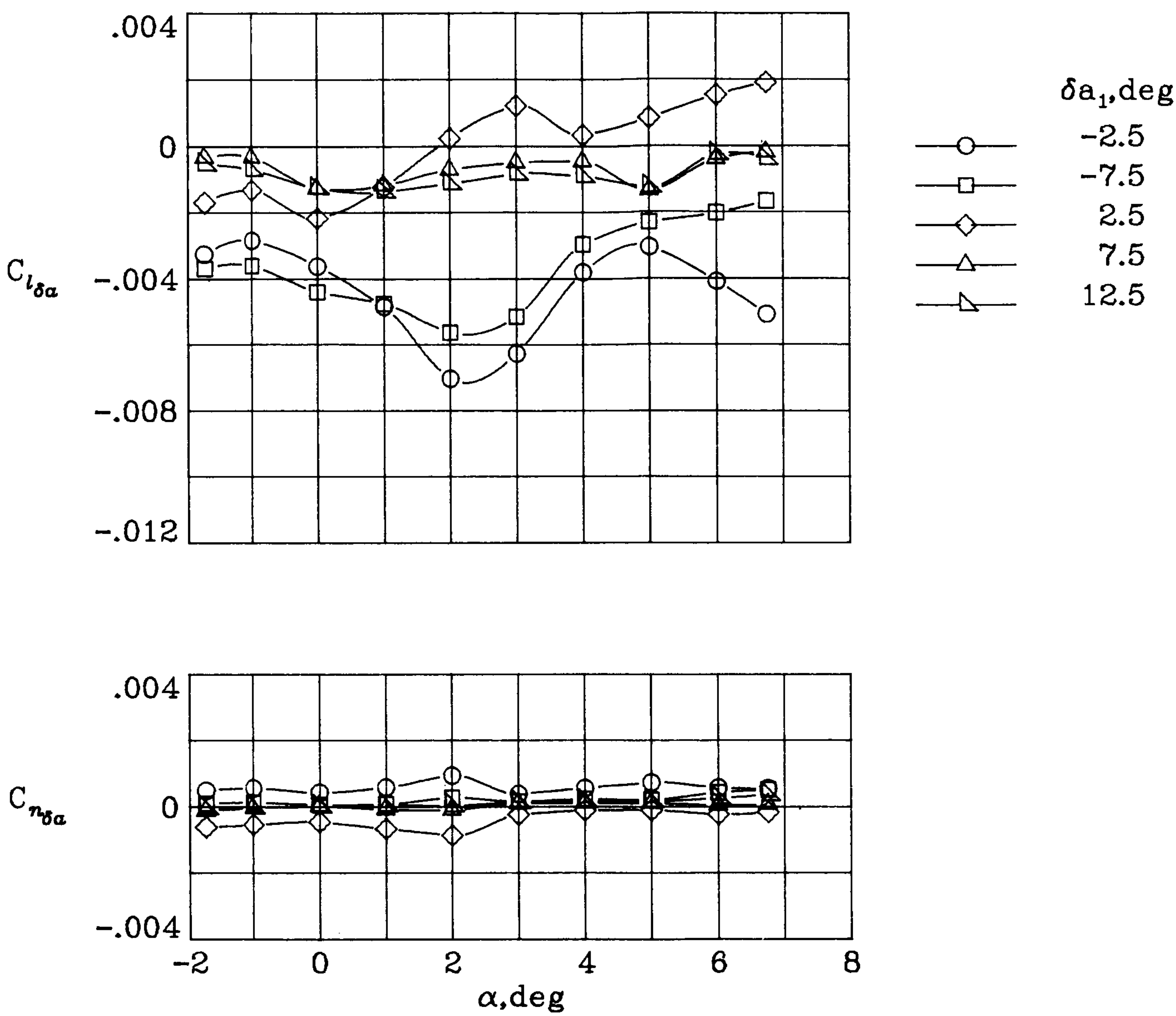

(e) $M_\infty = 0.84$.

Figure 25.- Continued.

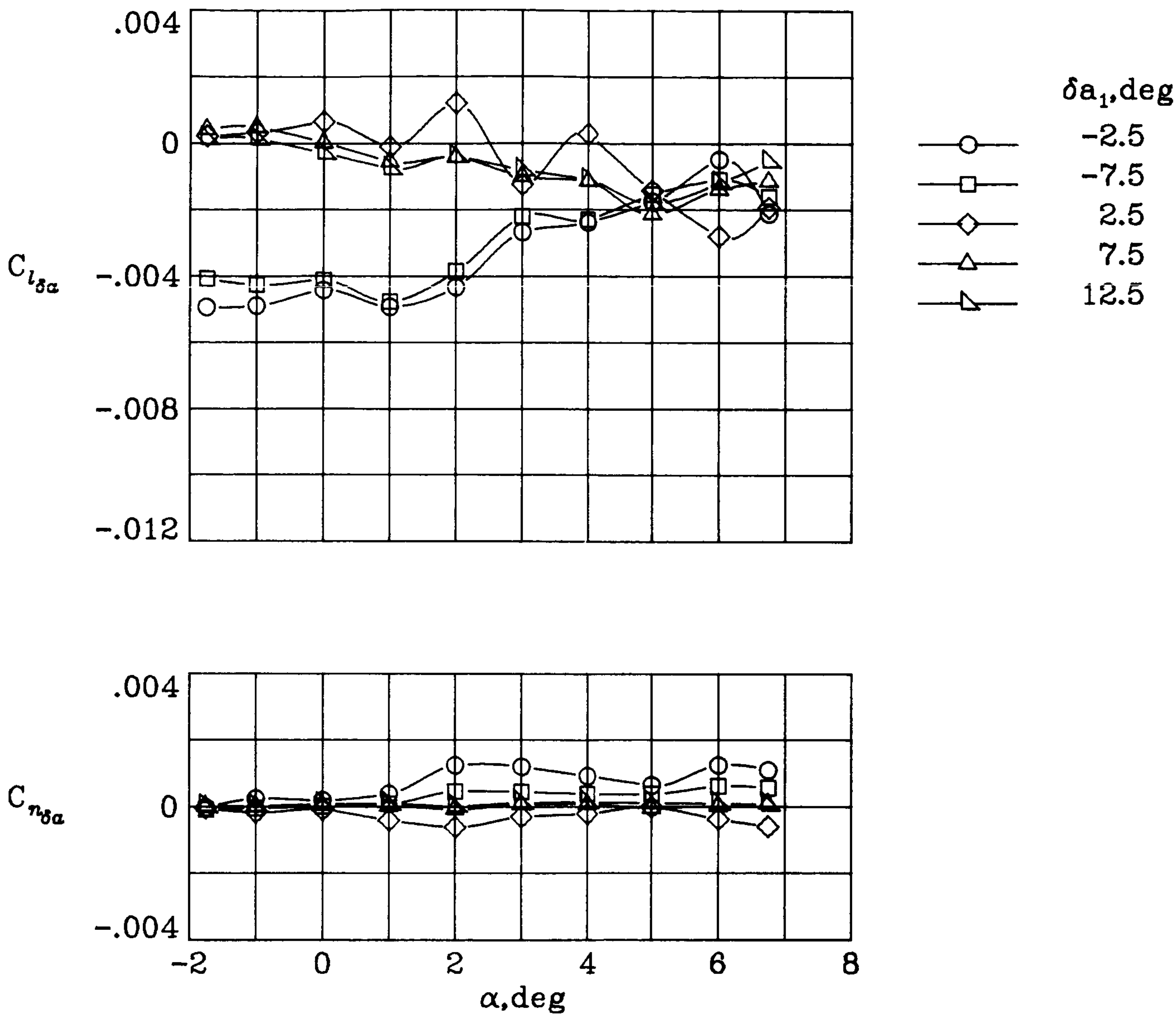

(f) $M_\infty = 0.86$.

Figure 25.- Continued.

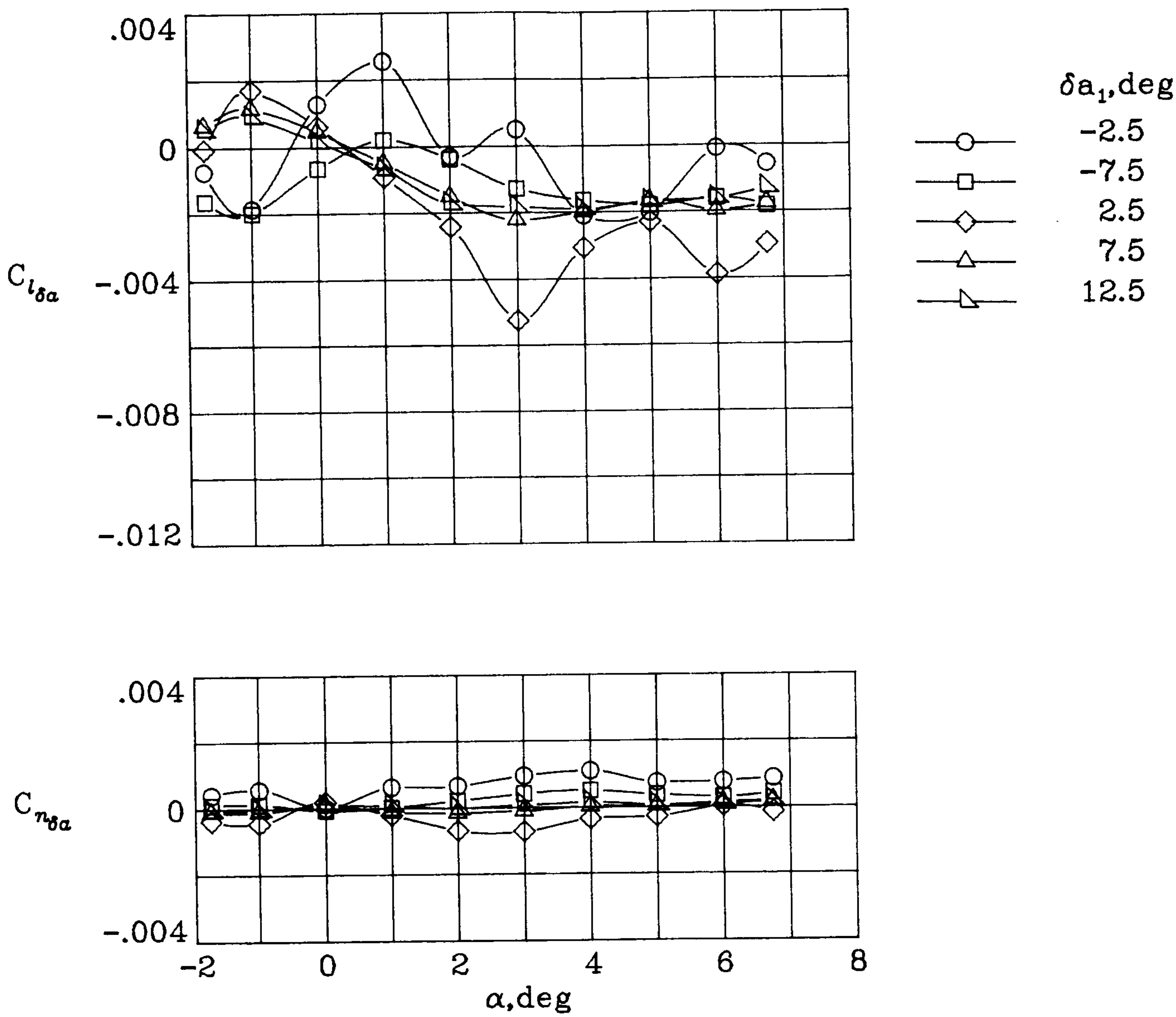

(g) $M_\infty = 0.90$.

Figure 25.- Concluded.

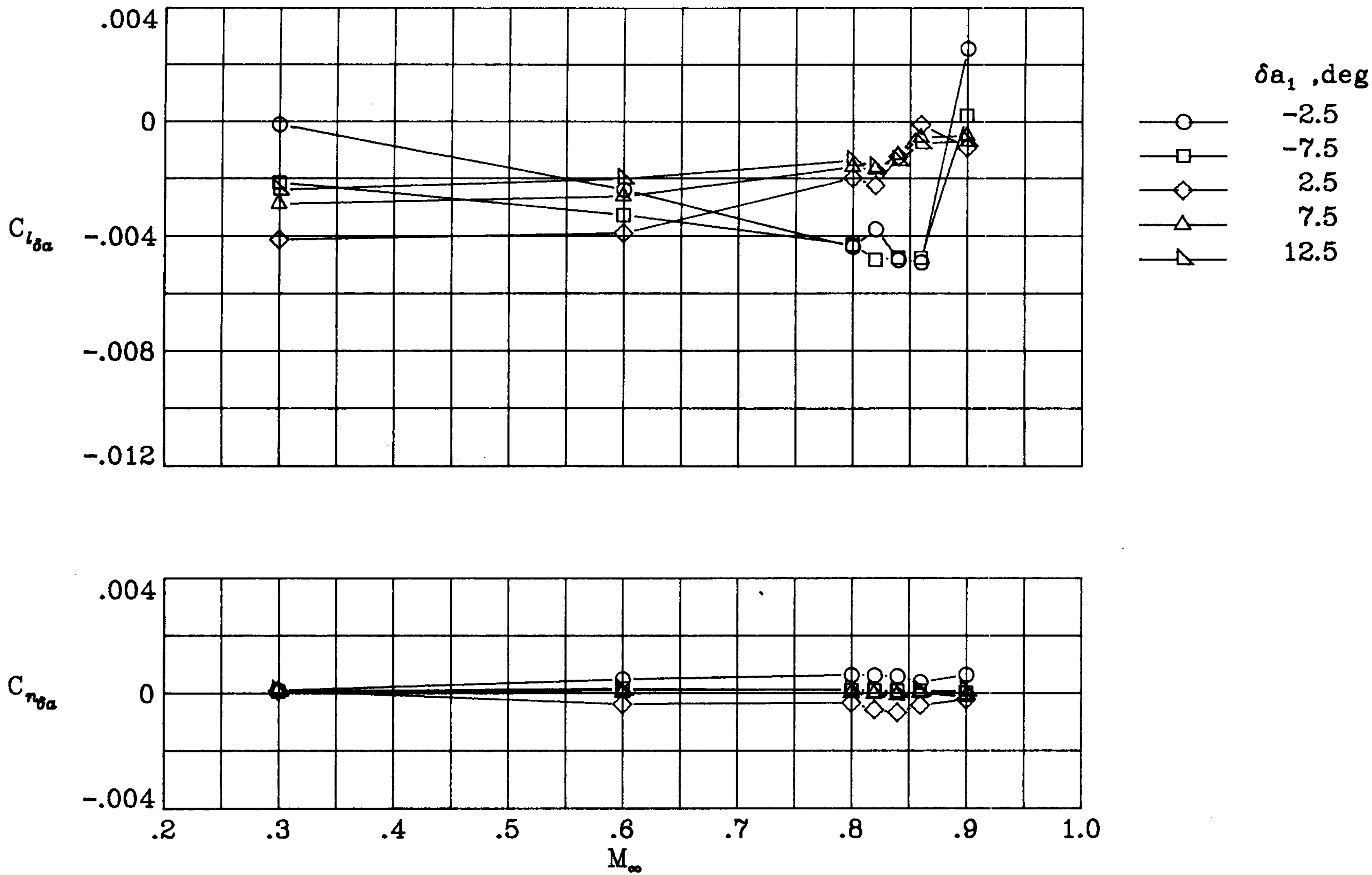

(a) $\alpha = 1°$.

Figure 26.- Variations of aileron-effectiveness parameters with Mach number for deflections of a_1. $\delta a_2 = 0°$.

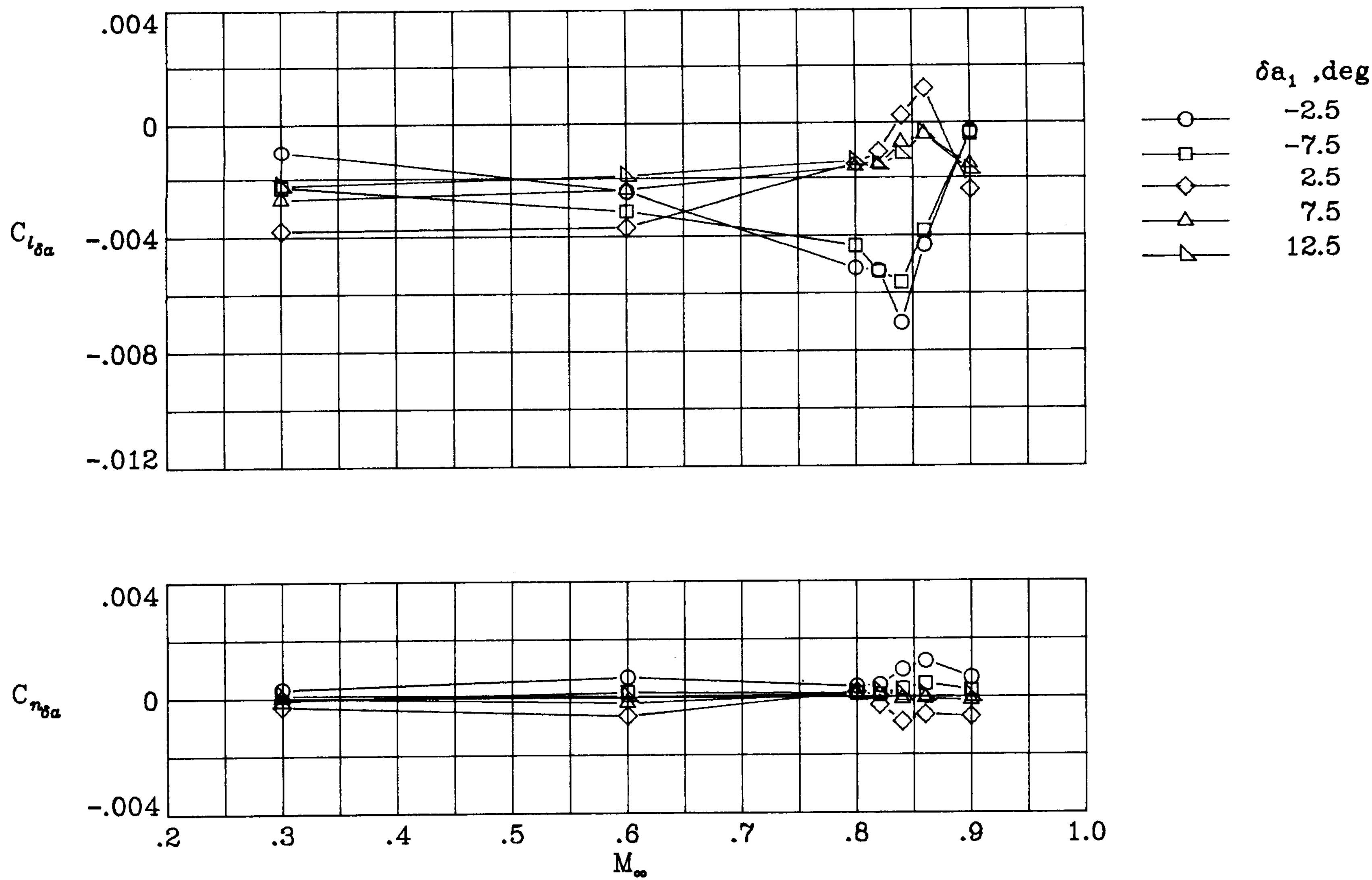

(b) $\alpha = 2°$.

Figure 26.- Continued.

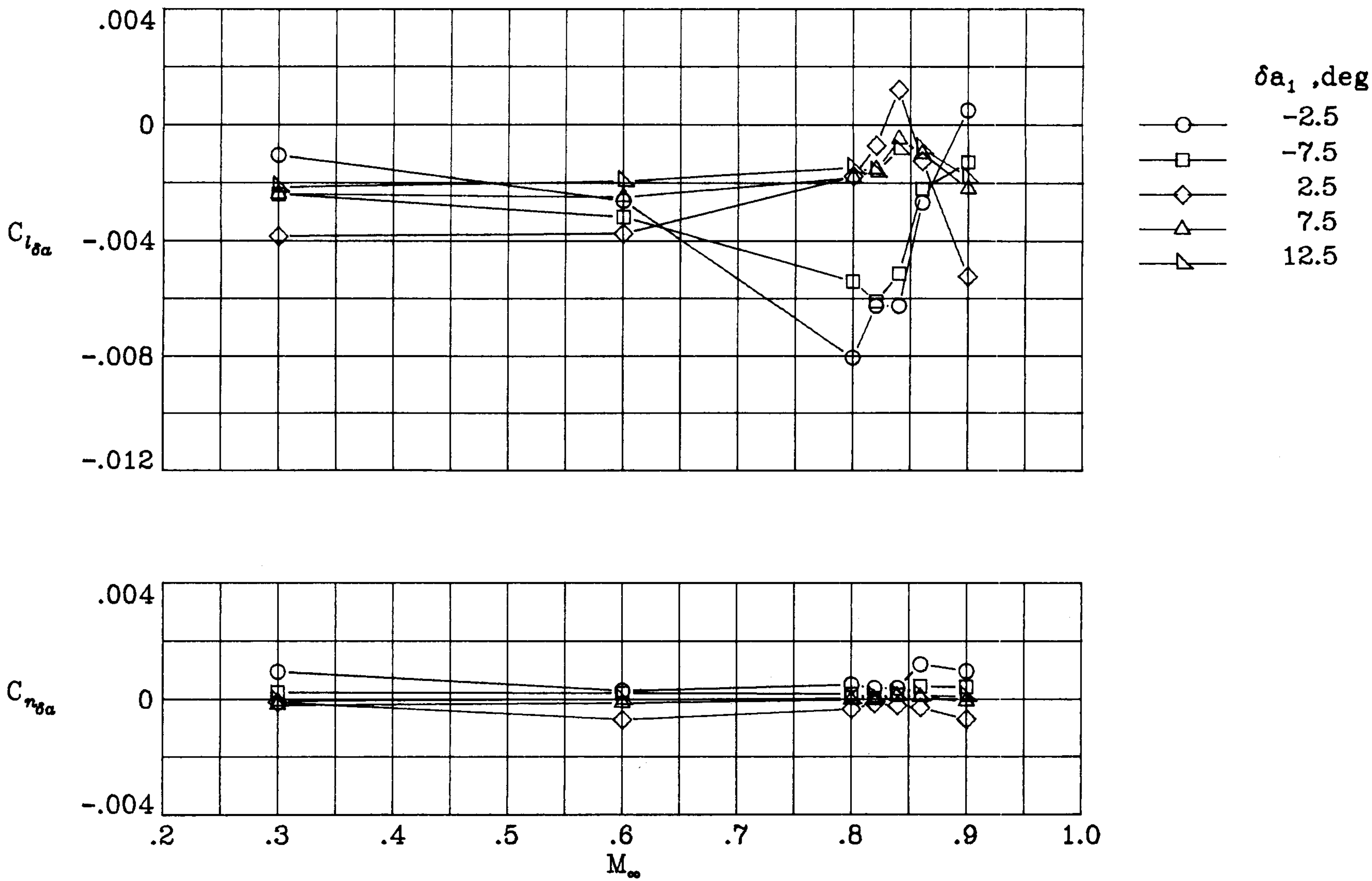

(c) $\alpha = 3°$.

Figure 26.- Continued.

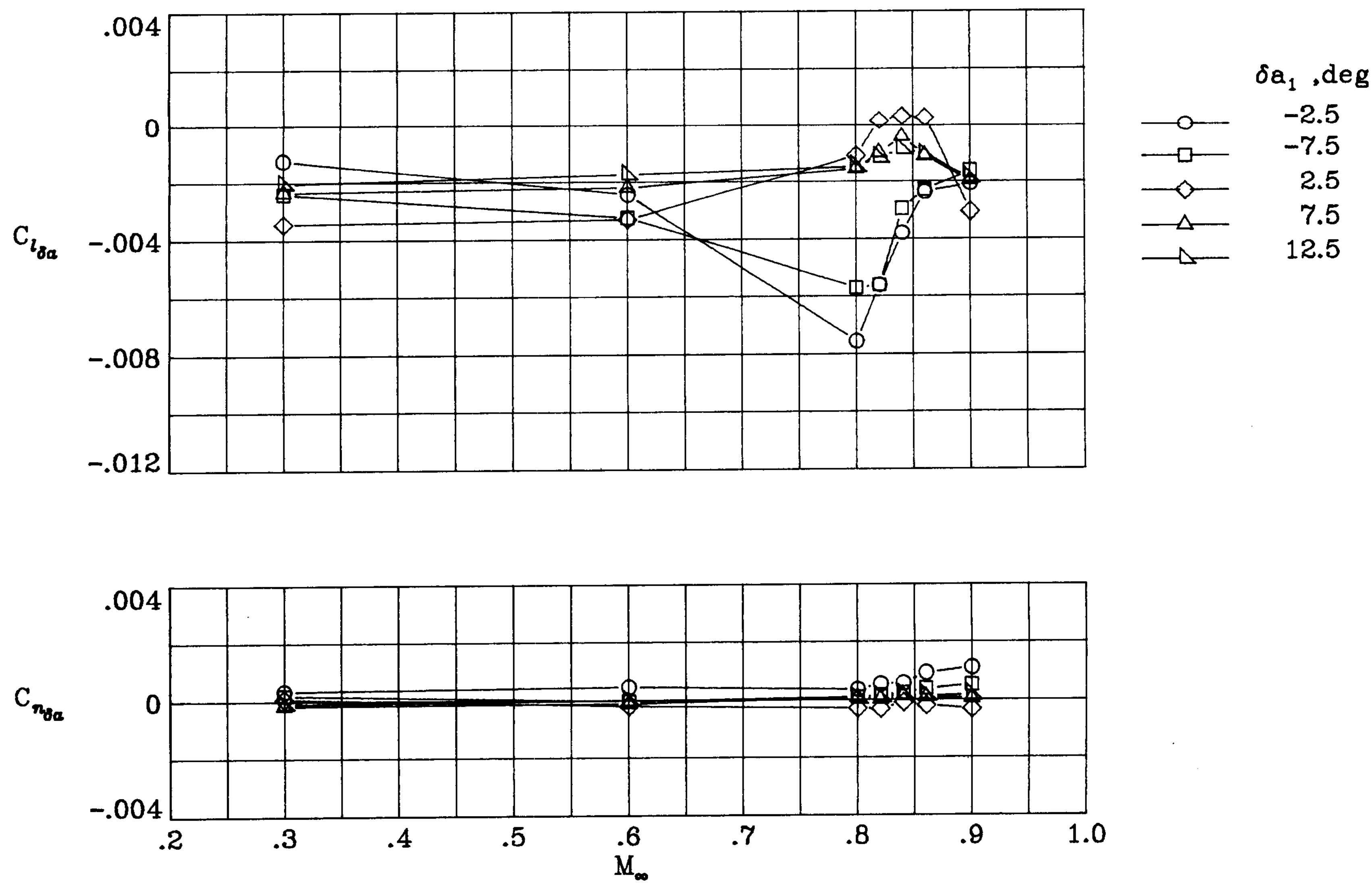

(d) $\alpha = 4°$.

Figure 26.- Concluded.

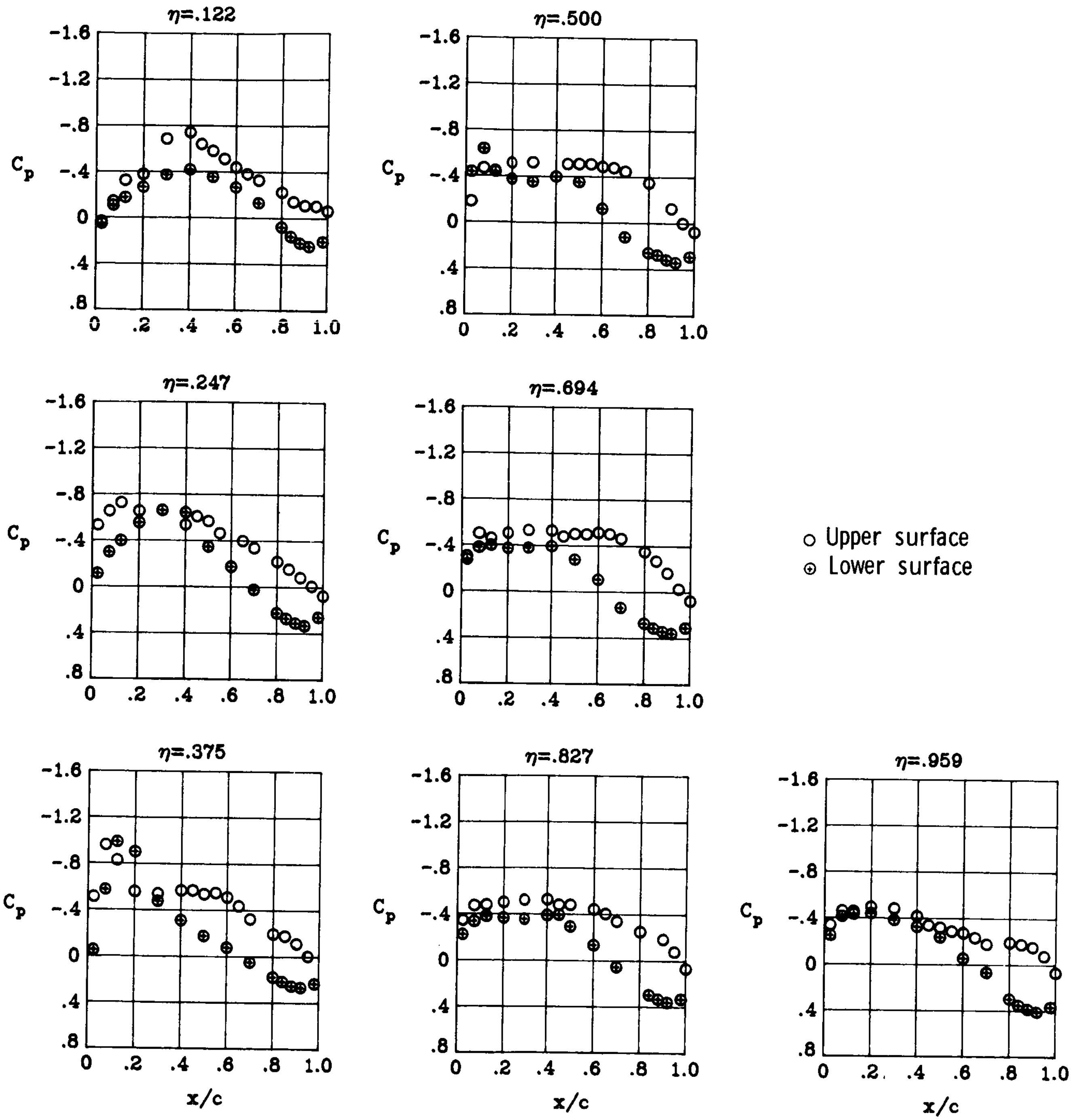

(a) $M_\infty = 0.82$; $\alpha = 1°$.

Figure 27.- Wing chordwise pressure distributions for $\delta a_1 = -2.5°$ at $M_\infty = 0.82$. $\delta a_2 = 0°$.

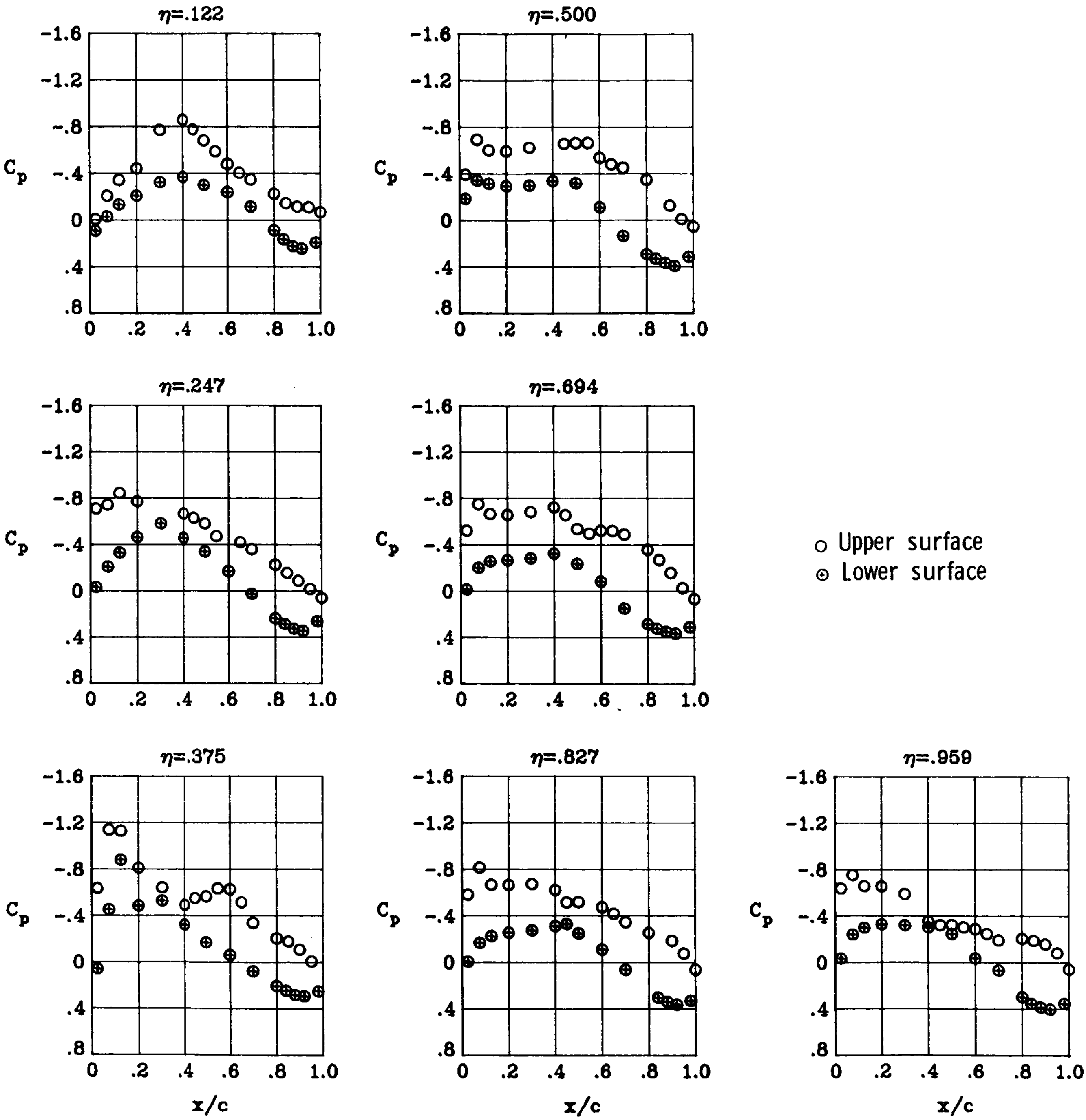

(b) $M_\infty = 0.82$; $\alpha = 2°$.

Figure 27.- Continued.

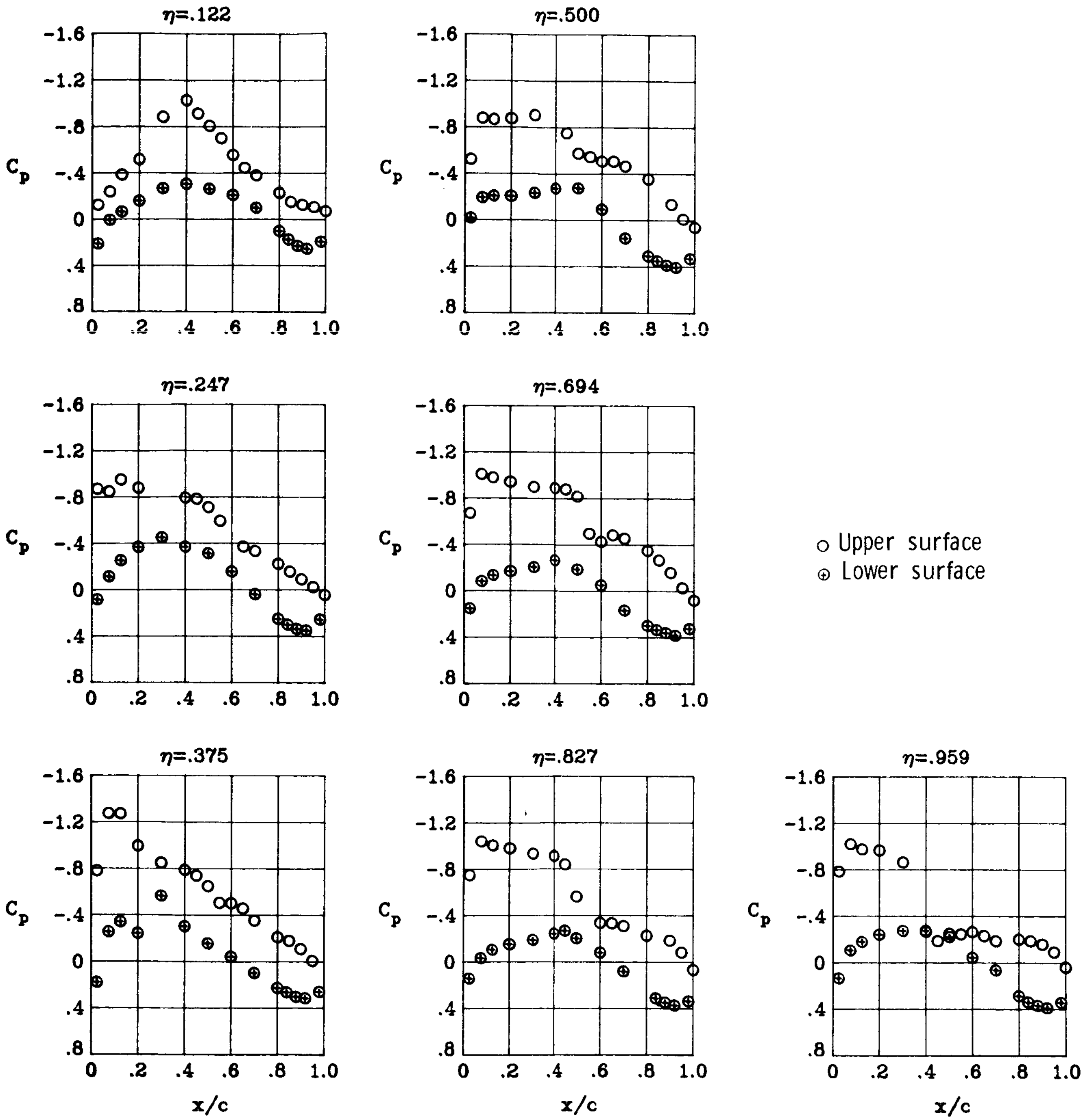

(c) $M_\infty = 0.82$; $\alpha = 3°$.

Figure 27.- Continued.

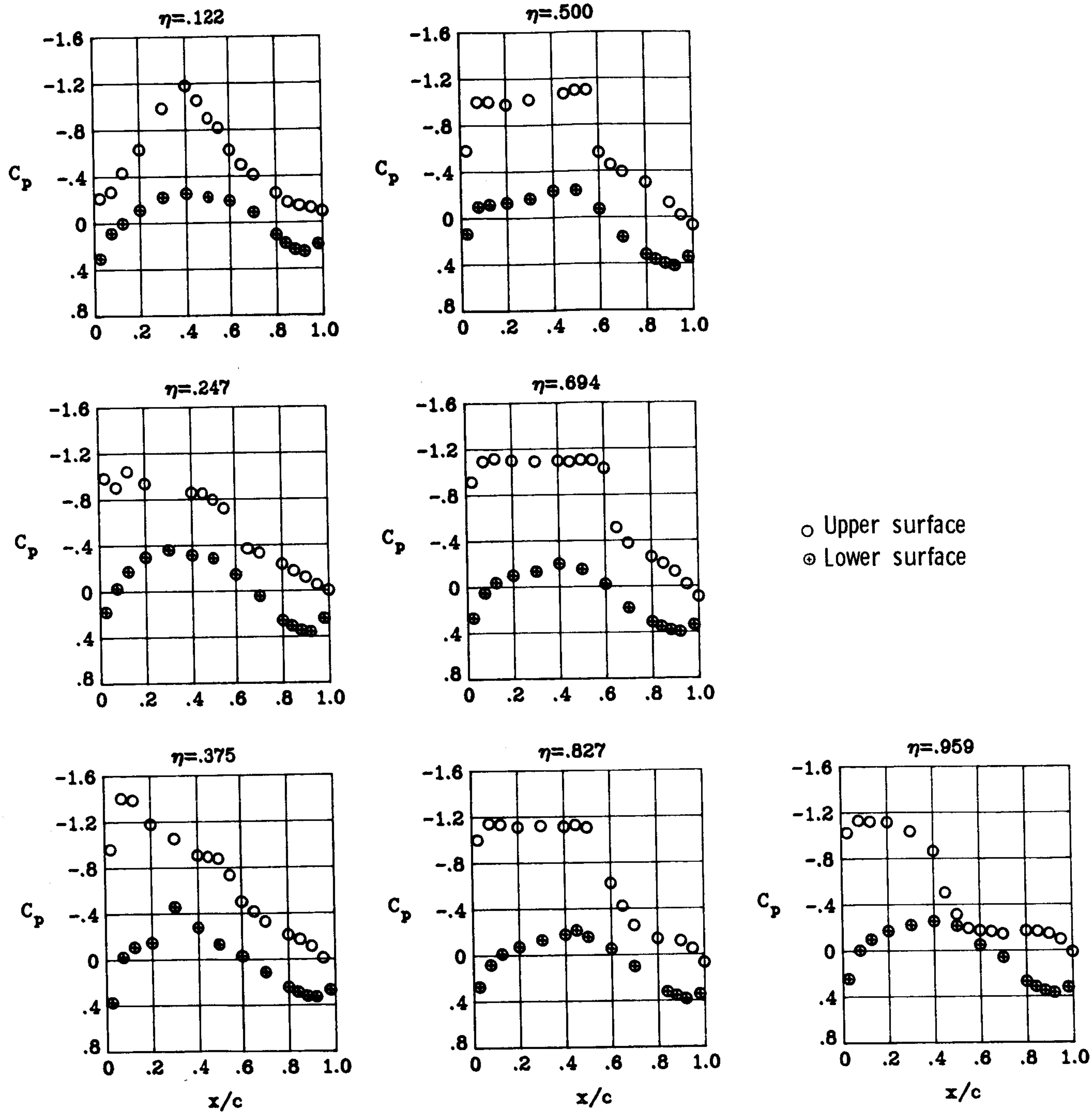

(d) $M_\infty = 0.82$; $\alpha = 4°$.

Figure 27.- Continued.

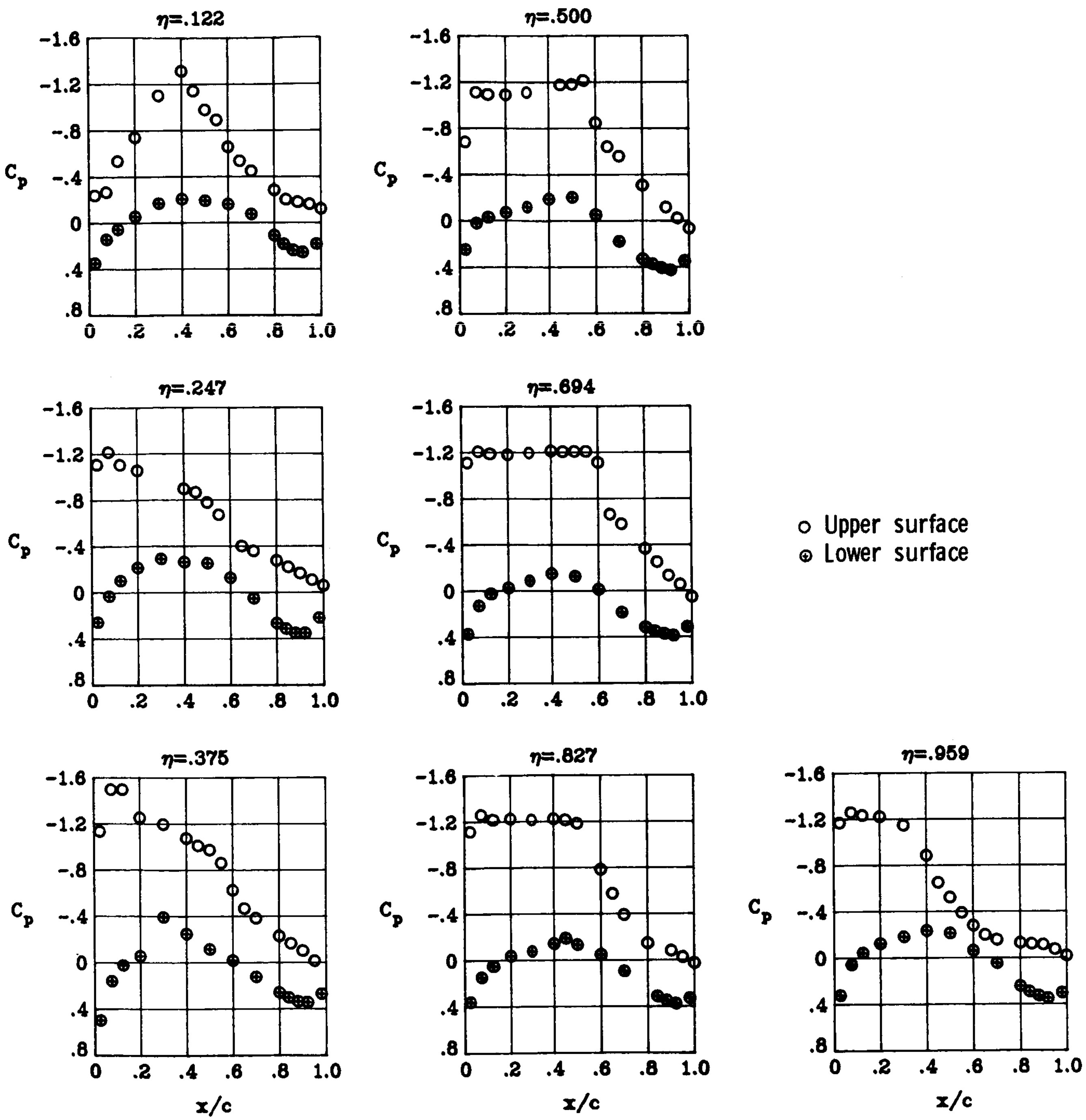

(e) $M_\infty = 0.82$; $\alpha = 5°$.

Figure 27.- Concluded.

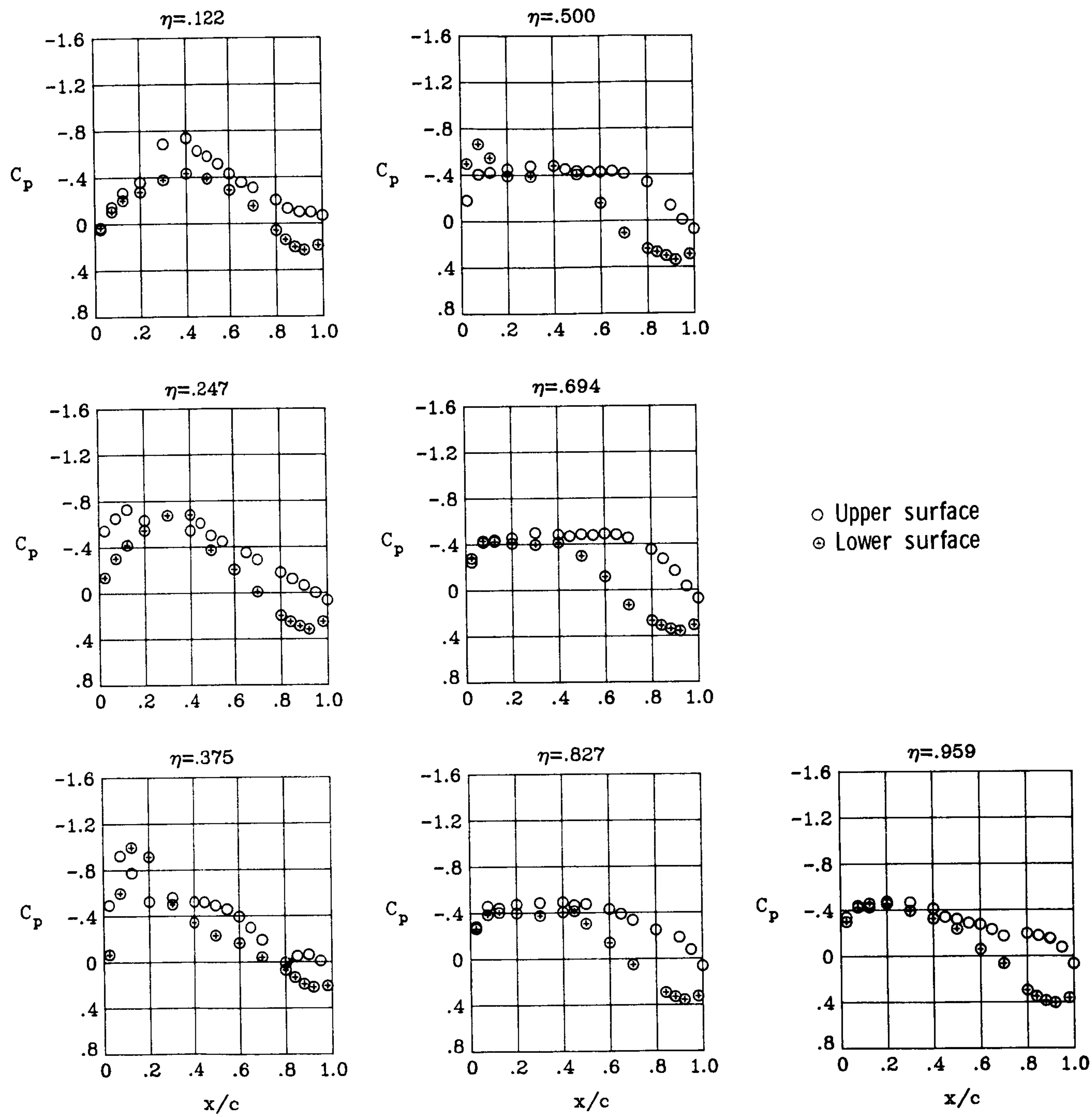

(a) $M_\infty = 0.82$; $\alpha = 1°$.

Figure 28.- Wing chordwise pressure distributions for $\delta a_1 = -7.5°$ at $M_\infty = 0.82$. $\delta a_2 = 0°$.

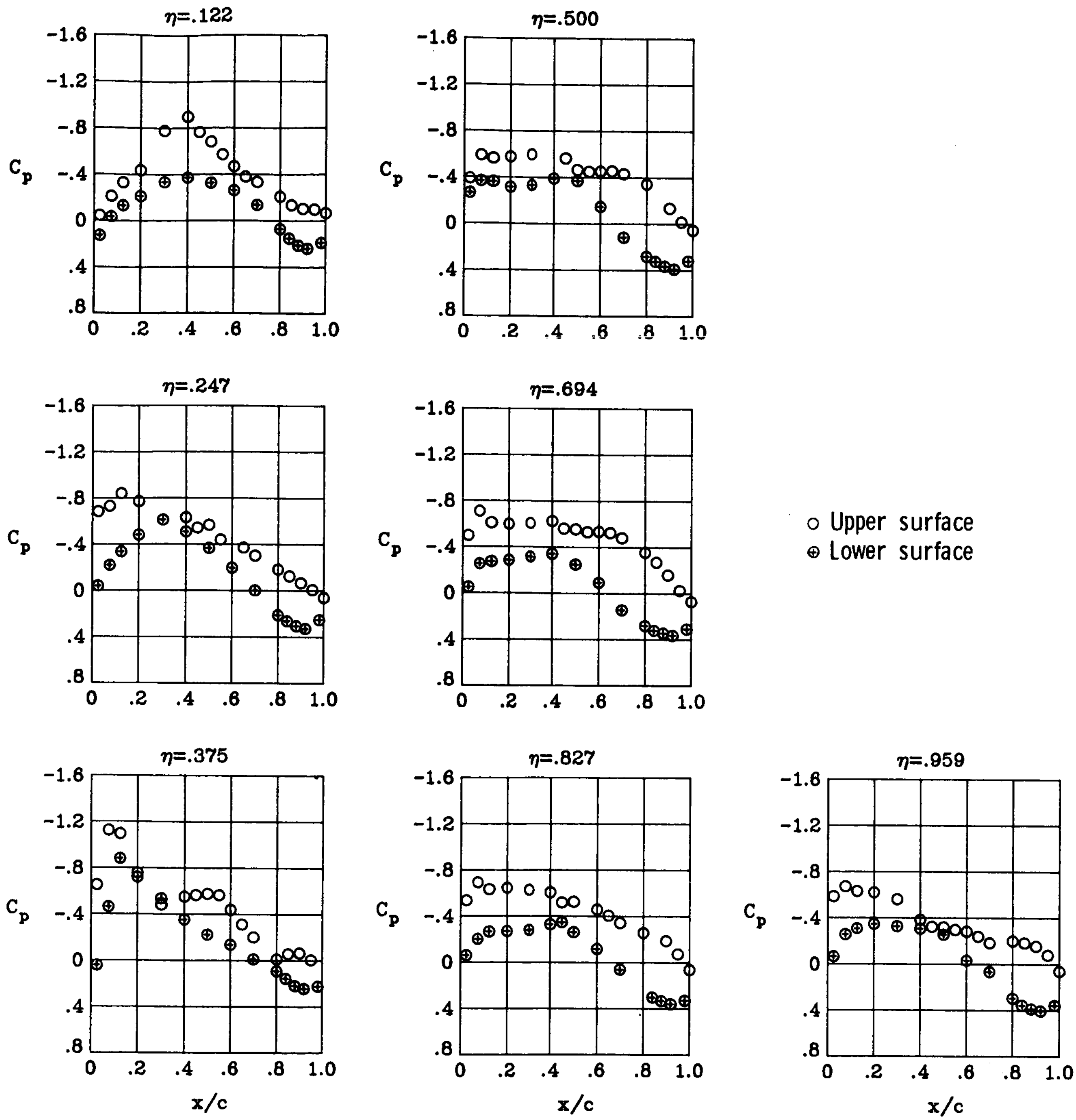

(b) $M_\infty = 0.82$; $\alpha = 2°$.

Figure 28.- Continued.

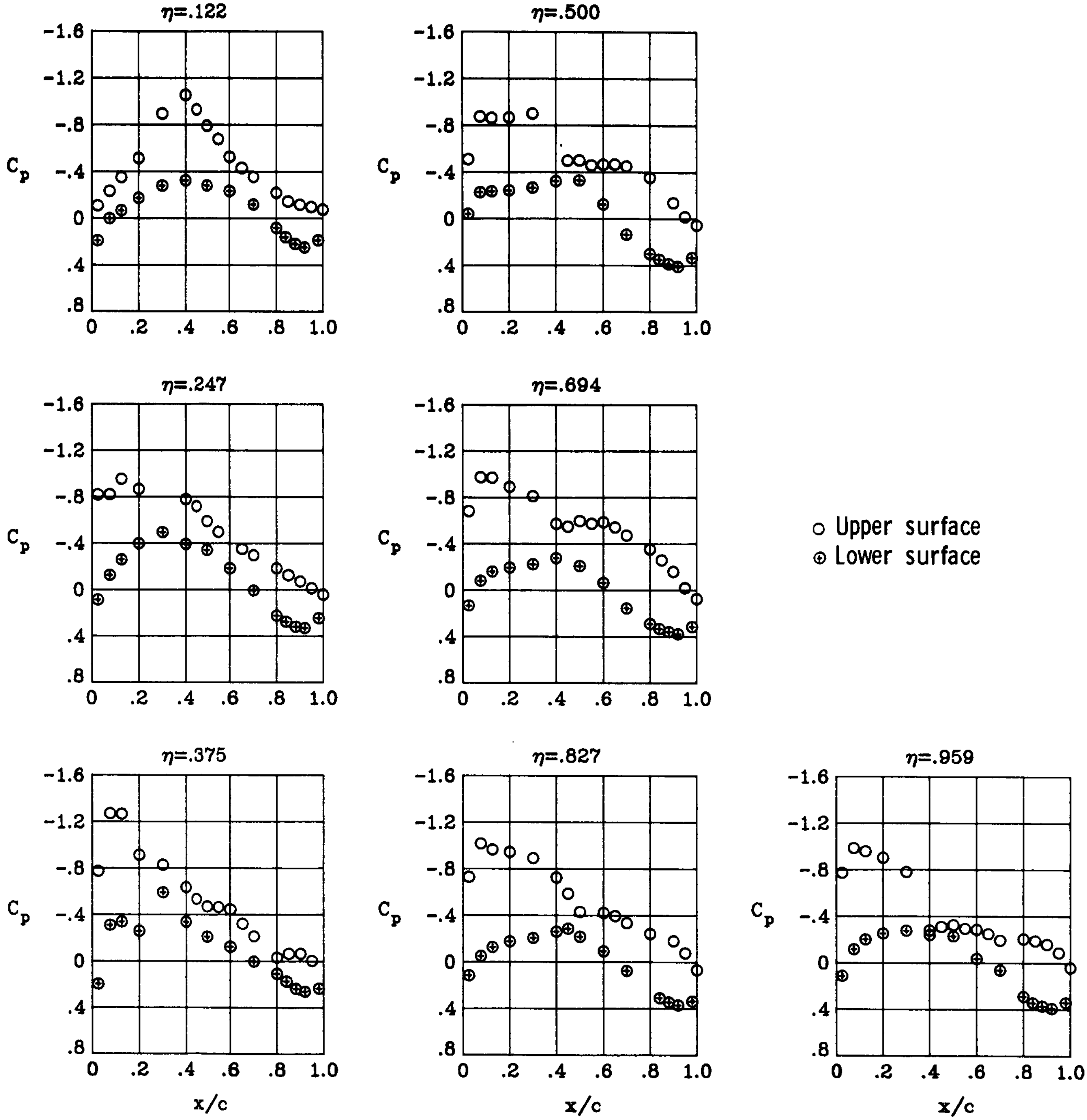

(c) $M_\infty = 0.82$; $\alpha = 3°$.

Figure 28.- Continued.

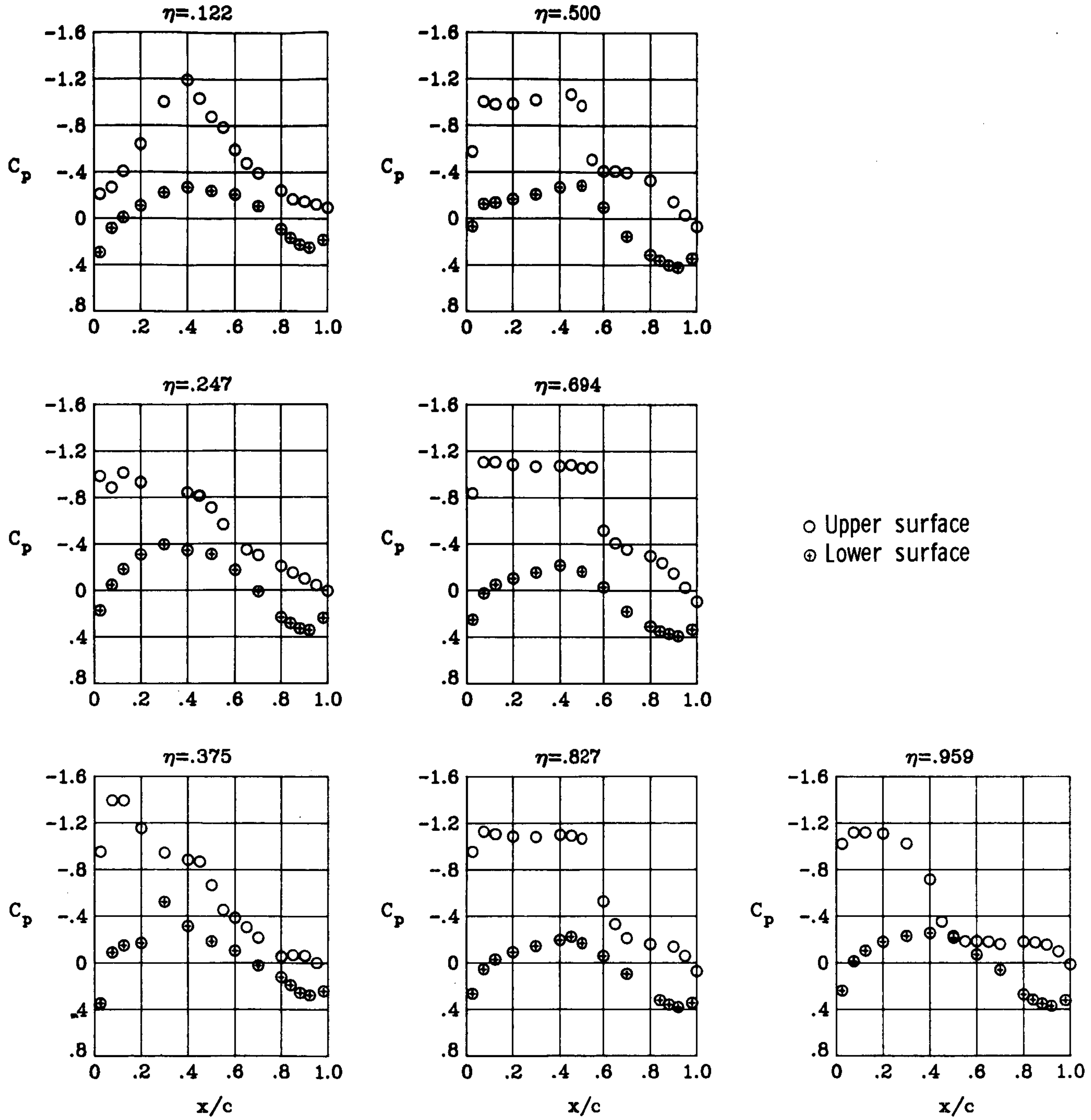

(d) $M_\infty = 0.82$; $\alpha = 4°$.

Figure 28.- Continued.

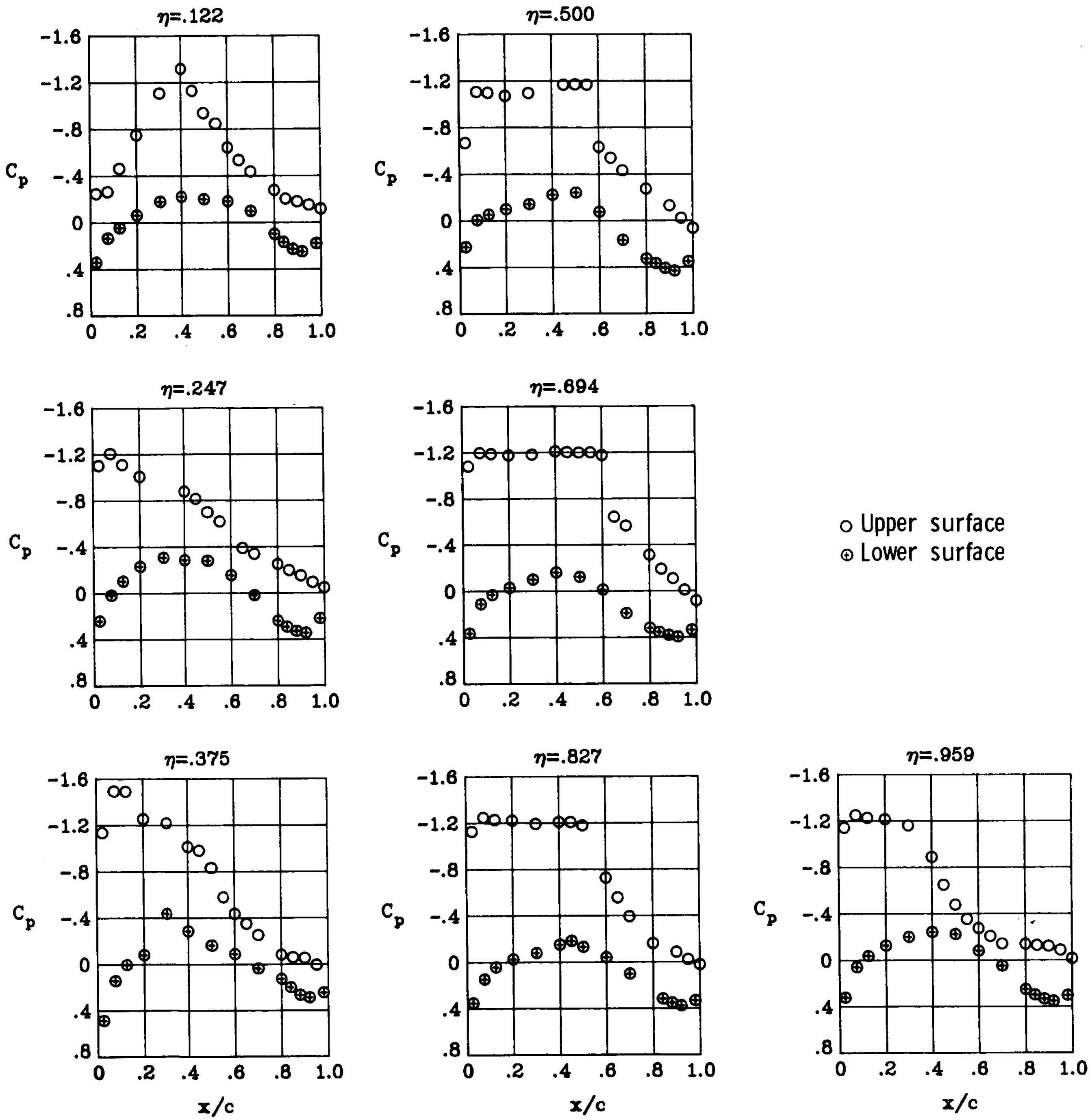

(e) $M_\infty = 0.82$; $\alpha = 5°$.

Figure 28.- Concluded.

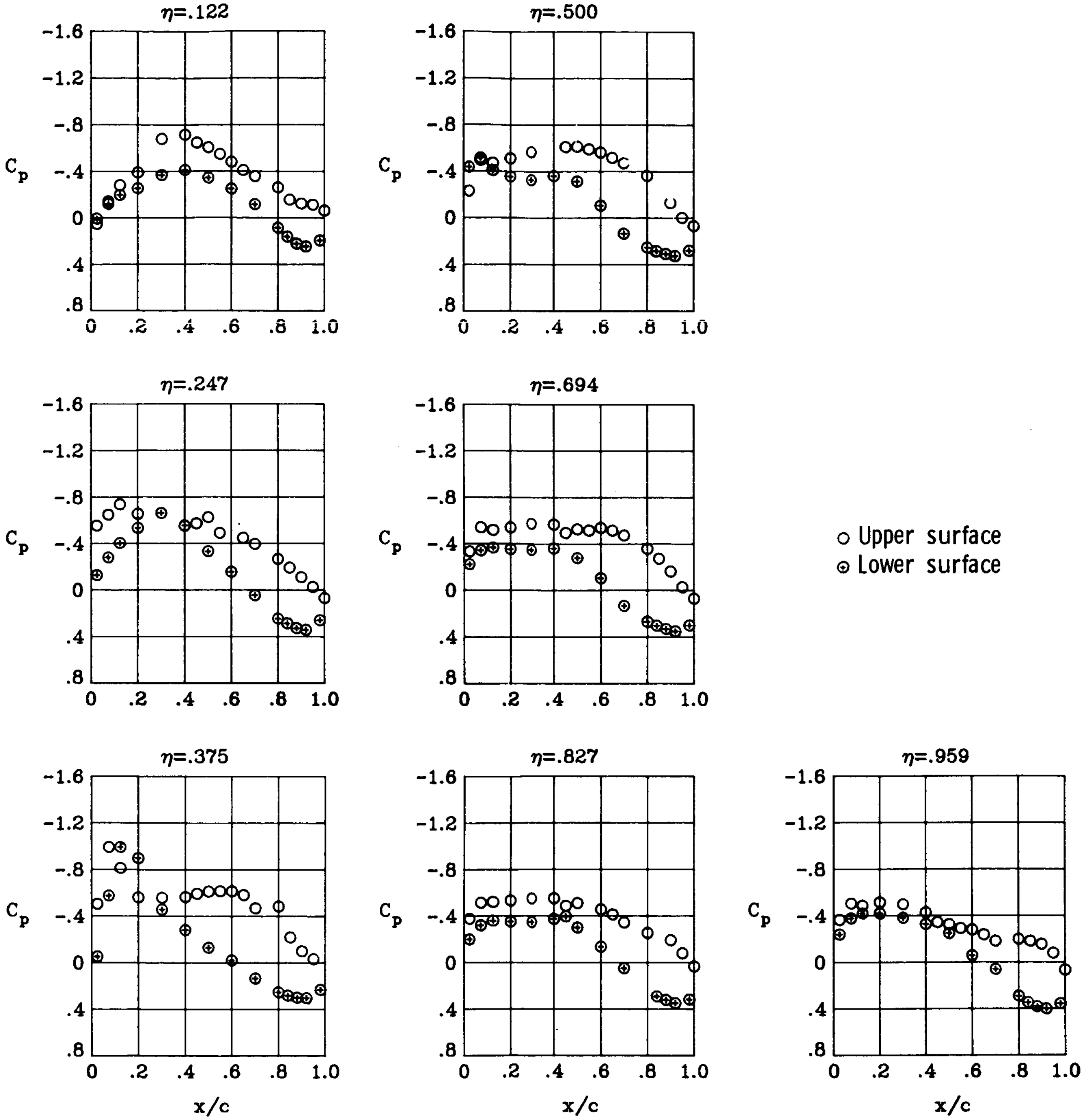

(a) $M_\infty = 0.82$; $\alpha = 1°$.

Figure 29.- Wing chordwise pressure distributions for $\delta a_1 = 2.5°$ at $M_\infty = 0.82$. $\delta a_2 = 0°$.

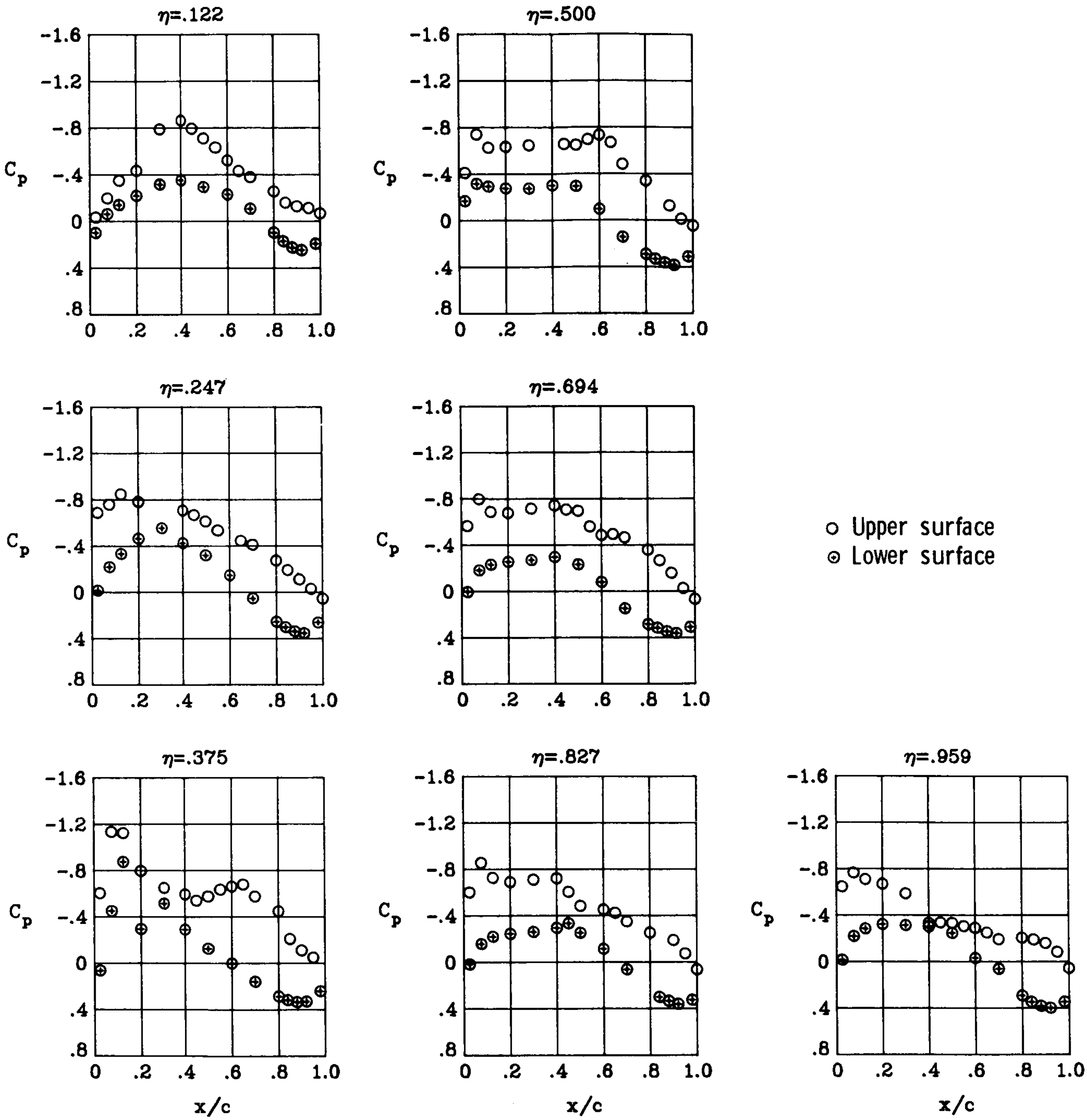

(b) $M_\infty = 0.82$; $\alpha = 2°$.

Figure 29.- Continued.

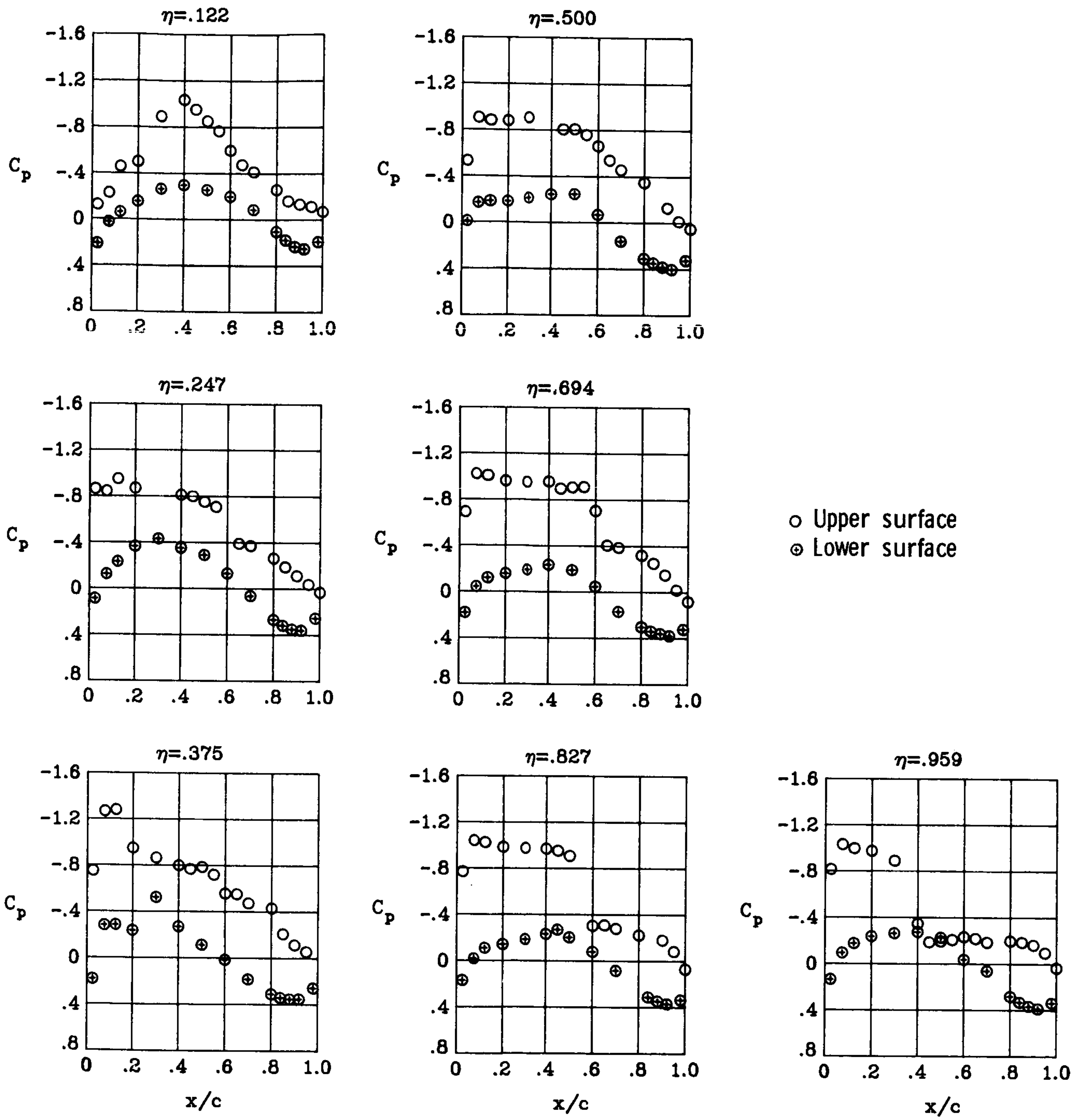

(c) $M_\infty = 0.82$; $\alpha = 3°$.

Figure 29.- Continued.

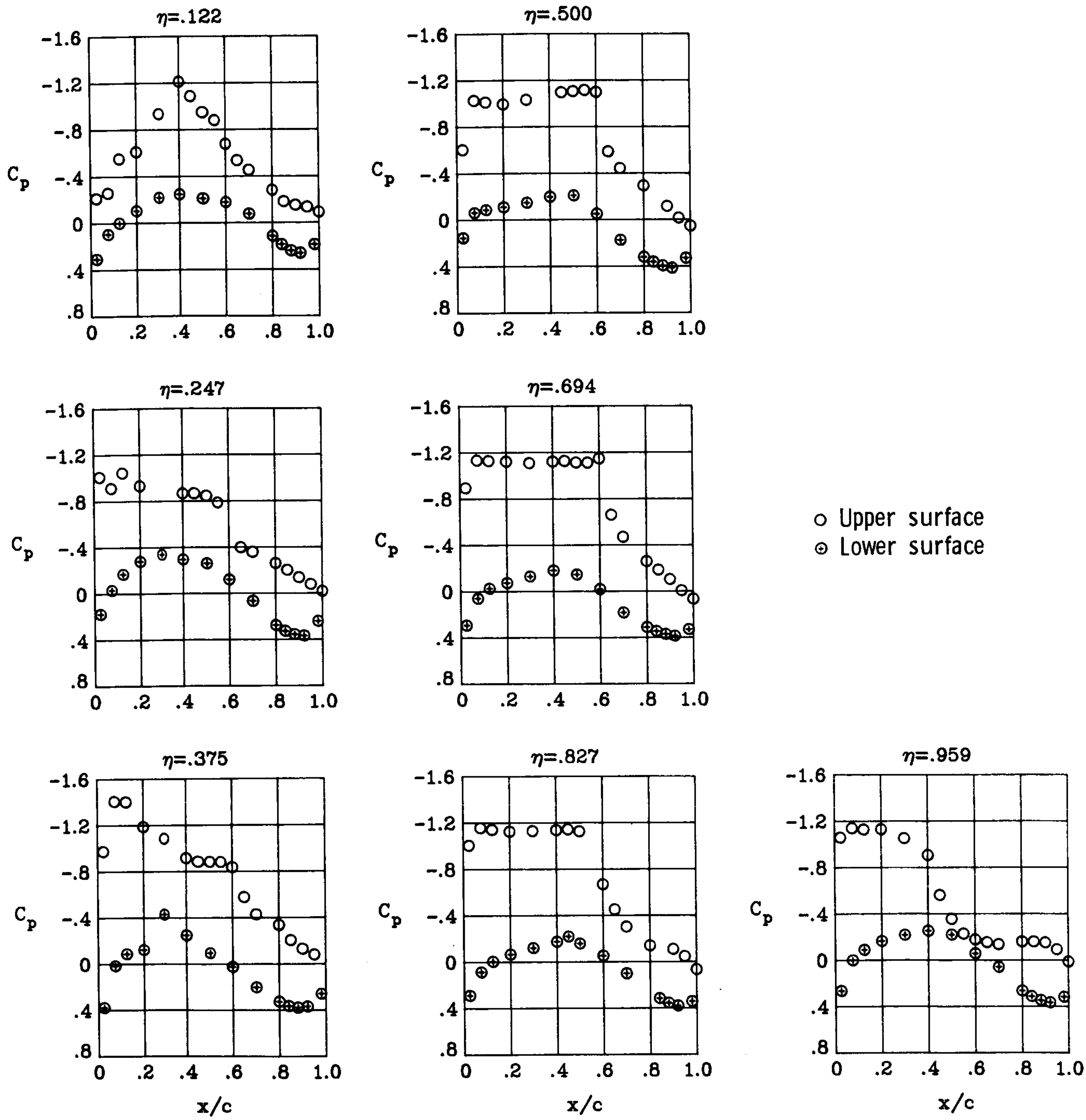

(d) $M_\infty = 0.82$; $\alpha = 4°$.

Figure 29.- Continued.

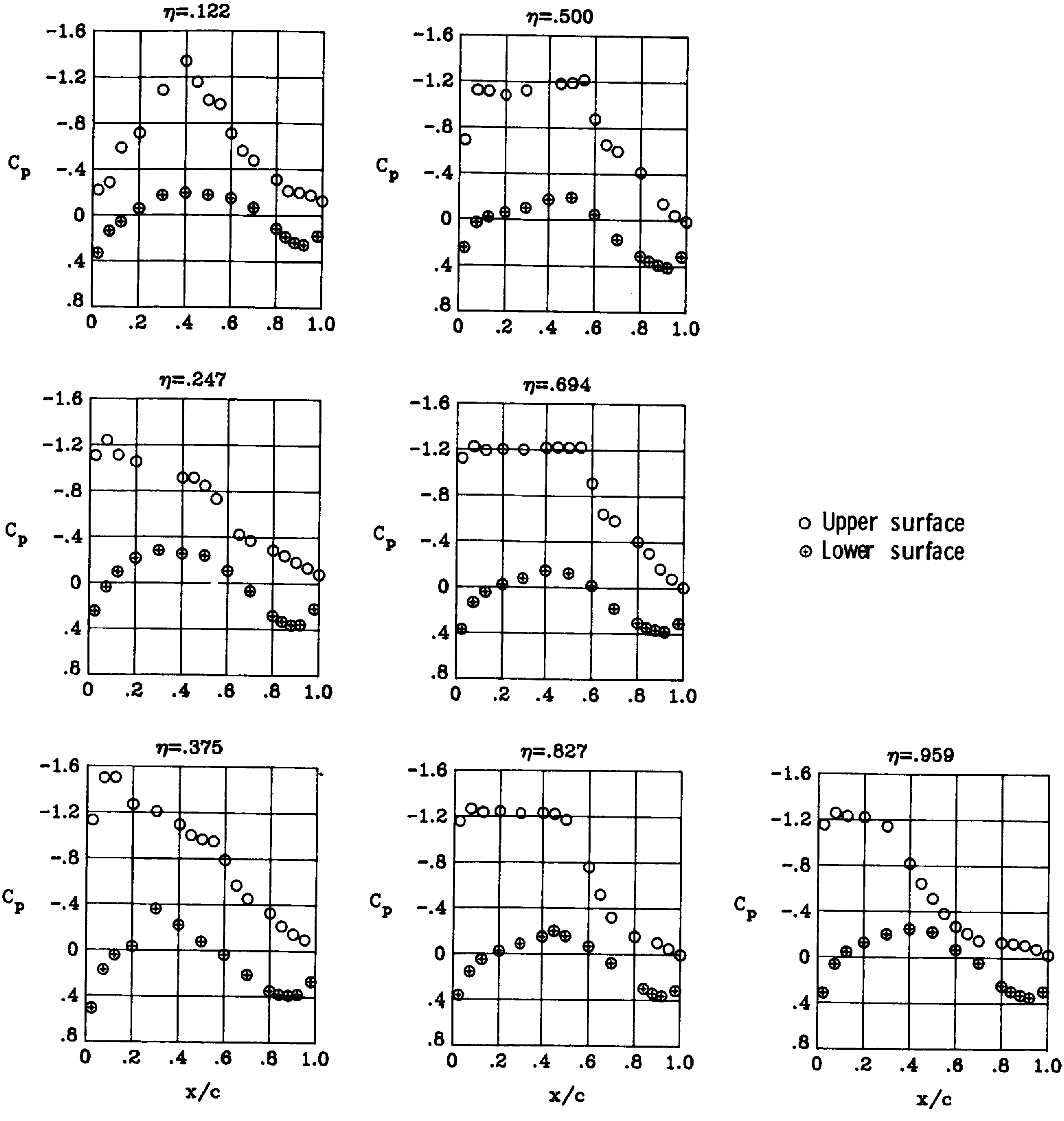

(e) $M_\infty = 0.82$; $\alpha = 5°$.

Figure 29.- Concluded.

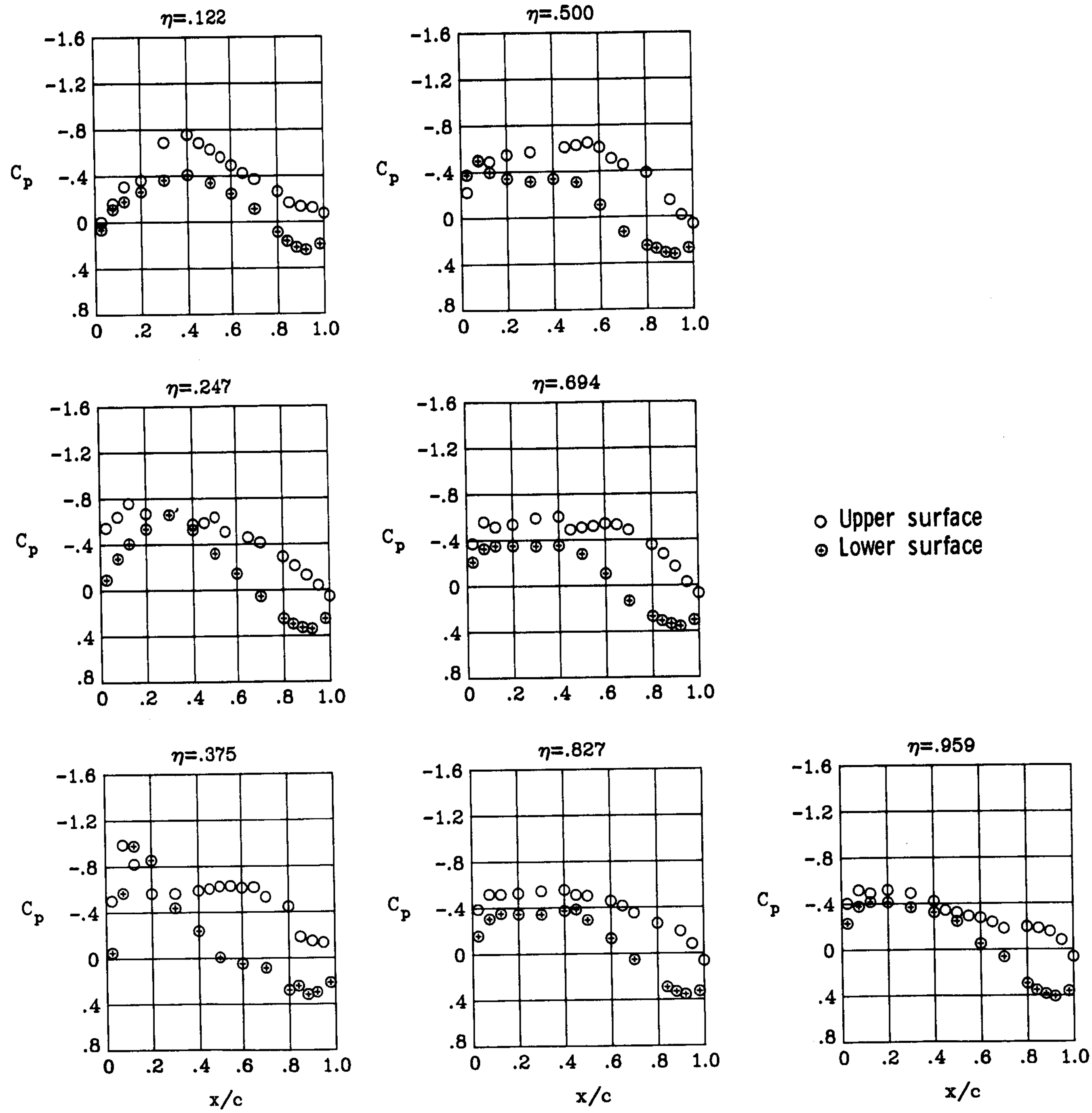

(a) $M_\infty = 0.82$; $\alpha = 1°$.

Figure 30.- Wing chordwise pressure distributions for $\delta a_1 = 7.5°$ at $M_\infty = 0.82$. $\delta a_2 = 0°$.

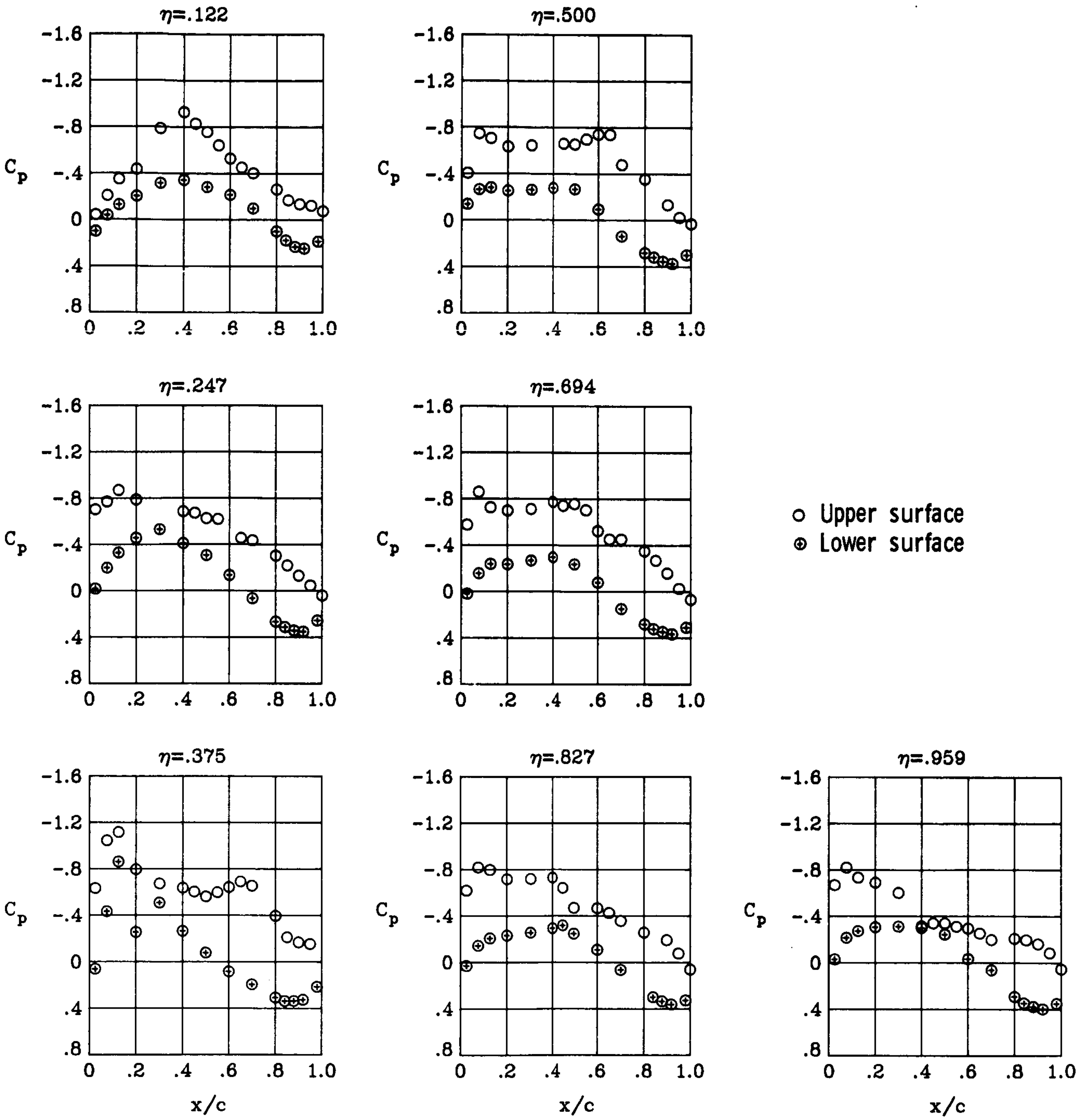

(b) $M_\infty = 0.82$; $\alpha = 2°$.

Figure 30.- Continued.

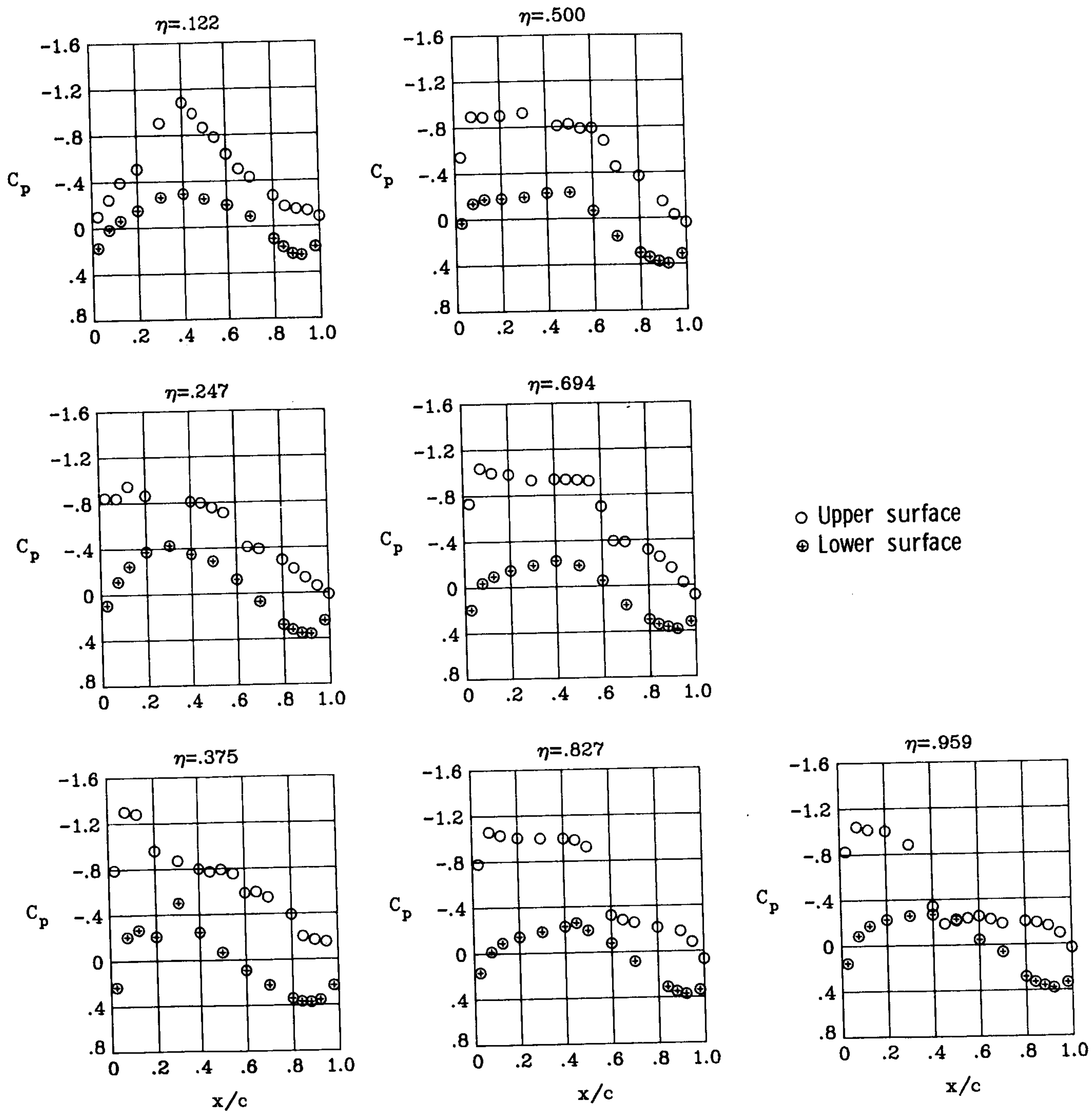

(c) $M_\infty = 0.82$; $\alpha = 3°$.

Figure 30.- Continued.

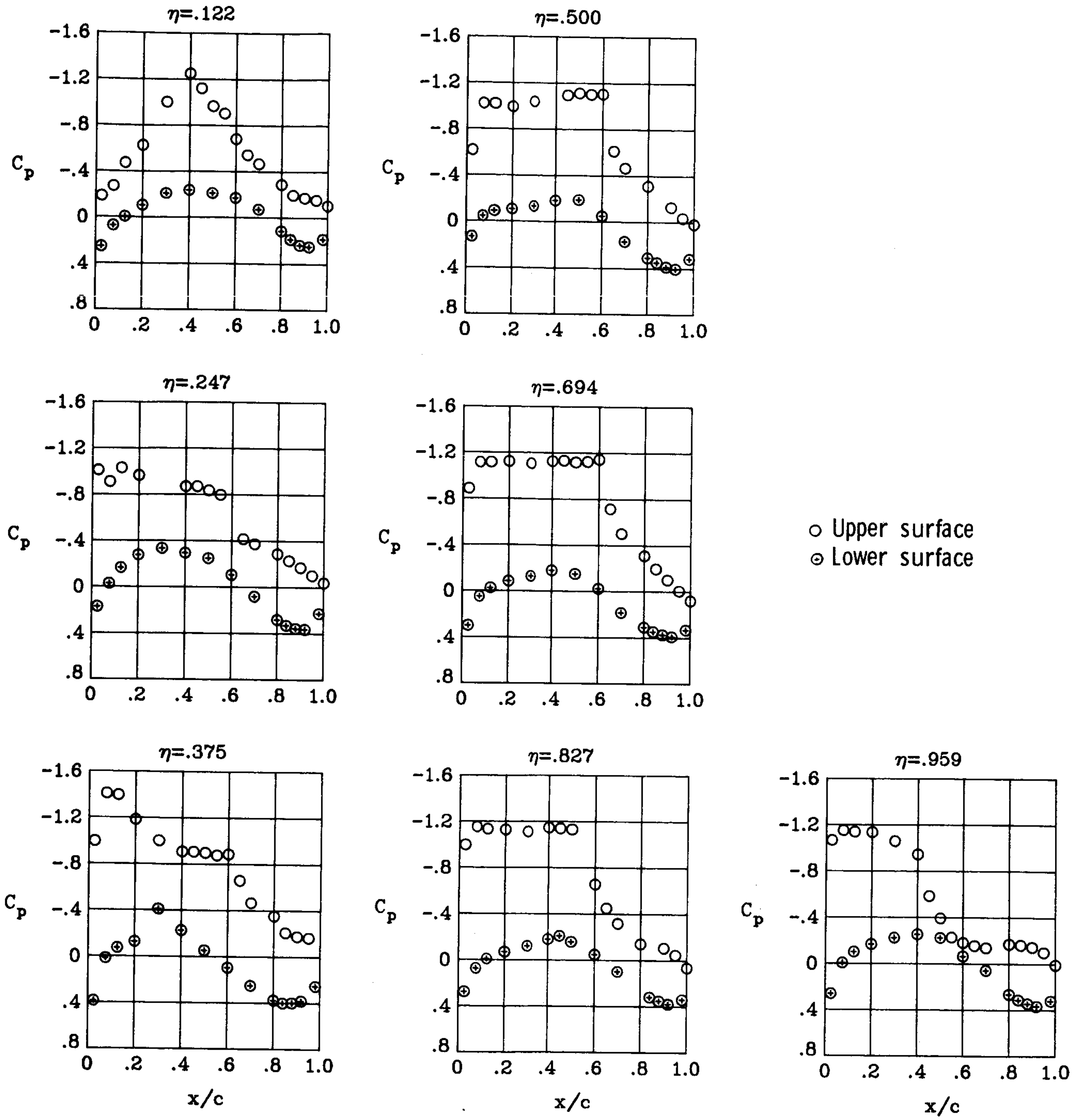

(d) $M_\infty = 0.82$; $\alpha = 4°$.

Figure 30.- Continued.

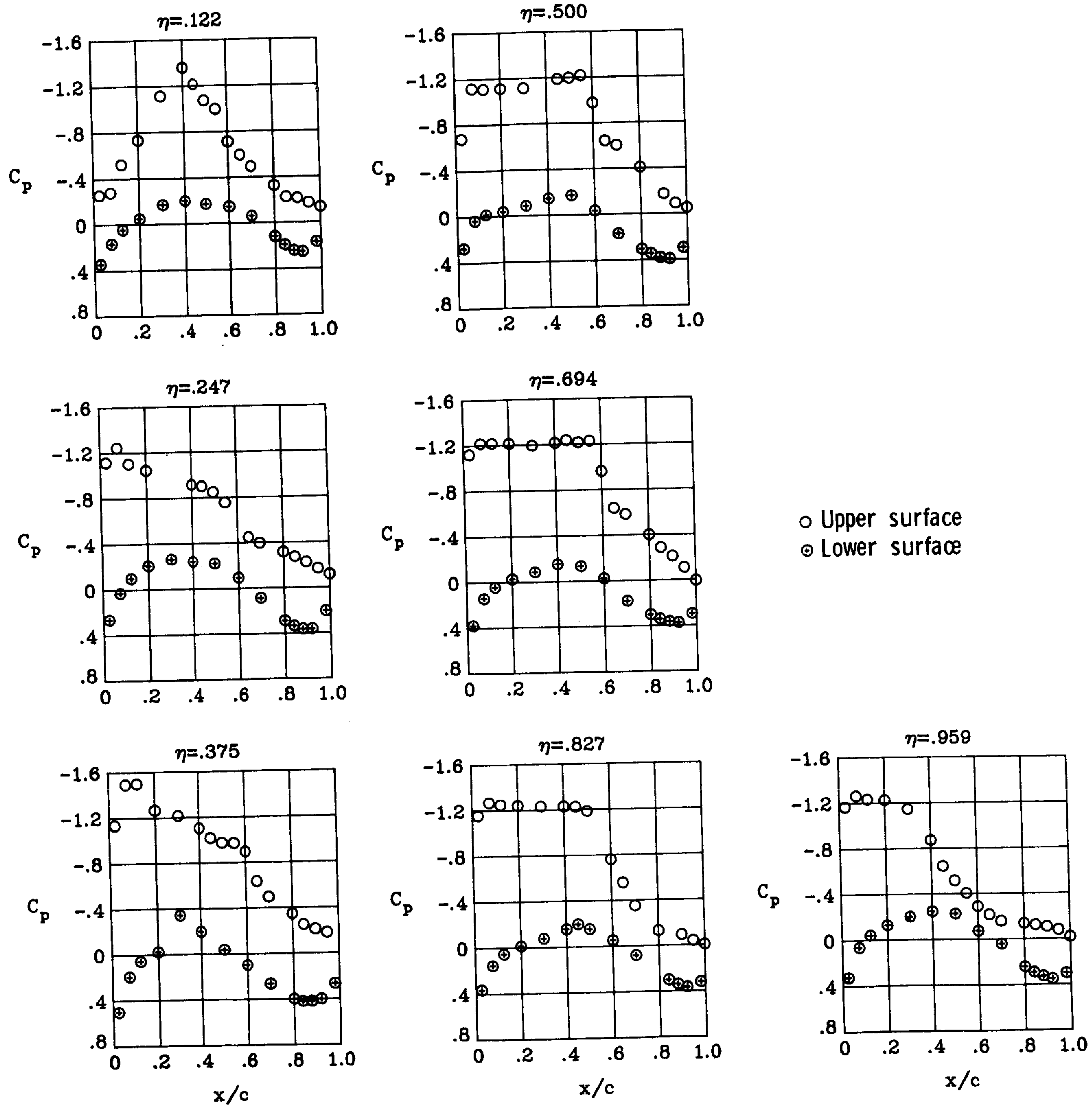

(e) $M_\infty = 0.82$; $\alpha = 5°$.

Figure 30.- Concluded.

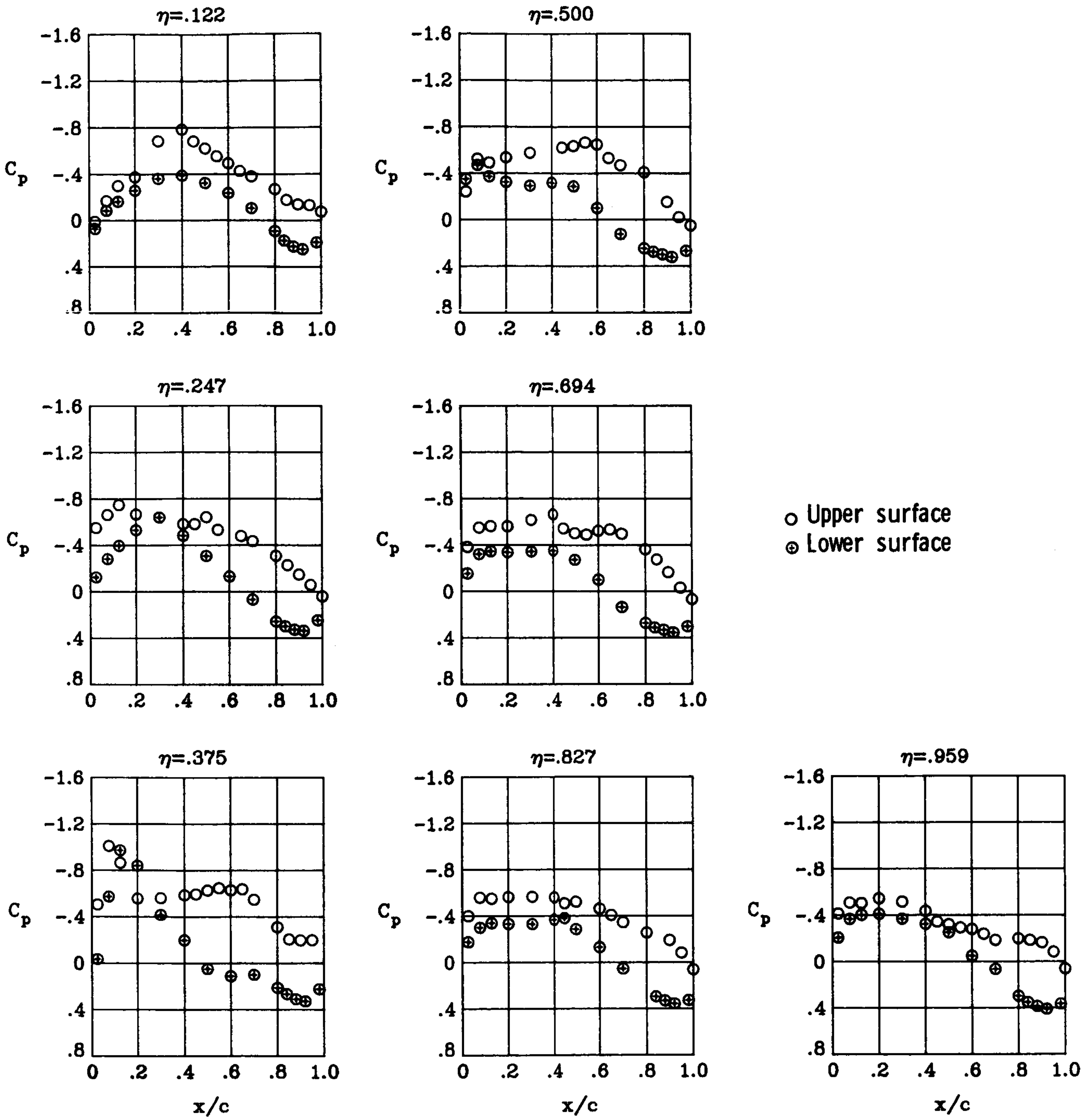

(a) $M_\infty = 0.82$; $\alpha = 1°$.

Figure 31.- Wing chordwise pressure distributions for $\delta a_1 = 12.5°$ at $M_\infty = 0.82$. $\delta a_2 = 0°$.

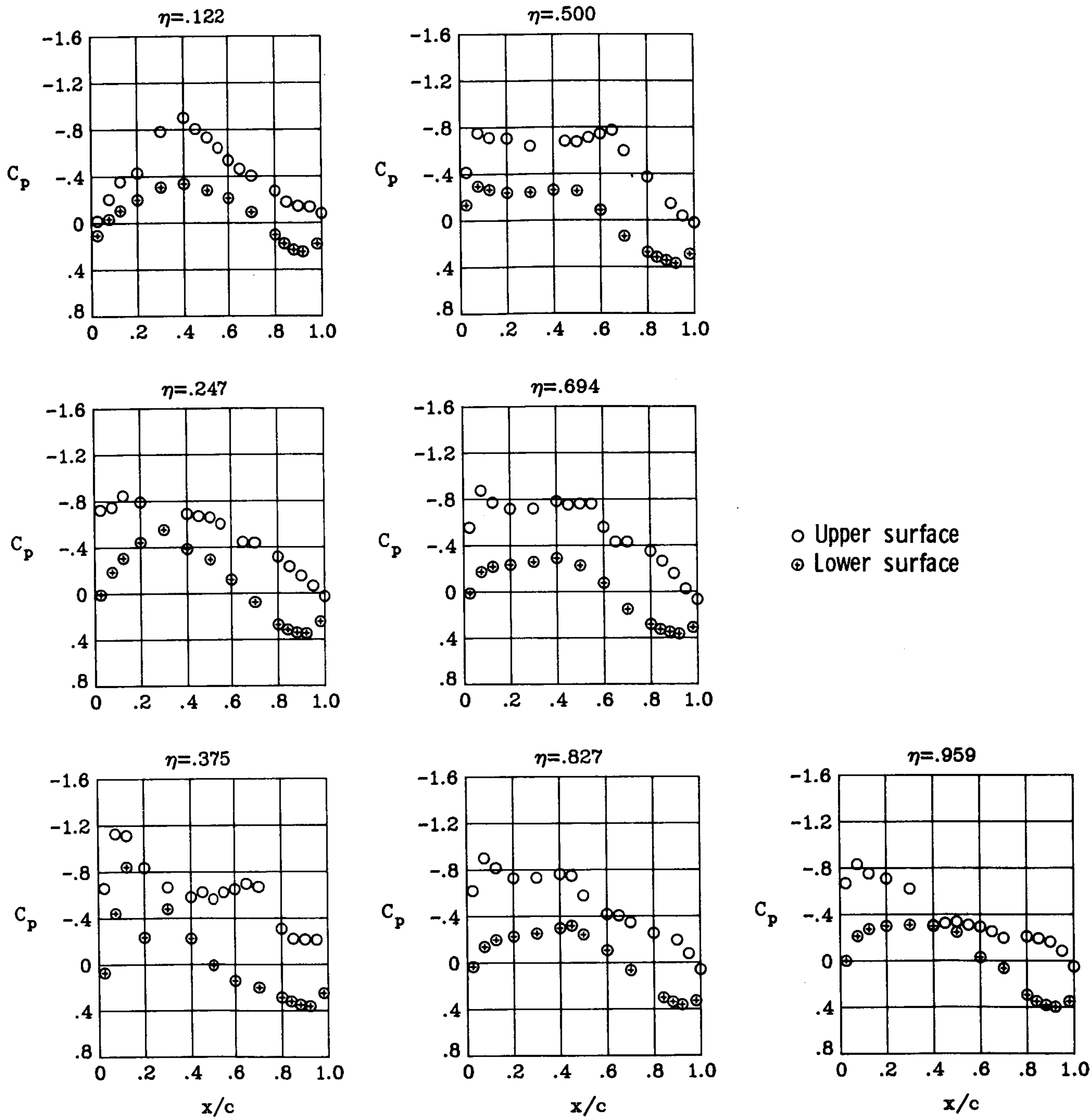

(b) $M_\infty = 0.82$; $\alpha = 2°$.

Figure 31.- Continued.

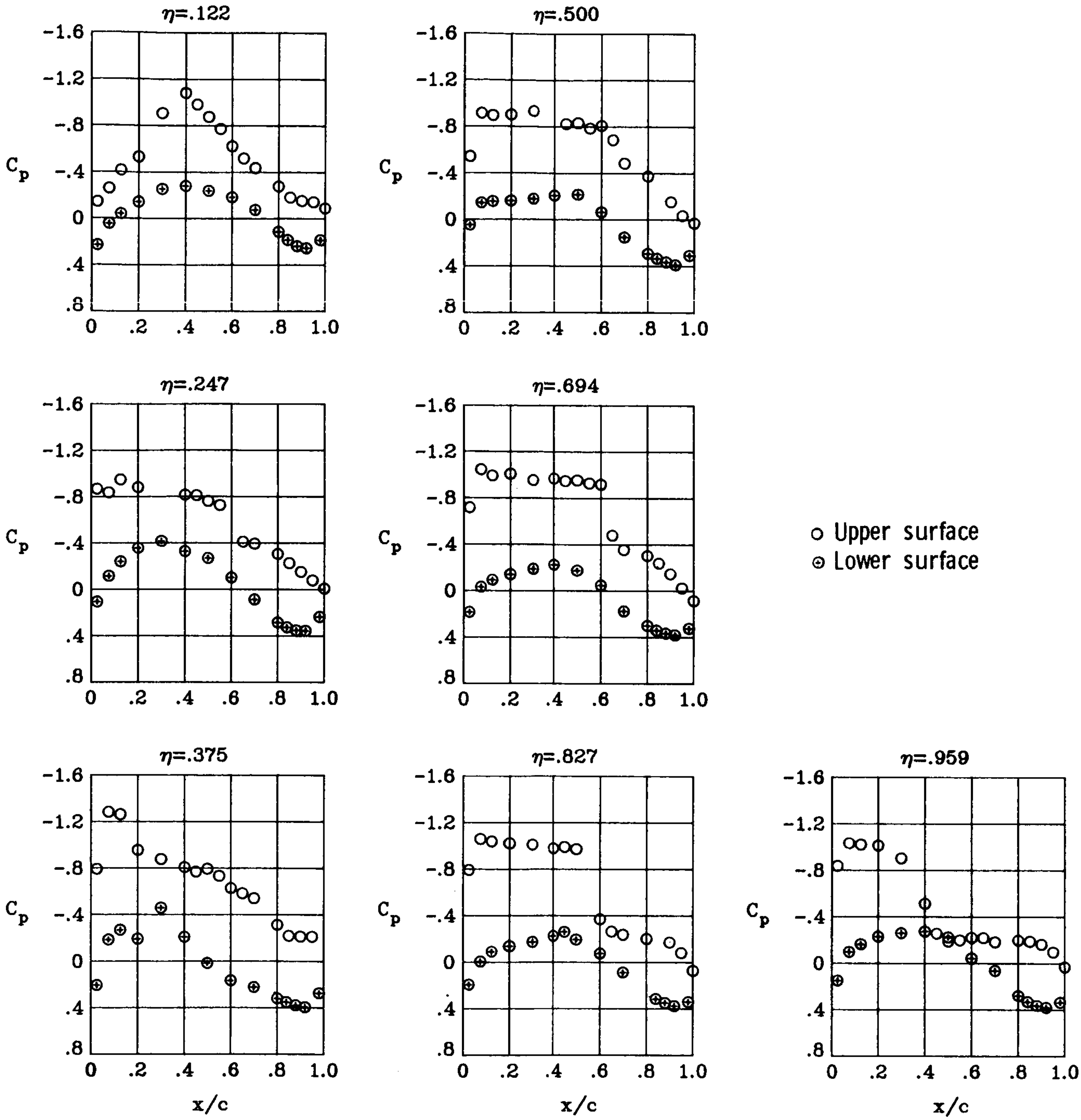

(c) $M_\infty = 0.82$; $\alpha = 3°$.

Figure 31.- Continued.

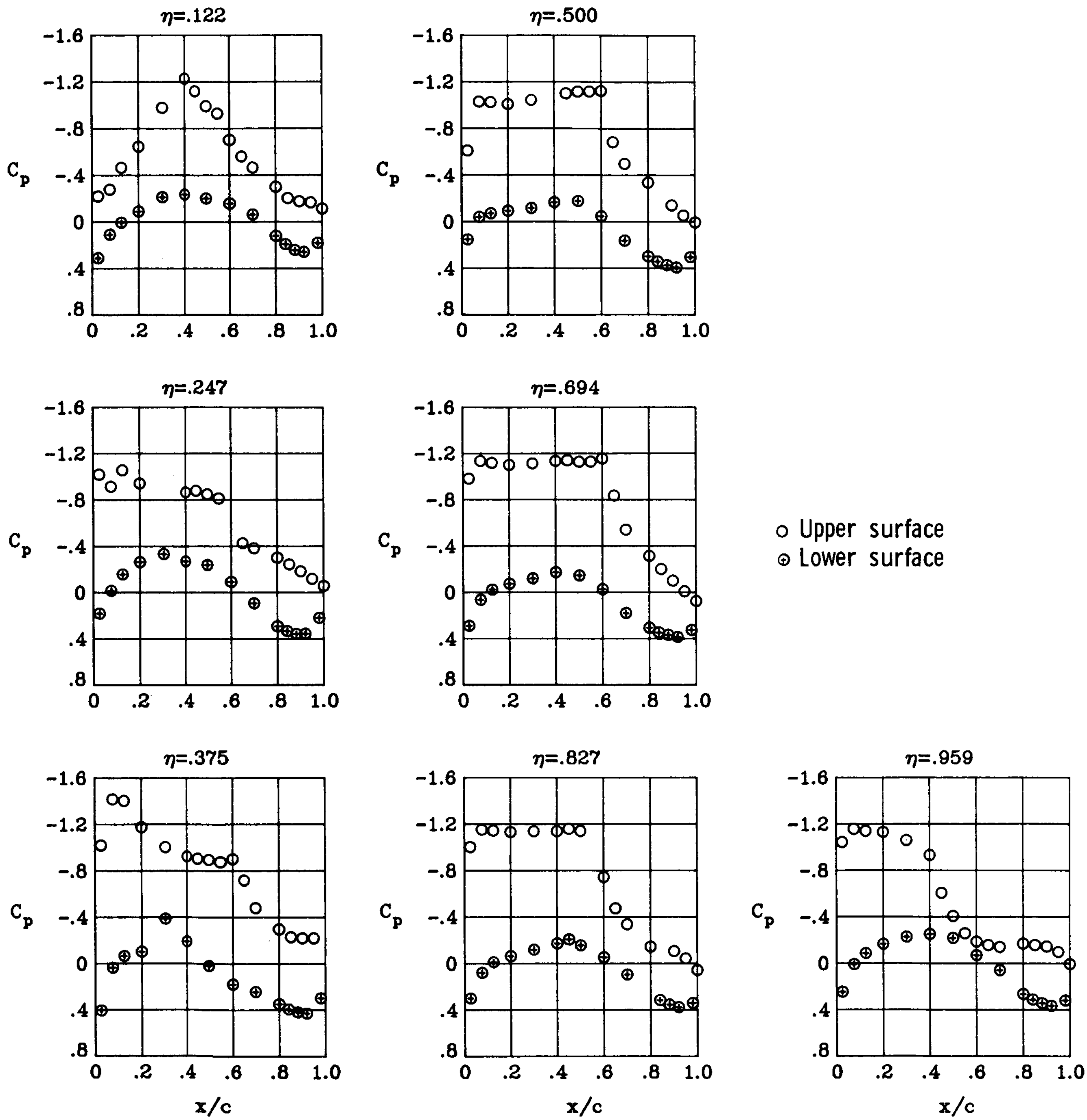

(d) M_∞ = 0.82; α = 4°.

Figure 31.- Continued.

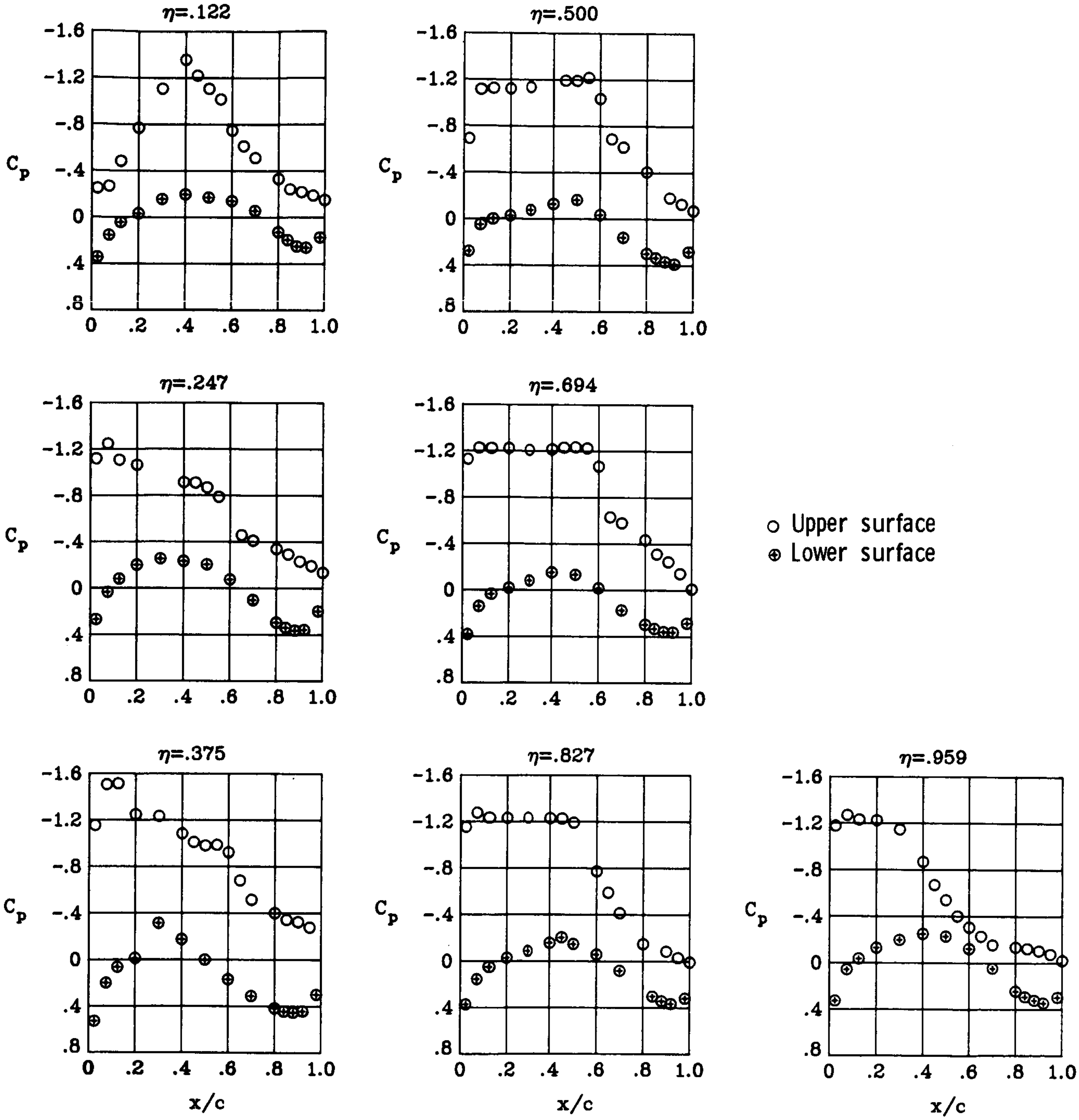

(e) M_∞ = 0.82; α = 5°.

Figure 31.- Concluded.

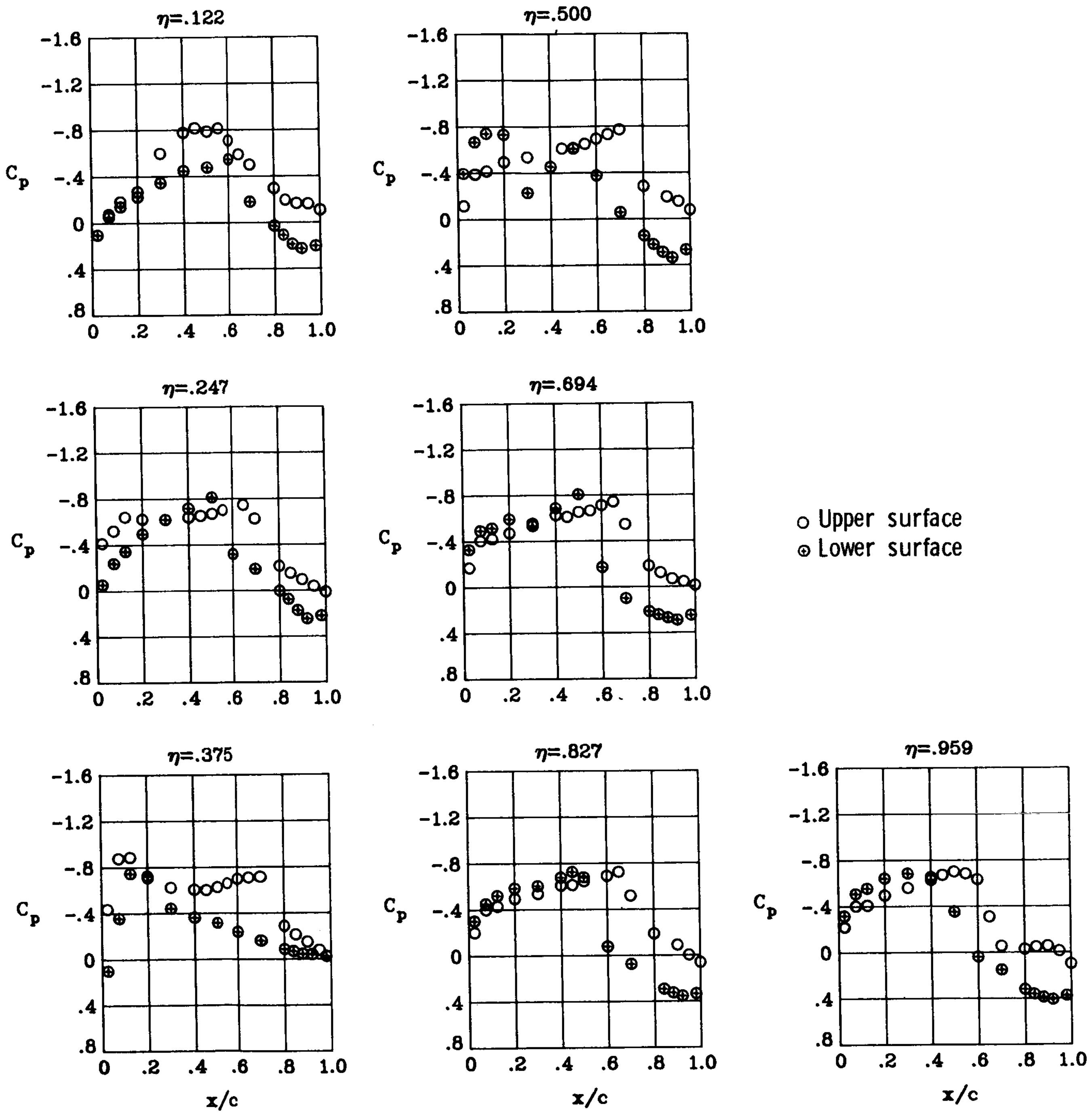

(a) $M_\infty = 0.90$; $\alpha = 1°$.

Figure 32.- Wing chordwise pressure distributions for $\delta a_1 = -7.5°$ at $M_\infty = 0.90$. $\delta a_2 = 0°$.

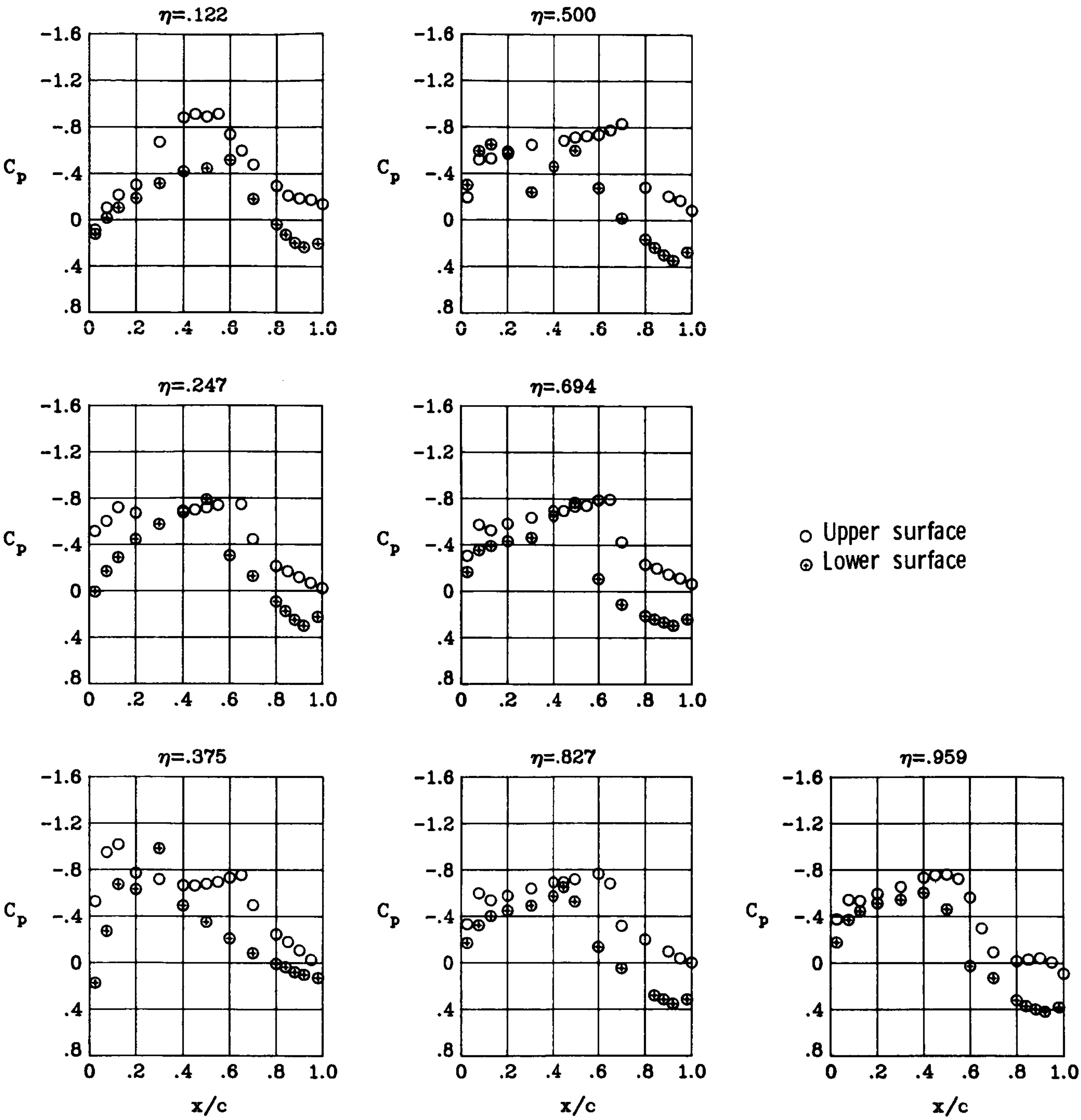

(b) $M_\infty = 0.90$; $\alpha = 2°$.

Figure 32.- Continued.

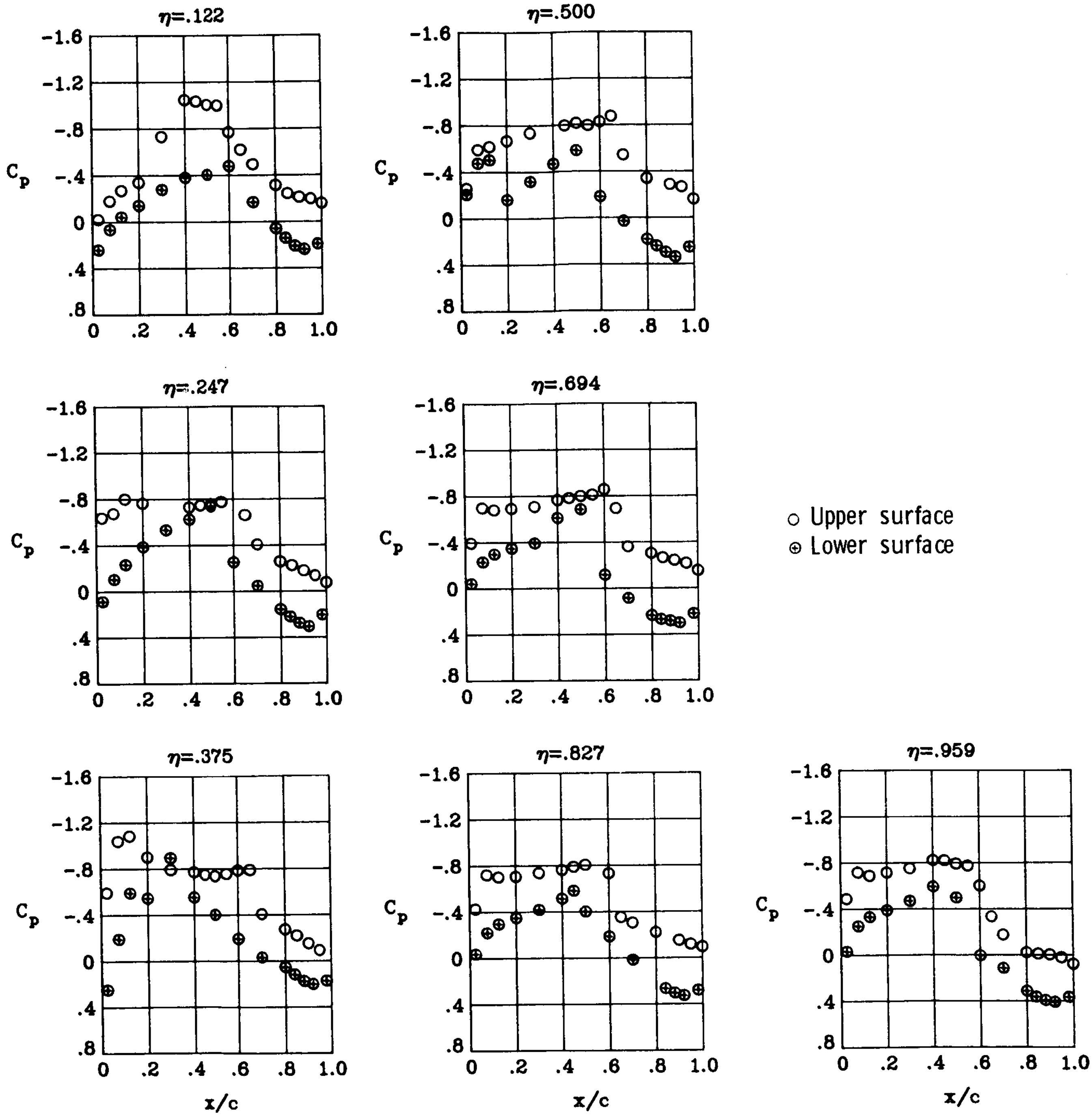

(c) $M_\infty = 0.90$; $\alpha = 3°$.

Figure 32.- Continued.

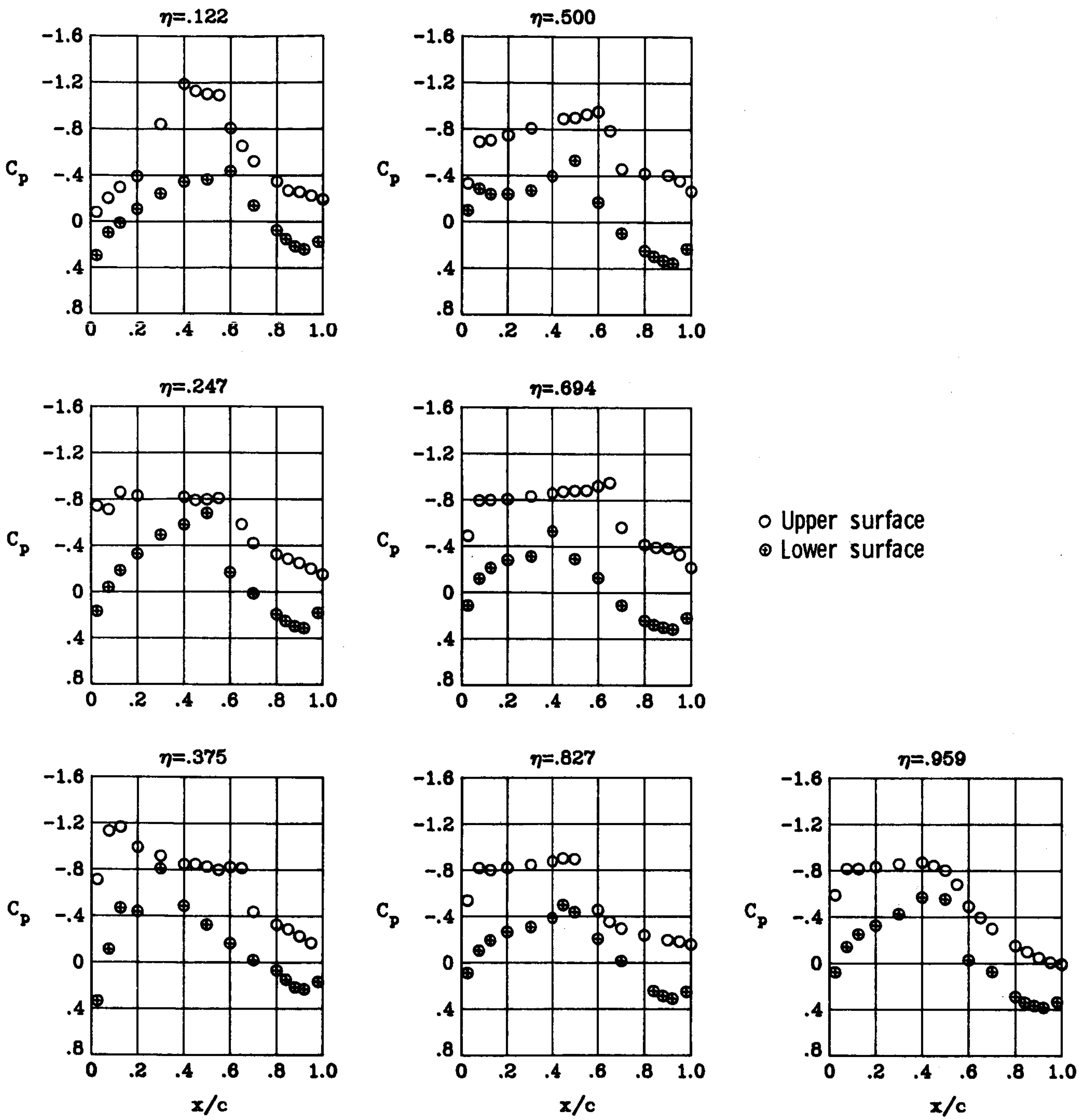

(d) $M_\infty = 0.90$; $\alpha = 4°$.

Figure 32.- Continued.

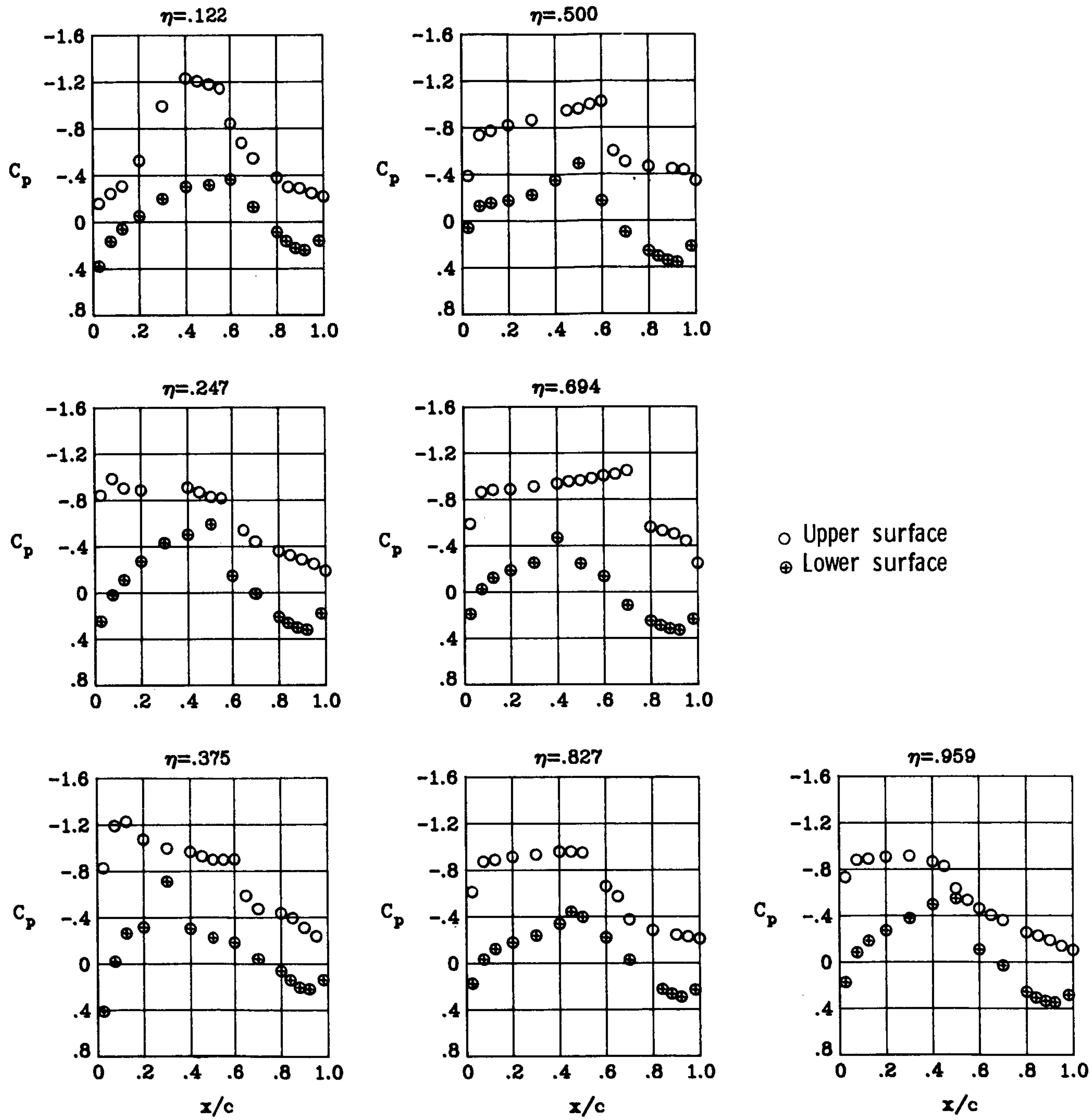

(e) $M_\infty = 0.90$; $\alpha = 5°$.

Figure 32.- Concluded.

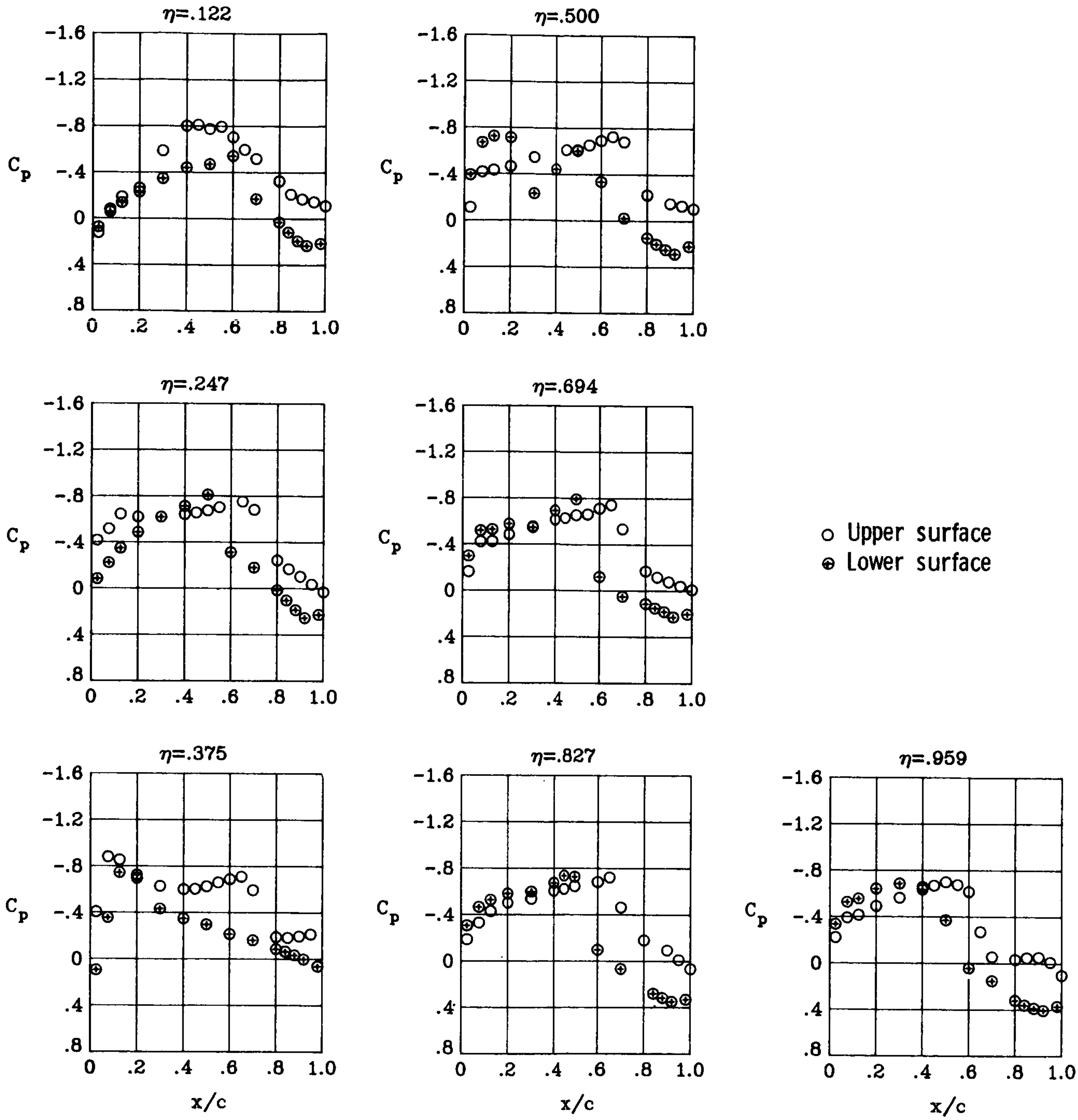

(a) $M_\infty = 0.90$; $\alpha = 1°$.

Figure 33.- Wing chordwise pressure distributions for $\delta a_1 = 7.5°$ at $M_\infty = 0.90$. $\delta a_2 = 0°$.

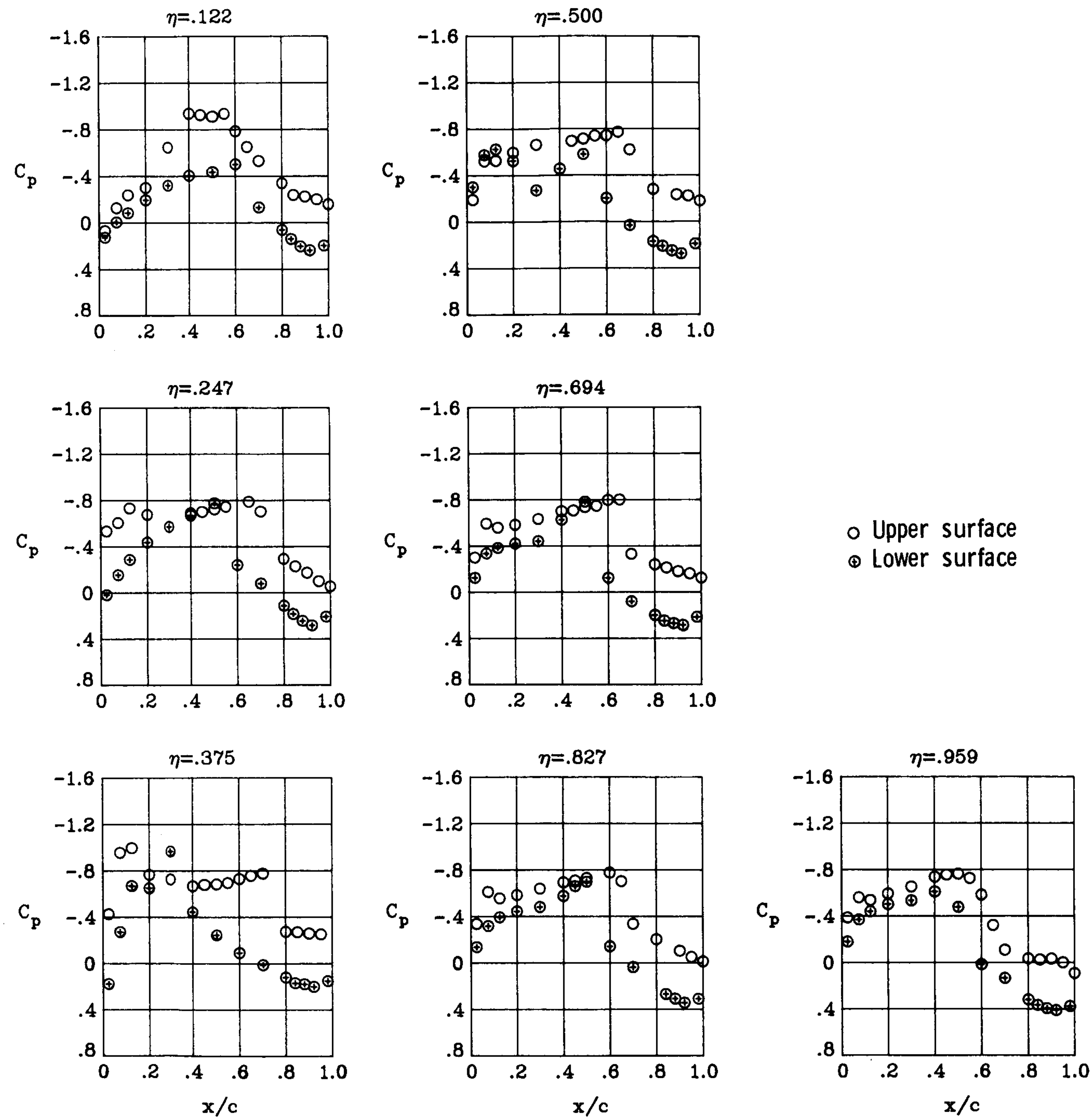

(b) $M_\infty = 0.90$; $\alpha = 2°$.

Figure 33.- Continued.

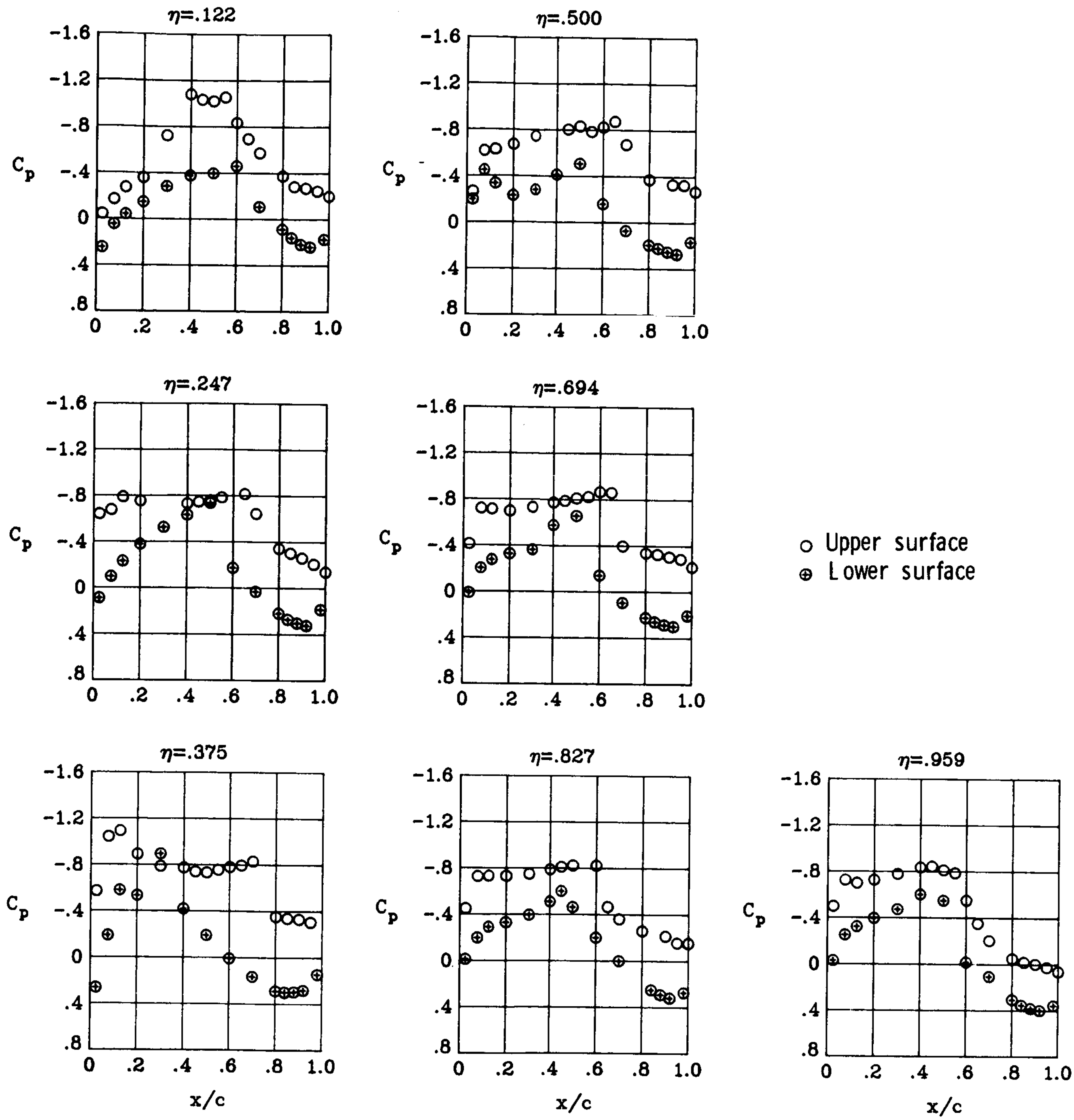

(c) $M_\infty = 0.90$; $\alpha = 3°$.

Figure 33.- Continued.

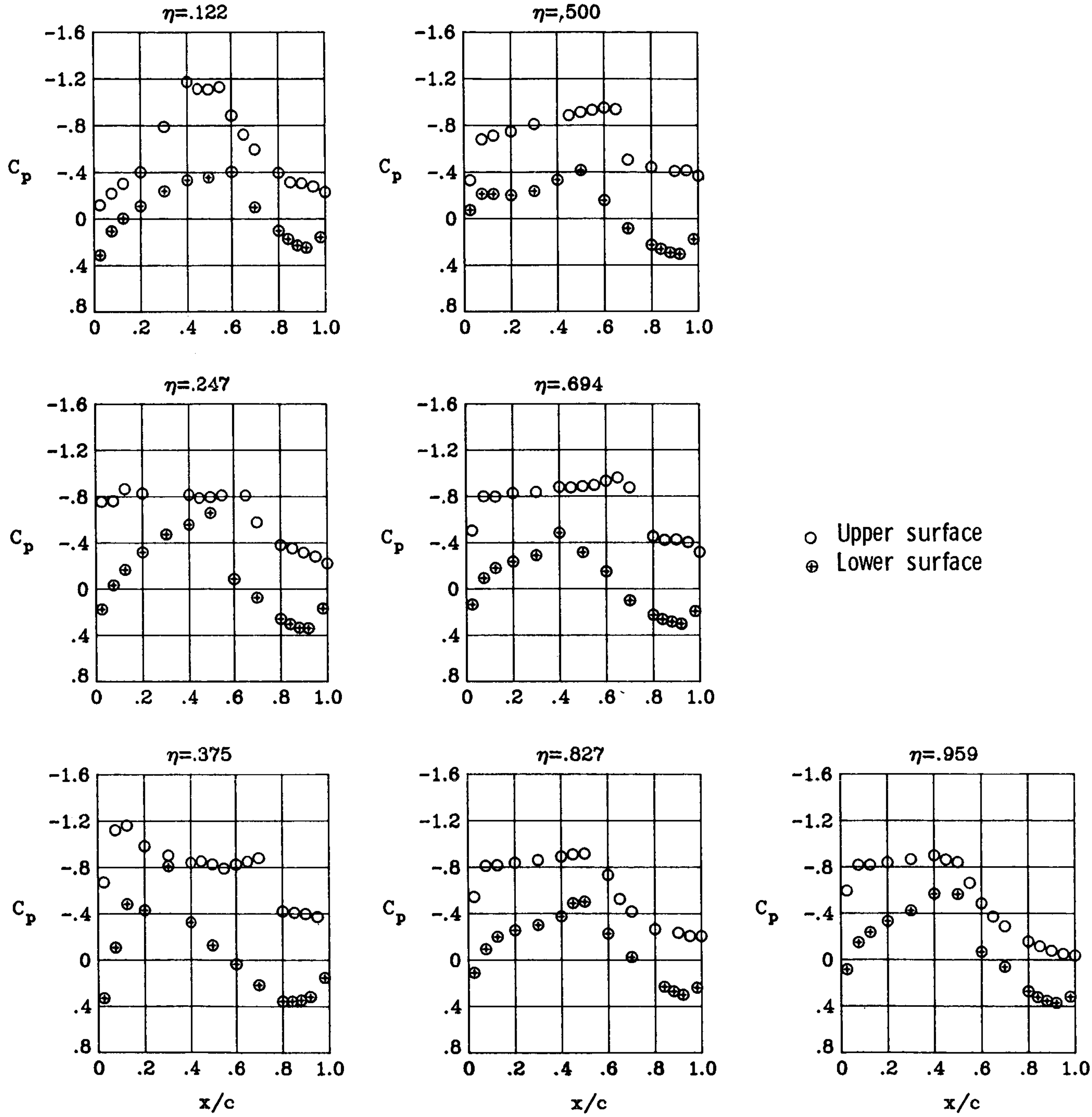

(d) $M_\infty = 0.90$; $\alpha = 4°$.

Figure 33.- Continued.

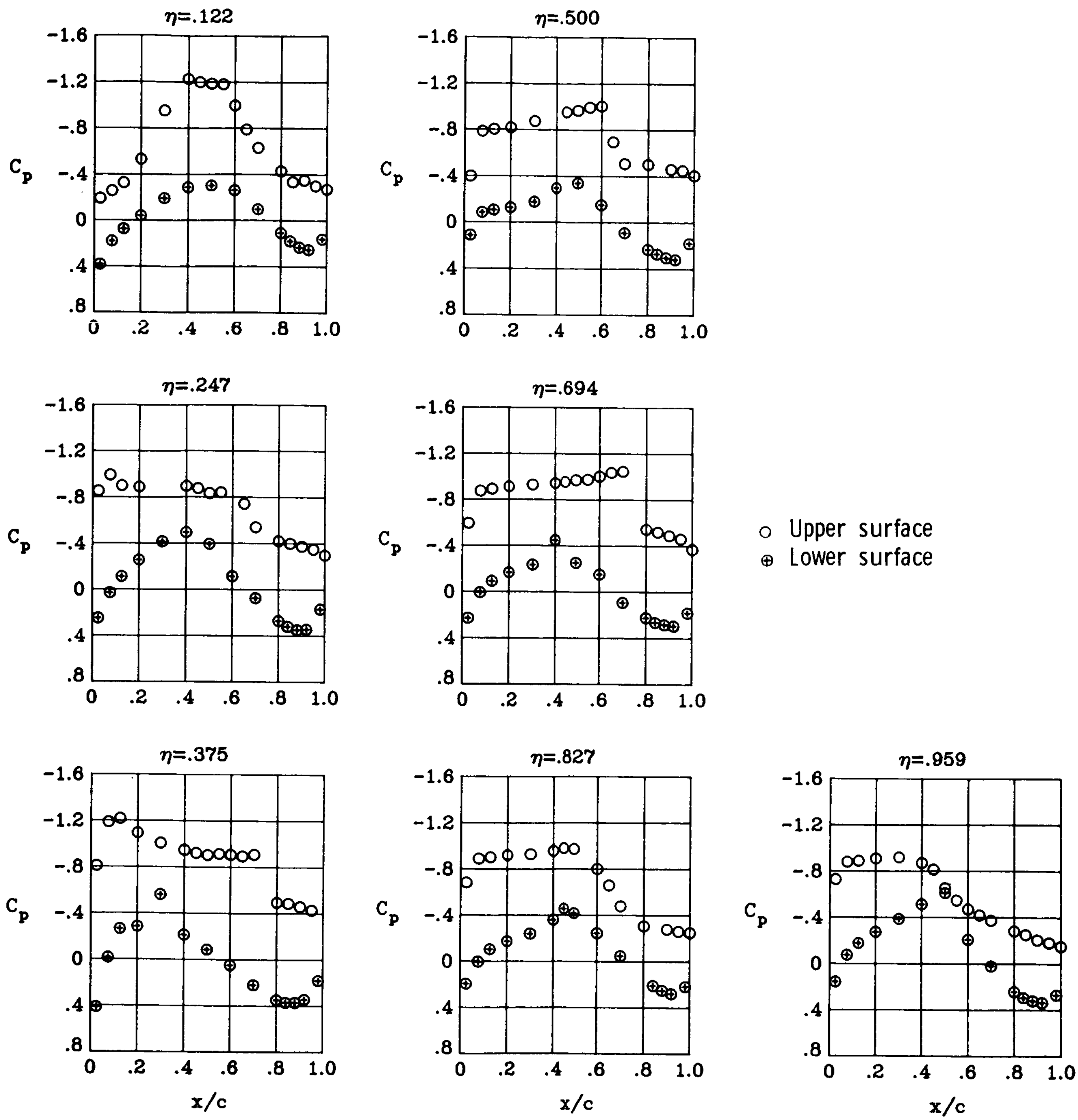

(e) $M_\infty = 0.90$; $\alpha = 5°$.

Figure 33.- Concluded.

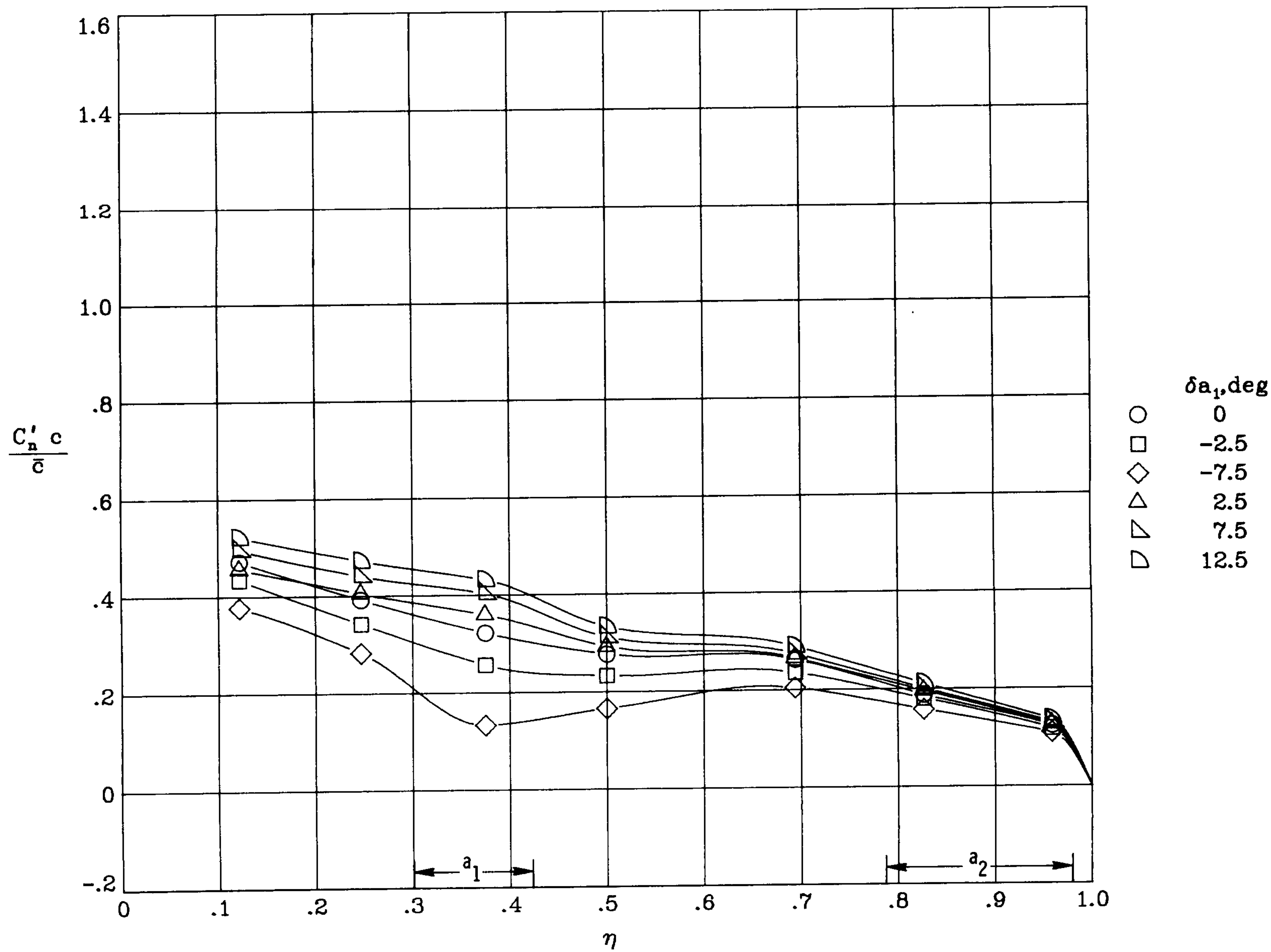

(a) $M_\infty = 0.82$; $\alpha = 1°$.

Figure 34.- Wing spanwise load distributions for deflections of a_1. $\delta a_2 = 0°$.

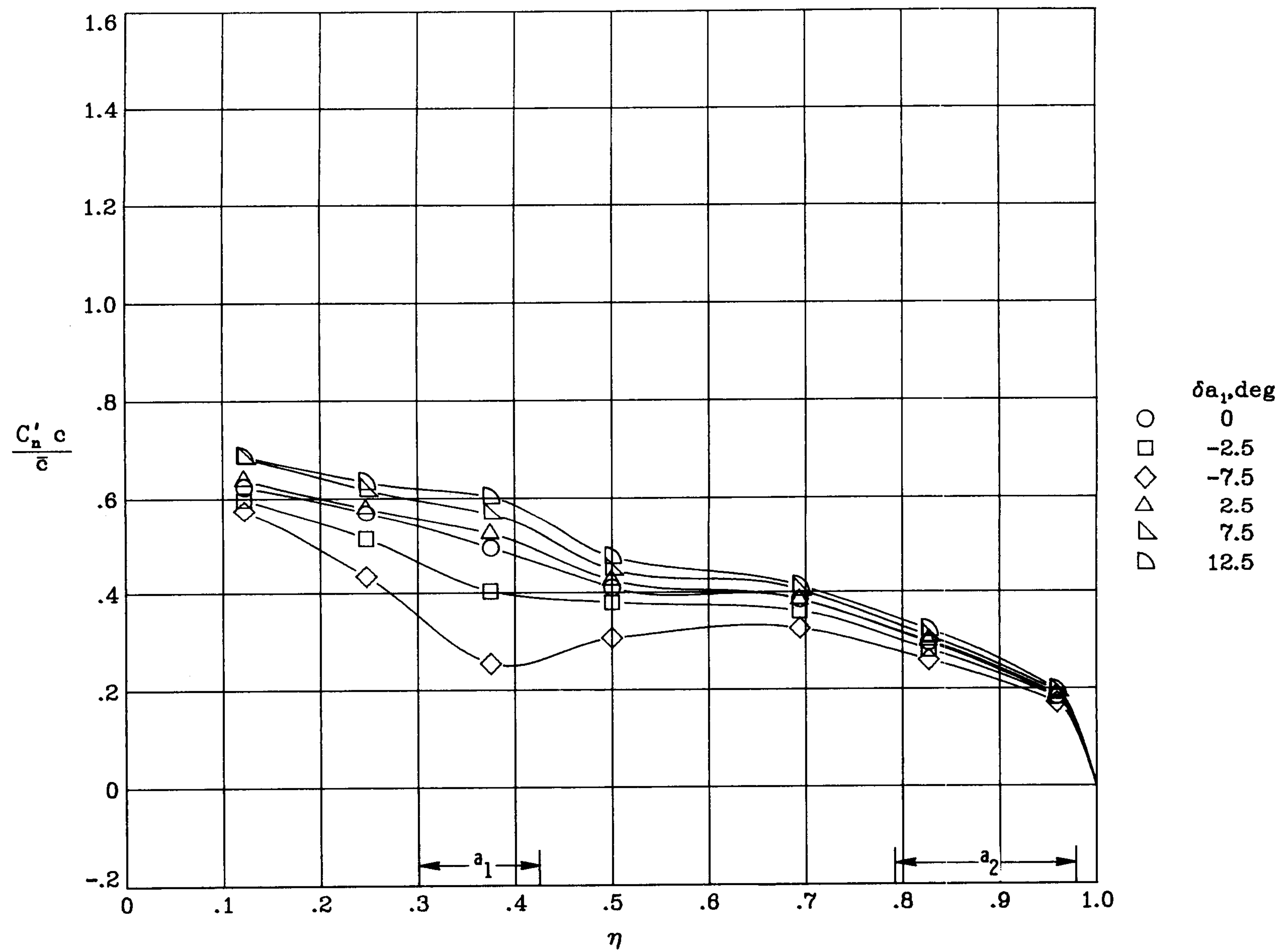

(b) $M_\infty = 0.82$; $\alpha = 2°$.

Figure 34.- Continued.

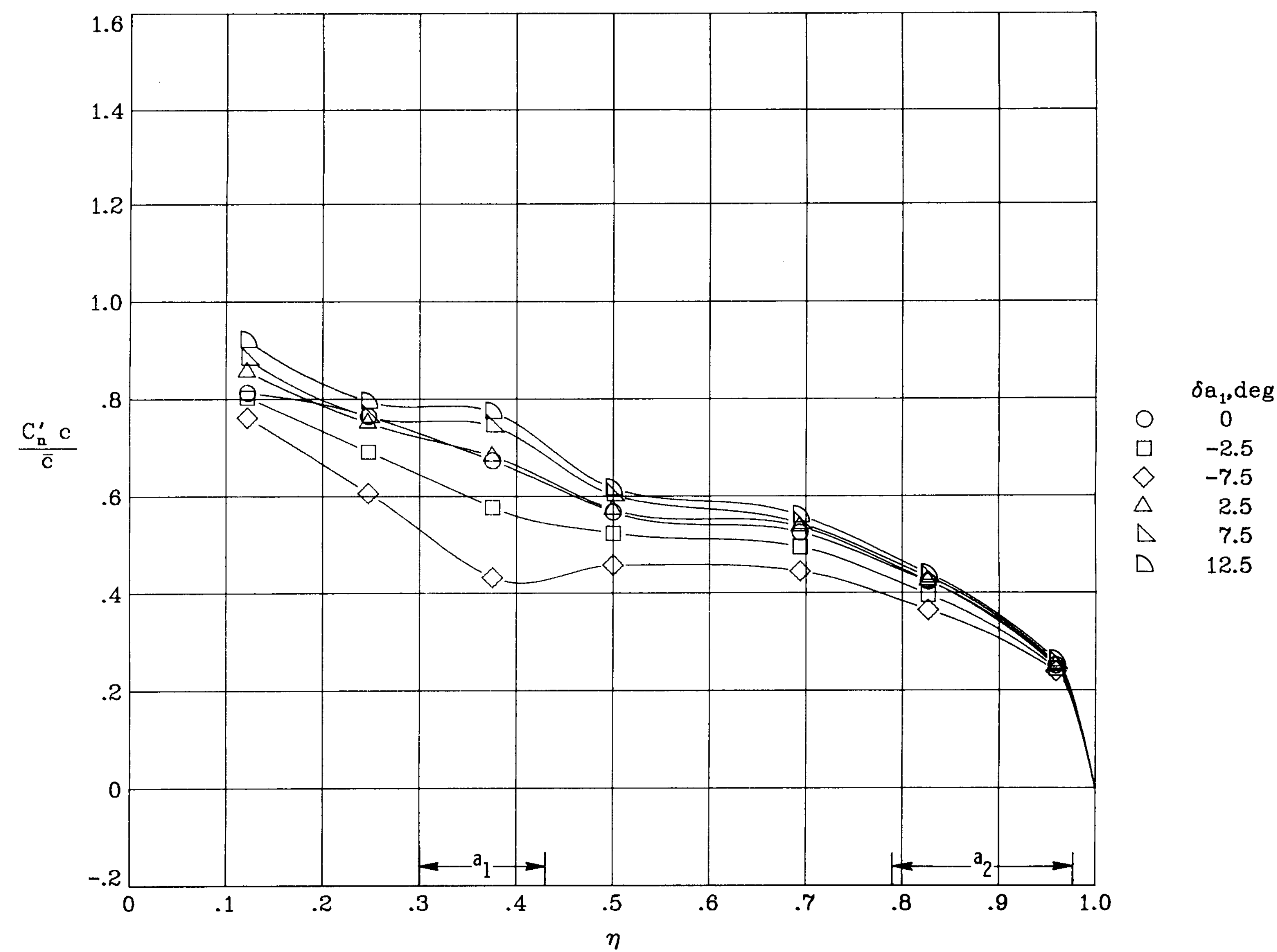

(c) $M_\infty = 0.82$; $\alpha = 3°$.

Figure 34.- Continued.

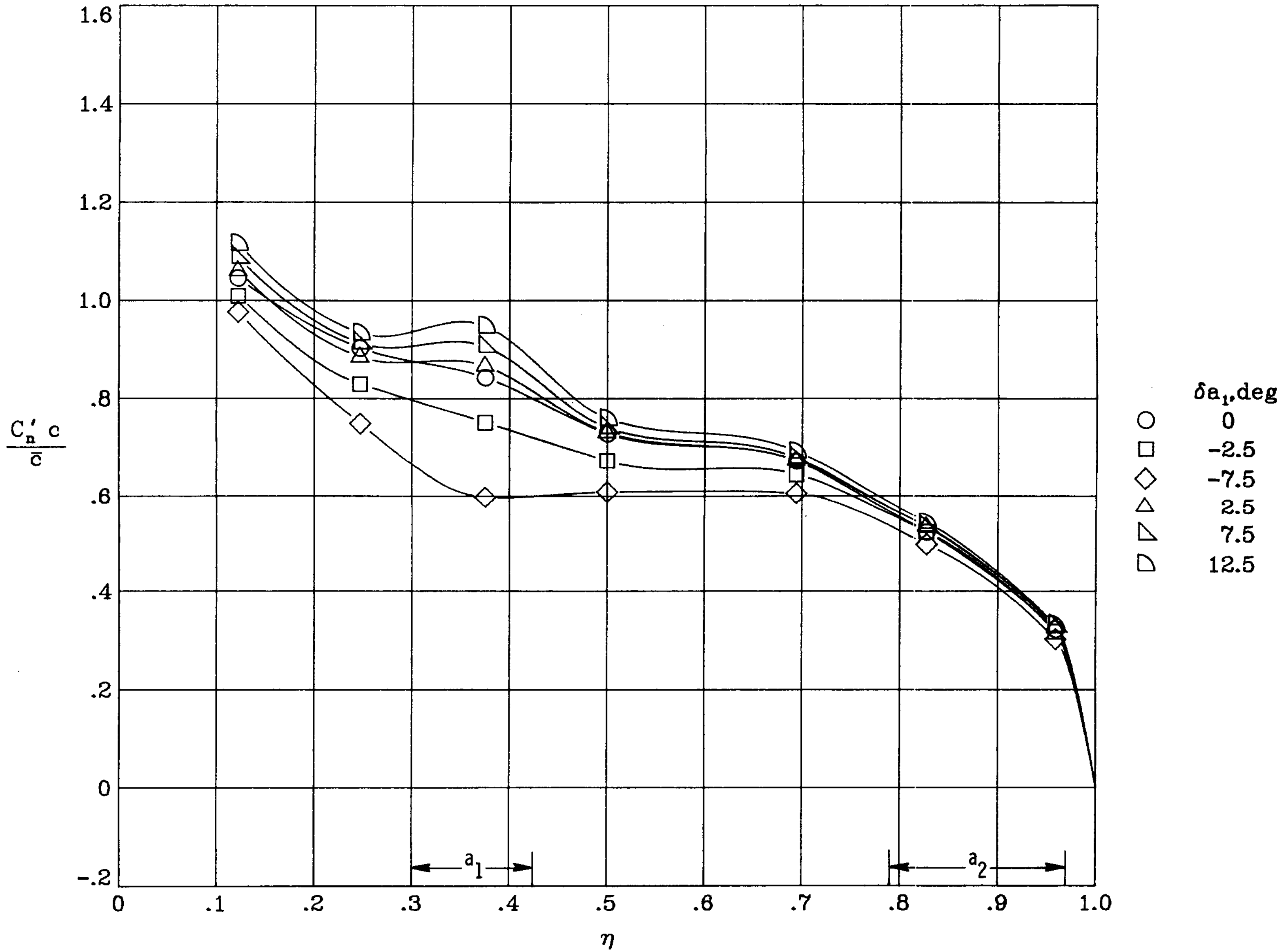

(d) $M_\infty = 0.82$; $\alpha = 4°$.

Figure 34.- Continued.

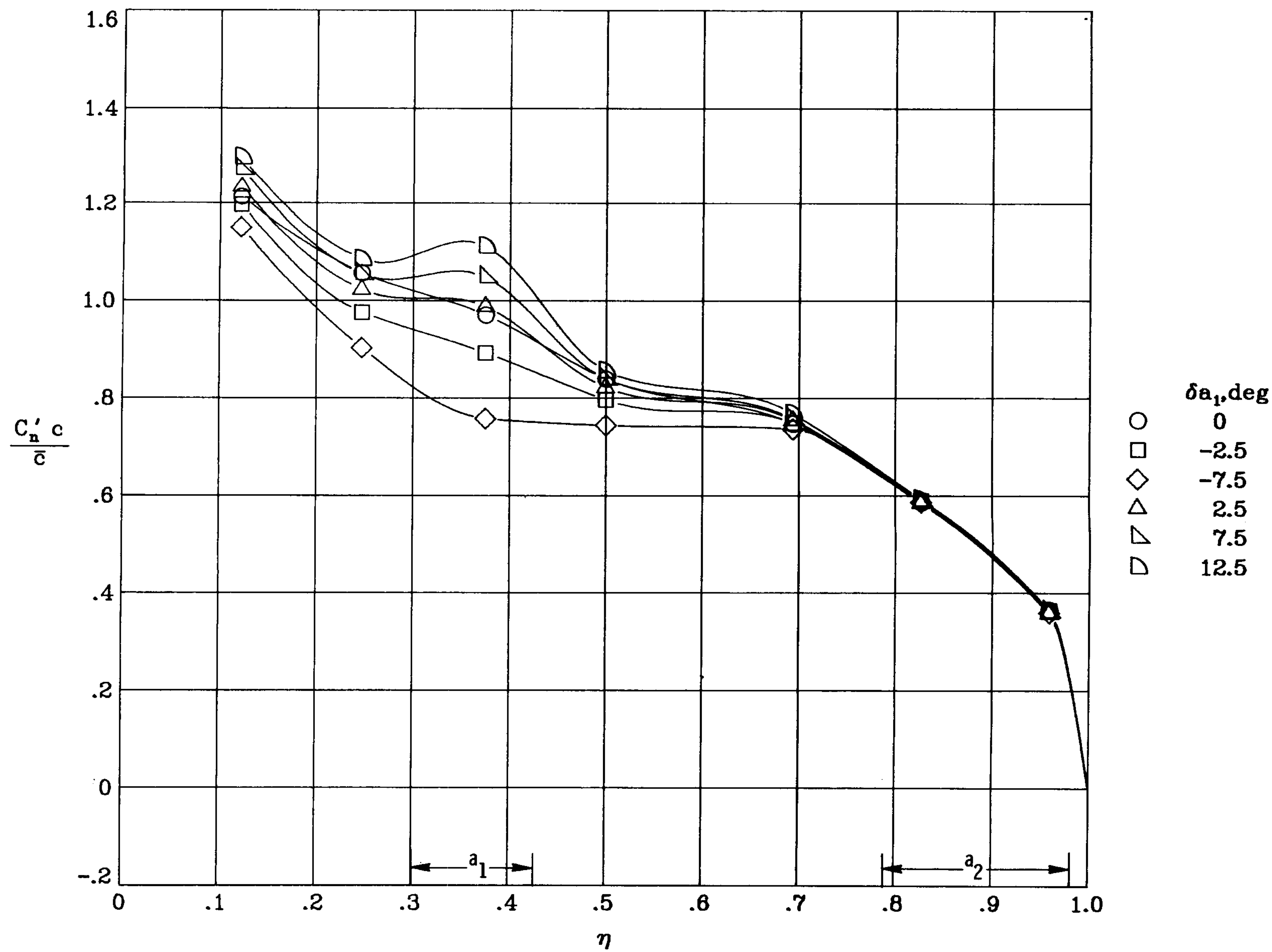

(e) $M_\infty = 0.82$; $\alpha = 5°$.

Figure 34.- Concluded.

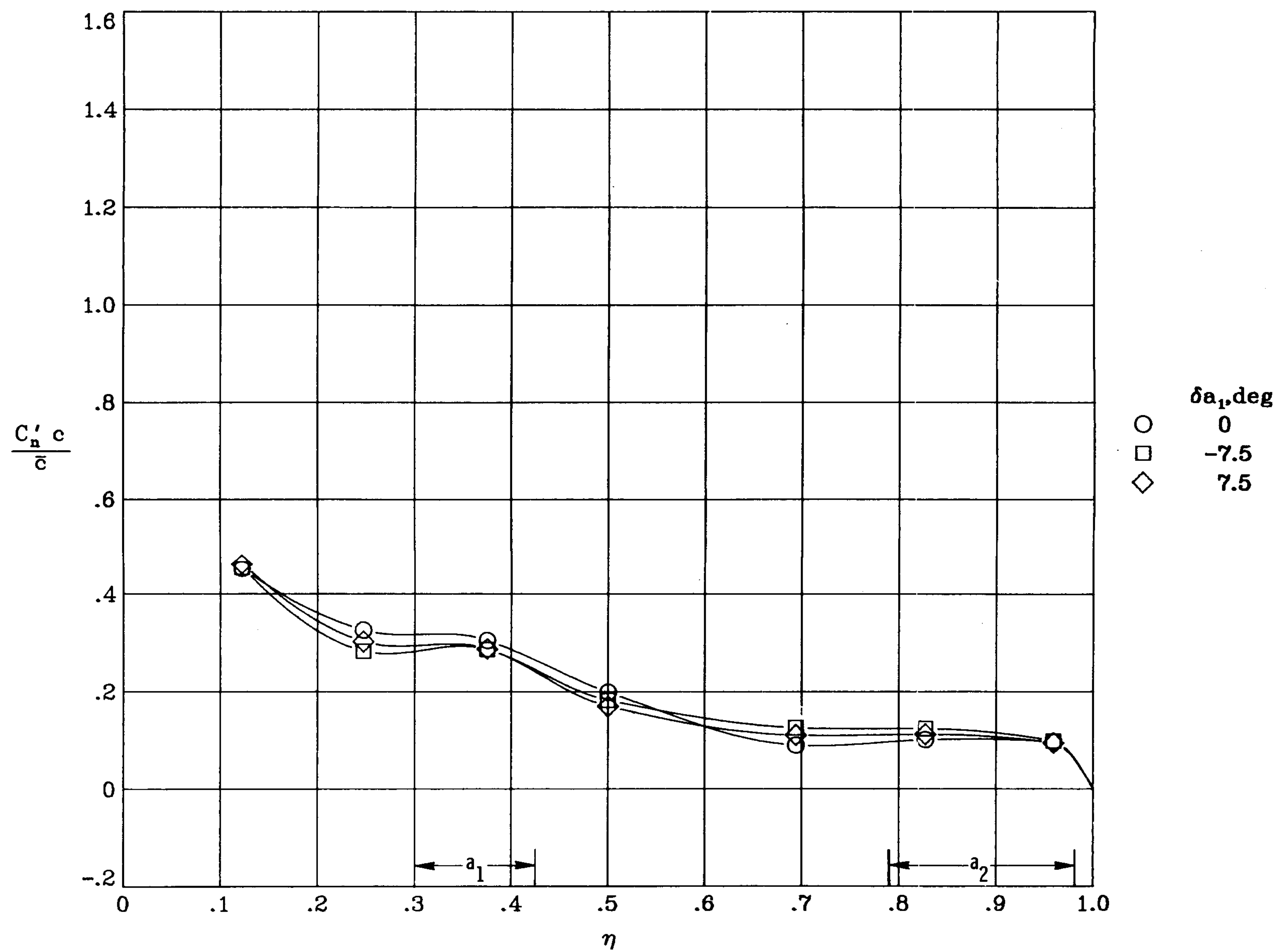

(a) $M_\infty = 0.90$; $\alpha = 1°$.

Figure 35.- Wing spanwise load distributions for deflections of a_1. $\delta a_2 = 0°$.

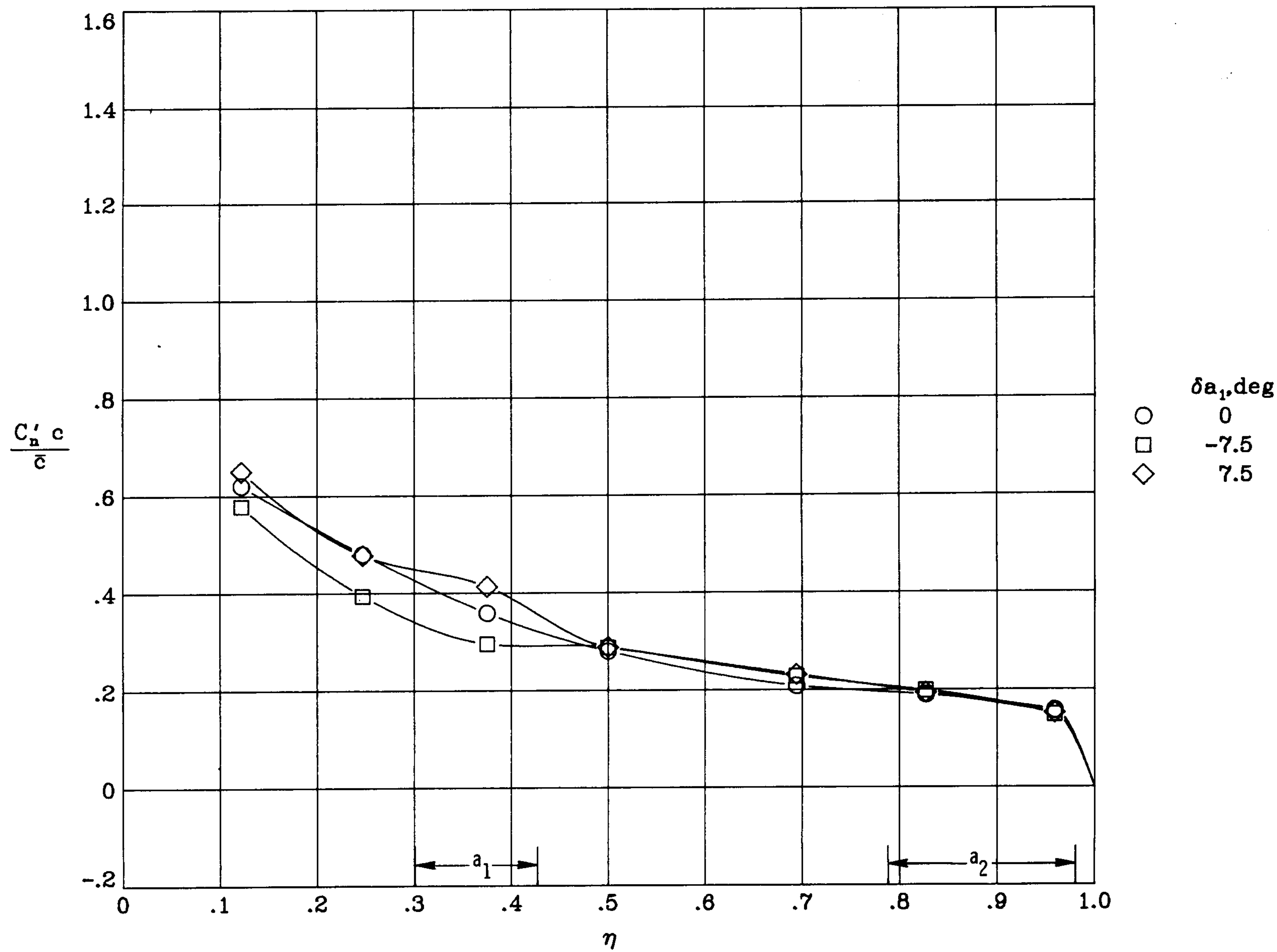

(b) $M_\infty = 0.90$; $\alpha = 2°$.

Figure 35.- Continued.

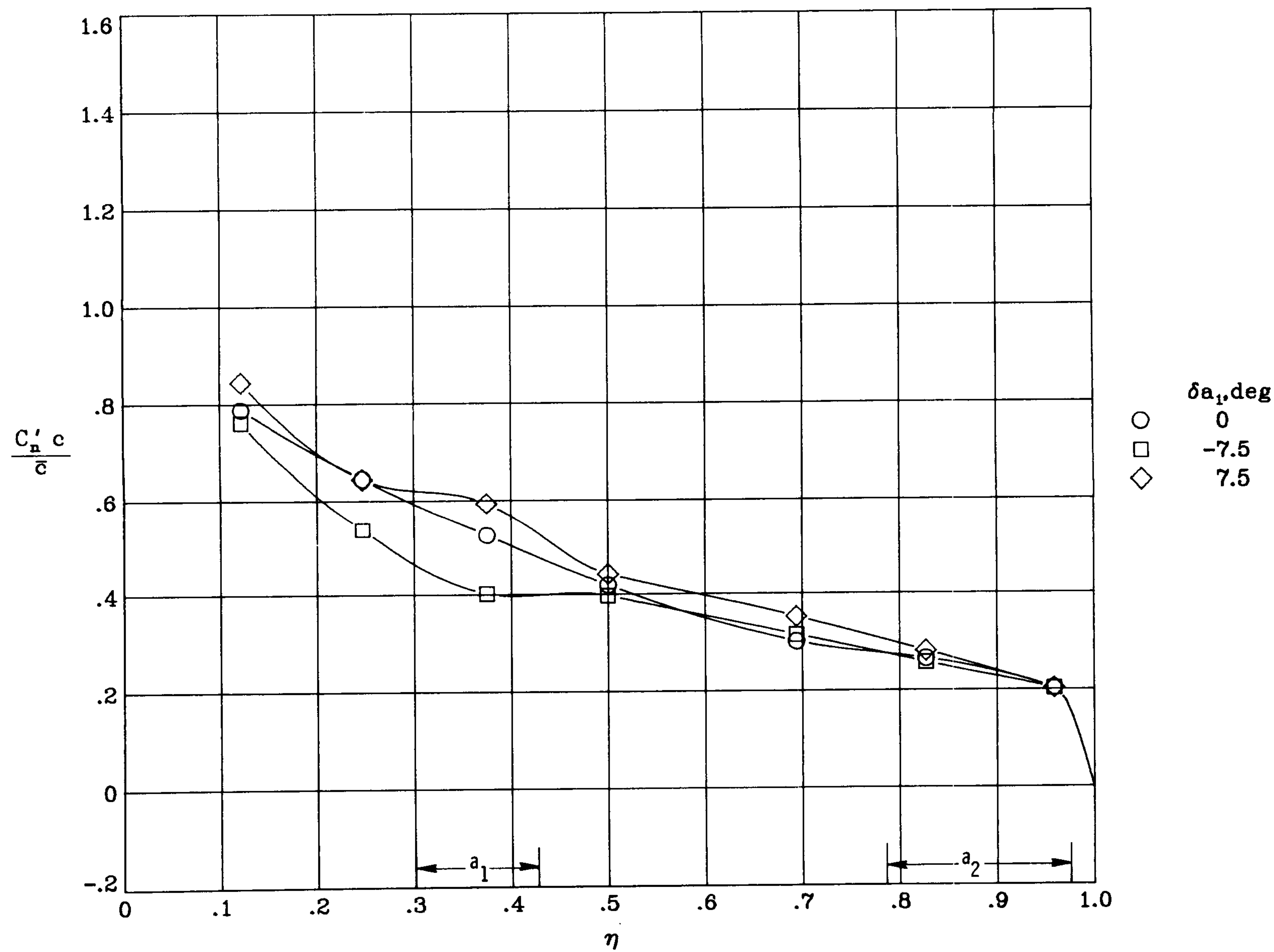

(c) $M_\infty = 0.90$; $\alpha = 3°$.

Figure 35.- Continued.

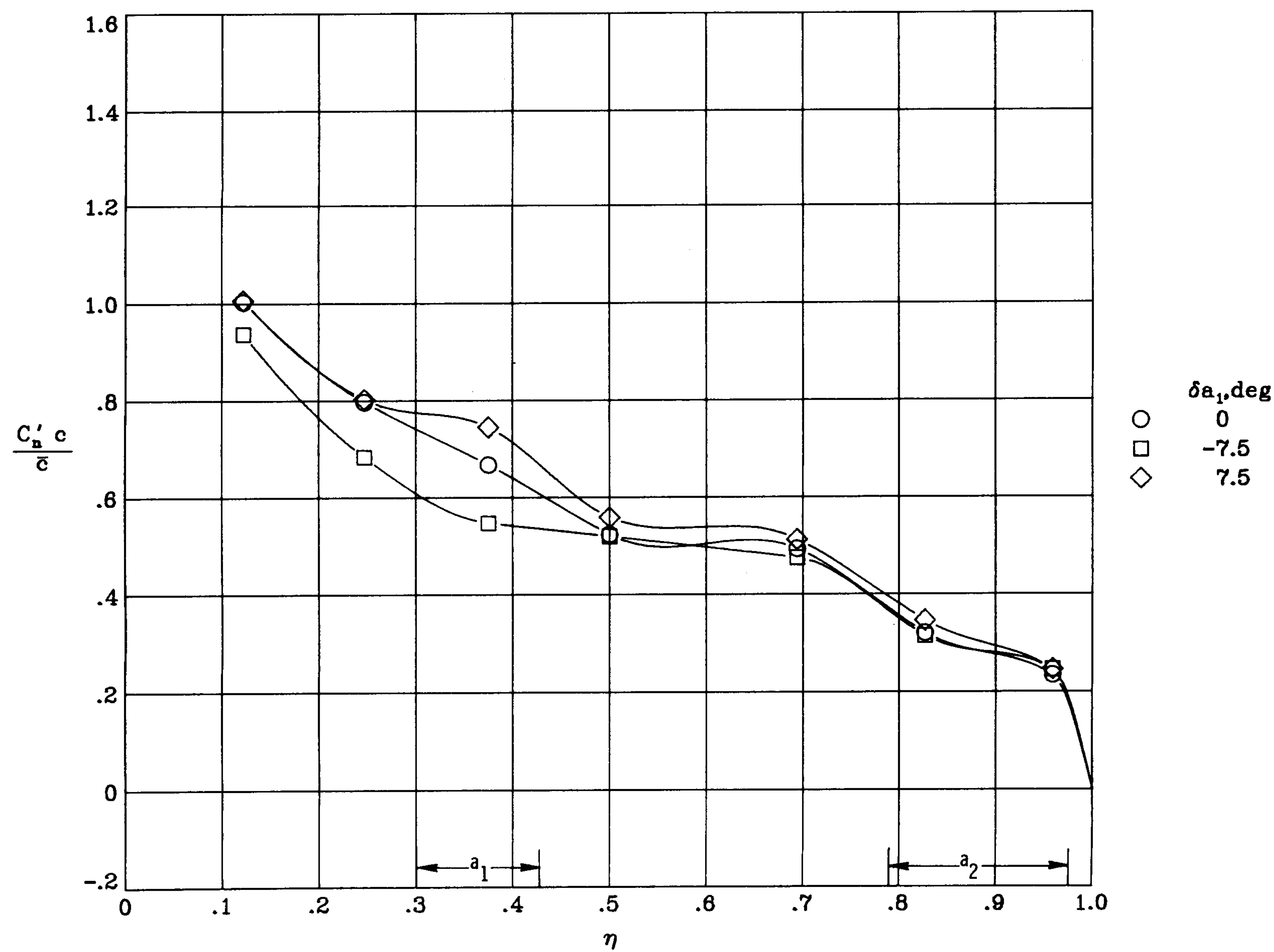

(d) $M_\infty = 0.90$; $\alpha = 4°$.

Figure 35.- Continued.

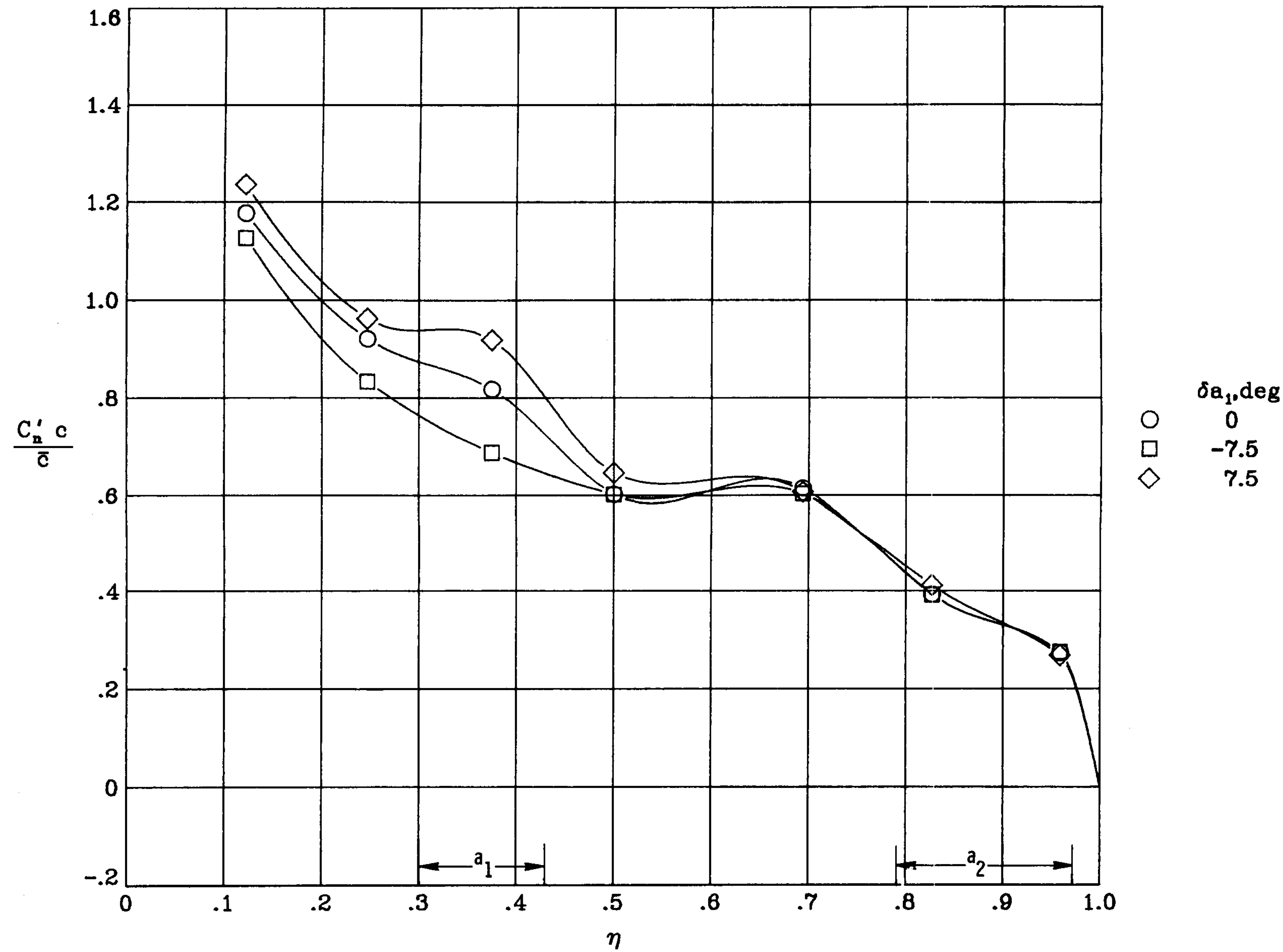

(e) $M_\infty = 0.90$; $\alpha = 5°$.

Figure 35.- Concluded.

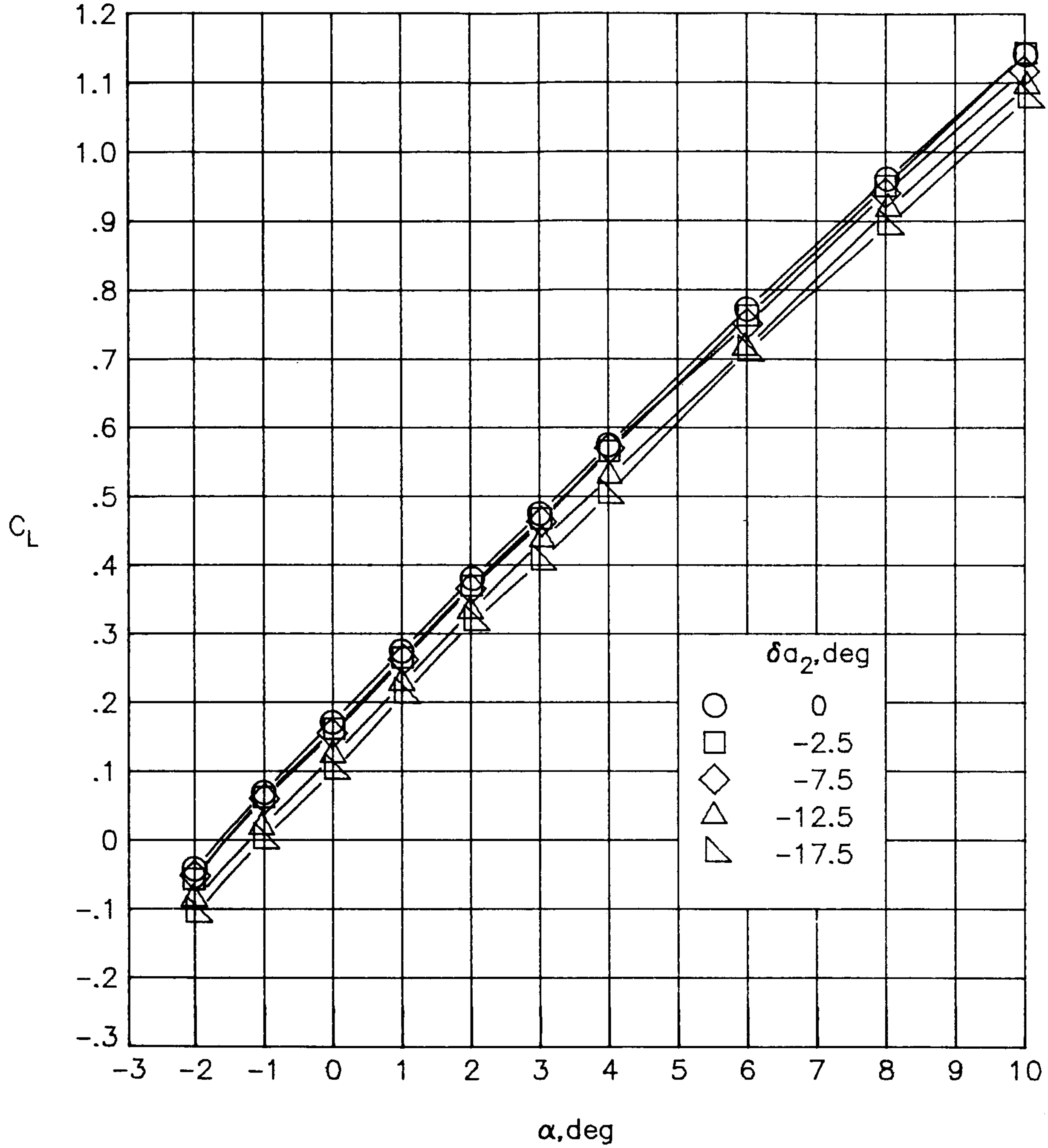

(a) $M_\infty = 0.30$.

Figure 36.- Variation of lift coefficient with angle of attack for deflections of a_2. $\delta a_1 = 0°$.

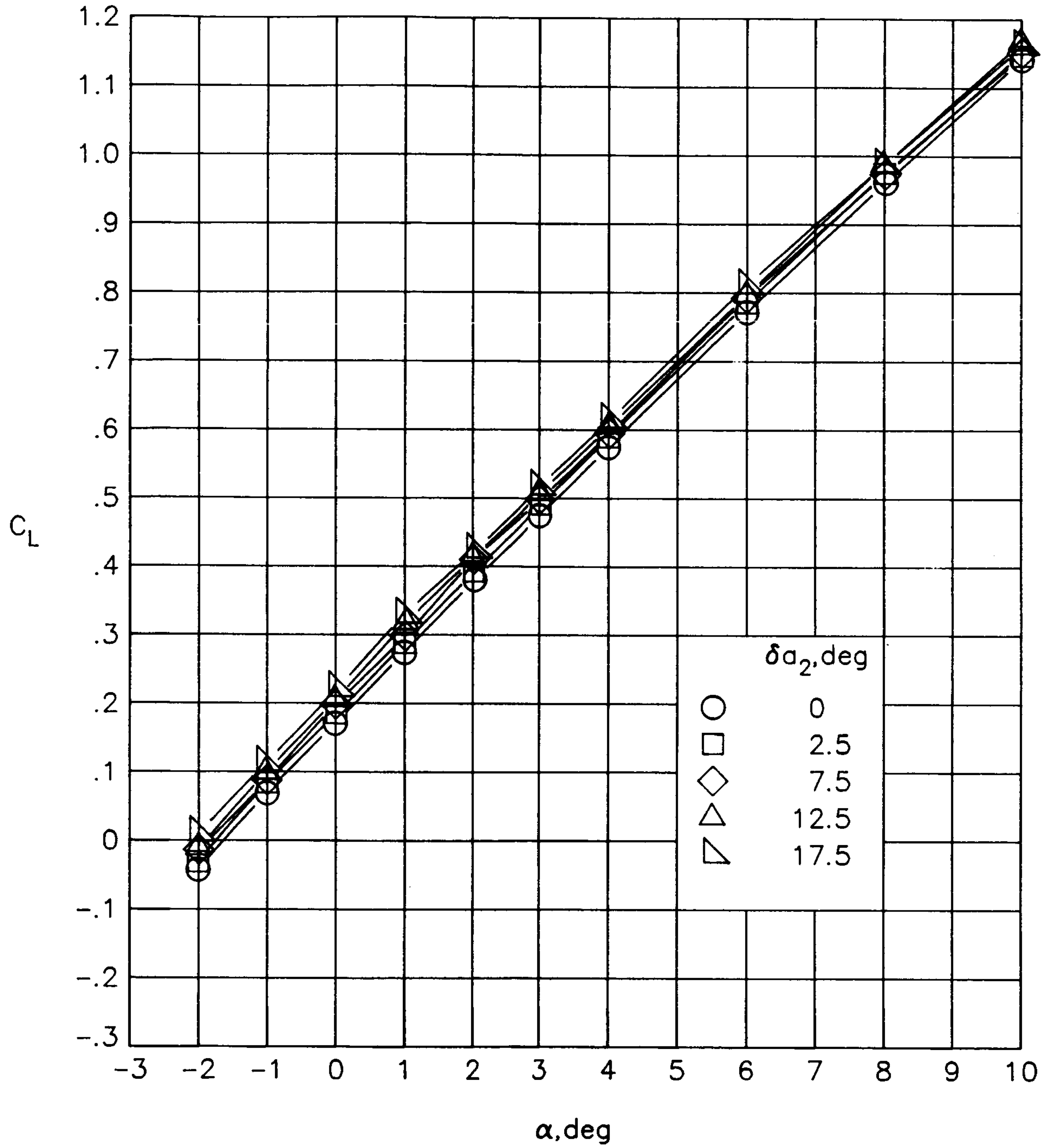

(a) Concluded.

Figure 36.- Continued.

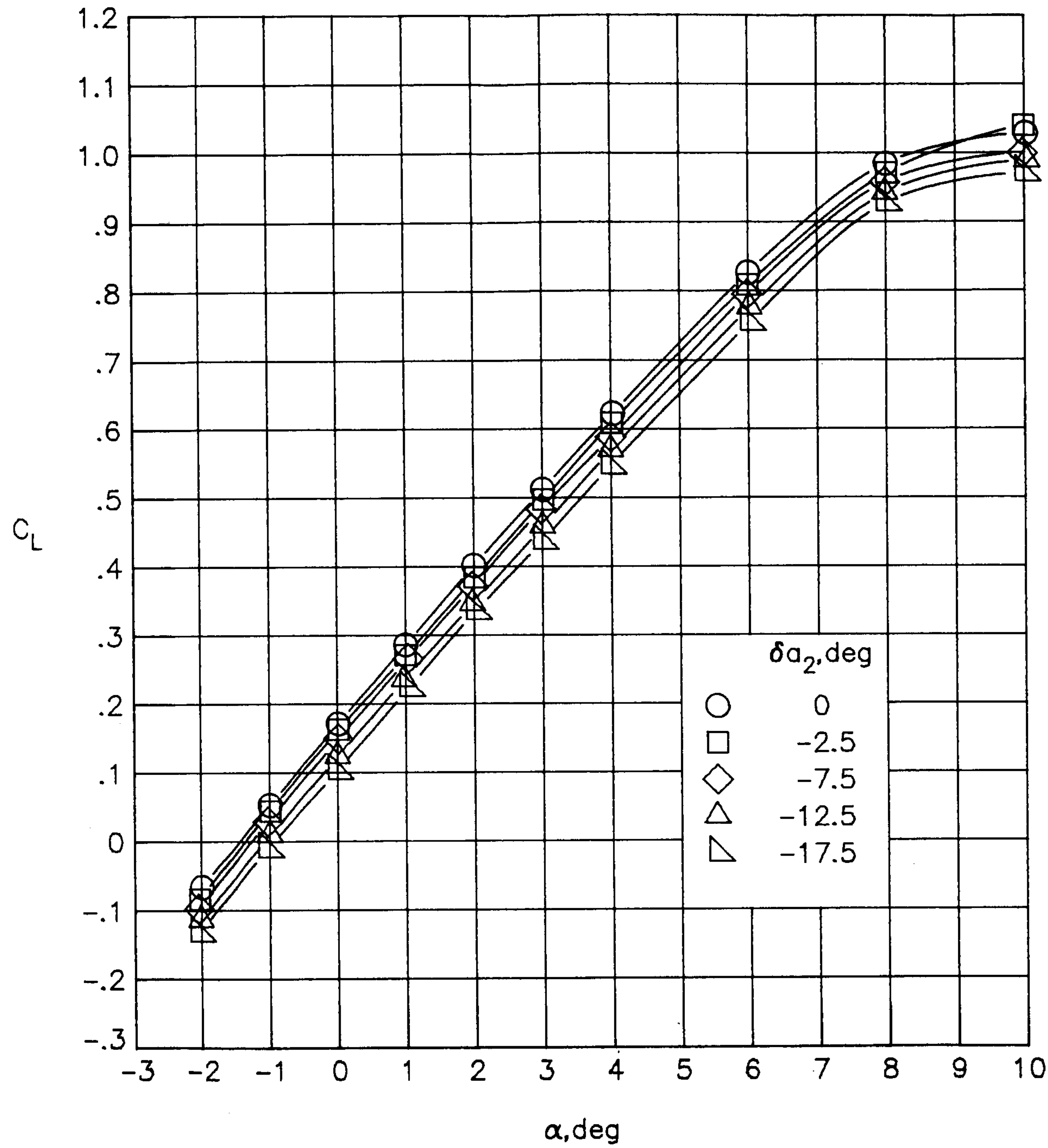

(b) $M_\infty = 0.60$.

Figure 36.- Continued.

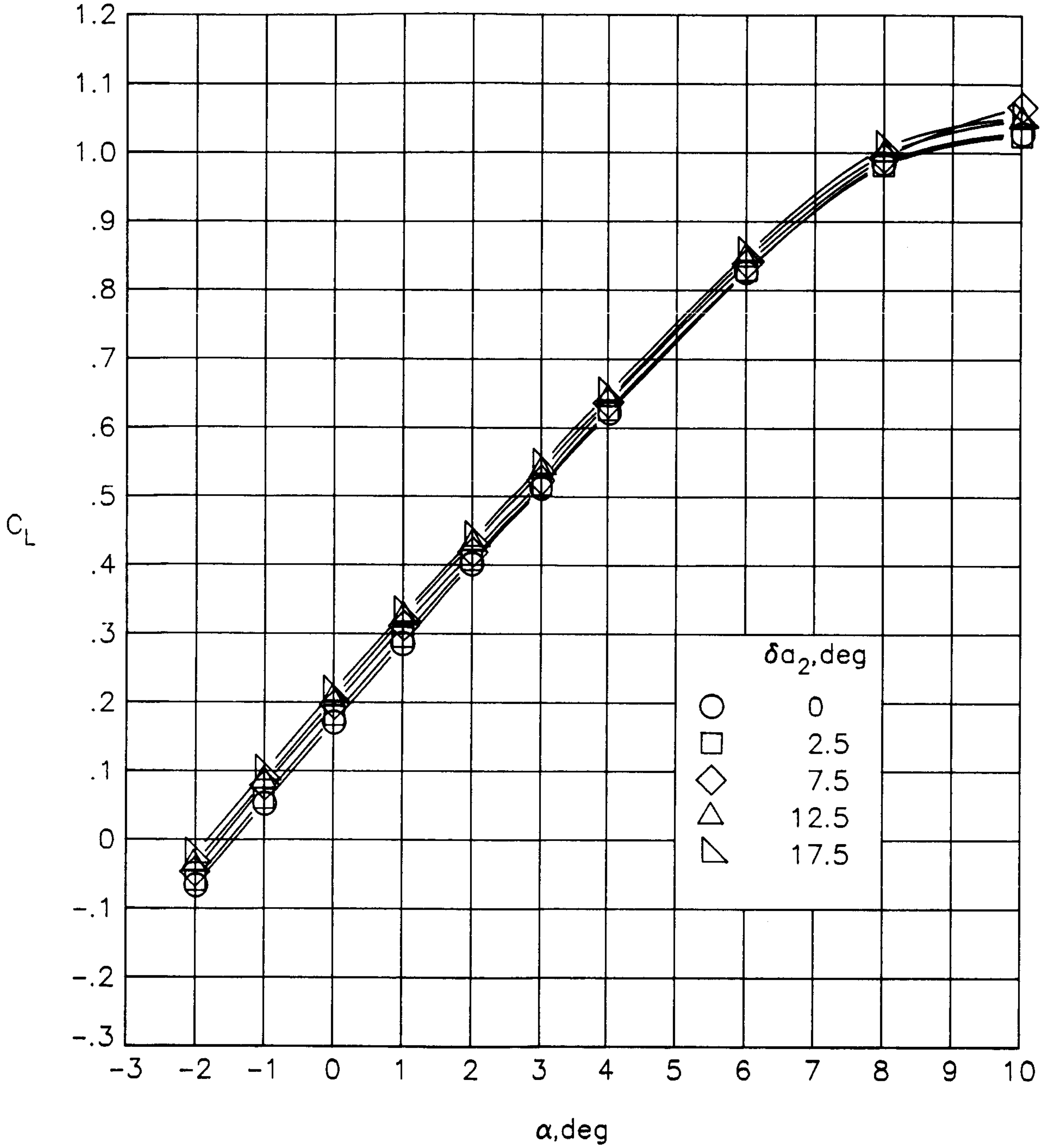

(b) Concluded.

Figure 36.- Continued.

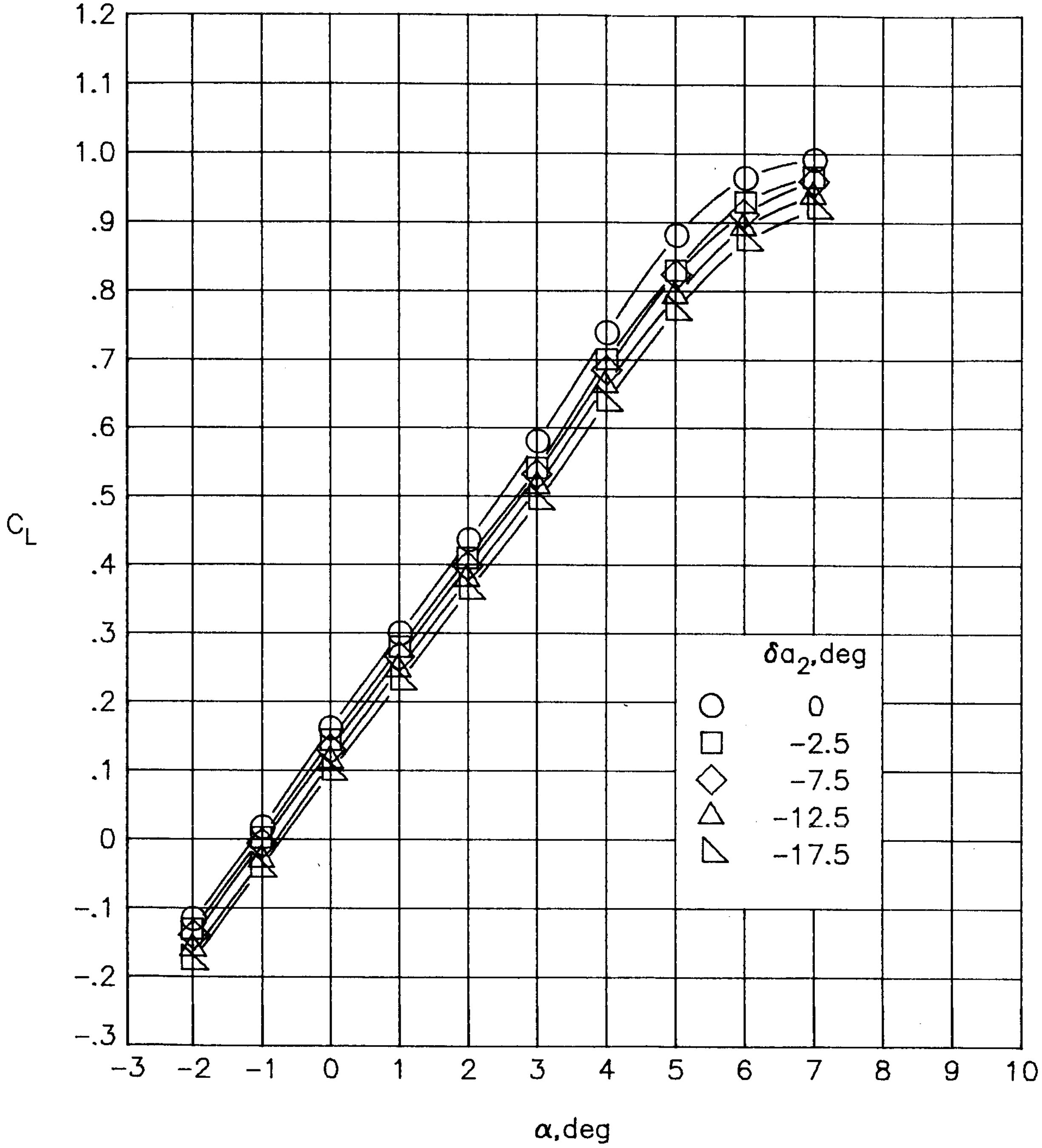

(c) $M_\infty = 0.80$.

Figure 36.- Continued.

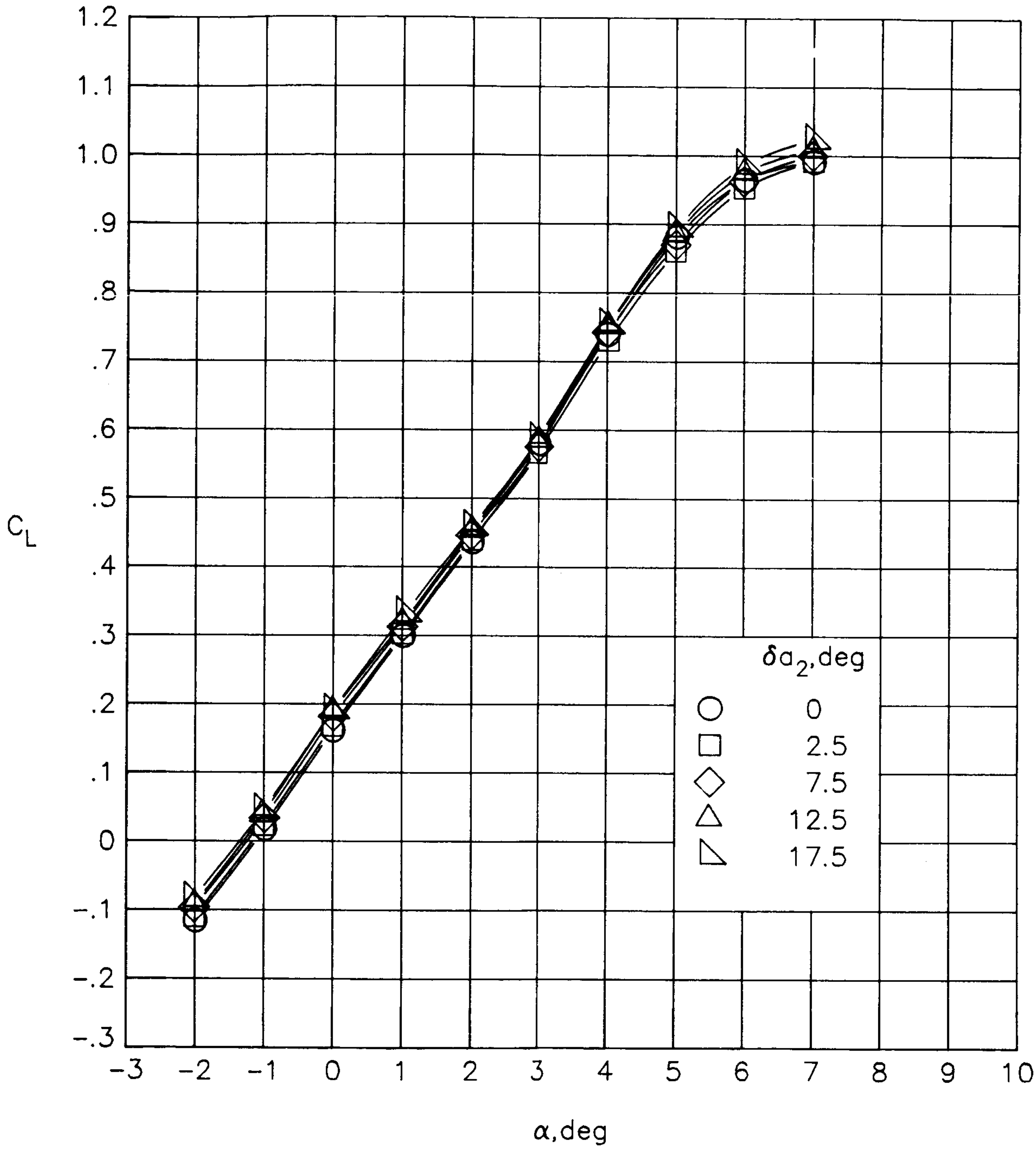

(c) Concluded.

Figure 36.- Continued.

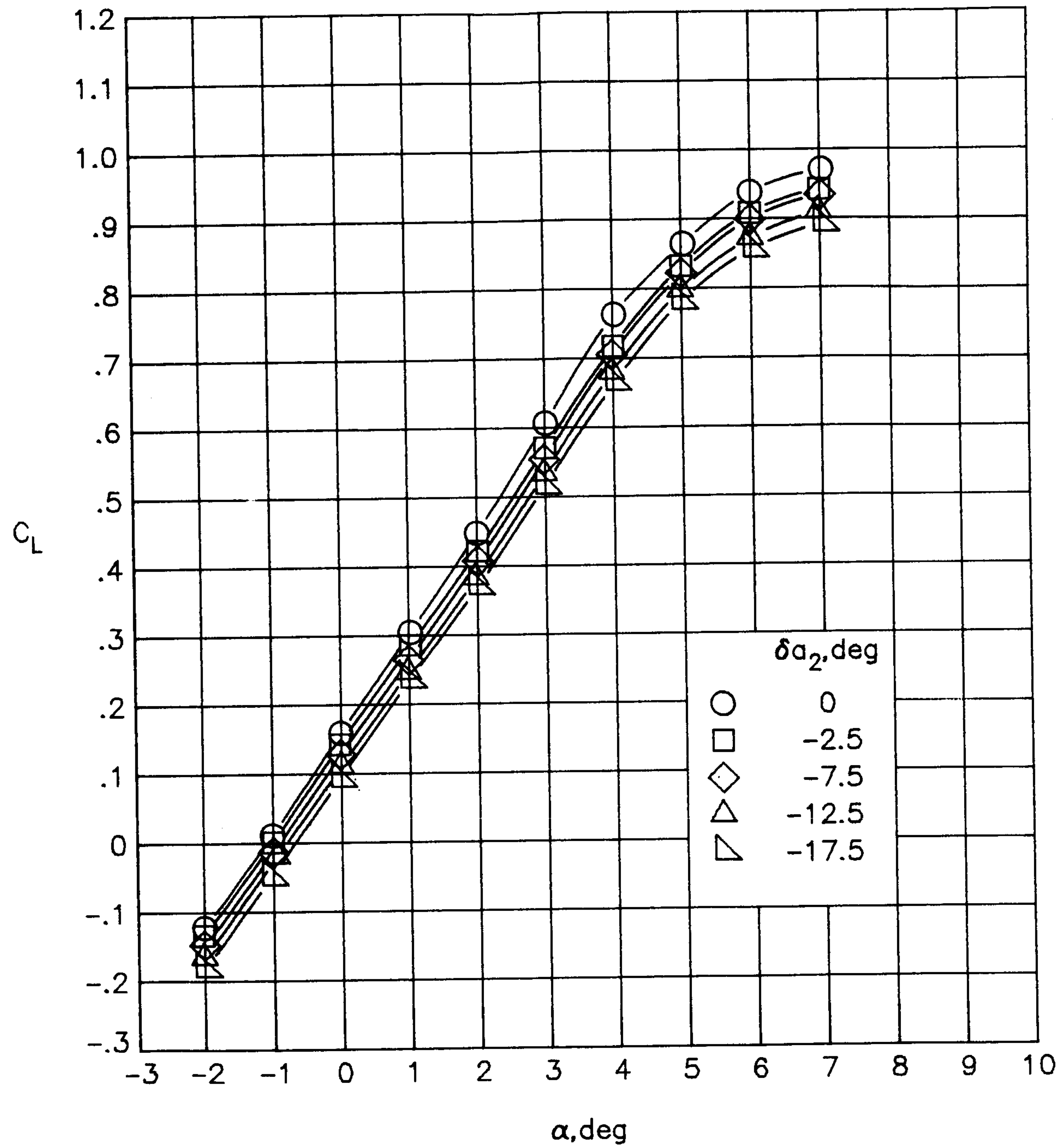

(d) M_∞ = 0.82.

Figure 36.- Continued.

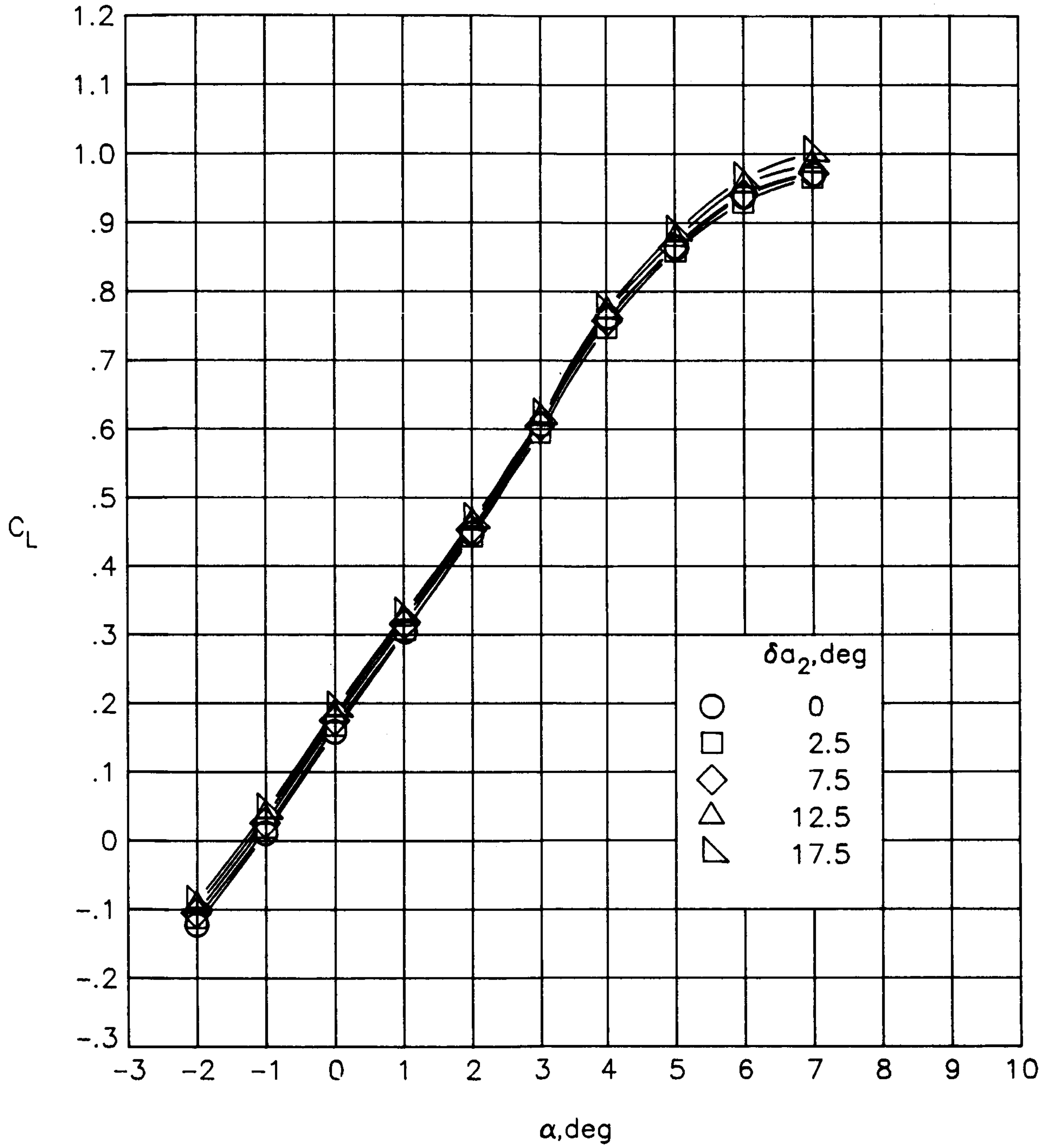

(d) Concluded.

Figure 36.- Continued.

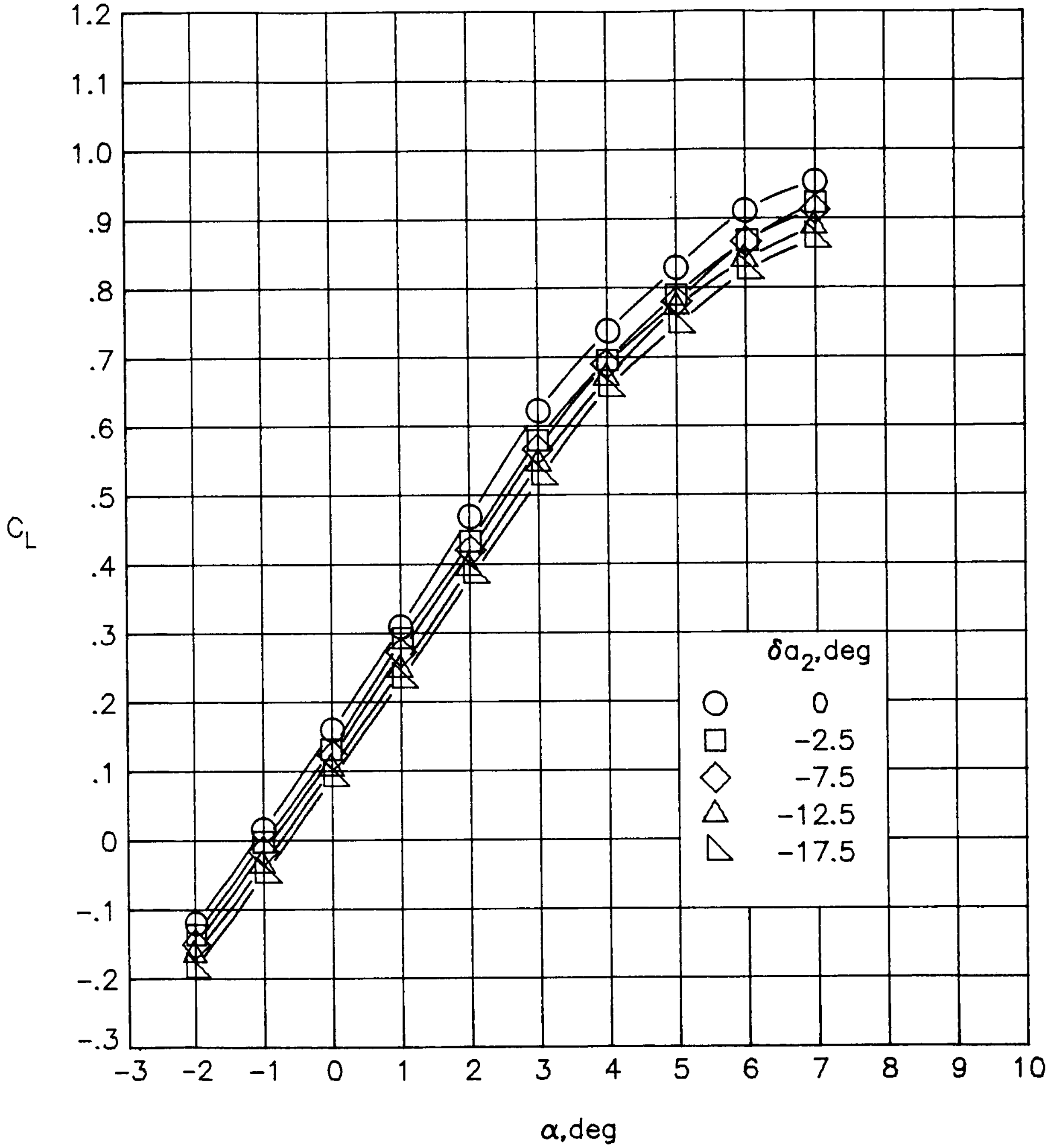

(e) M_∞ = 0.84.

Figure 36.- Continued.

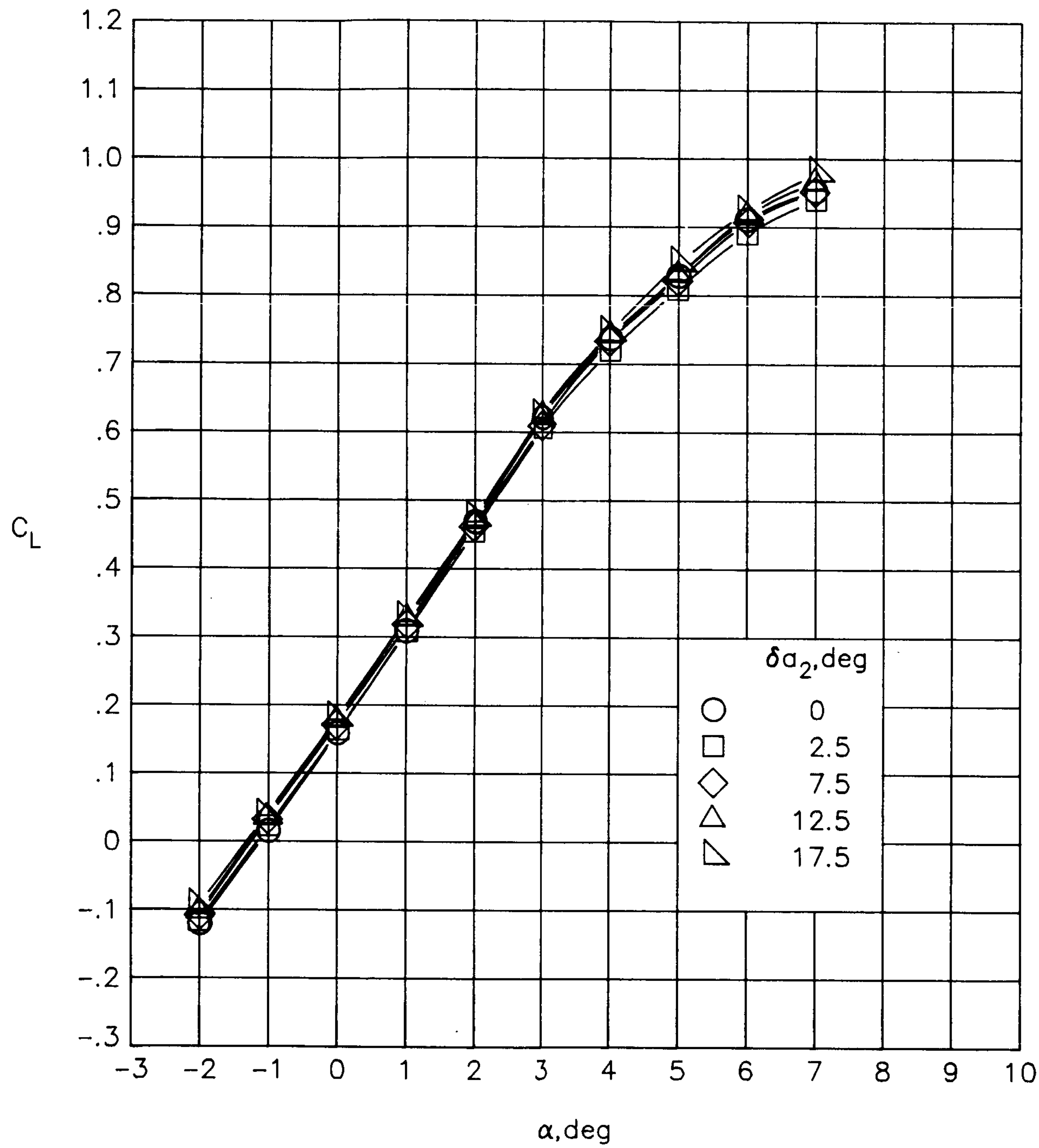

(e) Concluded.

Figure 36.- Continued.

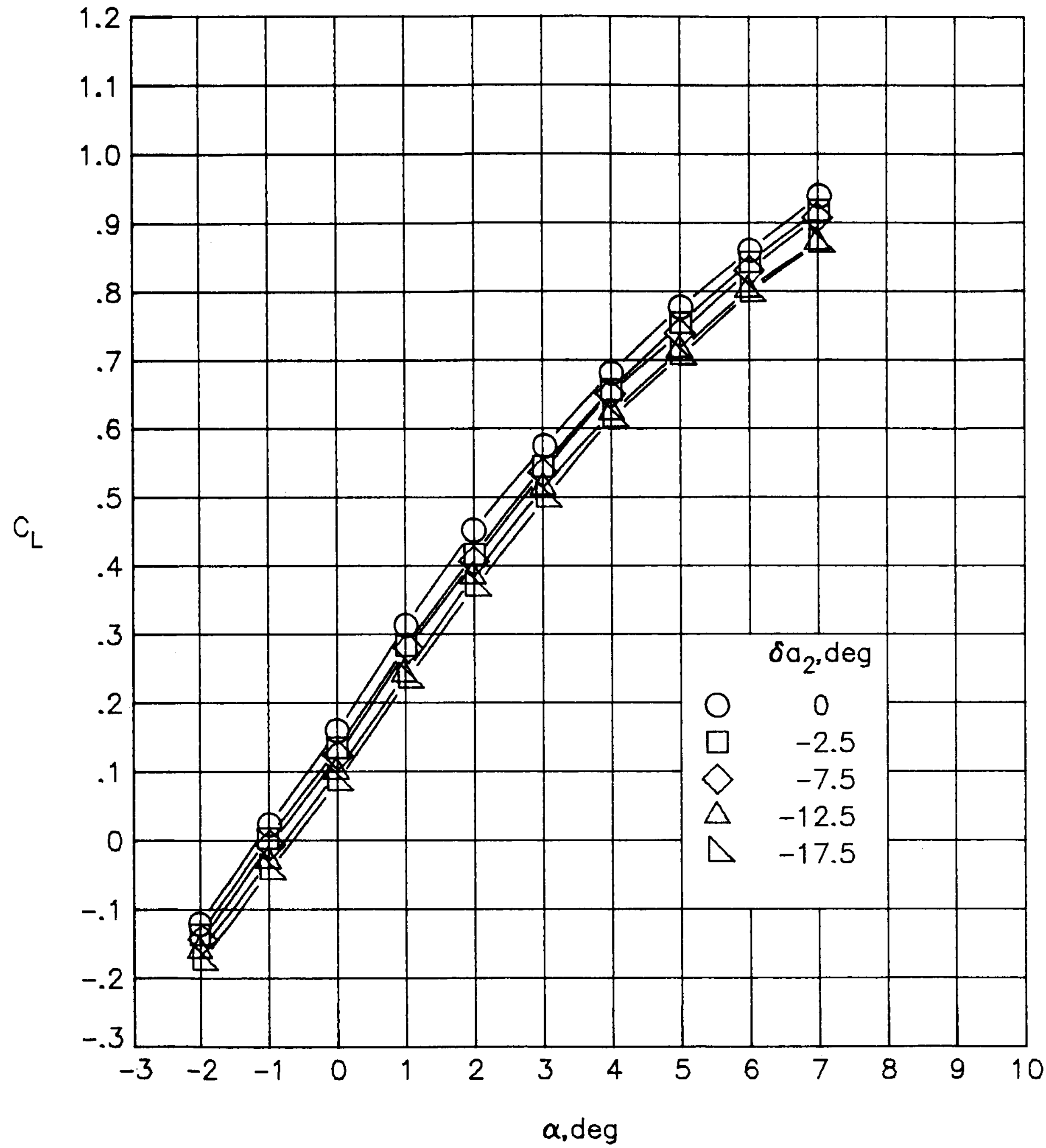

(f) $M_\infty = 0.86$.

Figure 36.- Continued.

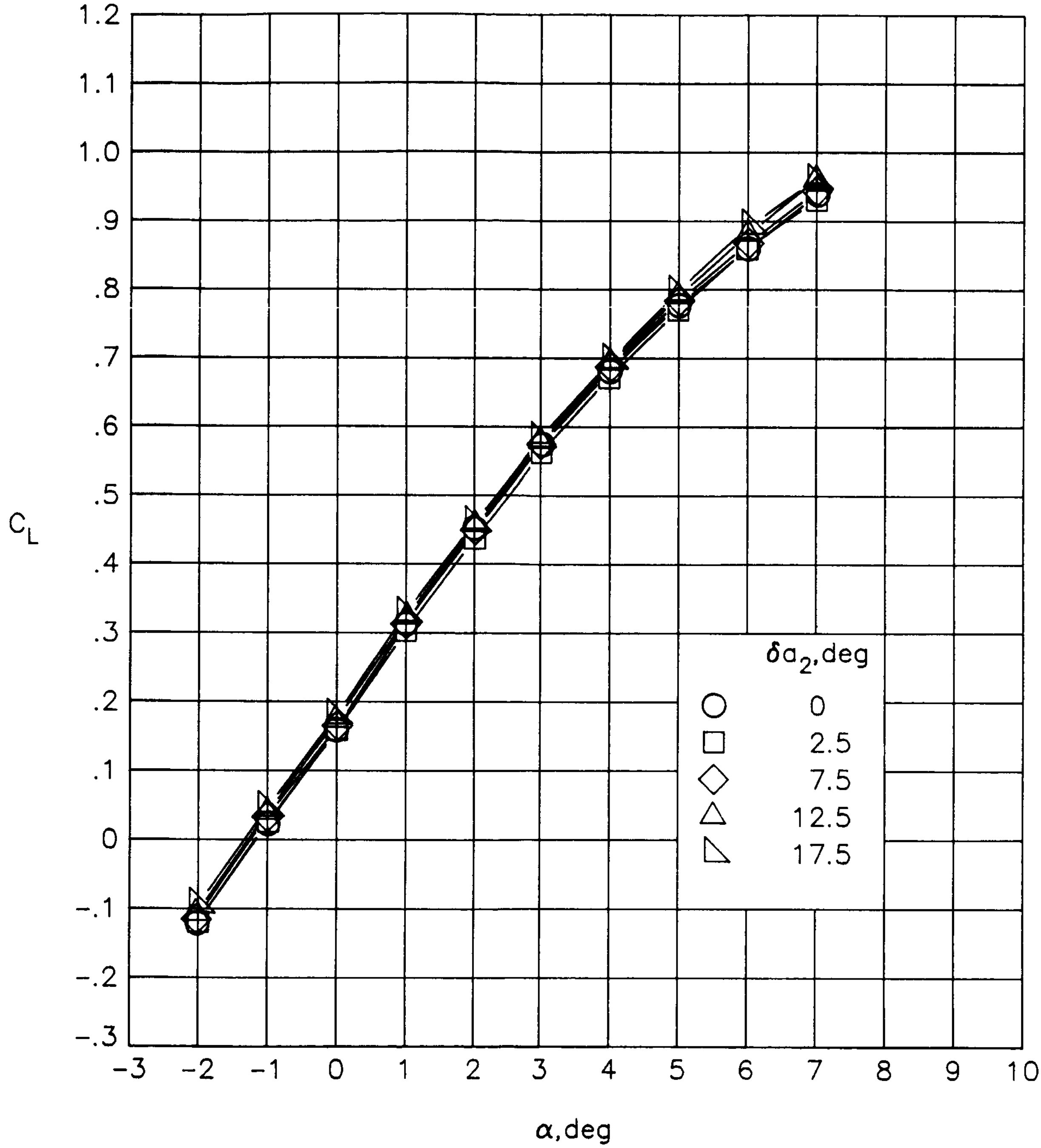

(f) Concluded.

Figure 36.- Continued.

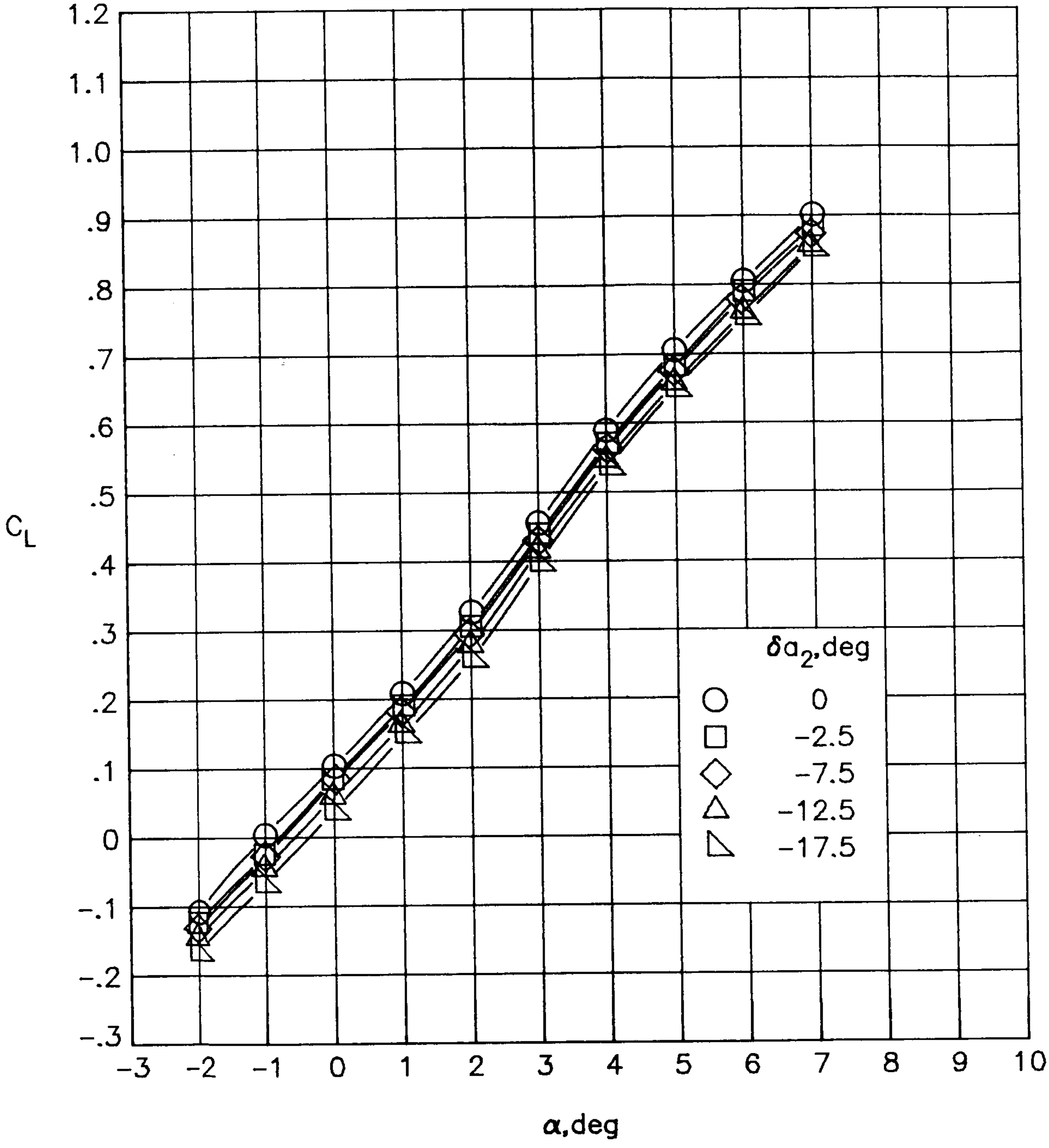

(g) $M_\infty = 0.90$.

Figure 36.- Continued.

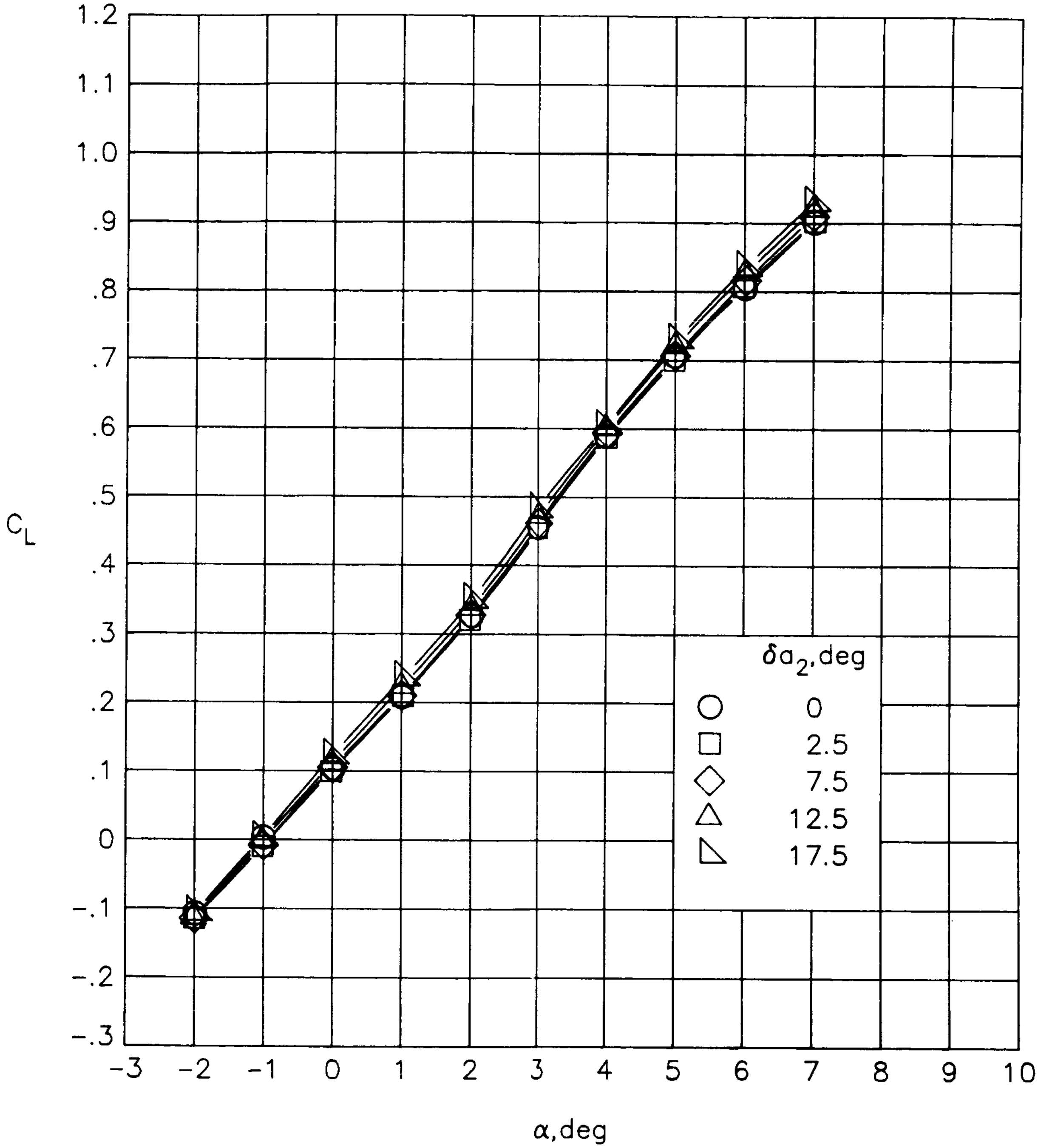

(q) Concluded.

Figure 36.- Concluded.

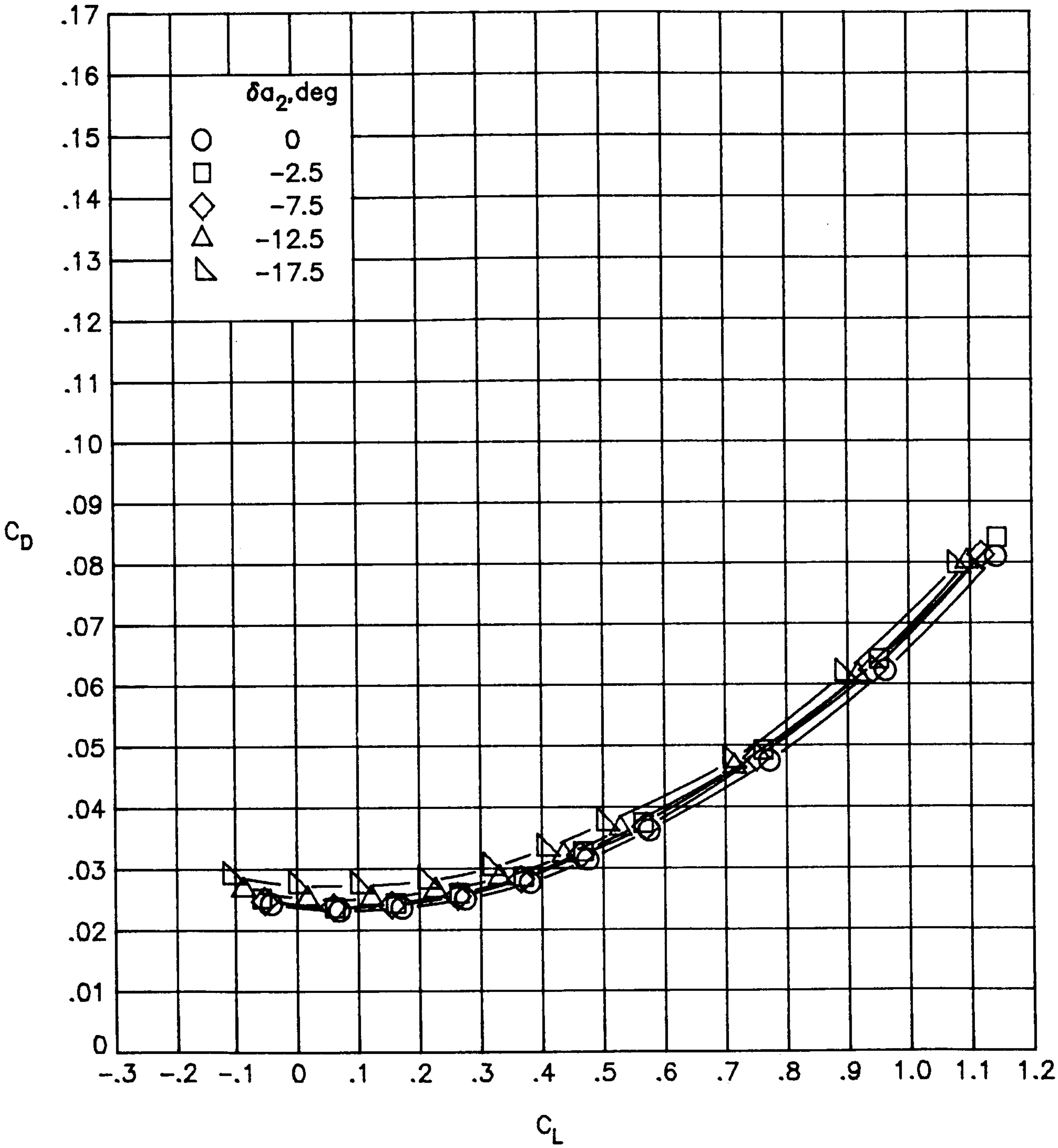

(a) $M_\infty = 0.30$.

Figure 37.- Variation of drag coefficient with lift coefficient for deflections of a_2. $\delta a_1 = 0°$.

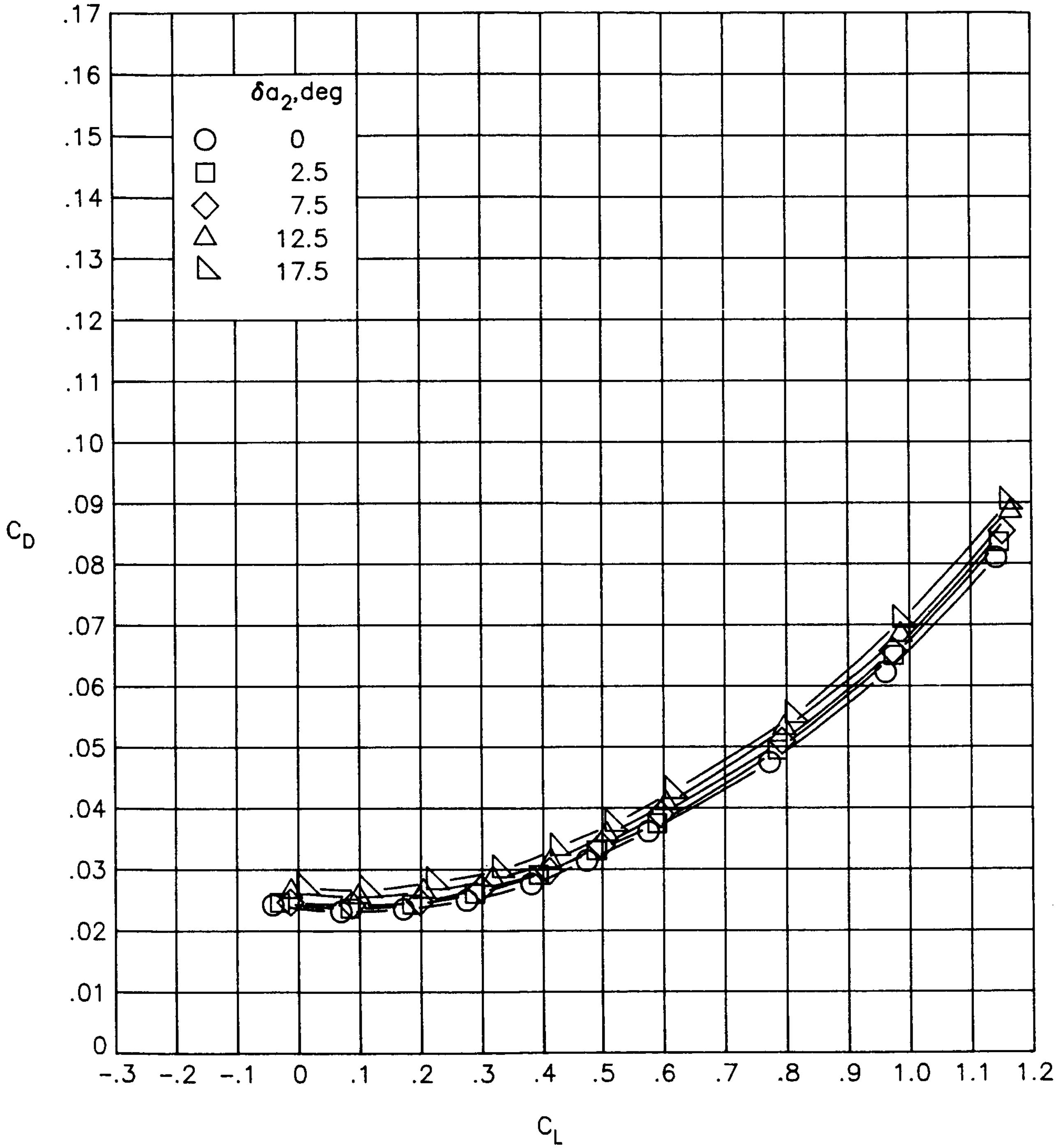

(a) Concluded.

Figure 37.- Continued.

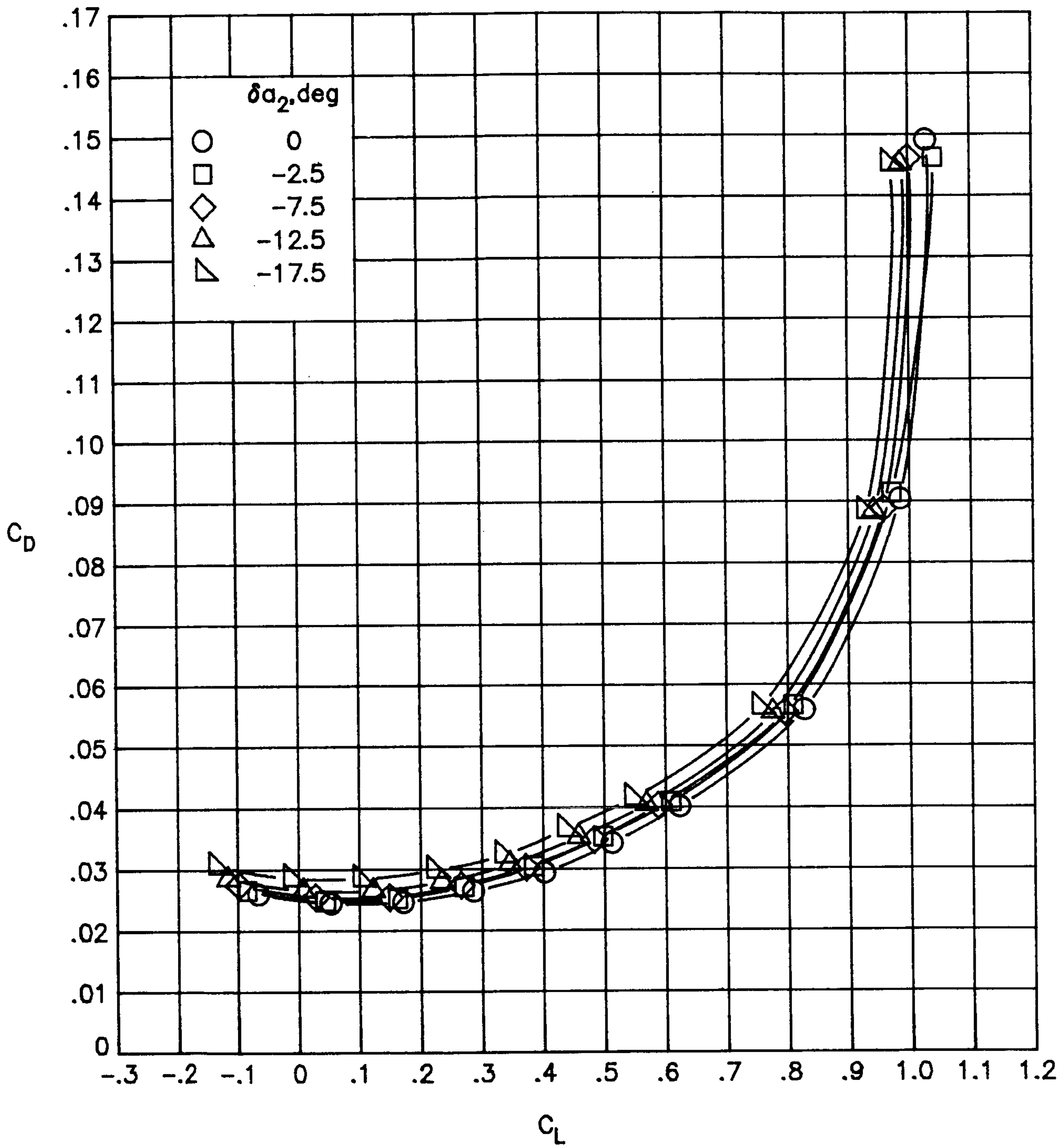

(b) $M_\infty = 0.60$.

Figure 37.- Continued.

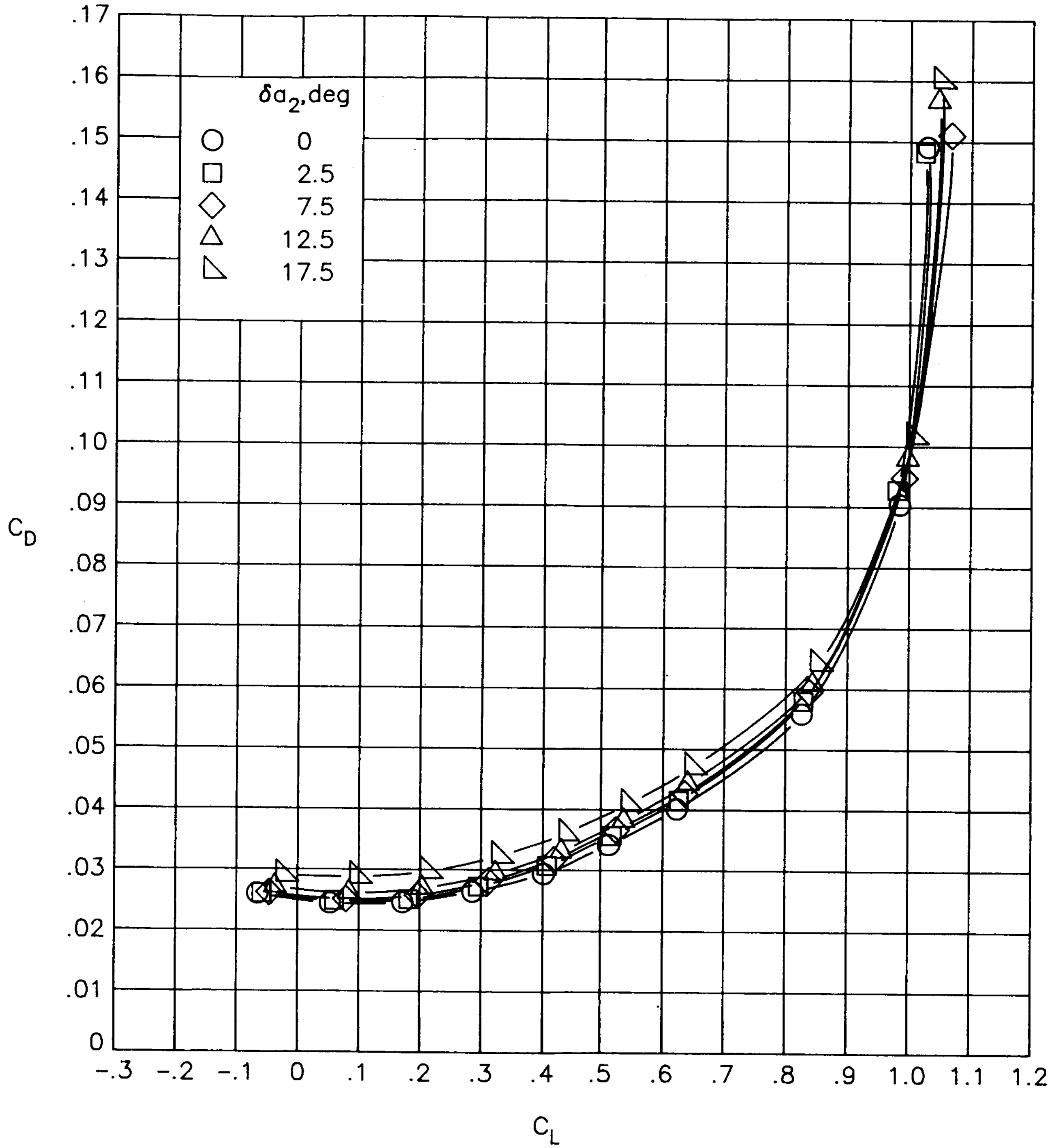

(b) Concluded.

Figure 37.- Continued.

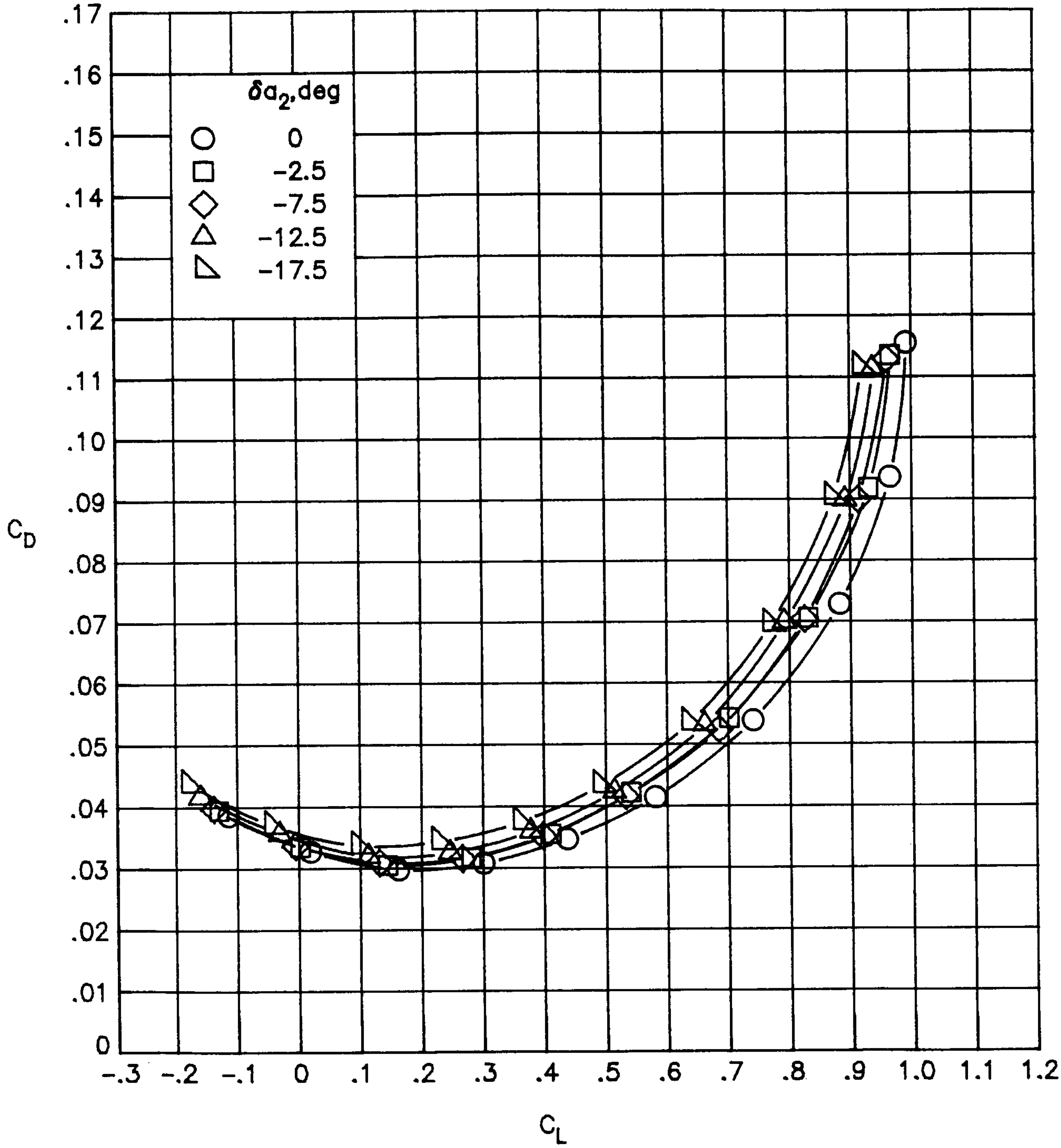

(c) $M_\infty = 0.80$.

Figure 37.- Continued.

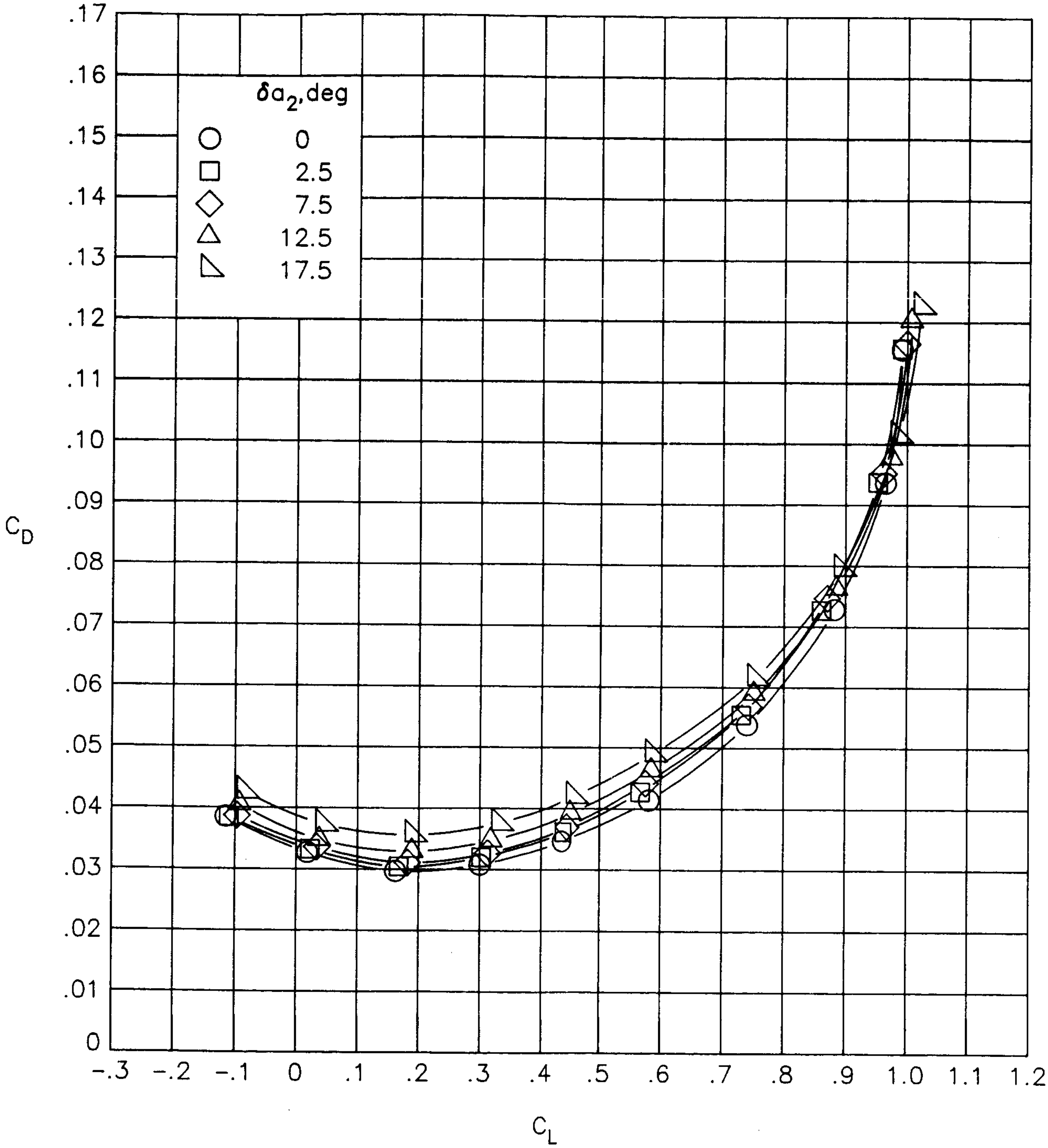

(c) Concluded.

Figure 37.- Continued.

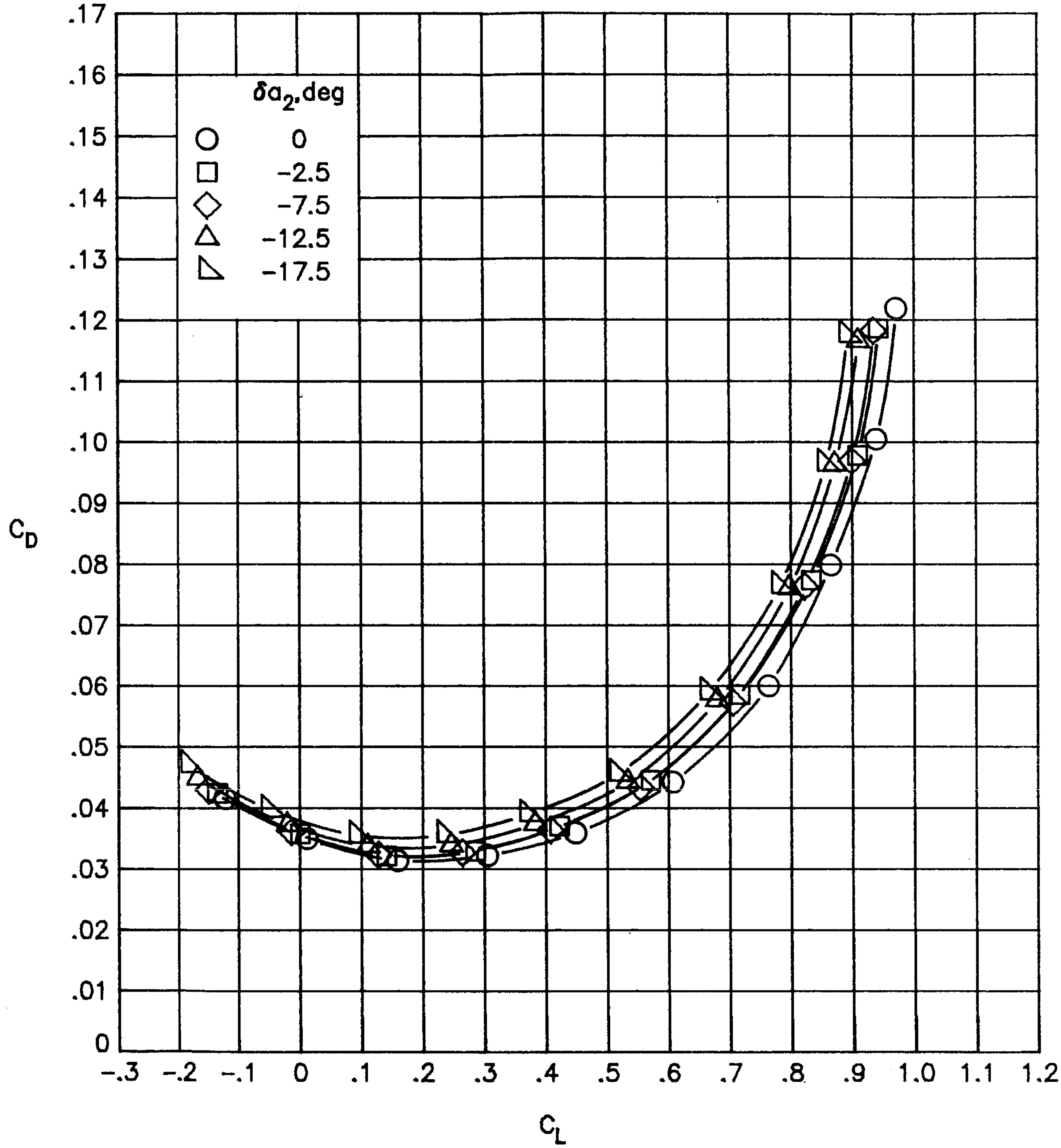

(d) $M_\infty = 0.82$.

Figure 37.- Continued.

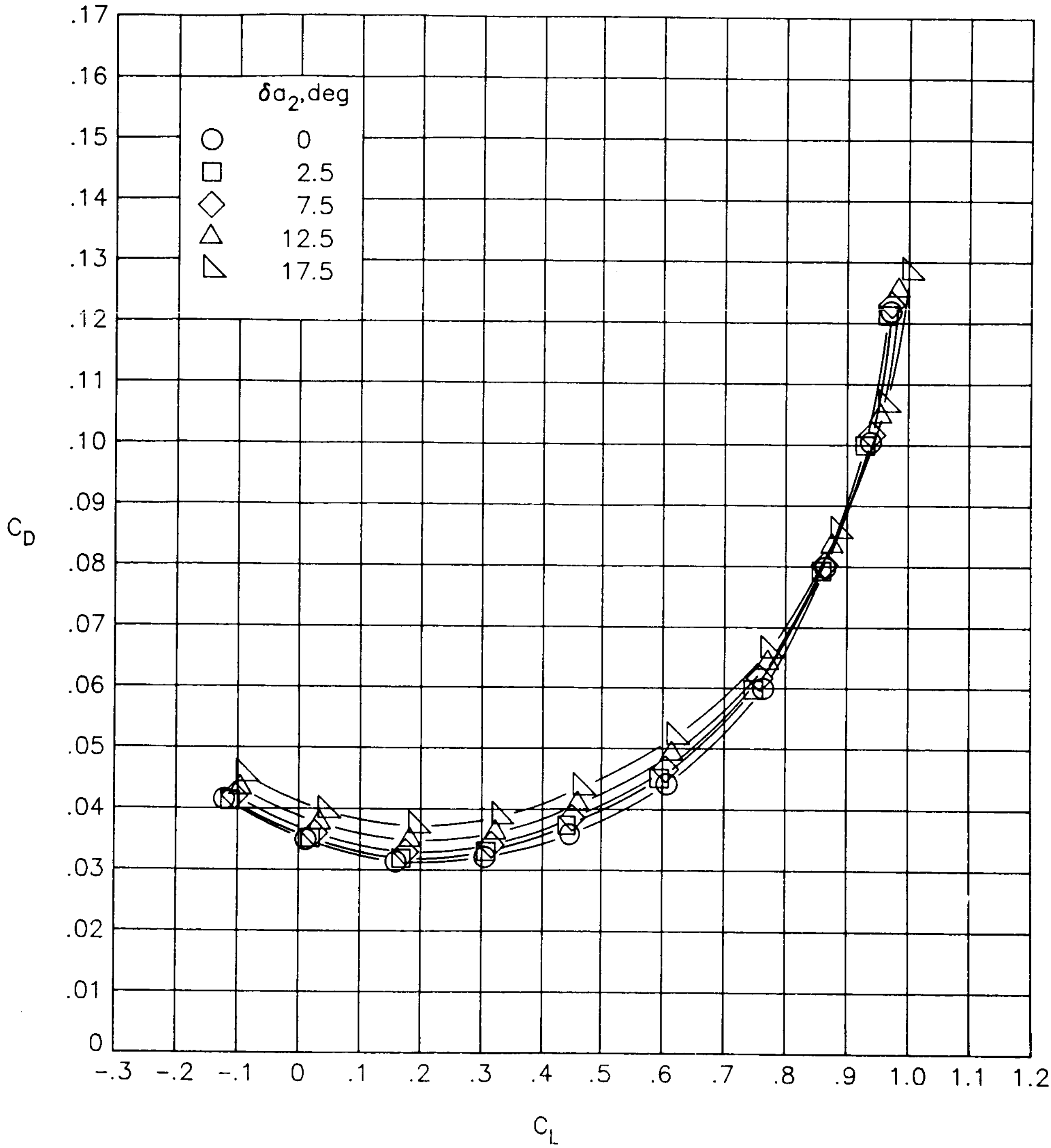

(d) Concluded.

Figure 37.- Continued.

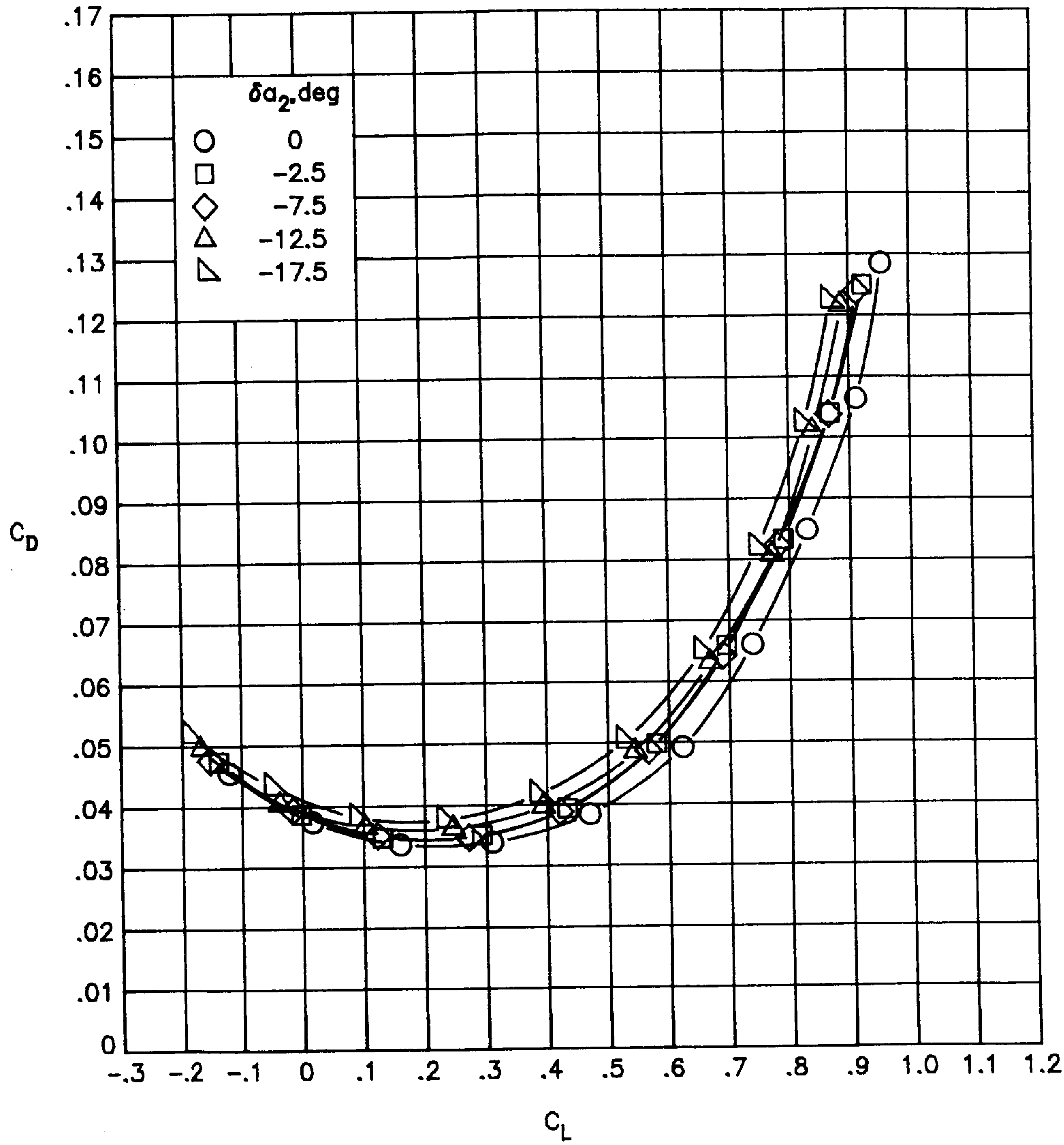

(e) $M_\infty = 0.84$.

Figure 37.- Continued.

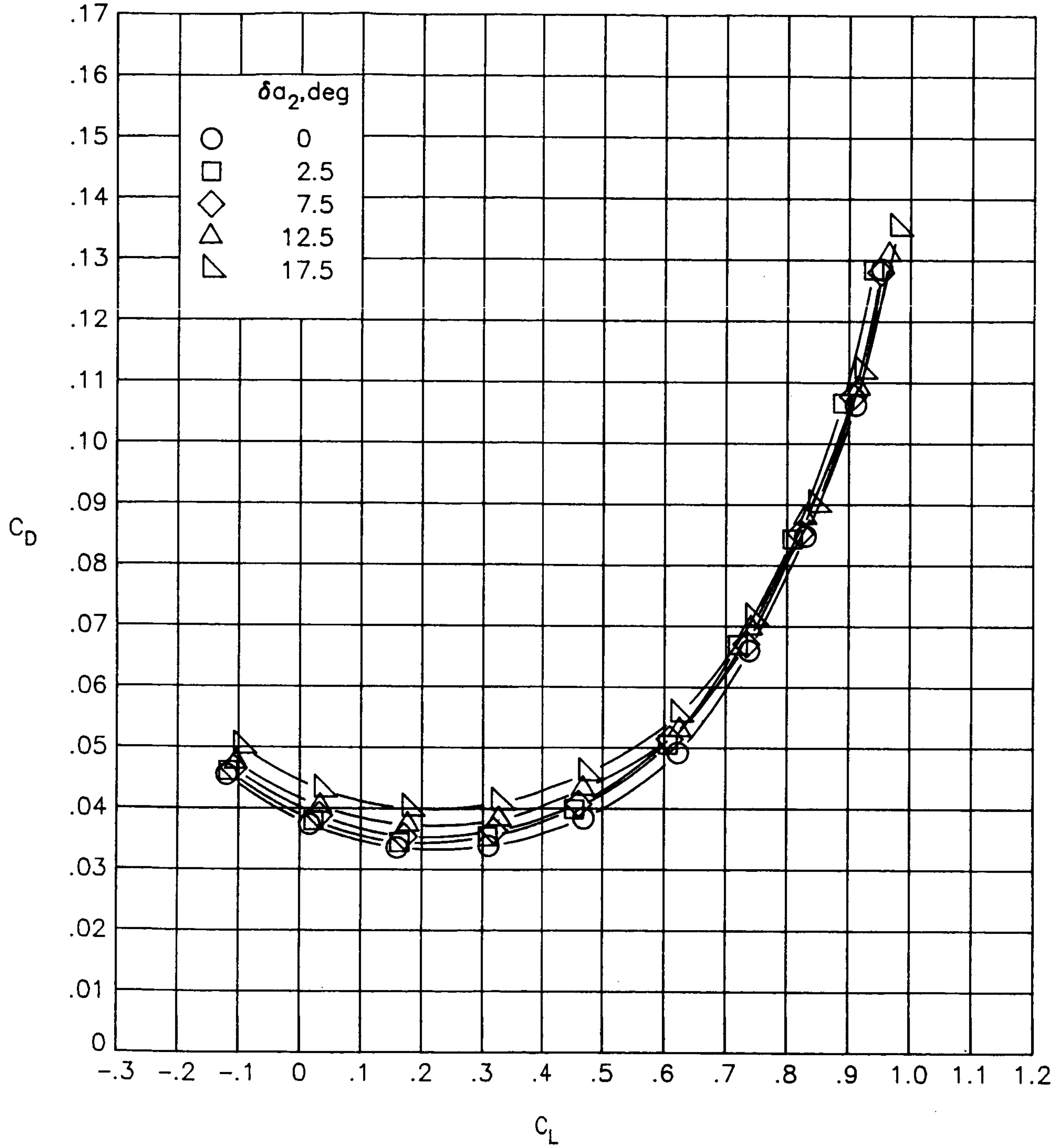

(e) Concluded.

Figure 37.- Continued.

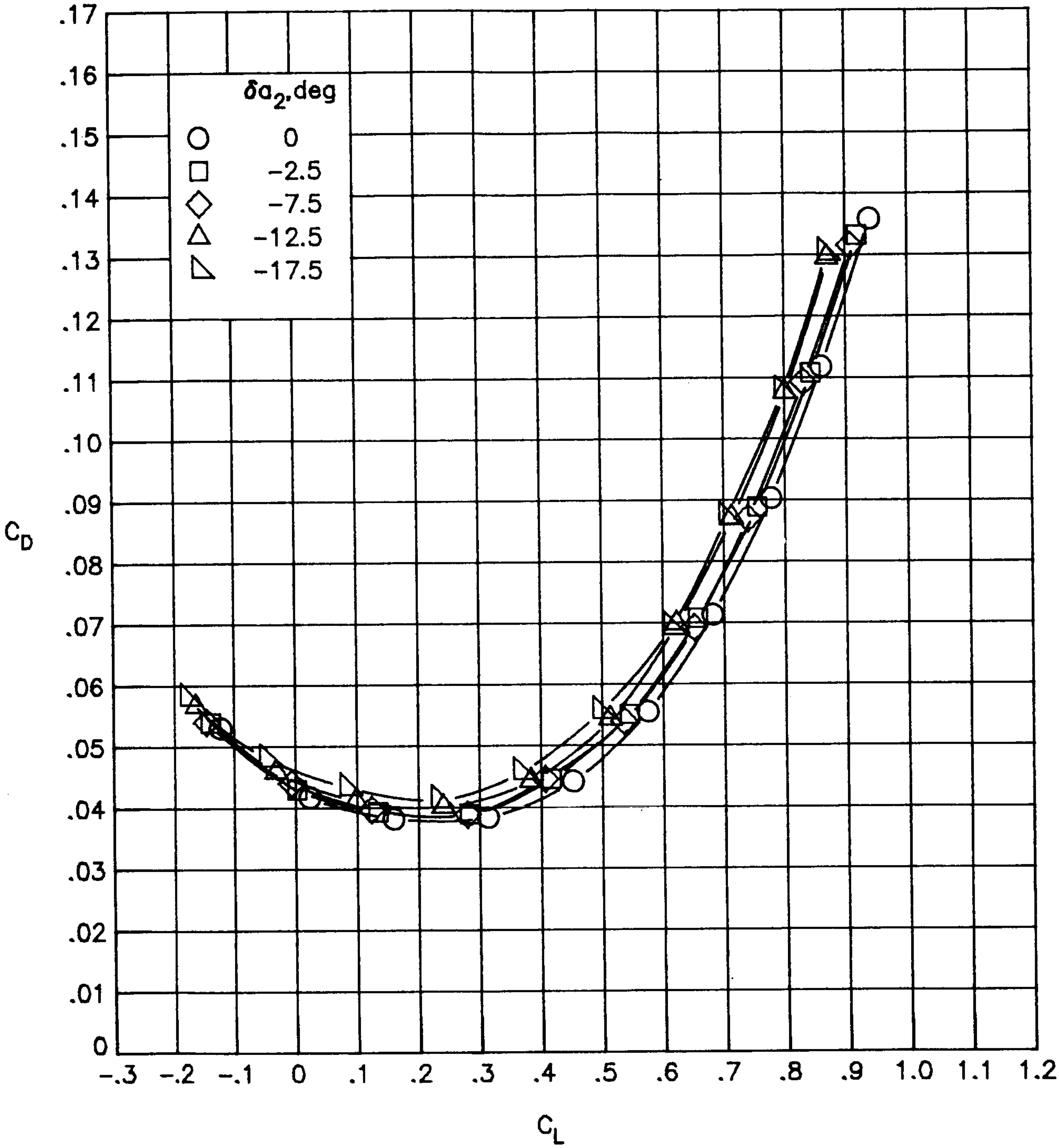

(f) $M_\infty = 0.86$.

Figure 37.- Continued.

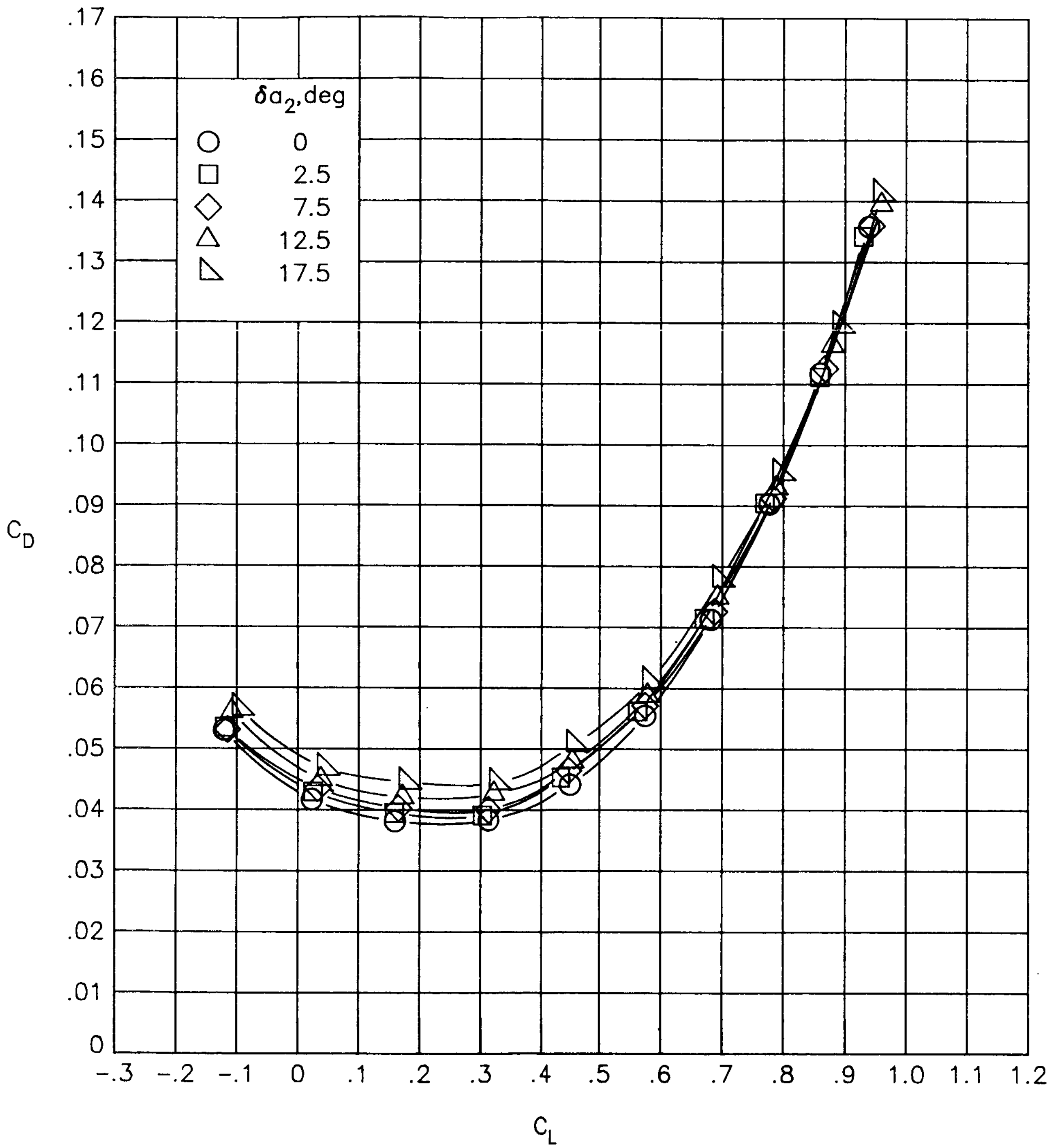

(f) Concluded.

Figure 37.- Continued.

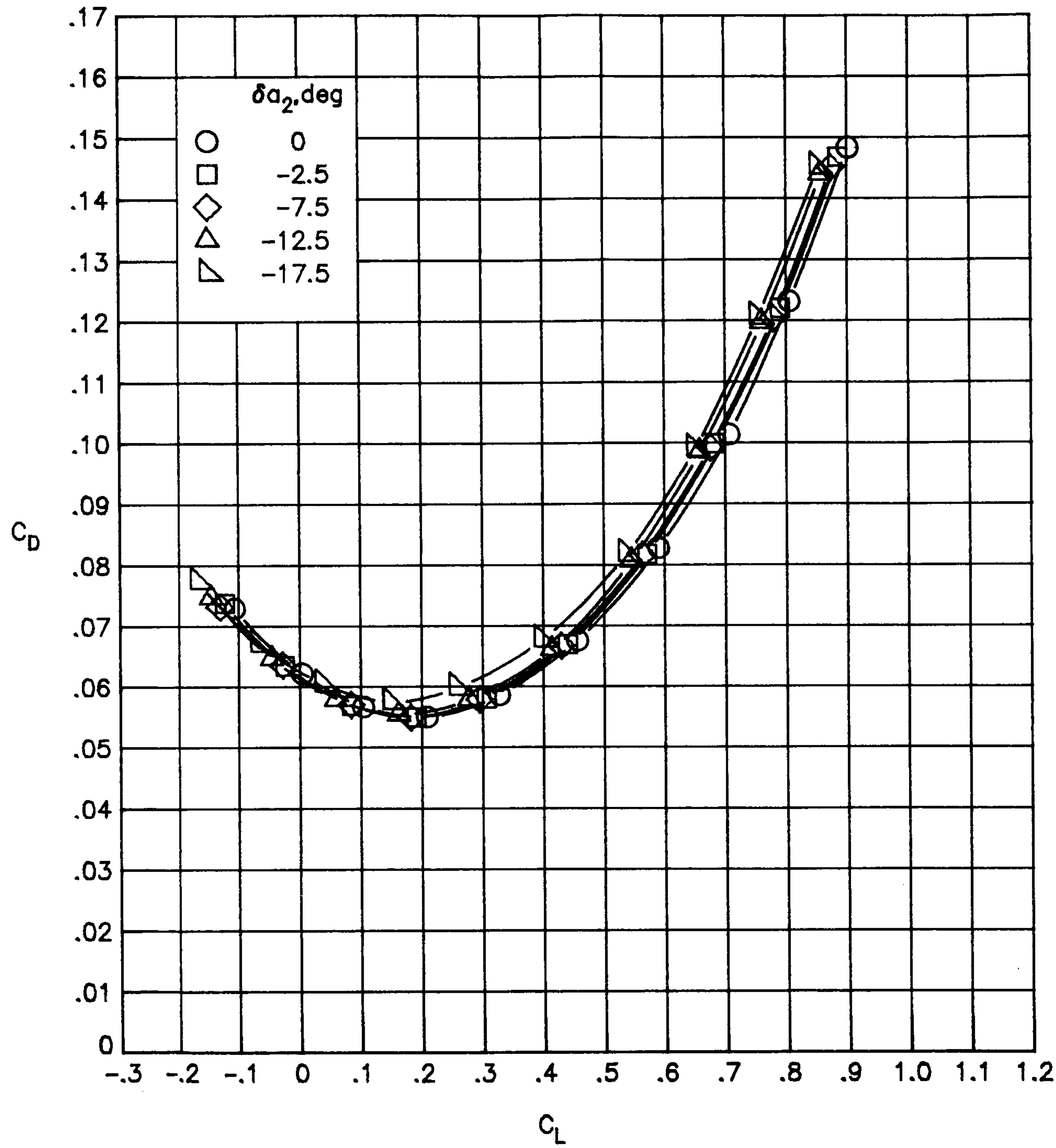

(g) M_∞ = 0.90.

Figure 37.- Continued.

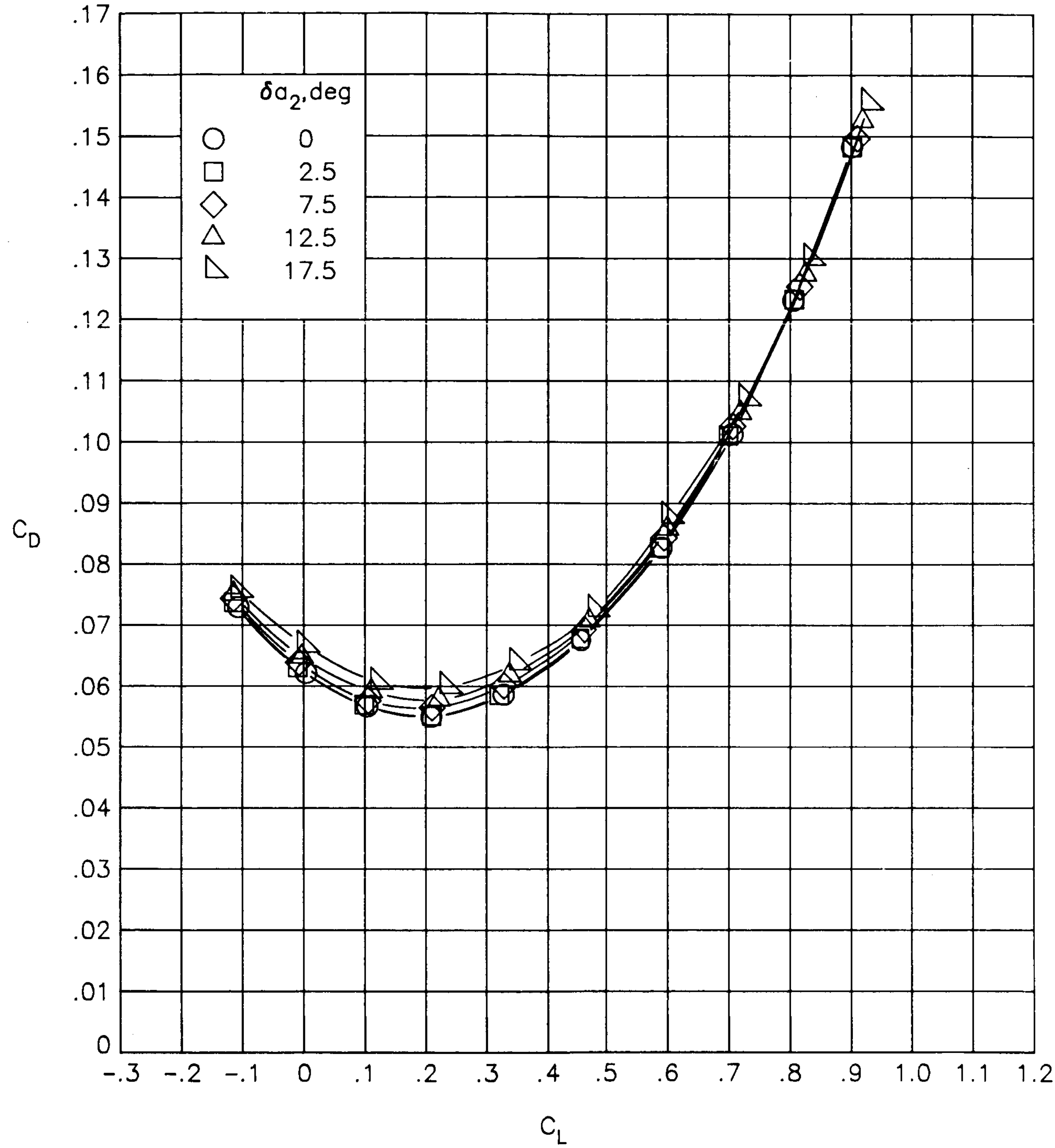

(g) Concluded.

Figure 37.- Concluded.

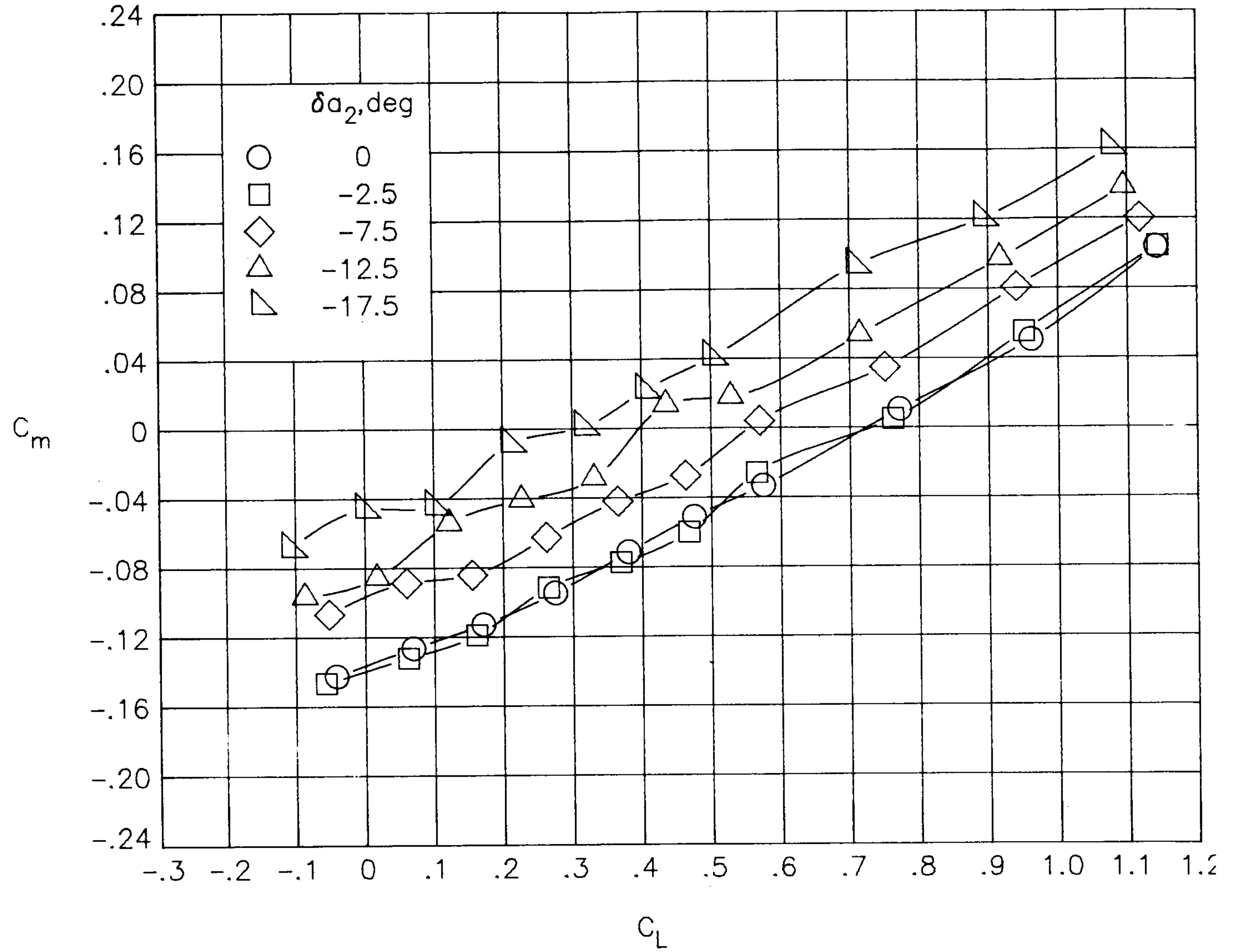

(a) $M_\infty = 0.30$.

Figure 38.- Variation of pitching-moment coefficient with lift coefficient for deflections of a_2. $\delta a_1 = 0°$.

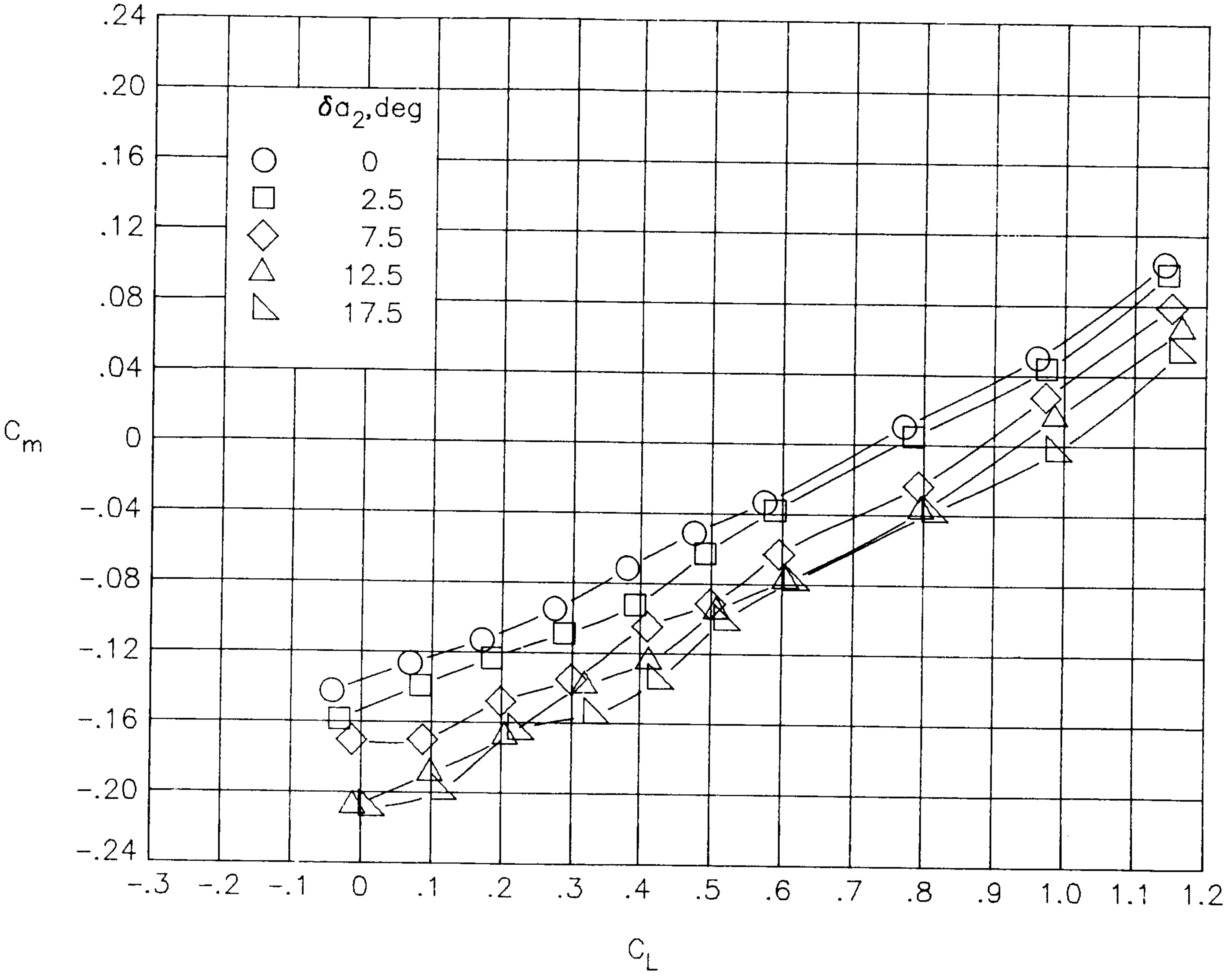

(a) Concluded.

Figure 38.- Continued.

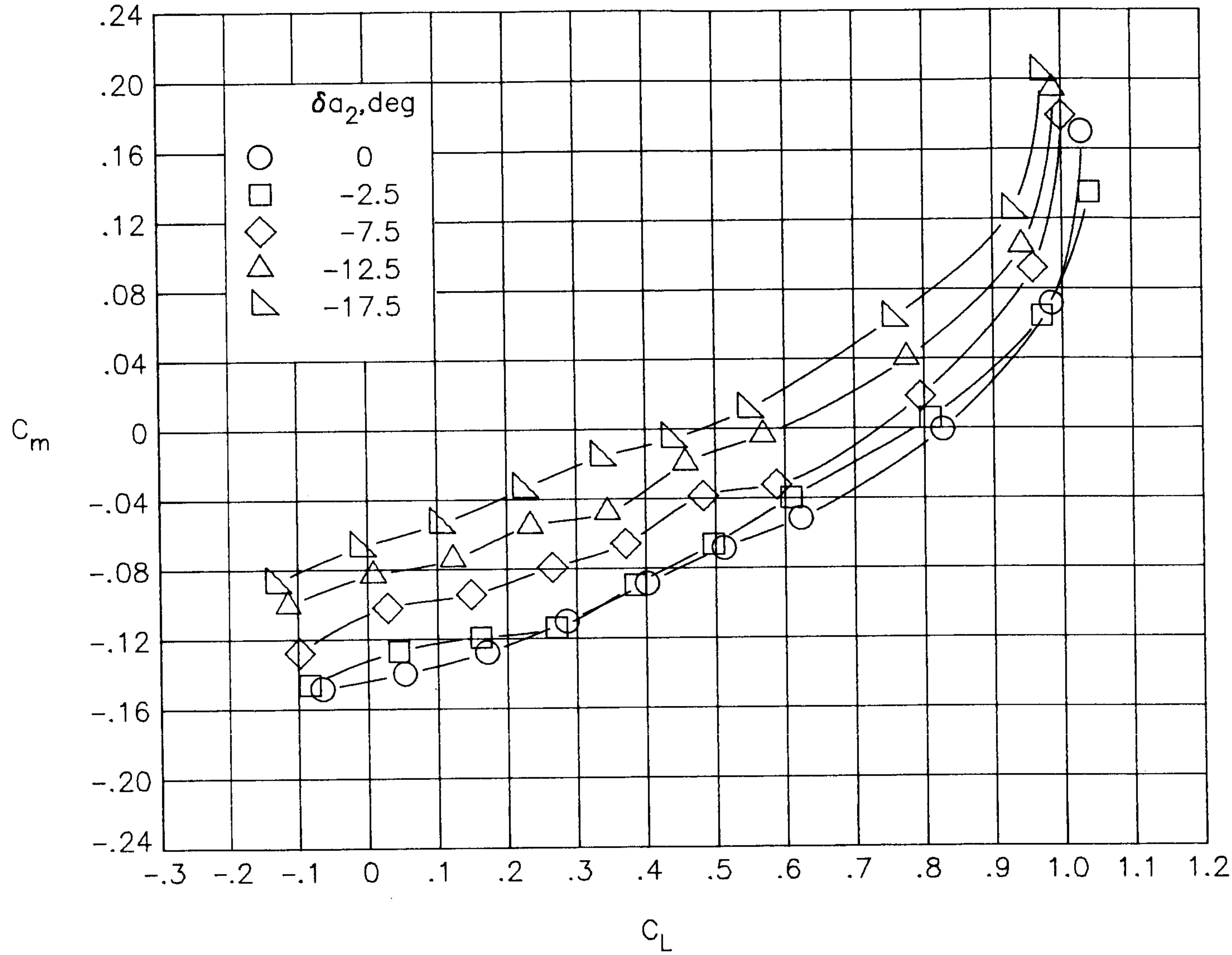

(b) $M_\infty = 0.60$.

Figure 38.- Continued.

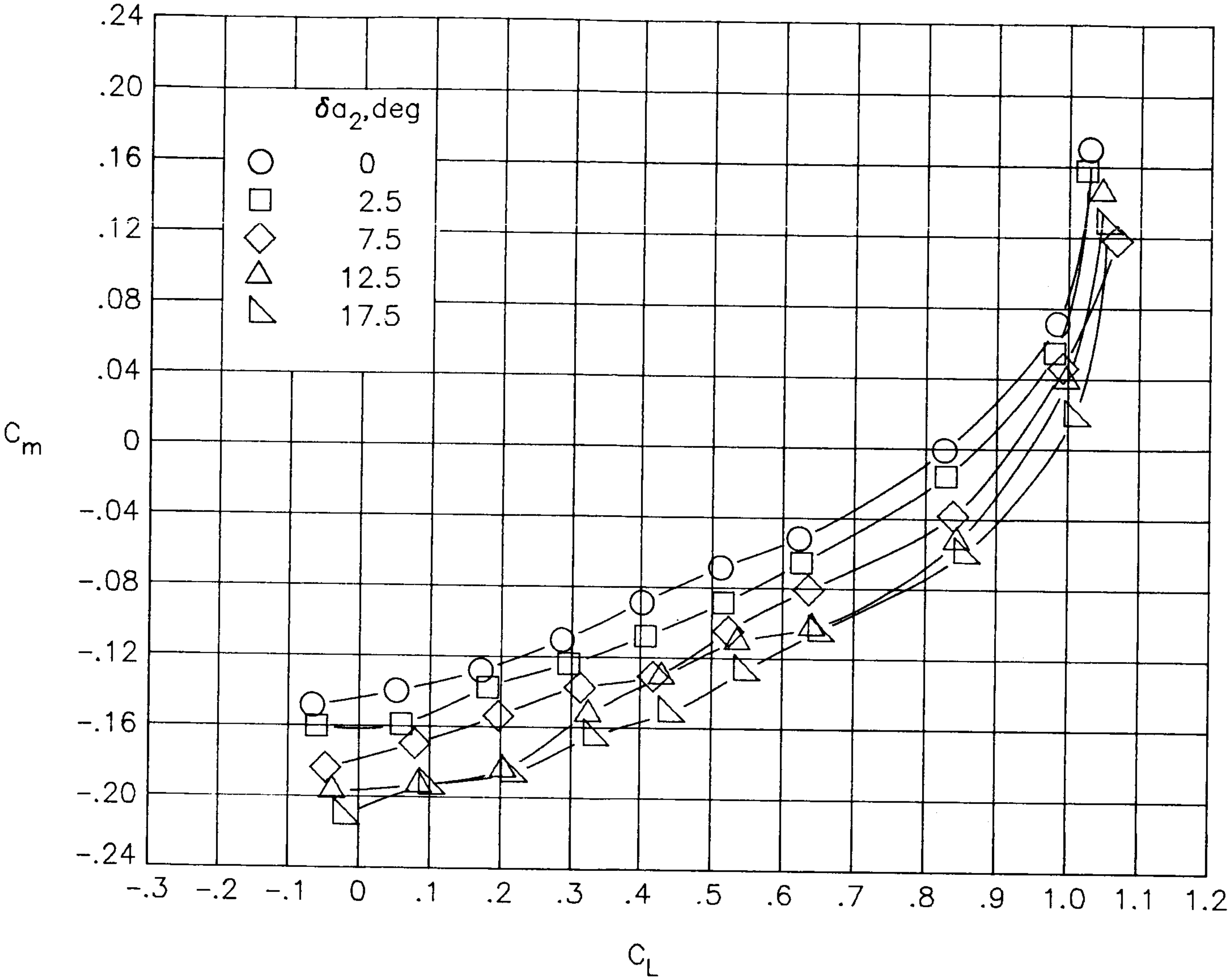

(b) Concluded.

Figure 38.- Continued.

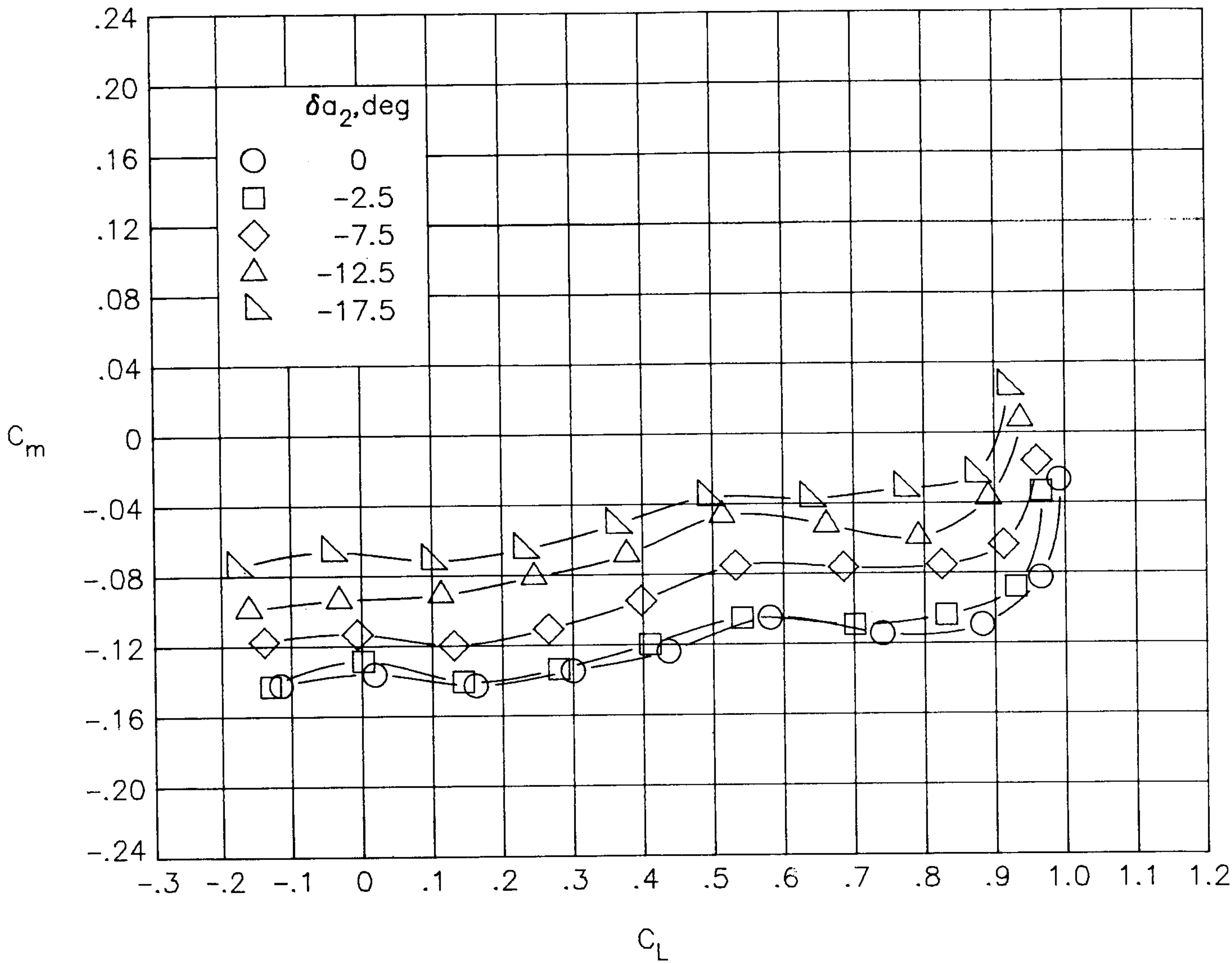

(c) $M_\infty = 0.80$.

Figure 38.- Continued.

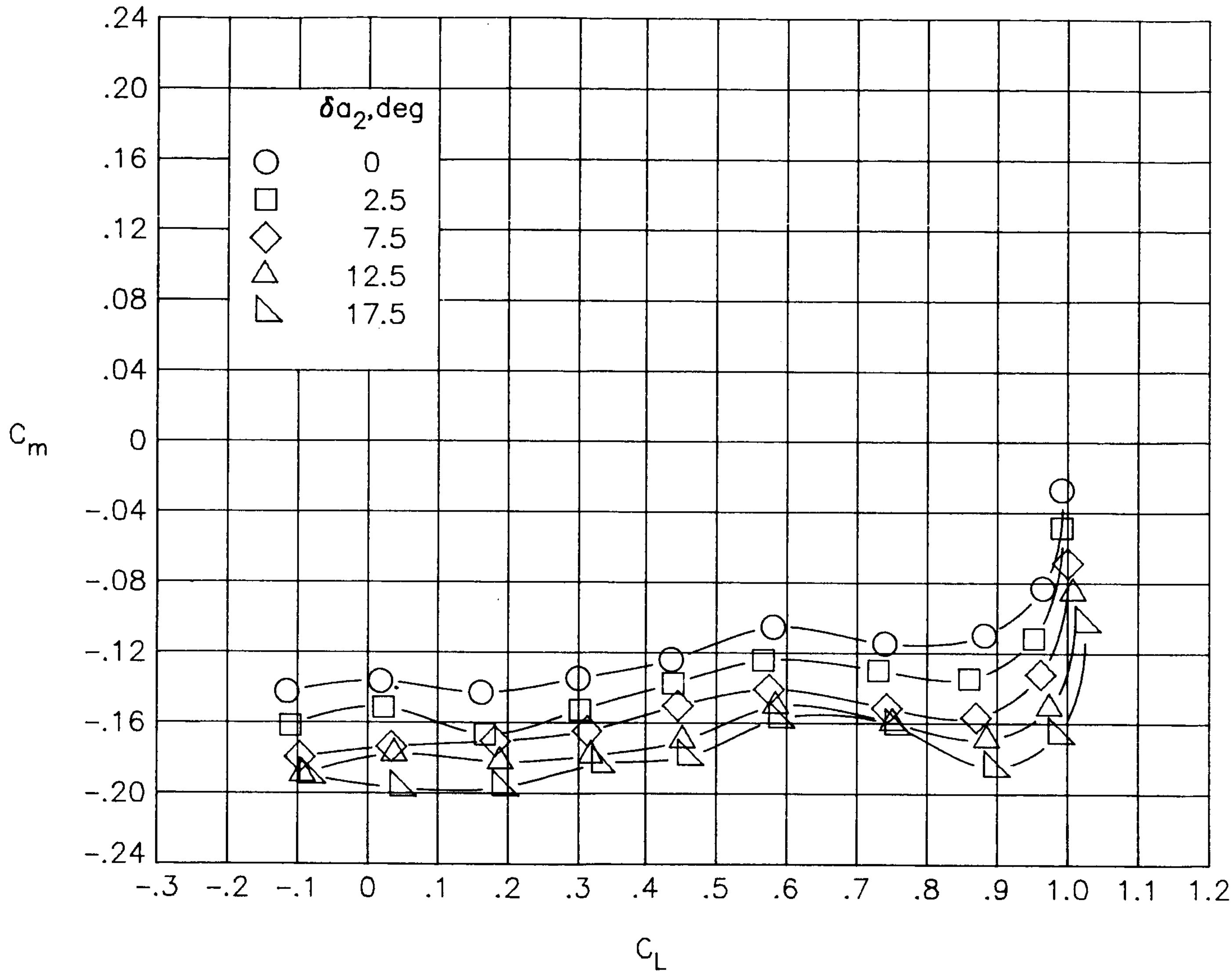

(c) Concluded.

Figure 38.- Continued.

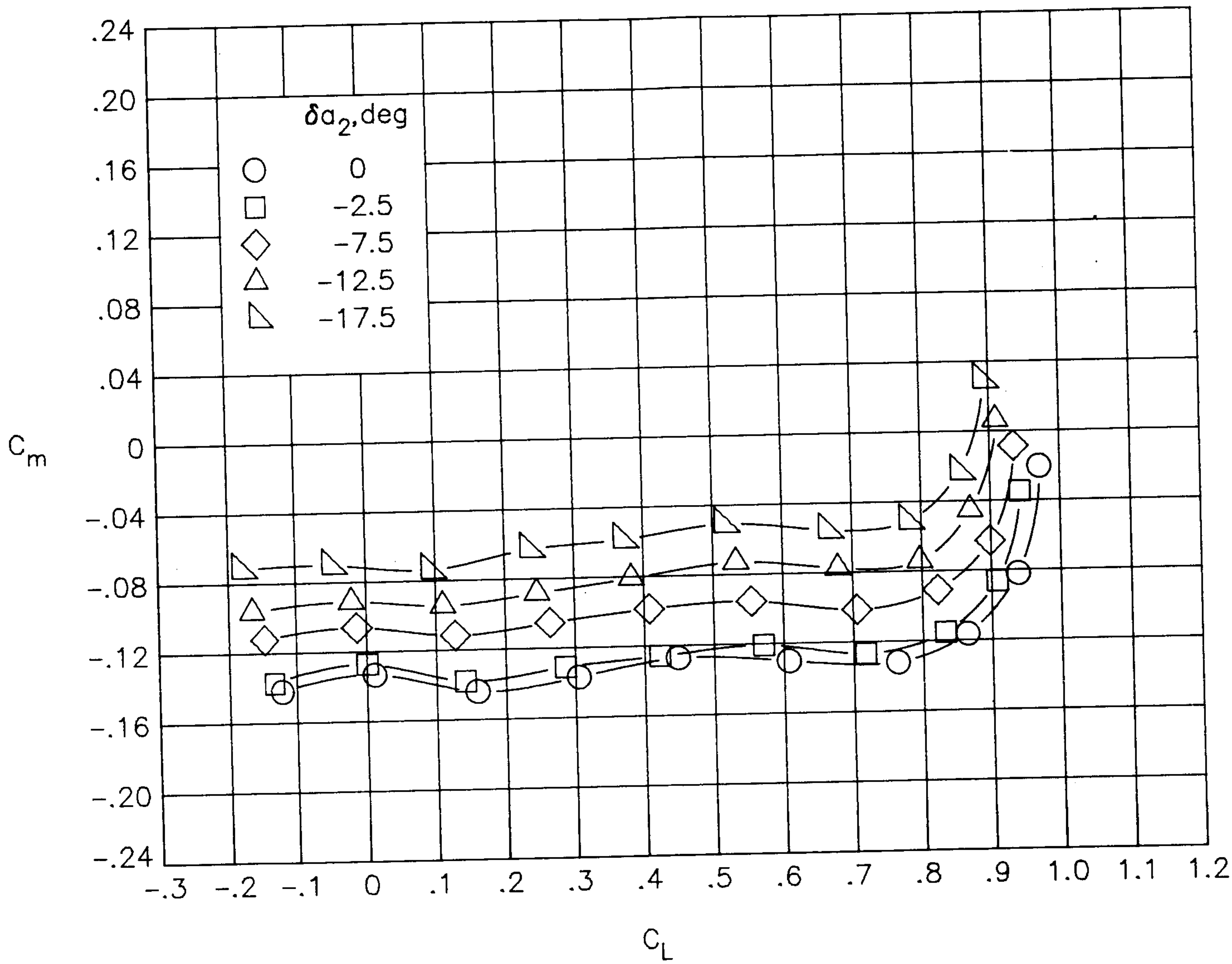

(d) $M_\infty = 0.82$.

Figure 38.- Continued.

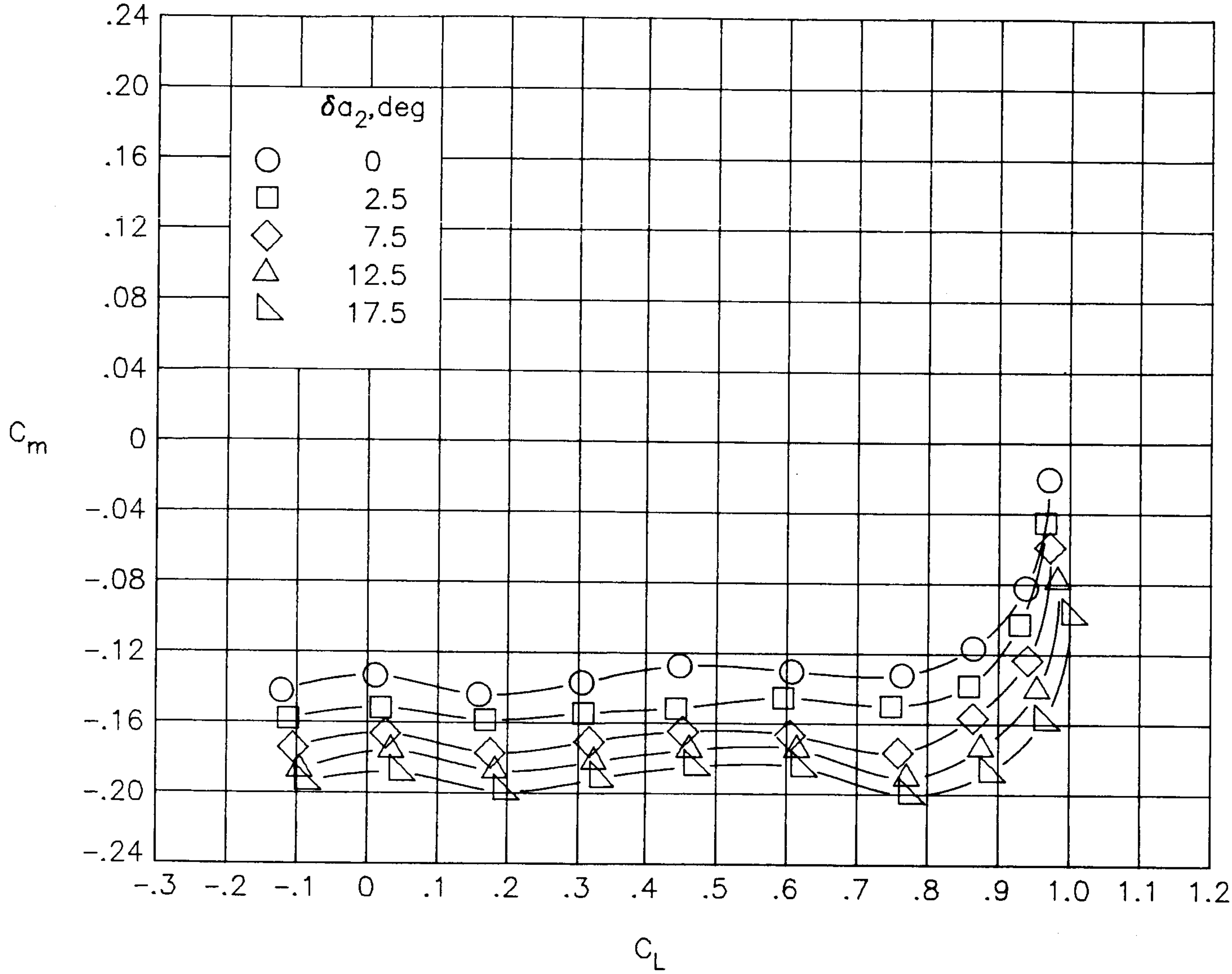

(d) Concluded.

Figure 38.- Continued.

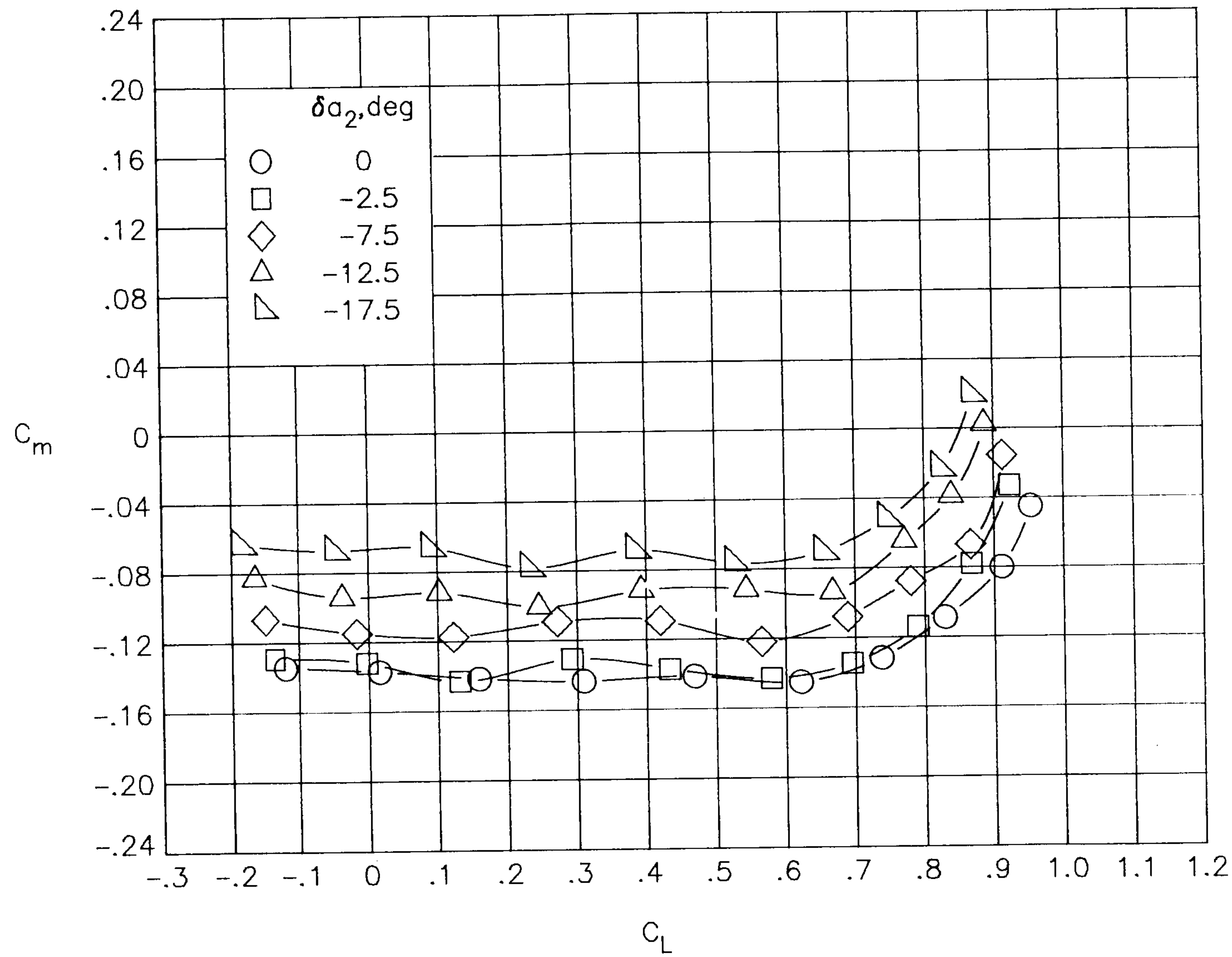

(e) $M_\infty = 0.84$.

Figure 38.- Continued.

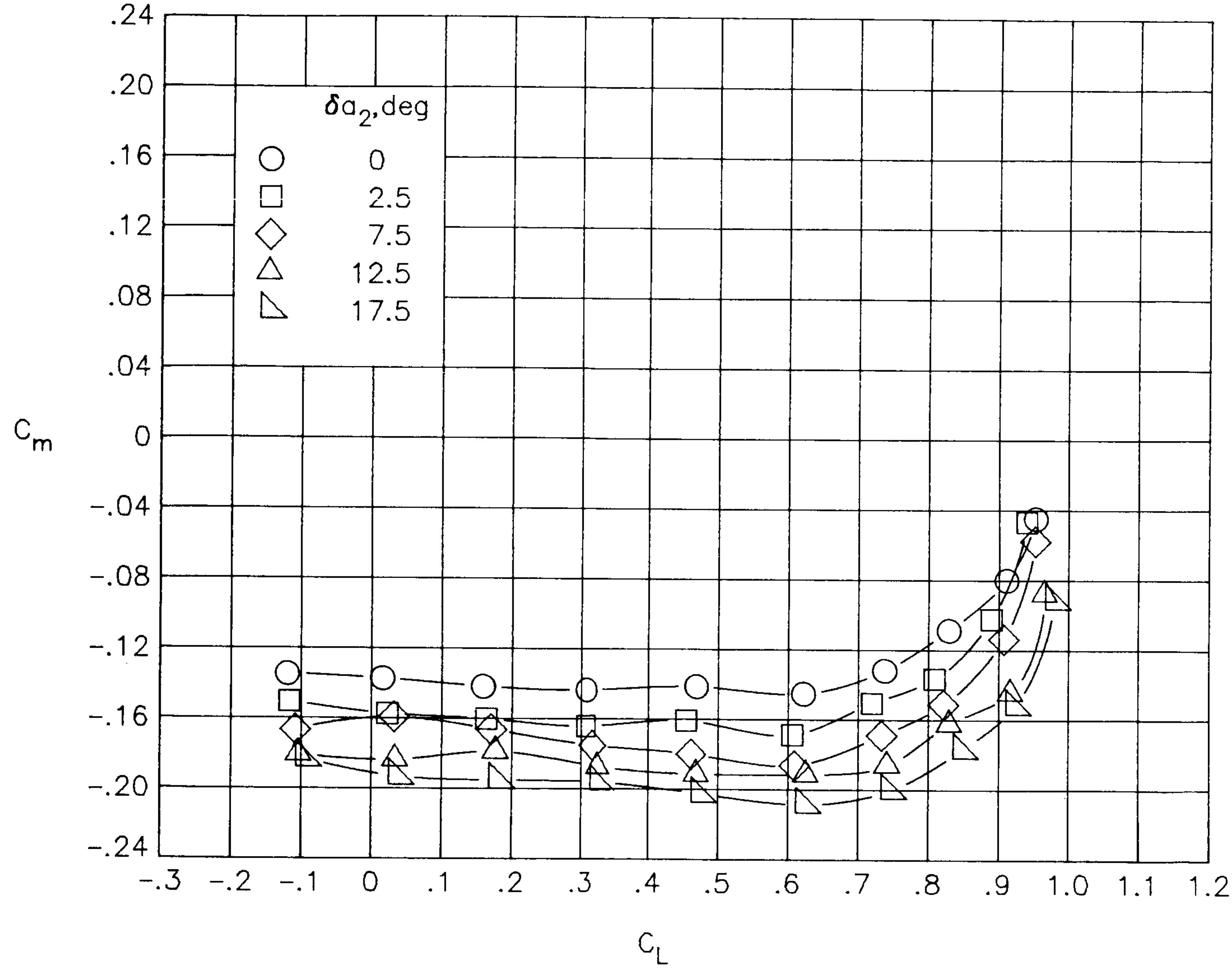

(e) Concluded.

Figure 38.- Continued.

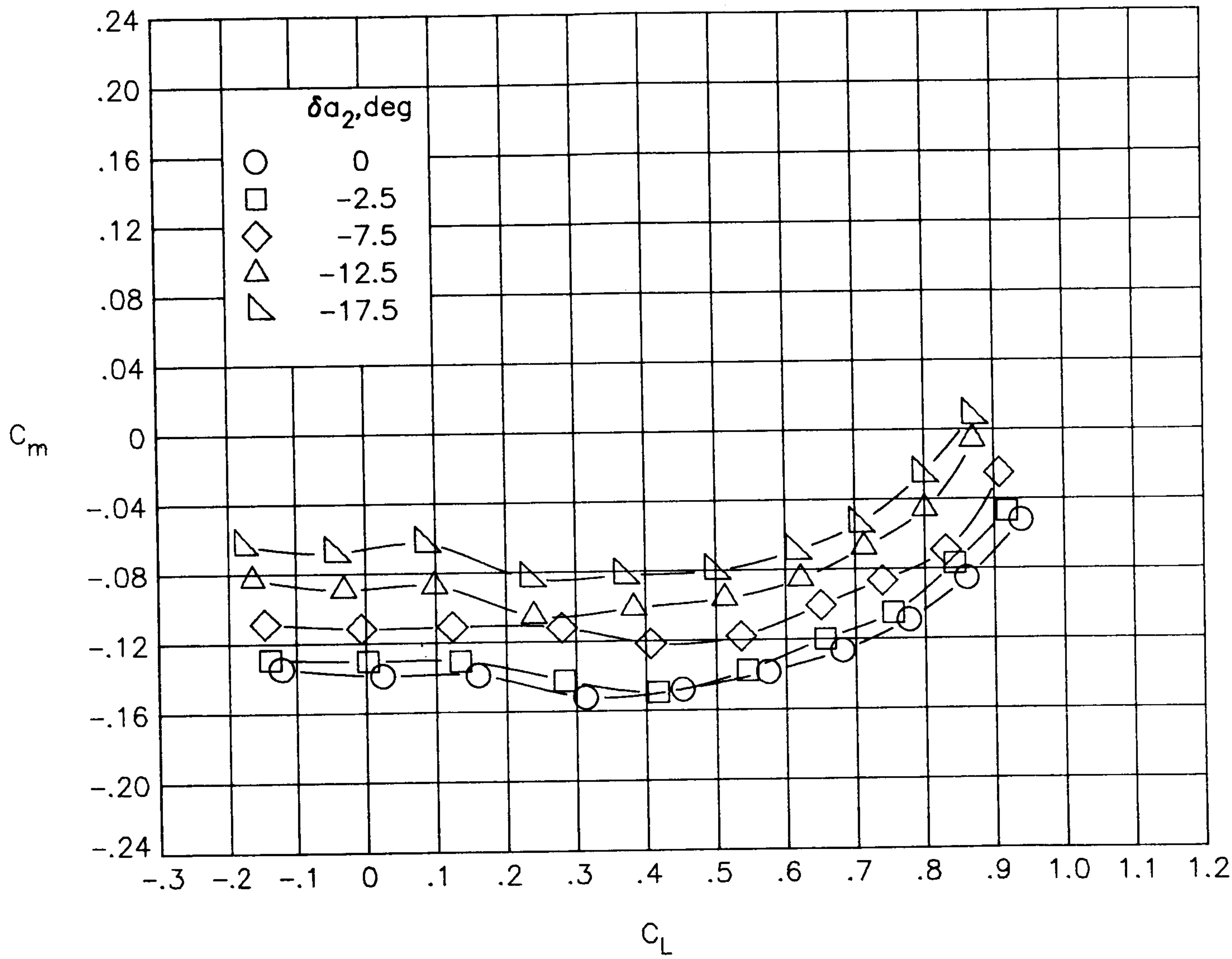

(f) $M_\infty = 0.86$.

Figure 38.- Continued.

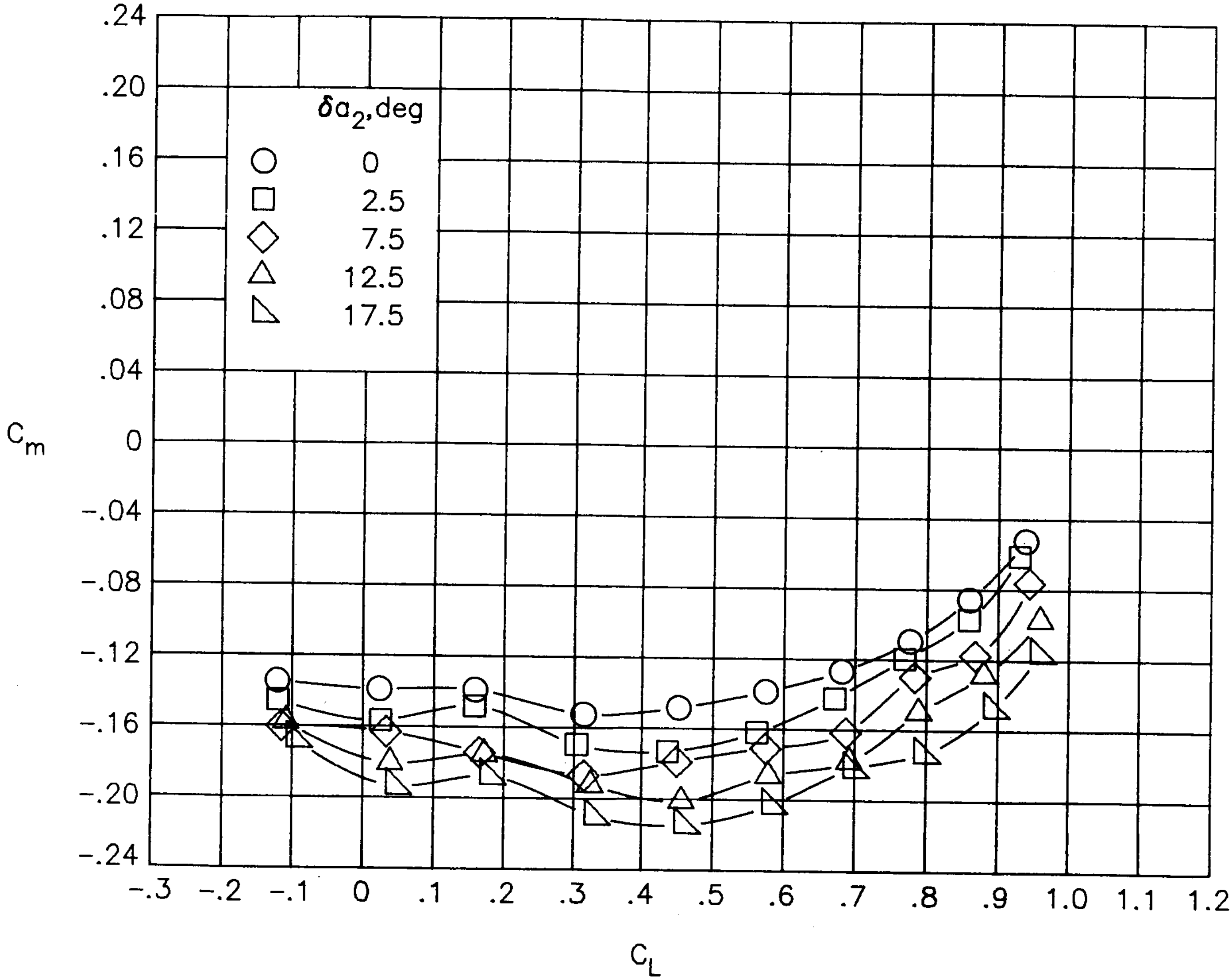

(f) Concluded.

Figure 38.- Continued.

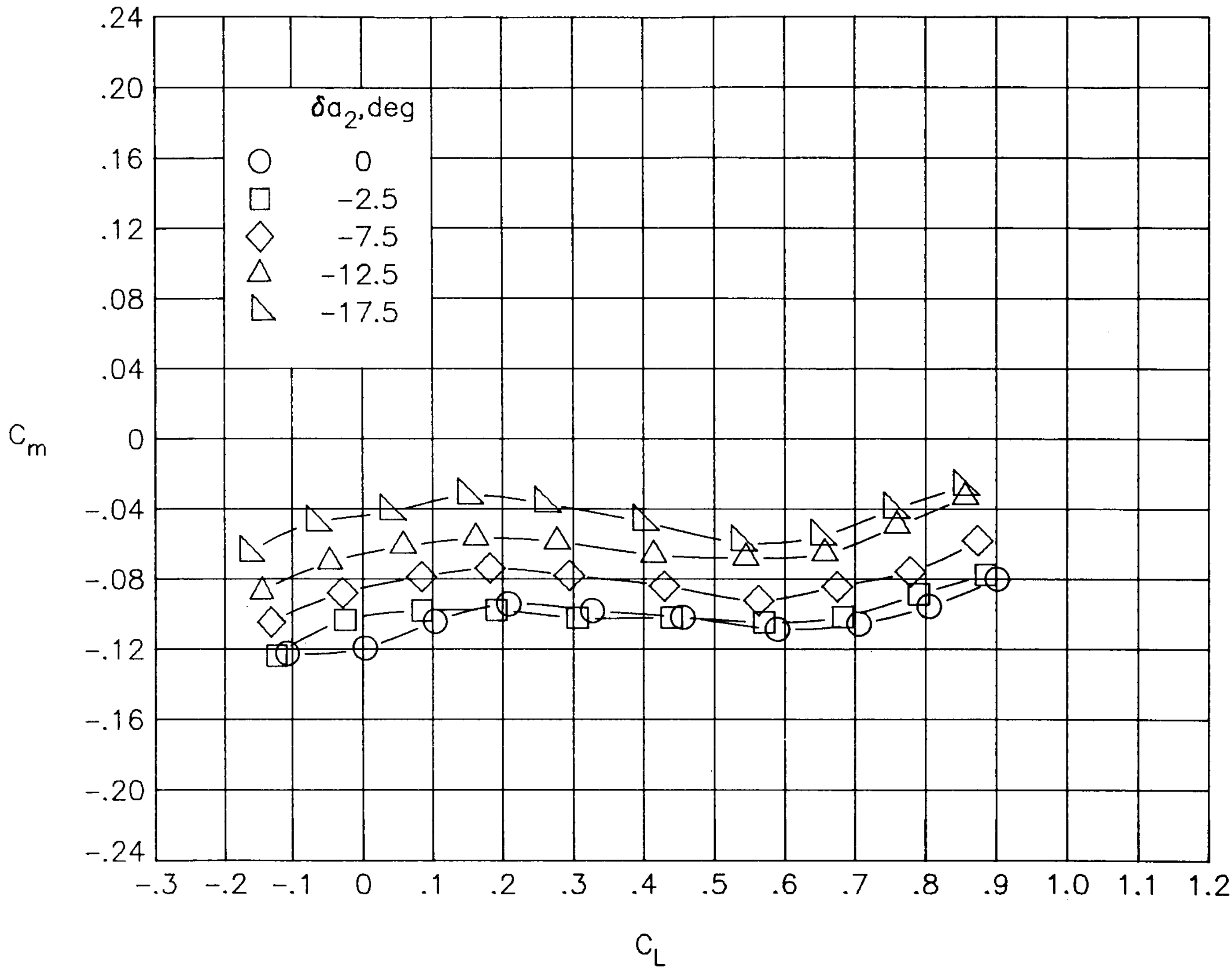

(g) $M_\infty = 0.90$.

Figure 38.- Continued.

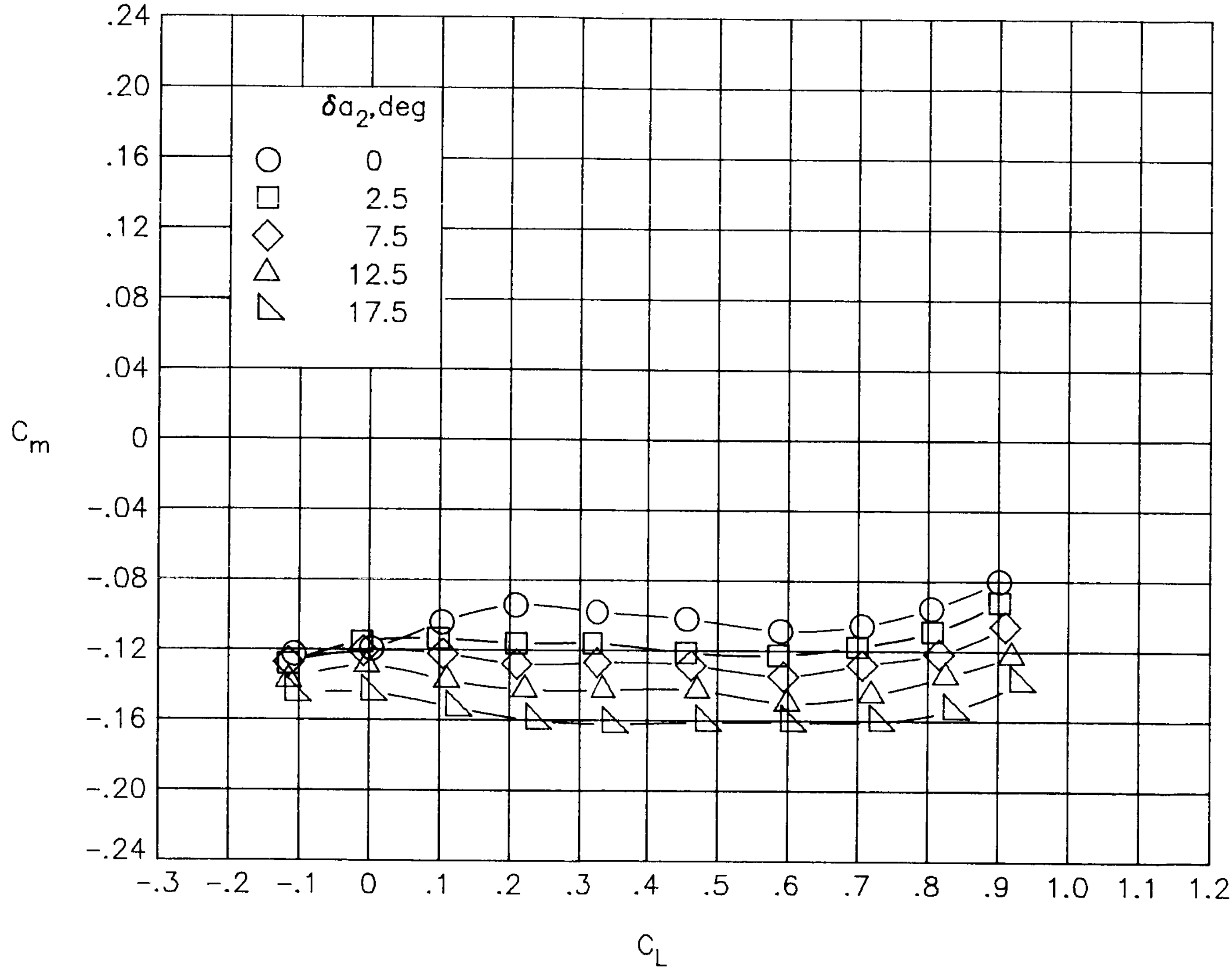

(g) Concluded.

Figure 38.- Concluded.

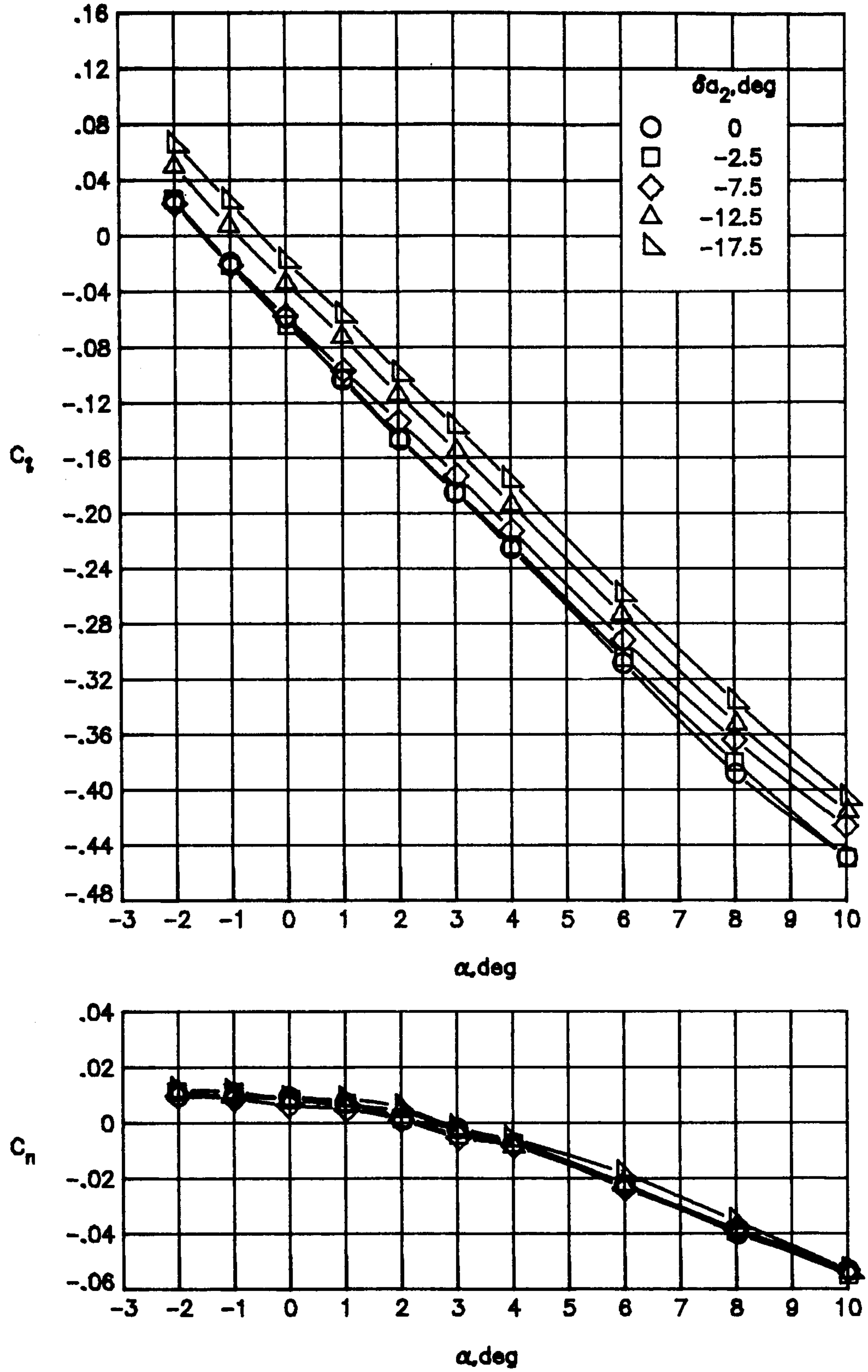

(a) $M_\infty = 0.30$.

Figure 39.- Variations of rolling-moment coefficient and yawing-moment coefficient with angle of attack for deflections of a_2. $\delta a_1 = 0°$.

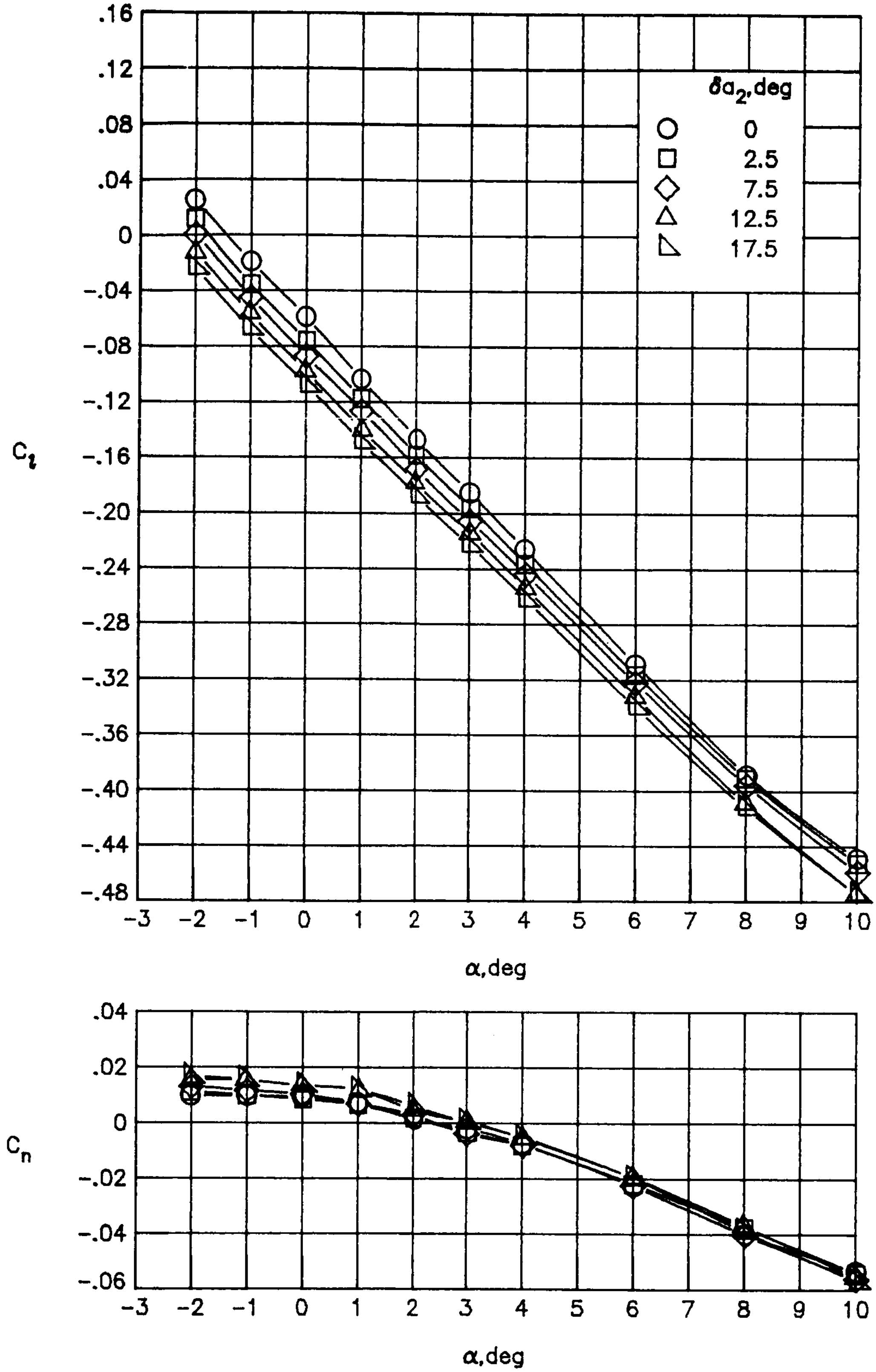

(a) Concluded.

Figure 39.- Continued.

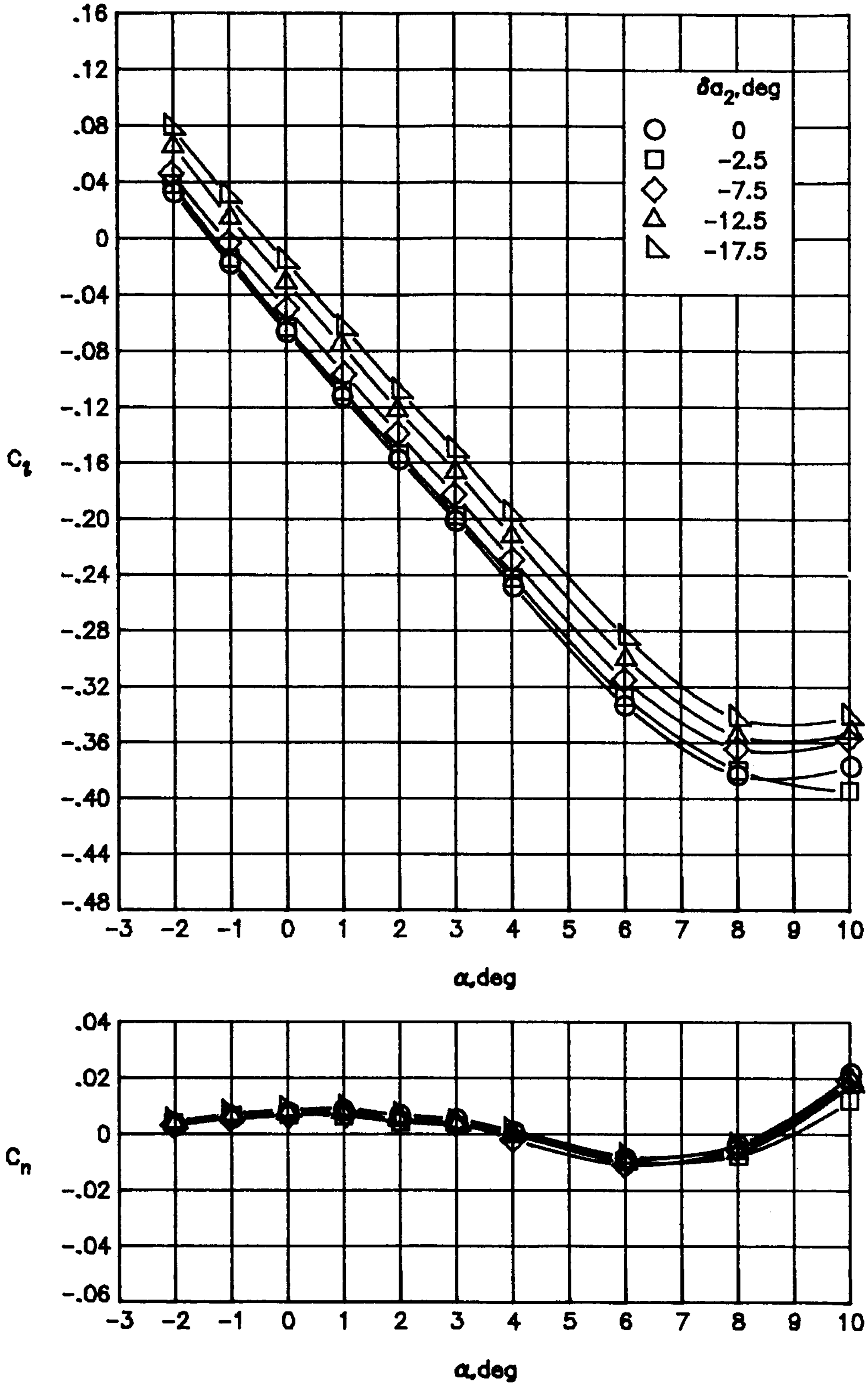

(b) $M_\infty = 0.60$.

Figure 39.- Continued.

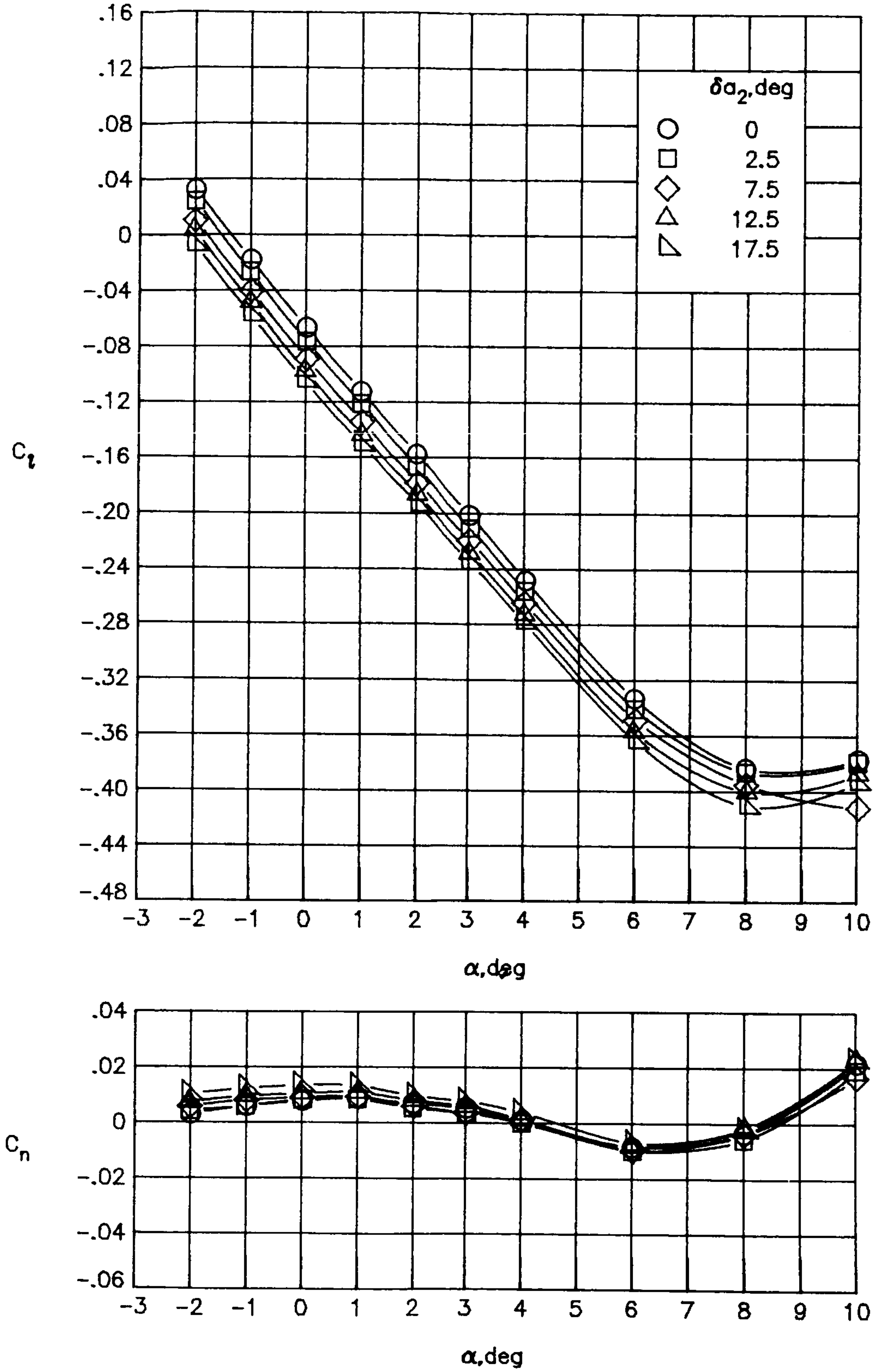

(b) Concluded.

Figure 39.- Continued.

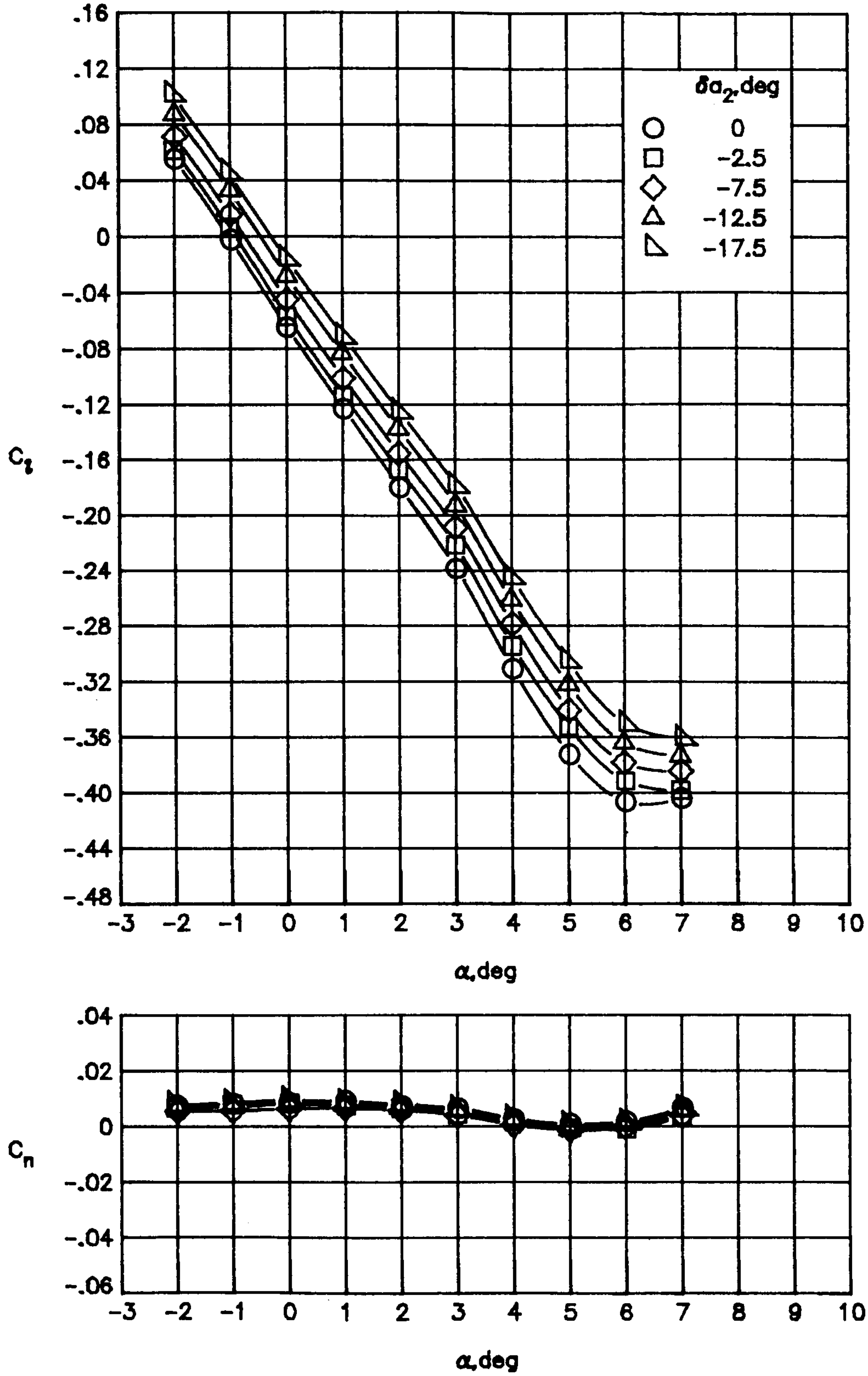

(c) $M_\infty = 0.80$.

Figure 39.- Continued.

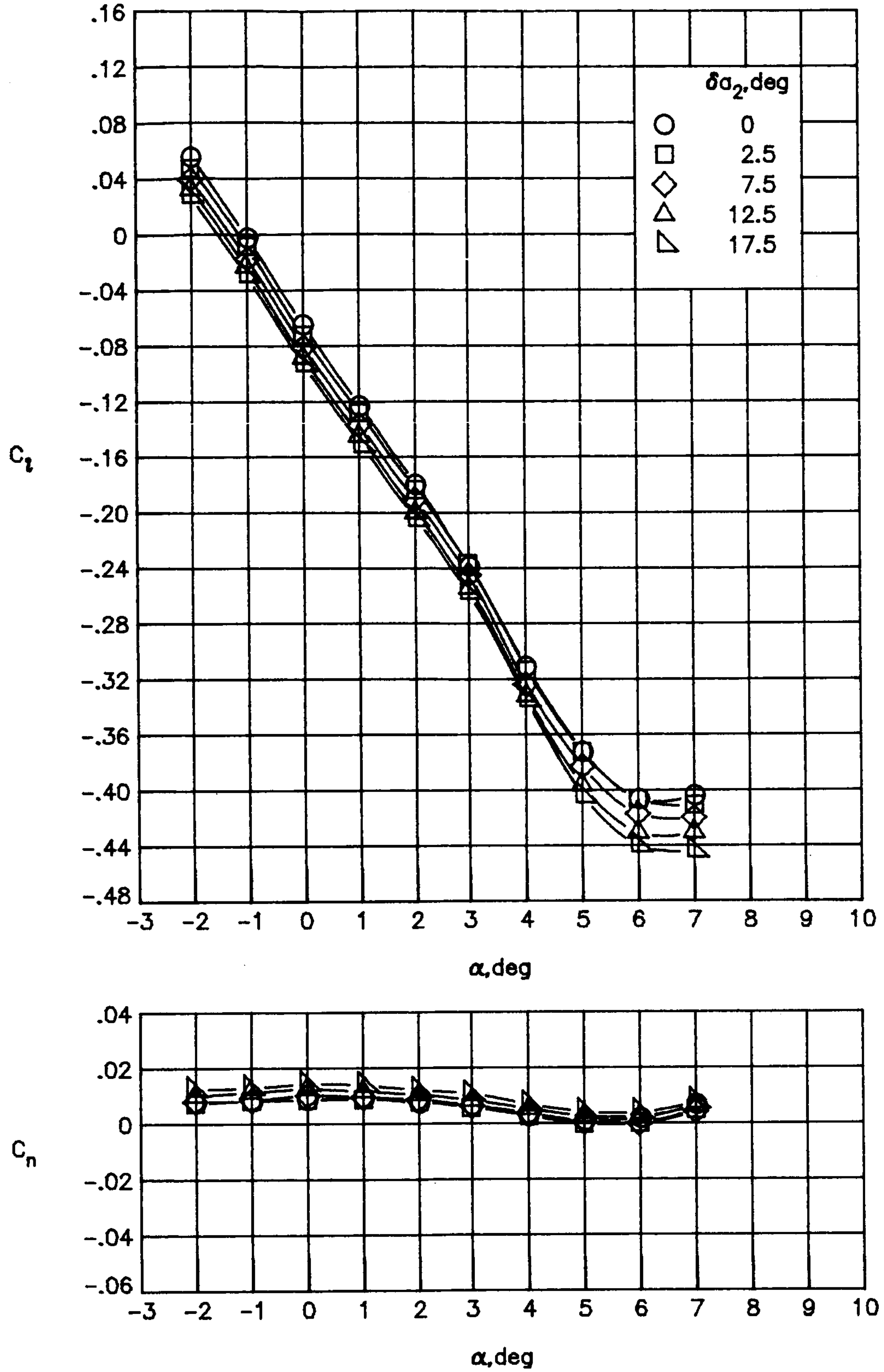

(c) Concluded.

Figure 39.- Continued.

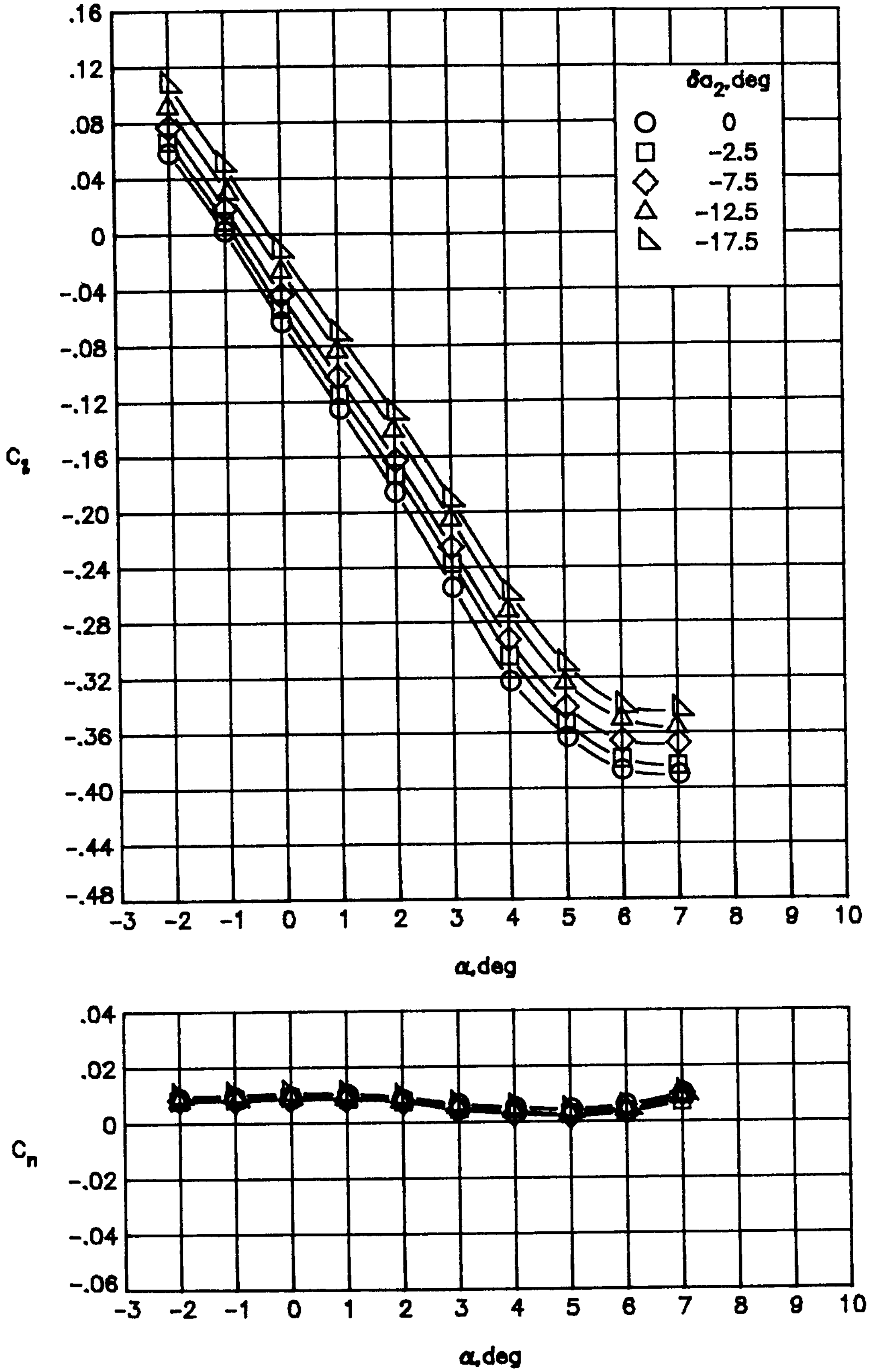

(d) $M_\infty = 0.82$.

Figure 39.- Continued.

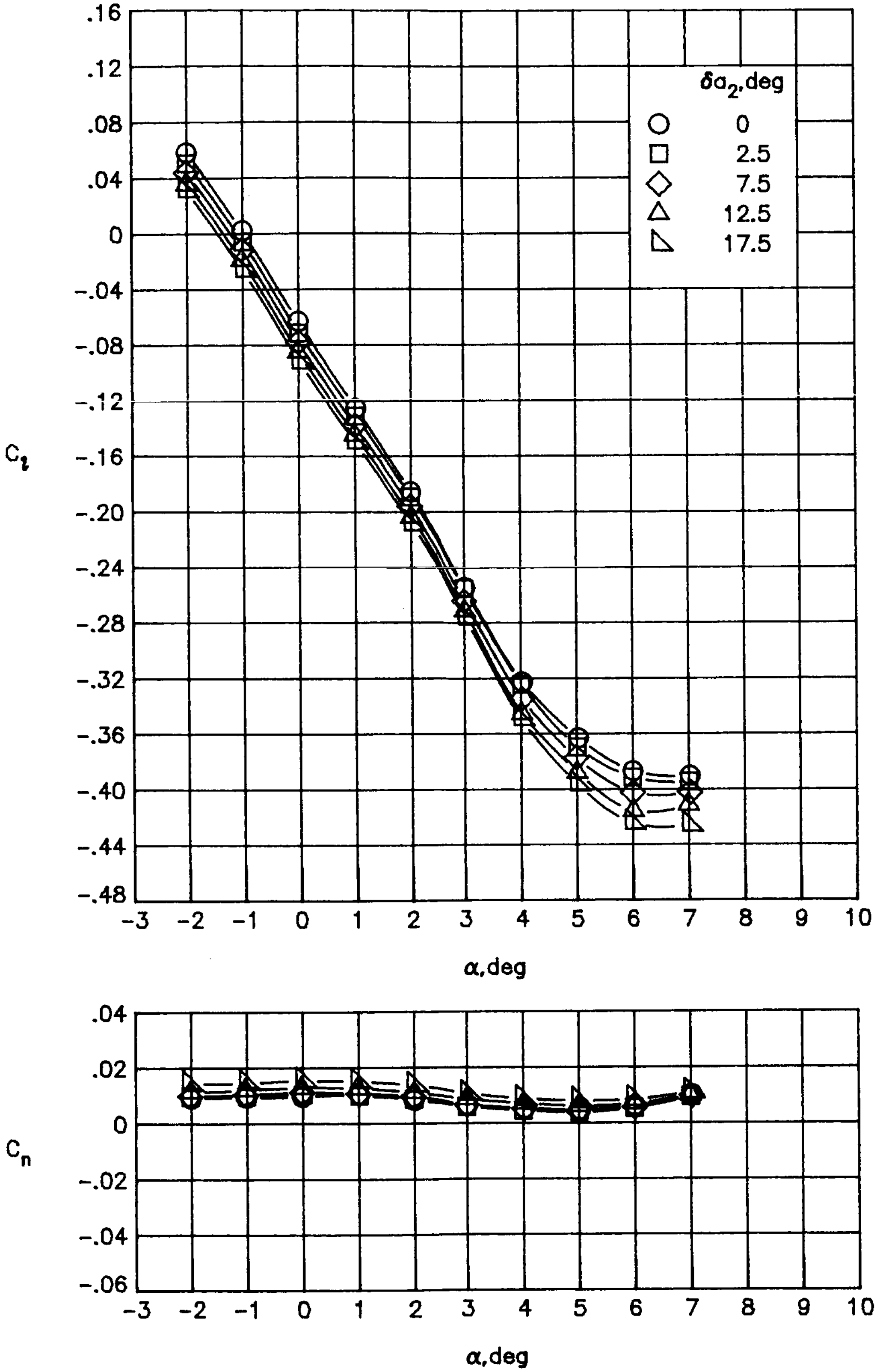

(d) Concluded.

Figure 39.- Continued.

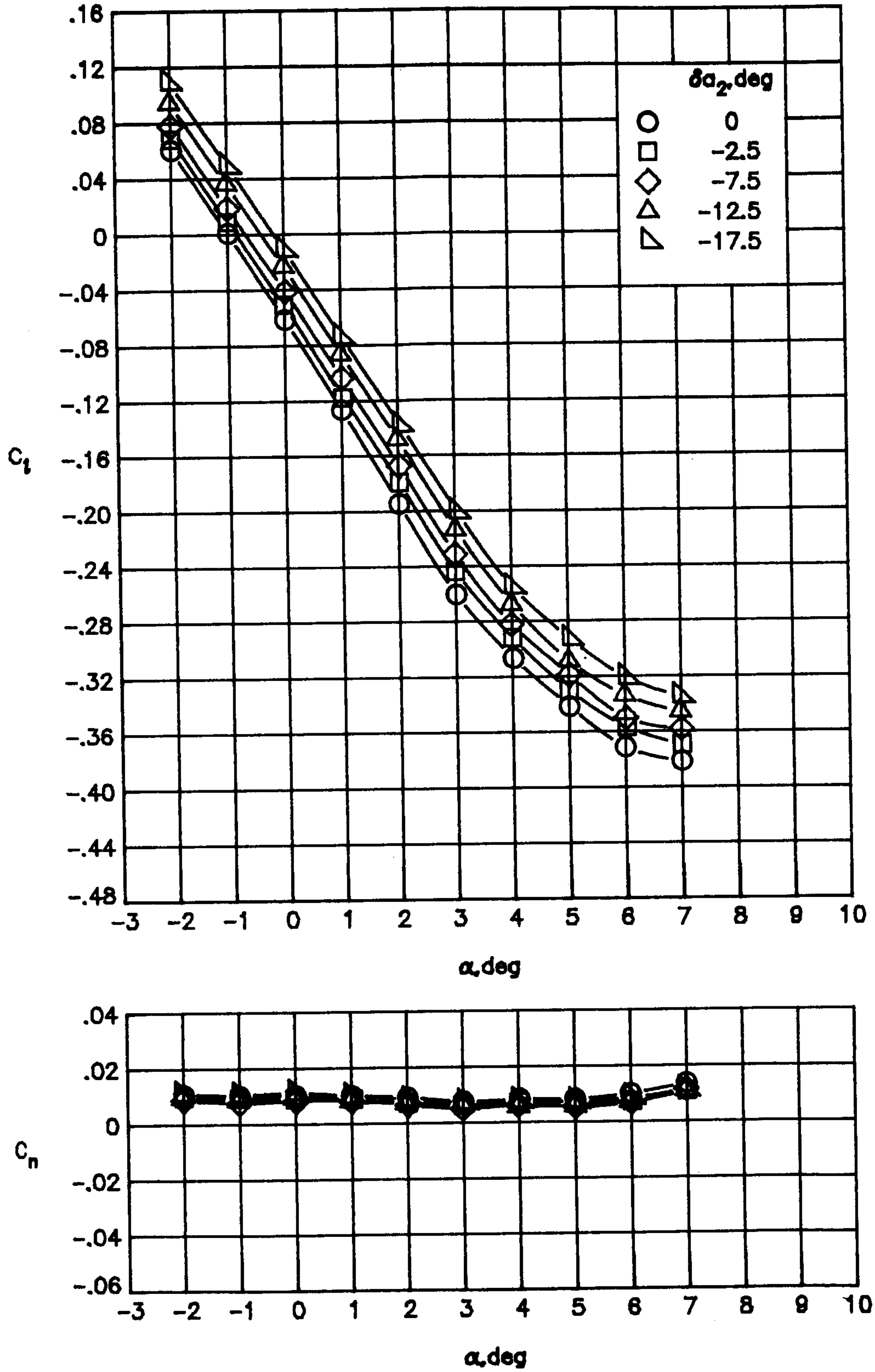

(e) $M_\infty = 0.84$.

Figure 39.- Continued.

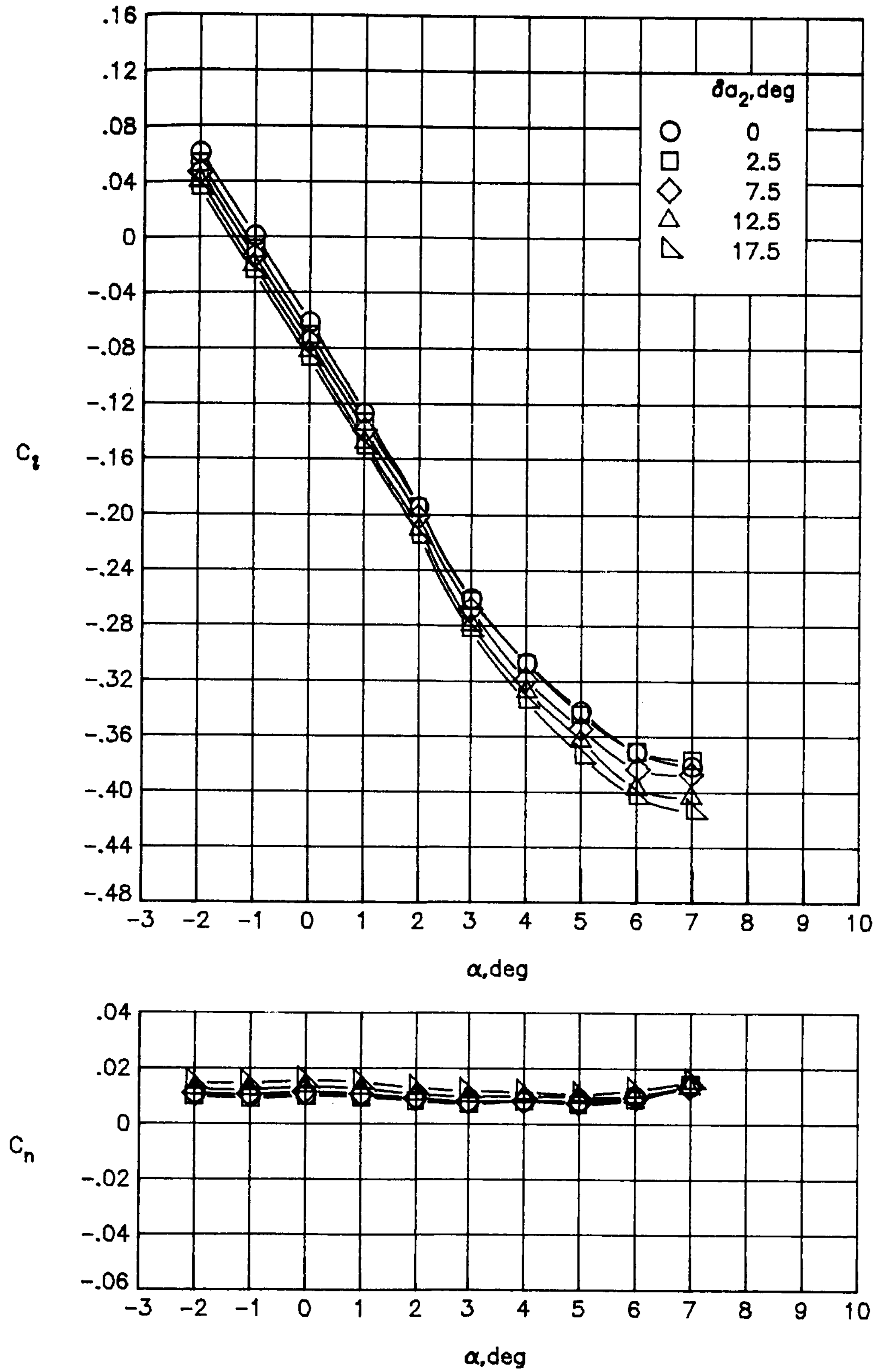

(e) Concluded.

Figure 39.- Continued.

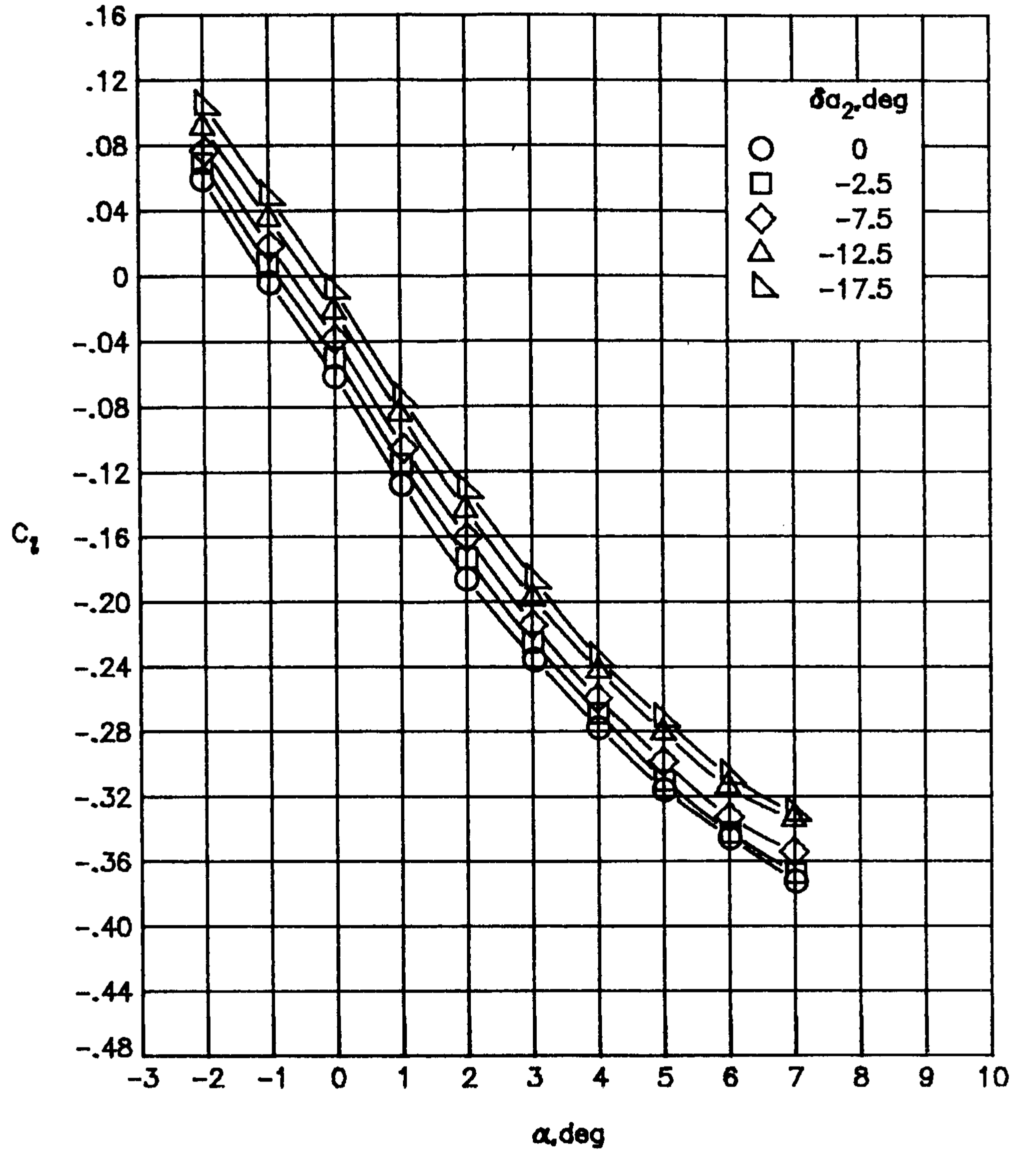

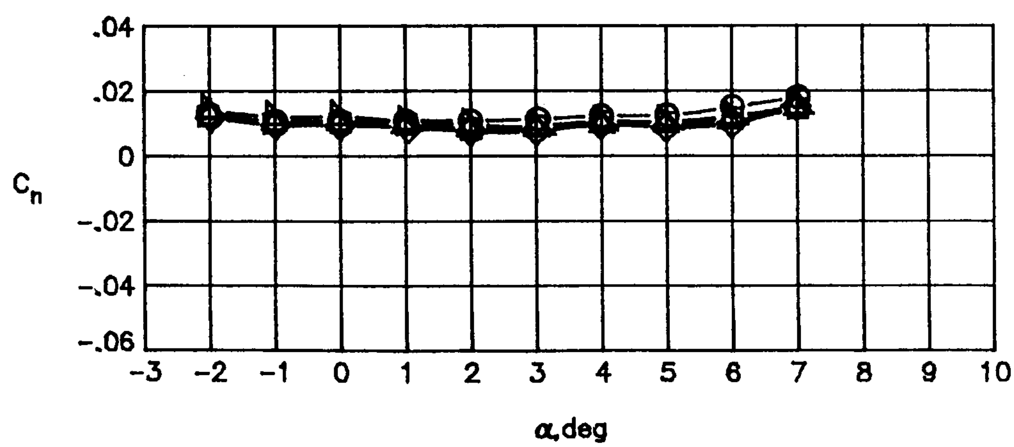

(f) $M_\infty = 0.86$.

Figure 39.- Continued.

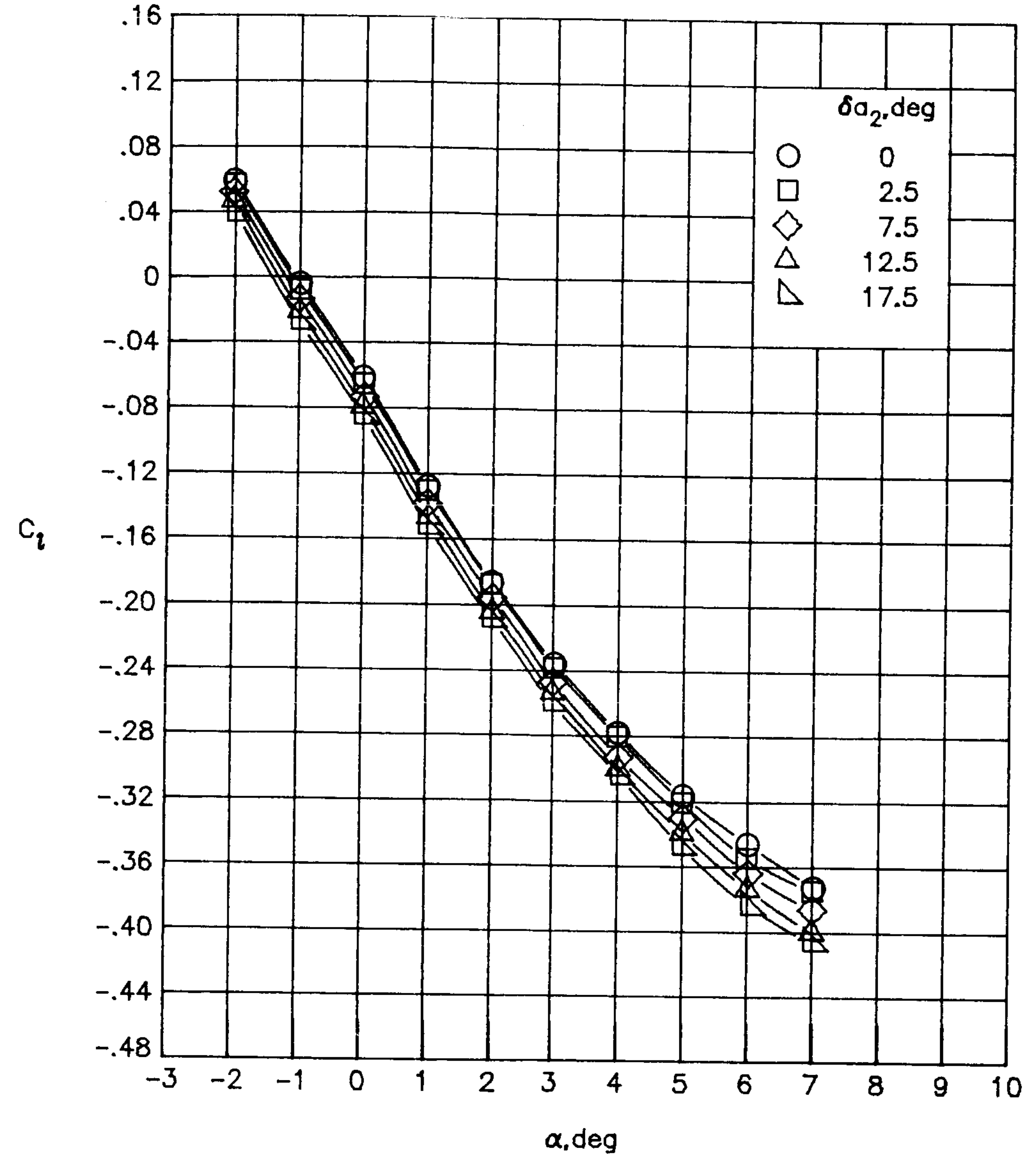

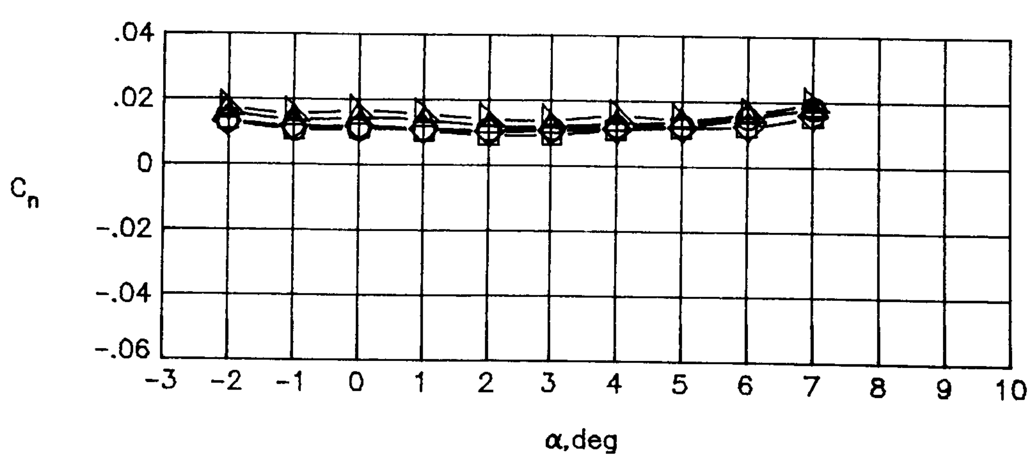

(f) Concluded.

Figure 39.- Continued.

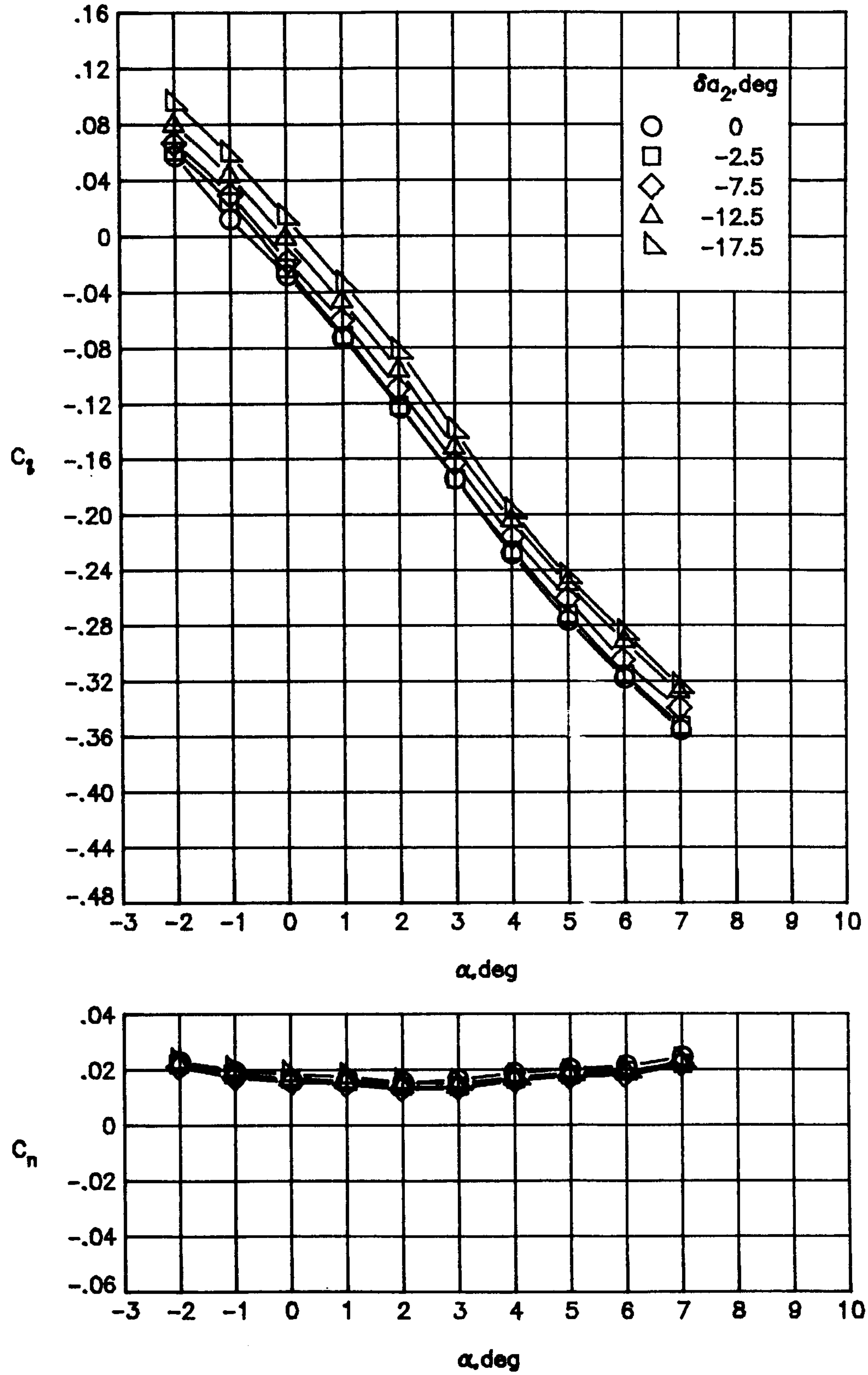

(g) $M_\infty = 0.90$.

Figure 39.- Continued.

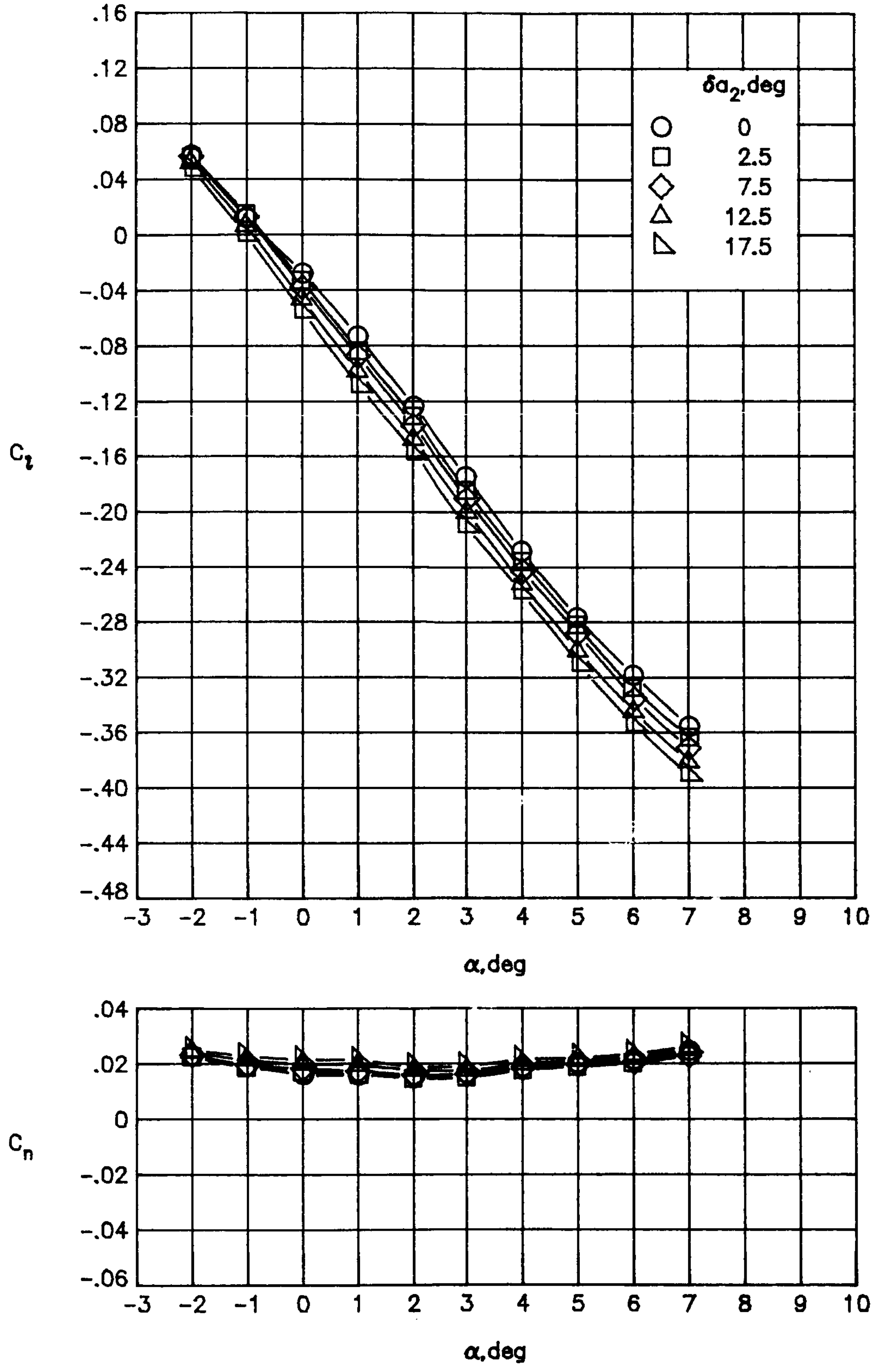

(g) Concluded.

Figure 39.- Concluded.

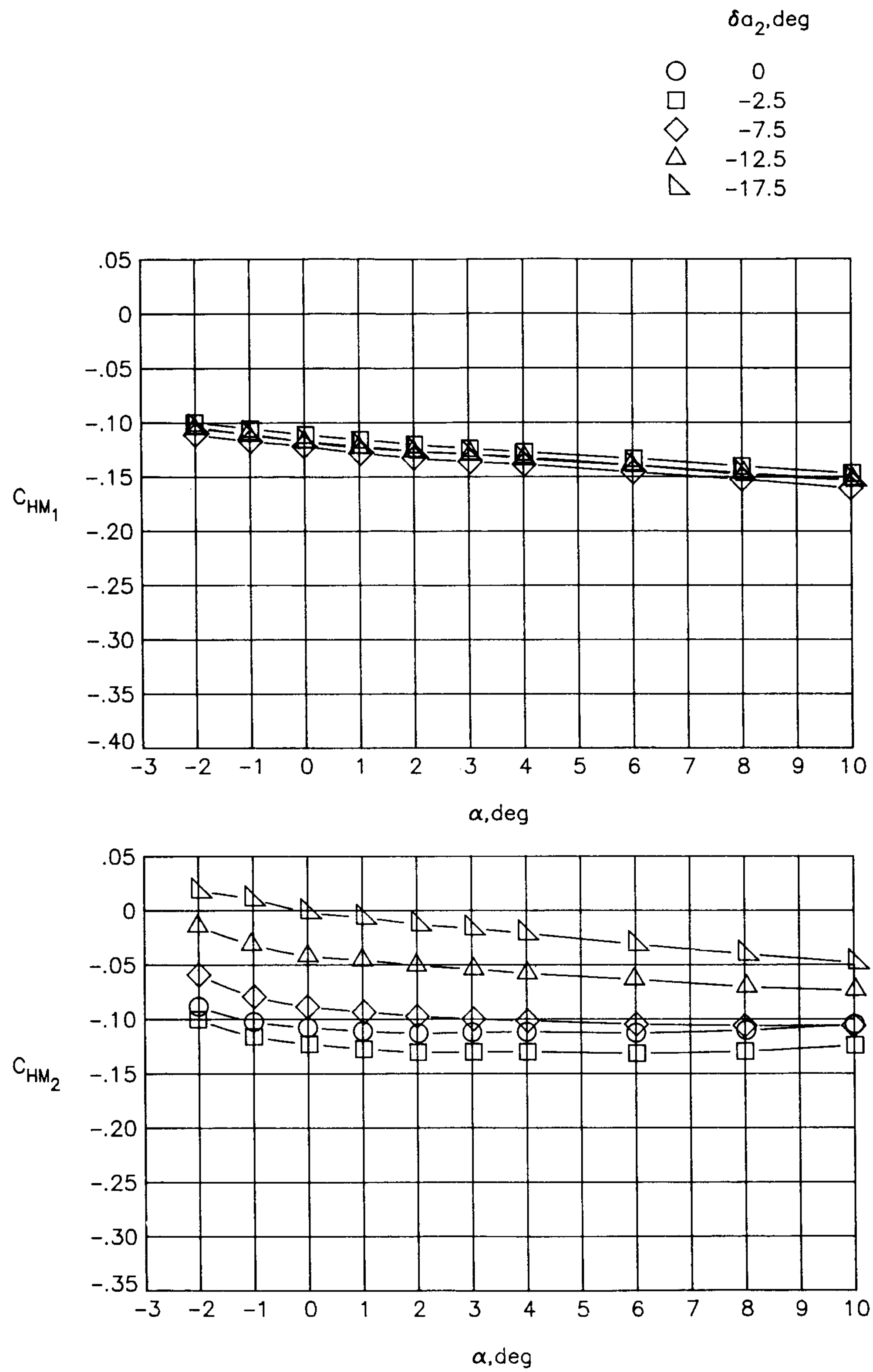

(a) $M_\infty = 0.30$.

Figure 40.- Variations of hinge-moment coefficients with angle of attack for deflections of a_2. $\delta a_1 = 0°$.

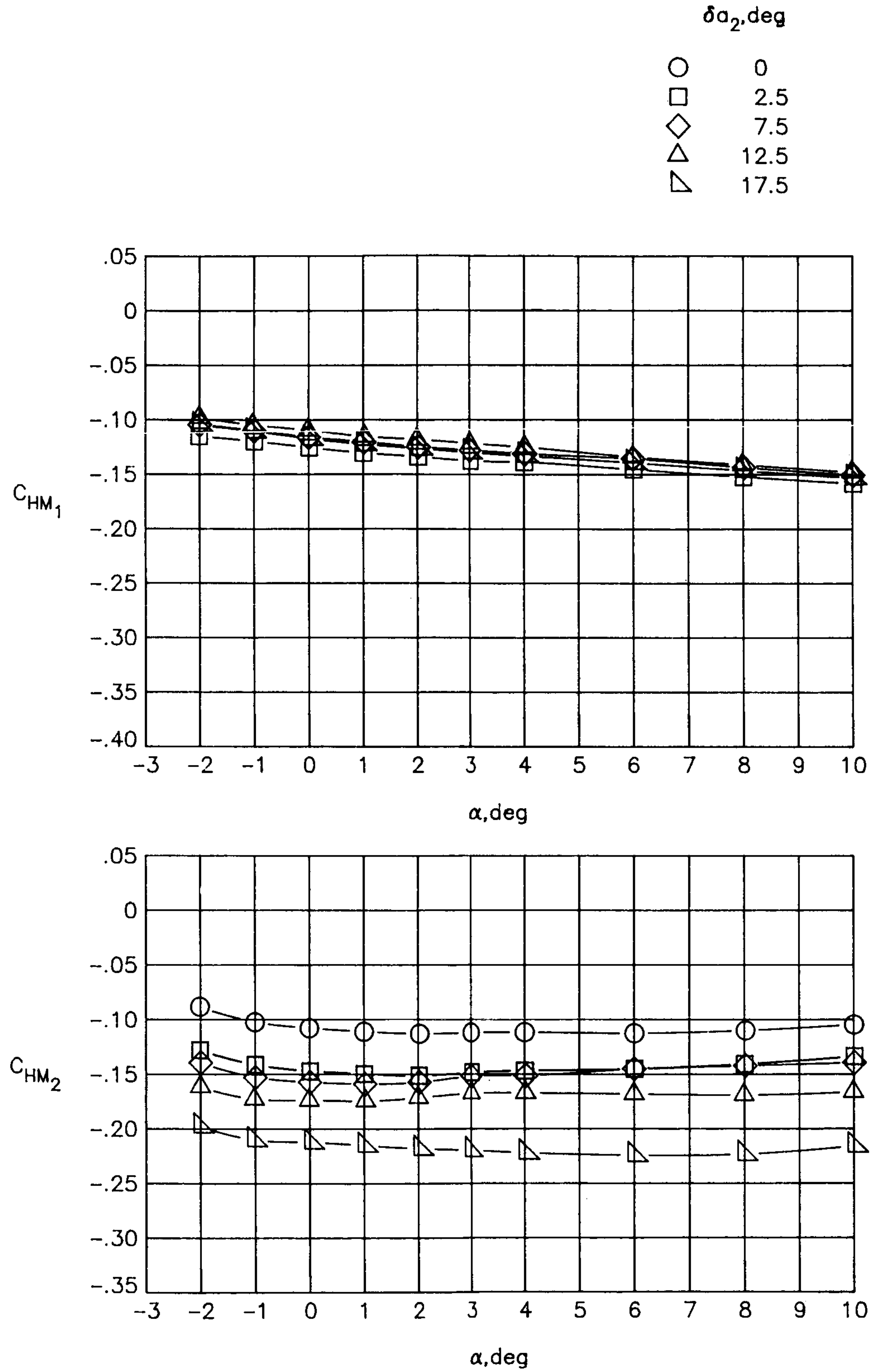

(a) Concluded.

Figure 40.- Continued.

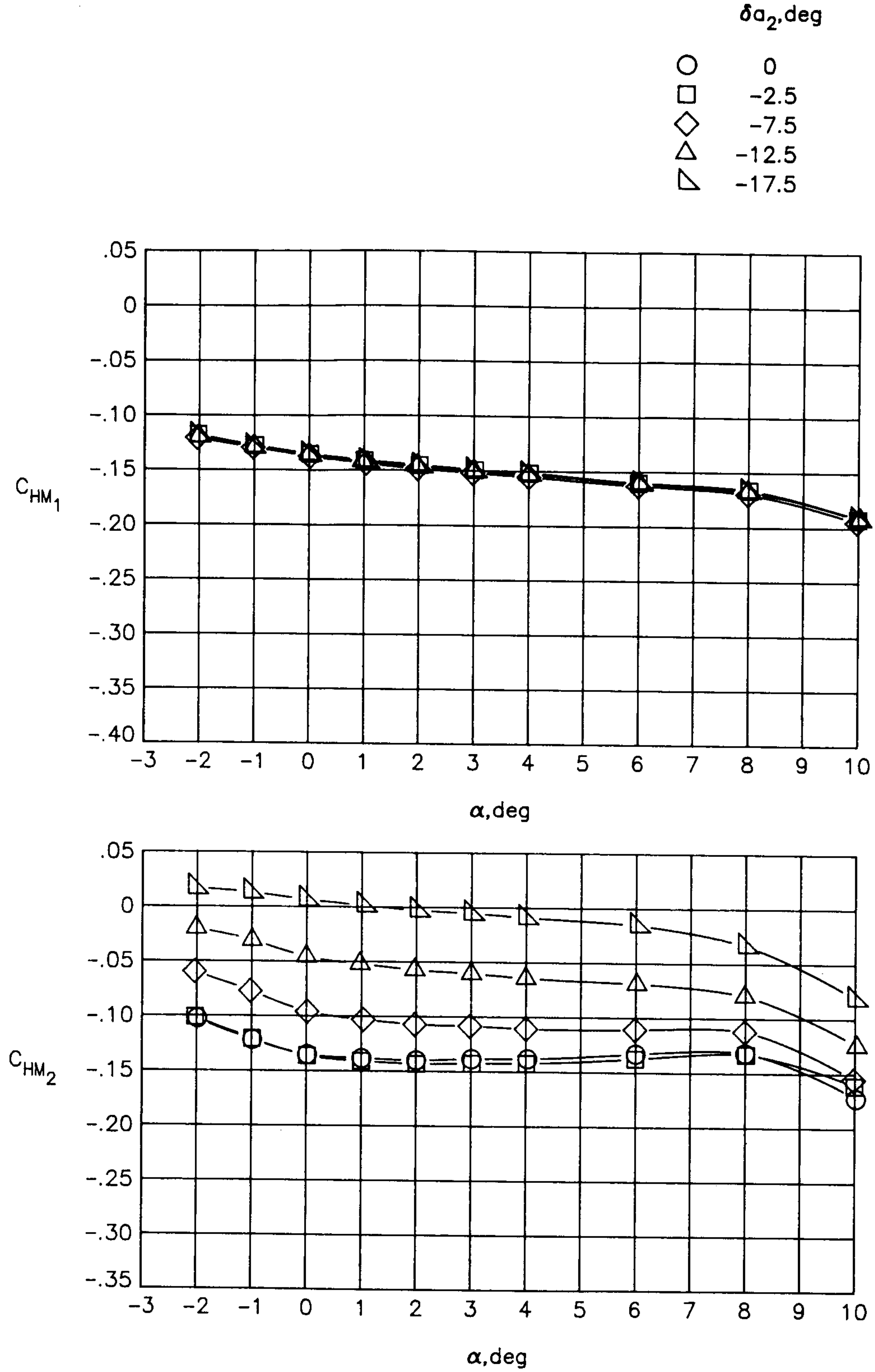

(b) $M_\infty = 0.60$.

Figure 40.- Continued.

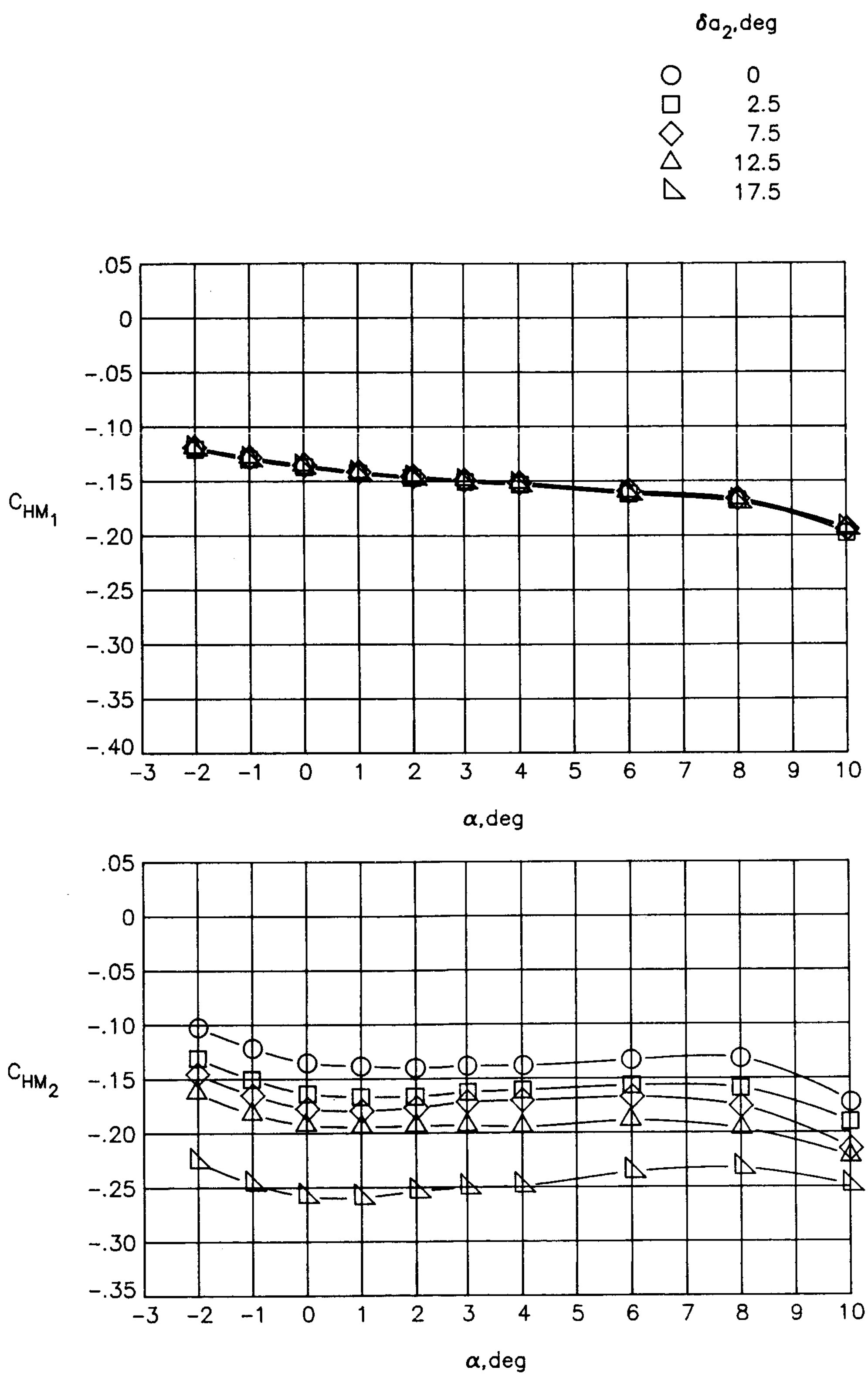

(b) Concluded.

Figure 40.- Continued.

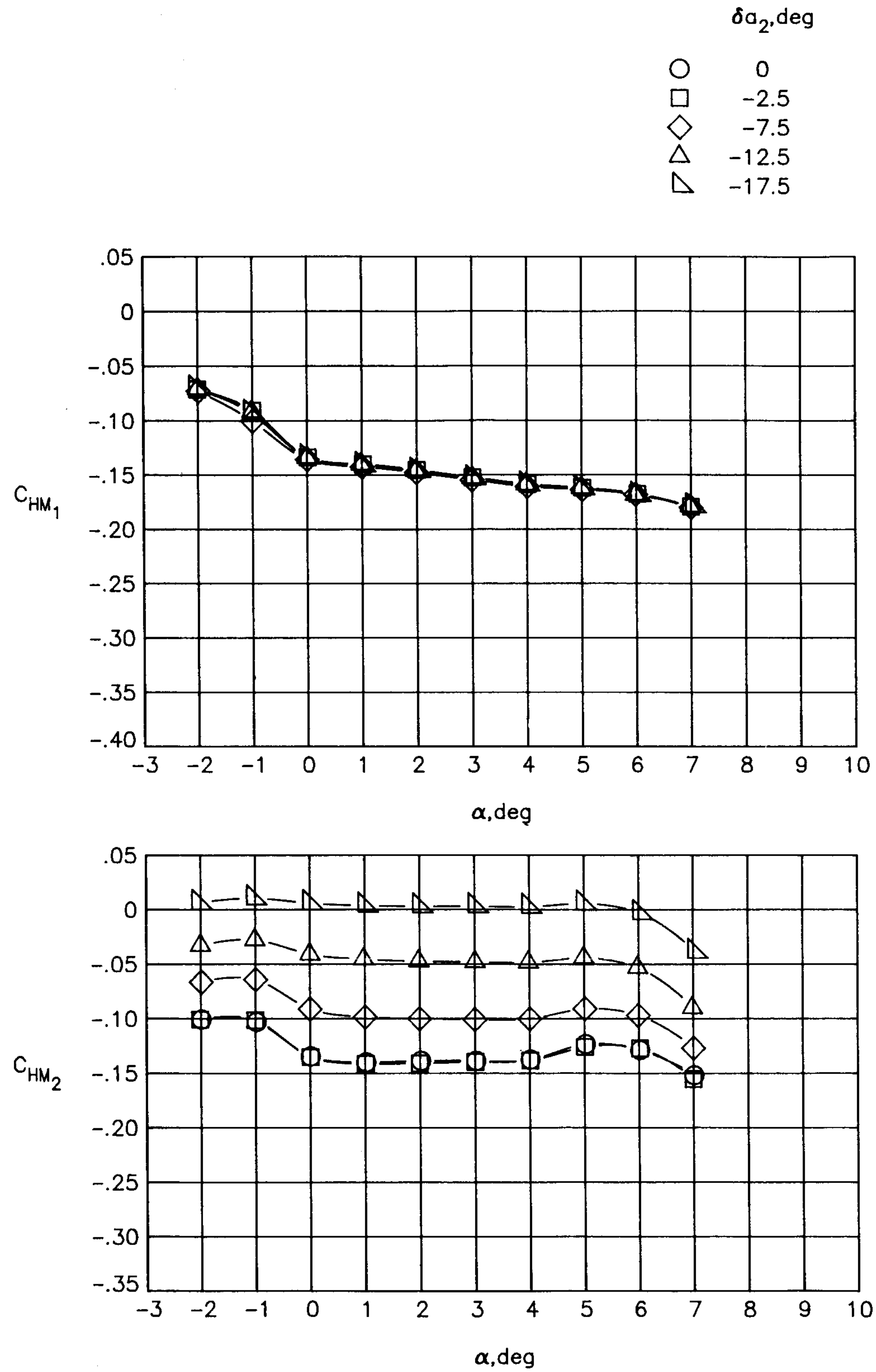

(c) $M_\infty = 0.80.$

Figure 40.- Continued.

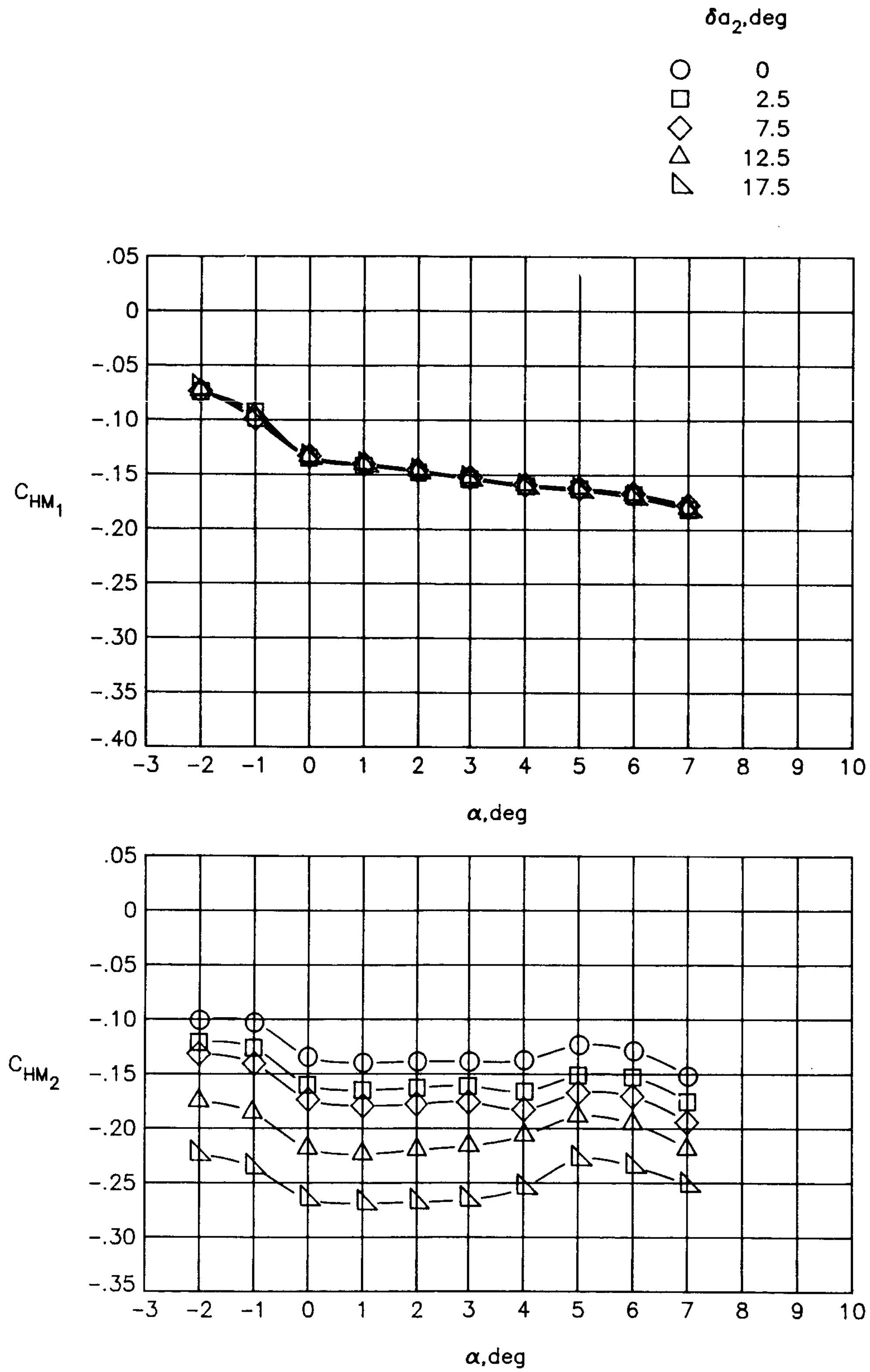

(c) Concluded.

Figure 40.- Continued.

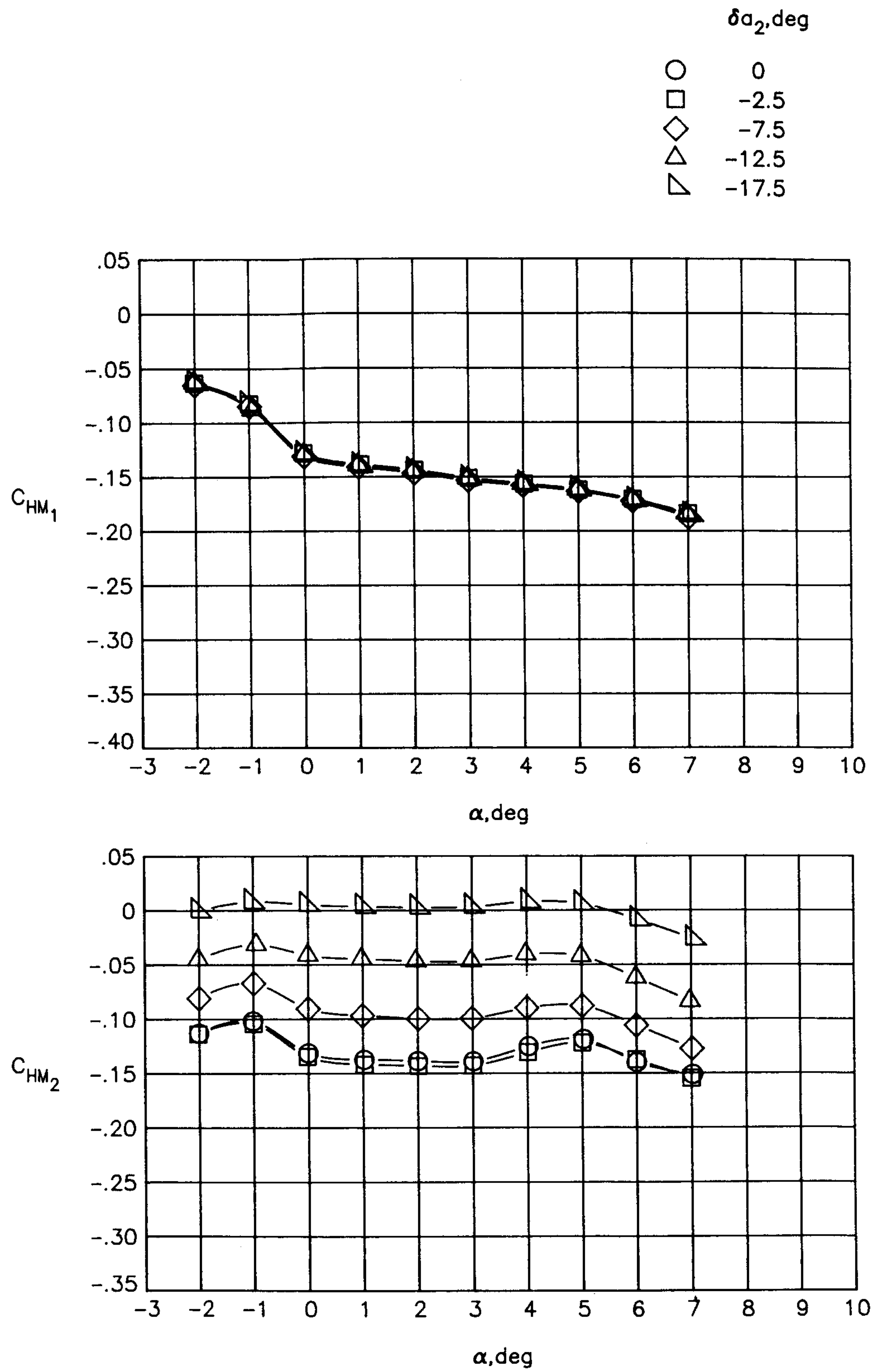

(d) $M_\infty = 0.82$.

Figure 40.- Continued.

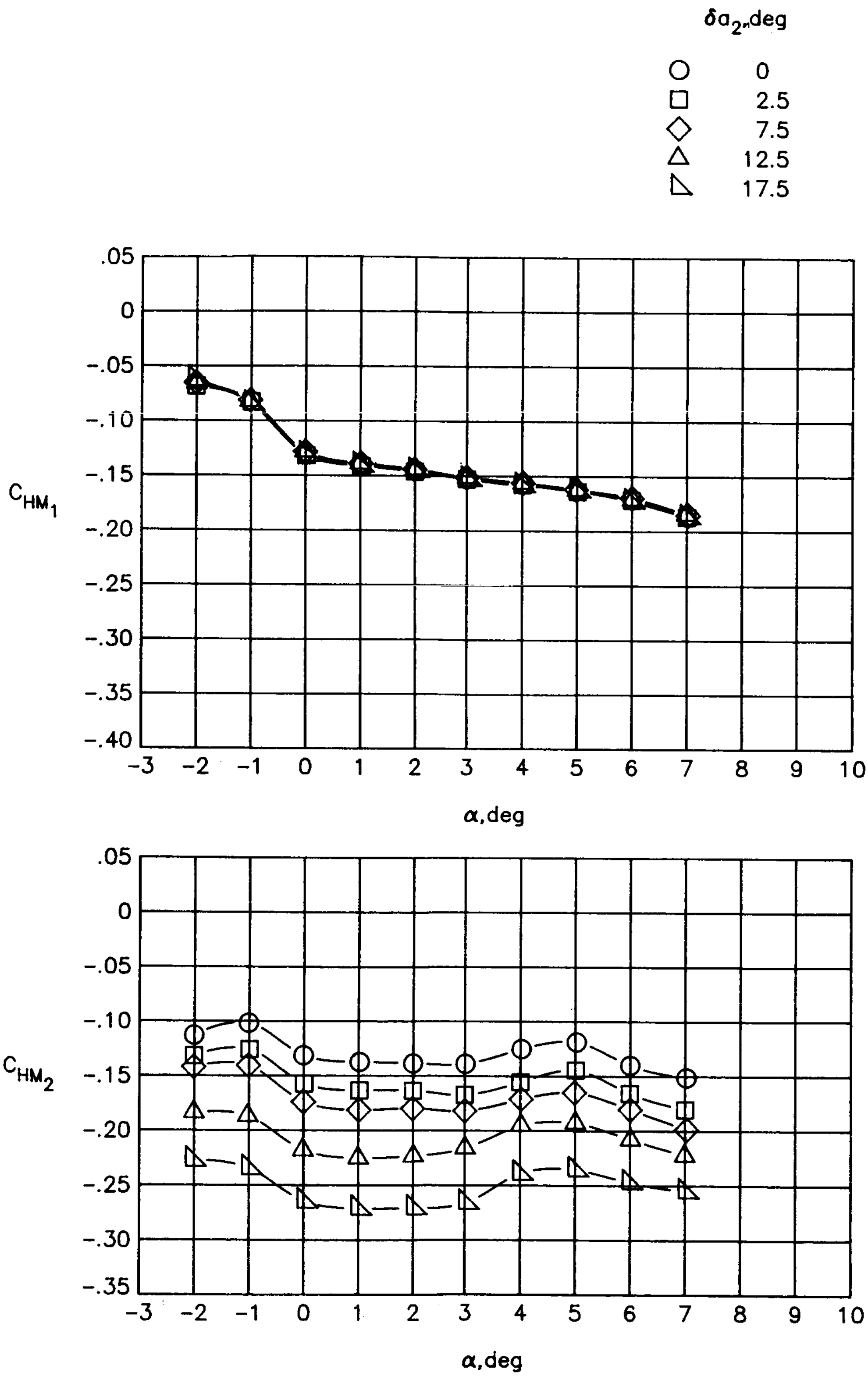

(d) Concluded.

Figure 40.- Continued.

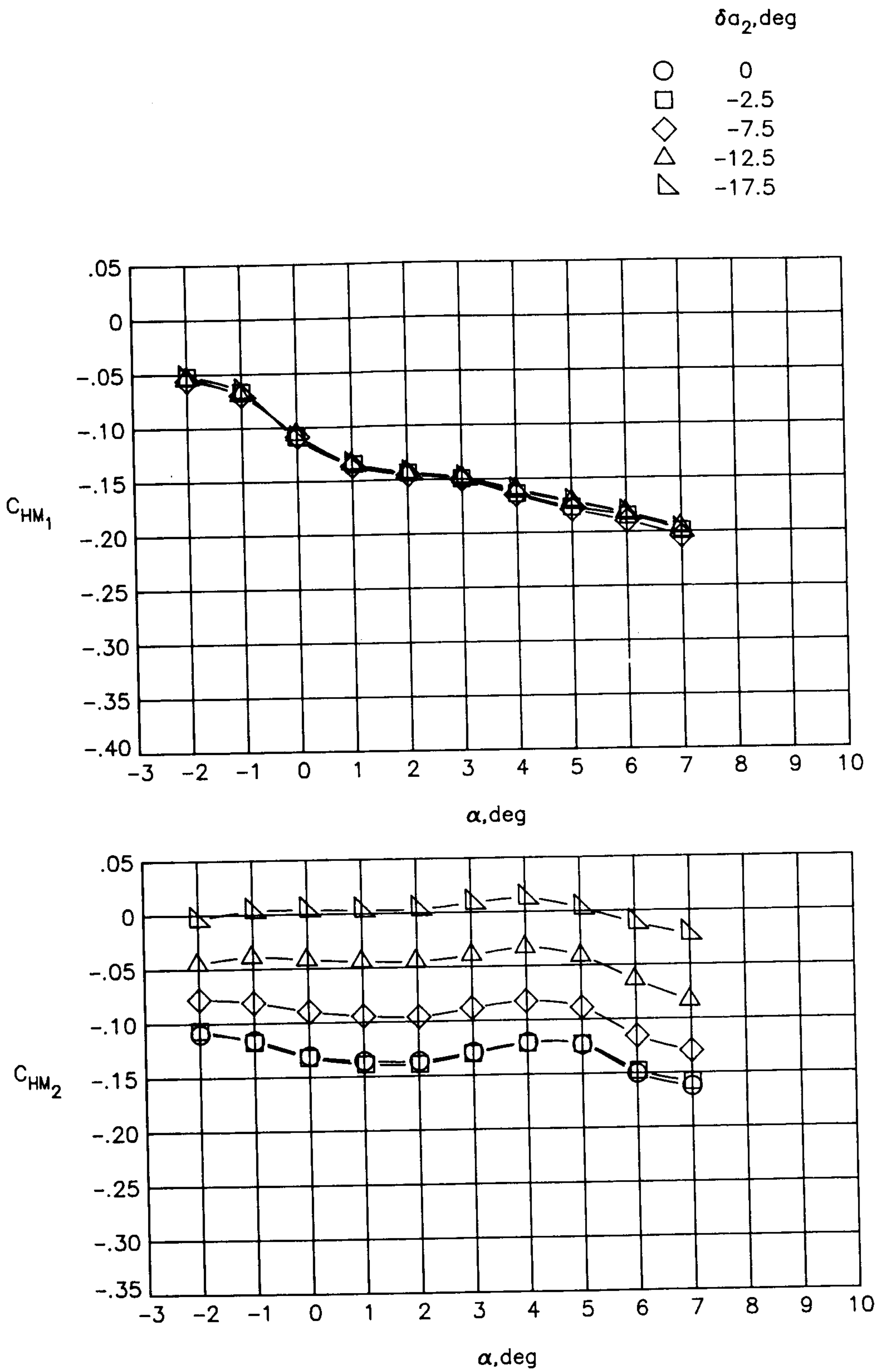

(e) $M_\infty = 0.84$.

Figure 40.- Continued.

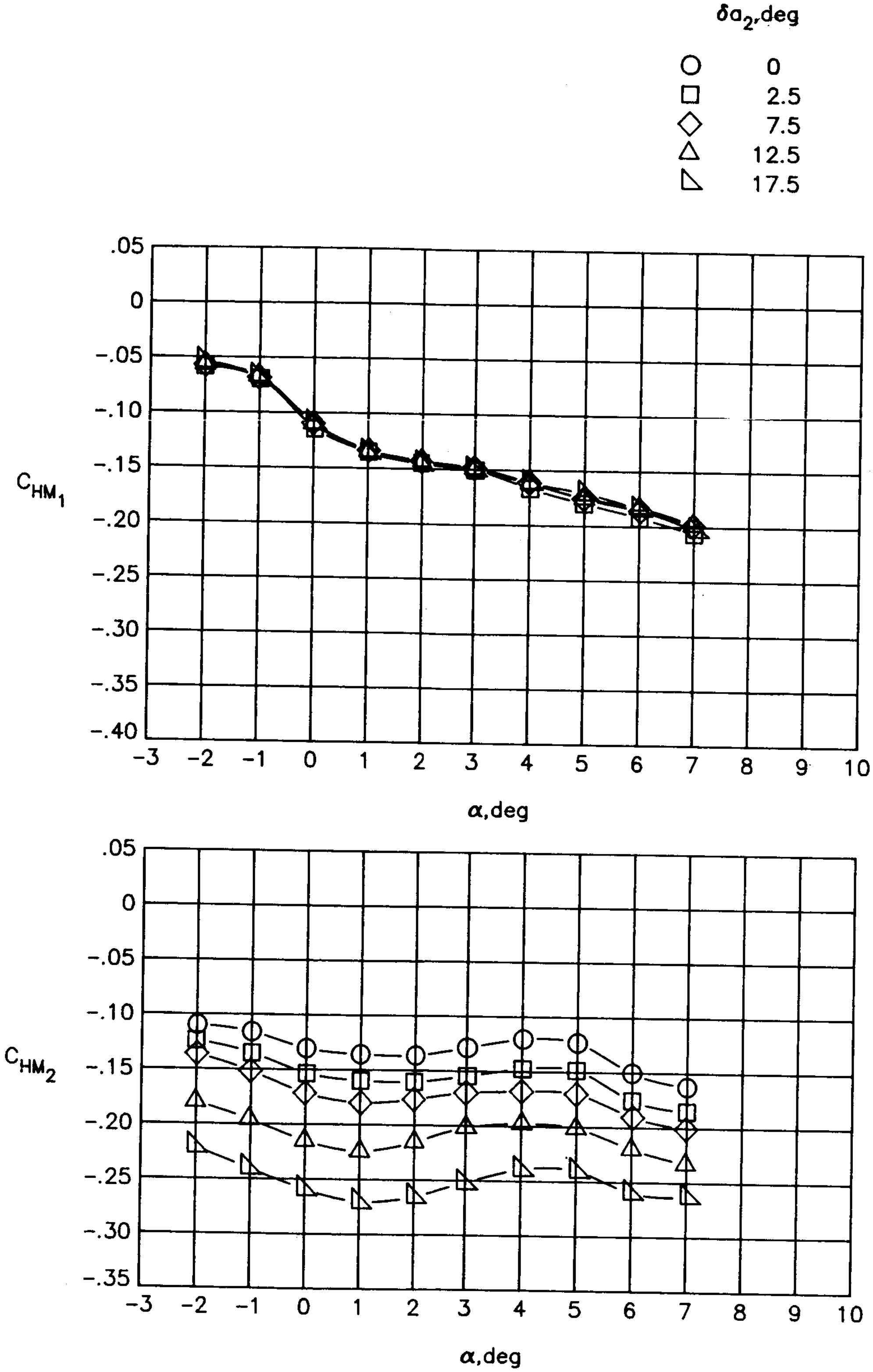

(e) Concluded.

Figure 40.- Continued.

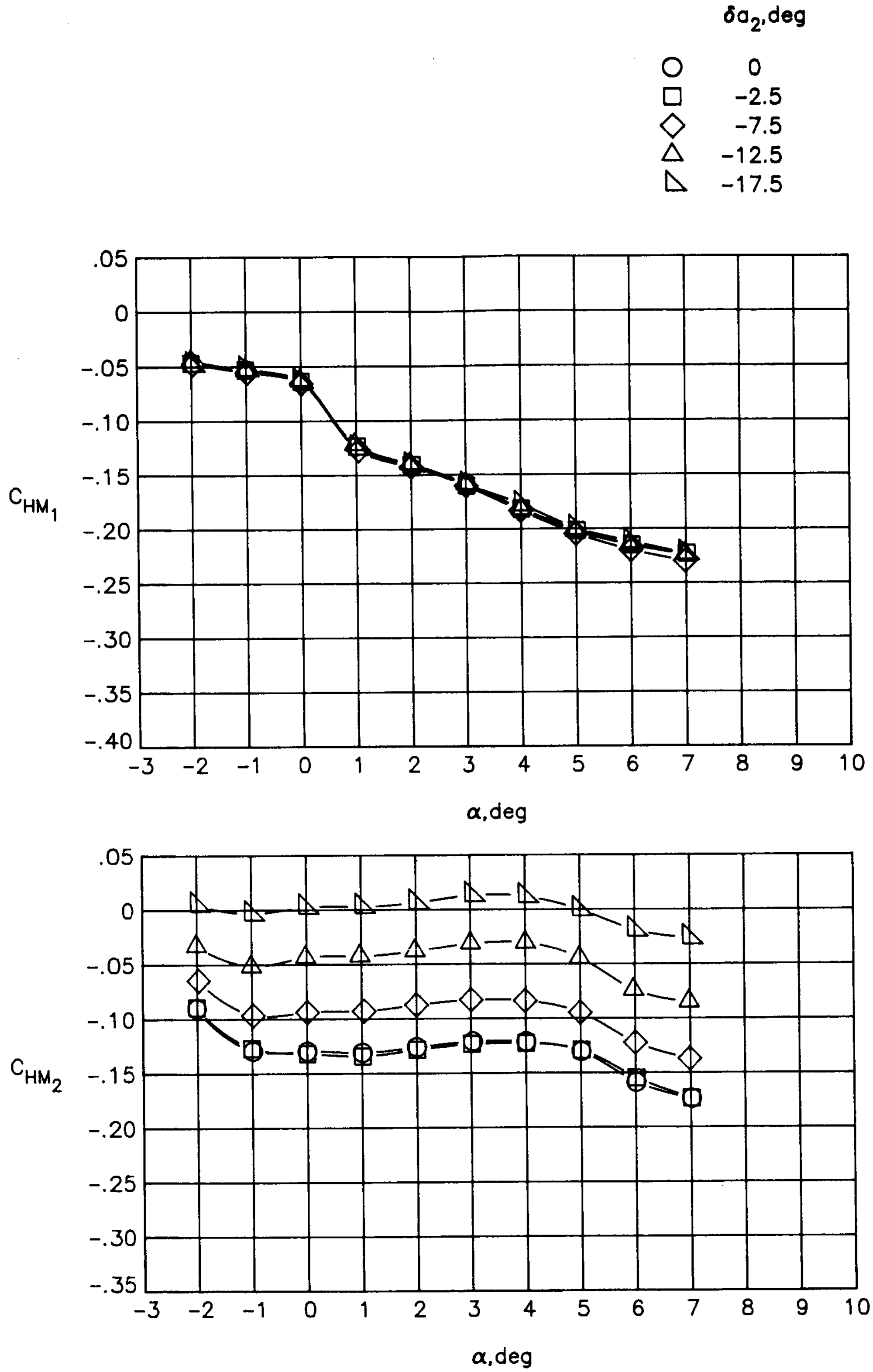

(f) $M_\infty = 0.86$.

Figure 40.- Continued.

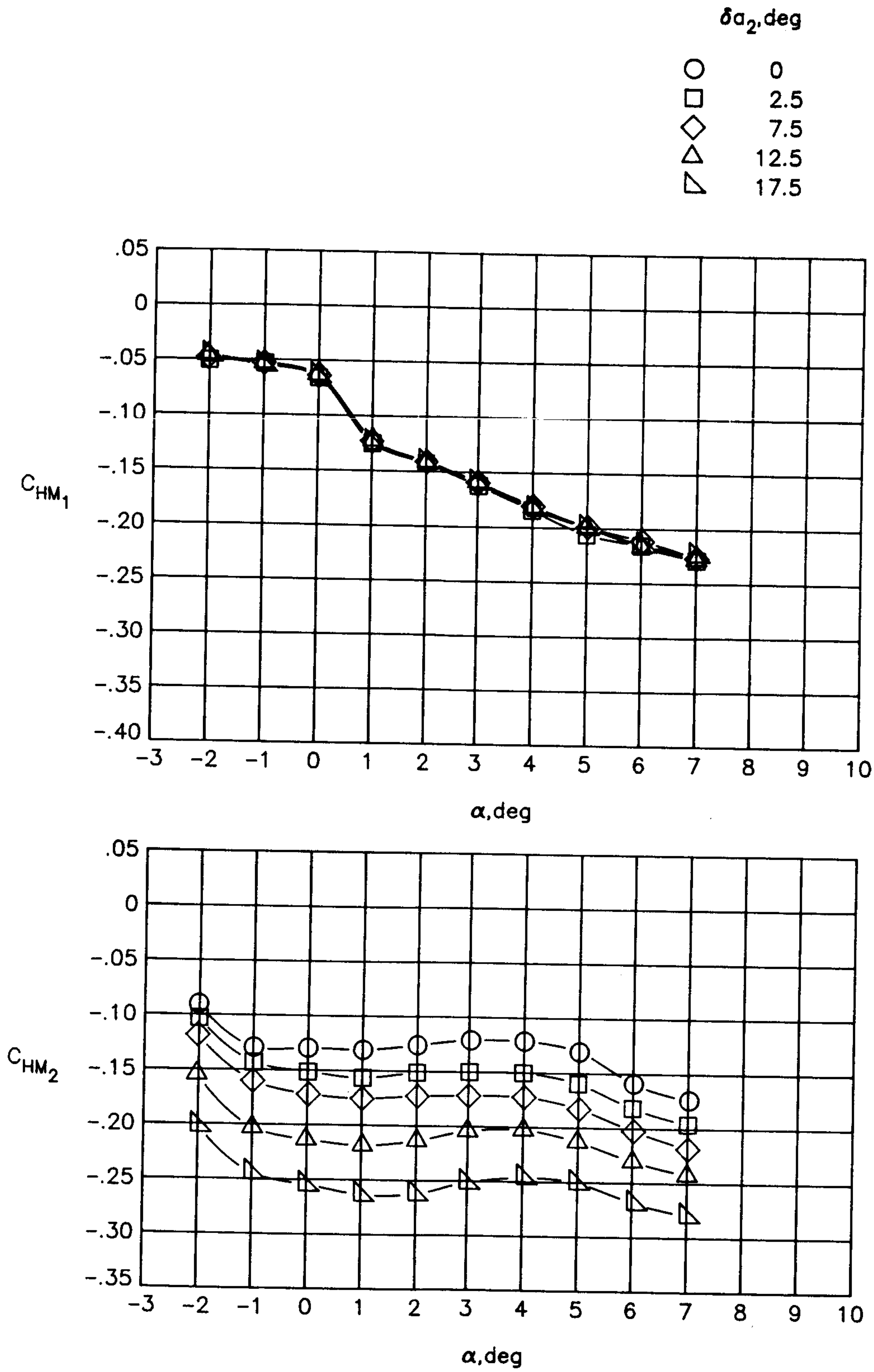

(f) Concluded.

Figure 40.- Continued.

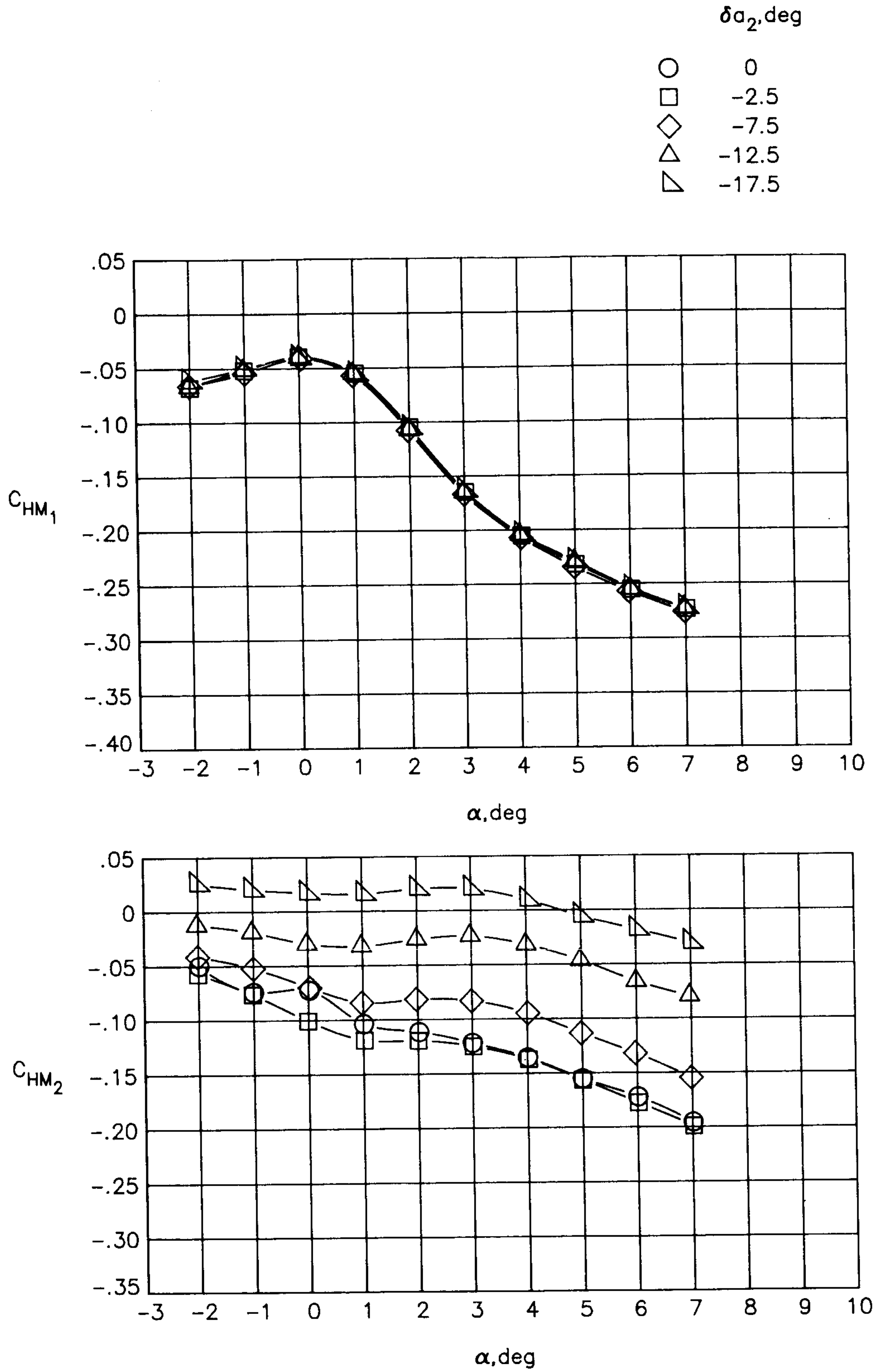

(g) M_∞ = 0.90.

Figure 40.- Continued.

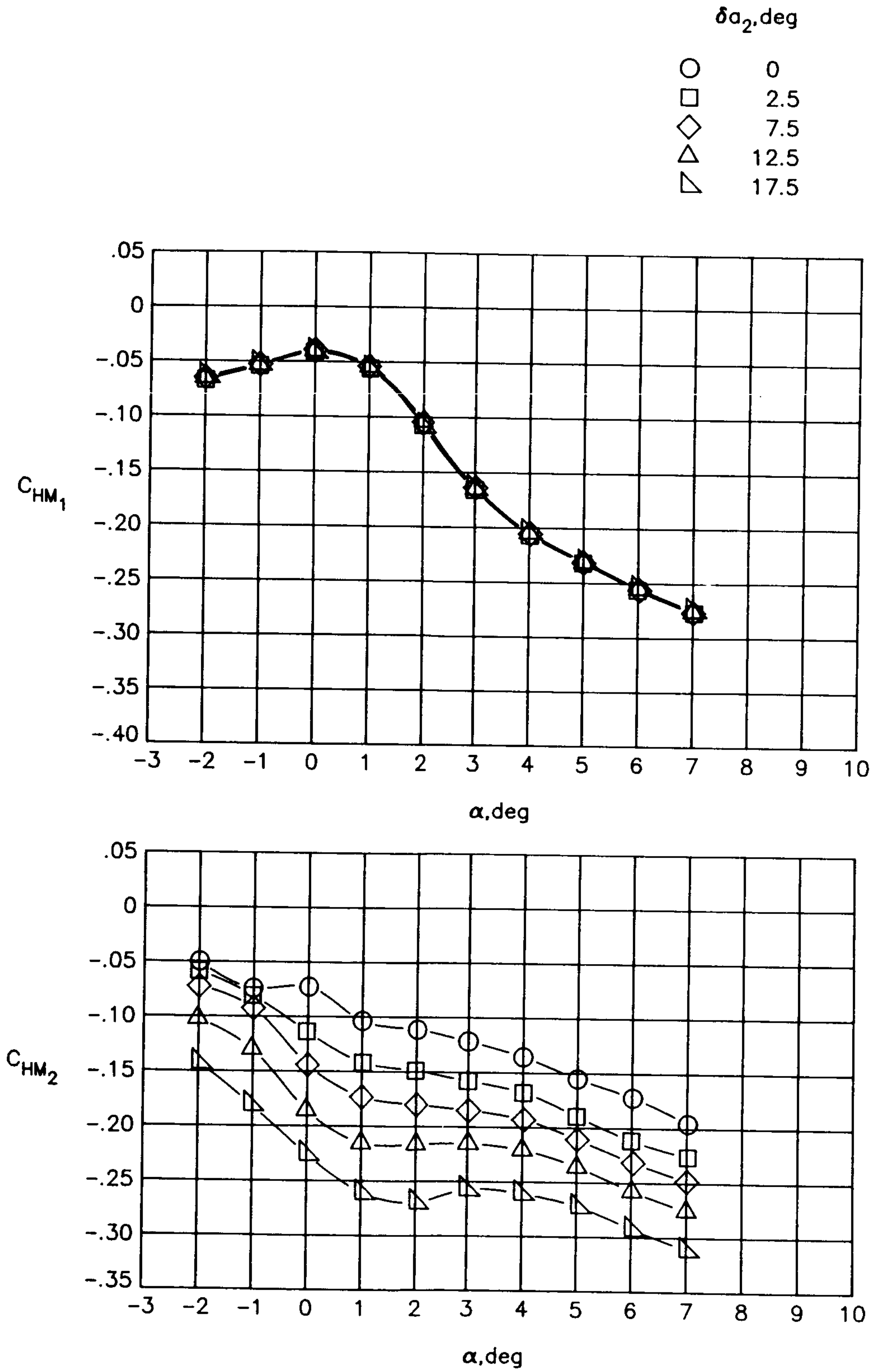

(g) Concluded.

Figure 40.- Concluded.

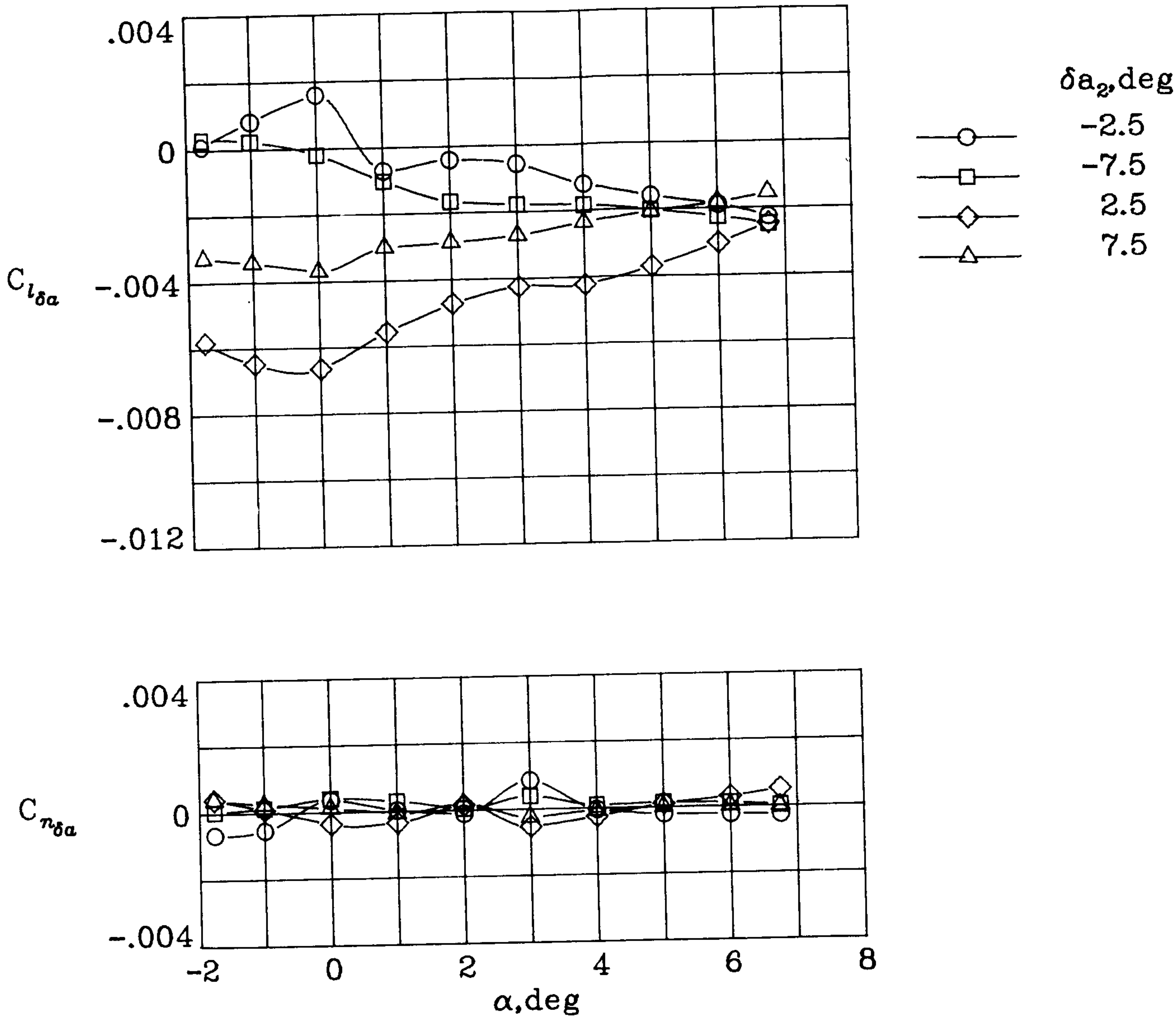

(a) M_∞ = 0.30.

Figure 41.- Variation of aileron-effectiveness parameters with angle of attack for deflections of a_2. δa_1 = 0°.

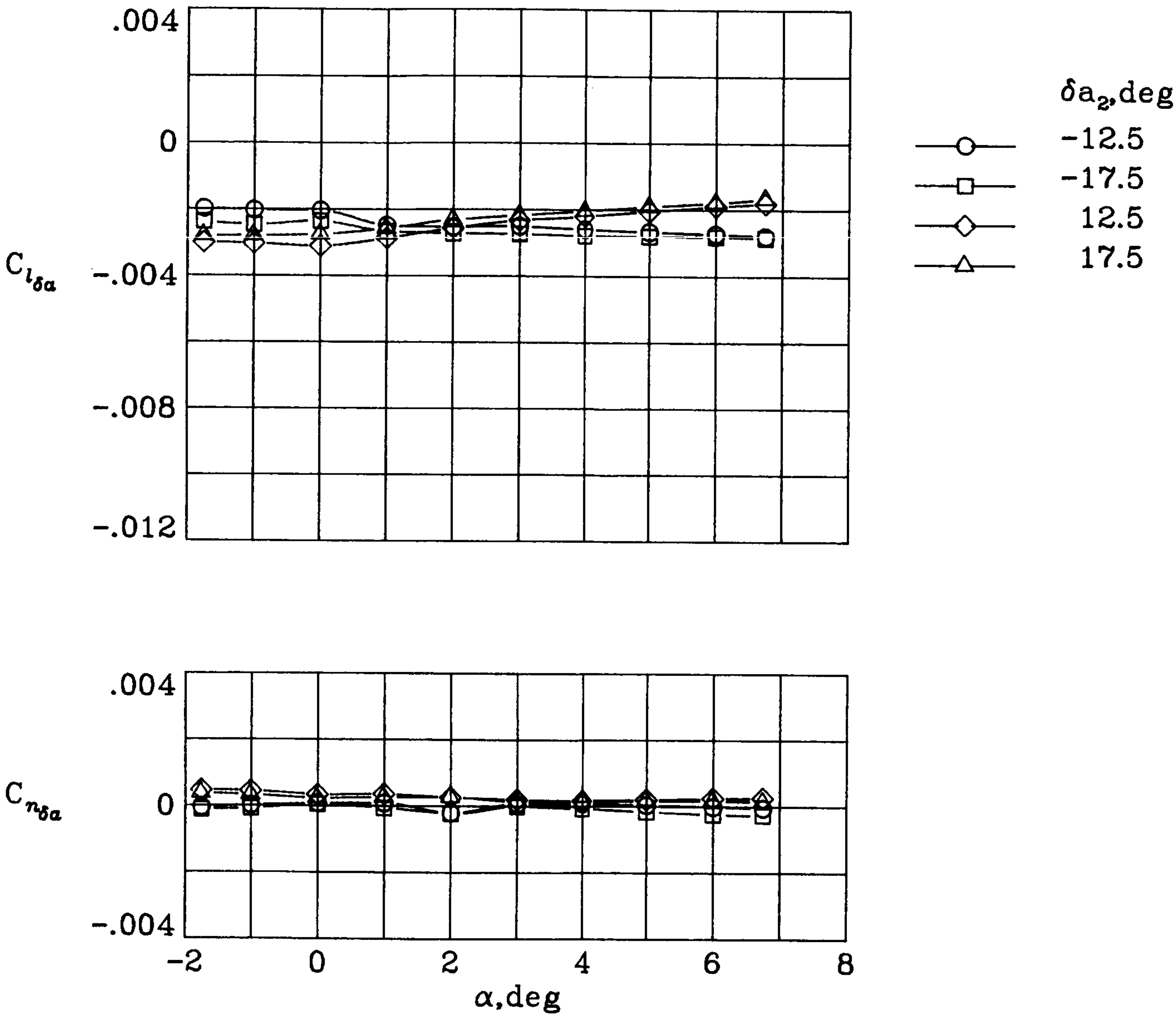

(a) Concluded.

Figure 41.- Continued.

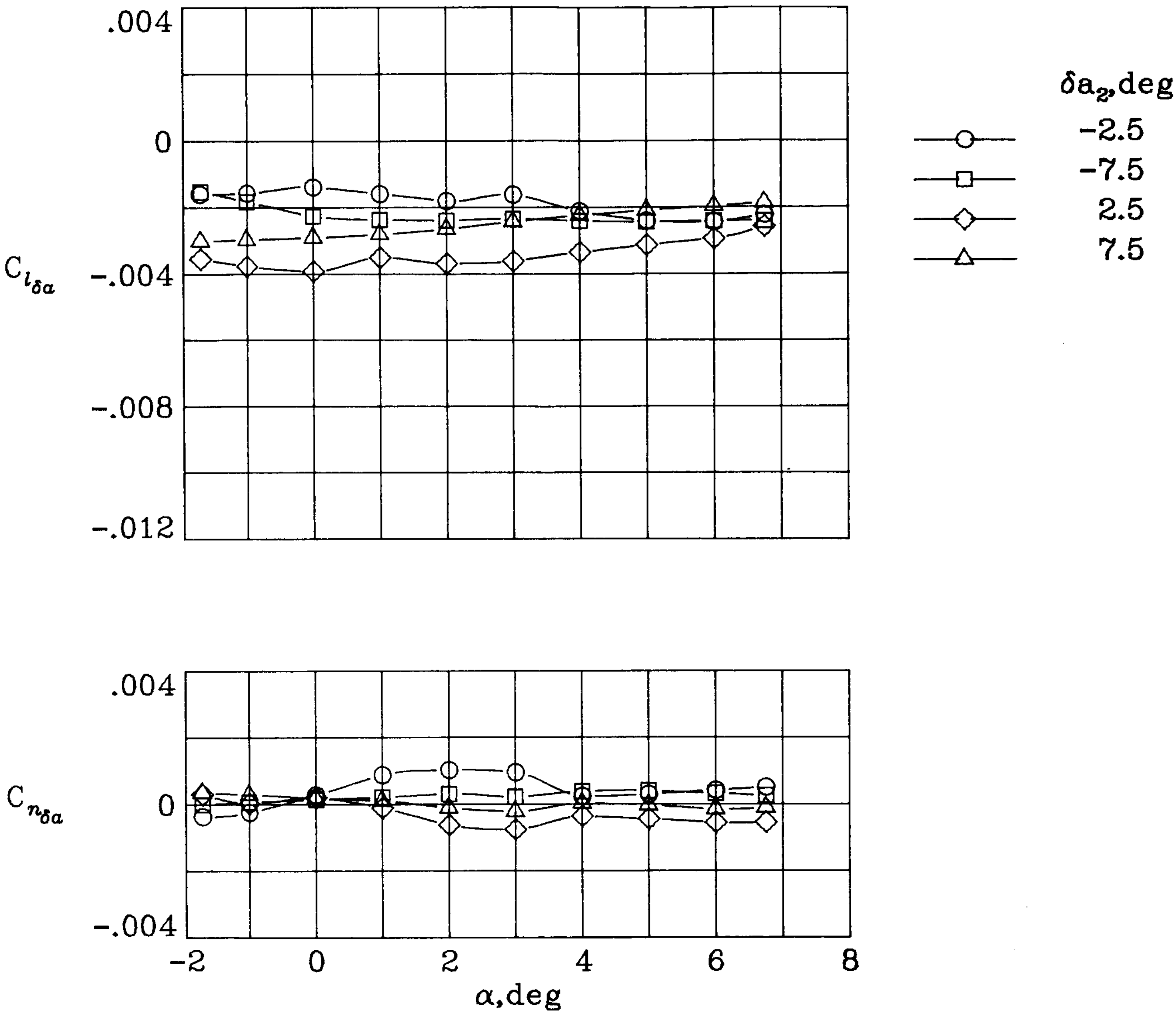

(b) M_∞ = 0.60.

Figure 41.- Continued.

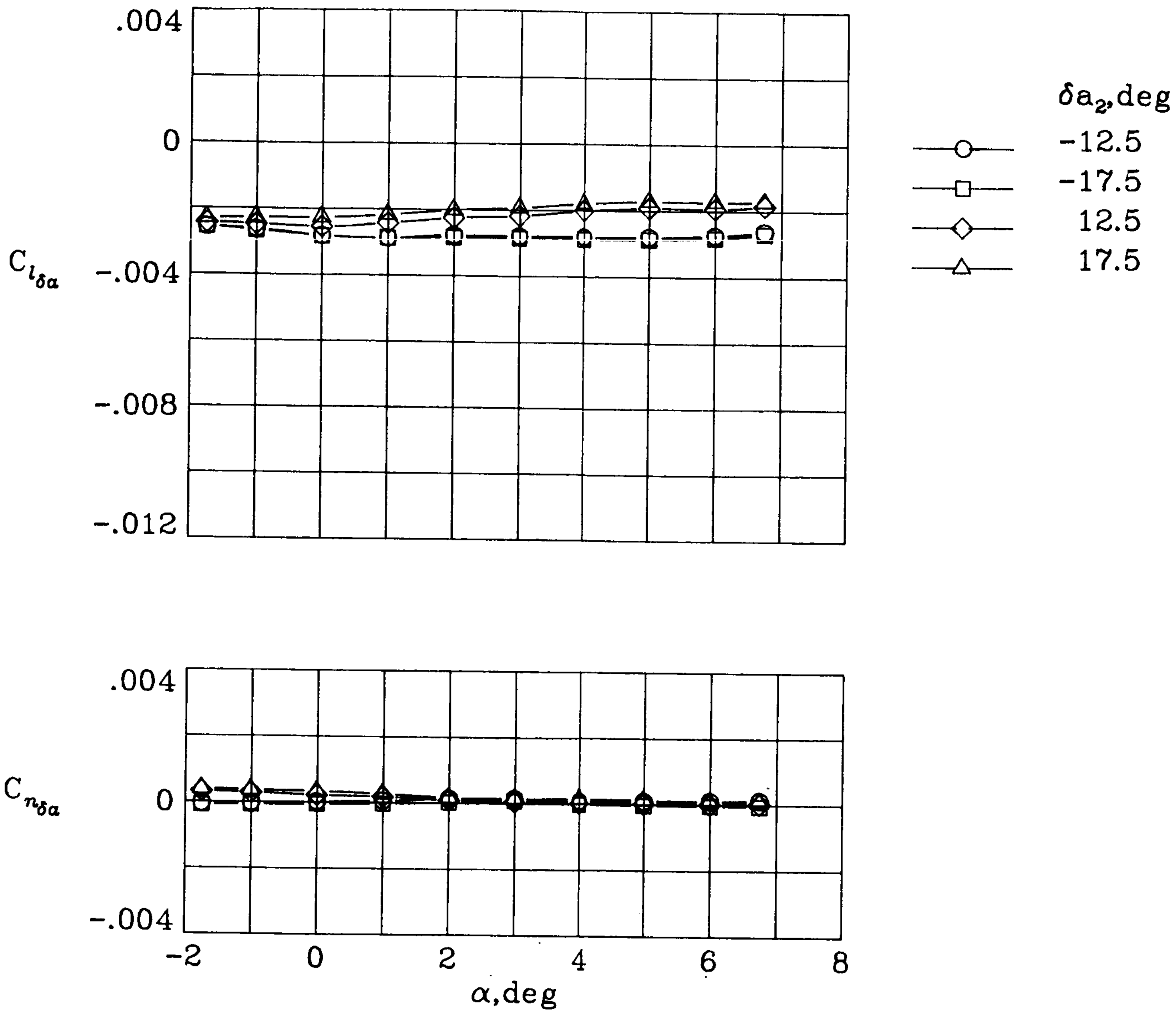

(b) Concluded.

Figure 41.- Continued.

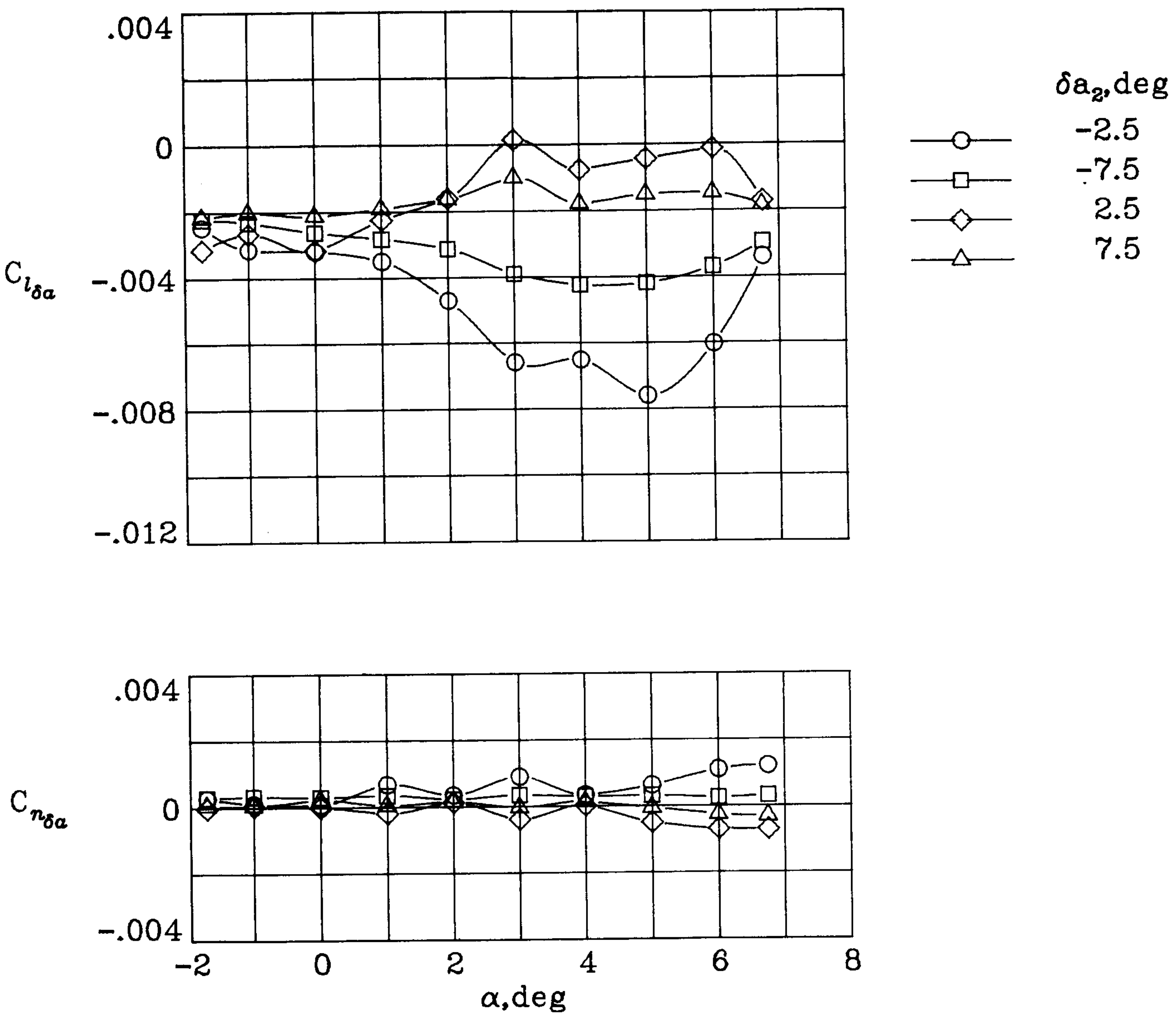

(c) $M_\infty = 0.80$.

Figure 41.- Continued.

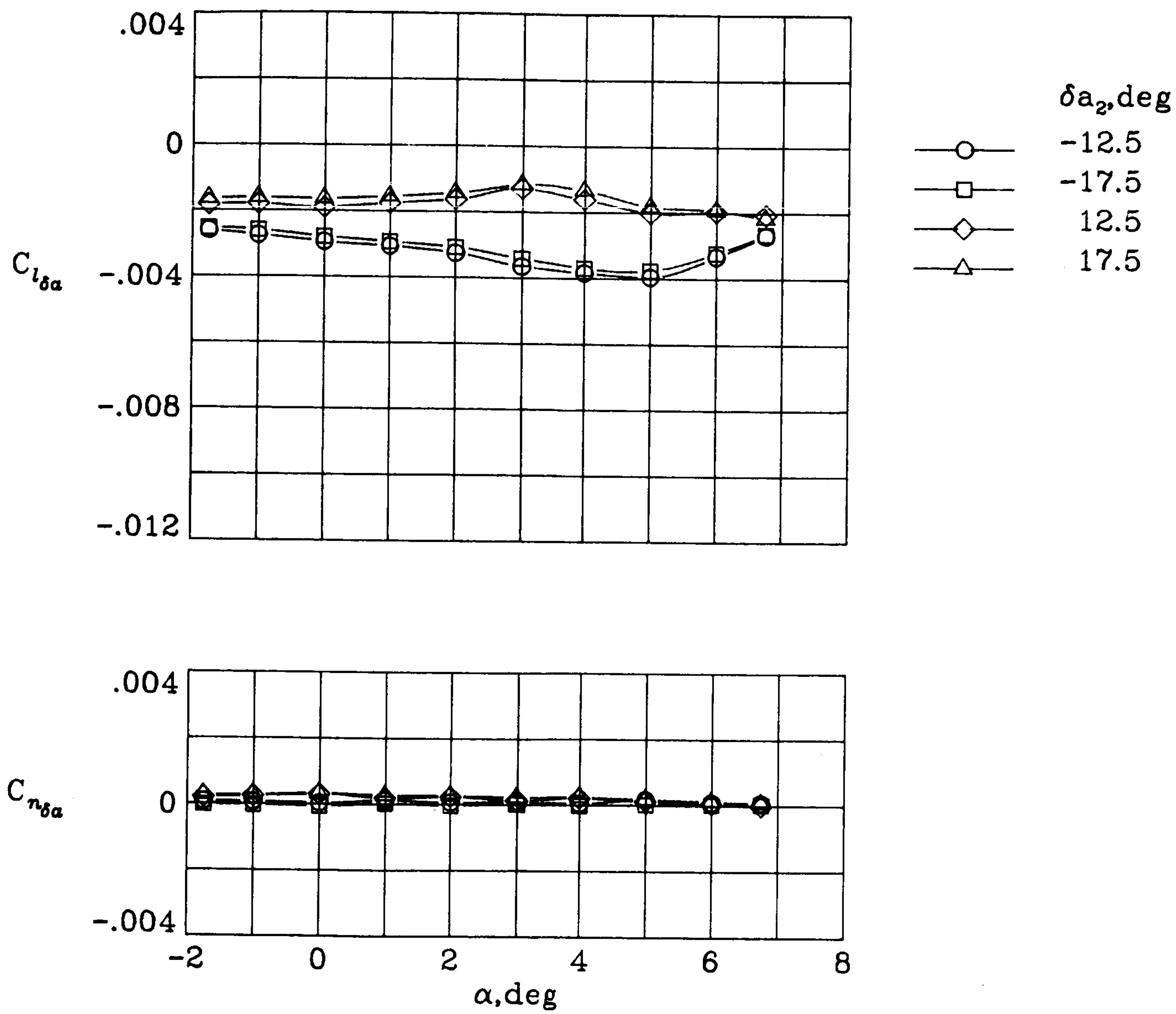

(c) Concluded.

Figure 41.- Continued.

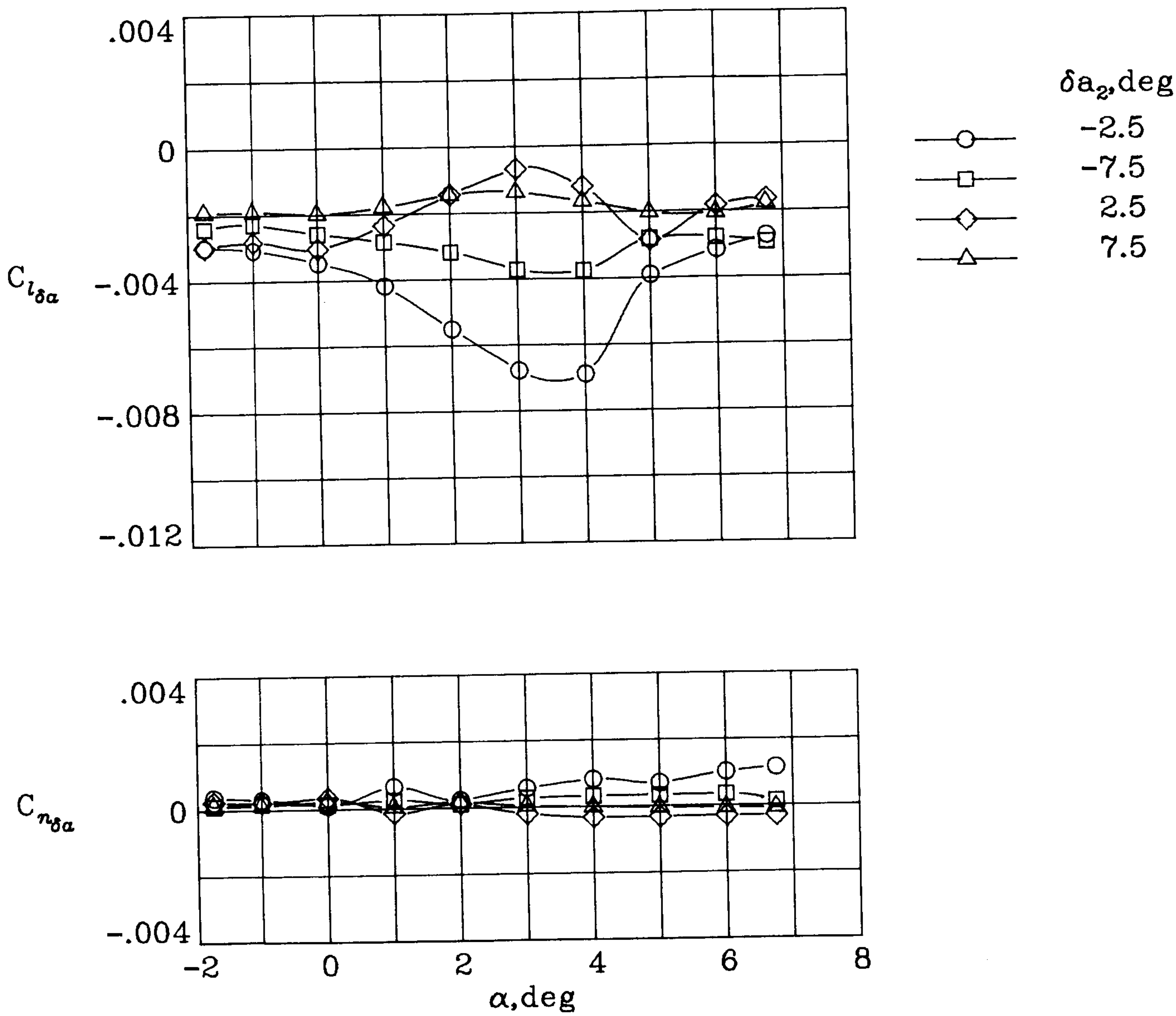

(d) $M_\infty = 0.82$.

Figure 41.- Continued.

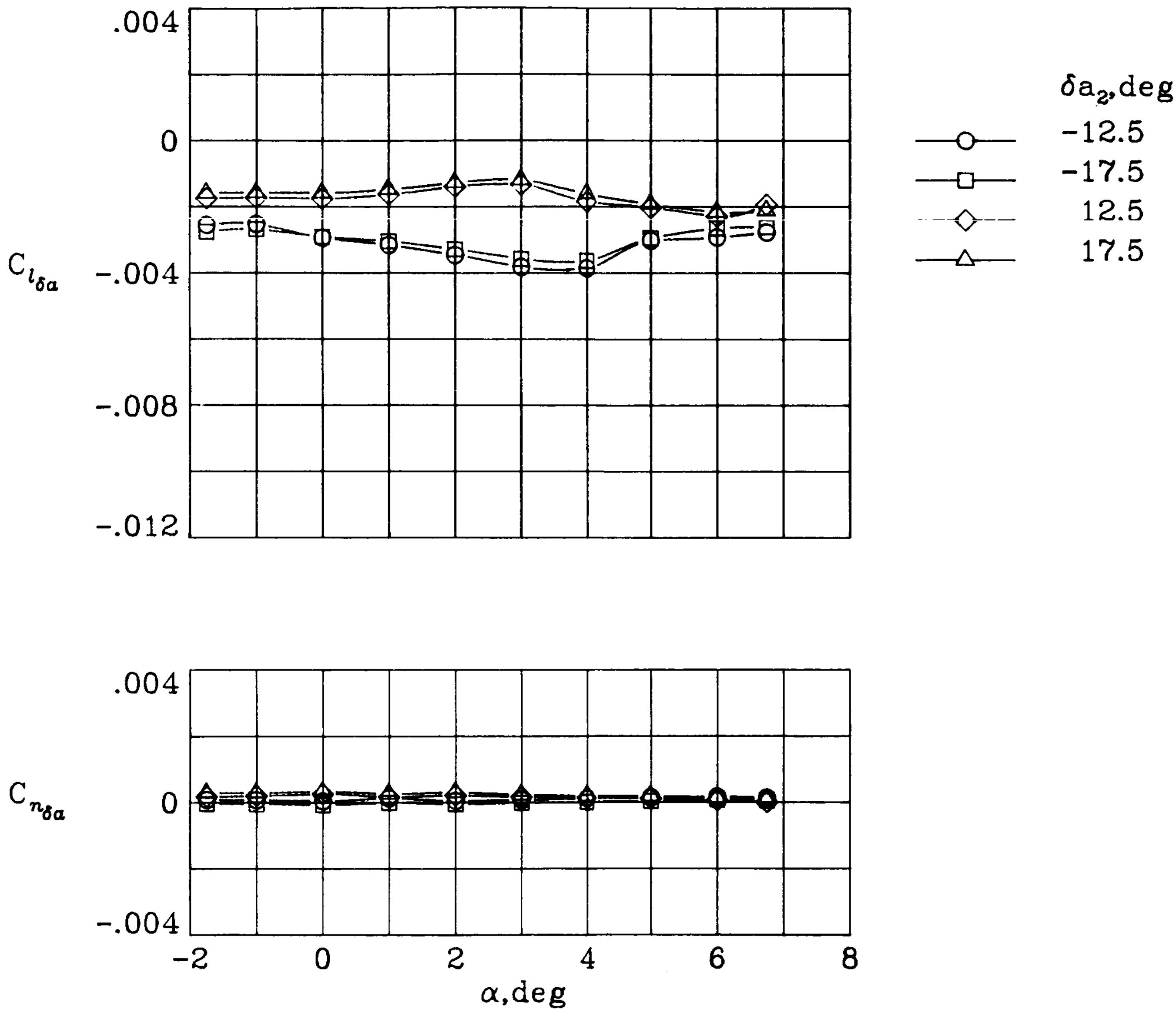

(d) Concluded.

Figure 41.- Continued.

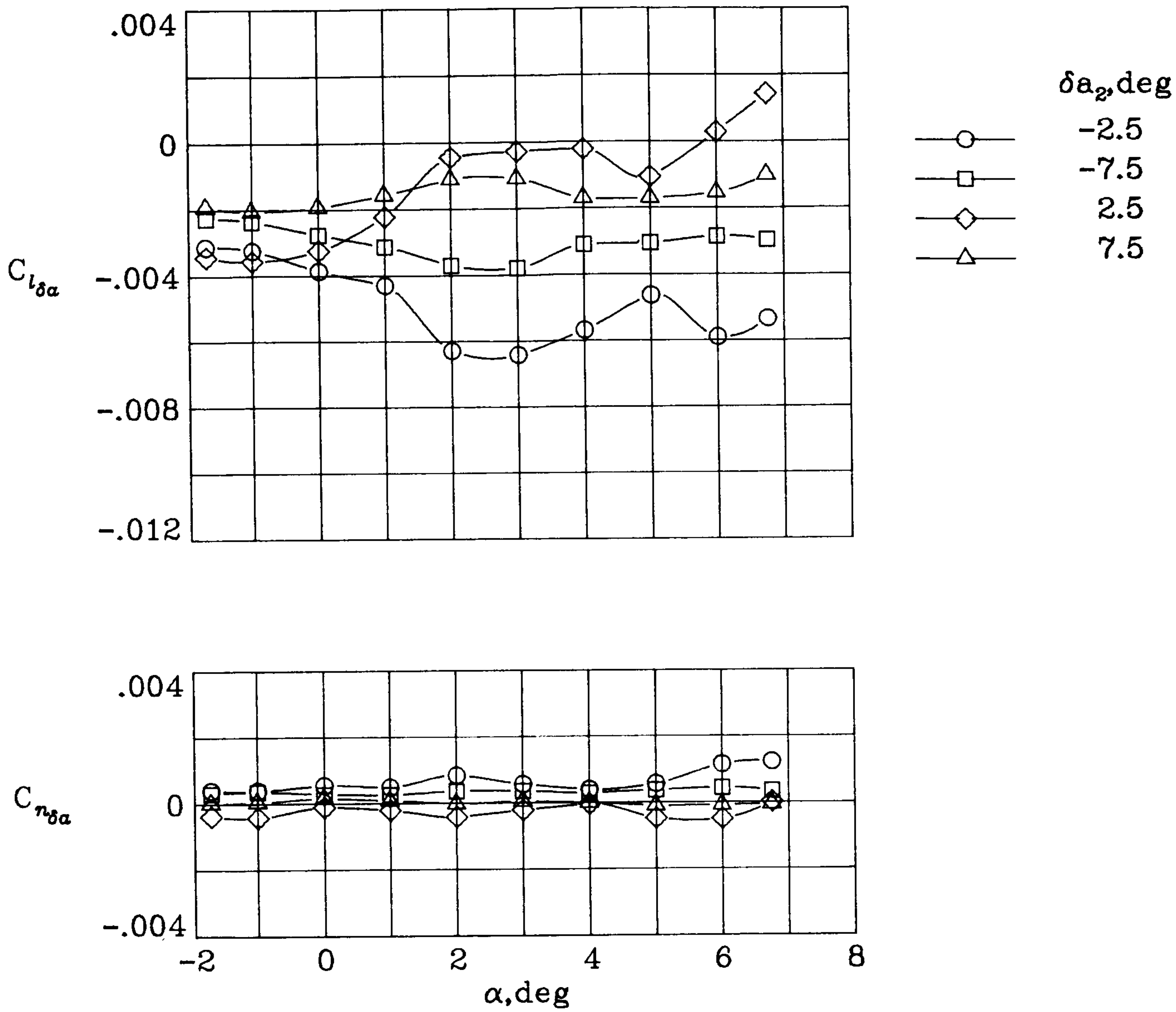

(e) $M_\infty = 0.84$.

Figure 41.- Continued.

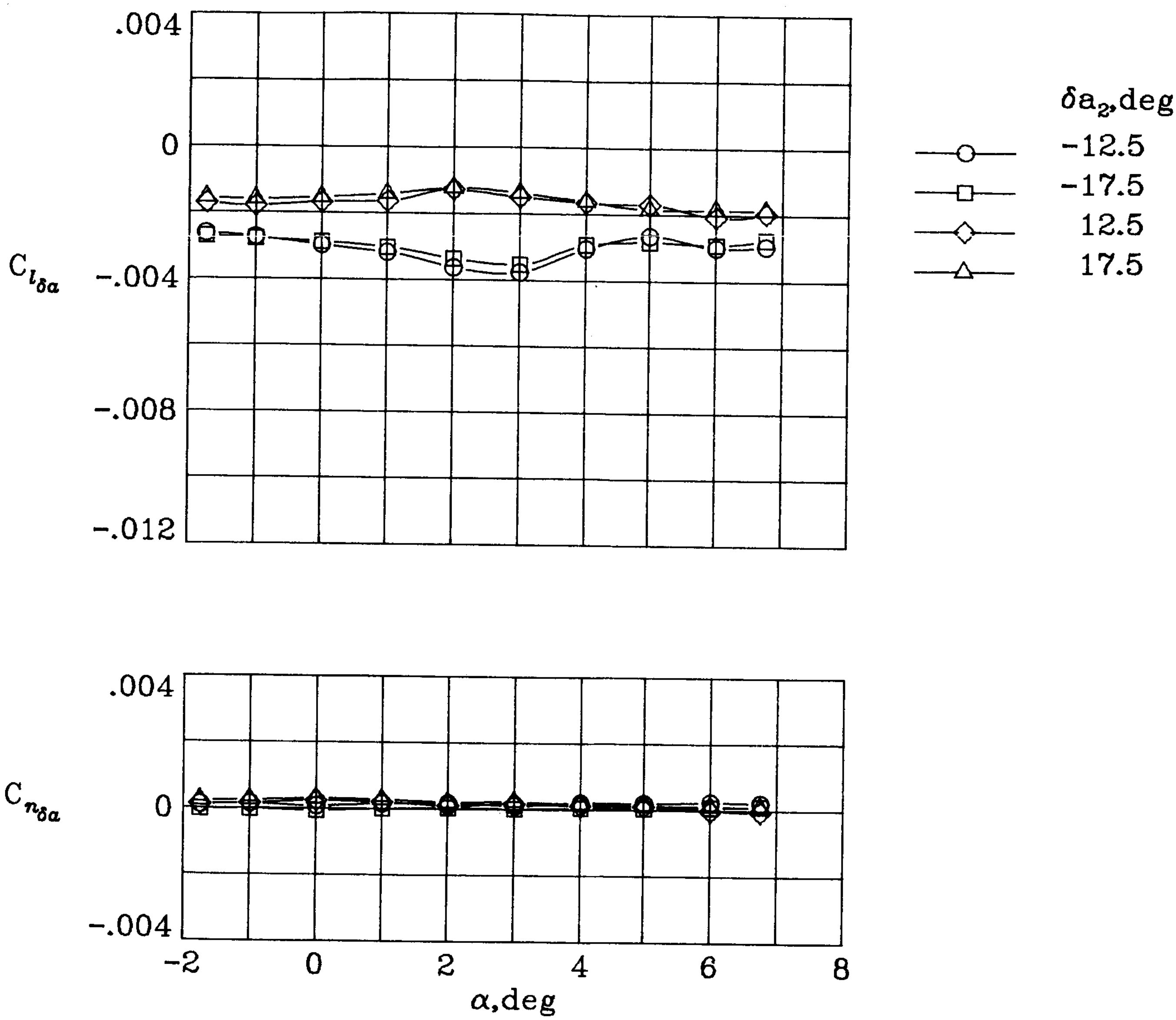

(e) Concluded.

Figure 41.- Continued.

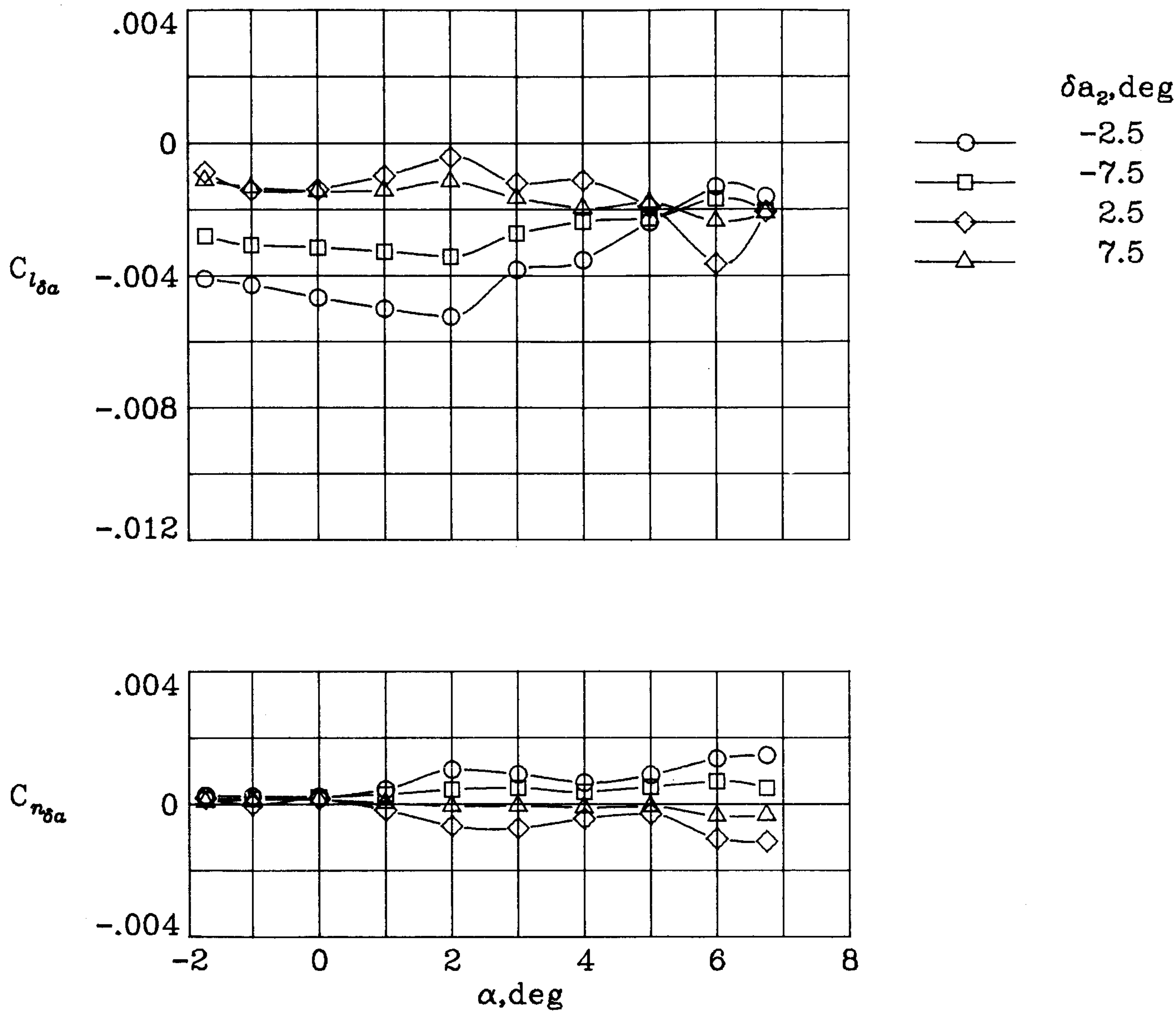

(f) $M_\infty = 0.86$.

Figure 41.- Continued.

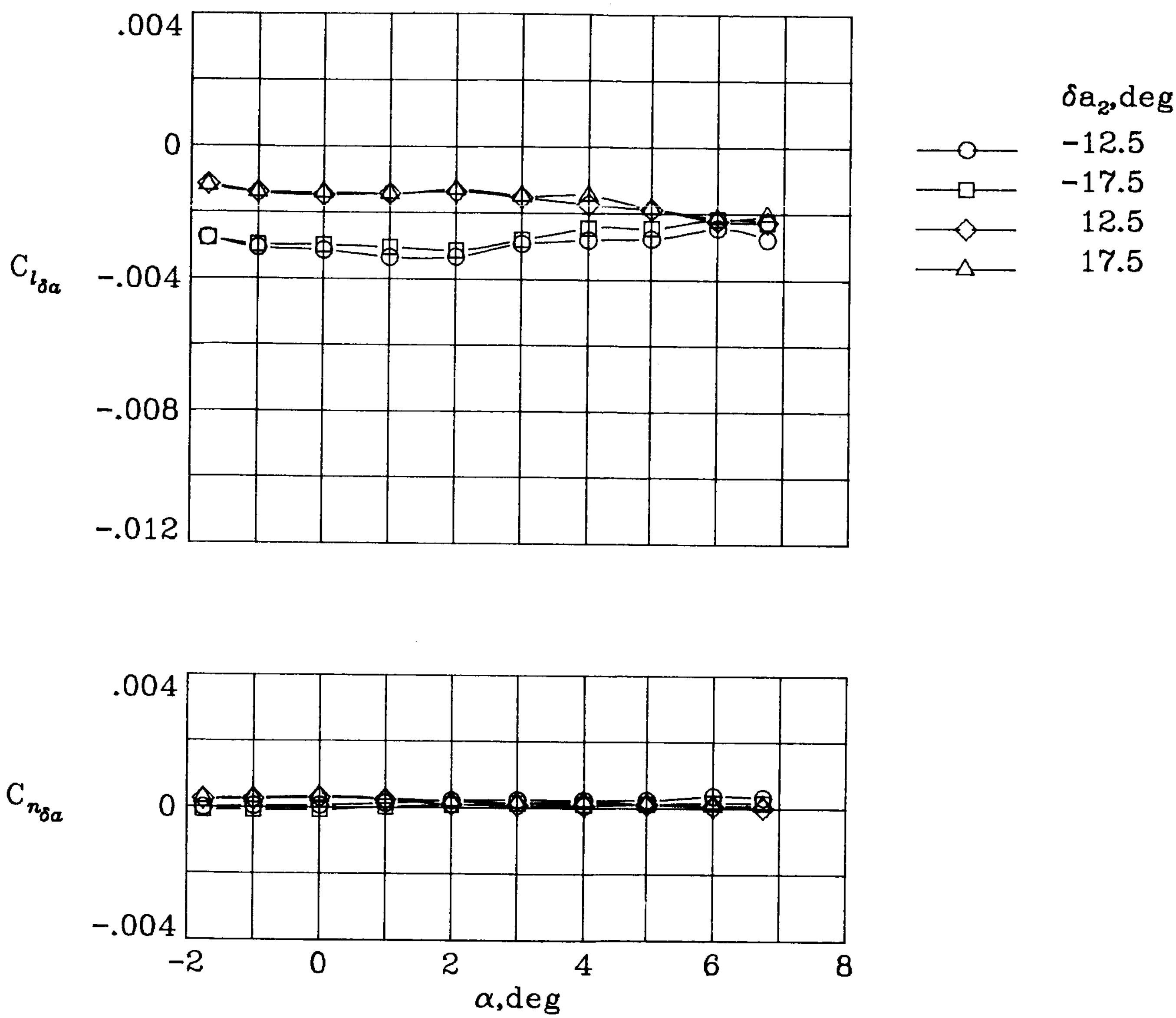

(f) Concluded.

Figure 41.- Continued.

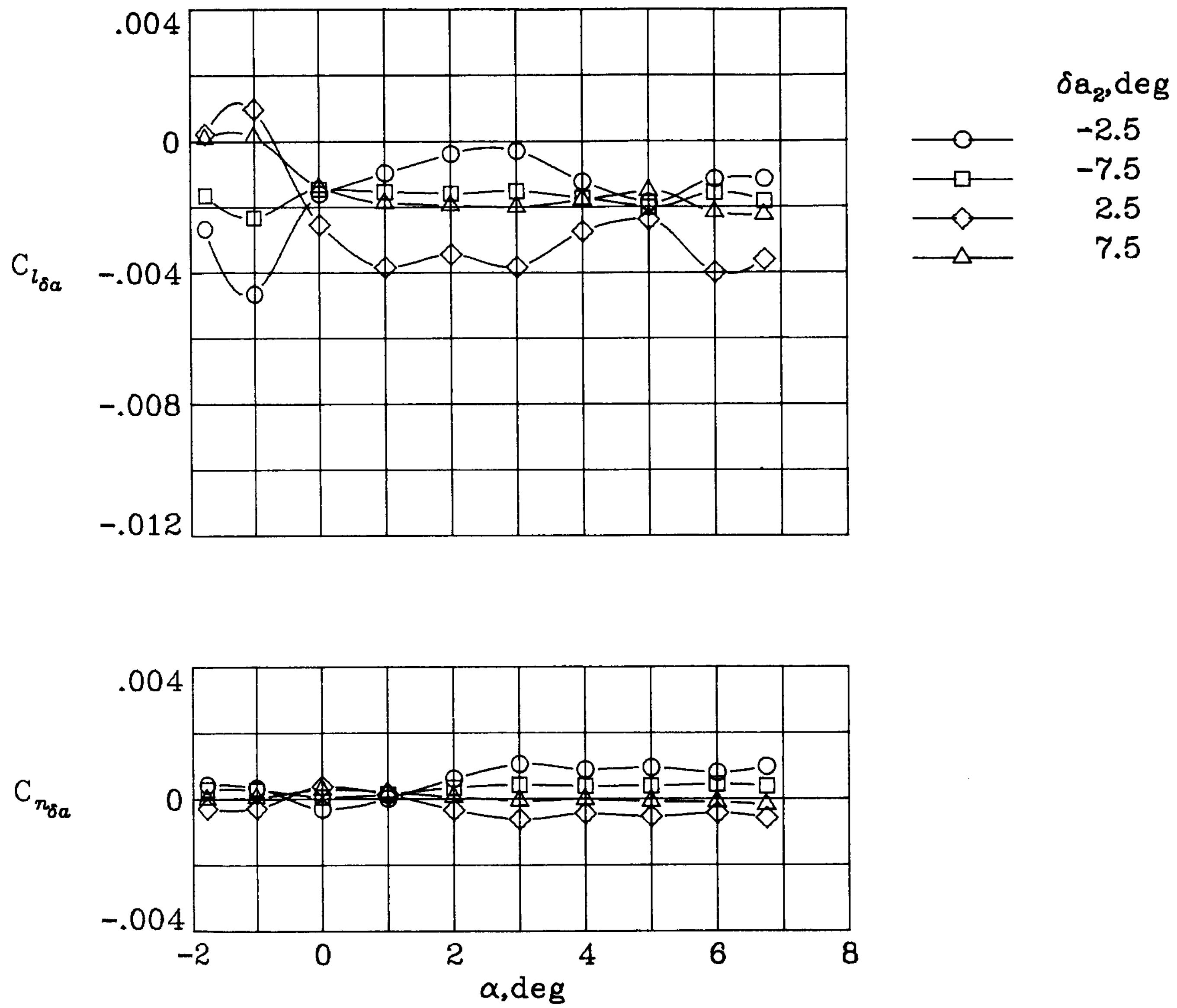

(g) $M_\infty = 0.90$.

Figure 41.- Continued.

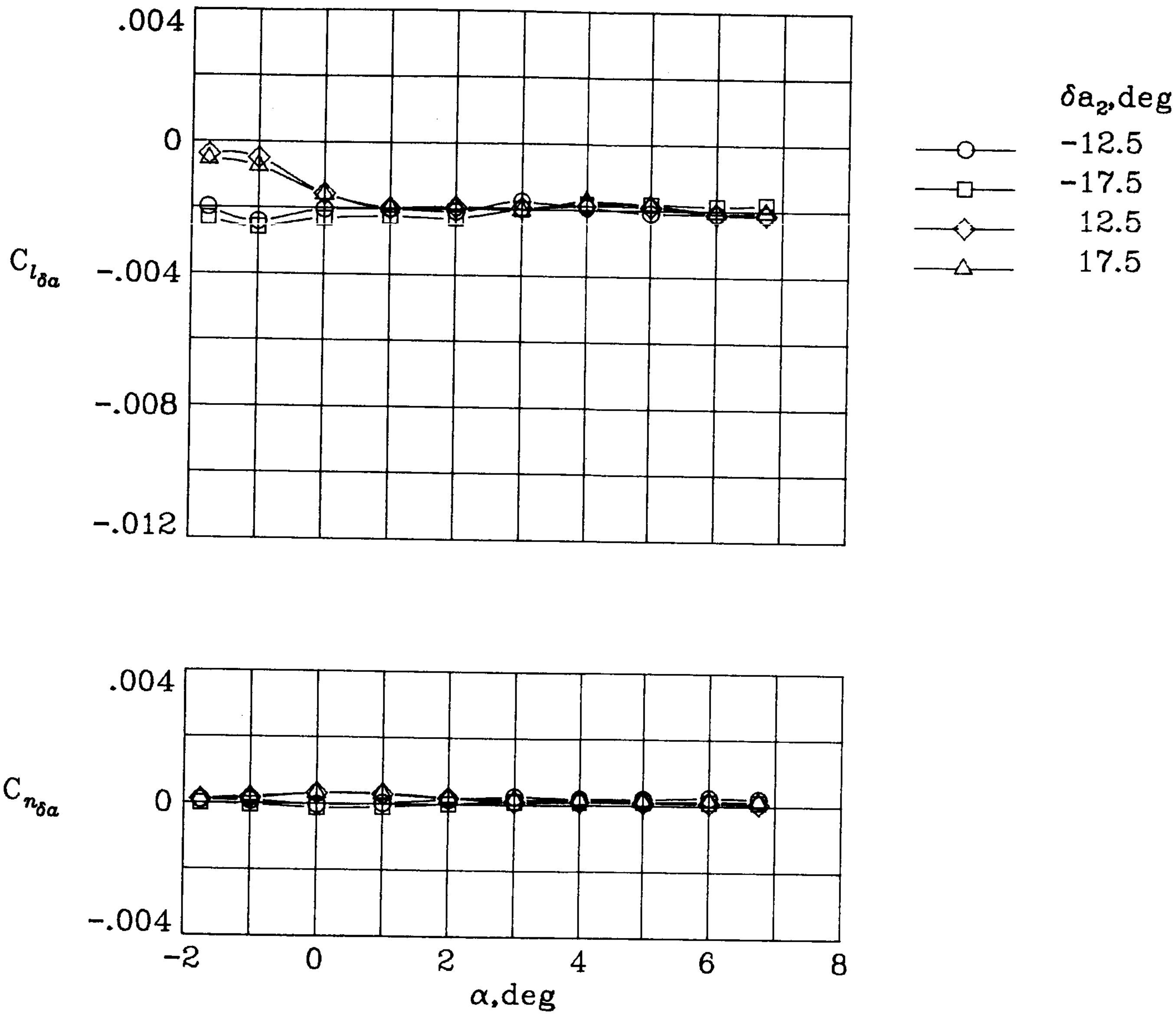

(g) Concluded.

Figure 41.- Concluded.

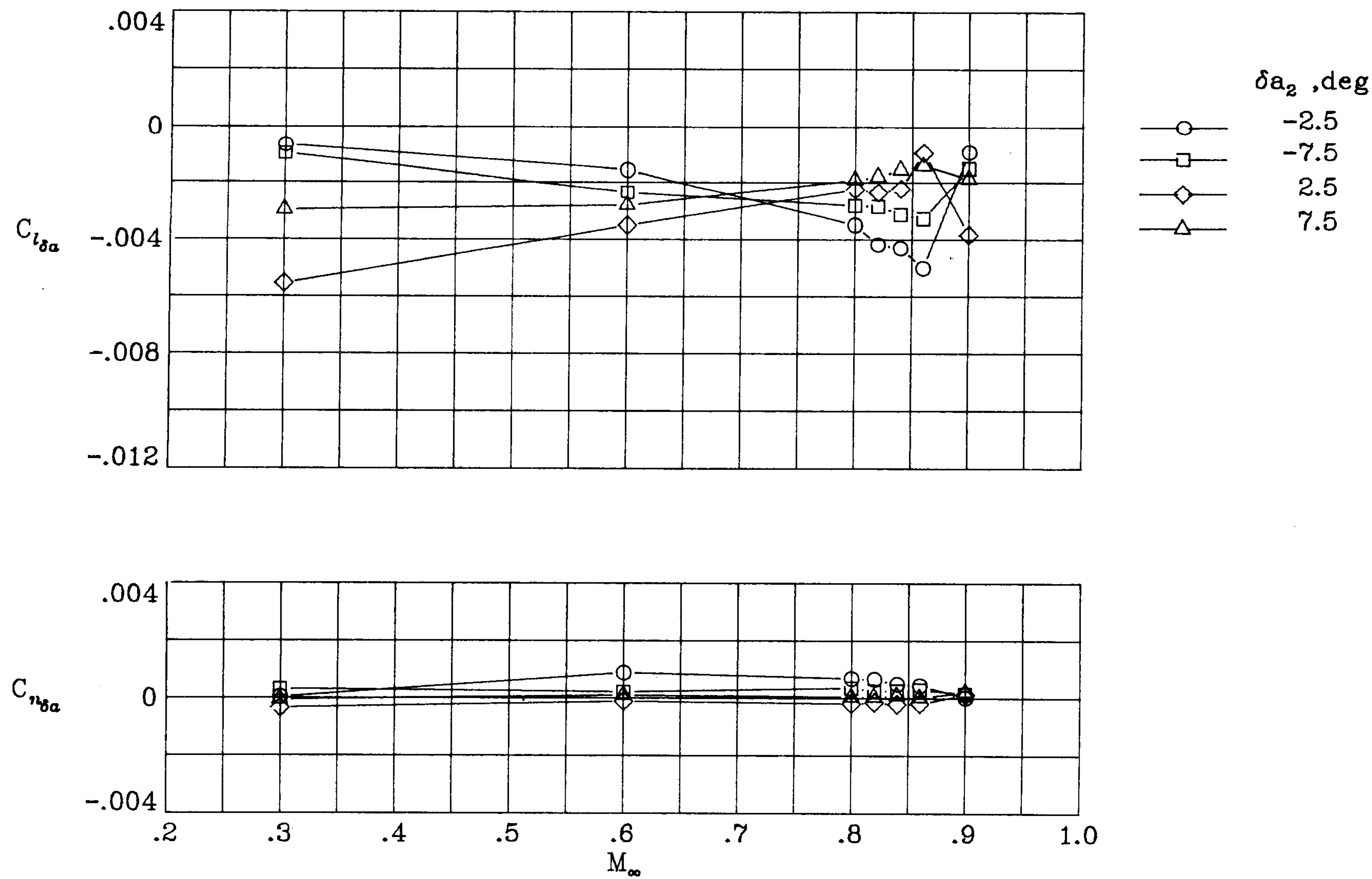

(a) $\alpha = 1°$.

Figure 42.- Variation of aileron-effectiveness parameters with Mach number for deflections of a_2. $\delta a_1 = 0°$.

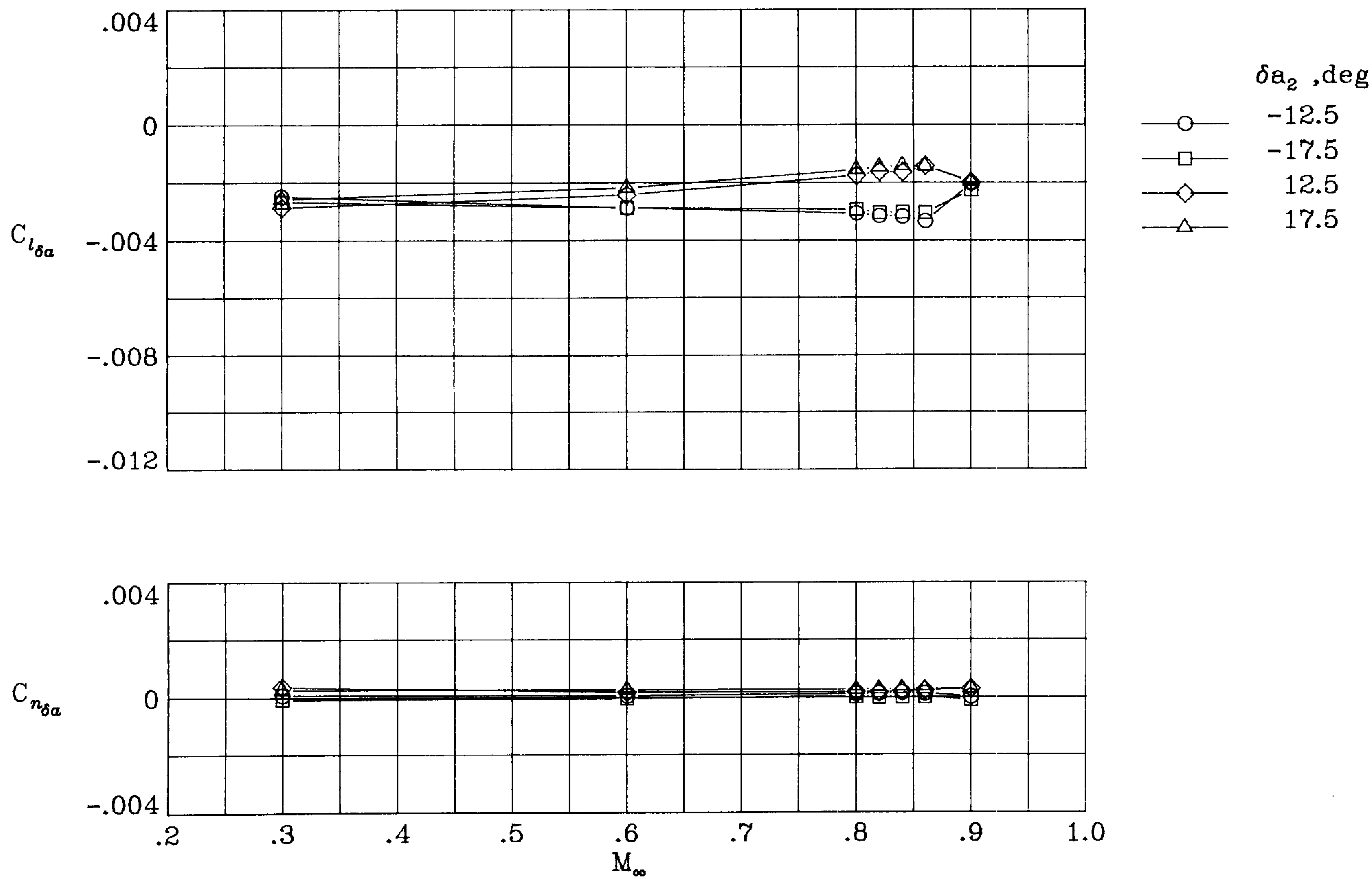

(a) Concluded.

Figure 42.- Continued.

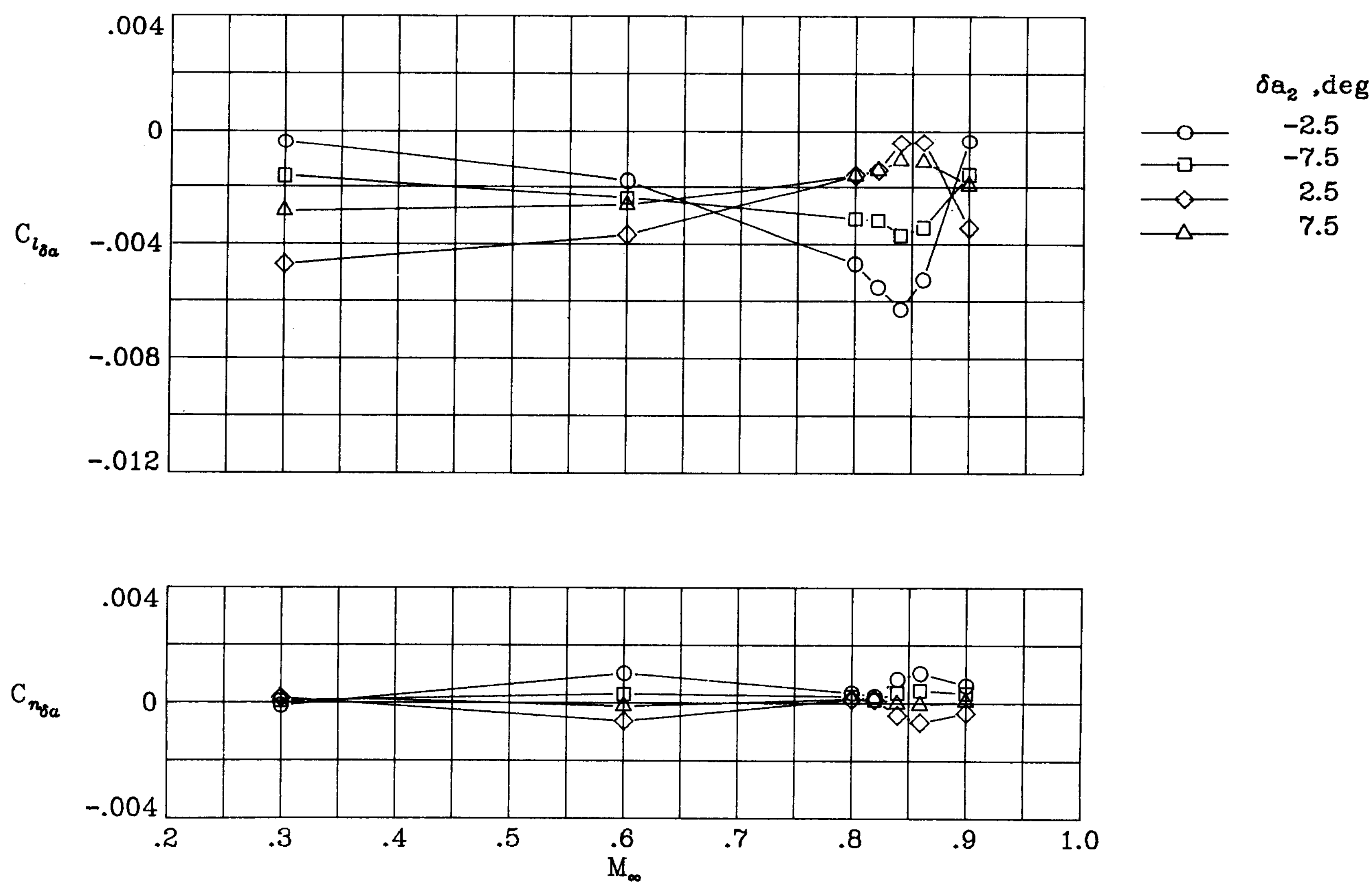

(b) $\alpha = 2°$.

Figure 42.- Continued.

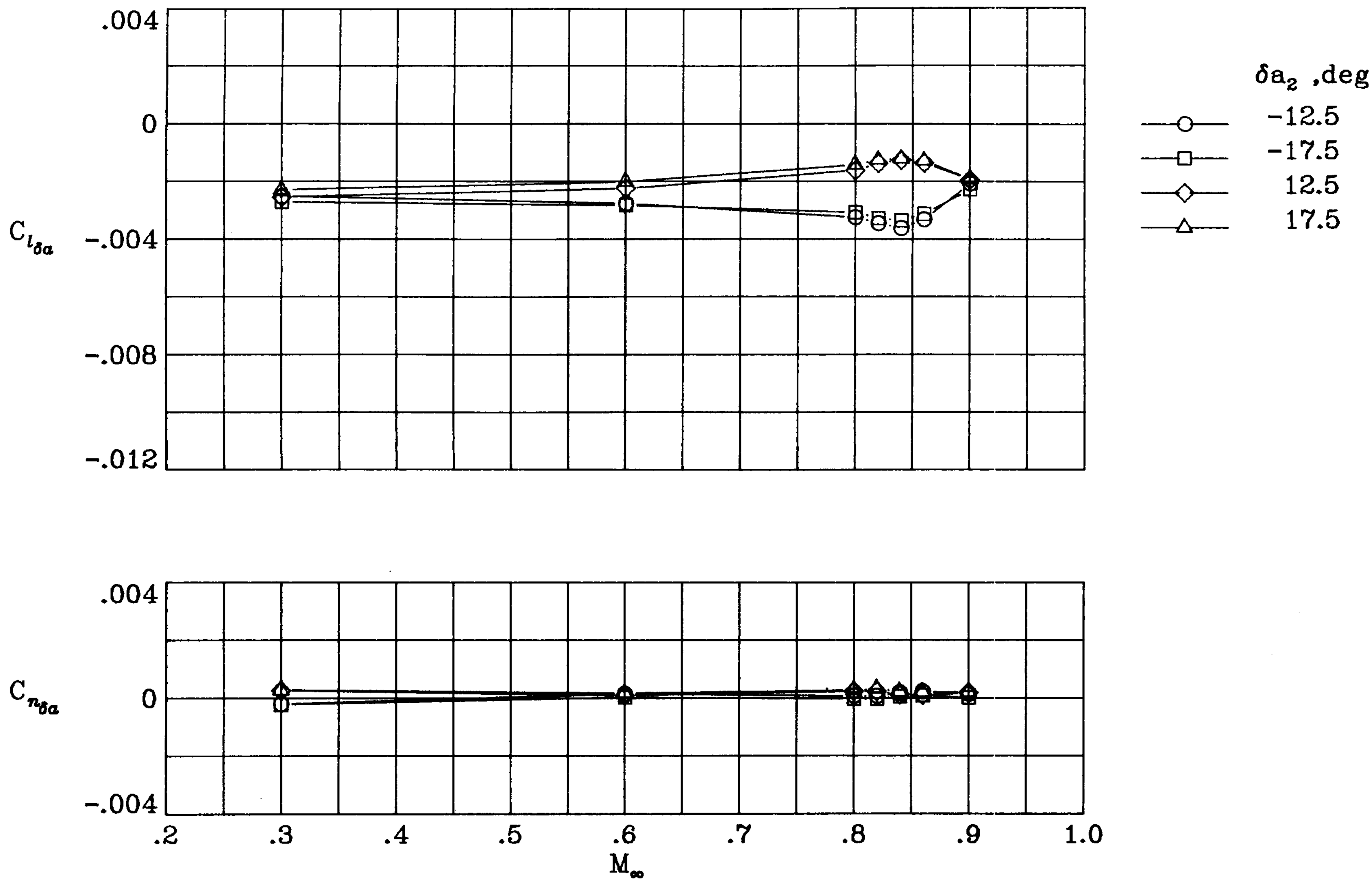

(b) Concluded.

Figure 42.- Continued.

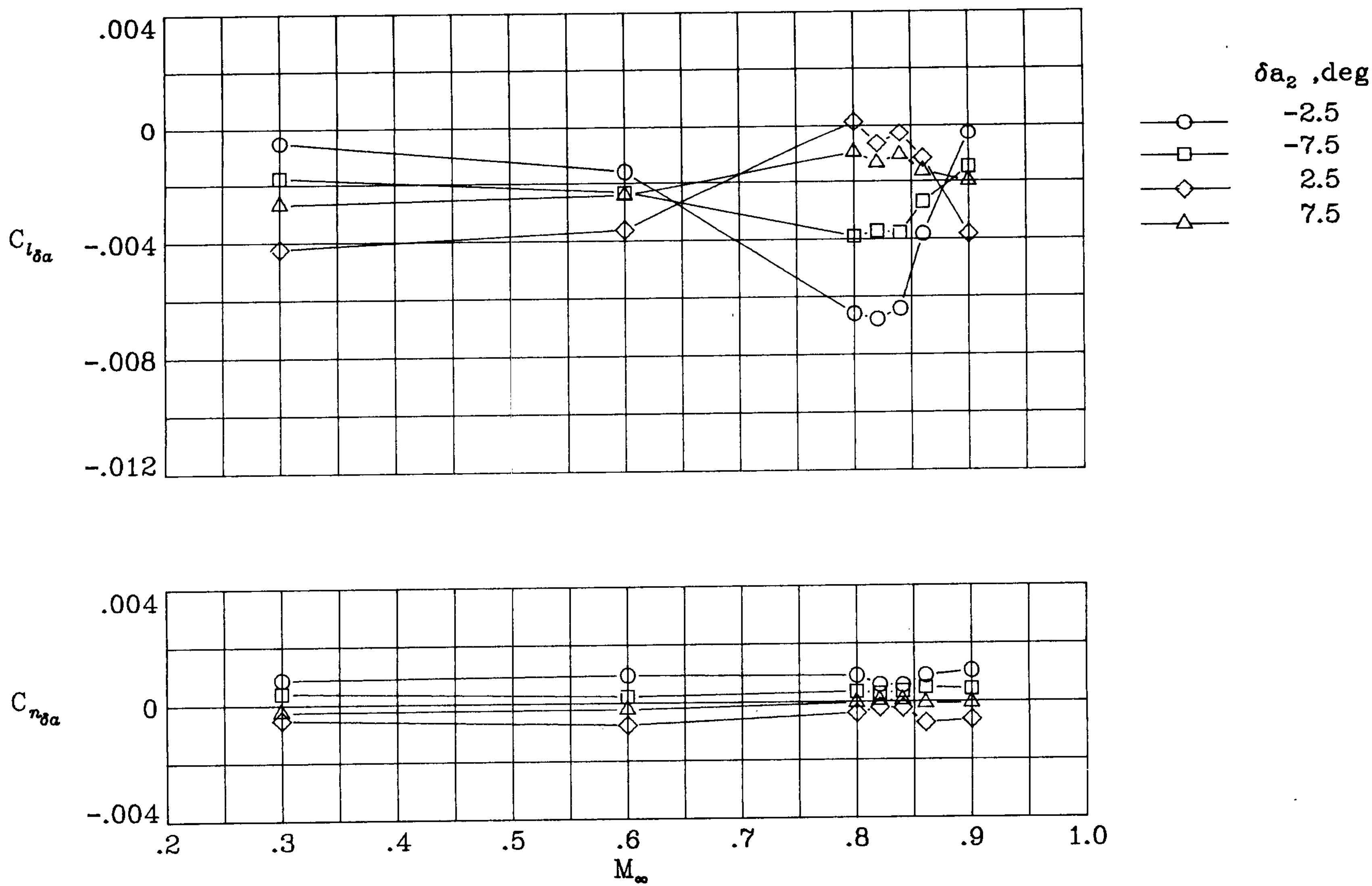

(c) $\alpha = 3°$.

Figure 42.- Continued.

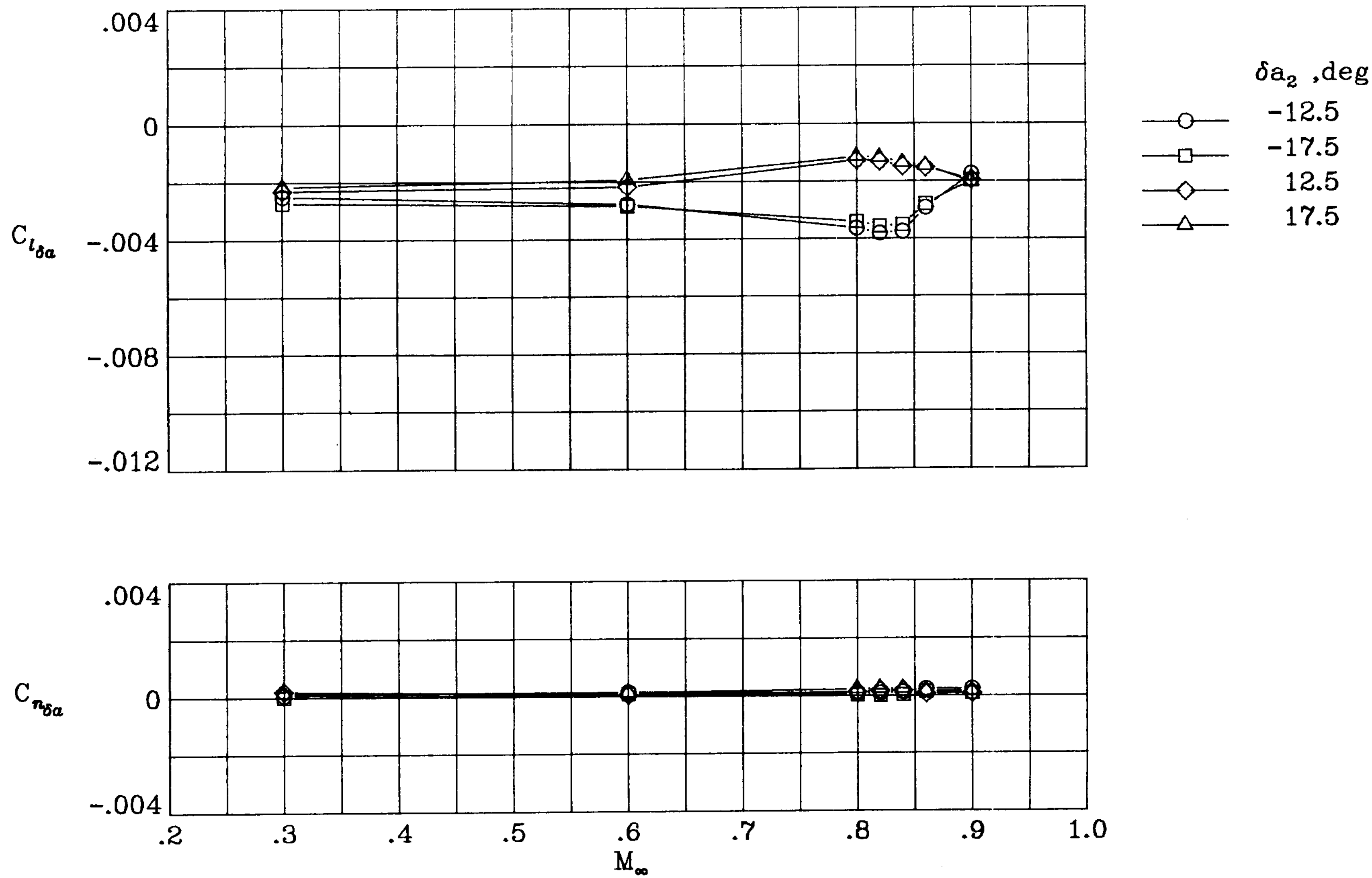

(c) Concluded.

Figure 42.- Continued.

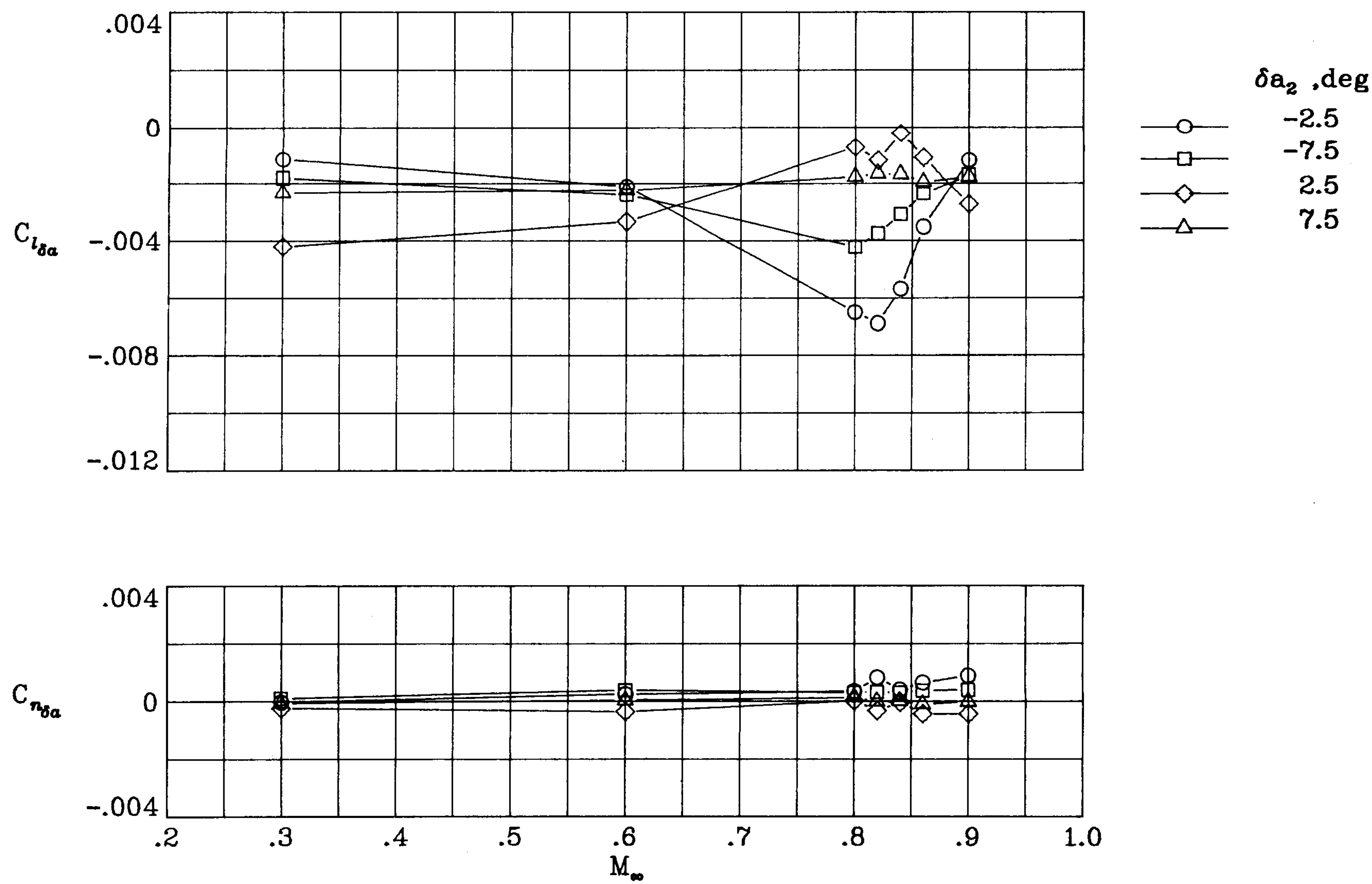

(d) $\alpha = 4°$.

Figure 42.- Continued.

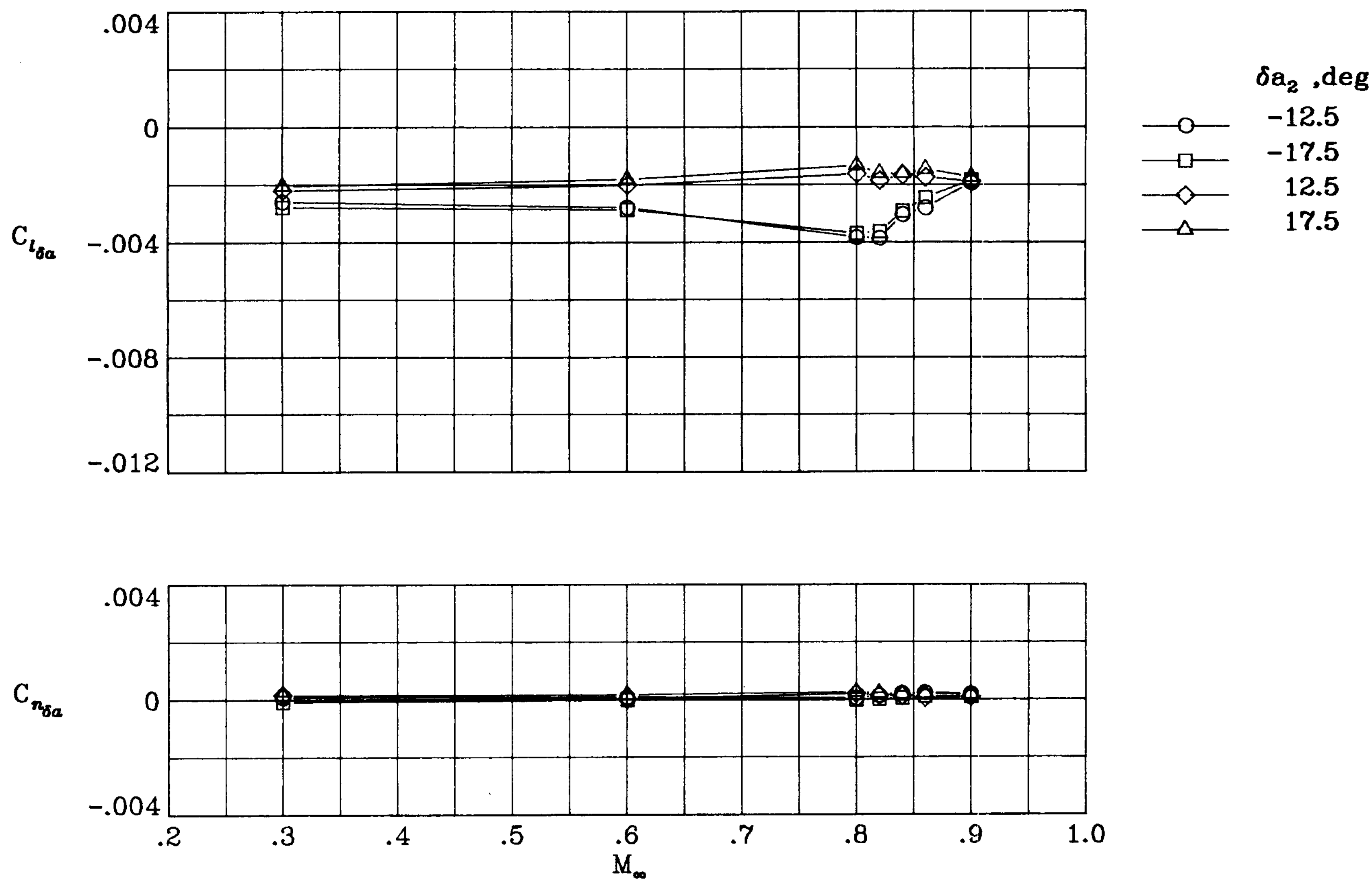

(d) Concluded.

Figure 42.- Concluded.

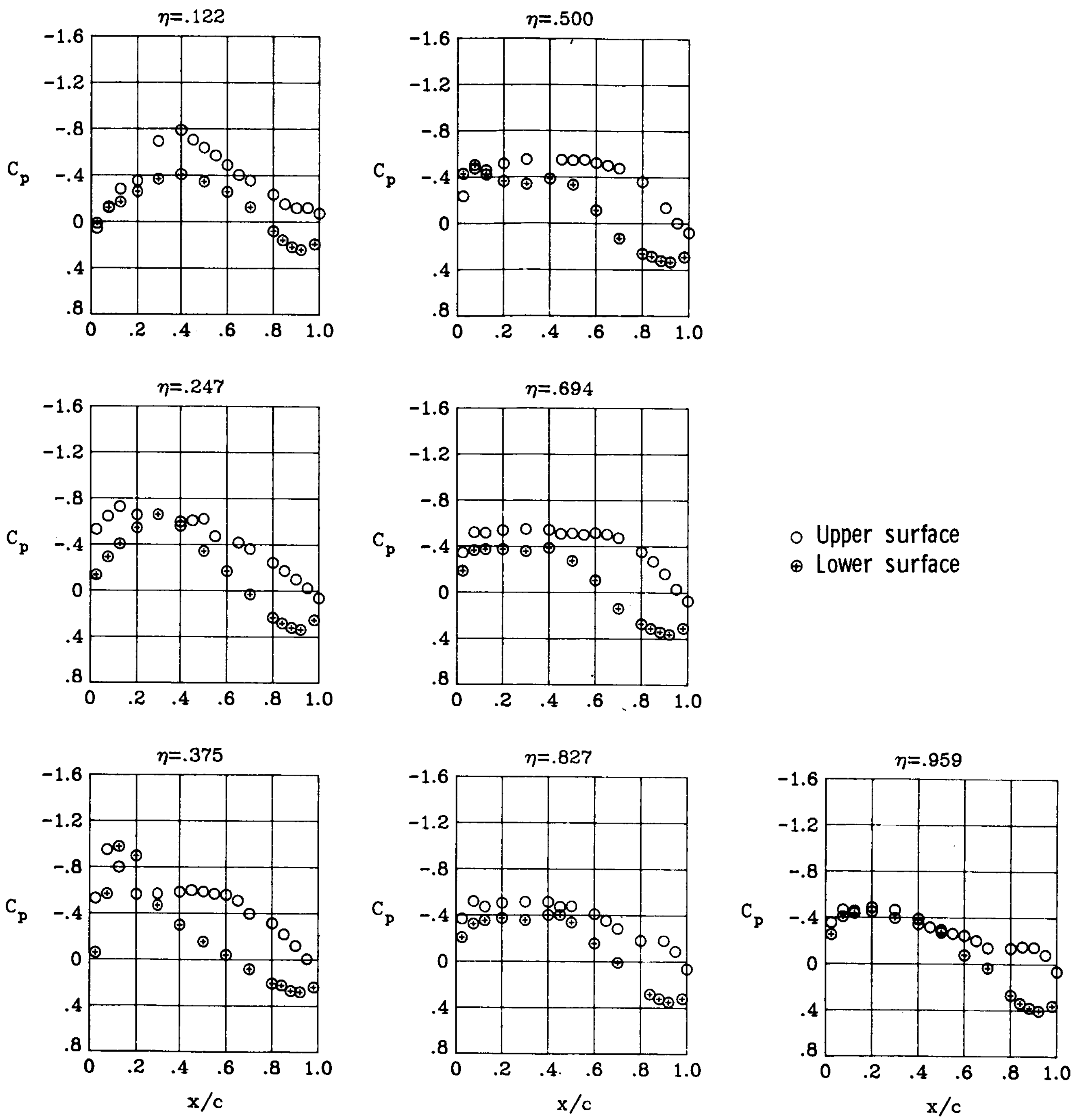

(a) $M_\infty = 0.82$; $\alpha = 1°$.

Figure 43.- Wing chordwise pressure distributions for $\delta a_2 = -2.5°$ at $M_\infty = 0.82$. $\delta a_1 = 0°$.

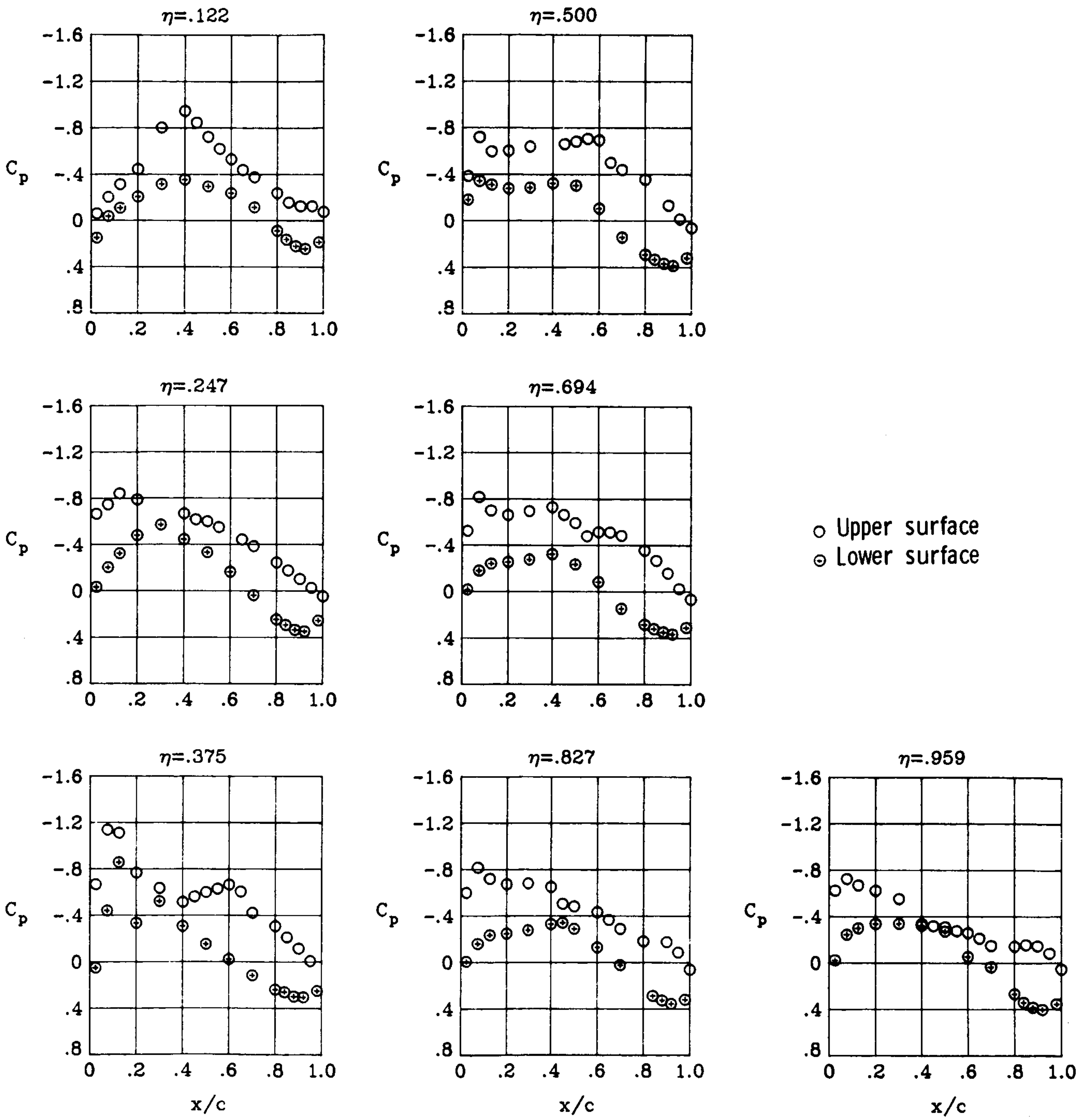

(b) $M_\infty = 0.82$; $\alpha = 2°$.

Figure 43.- Continued.

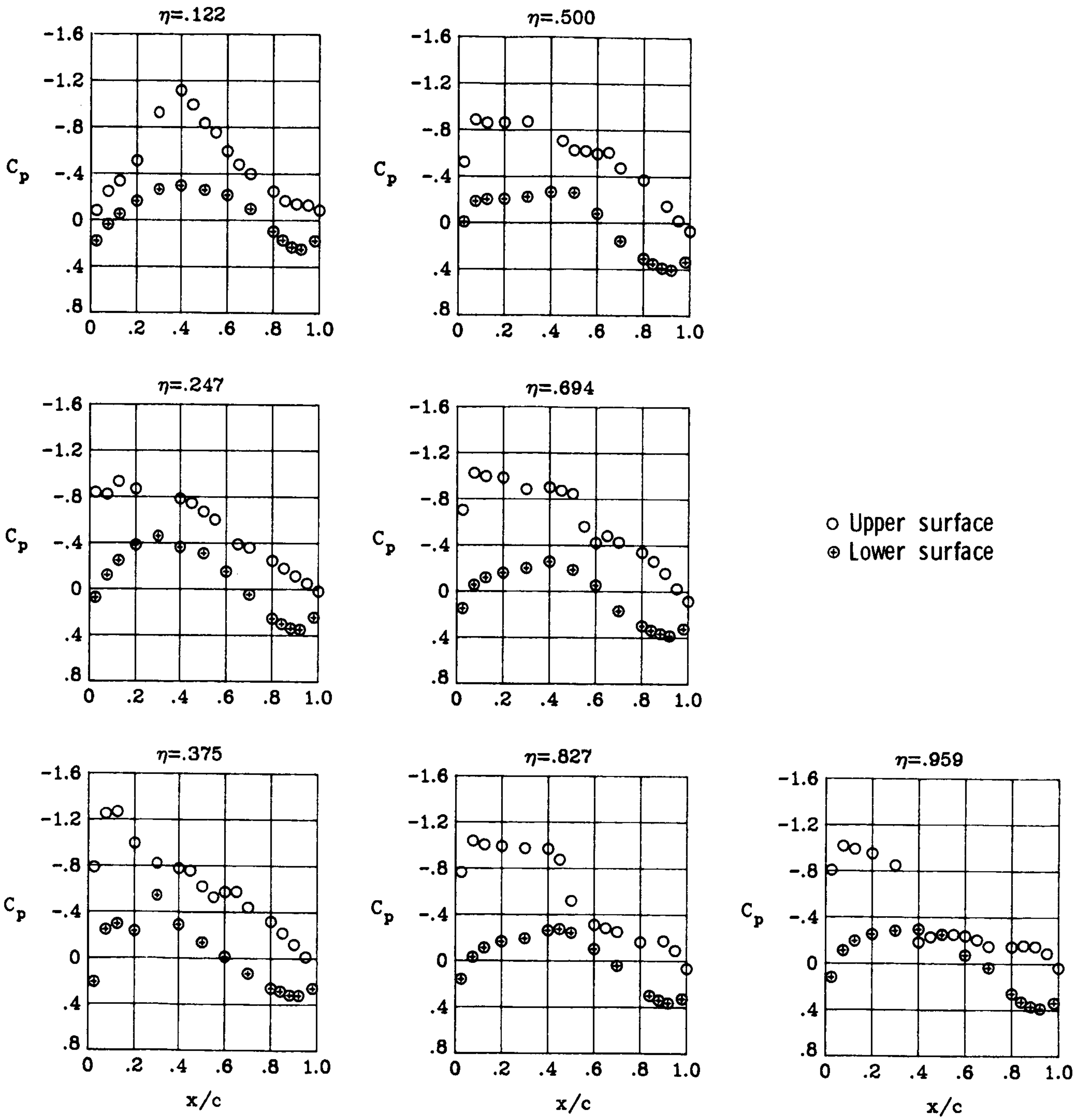

(c) $M_\infty = 0.82$; $\alpha = 3°$.

Figure 43.- Continued.

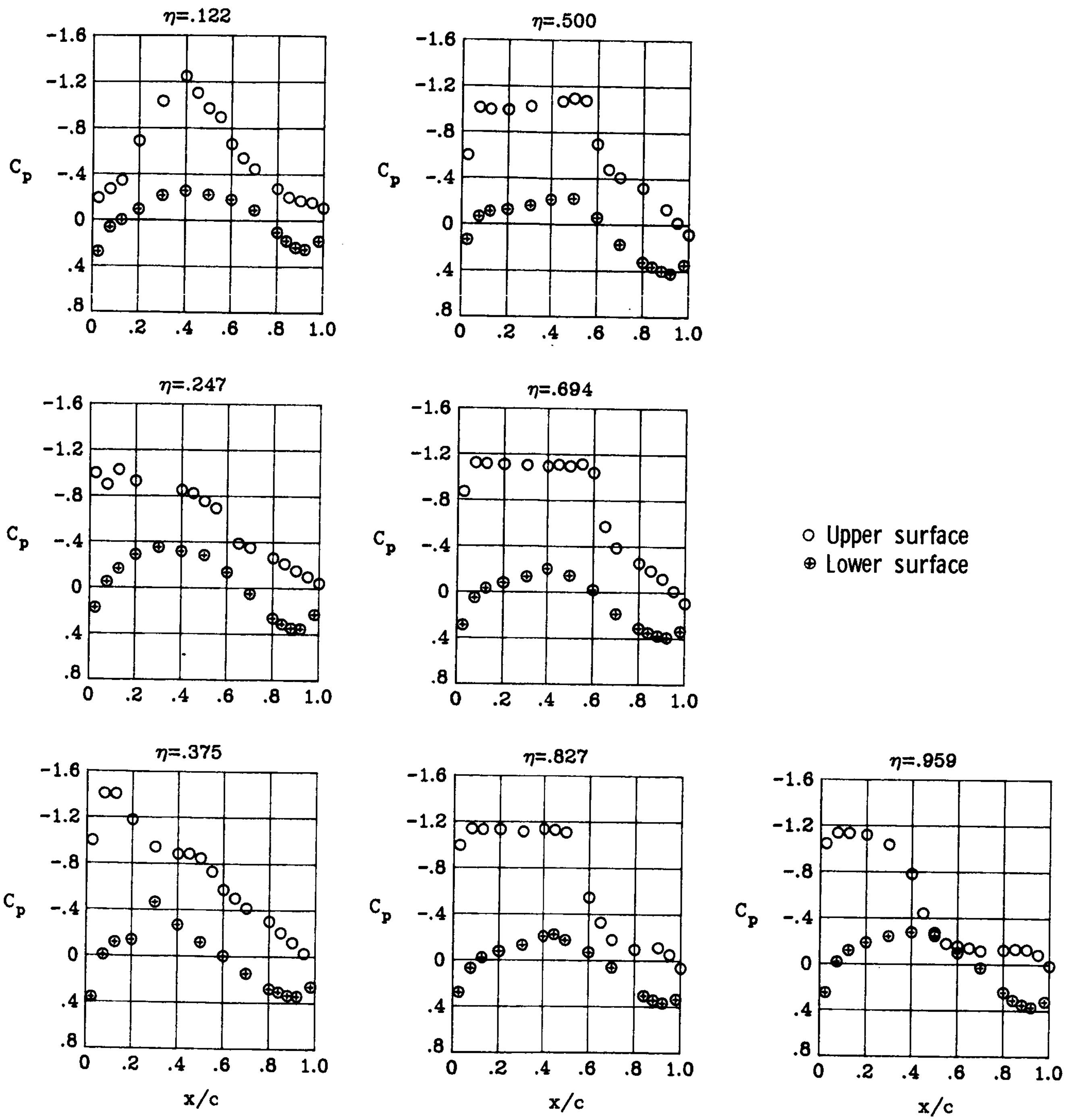

(d) $M_\infty = 0.82$; $\alpha = 4°$.

Figure 43.- Continued.

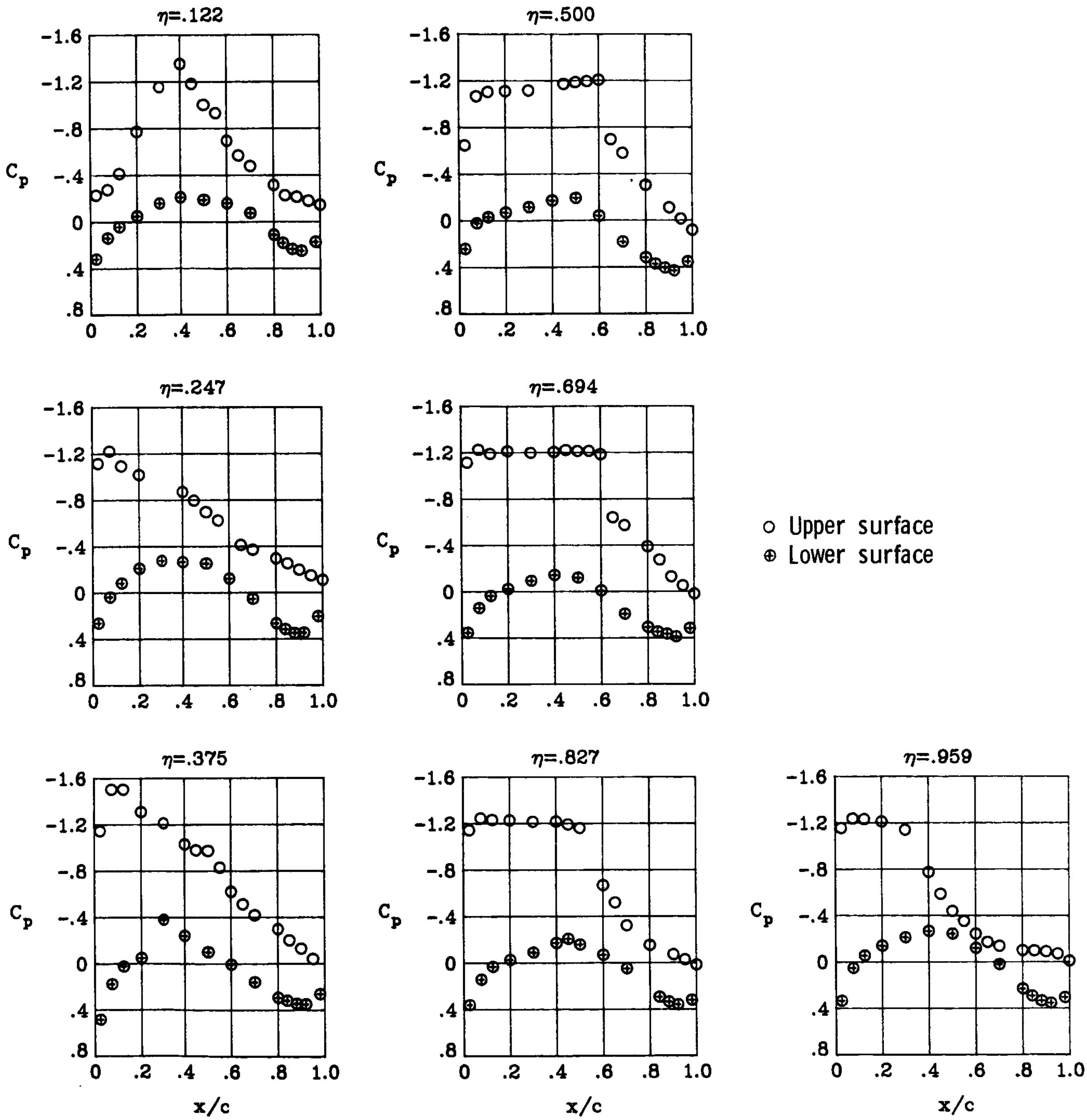

(e) $M_\infty = 0.82$; $\alpha = 5°$.

Figure 43.- Concluded.

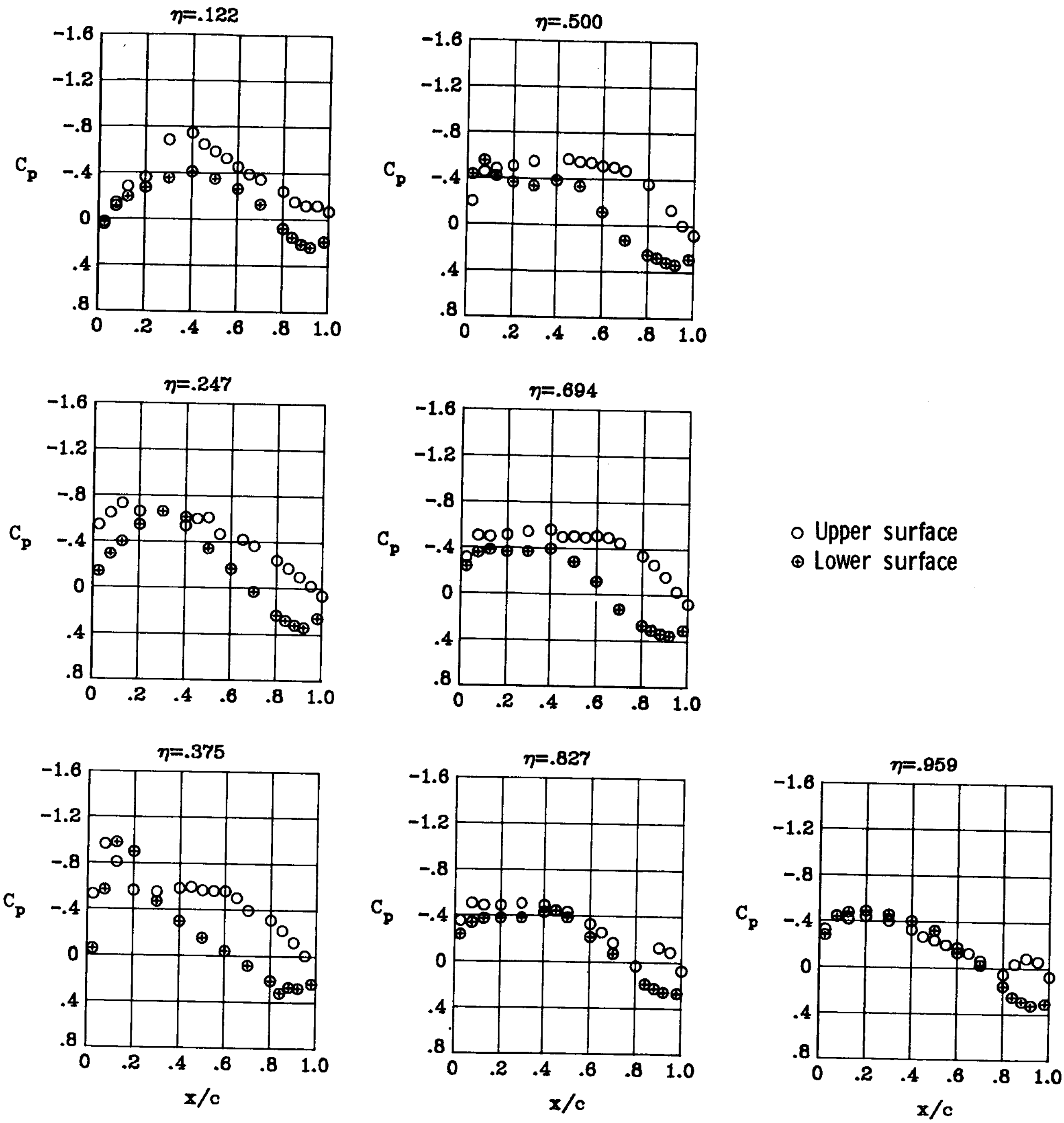

(a) $M_\infty = 0.82$; $\alpha = 1°$.

Figure 44.- Wing chordwise pressure distributions for $\delta a_2 = -7.5°$ at $M_\infty = 0.82$. $\delta a_1 = 0°$.

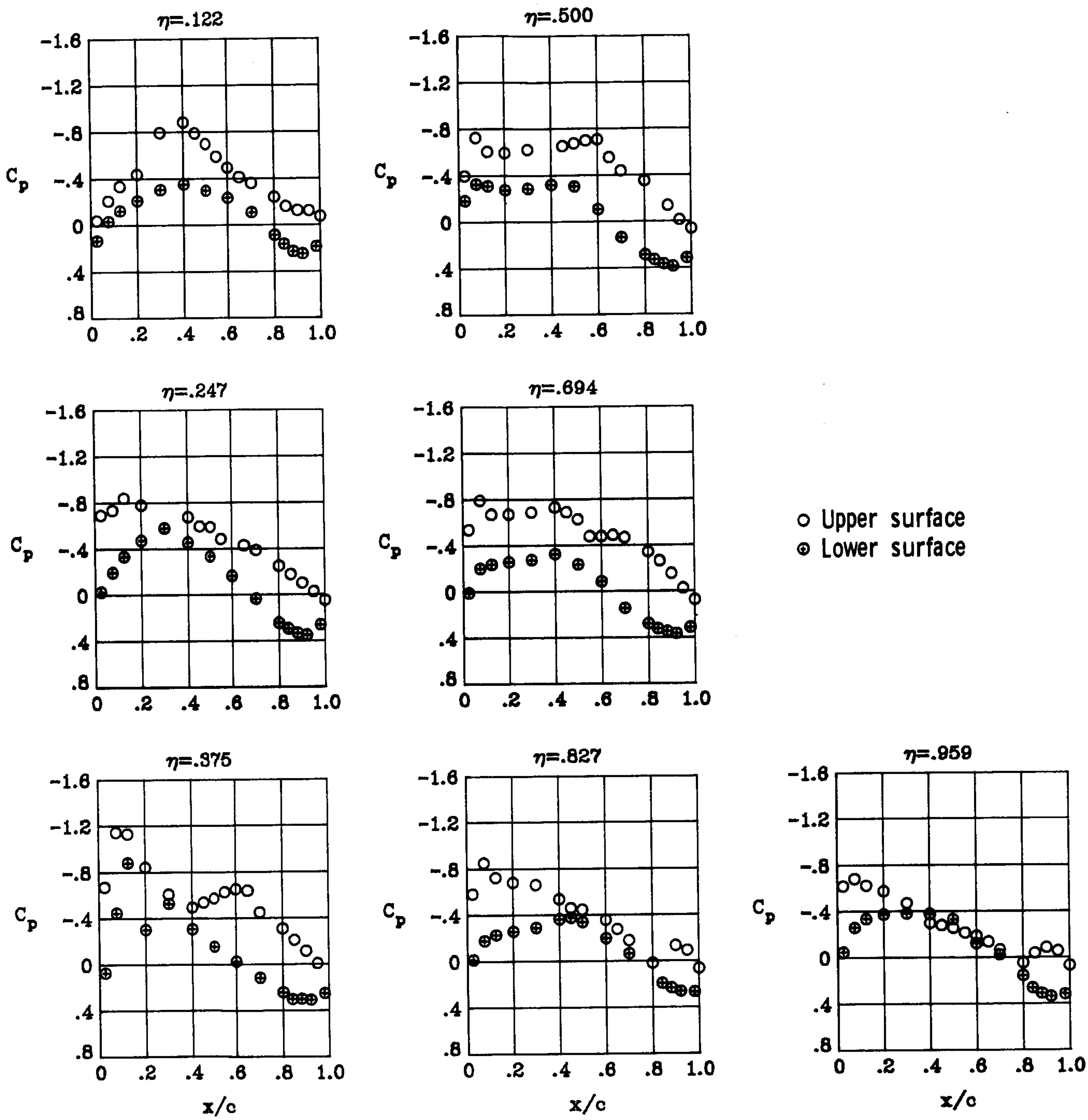

(b) $M_\infty = 0.82$; $\alpha = 2°$.

Figure 44.- Continued.

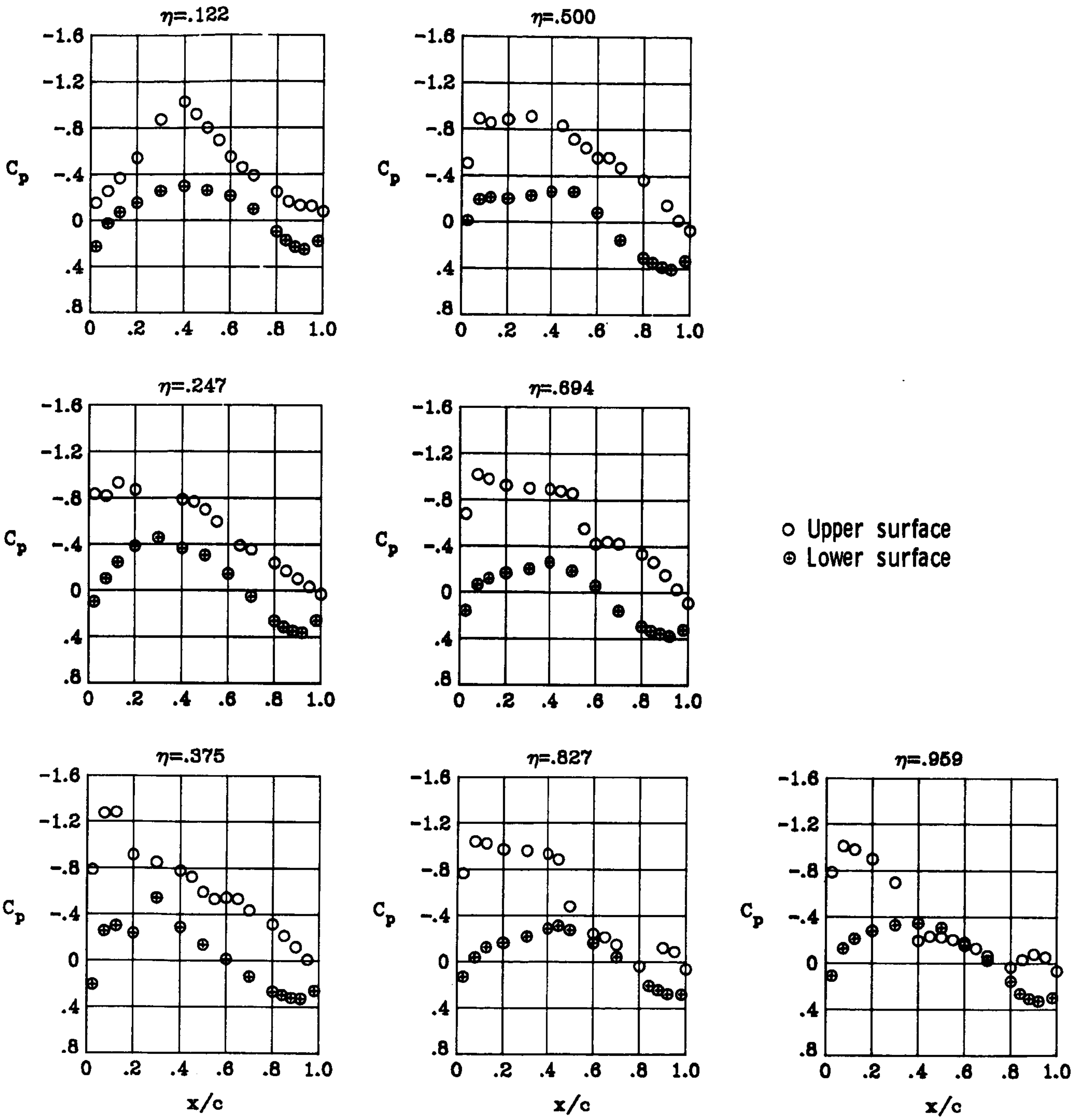

(c) $M_\infty = 0.82$; $\alpha = 3°$.

Figure 44.- Continued.

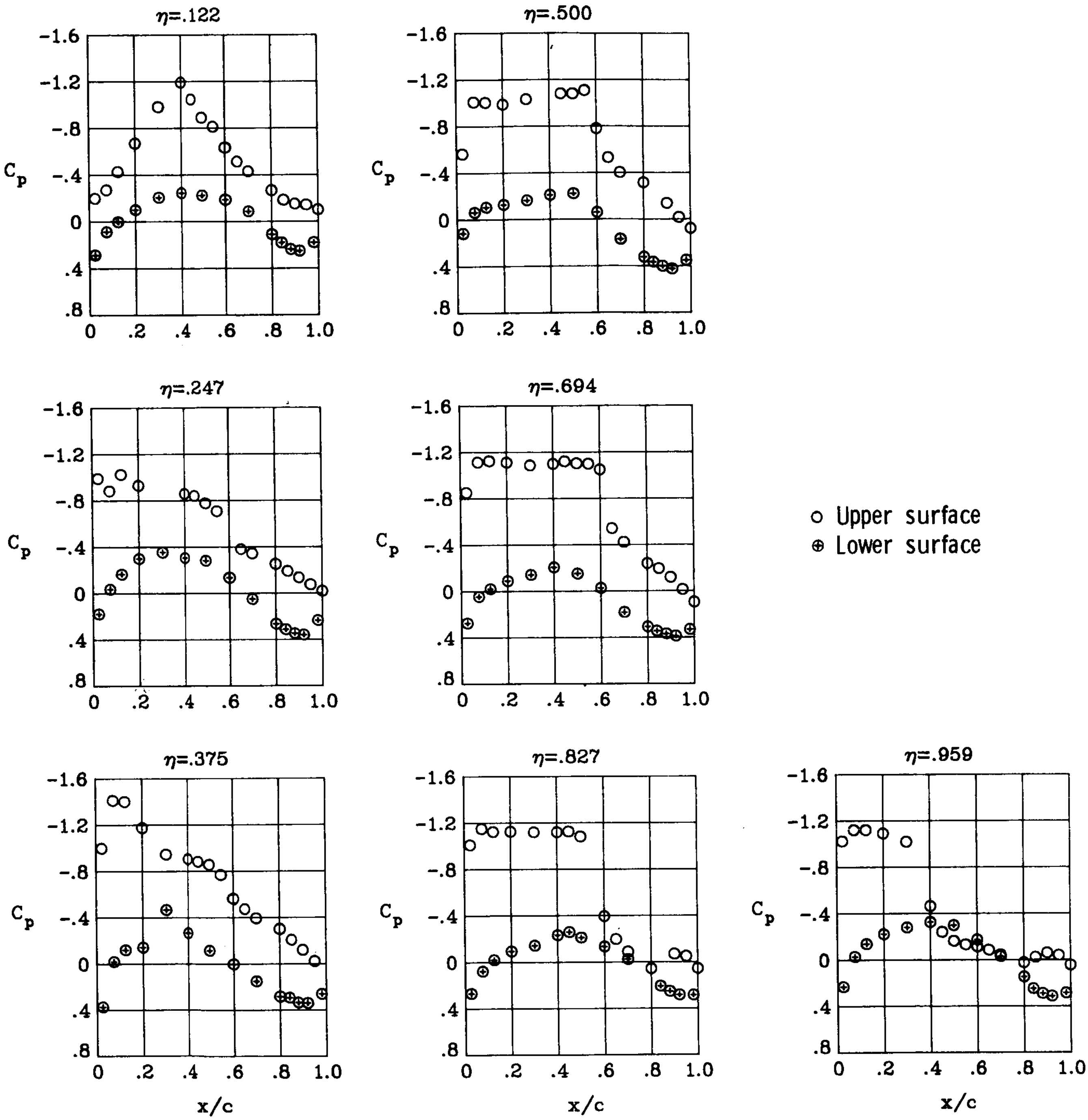

(d) $M_\infty = 0.82$; $\alpha = 4°$.

Figure 44.- Continued.

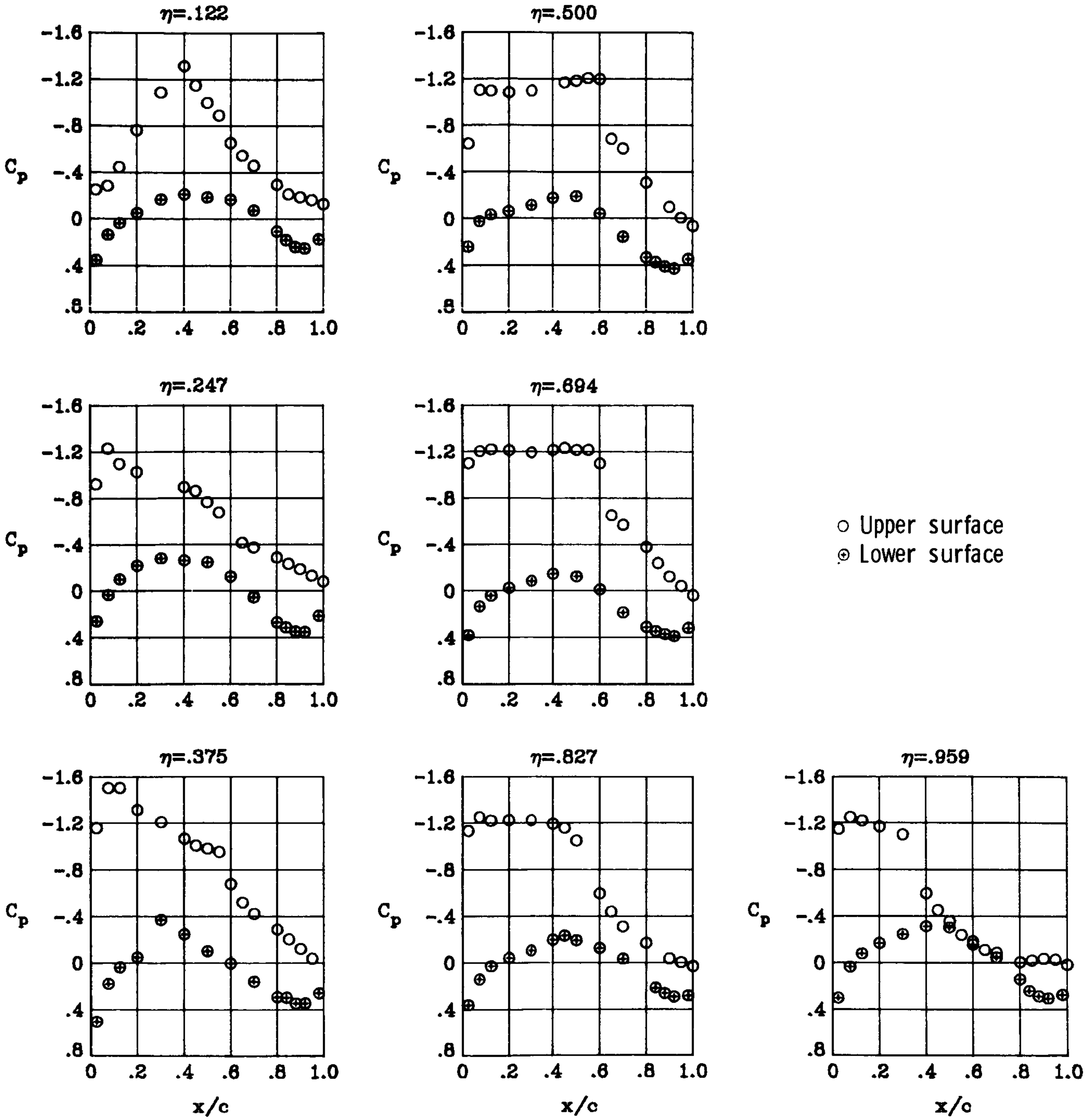

(e) $M_\infty = 0.82$; $\alpha = 5°$.

Figure 44.- Concluded.

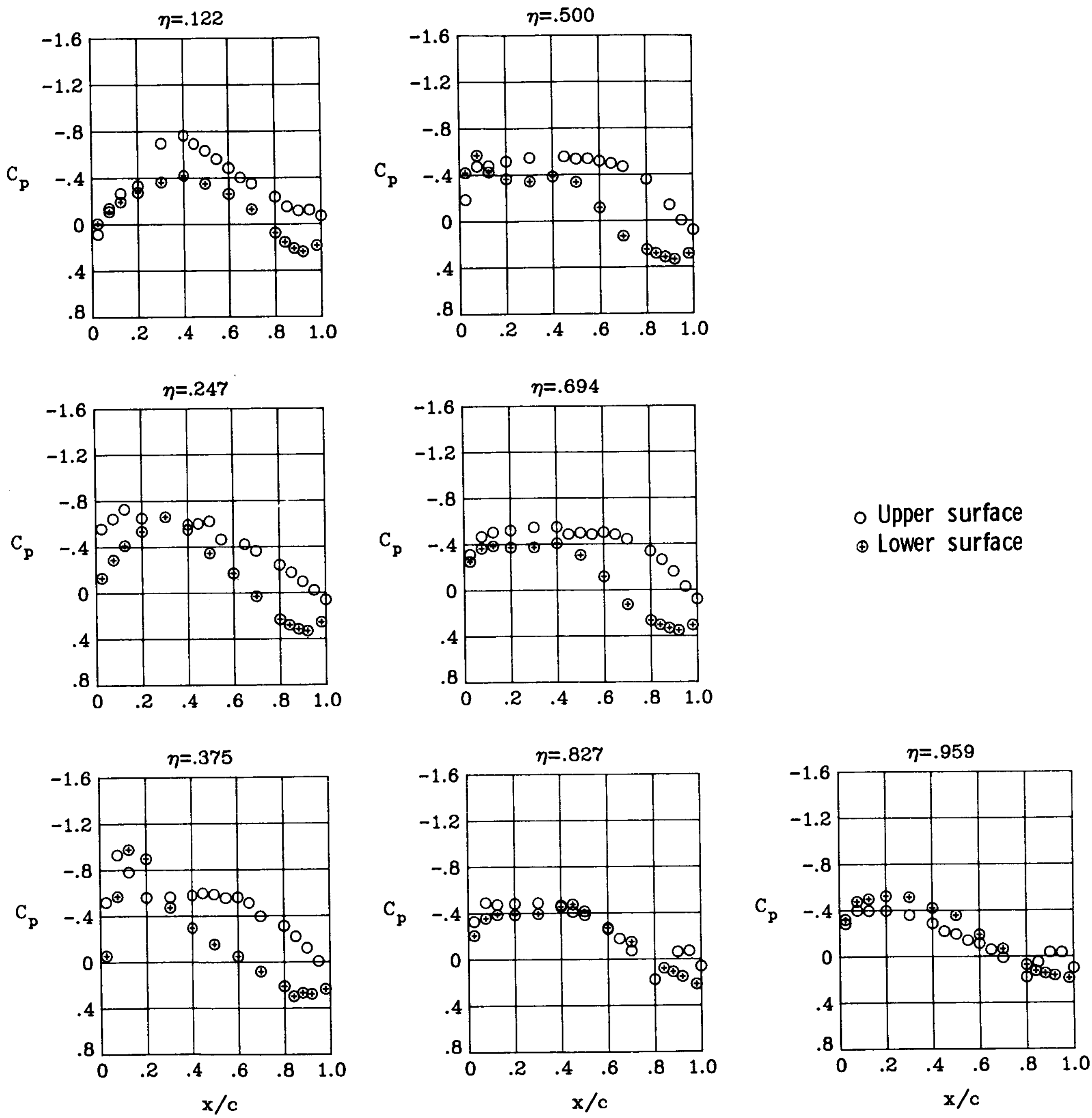

(a) $M_\infty = 0.82$; $\alpha = 1°$.

Figure 45.- Wing chordwise pressure distributions for $\delta a_2 = -12.5°$ at $M_\infty = 0.82$. $\delta a_1 = 0°$.

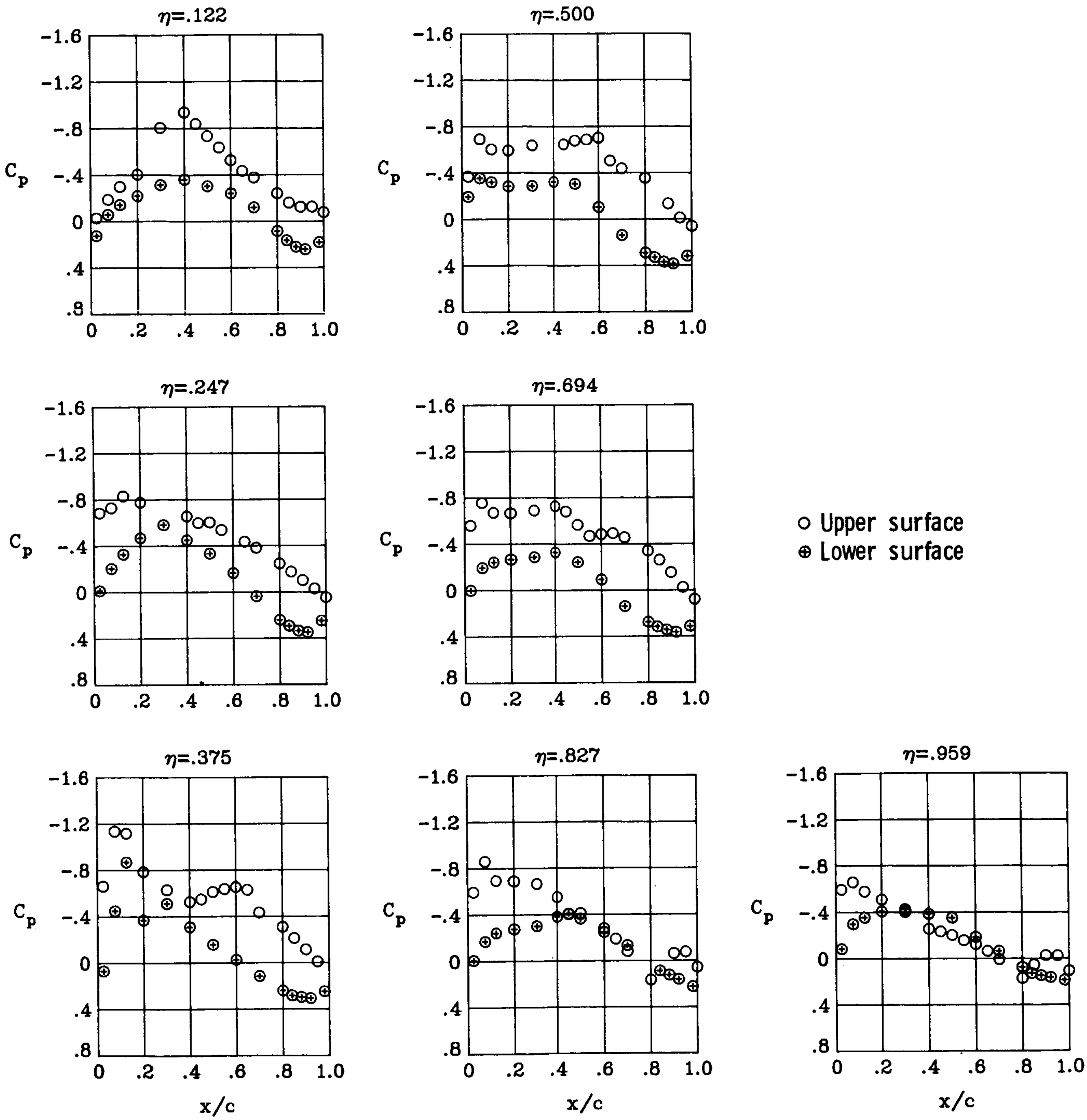

(b) $M_\infty = 0.82;\ \alpha = 2°.$

Figure 45.- Continued.

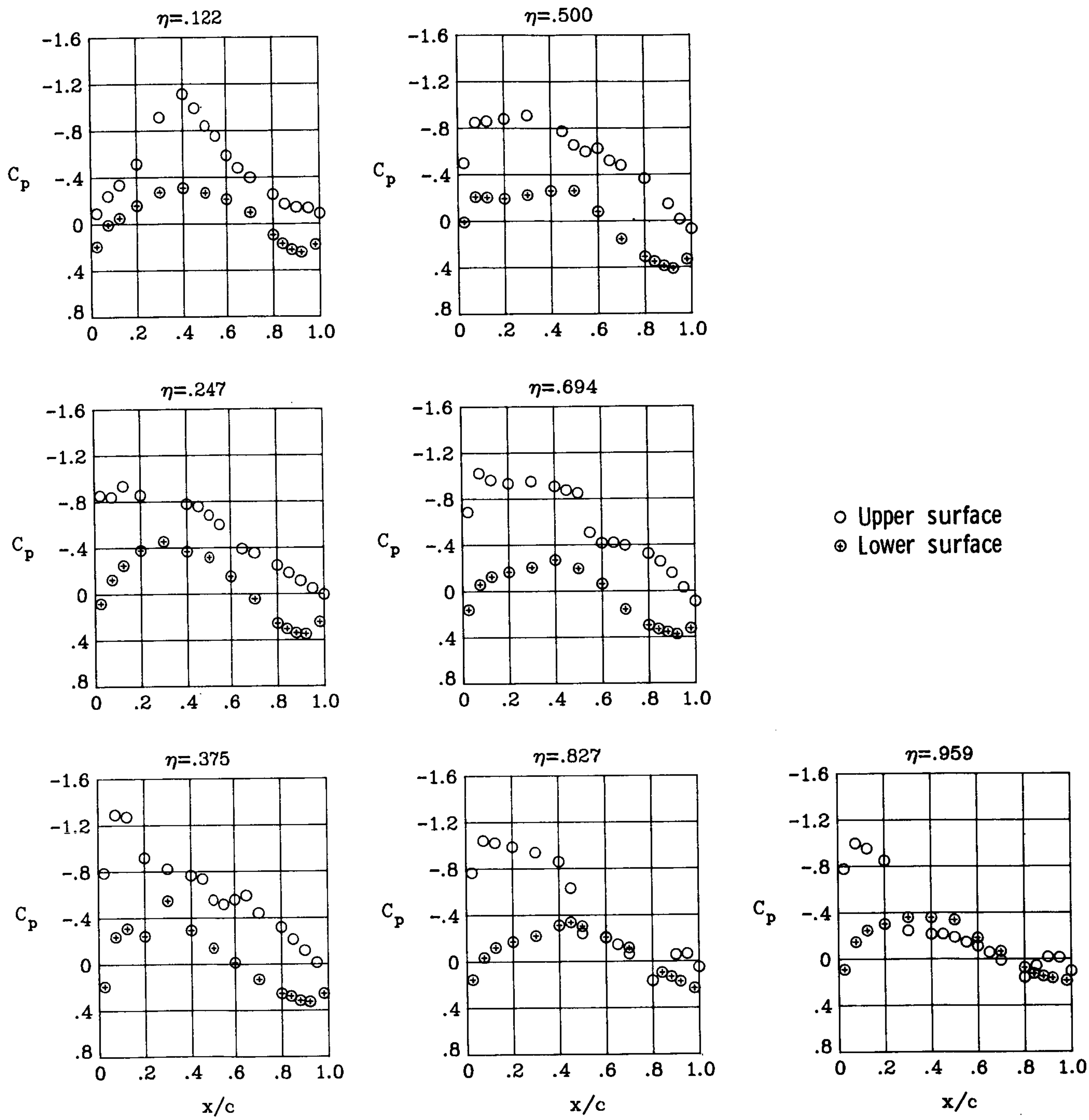

(c) $M_\infty = 0.82$; $\alpha = 3°$.

Figure 45.- Continued.

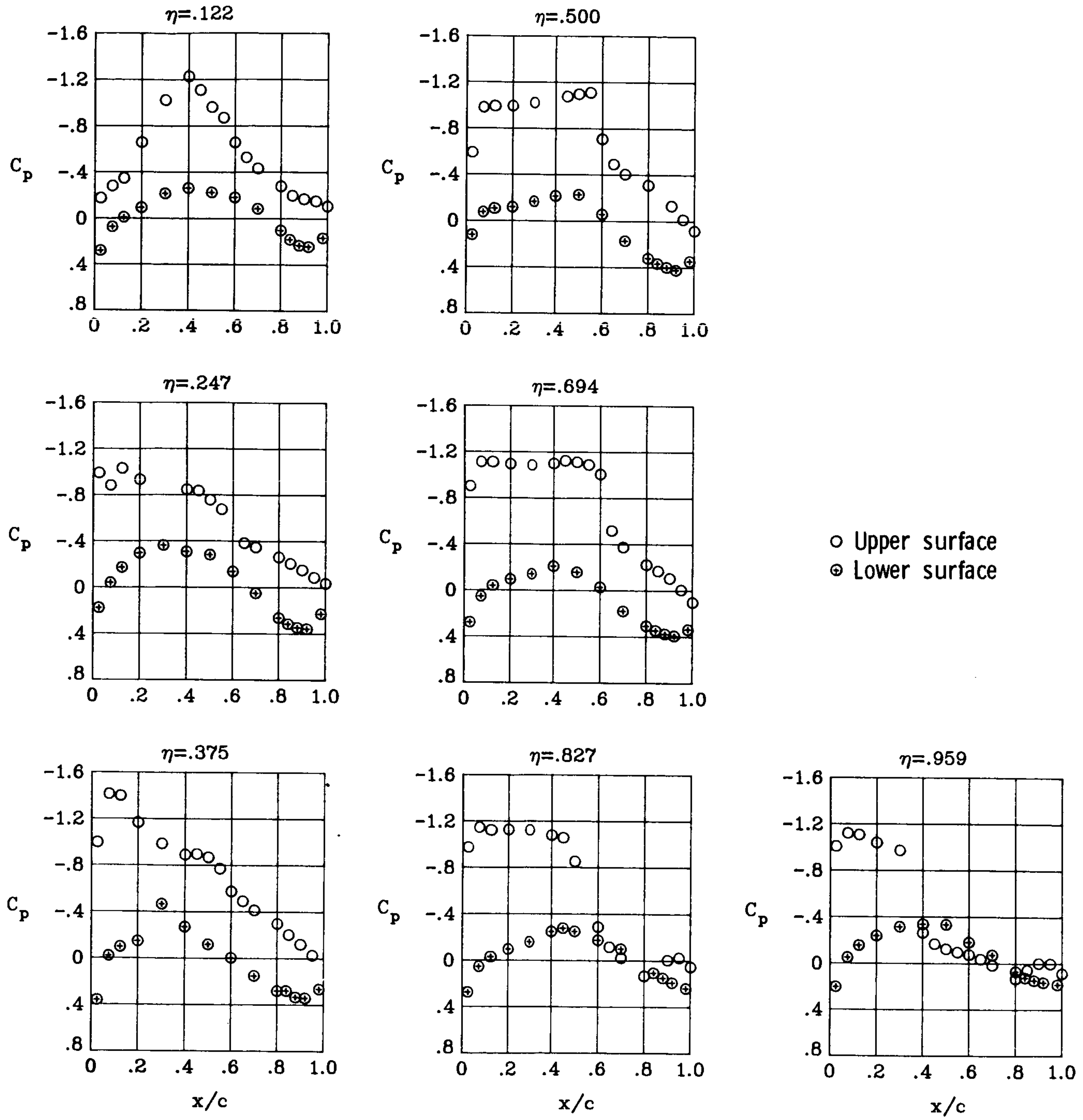

(d) $M_\infty = 0.82$; $\alpha = 4°$.

Figure 45.- Continued.

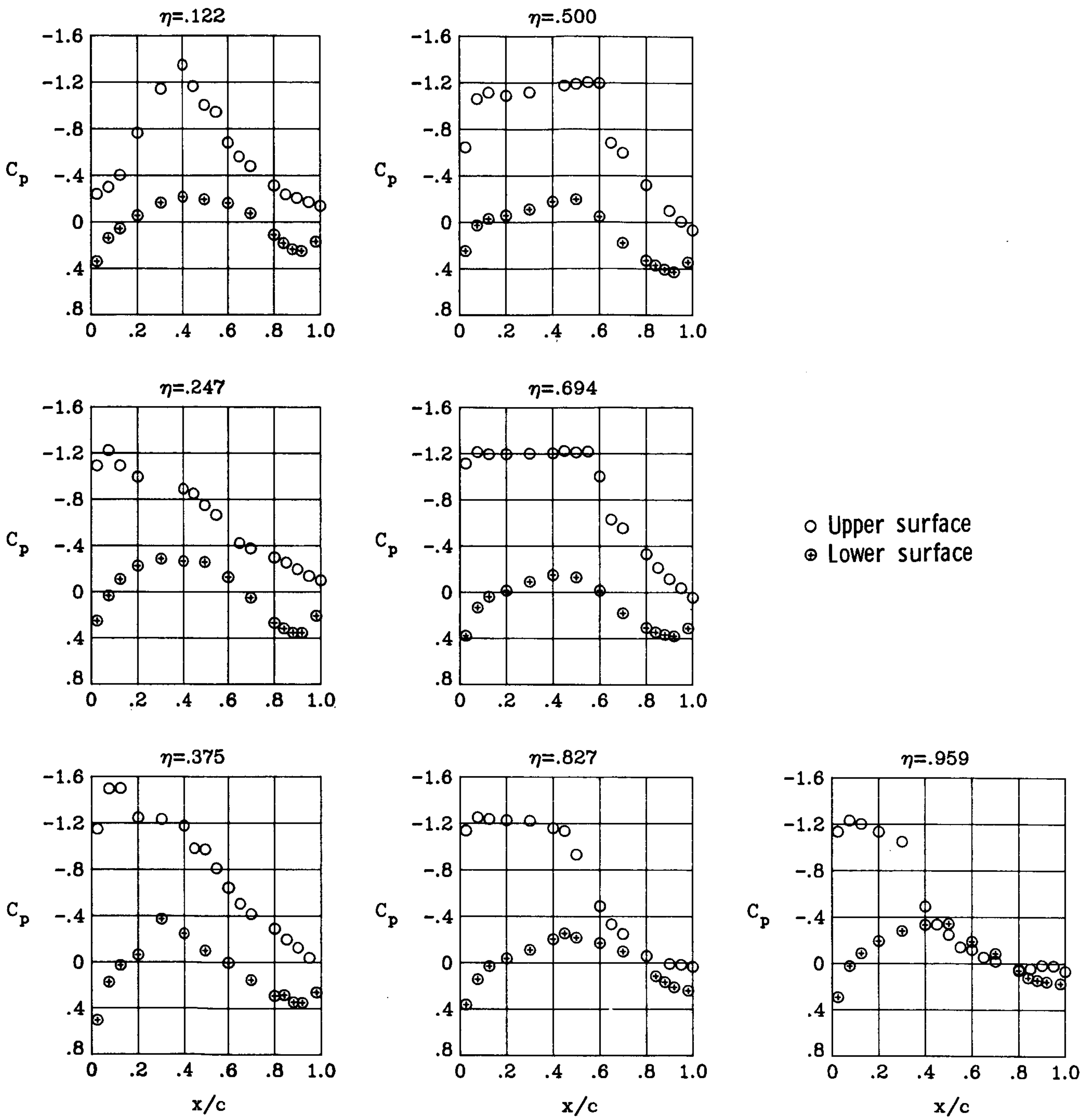

(e) $M_\infty = 0.82$; $\alpha = 5°$.

Figure 45.- Concluded.

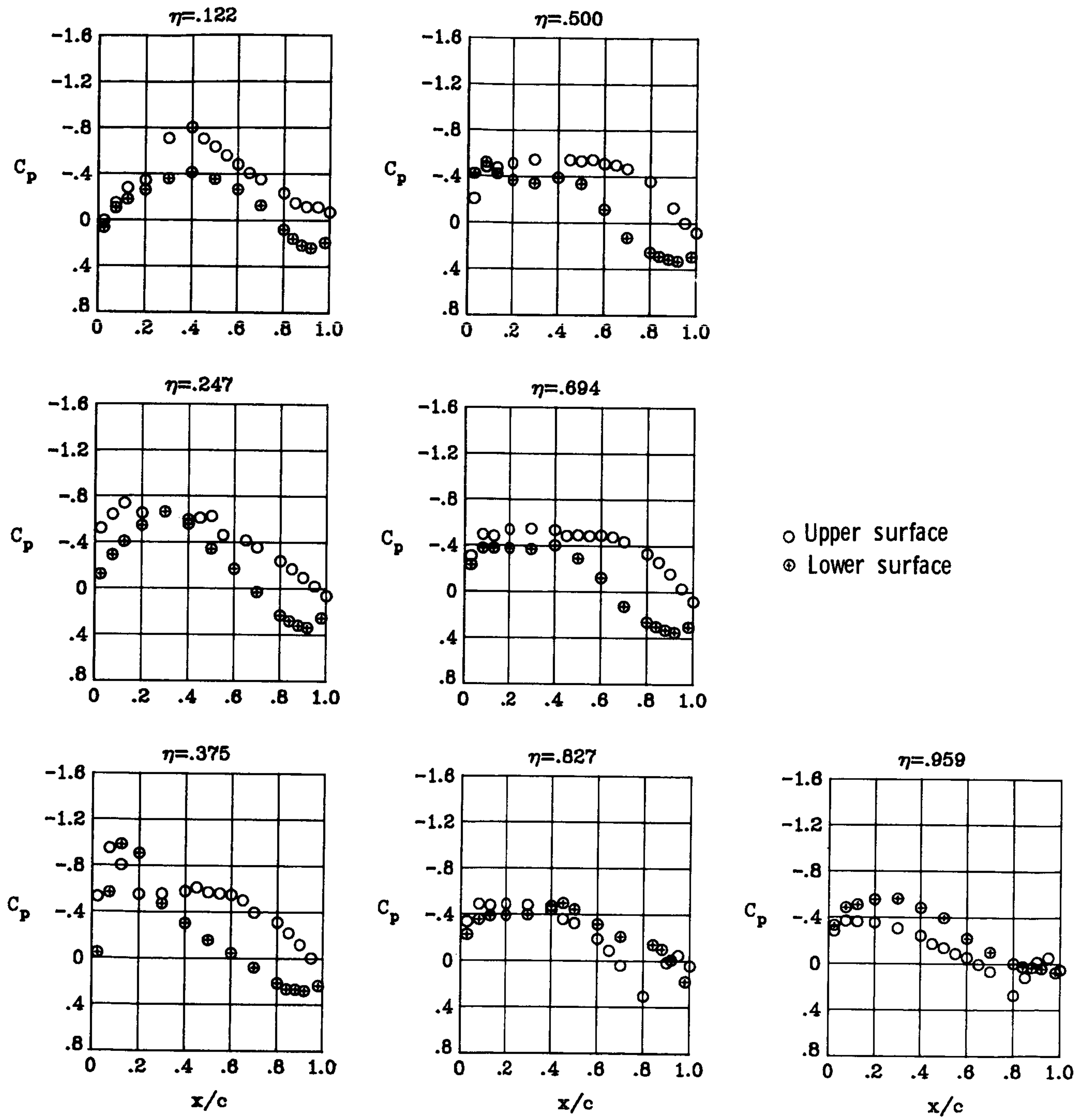

(a) $M_\infty = 0.82$; $\alpha = 1°$.

Figure 46.- Wing chordwise pressure distributions for $\delta a_2 = -17.5°$ at $M_\infty = 0.82$. $\delta a_1 = 0°$.

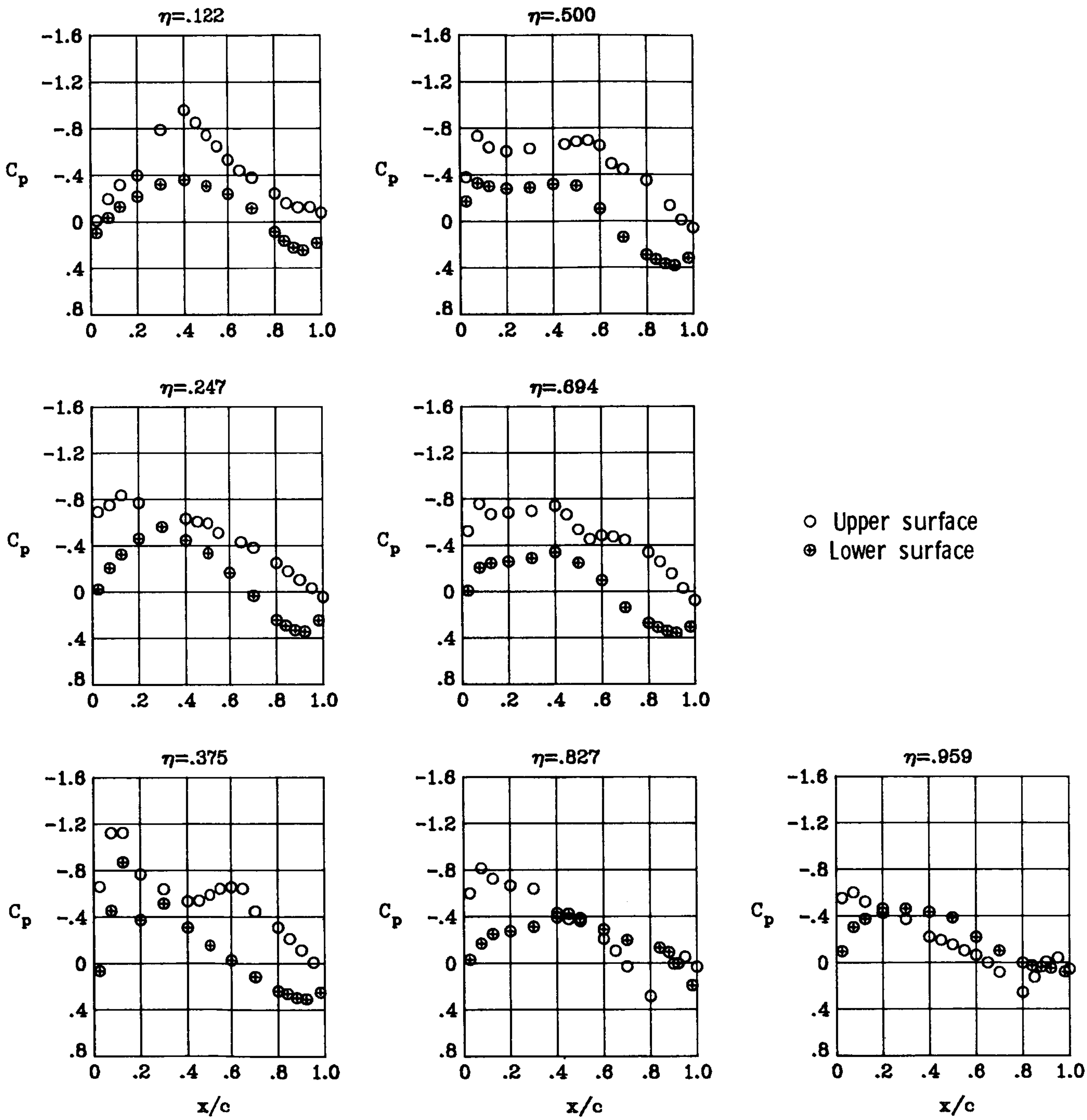

(b) $M_\infty = 0.82$; $\alpha = 2°$.

Figure 46.- Continued.

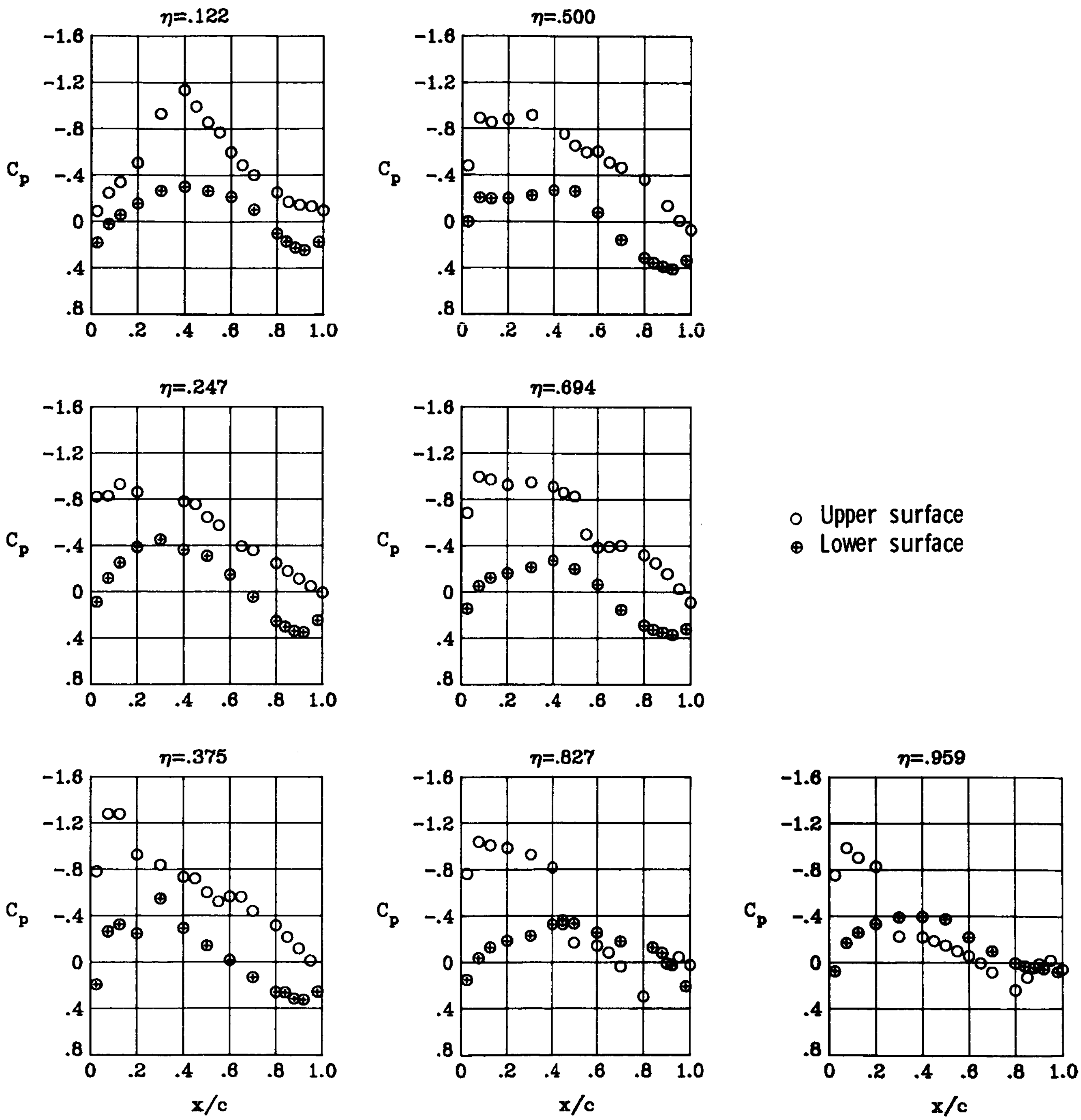

(c) $M_\infty = 0.82$; $\alpha = 3°$.

Figure 46.- Continued.

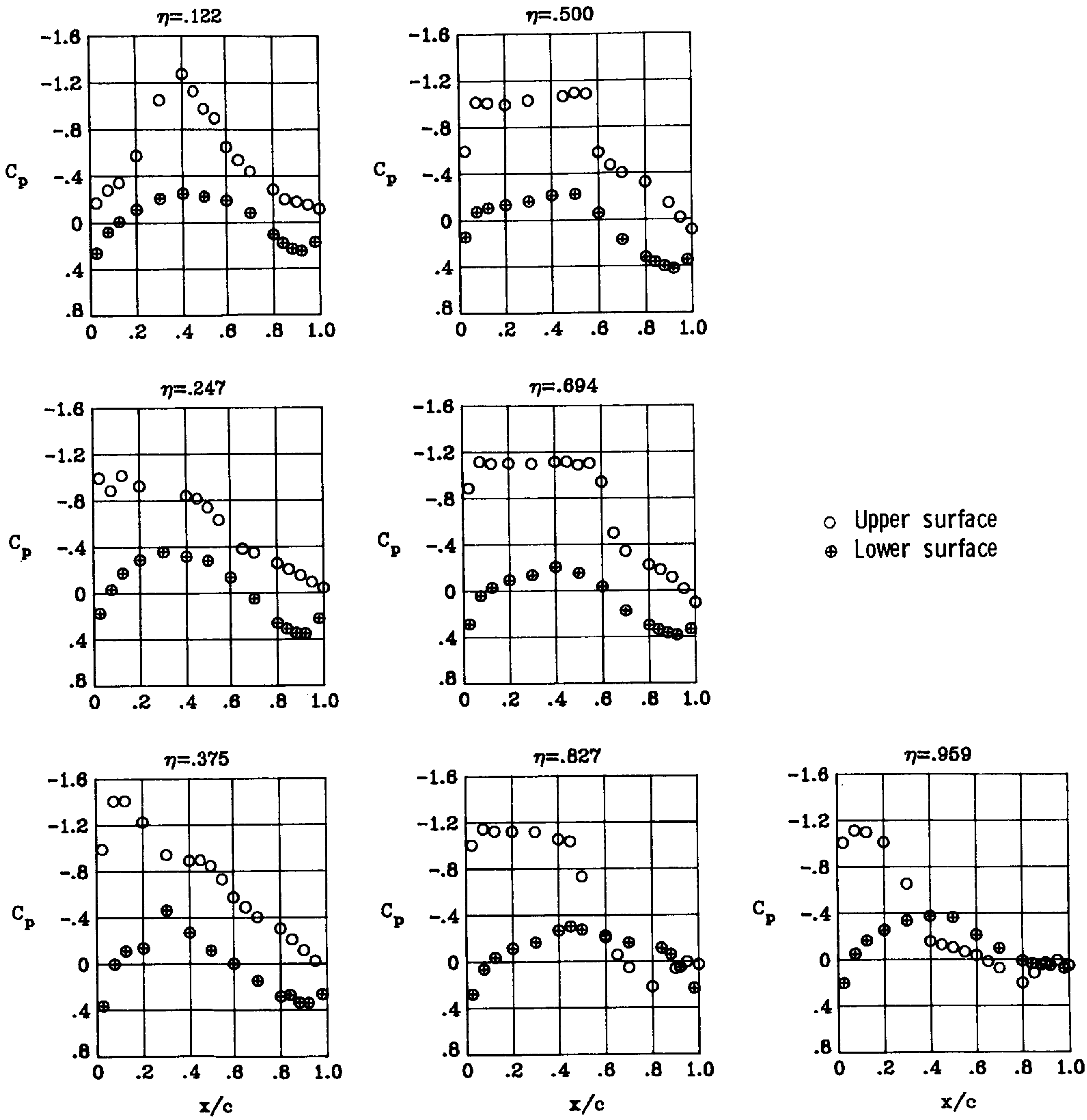

(d) $M_\infty = 0.82$; $\alpha = 4°$.

Figure 46.- Continued.

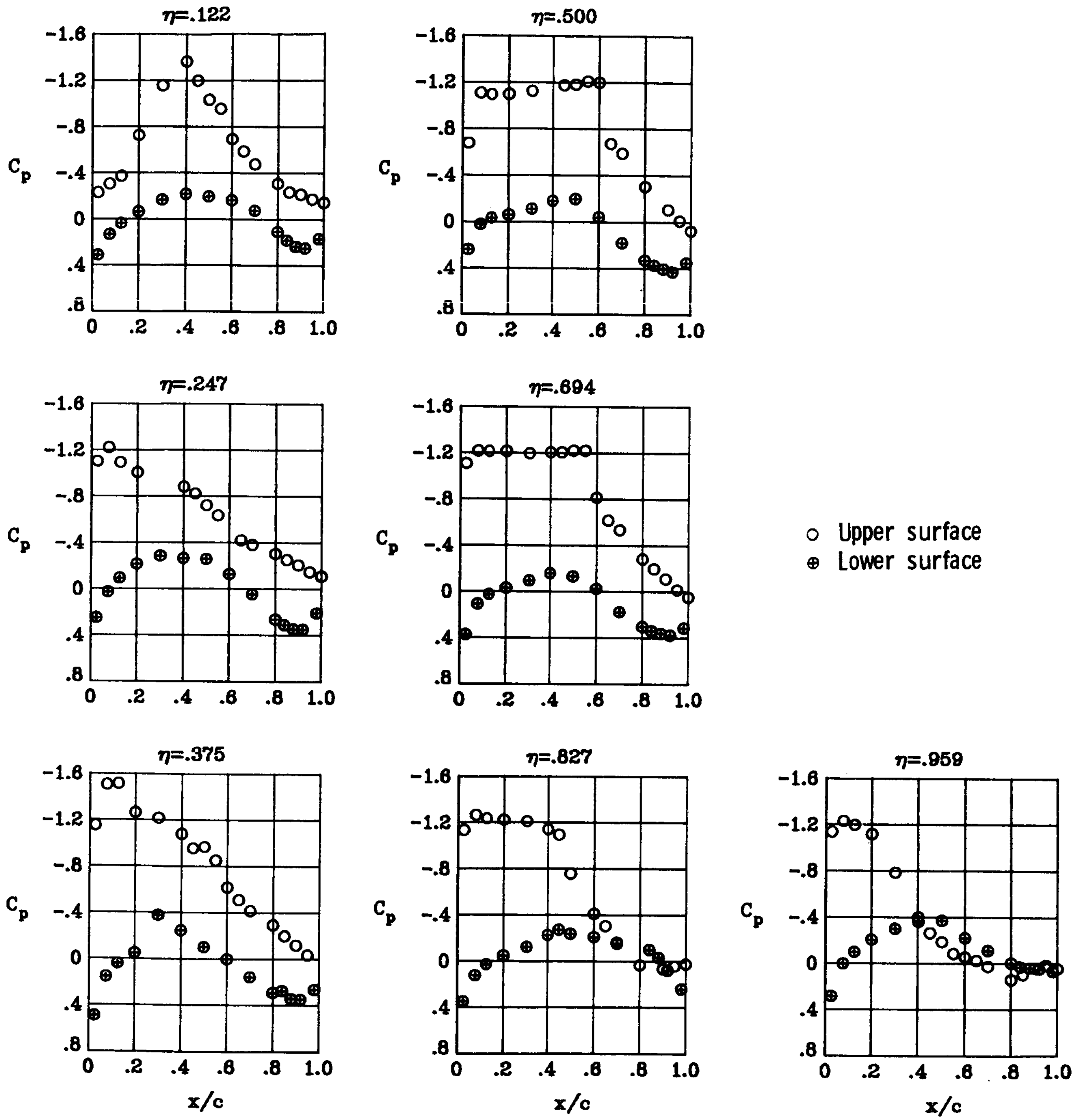

(e) $M_\infty = 0.82$; $\alpha = 5°$.

Figure 46.- Concluded.

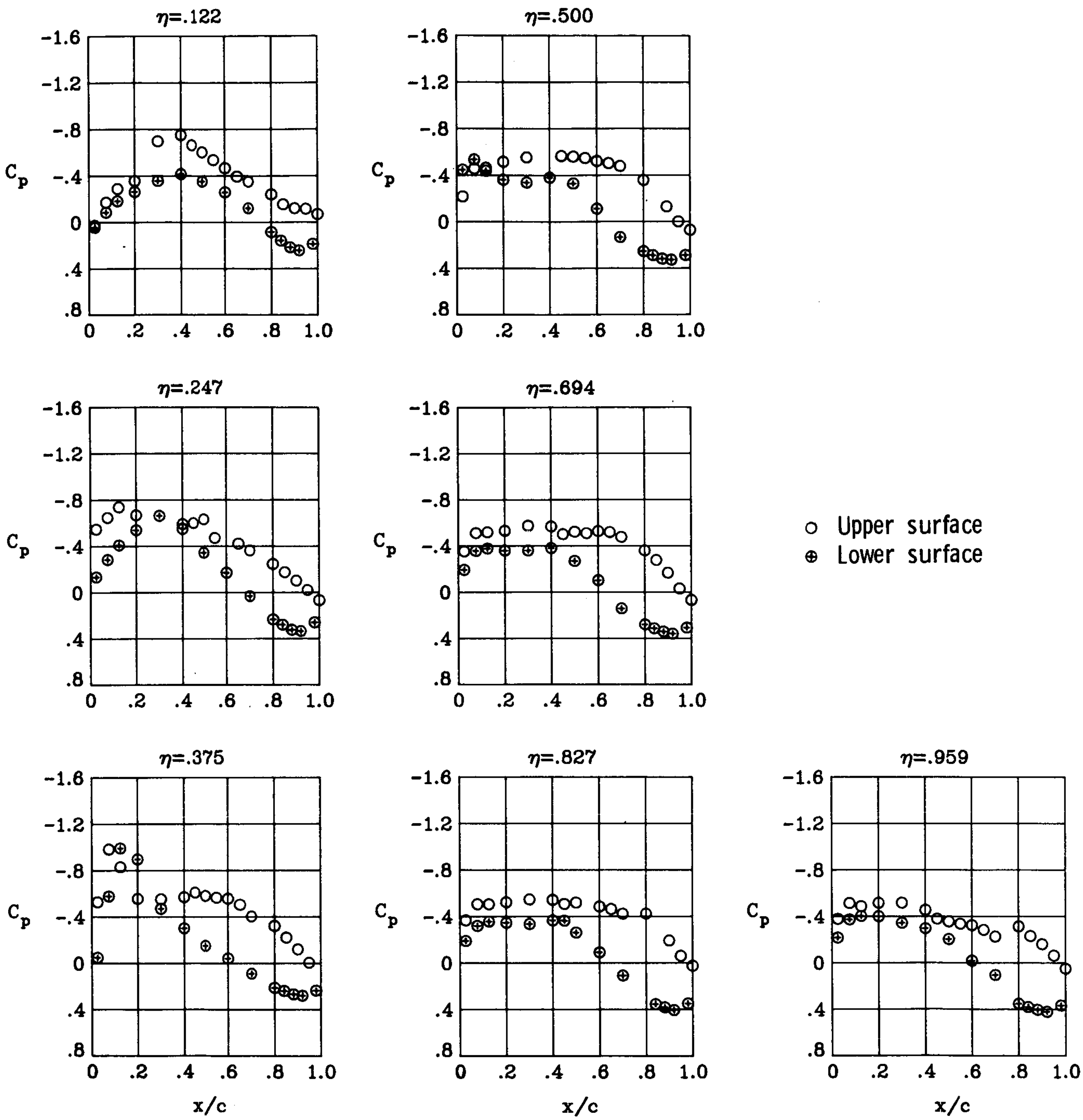

(a) $M_\infty = 0.82$; $\alpha = 1°$.

Figure 47.- Wing chordwise pressure distributions for $\delta a_2 = 2.5°$ at $M_\infty = 0.82$. $\delta a_1 = 0°$.

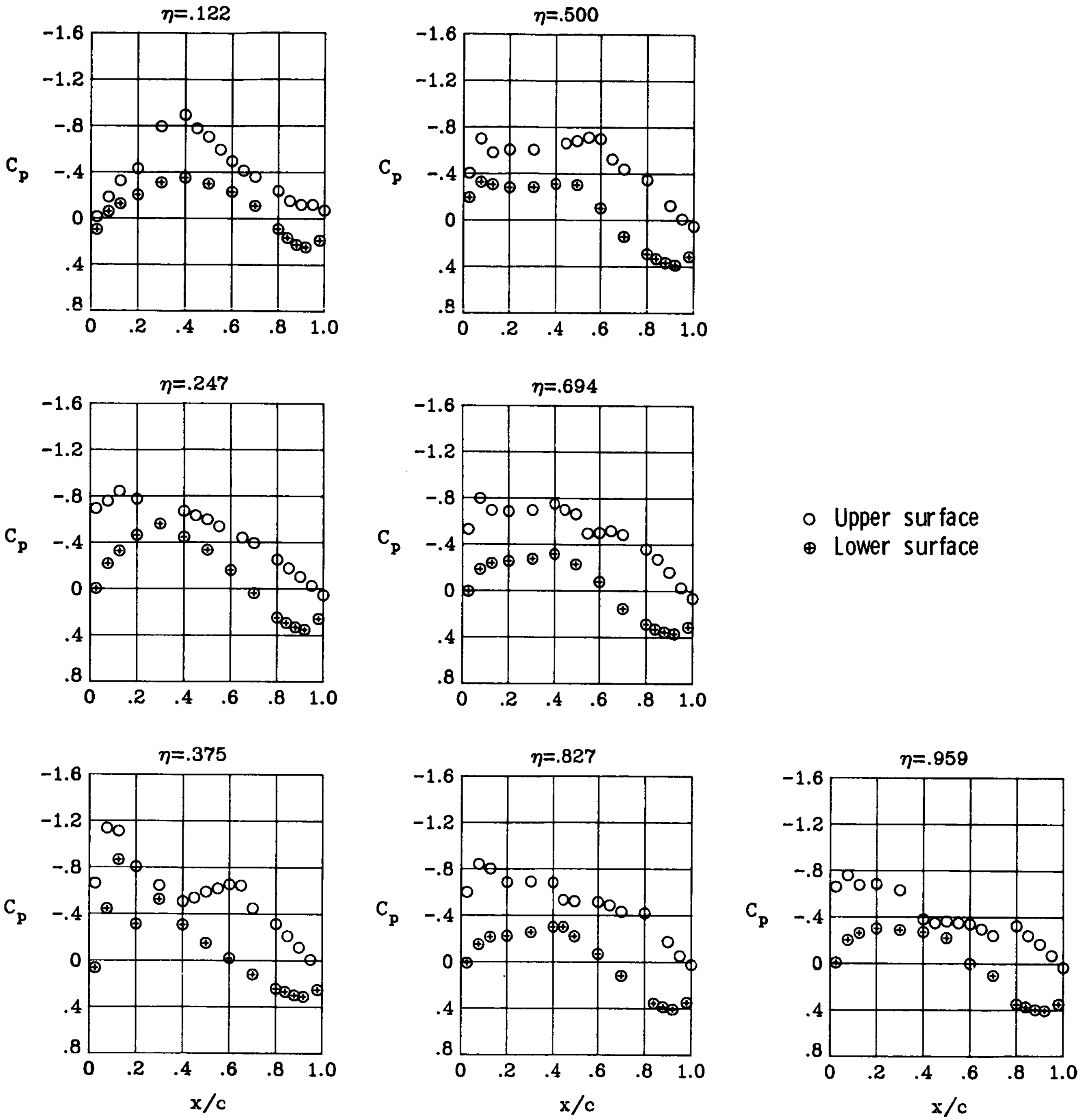

(b) $M_\infty = 0.82$; $\alpha = 2°$.

Figure 47.- Continued.

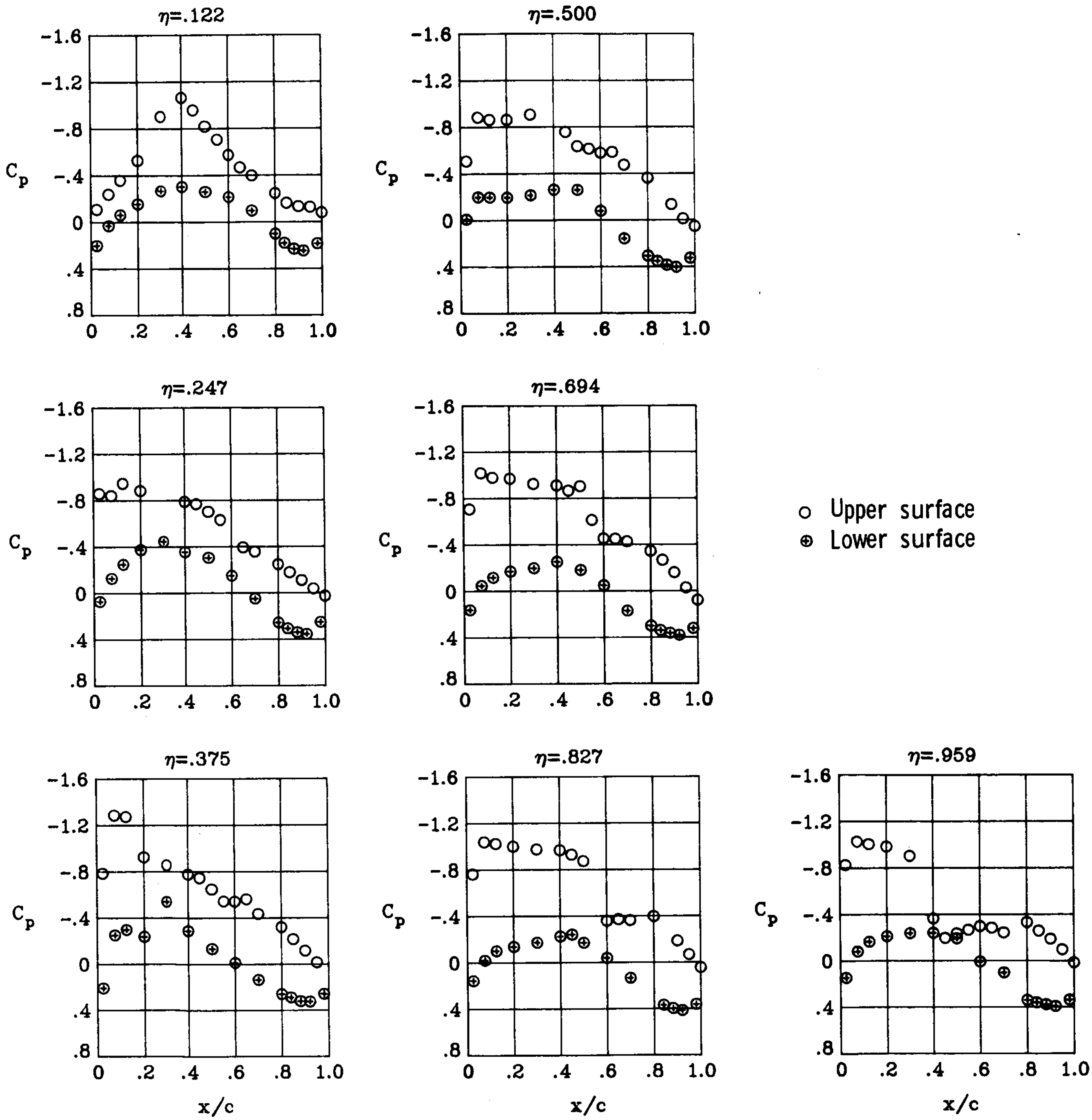

(c) $M_\infty = 0.82$; $\alpha = 3°$.

Figure 47.- Continued.

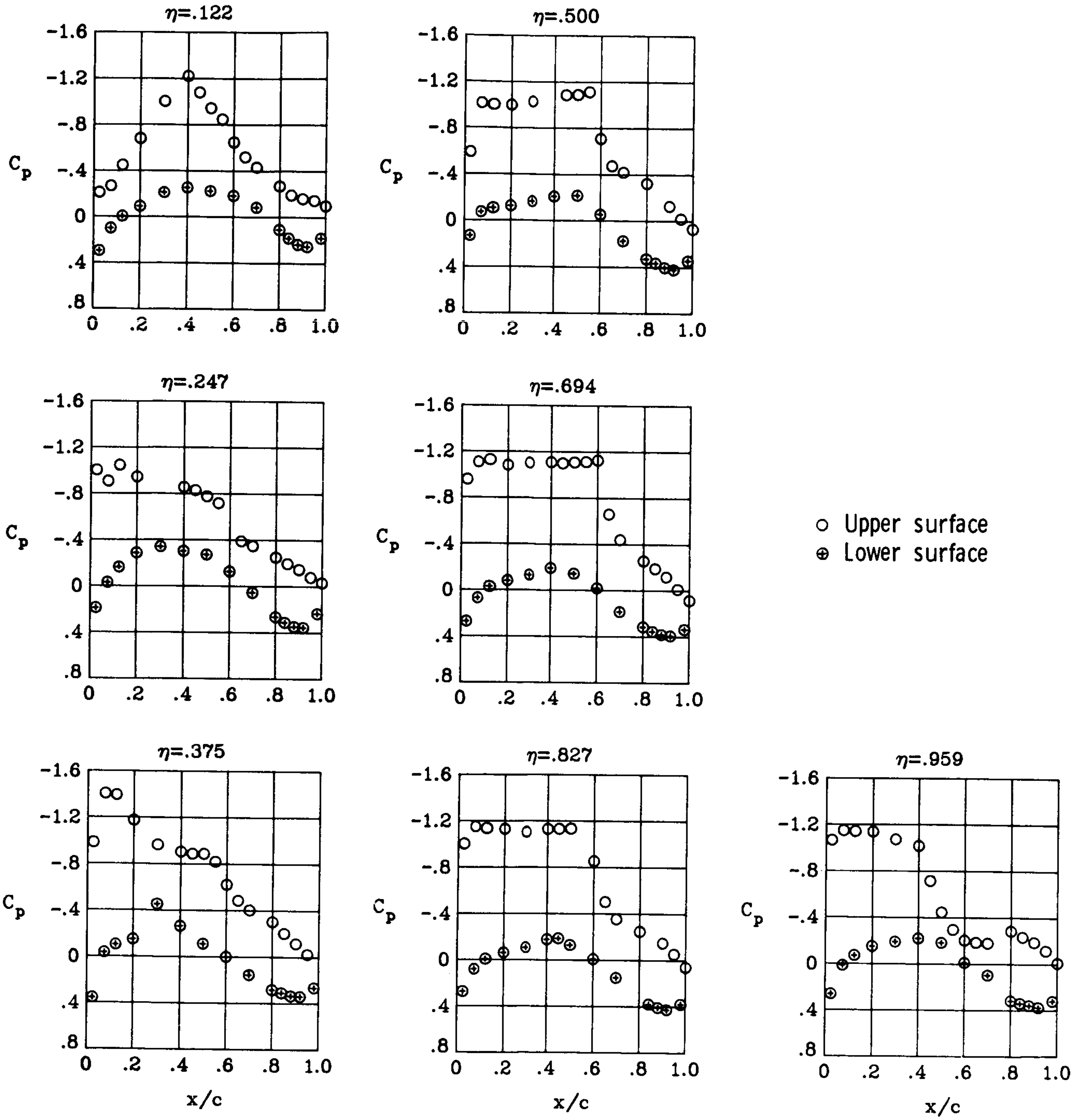

(d) $M_\infty = 0.82$; $\alpha = 4°$.

Figure 47.- Continued.

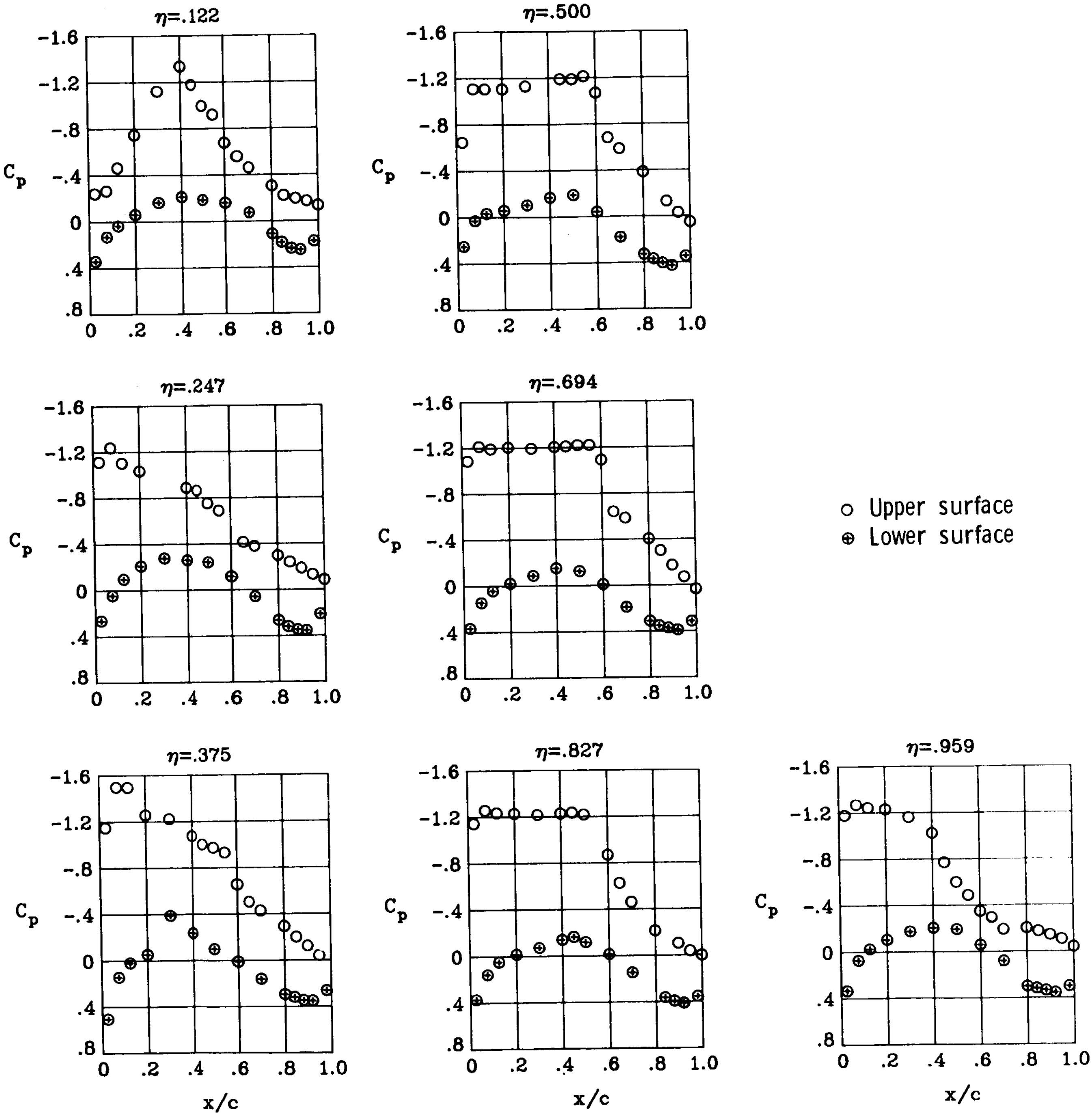

(e) $M_\infty = 0.82$; $\alpha = 5°$.

Figure 47.- Concluded.

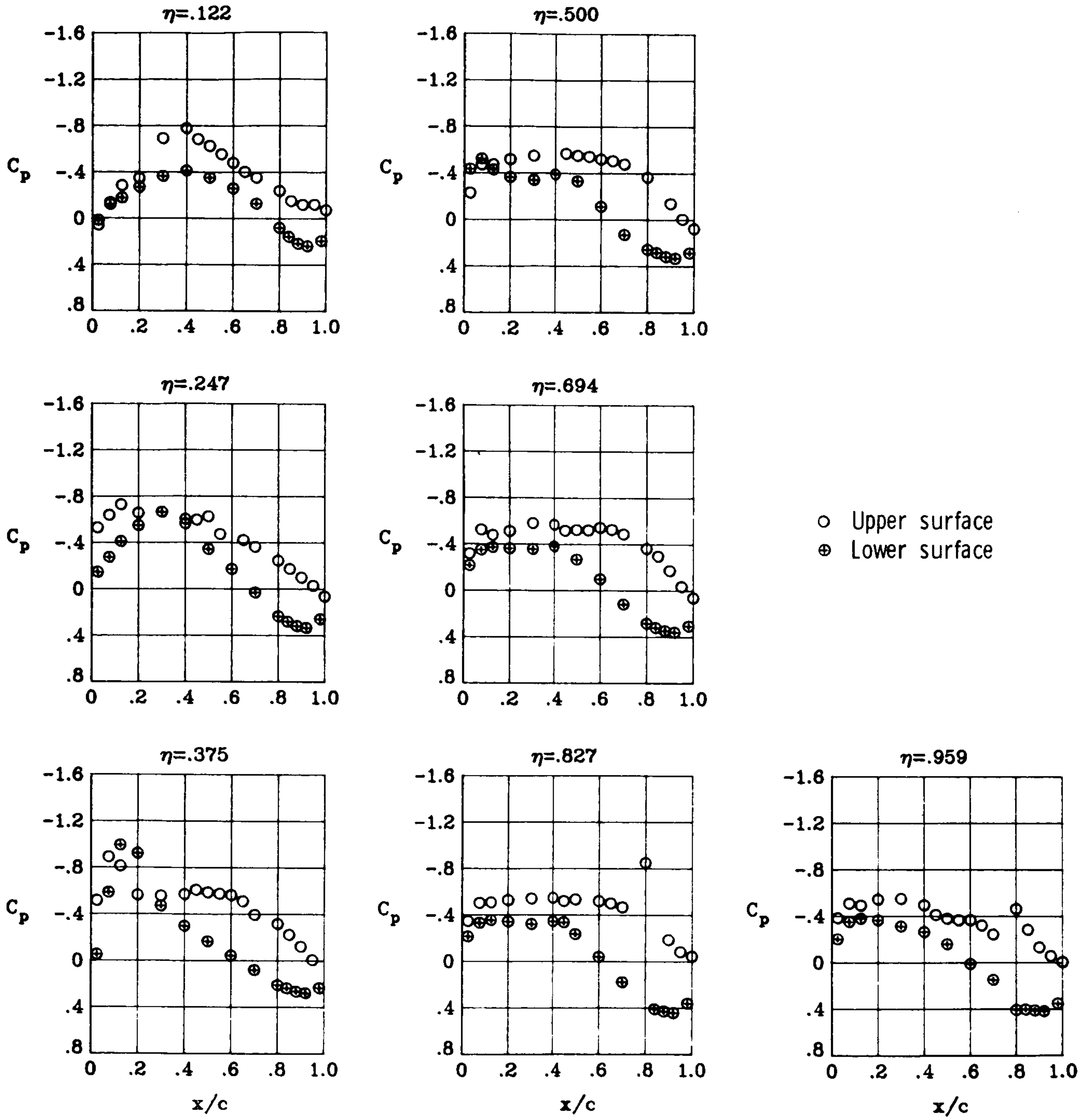

(a) $M_\infty = 0.82$; $\alpha = 1°$.

Figure 48.- Wing chordwise pressure distributions for $\delta a_2 = 7.5°$ at $M_\infty = 0.82$. $\delta a_1 = 0°$.

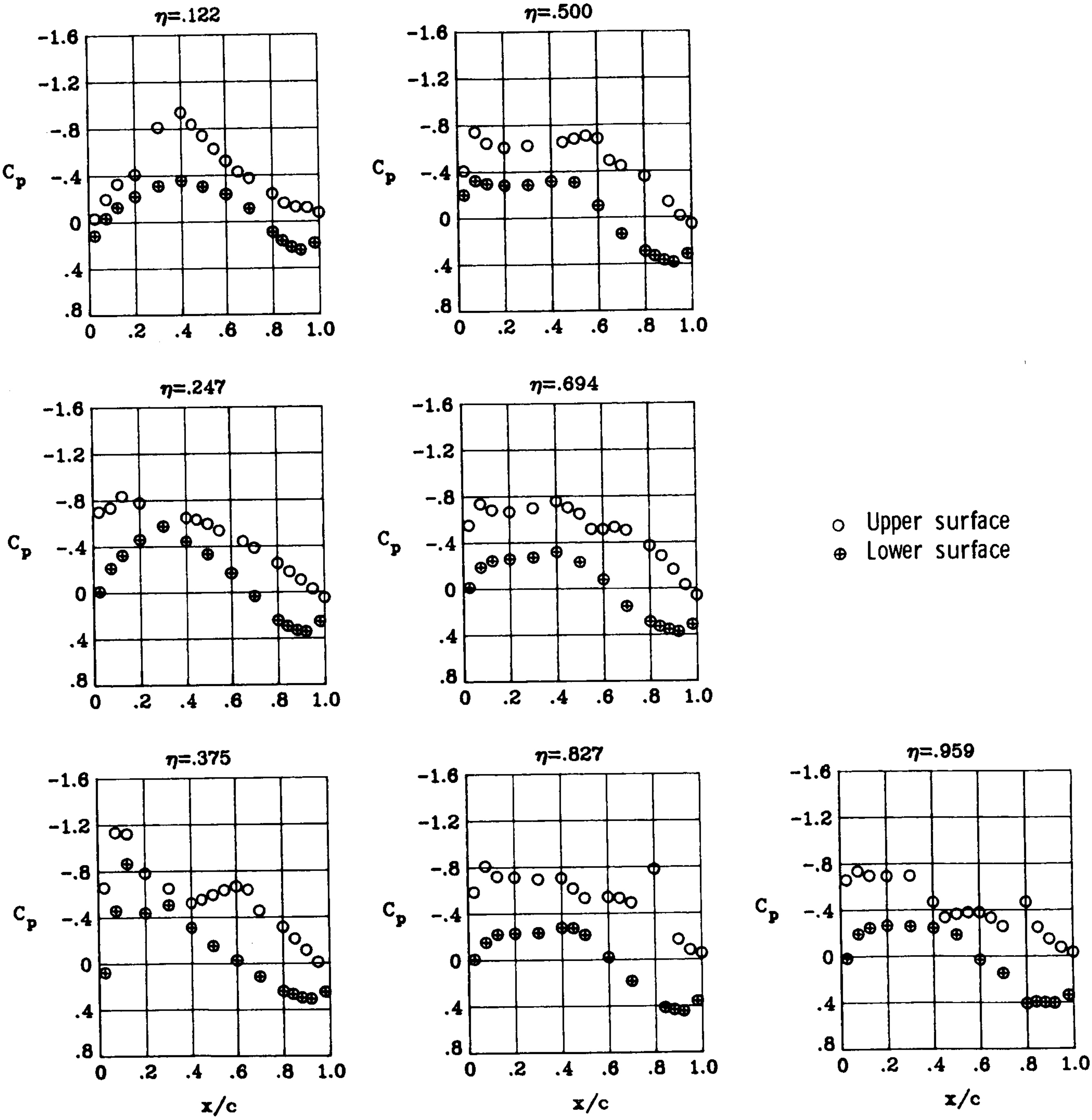

(b) $M_\infty = 0.82$; $\alpha = 2°$.

Figure 48.- Continued.

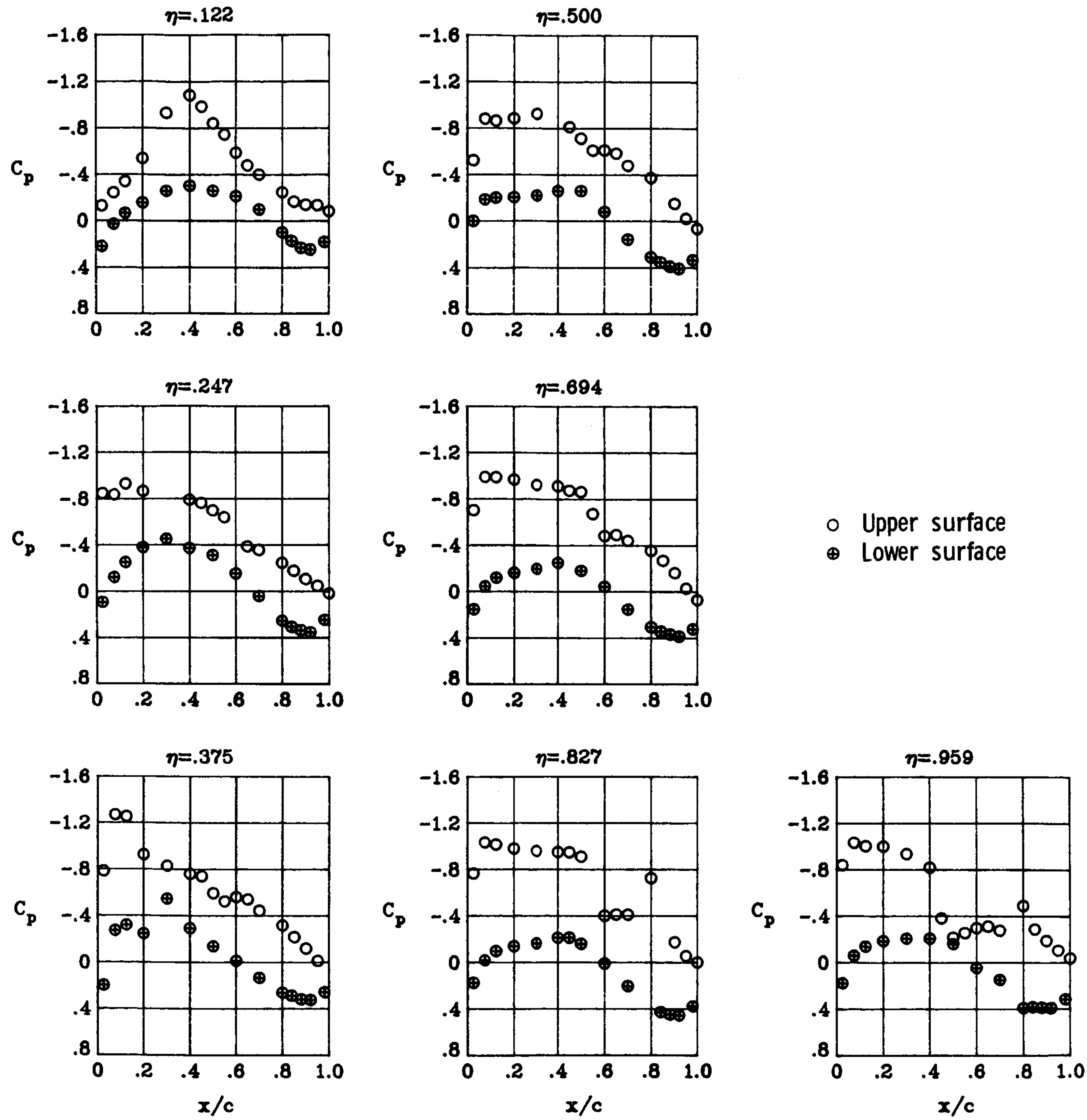

(c) $M_\infty = 0.82$; $\alpha = 3°$.

Figure 48.- Continued.

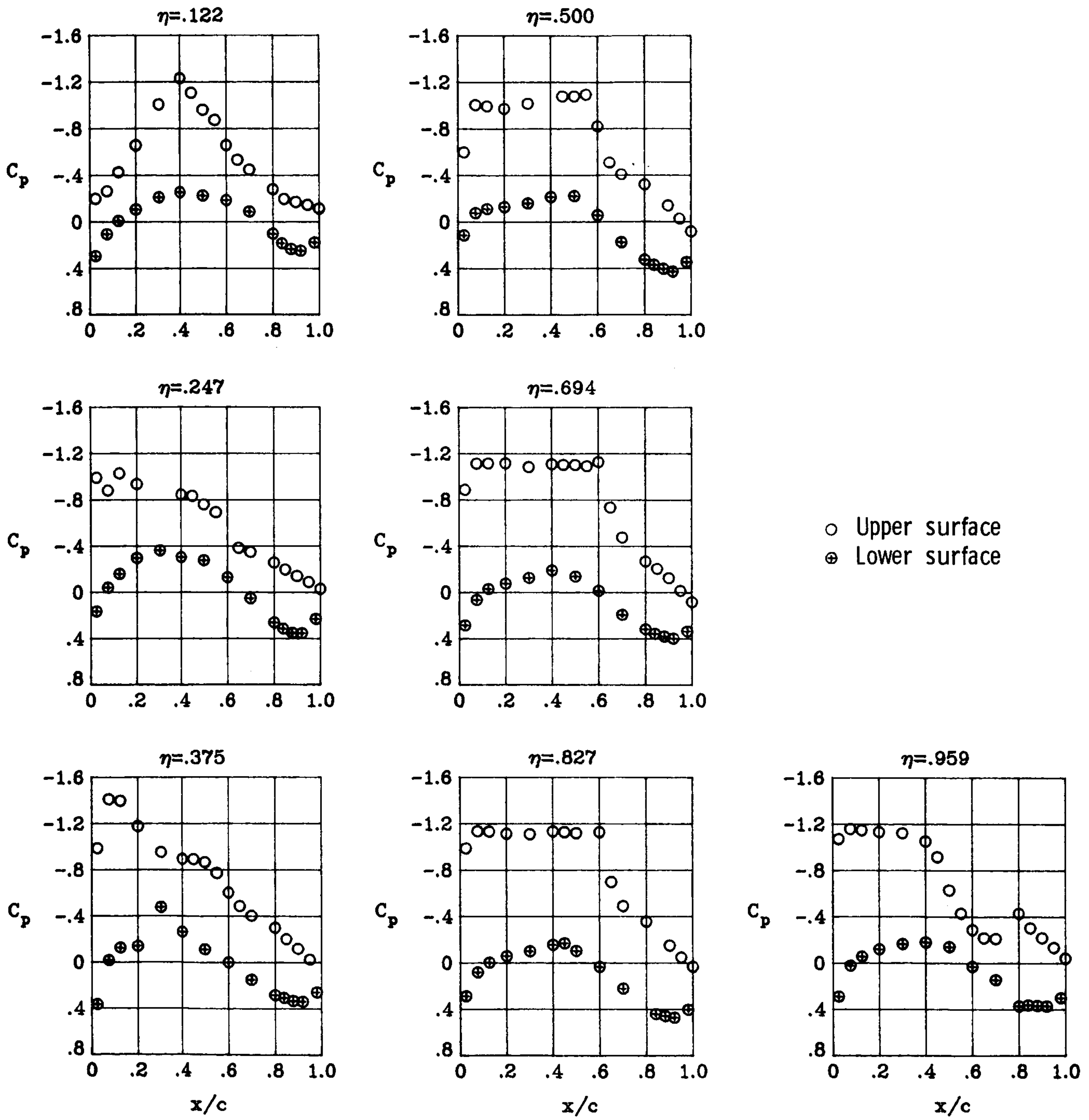

(d) $M_\infty = 0.82$; $\alpha = 4°$.

Figure 48.- Continued.

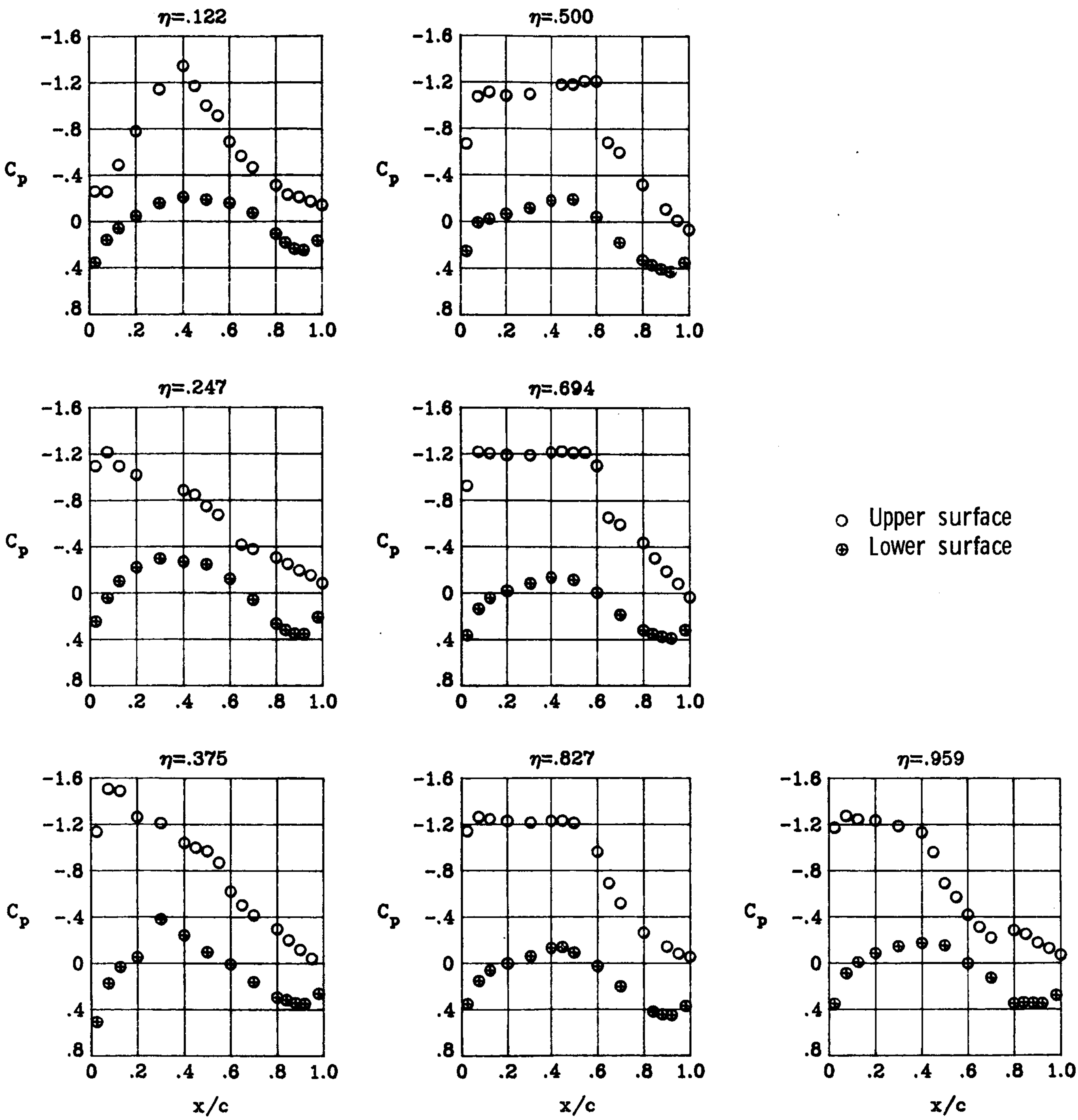

(e) $M_\infty = 0.82$; $\alpha = 5°$.

Figure 48.- Concluded.

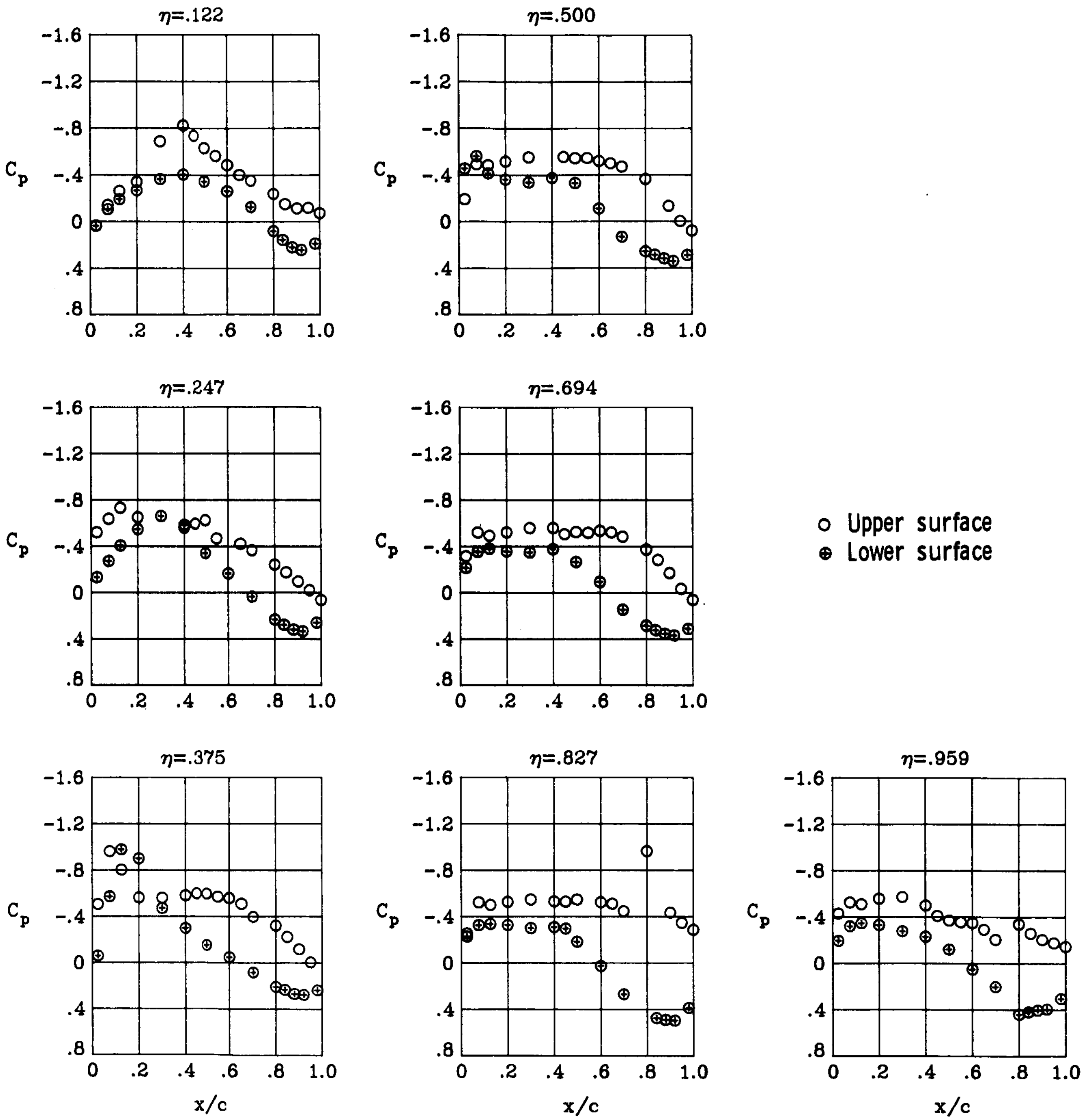

(a) $M_\infty = 0.82$; $\alpha = 1°$.

Figure 49.- Wing chordwise pressure distributions for $\delta a_2 = 12.5°$ at $M_\infty = 0.82$. $\delta a_1 = 0°$.

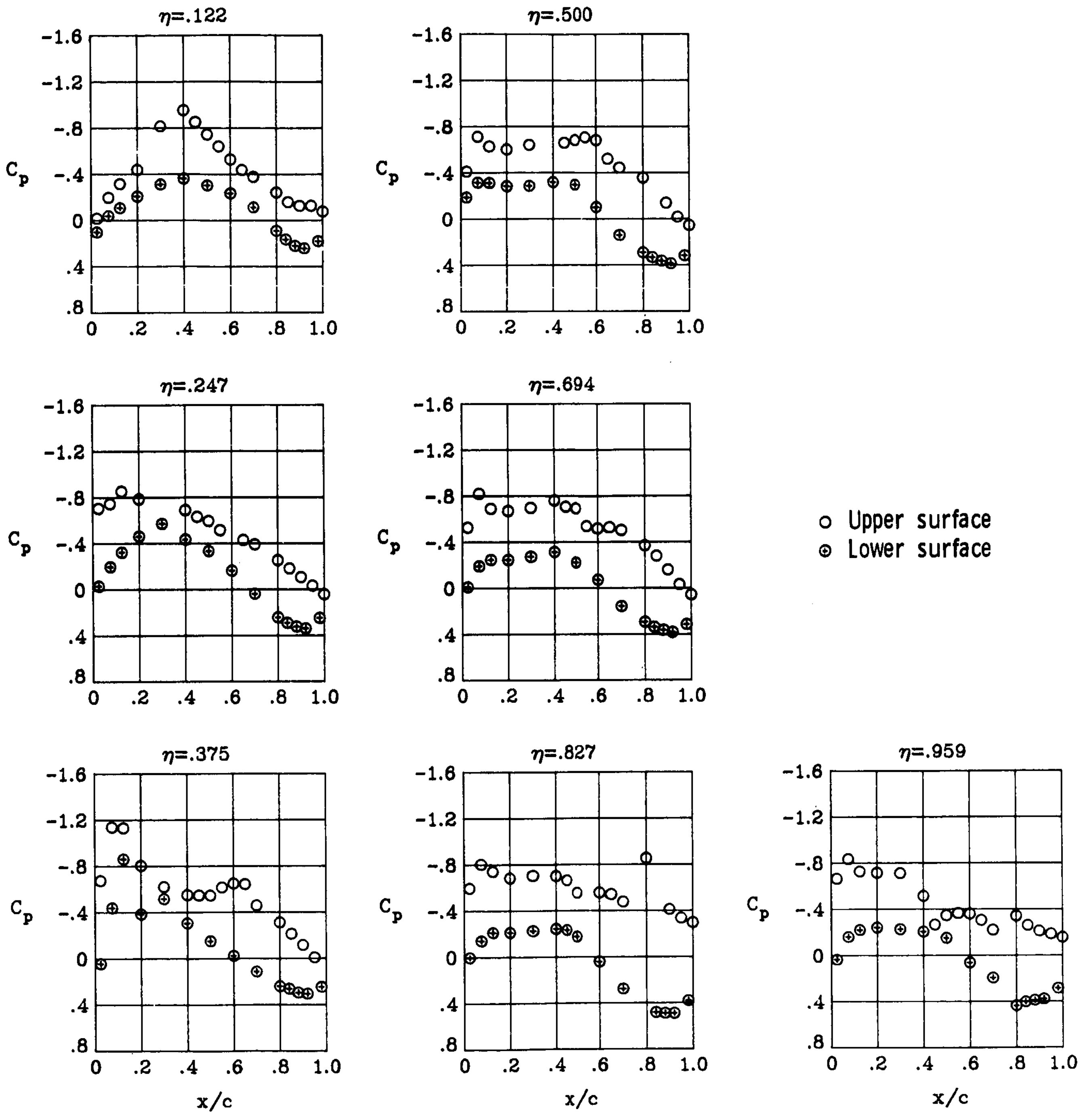

(b) $M_\infty = 0.82$; $\alpha = 2°$.

Figure 49.- Continued.

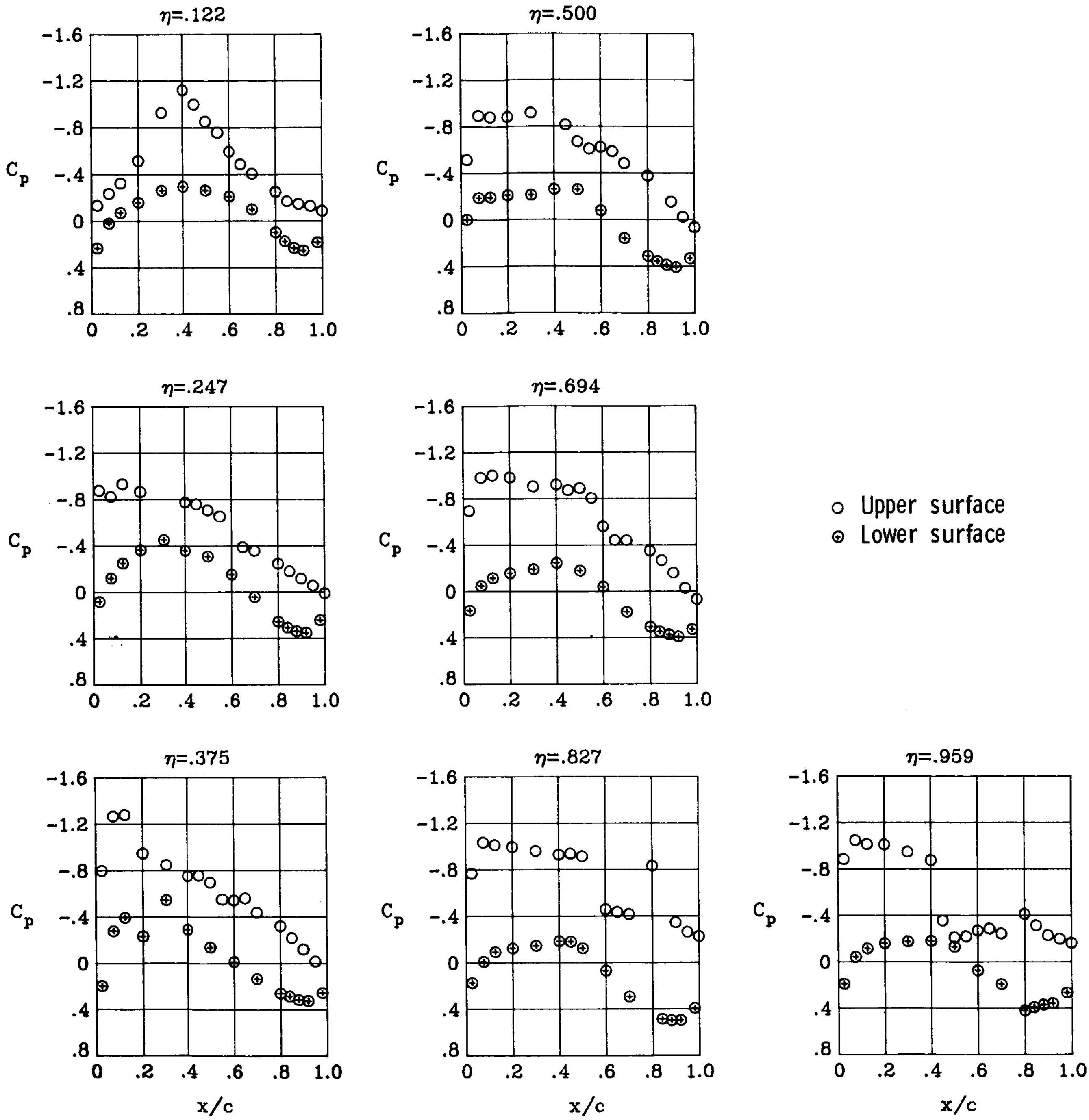

(c) $M_\infty = 0.82$; $\alpha = 3°$.

Figure 49.- Continued.

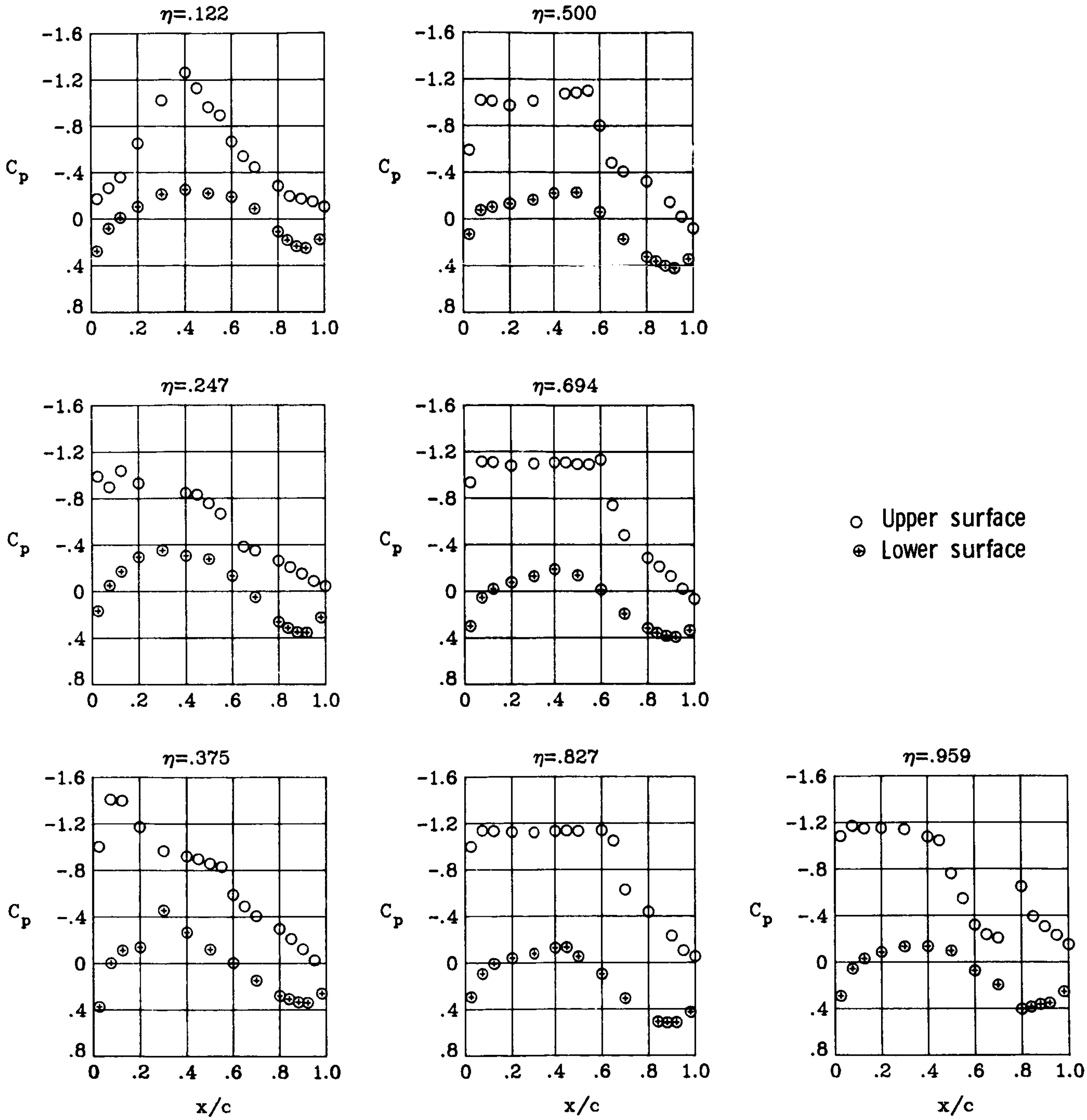

(d) $M_\infty = 0.82$; $\alpha = 4°$.

Figure 49.- Continued.

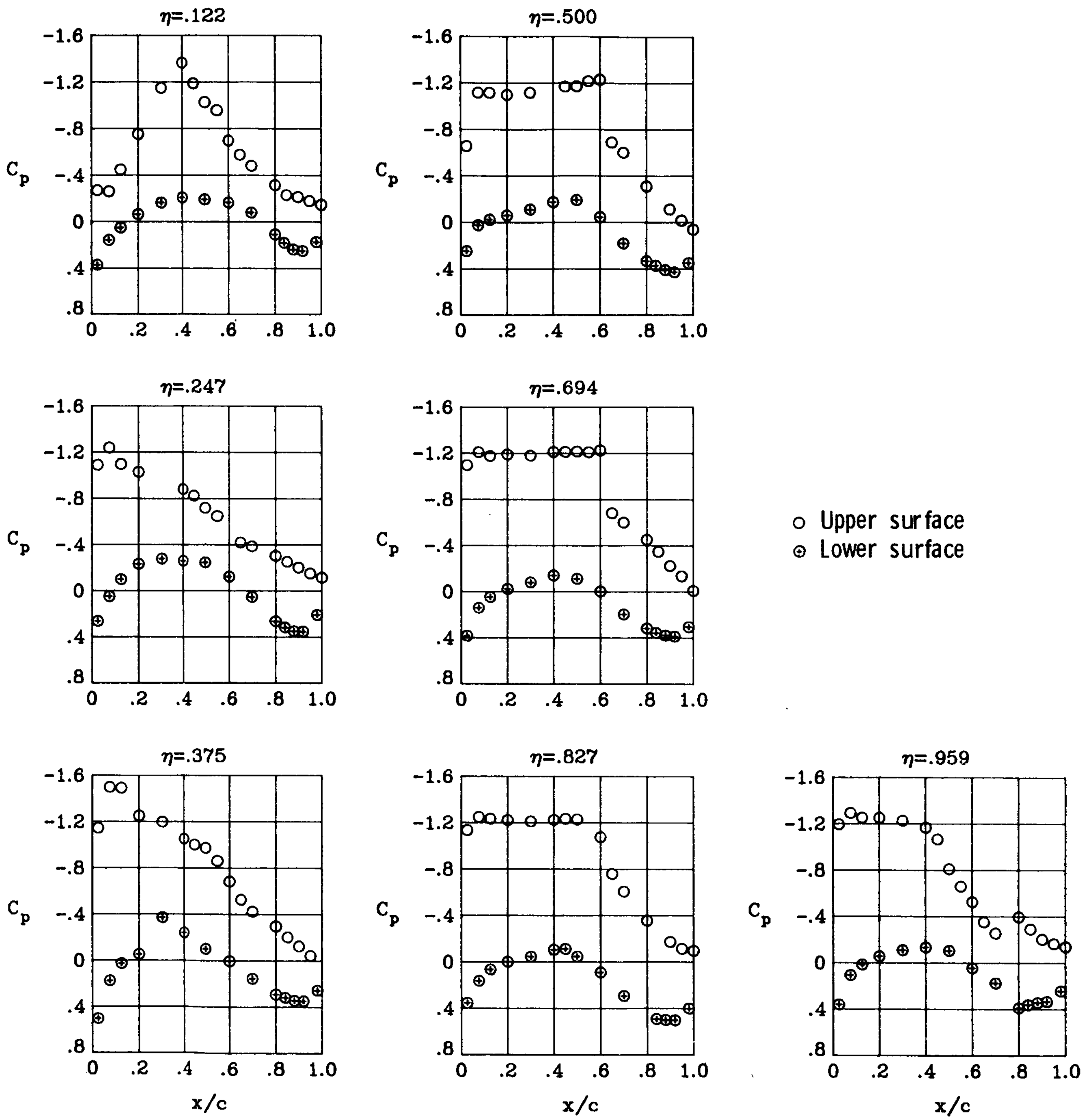

(e) $M_\infty = 0.82$; $\alpha = 5°$.

Figure 49.- Concluded.

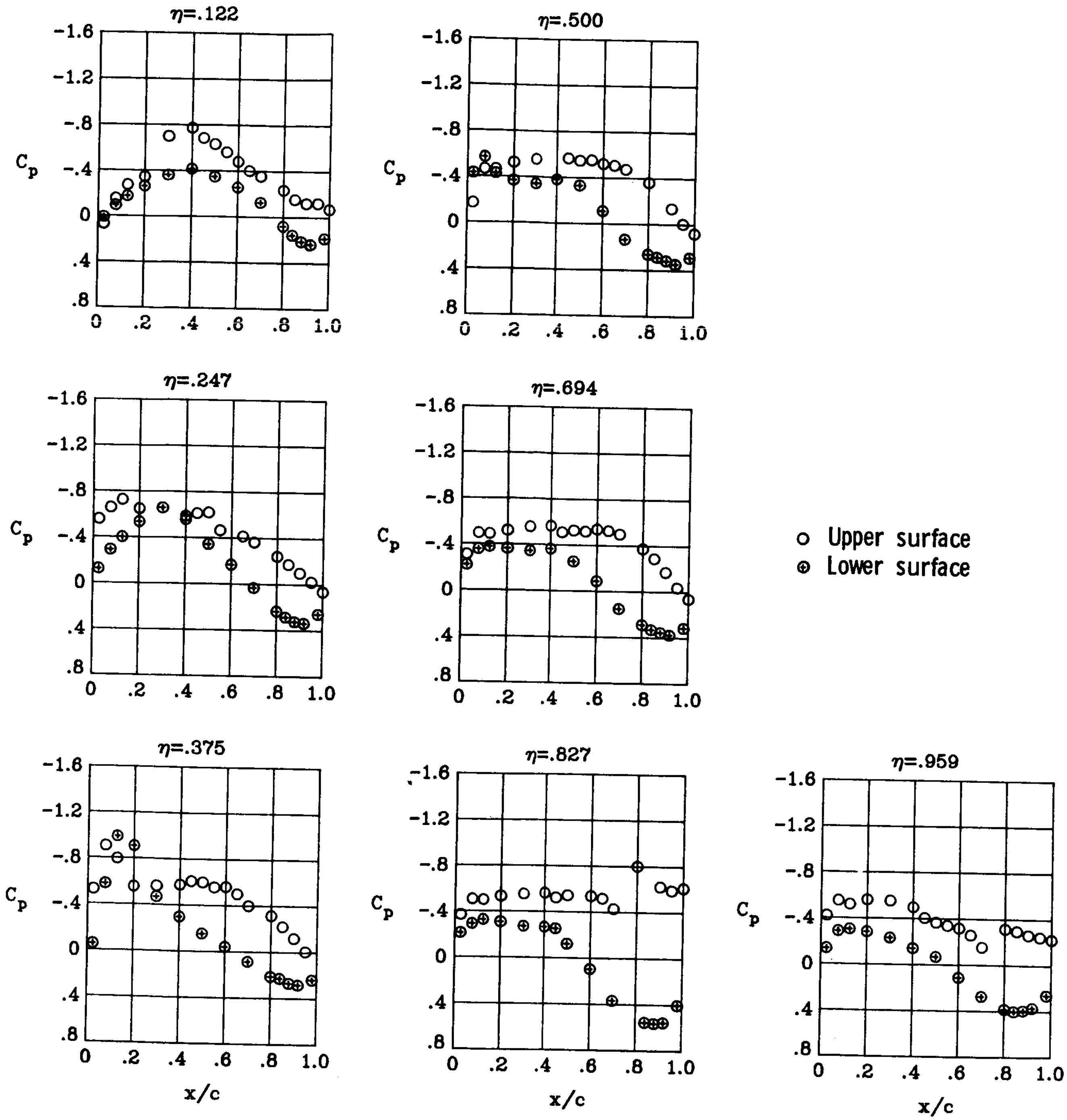

(a) $M_\infty = 0.82$; $\alpha = 1°$.

Figure 50.- Wing chordwise pressure distributions for $\delta a_2 = 17.5°$ at $M_\infty = 0.82$. $\delta a_1 = 0°$.

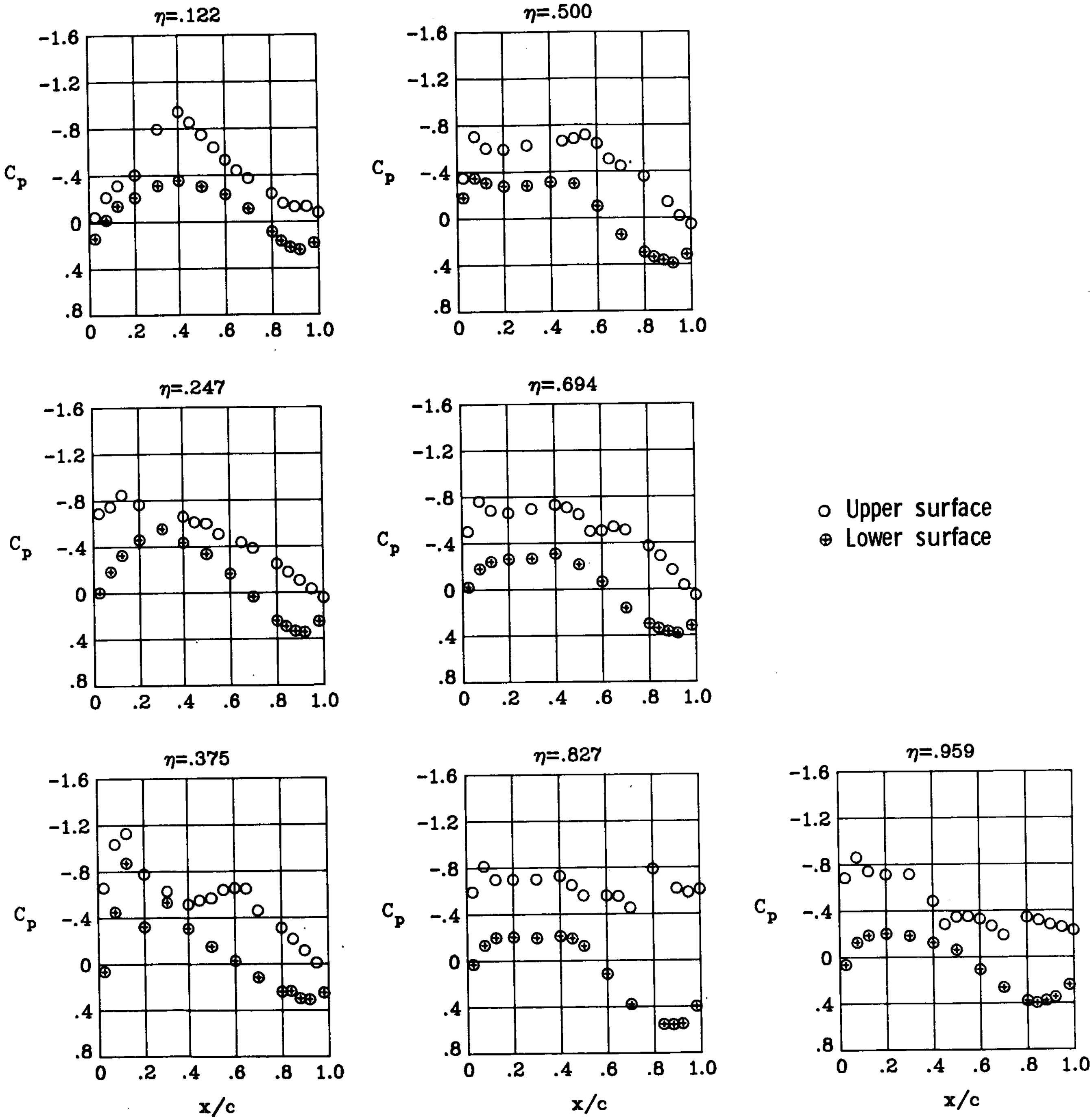

(b) $M_\infty = 0.82$; $\alpha = 2°$.

Figure 50.- Continued.

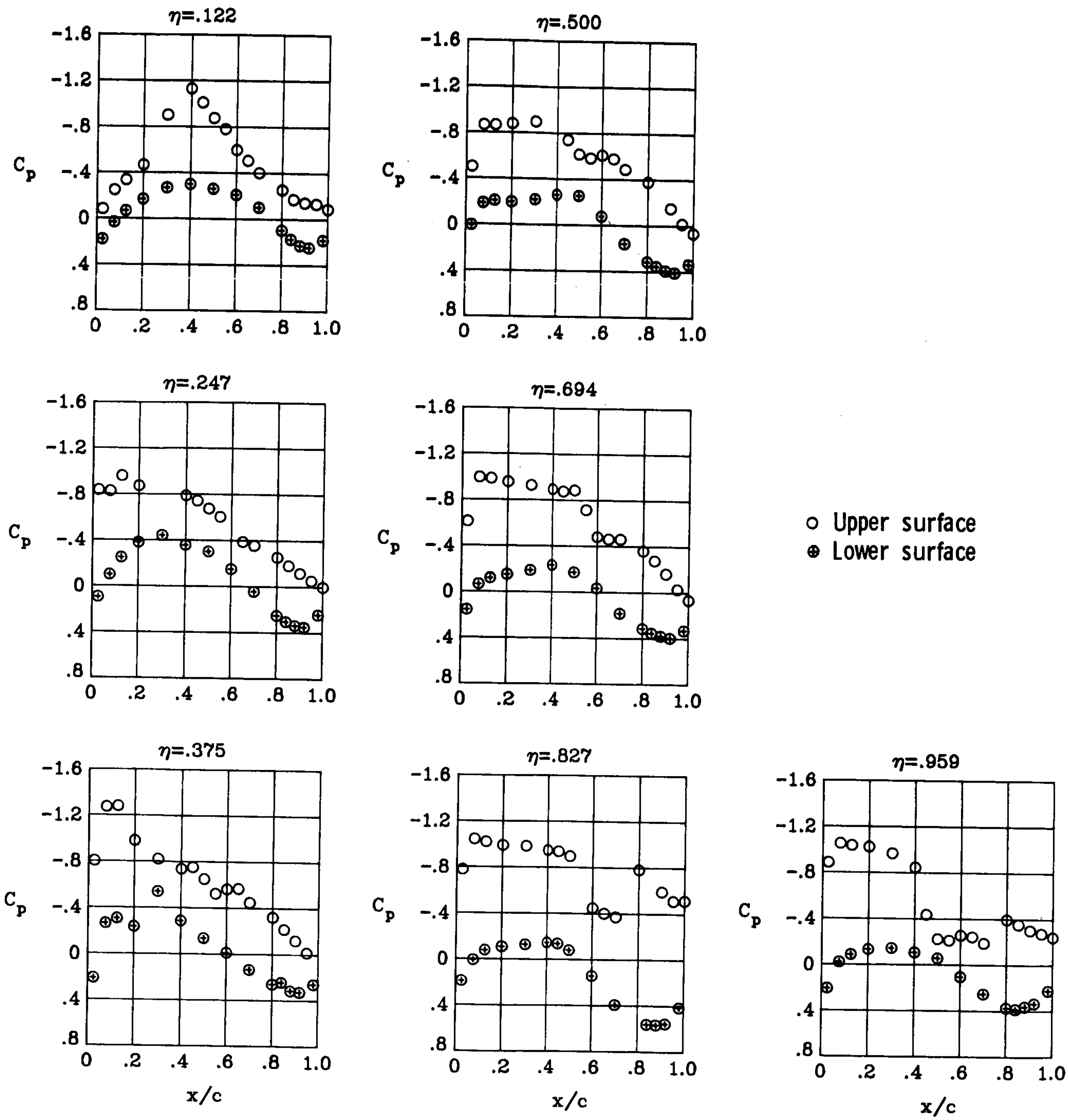

(c) $M_\infty = 0.82$; $\alpha = 3°$.

Figure 50.- Continued.

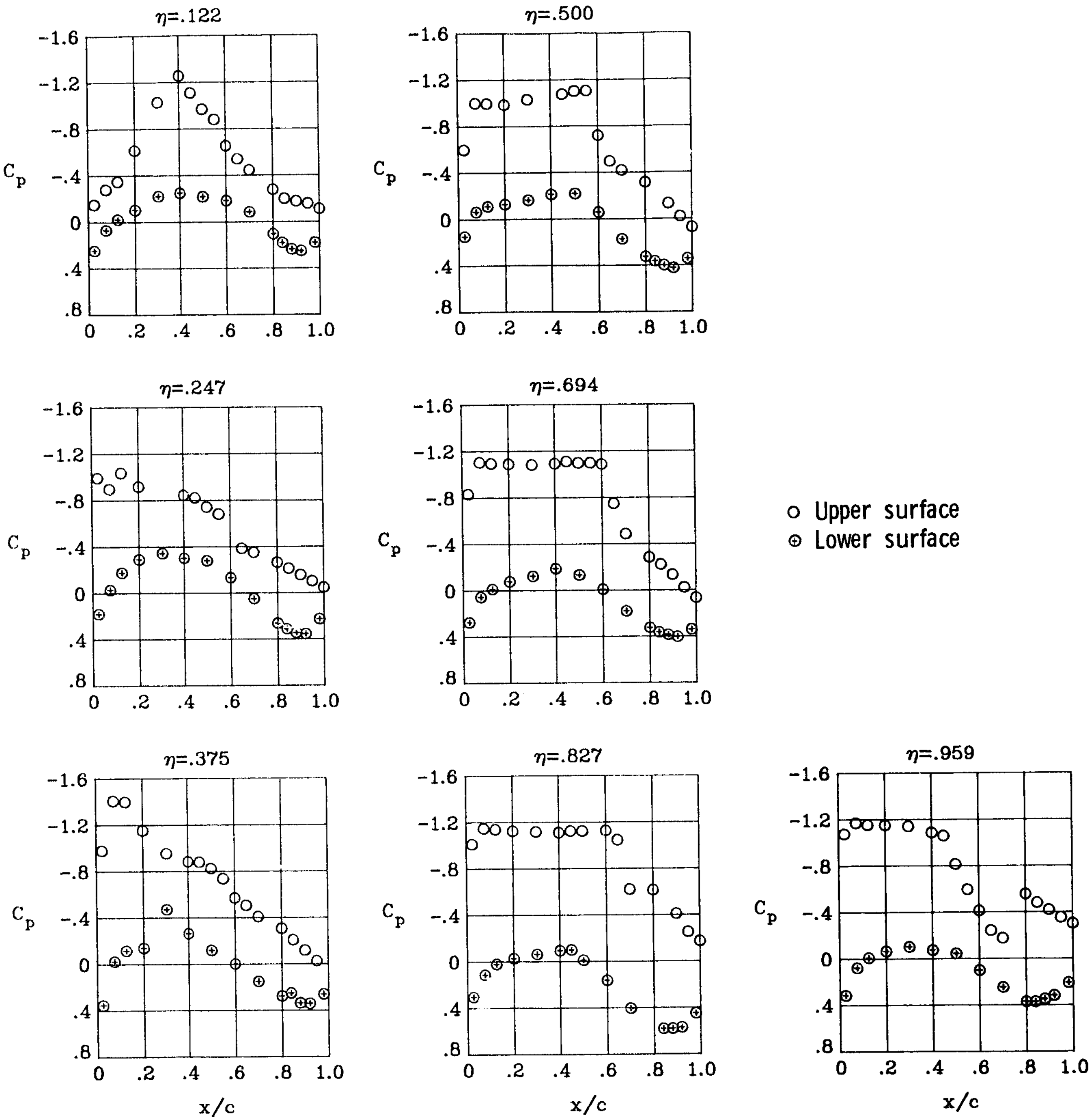

(d) $M_\infty = 0.82$; $\alpha = 4°$.

Figure 50.- Continued.

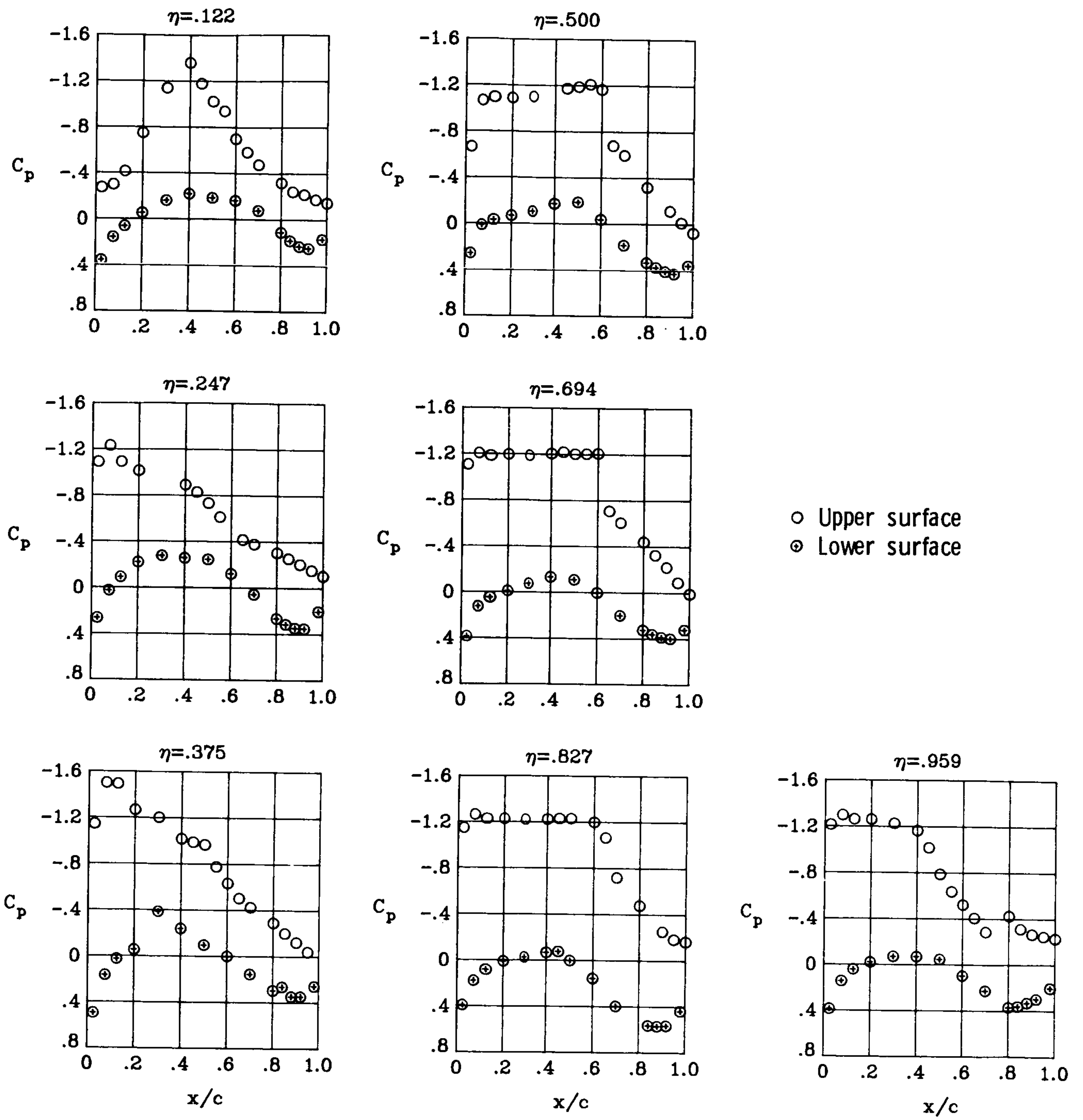

(e) $M_\infty = 0.82$; $\alpha = 5°$.

Figure 50.- Concluded.

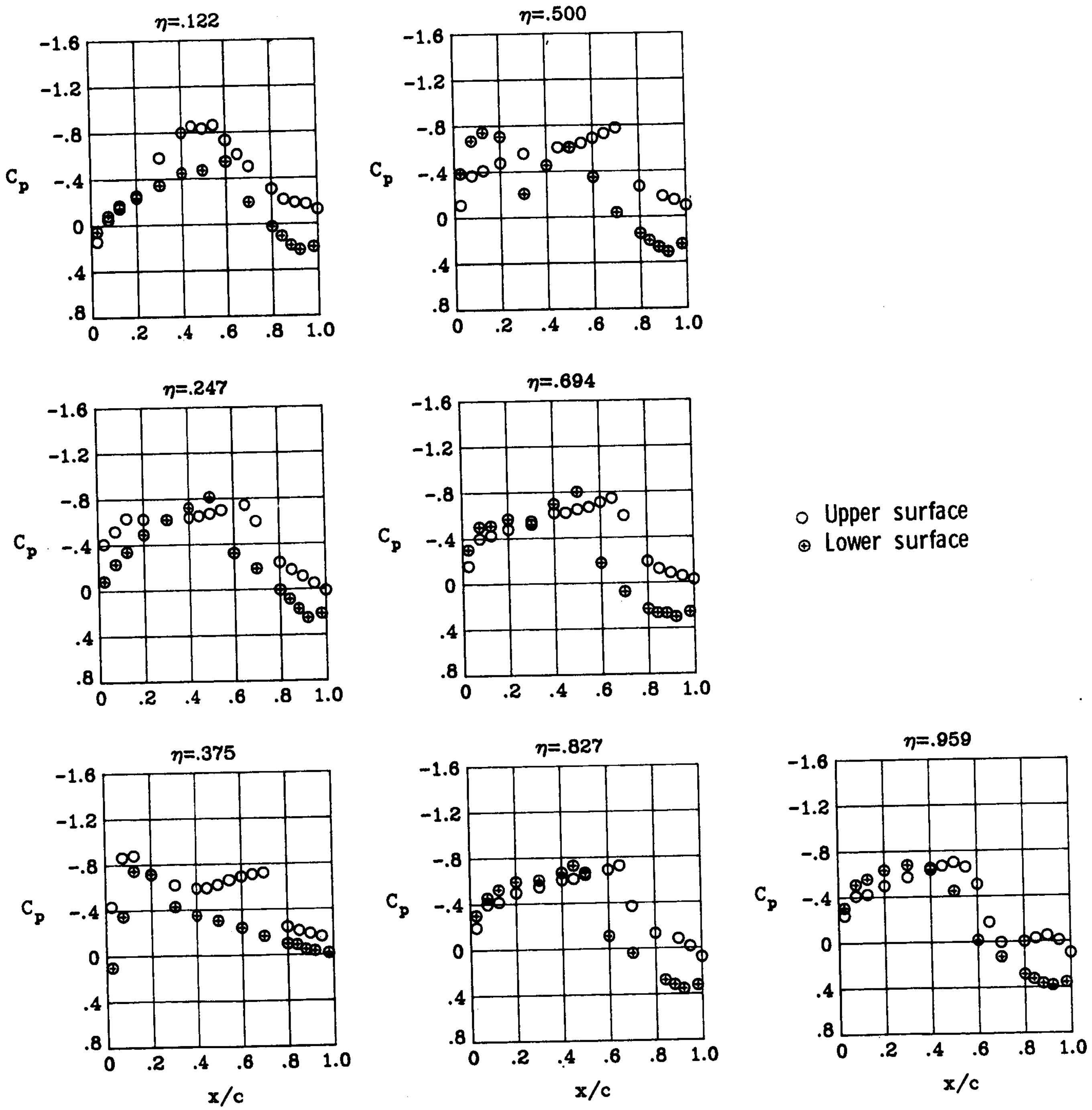

(a) $M_\infty = 0.90$; $\alpha = 1°$.

Figure 51.- Wing chordwise pressure distributions for $\delta a_2 = -2.5°$ at $M_\infty = 0.90$. $\delta a_1 = 0°$.

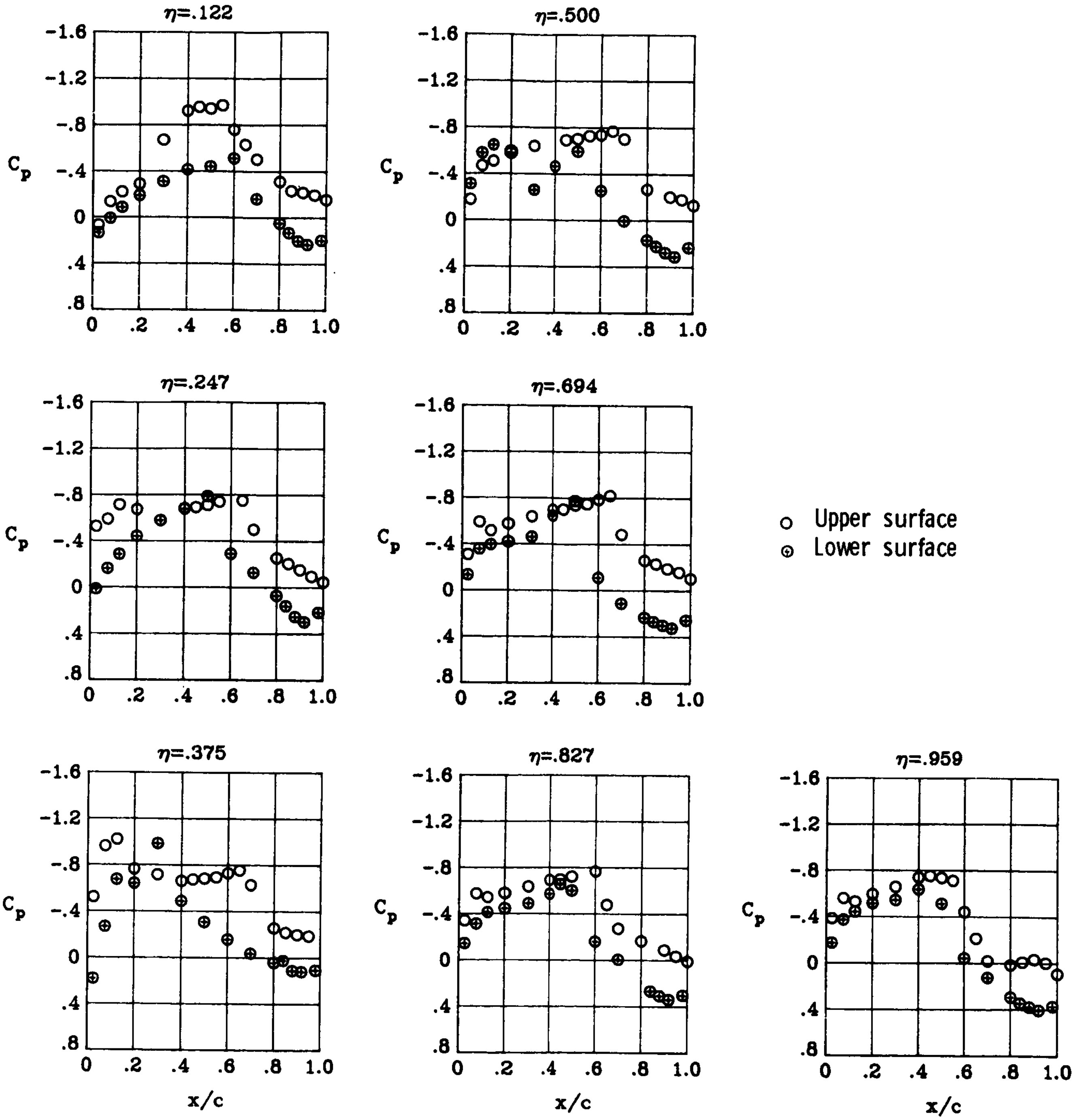

(b) $M_\infty = 0.90$; $\alpha = 2°$.

Figure 51.- Continued.

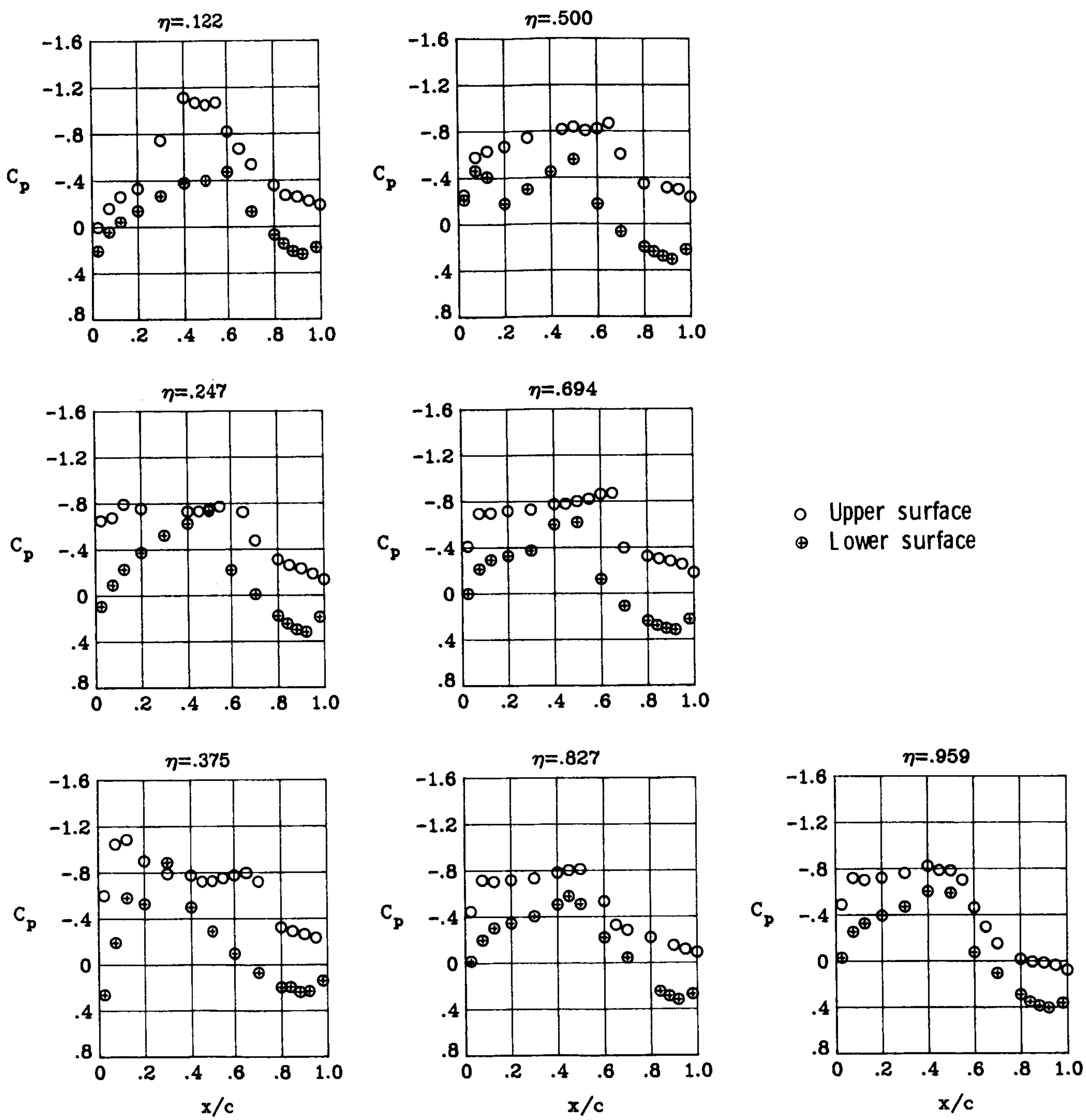

(c) $M_\infty = 0.90$; $\alpha = 3°$.

Figure 51.- Continued.

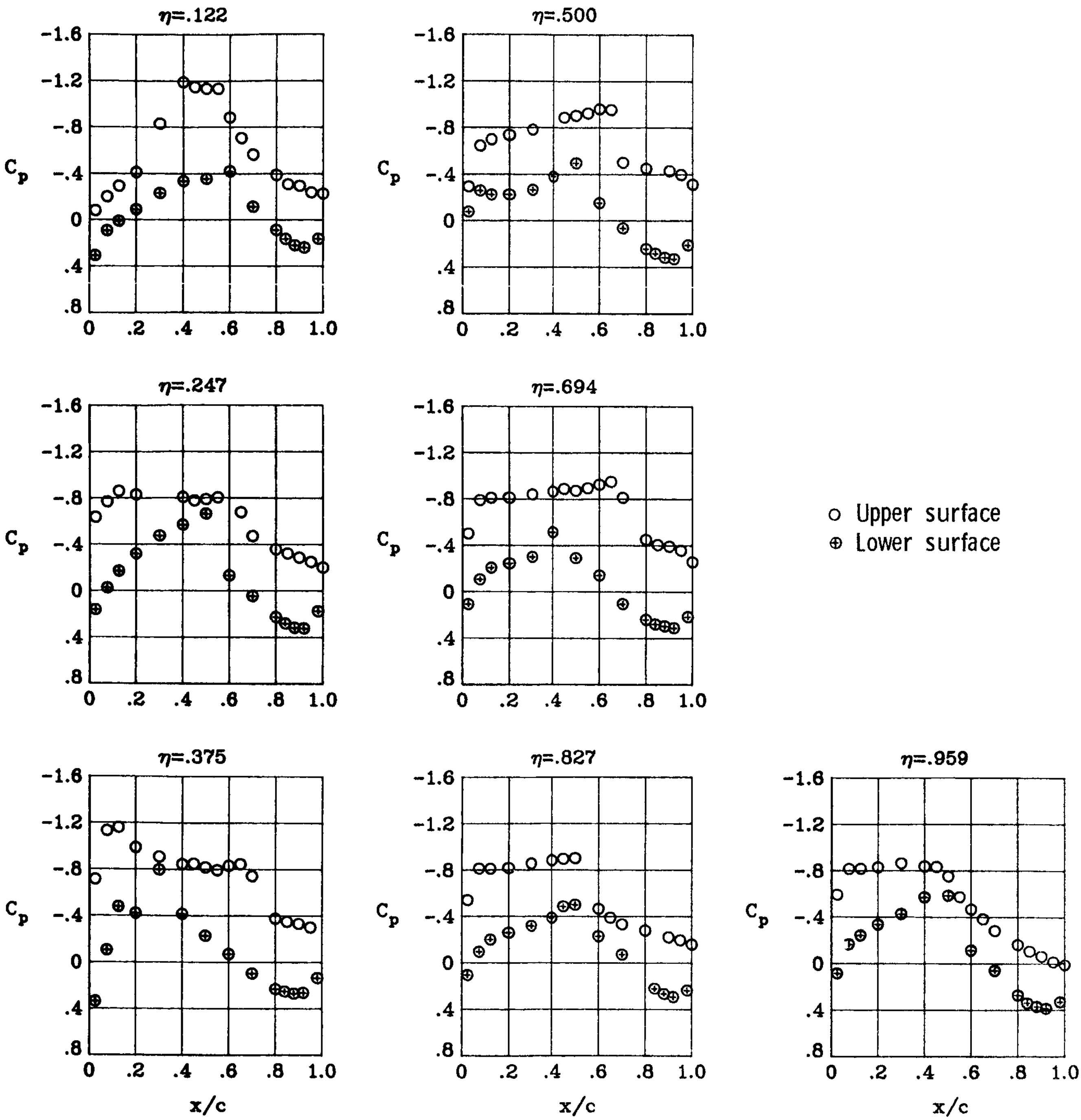

(d) $M_\infty = 0.90$; $\alpha = 4°$.

Figure 51.- Continued.

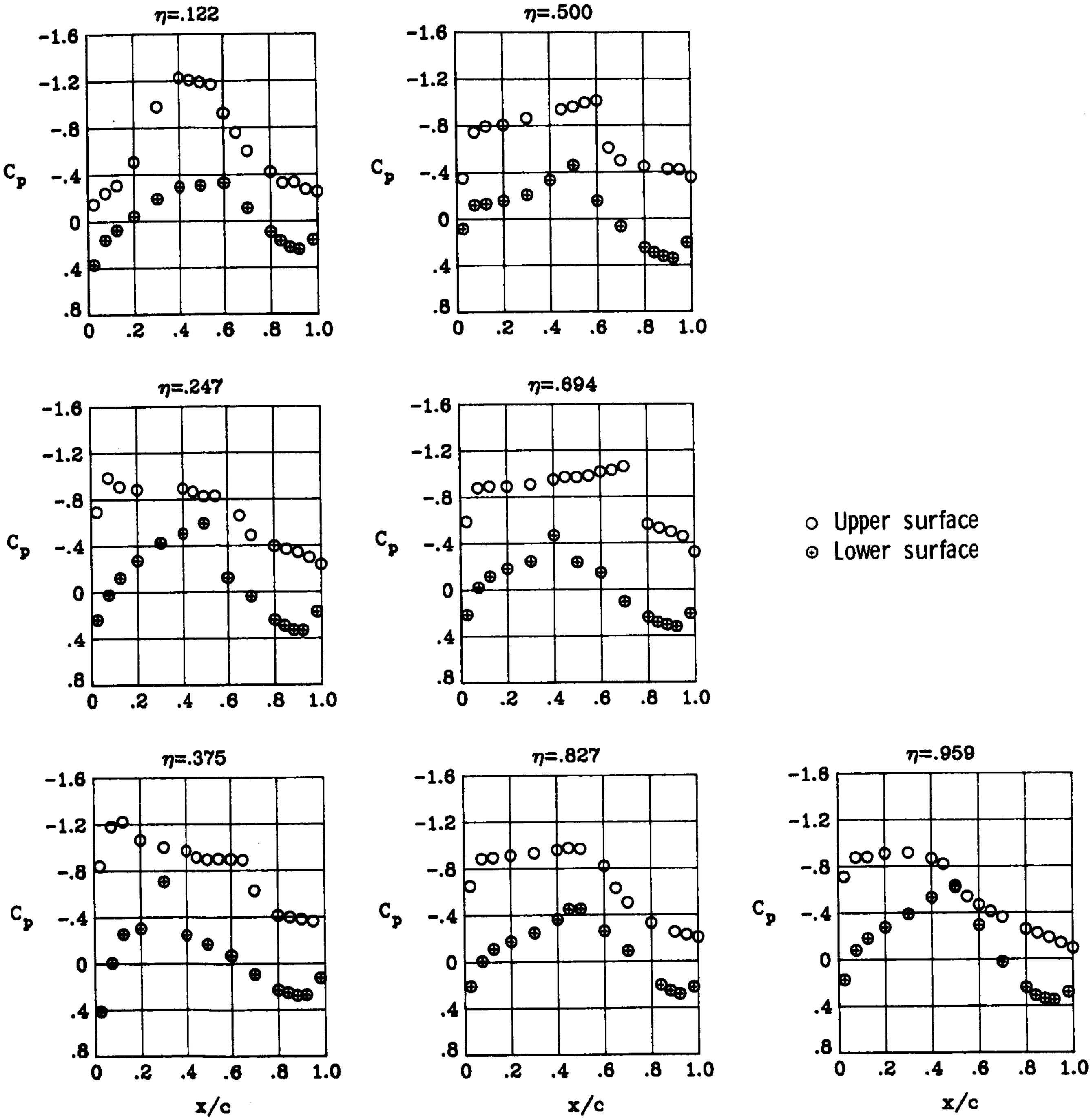

(e) $M_\infty = 0.90$; $\alpha = 5°$.

Figure 51.- Concluded.

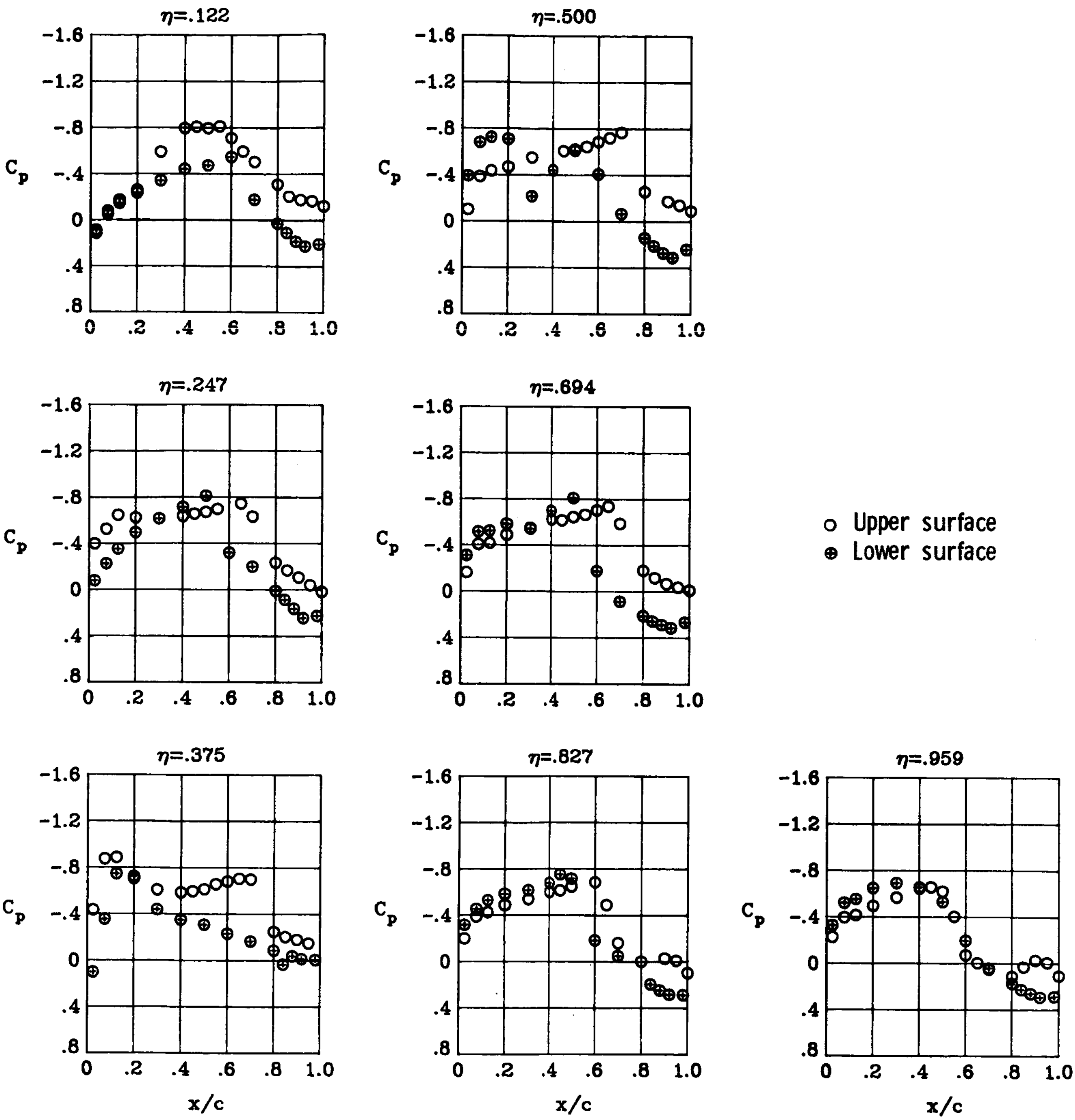

(a) $M_\infty = 0.90$; $\alpha = 1°$.

Figure 52.- Wing chordwise pressure distributions for $\delta a_2 = -7.5°$ at $M_\infty = 0.90$. $\delta a_1 = 0°$.

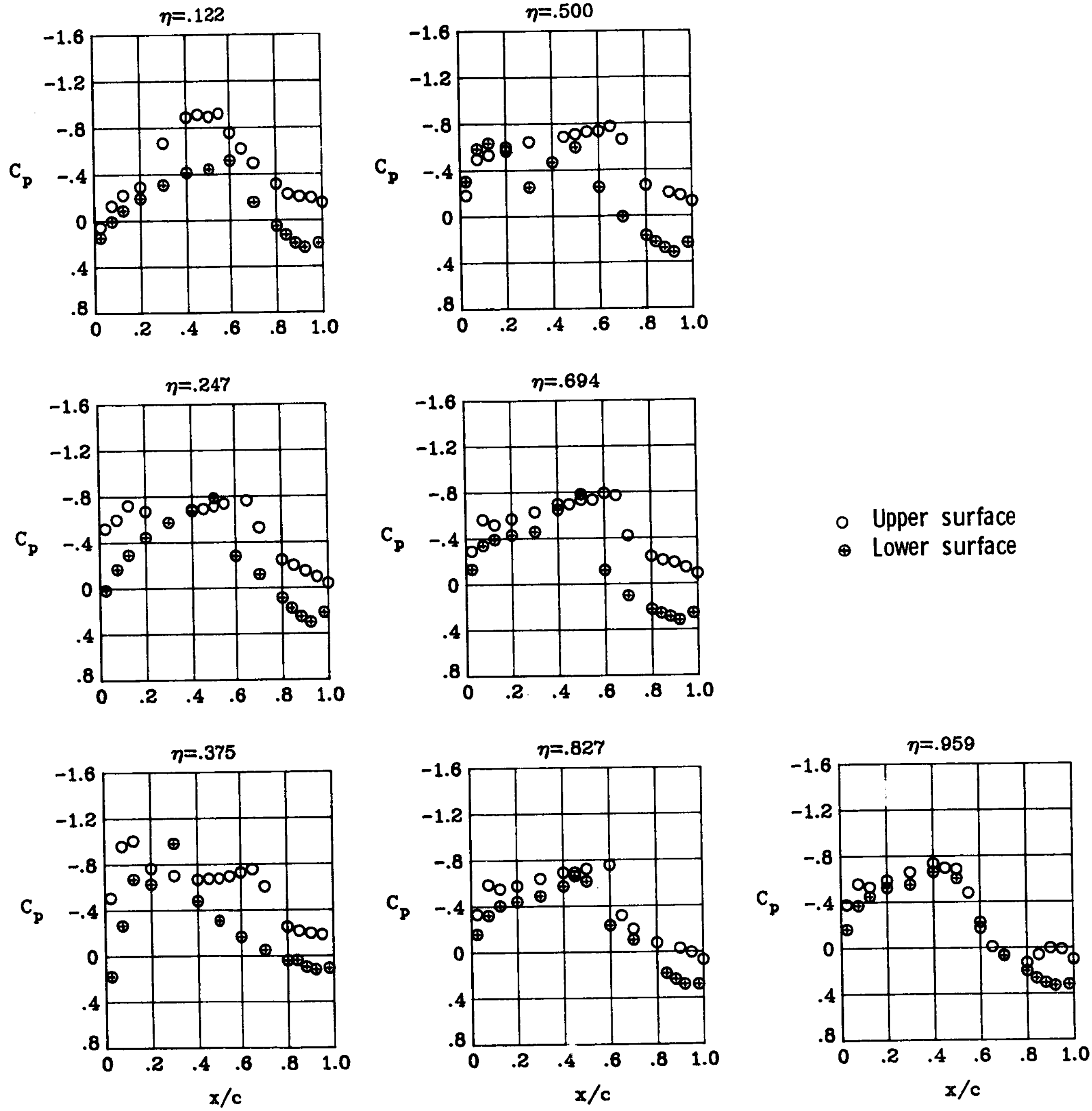

(b) M_∞ = 0.90; α = 2°.

Figure 52. - Continued.

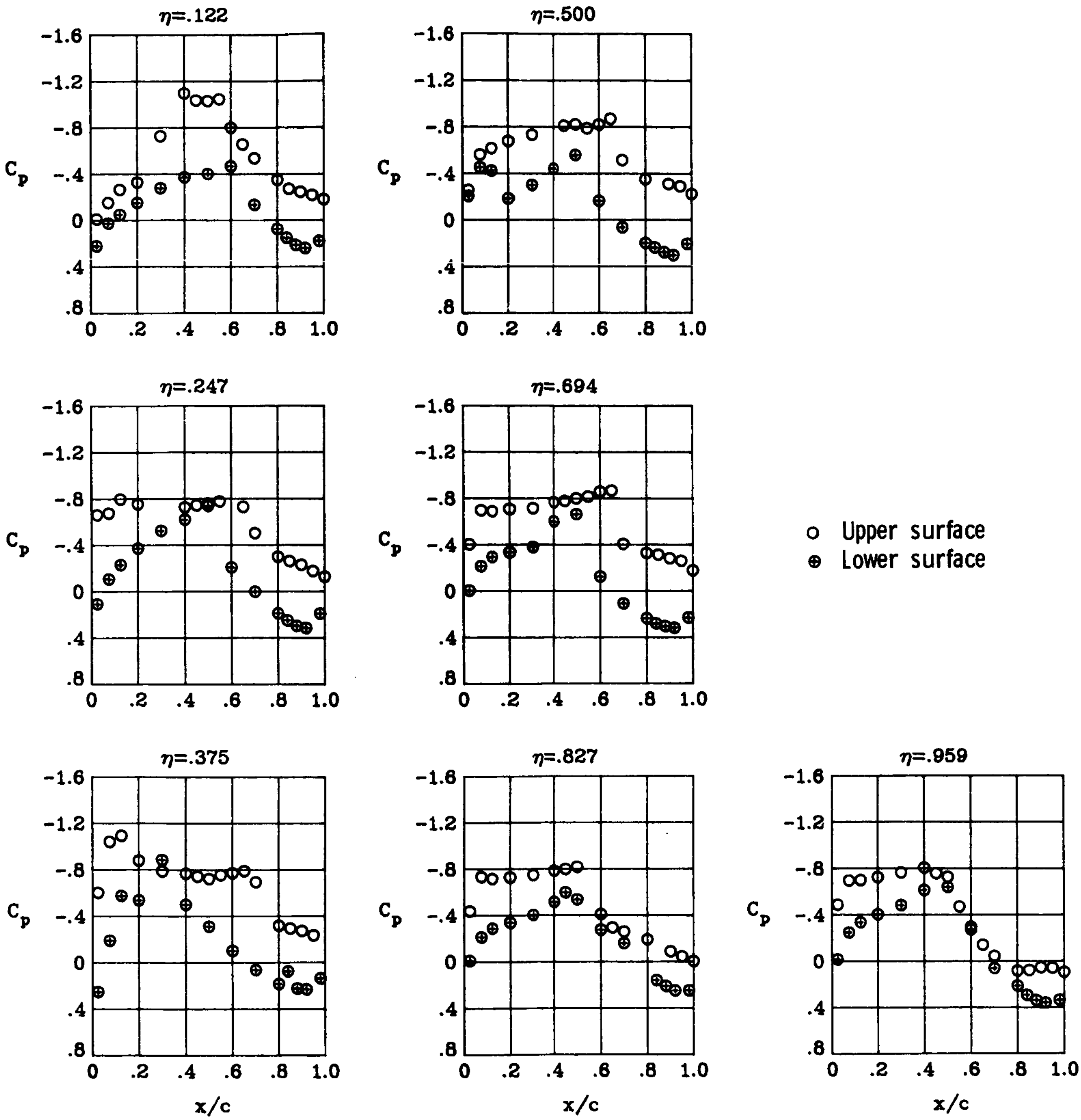

(c) $M_\infty = 0.90$; $\alpha = 3°$.

Figure 52.- Continued.

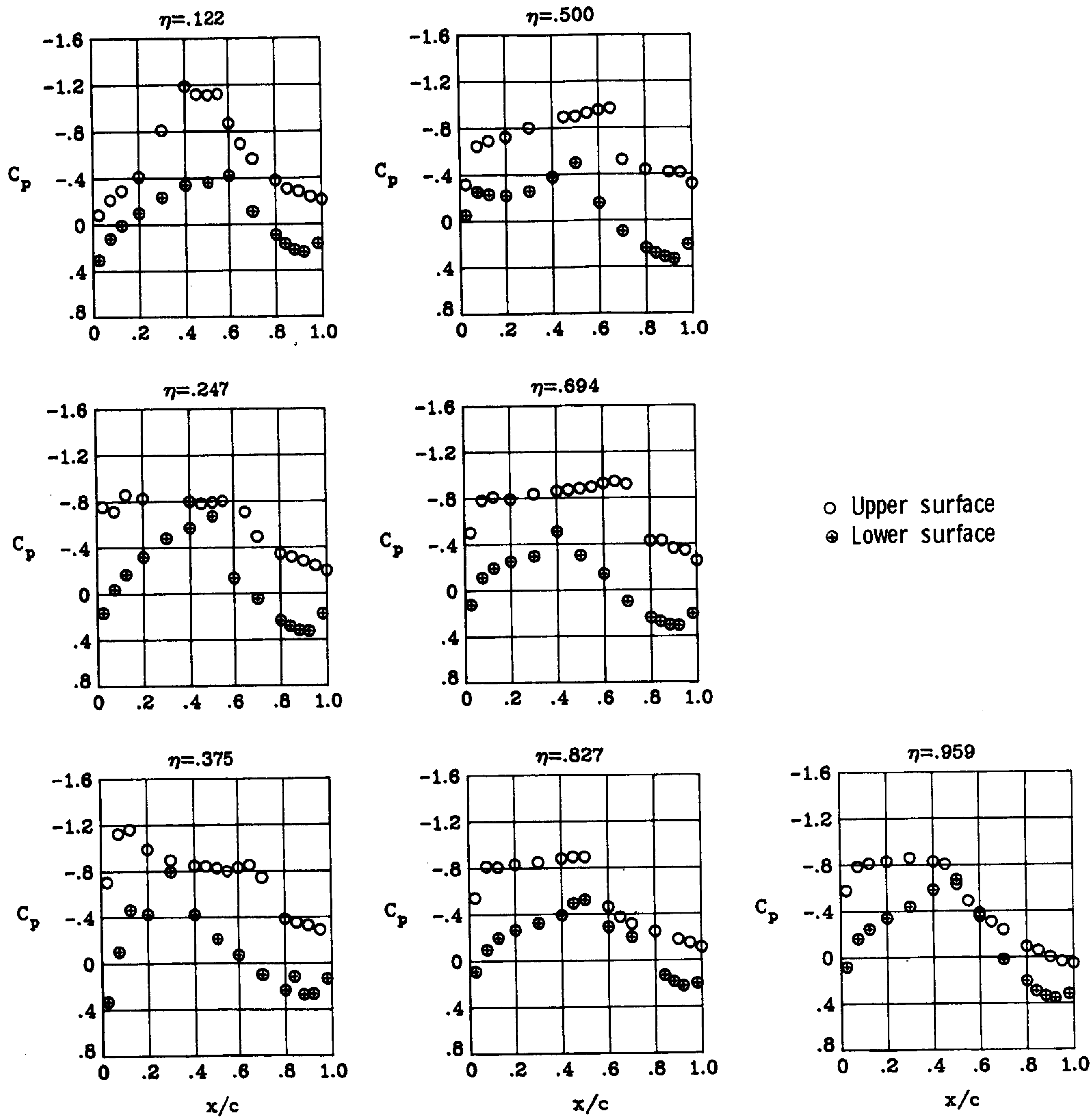

(d) $M_\infty = 0.90$; $\alpha = 4°$.

Figure 52.- Continued.

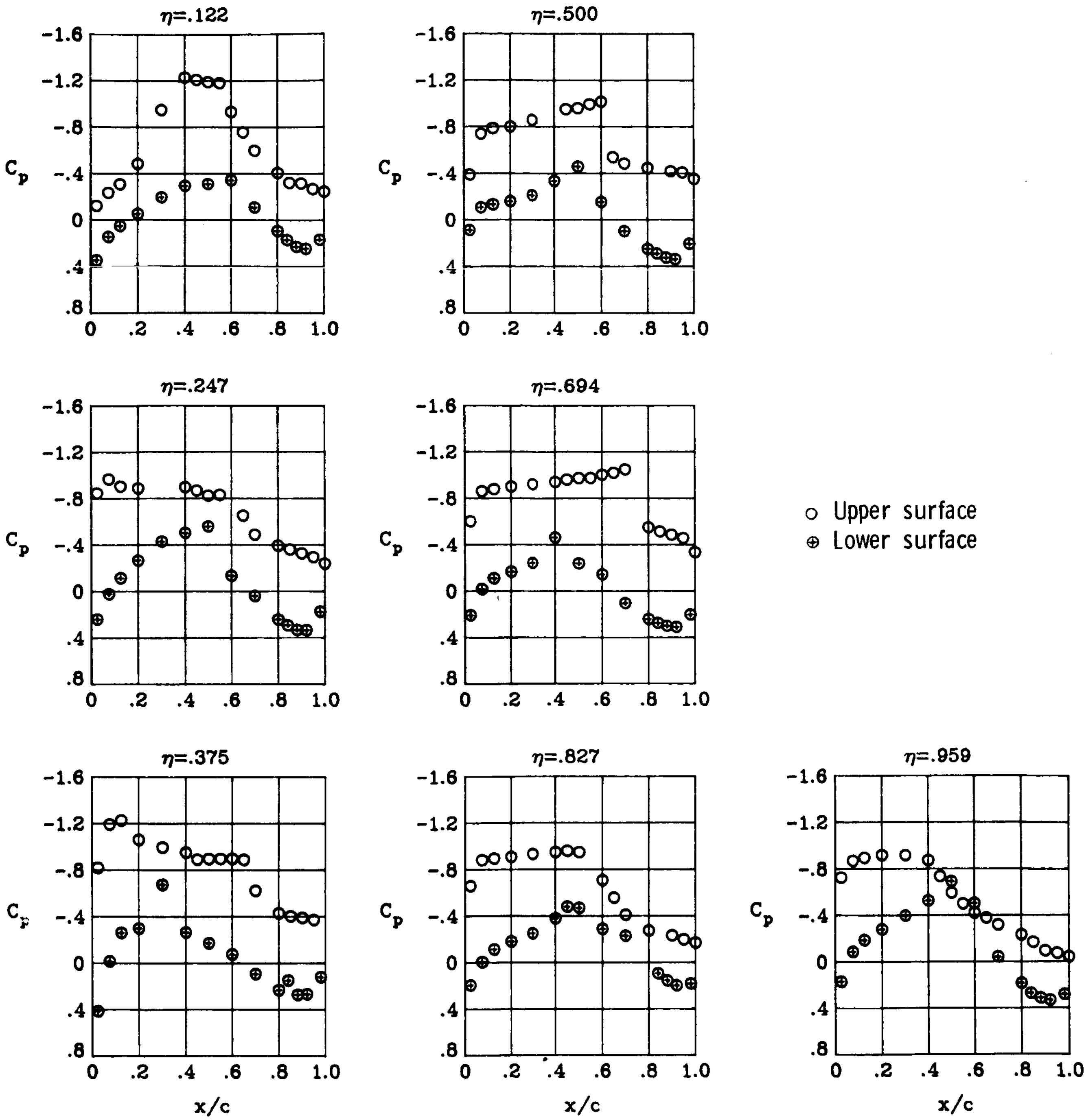

(e) $M_\infty = 0.90$; $\alpha = 5°$.

Figure 52.- Concluded.

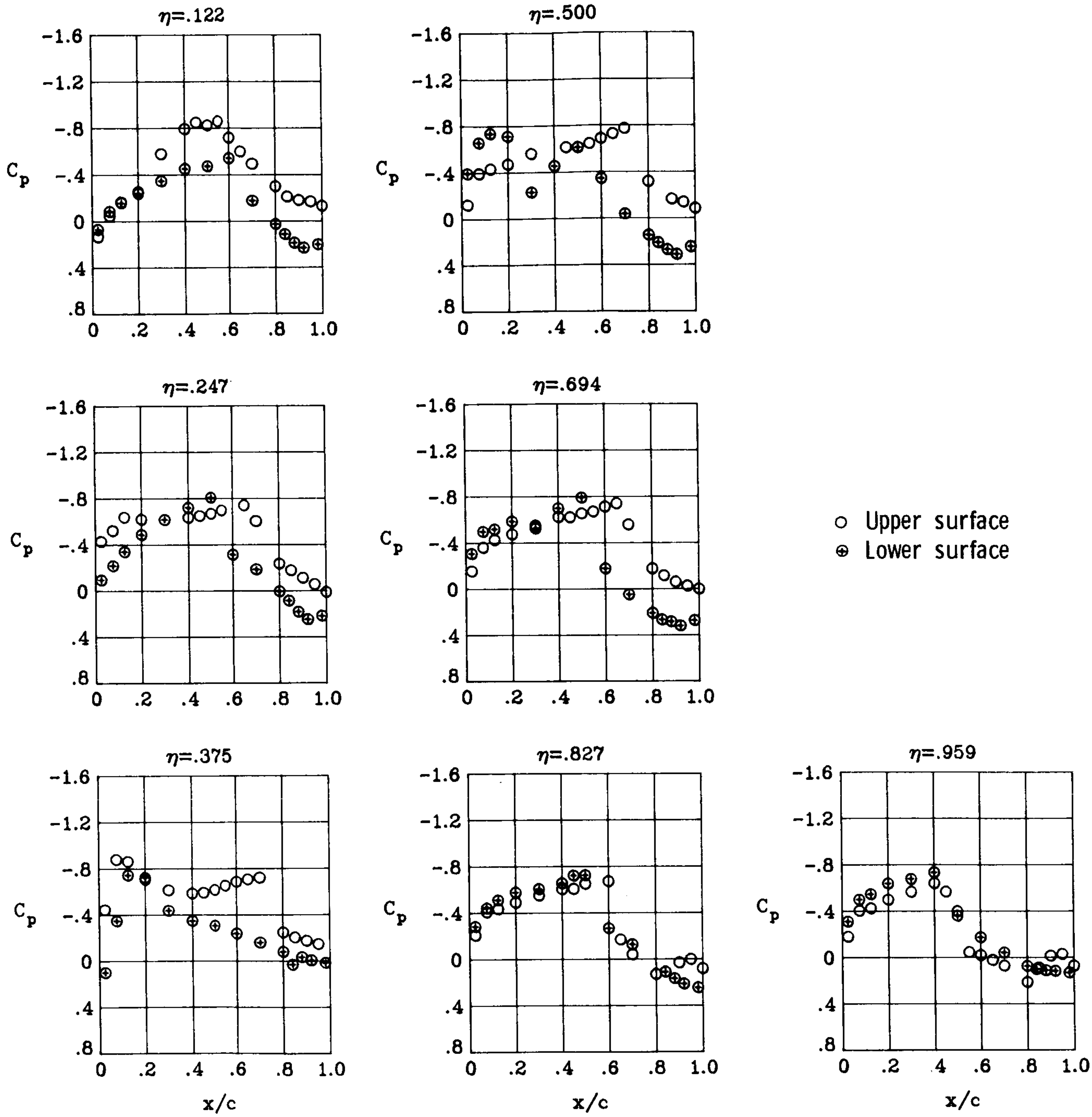

(a) $M_\infty = 0.90$; $\alpha = 1°$.

Figure 53.- Wing chordwise pressure distributions for $\delta a_2 = -12.5°$ at $M_\infty = 0.90$. $\delta a_1 = 0°$.

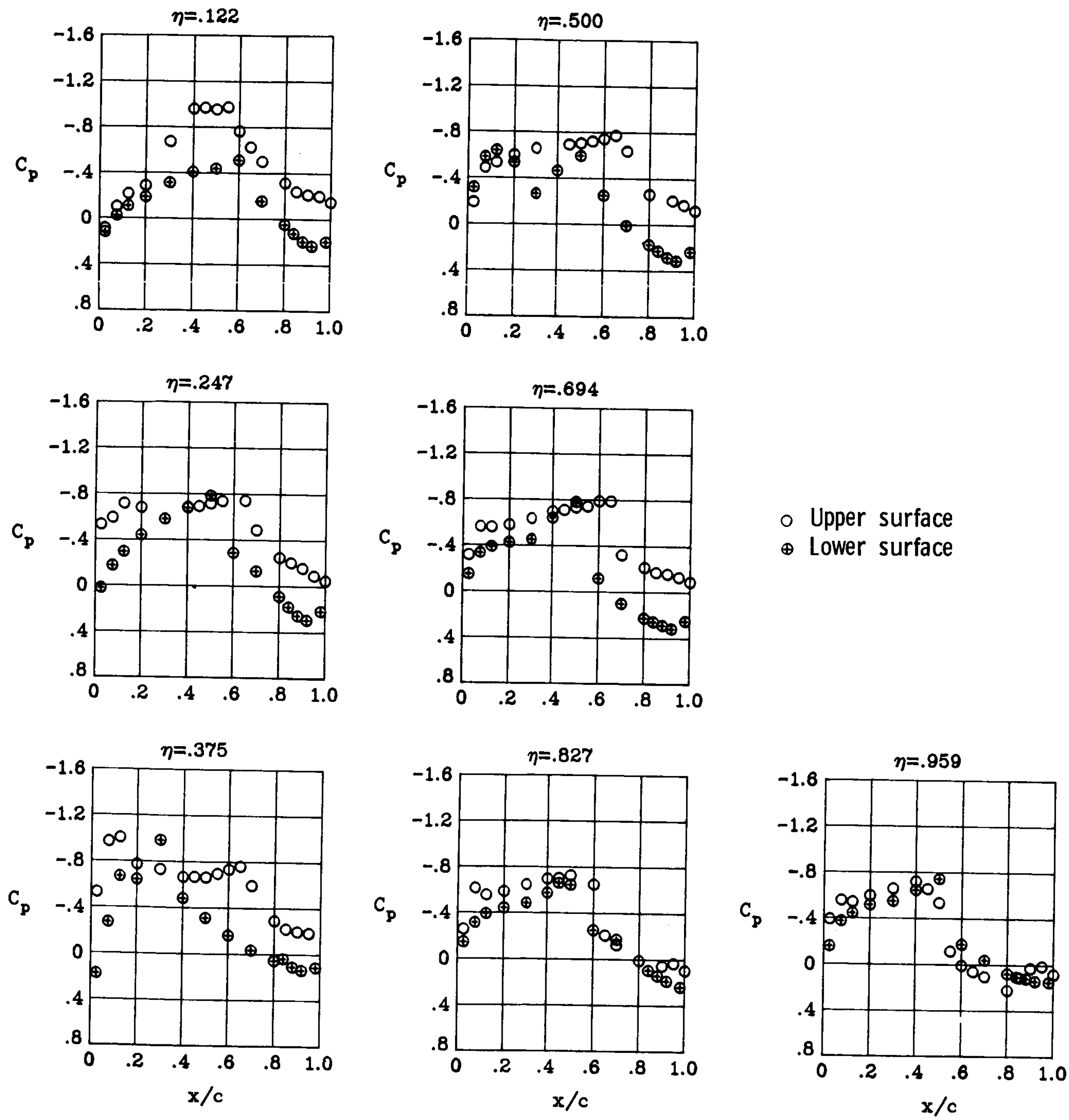

(b) $M_\infty = 0.90$; $\alpha = 2°$.

Figure 53.- Continued.

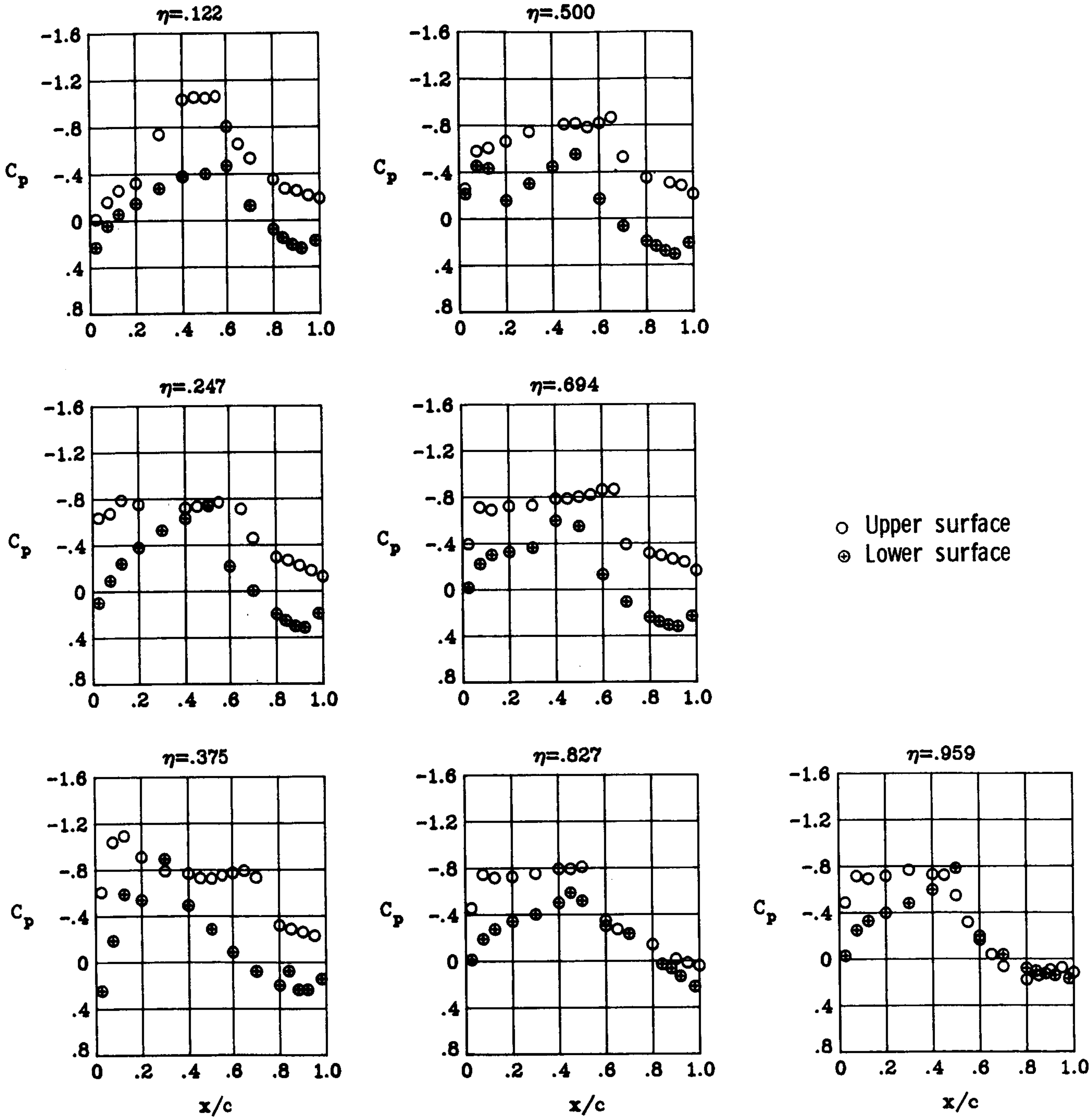

(c) $M_\infty = 0.90$; $\alpha = 3°$.

Figure 53.- Continued.

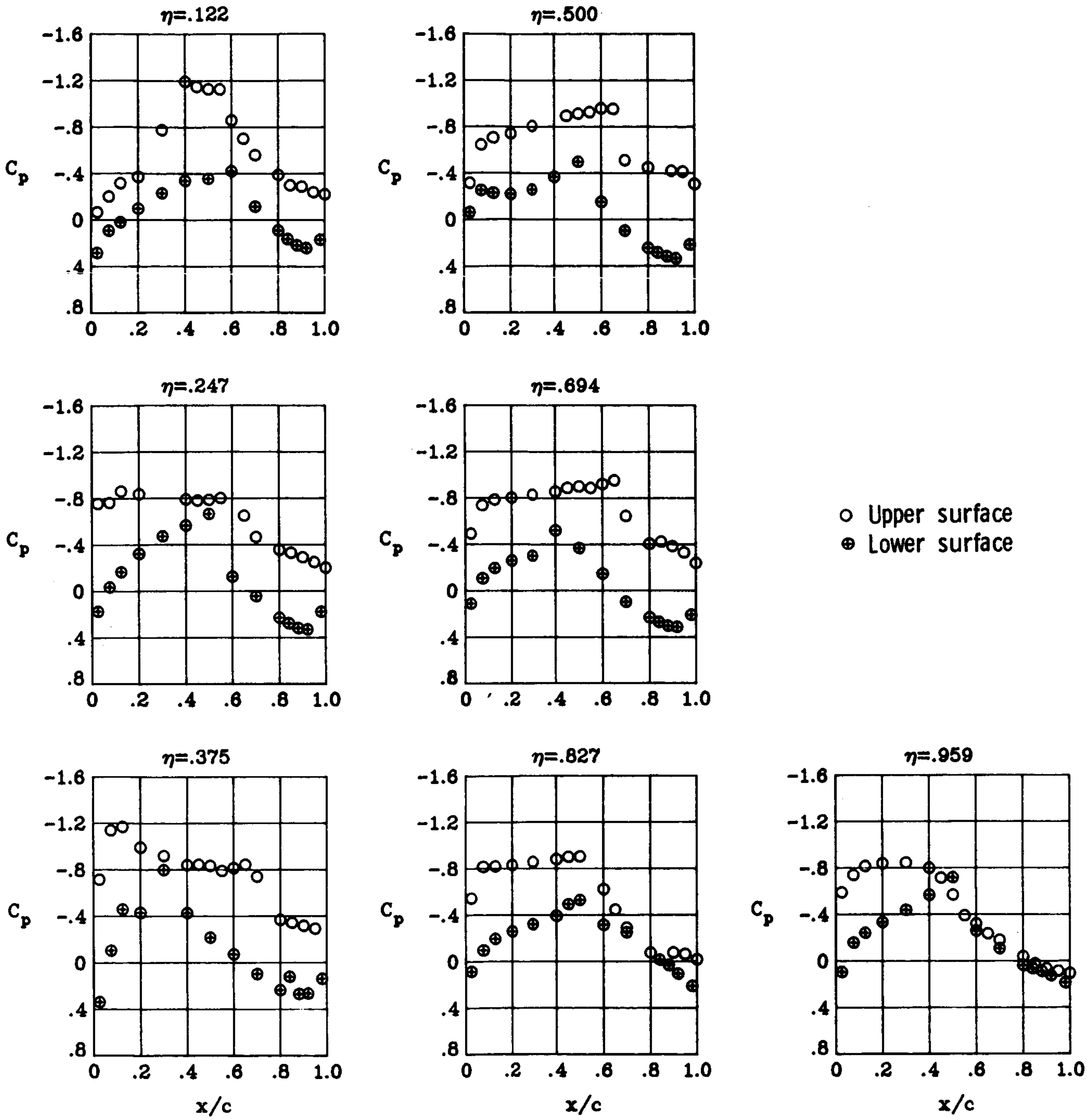

(d) M_∞ = 0.90; α = 4°.

Figure 53.- Continued.

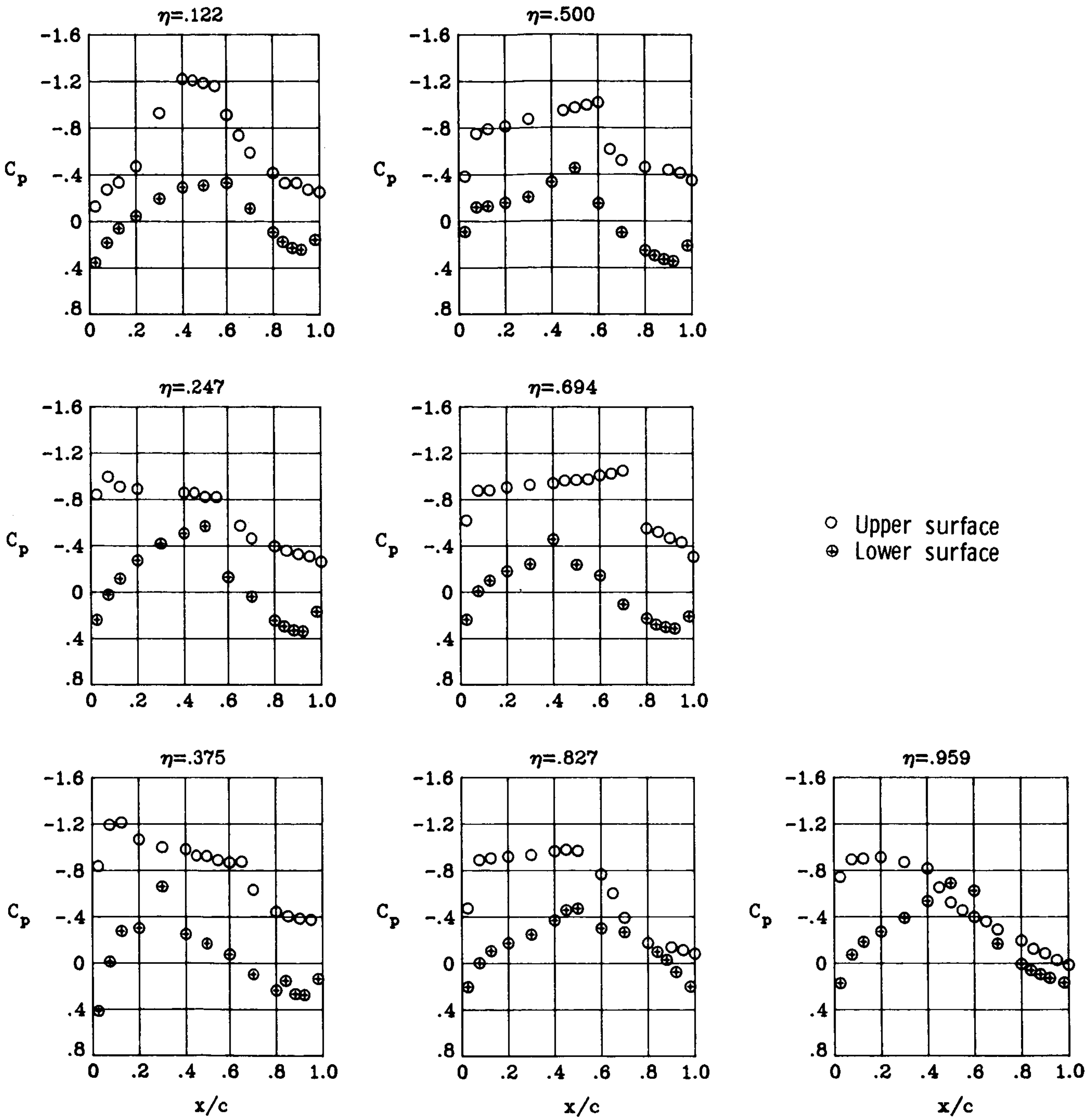

(e) $M_\infty = 0.90$; $\alpha = 5°$.

Figure 53.- Concluded.

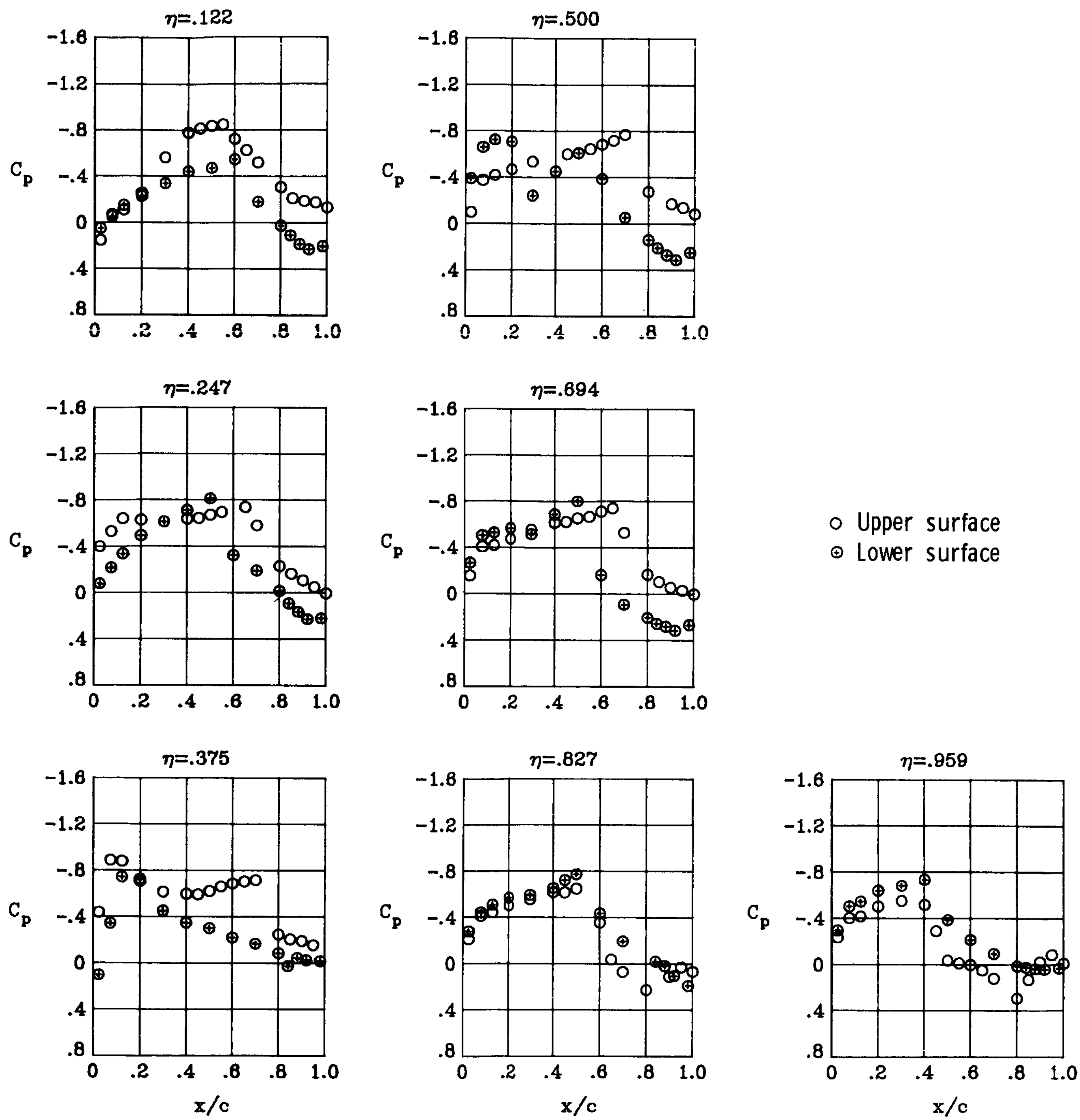

(a) $M_\infty = 0.90$; $\alpha = 1°$.

Figure 54.- Wing chordwise pressure distributions for $\delta a_2 = -17.5°$ at $M_\infty = 0.90$. $\delta a_1 = 0°$.

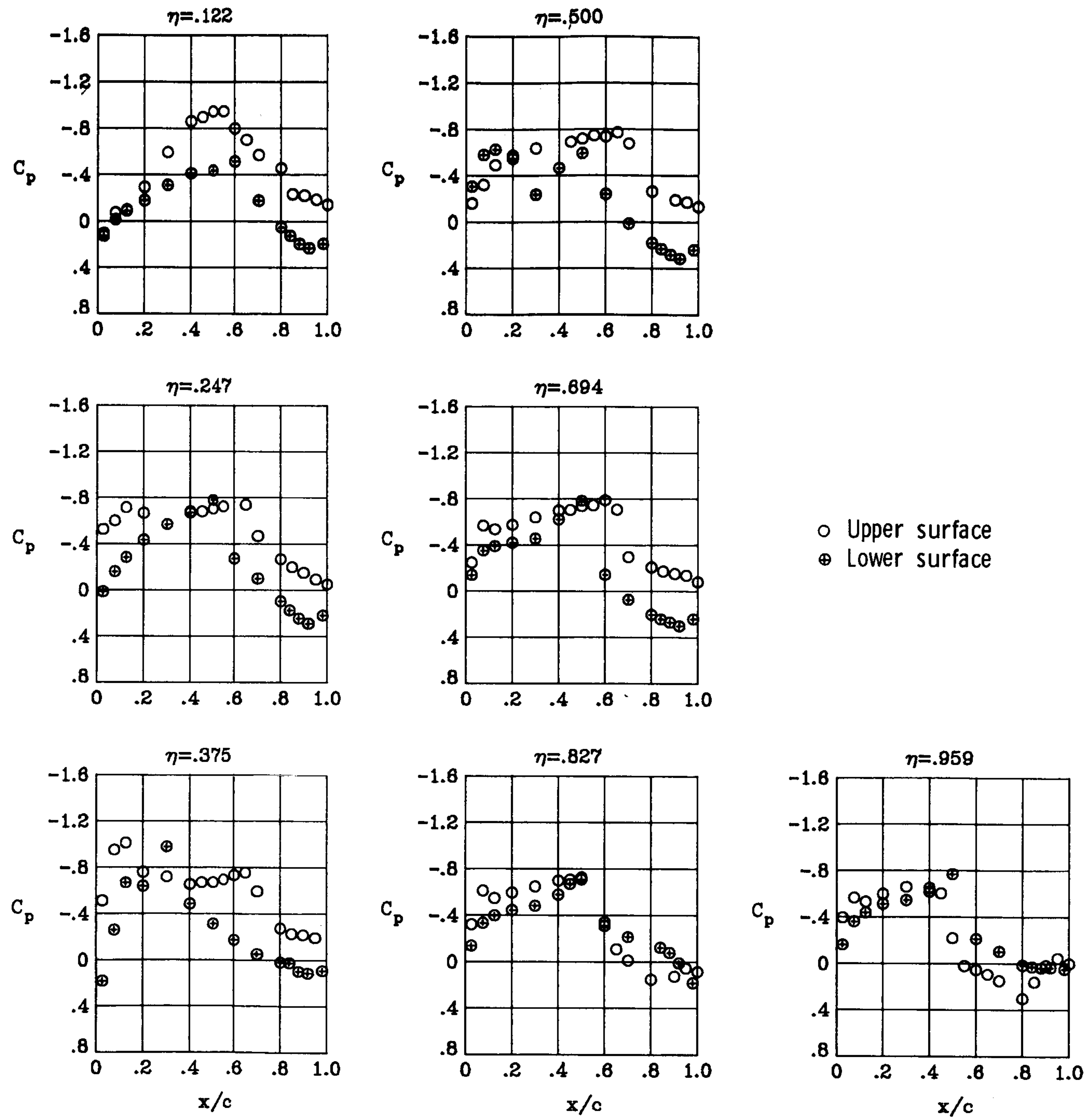

(b) $M_\infty = 0.90$; $\alpha = 2°$.

Figure 54.- Continued.

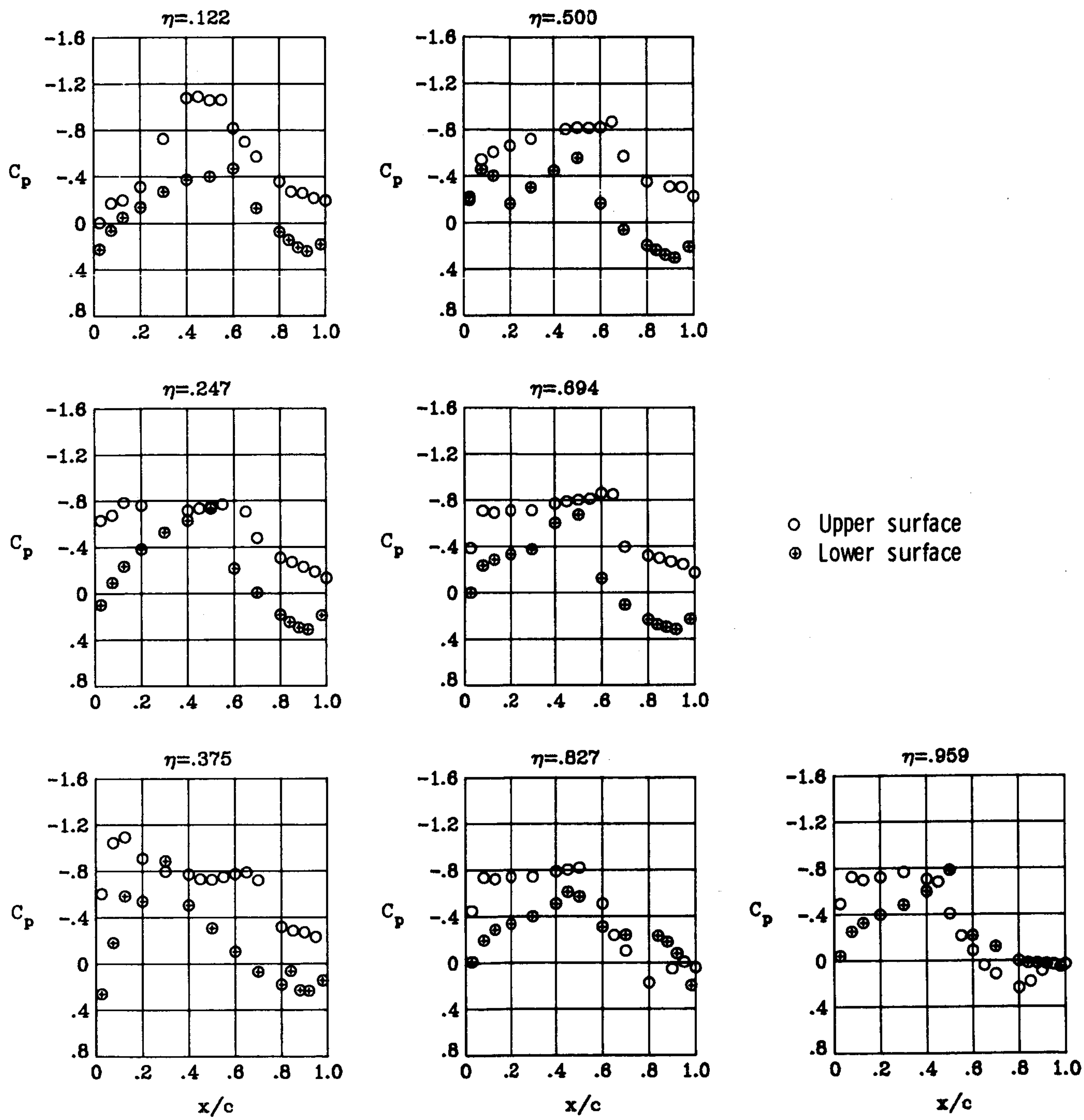

(c) $M_\infty = 0.90;\ \alpha = 3°.$

Figure 54.- Continued.

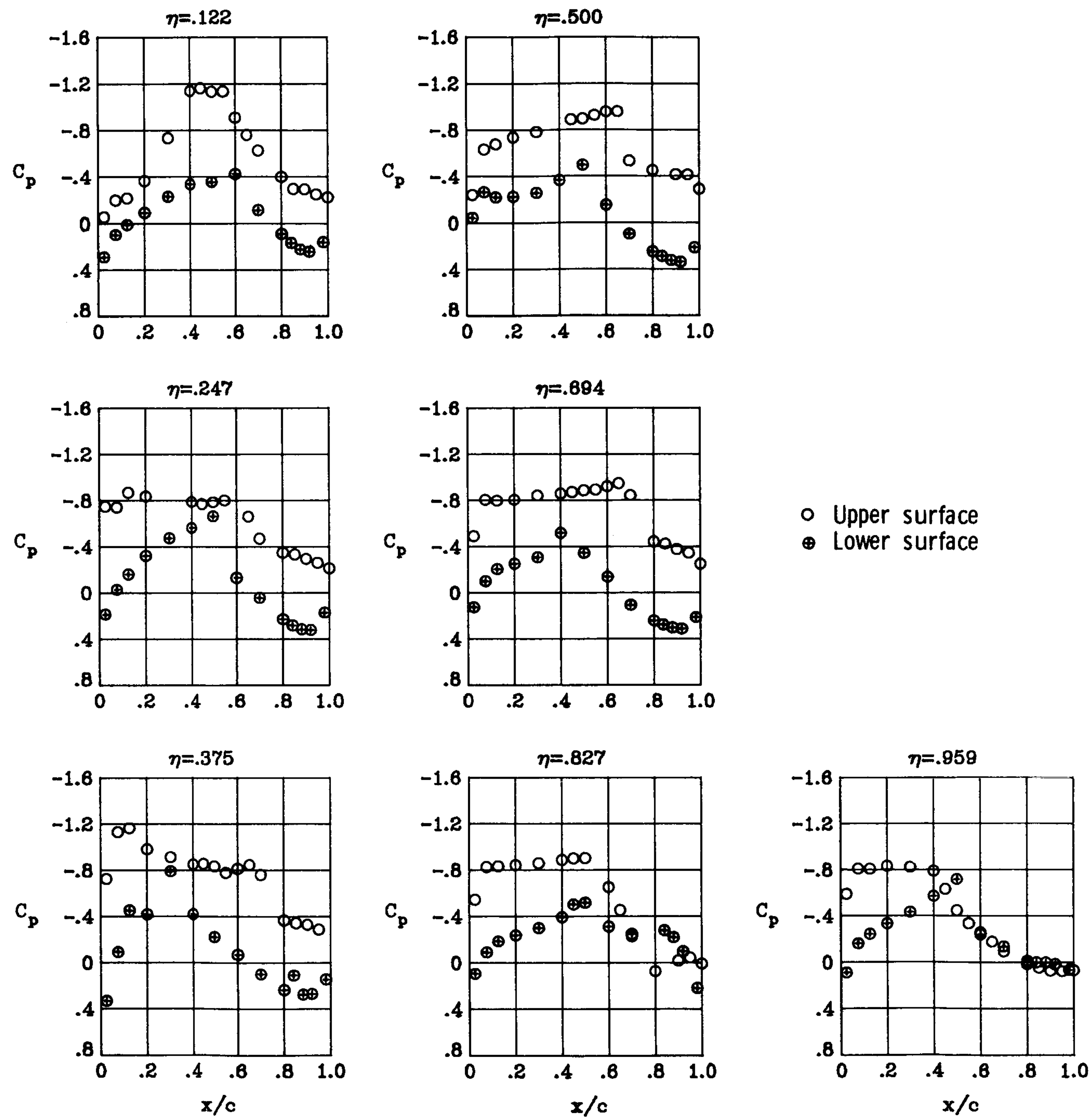

(d) $M_\infty = 0.90$; $\alpha = 4°$.

Figure 54.- Continued.

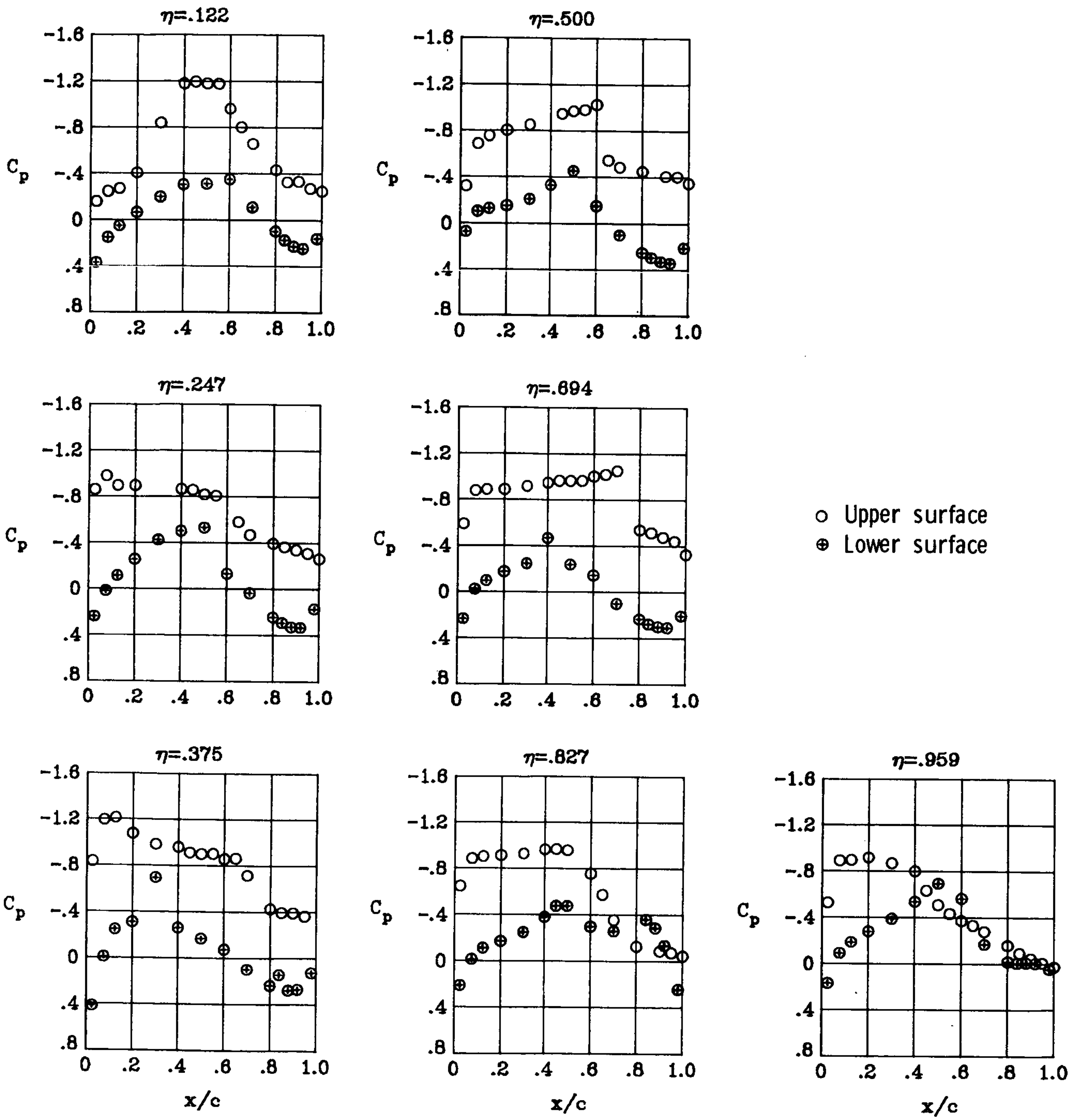

(e) $M_\infty = 0.90$; $\alpha = 5°$.

Figure 54.- Concluded.

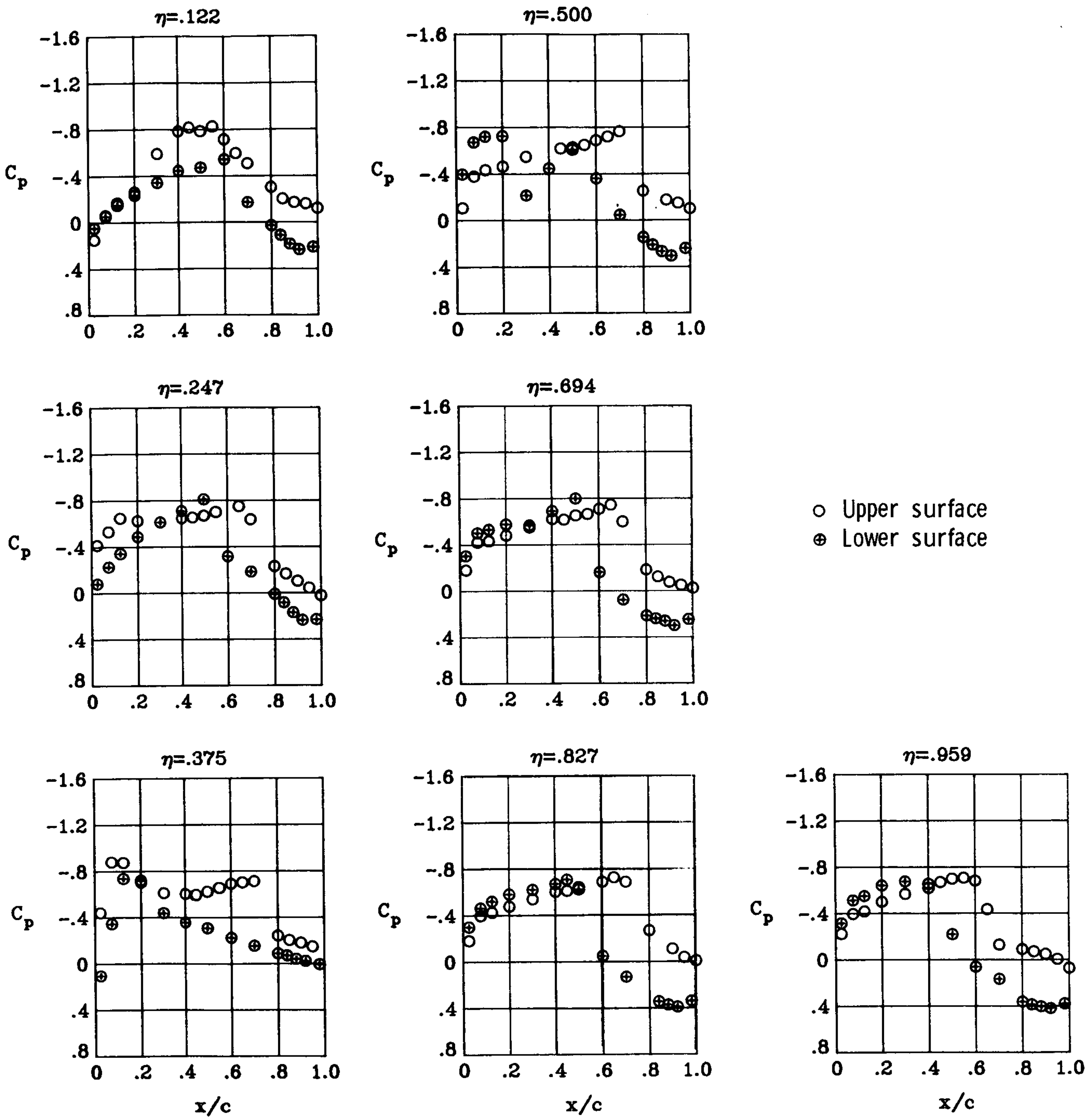

(a) $M_\infty = 0.90$; $\alpha = 1°$.

Figure 55.- Wing chordwise pressure distributions for $\delta a_2 = 2.5°$ at $M_\infty = 0.90$. $\delta a_1 = 0°$.

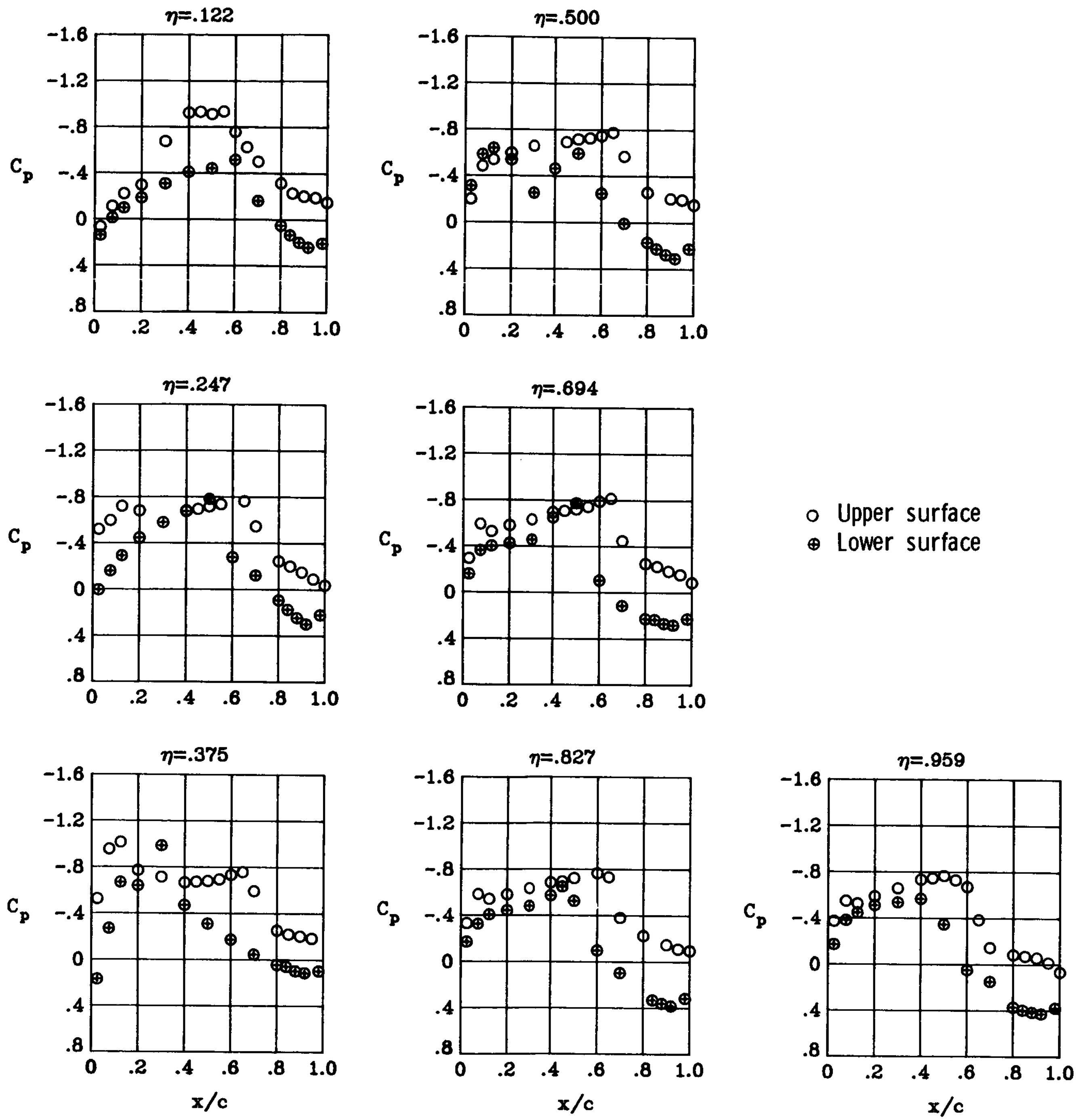

(b) $M_\infty = 0.90$; $\alpha = 2°$.

Figure 55.- Continued.

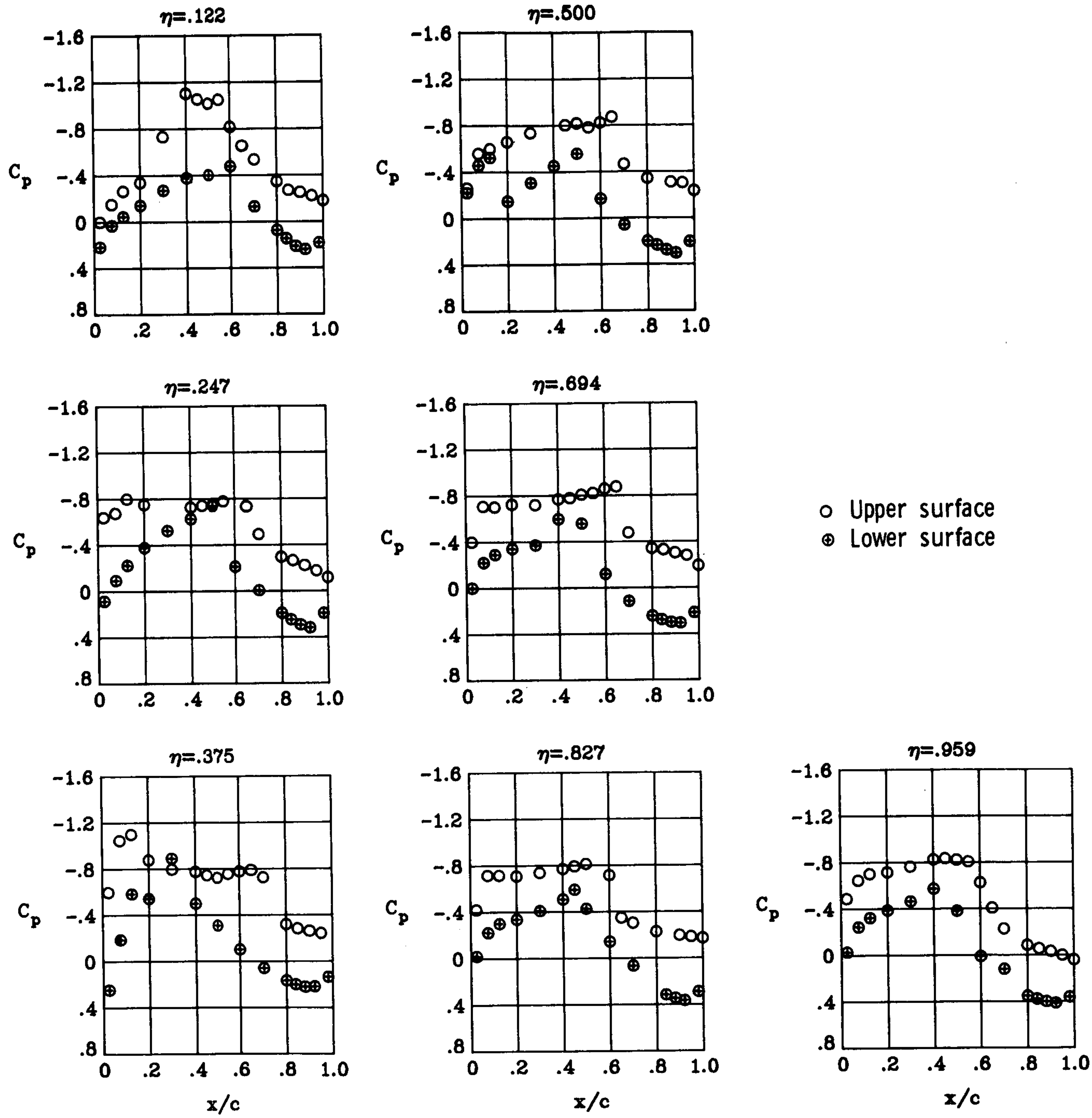

(c) $M_\infty = 0.90$; $\alpha = 3°$.

Figure 55.- Continued.

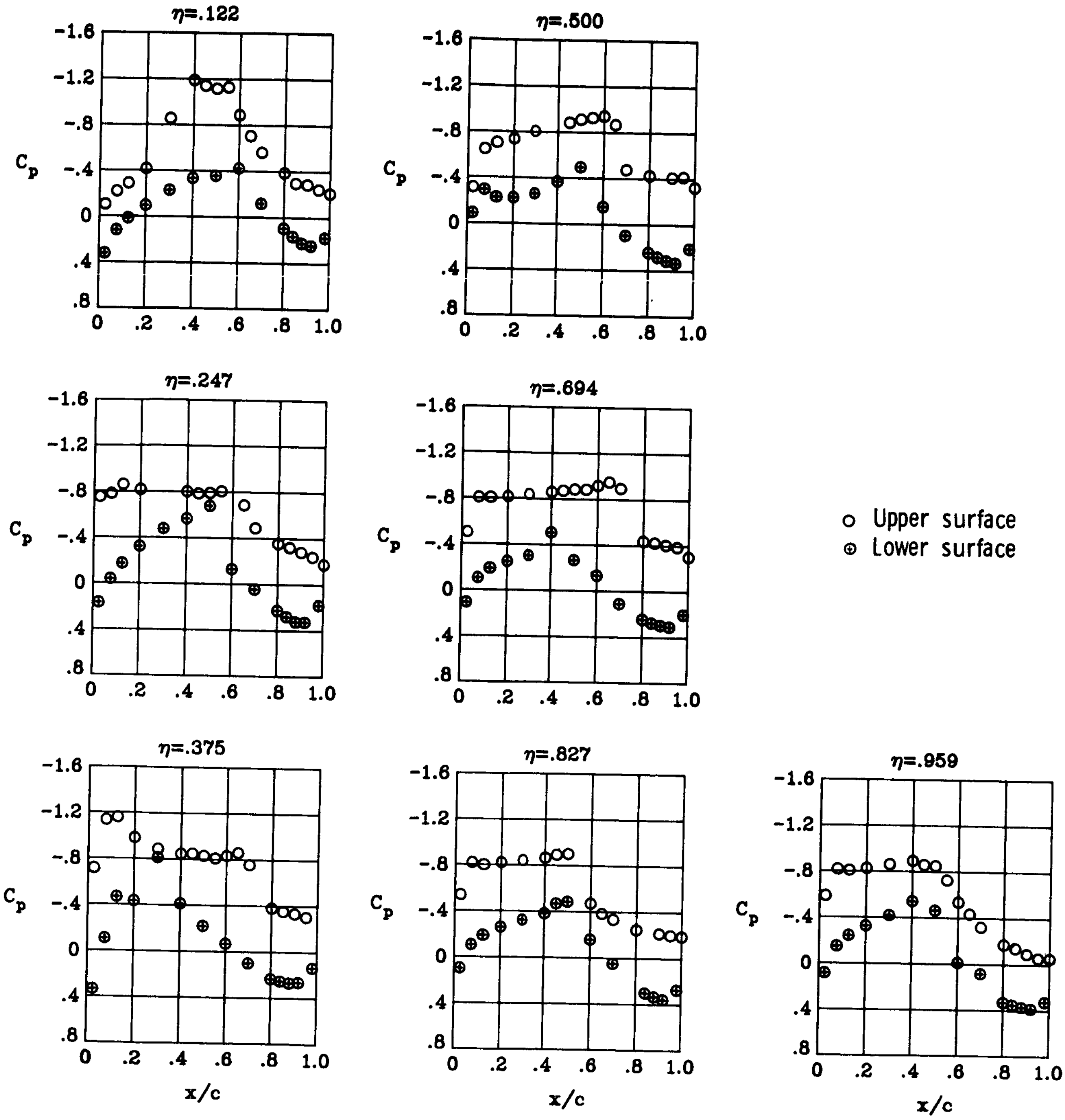

(d) $M_\infty = 0.90$; $\alpha = 4°$.

Figure 55.- Continued.

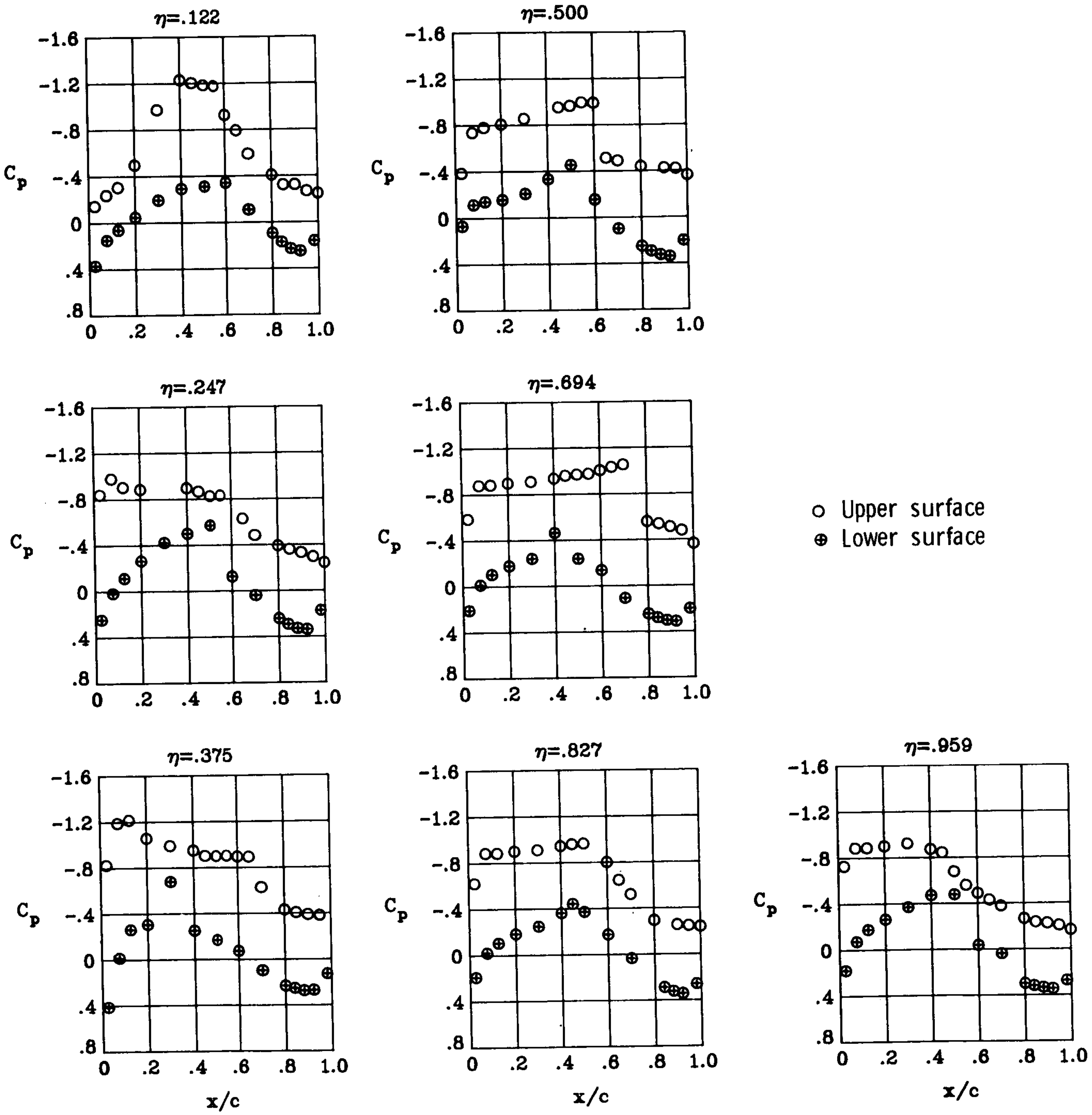

(e) $M_\infty = 0.90$; $\alpha = 5°$.

Figure 55.- Concluded.

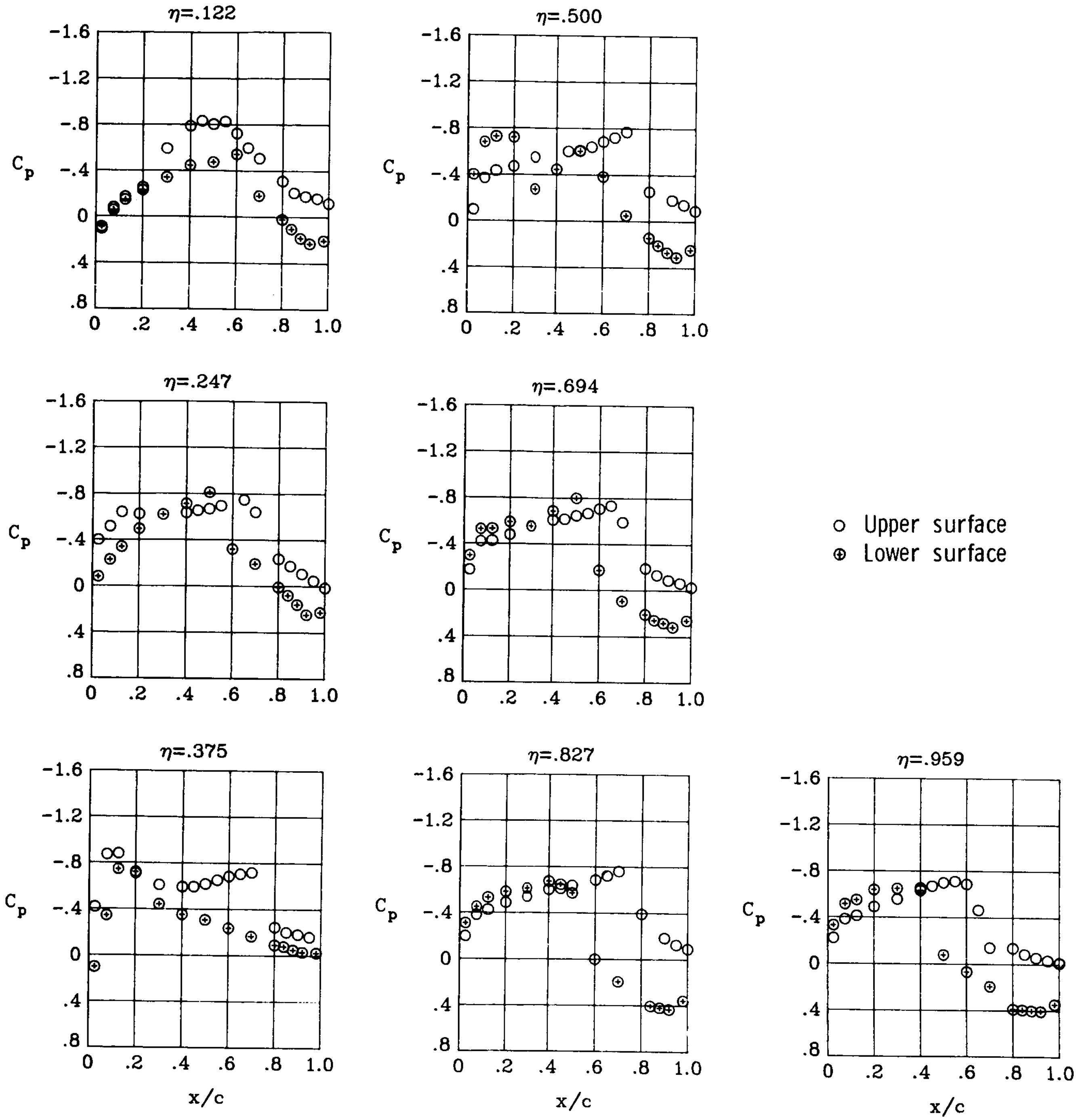

(a) $M_\infty = 0.90$; $\alpha = 1°$.

Figure 56.- Wing chordwise pressure distributions for $\delta a_2 = 7.5°$ at $M_\infty = 0.90$. $\delta a_1 = 0°$.

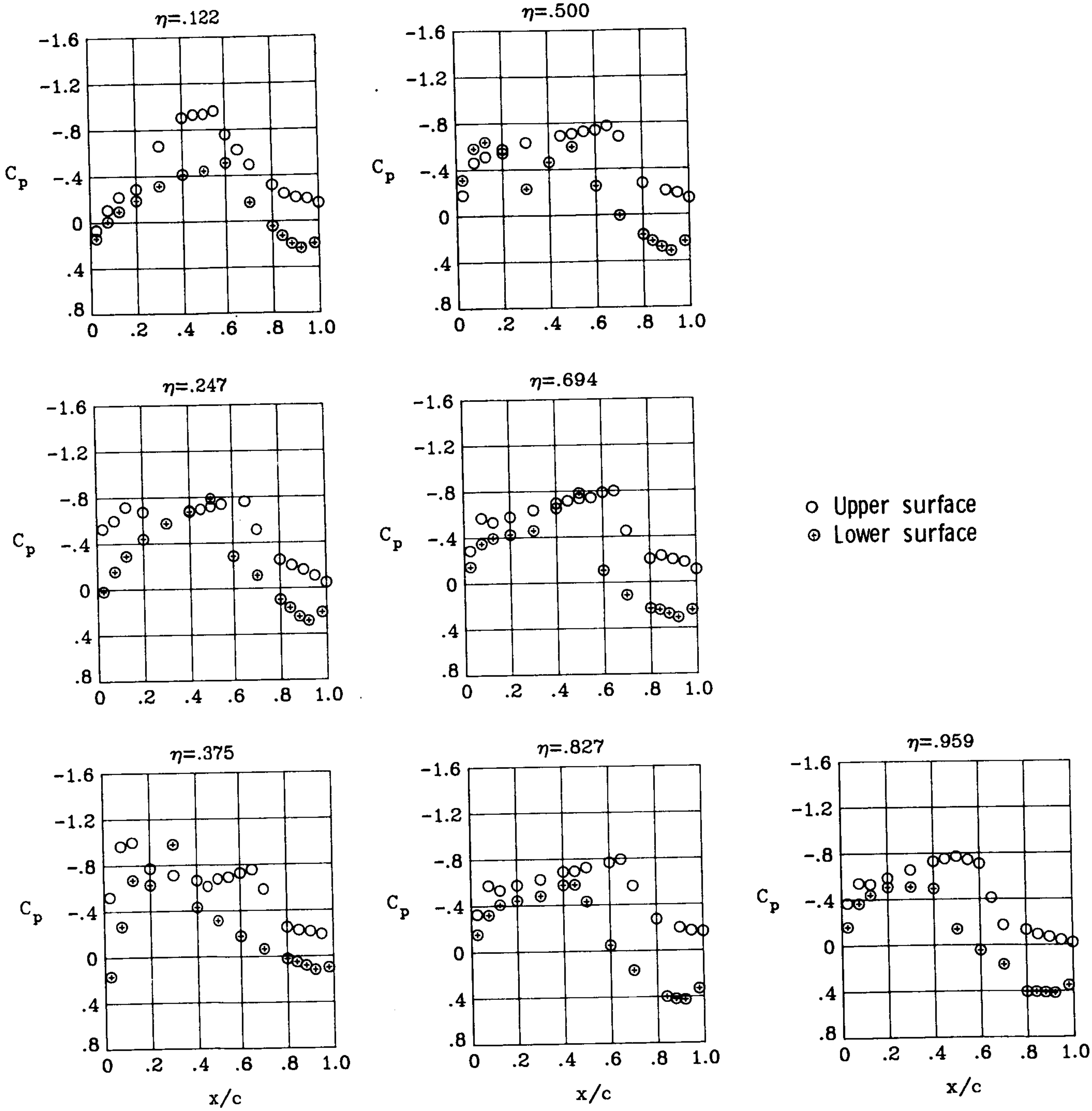

(b) $M_\infty = 0.90$; $\alpha = 2°$.

Figure 56.- Continued.

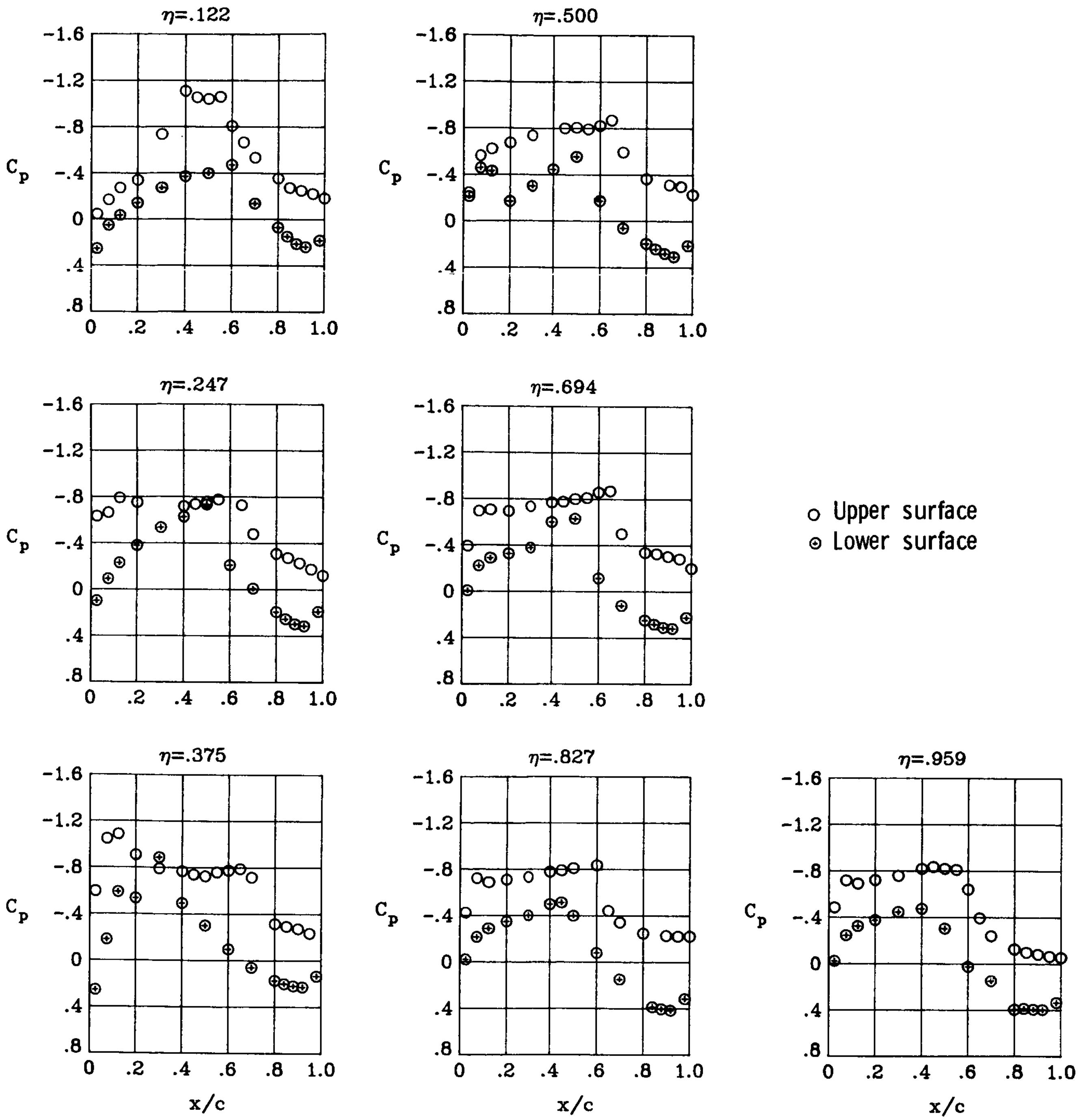

(c) $M_\infty = 0.90$; $\alpha = 3°$.

Figure 56.- Continued.

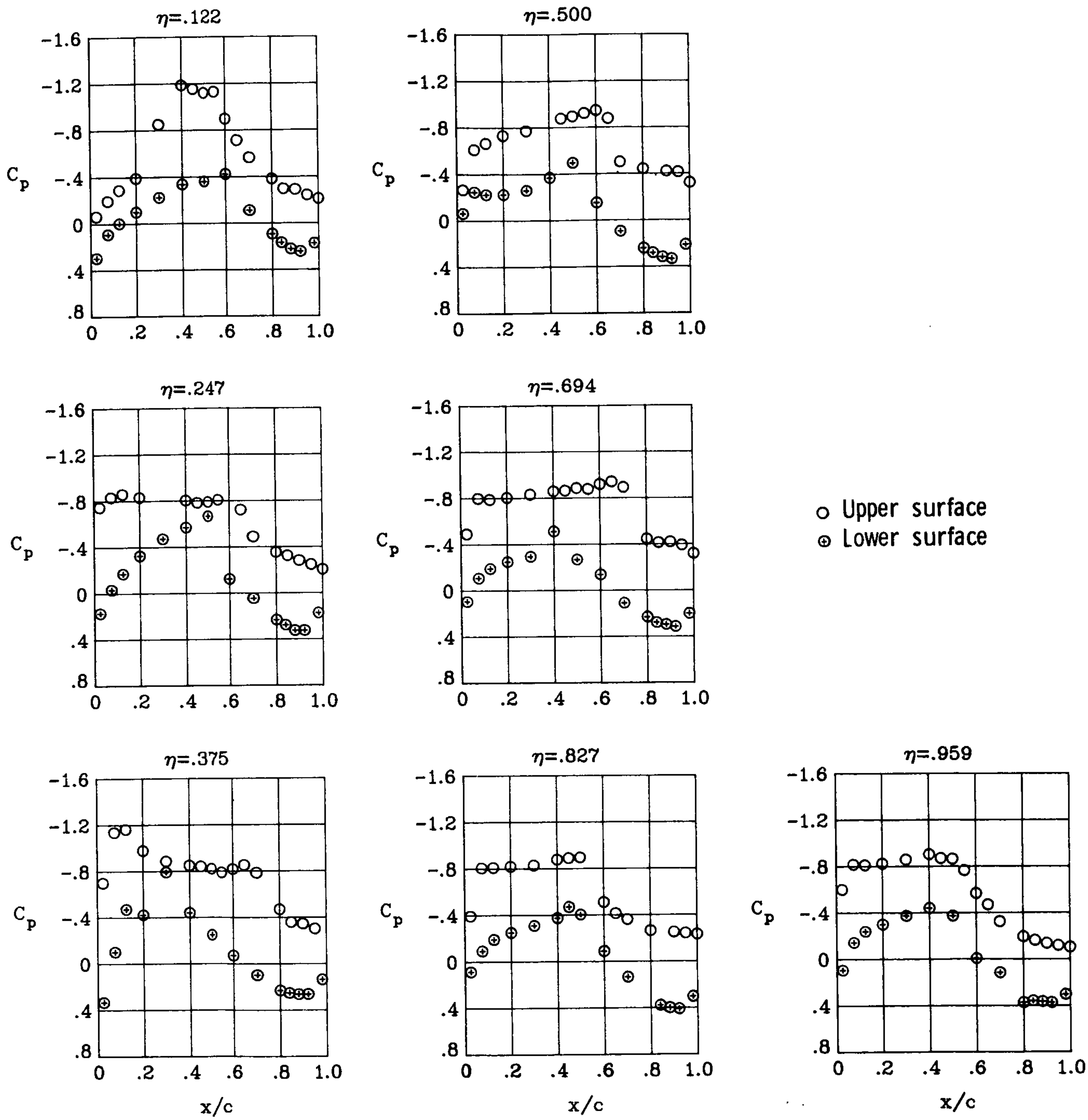

(d) $M_\infty = 0.90$; $\alpha = 4°$.

Figure 56.- Continued.

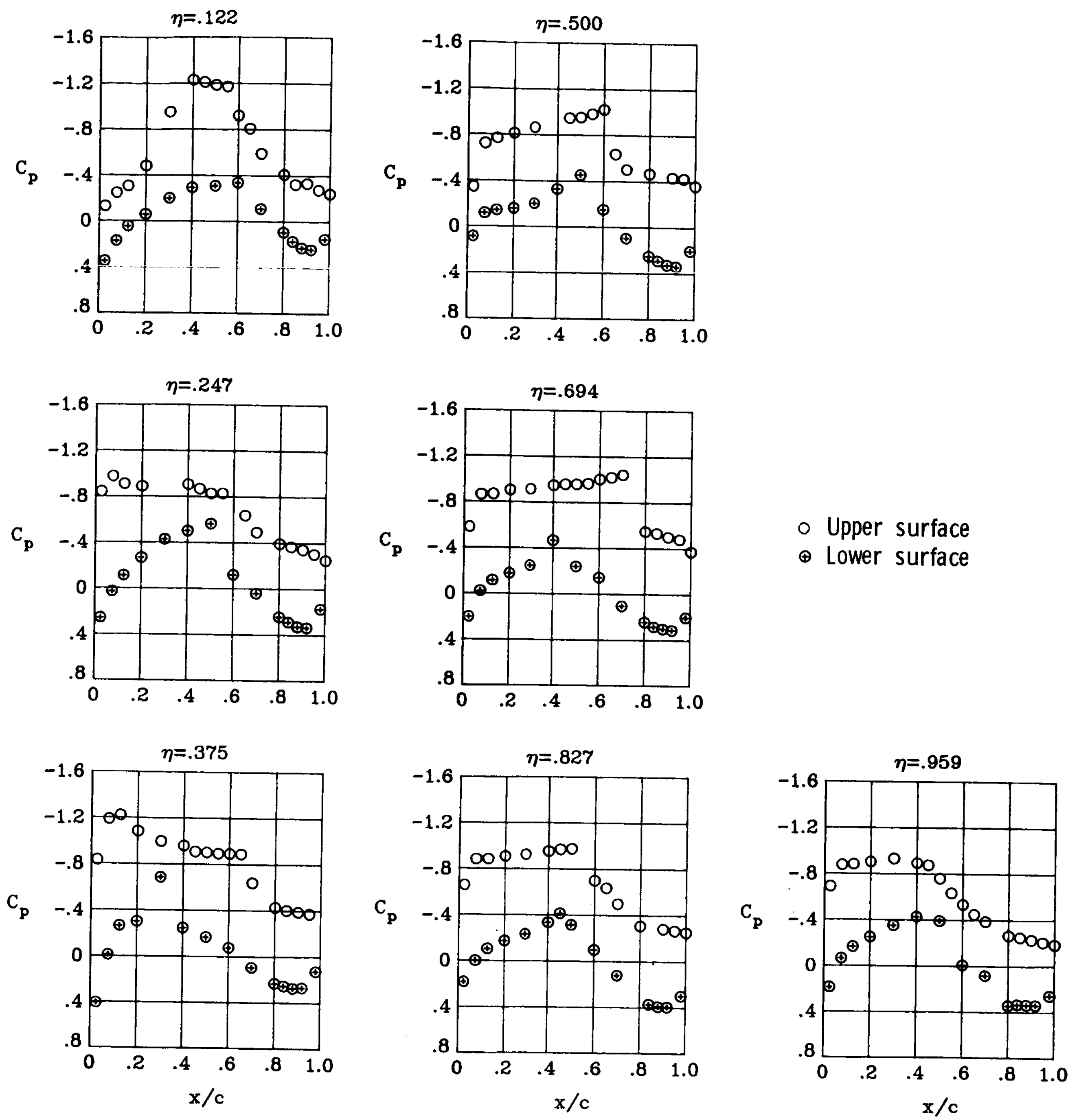

(e) $M_\infty = 0.90$; $\alpha = 5°$.

Figure 56.- Concluded.

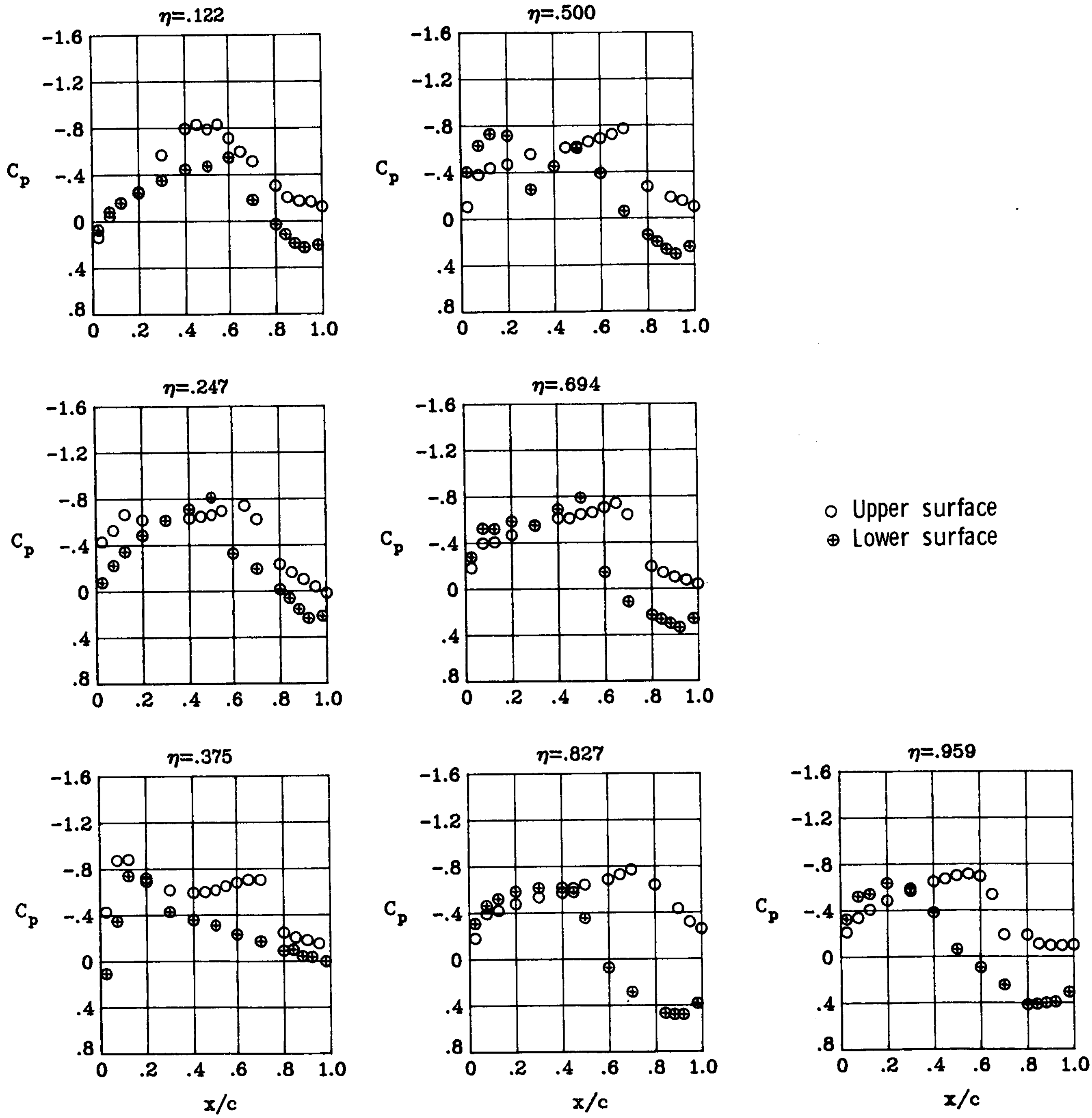

(a) $M_\infty = 0.90$; $\alpha = 1°$.

Figure 57.- Wing chordwise pressure distributions for $\delta a_2 = 12.5°$ at $M_\infty = 0.90$. $\delta a_1 = 0°$.

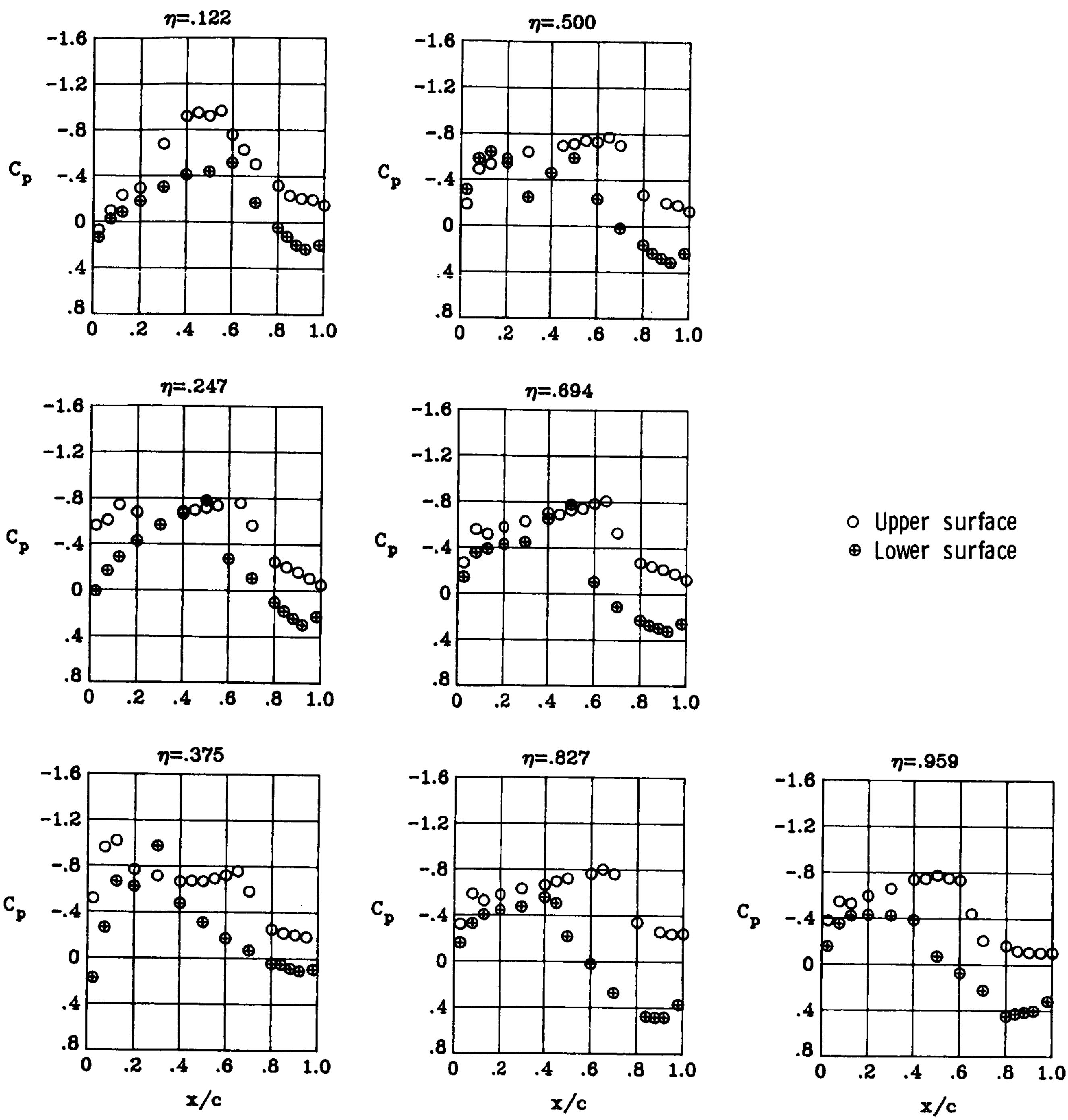

(b) $M_\infty = 0.90$; $\alpha = 2°$.

Figure 57.- Continued.

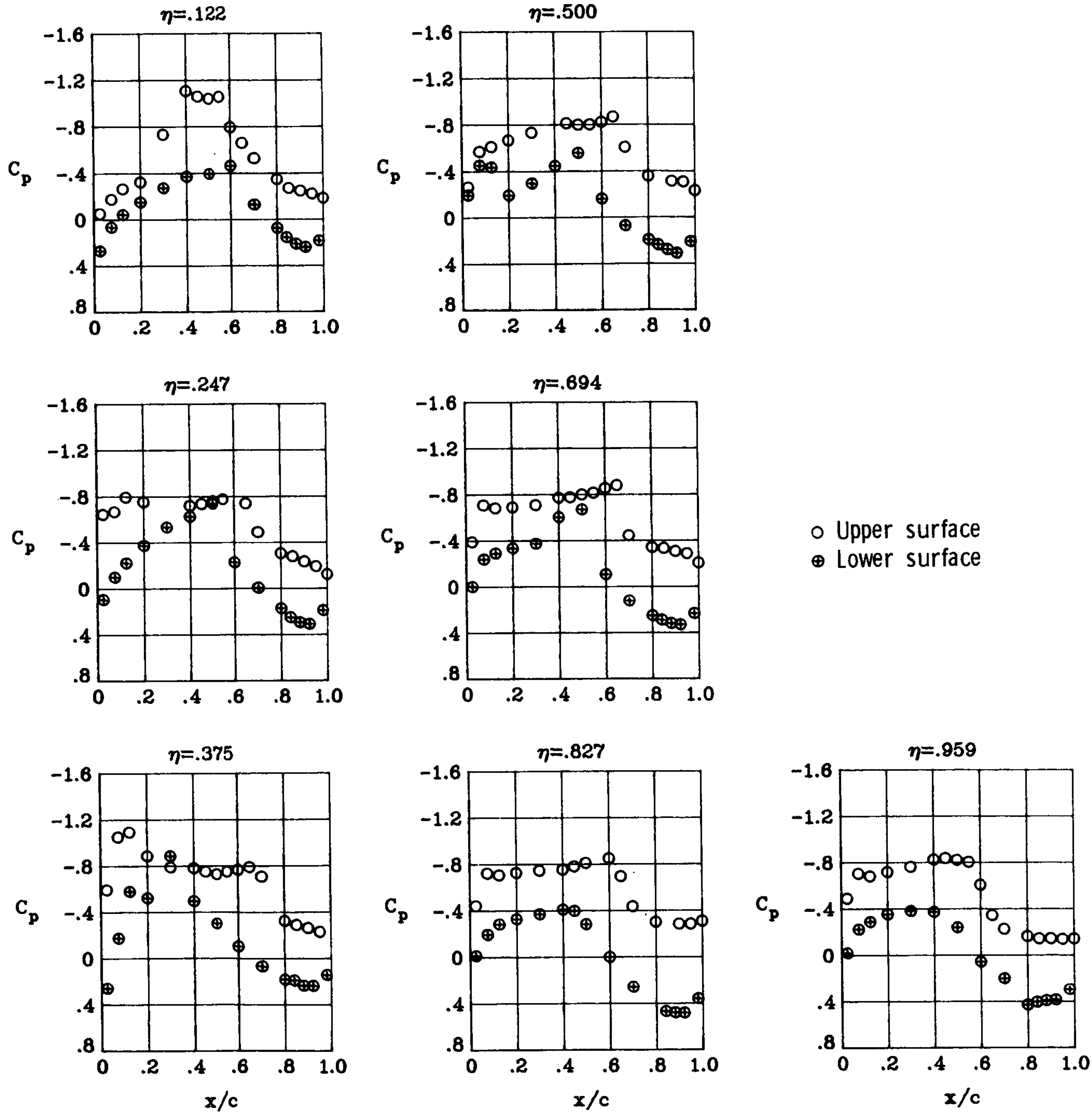

(c) $M_\infty = 0.90$; $\alpha = 3°$.

Figure 57.- Continued.

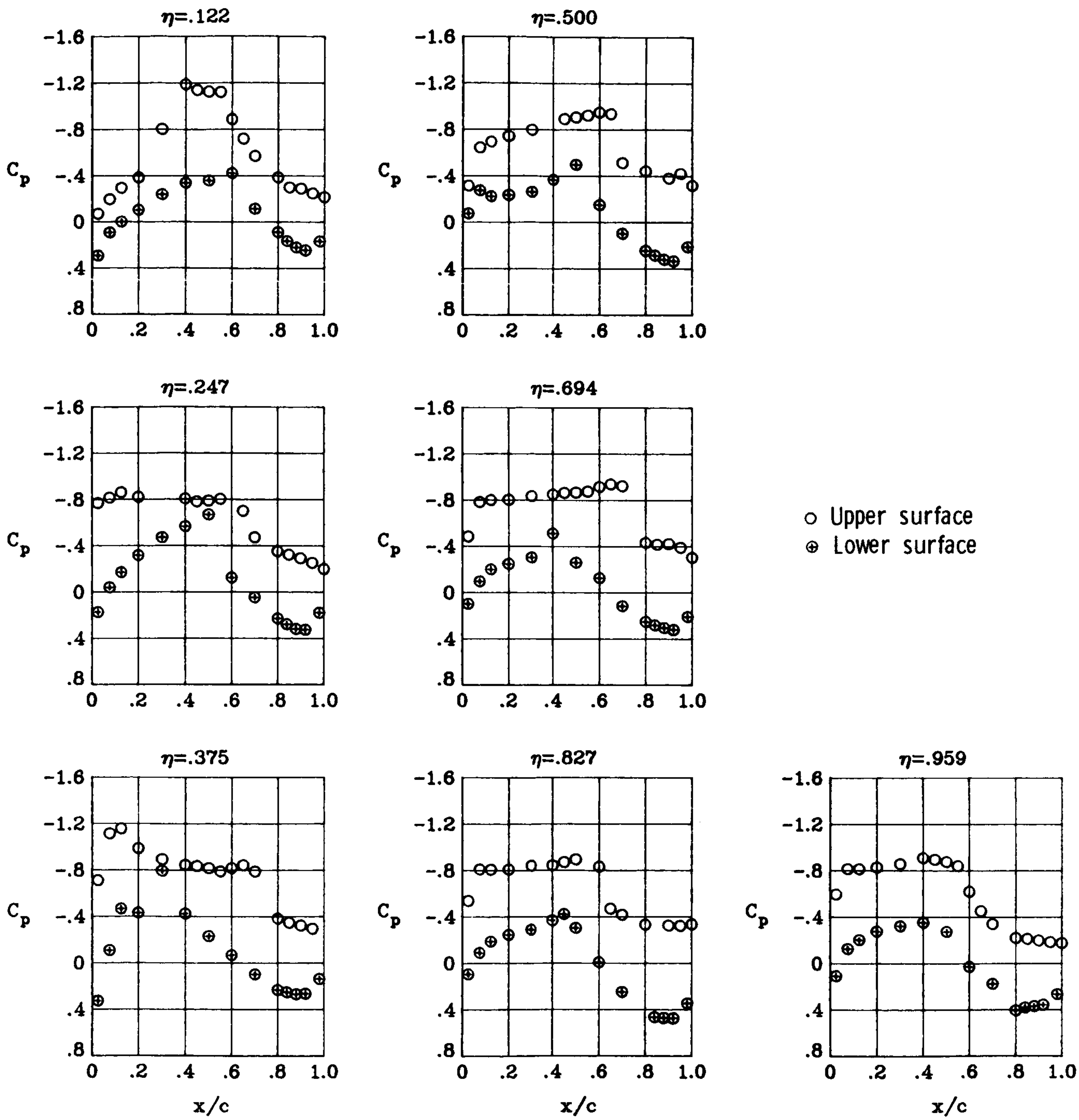

(d) $M_\infty = 0.90$; $\alpha = 4°$.

Figure 57.- Continued.

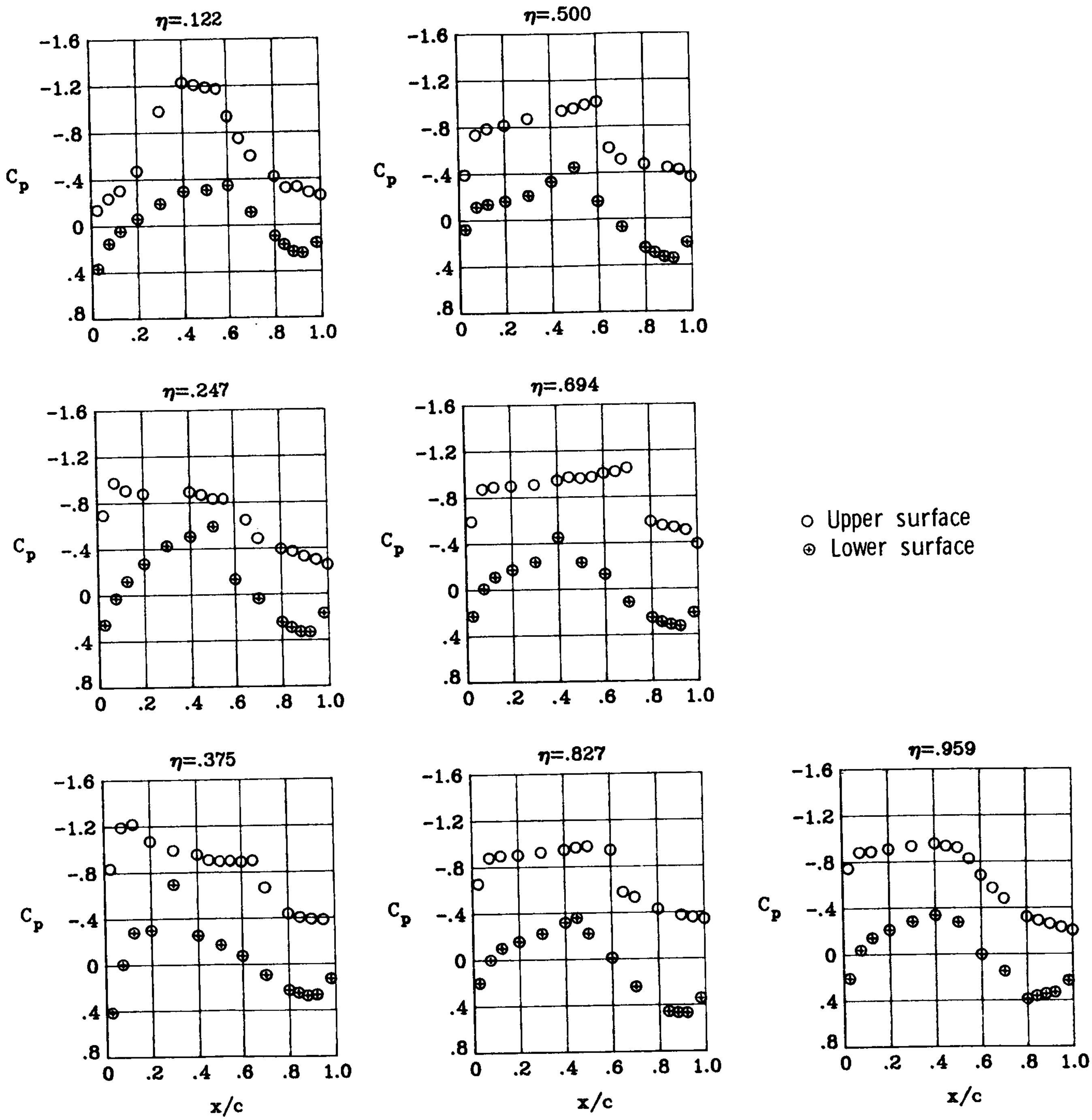

(e) $M_\infty = 0.90$; $\alpha = 5°$.

Figure 57.- Concluded.

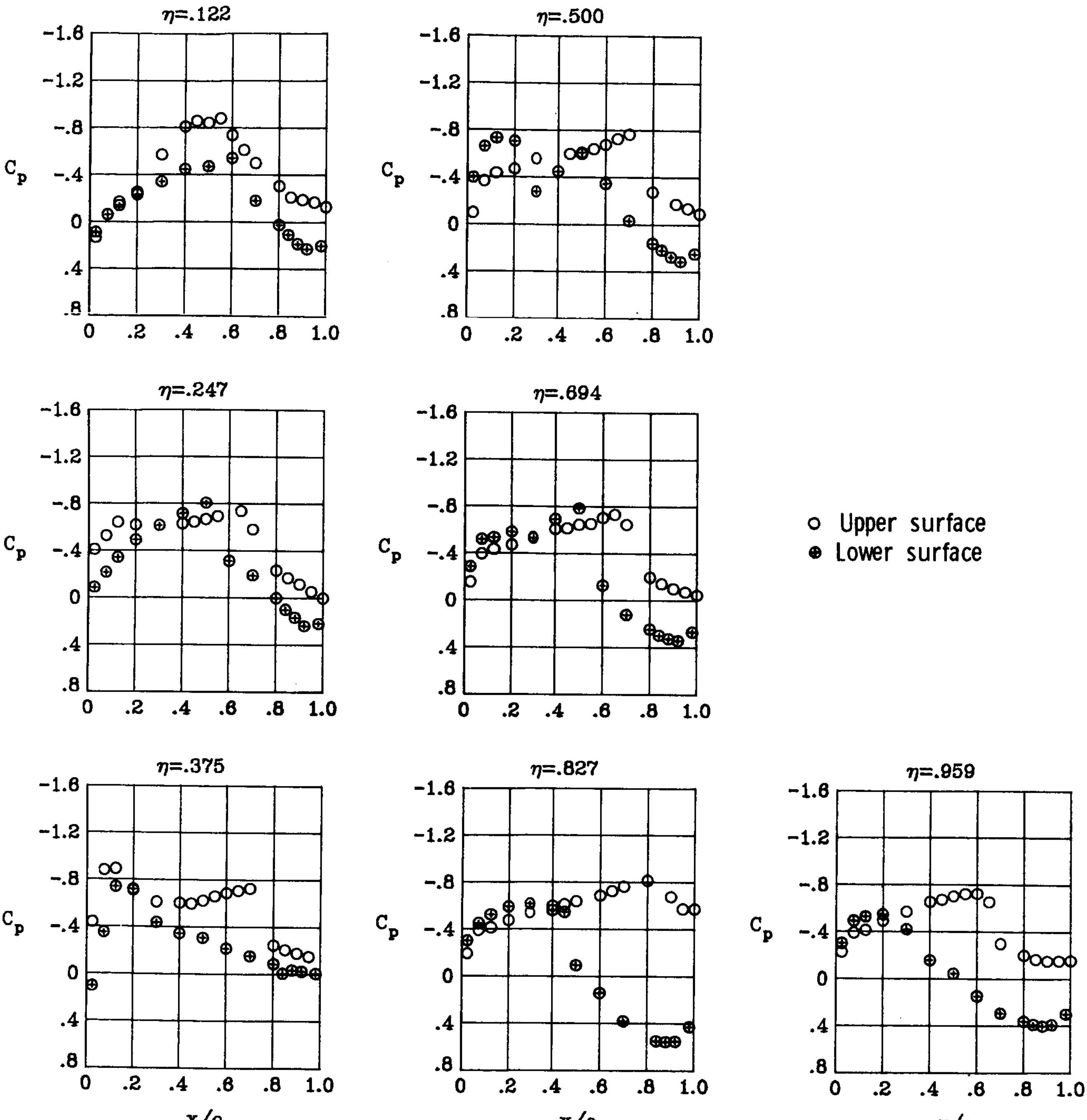

(a) $M_\infty = 0.90$; $\alpha = 1°$.

Figure 58.- Wing chordwise pressure distributions for $\delta a_2 = 17.5°$ at $M_\infty = 0.90$. $\delta a_1 = 0°$.

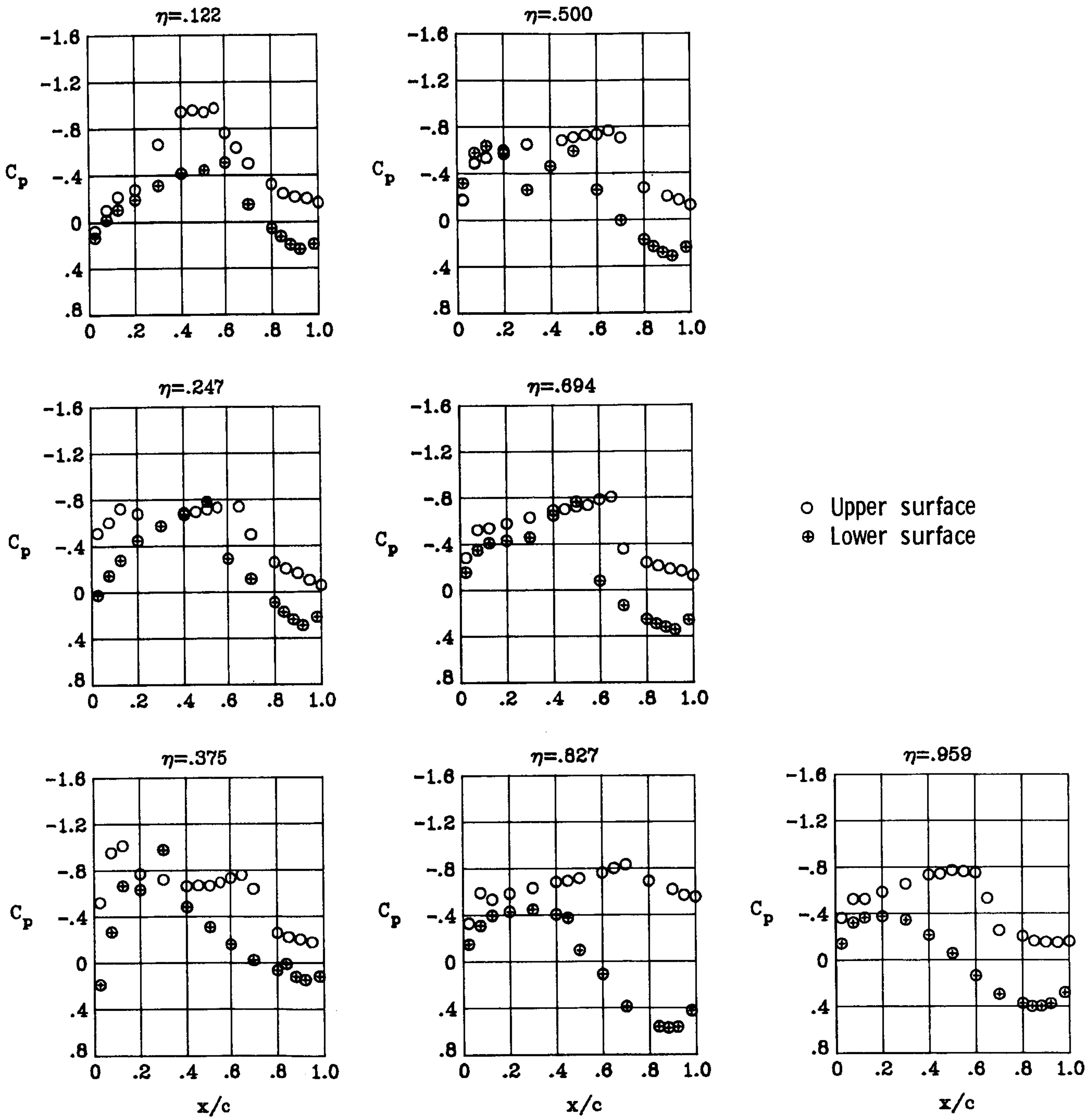

(b) $M_\infty = 0.90$; $\alpha = 2°$.

Figure 58.- Continued.

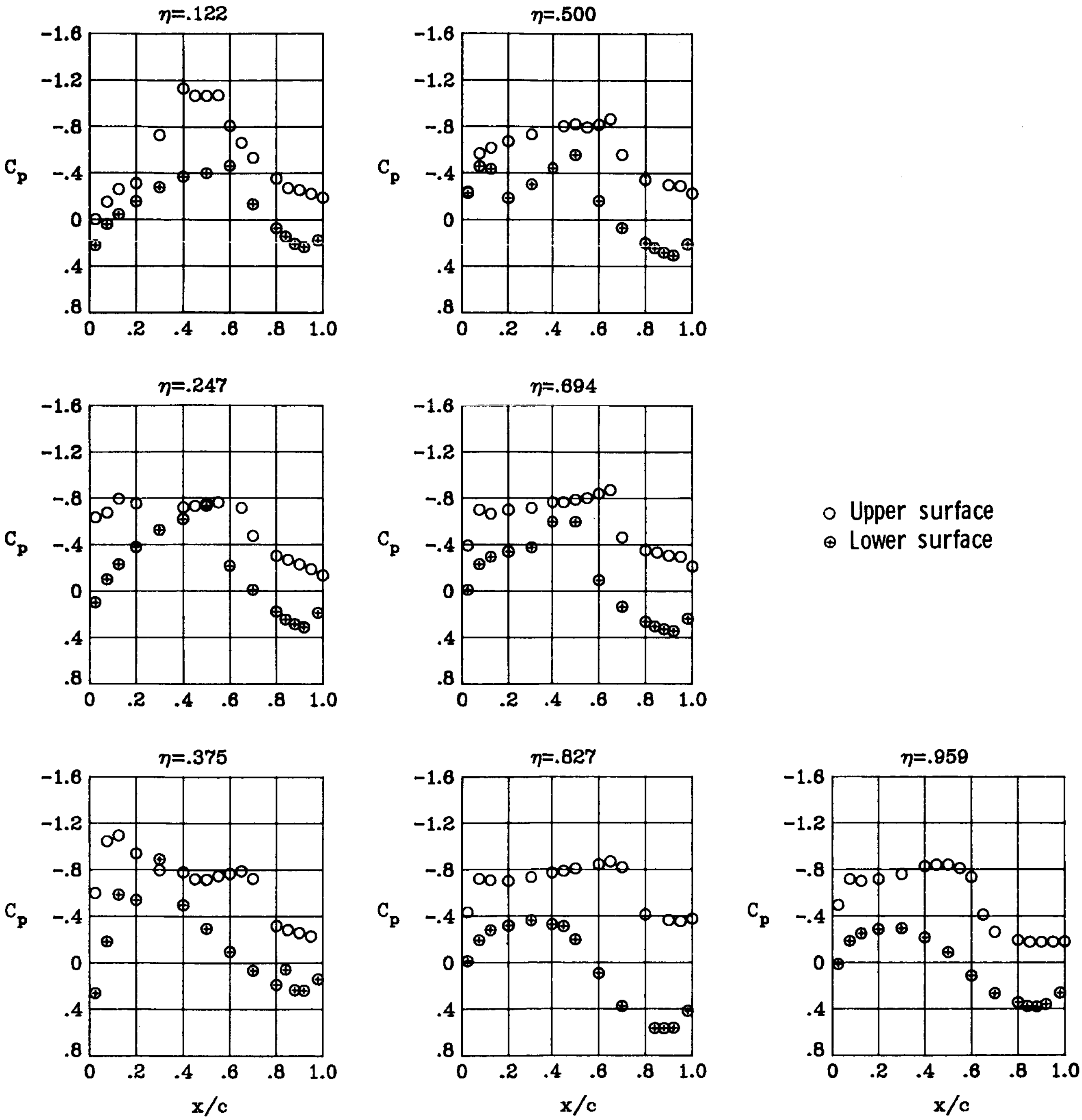

(c) $M_\infty = 0.90$; $\alpha = 3°$.

Figure 58.- Continued.

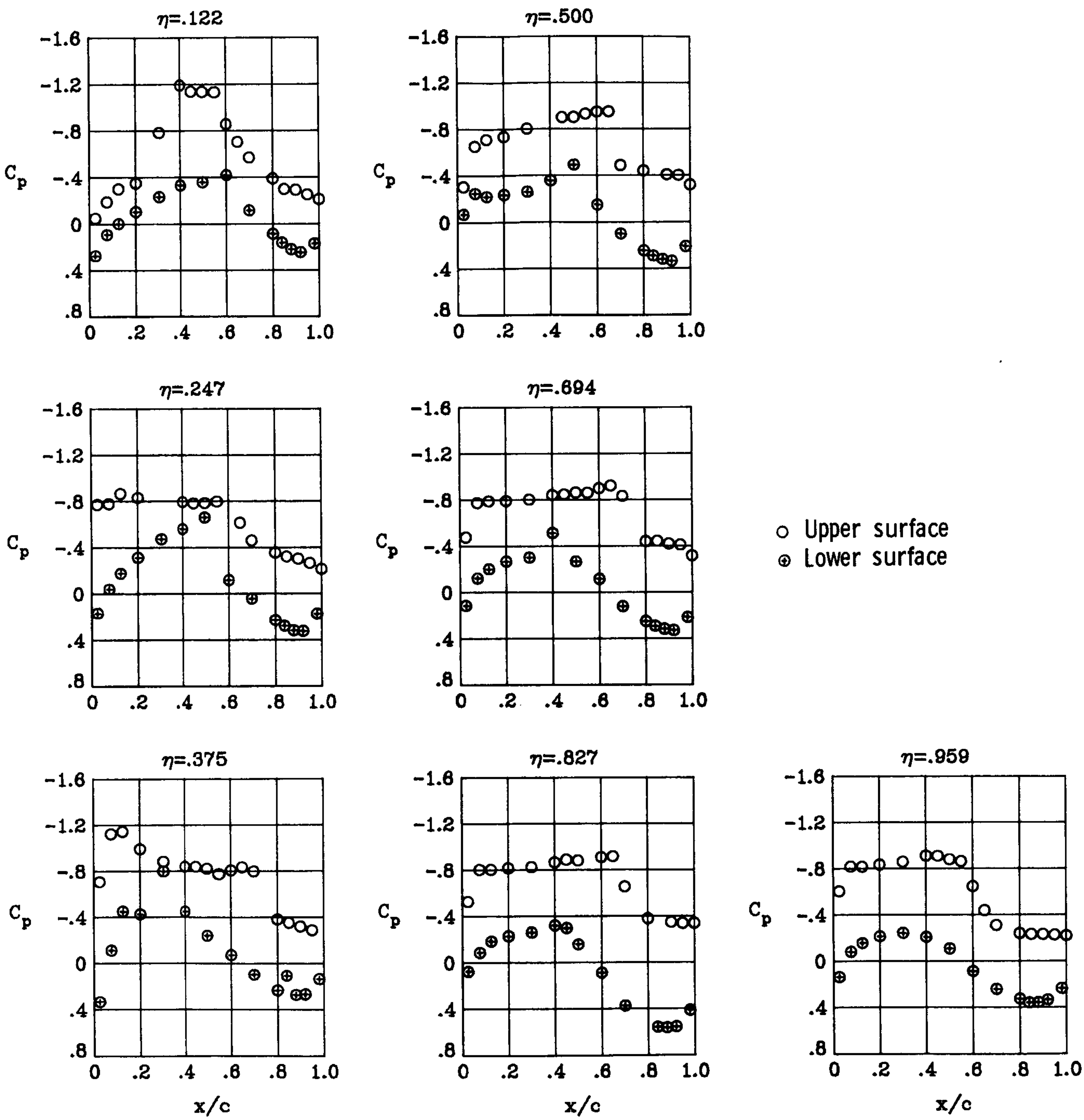

(d) $M_\infty = 0.90$; $\alpha = 4°$.

Figure 58.- Continued.

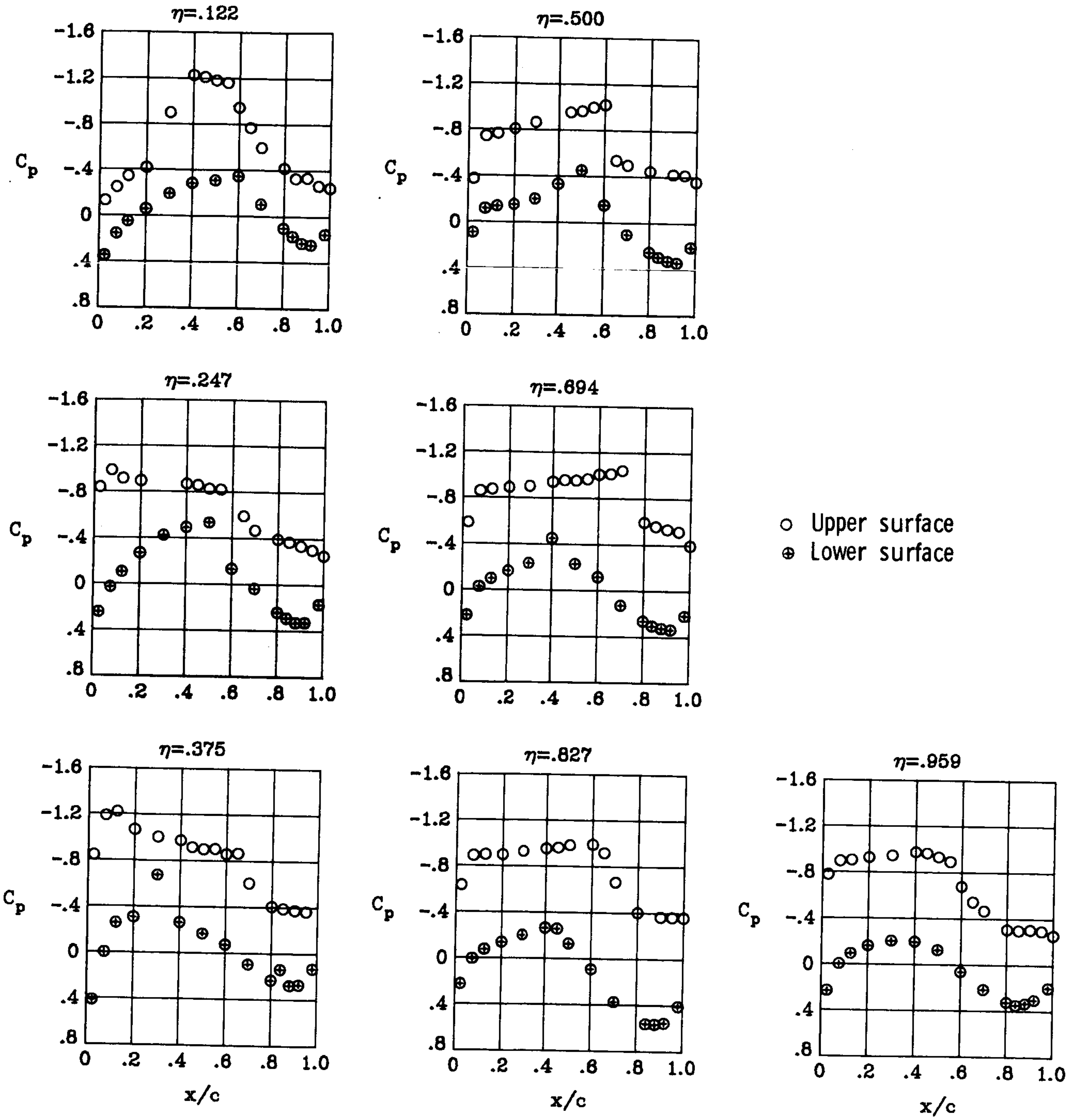

(e) M_∞ = 0.90; α = 5°.

Figure 58.- Concluded.

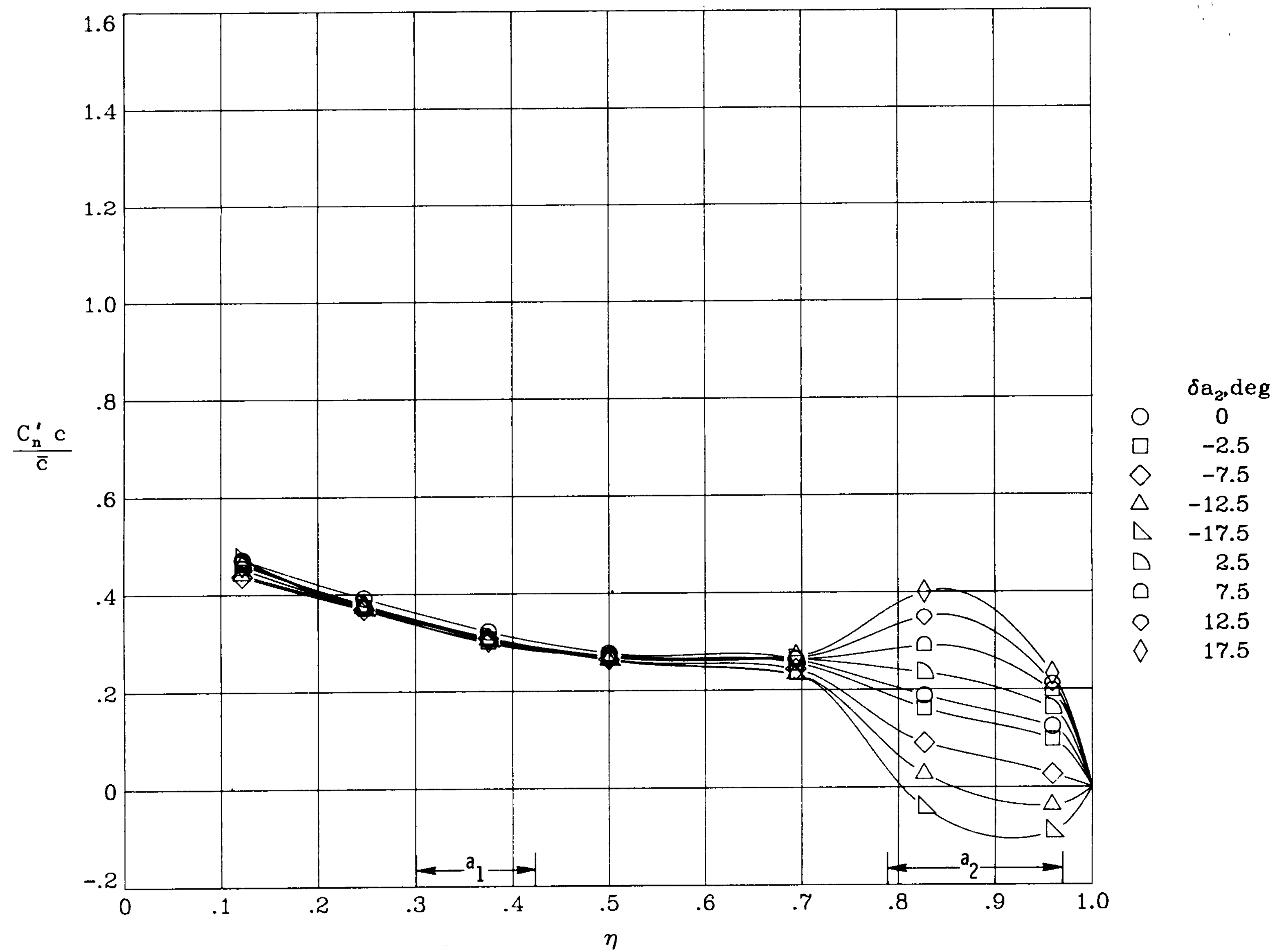

(a) $M_\infty = 0.82$; $\alpha = 1°$.

Figure 59.- Wing spanwise load distributions for deflections of a_2. $\delta a_1 = 0°$.

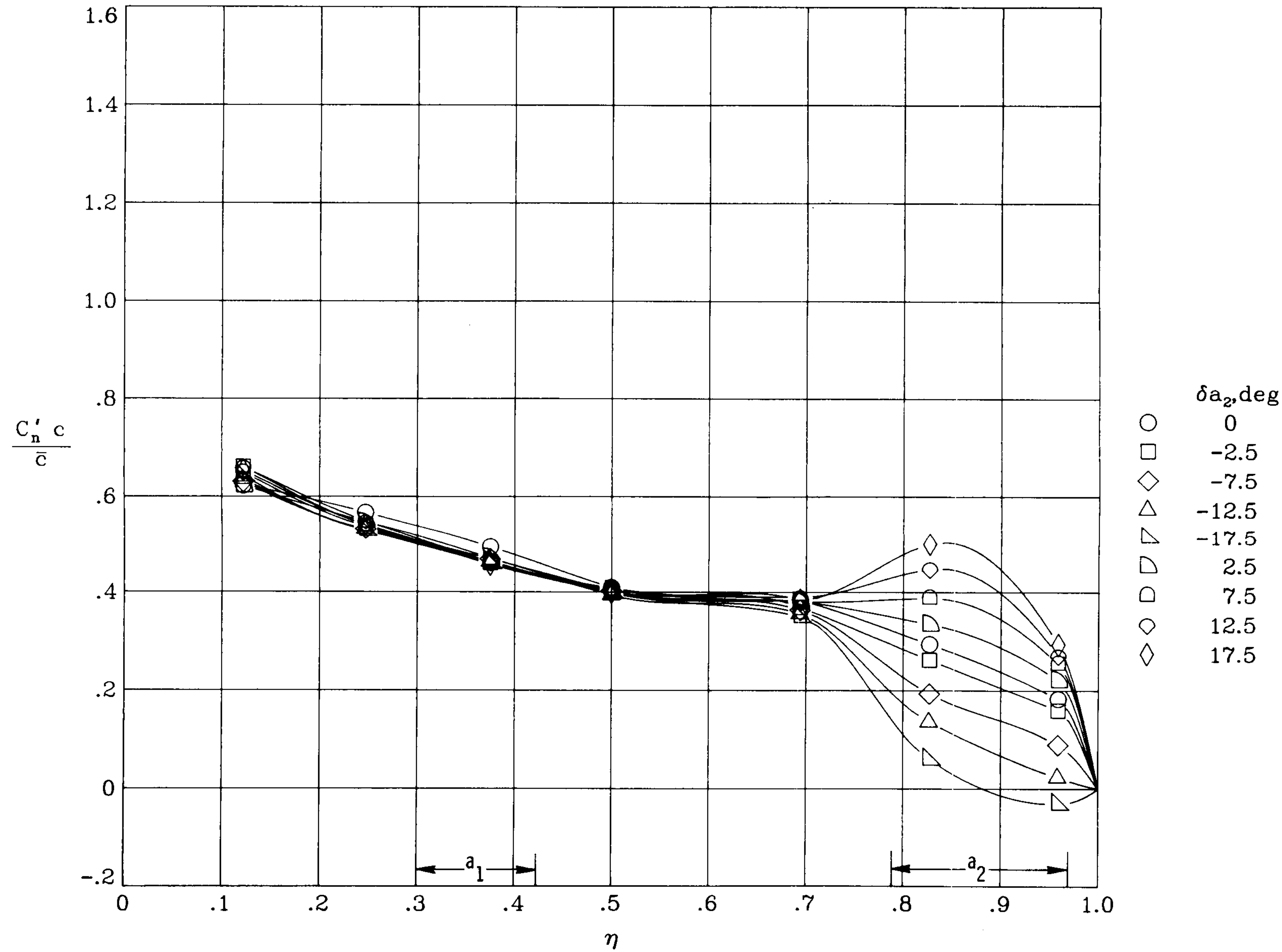

(b) $M_\infty = 0.82$; $\alpha = 2°$.

Figure 59.- Continued.

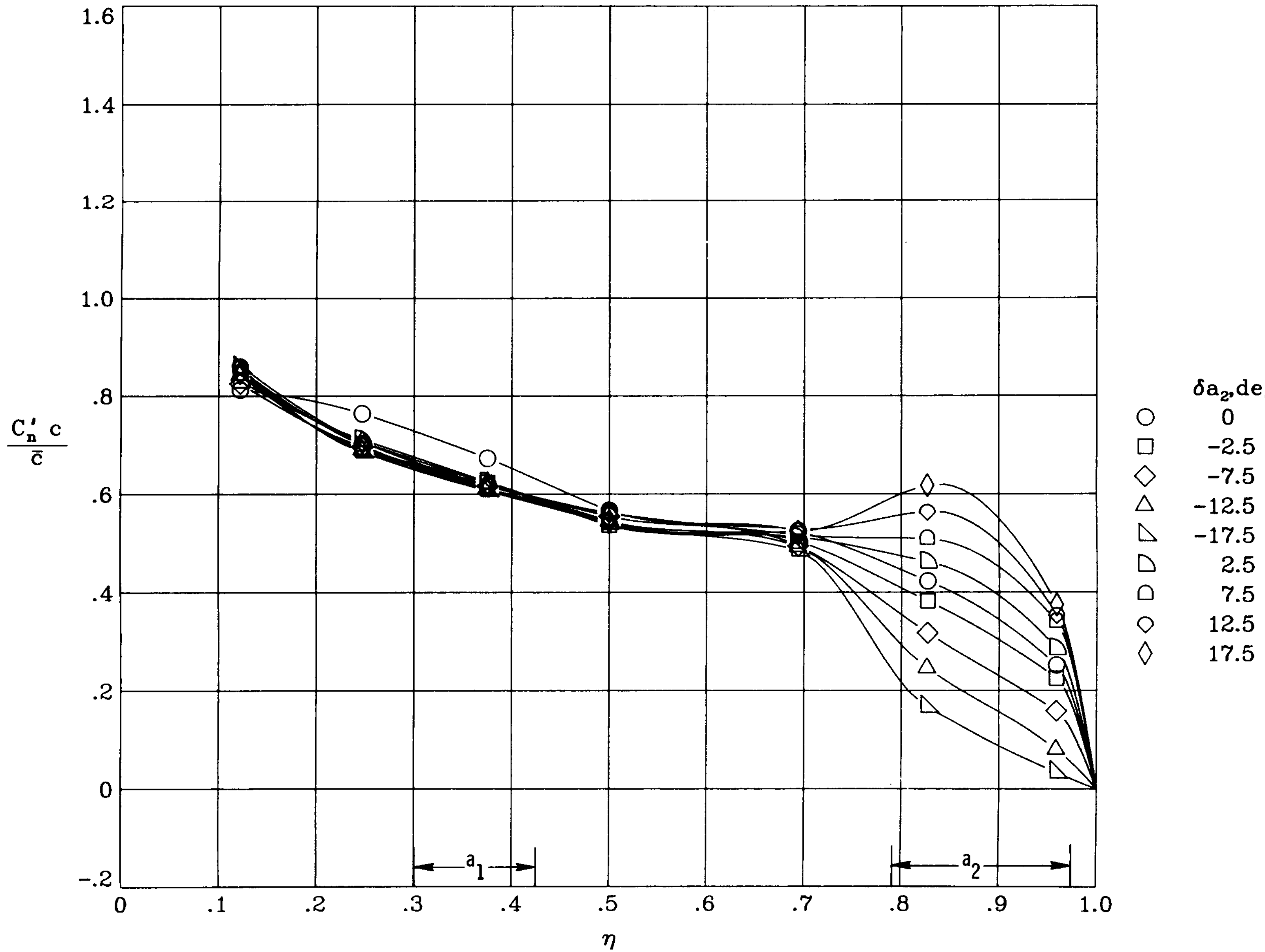

(c) $M_\infty = 0.82$; $\alpha = 3°$.

Figure 59.- Continued.

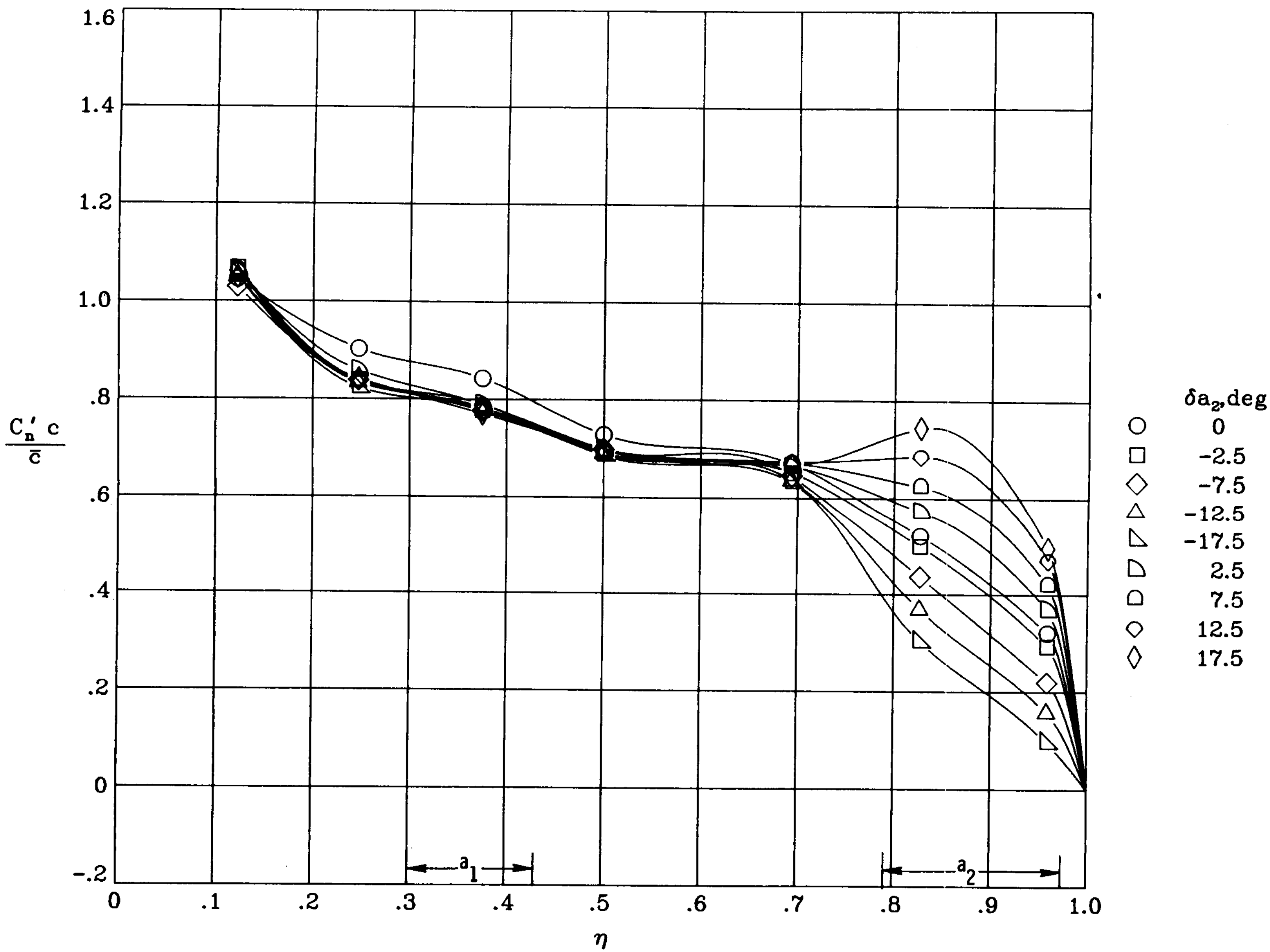

(d) $M_\infty = 0.82$; $\alpha = 4°$.

Figure 59.- Continued.

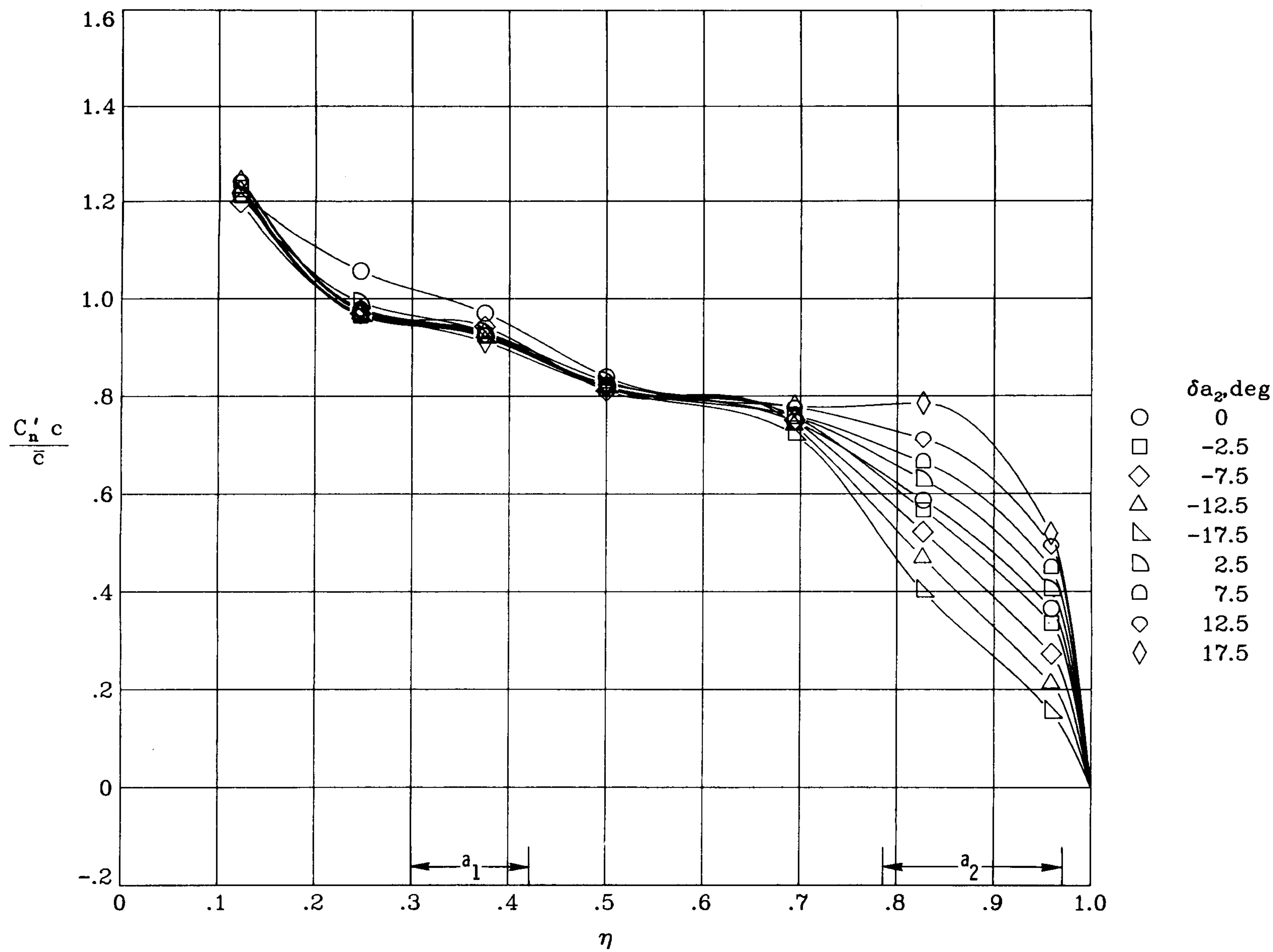

(e) $M_\infty = 0.82$; $\alpha = 5°$.

Figure 59.- Concluded.

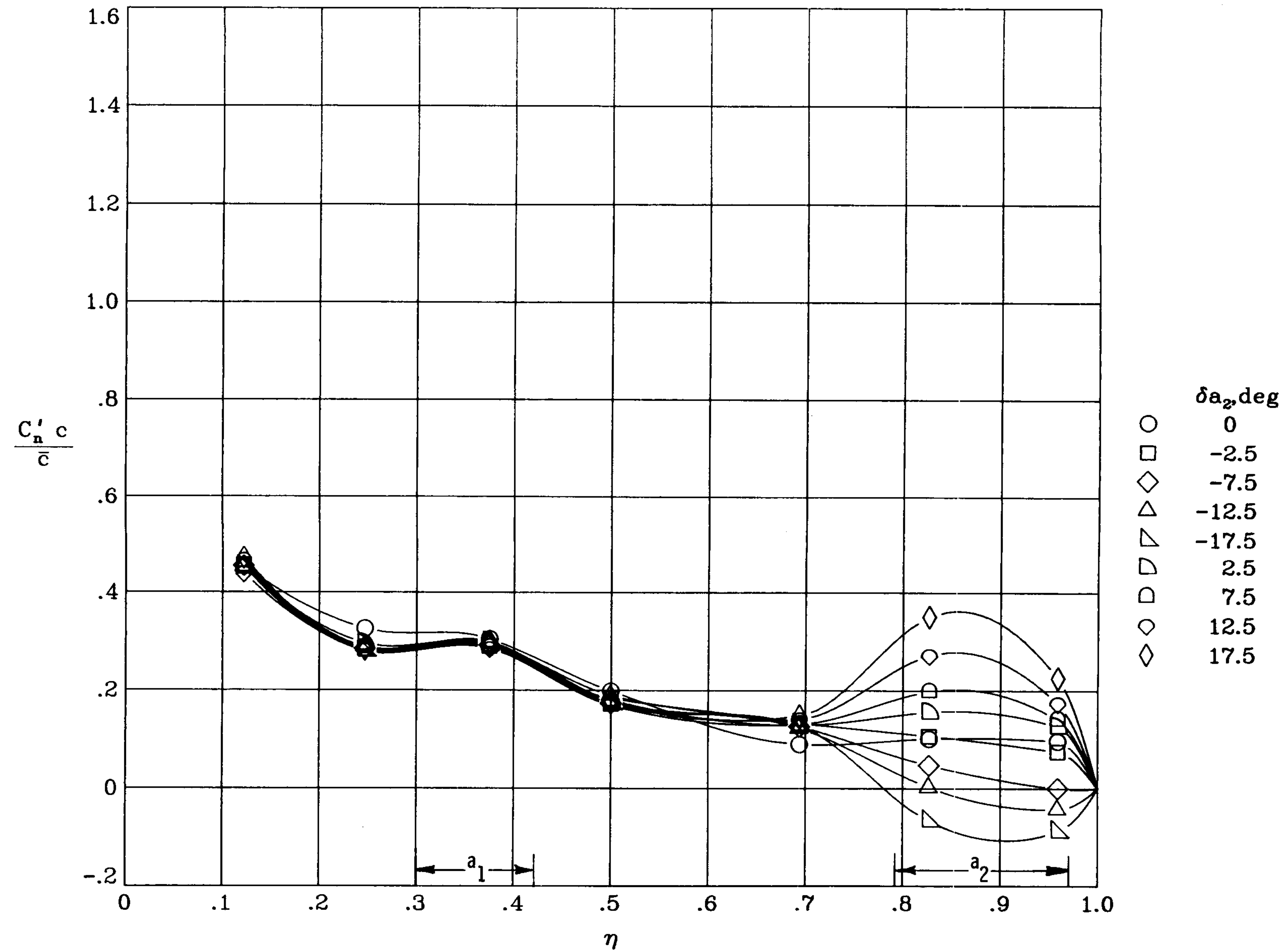

(a) $M_\infty = 0.90$; $\alpha = 1°$.

Figure 60.- Wing spanwise load distributions for deflections of a_2. $\delta a_1 = 0°$.

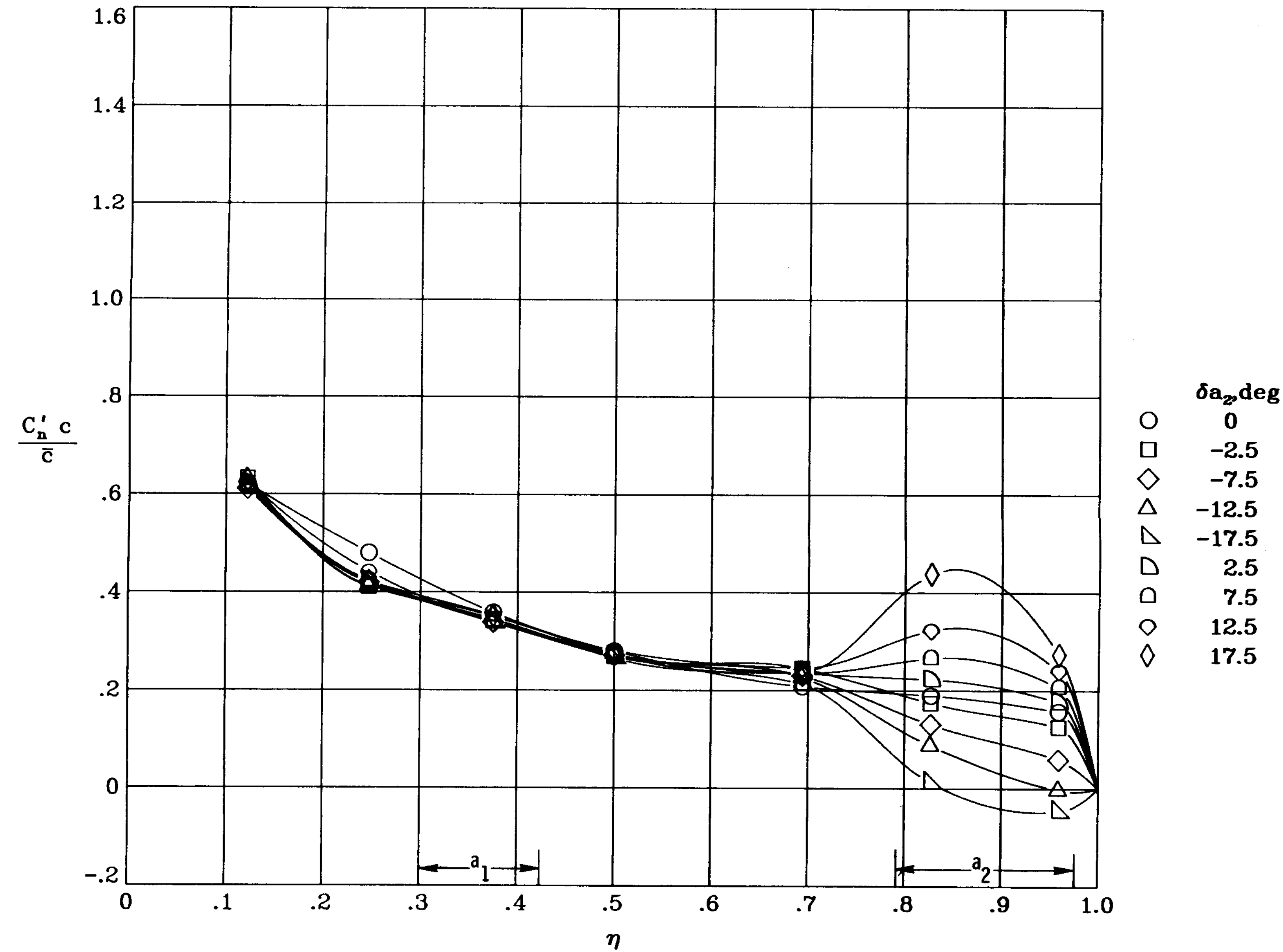

(b) $M_\infty = 0.90$; $\alpha = 2°$.

Figure 60.- Continued.

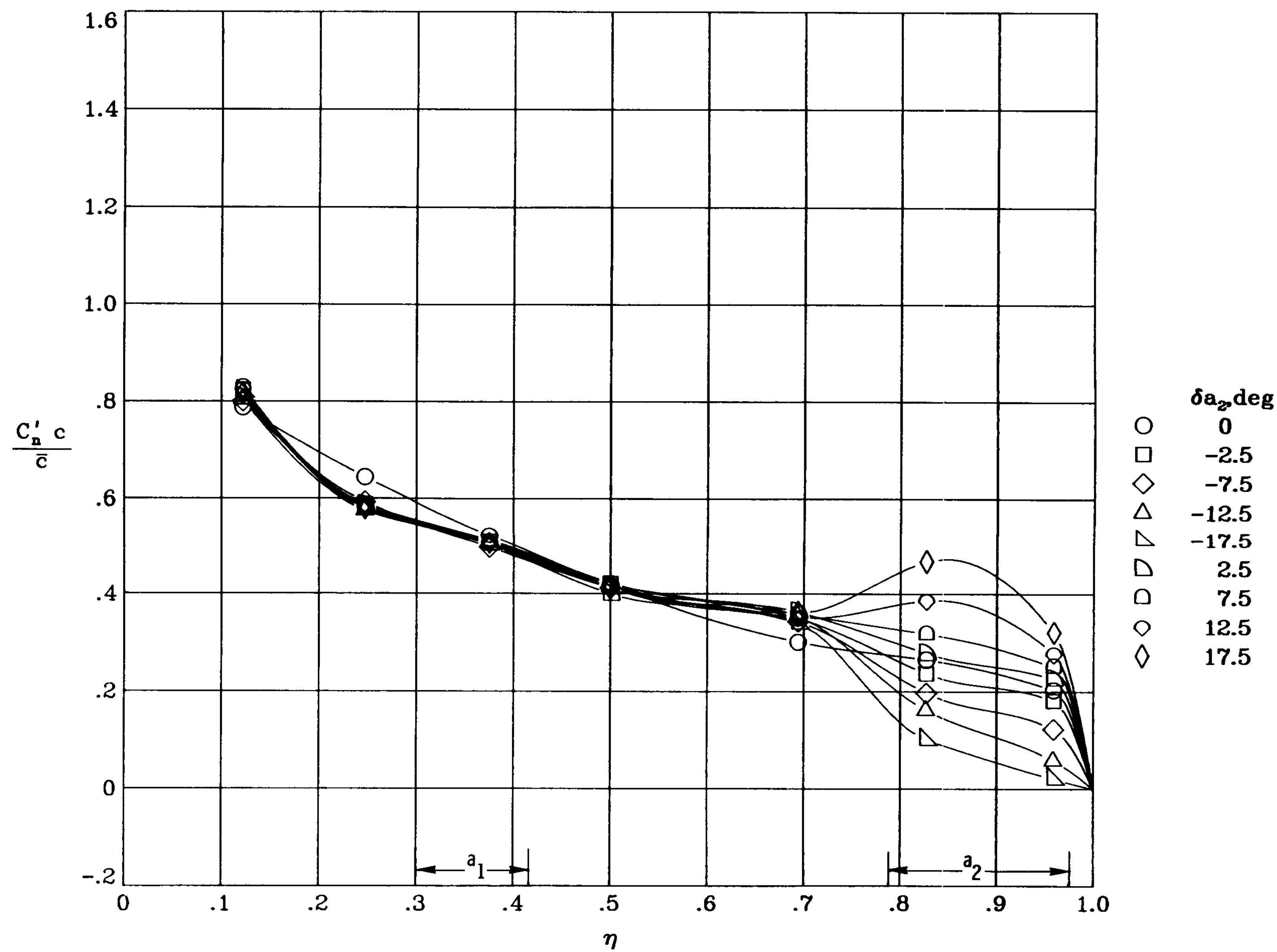

(c) $M_\infty = 0.90$; $\alpha = 3°$.

Figure 60.- Continued.

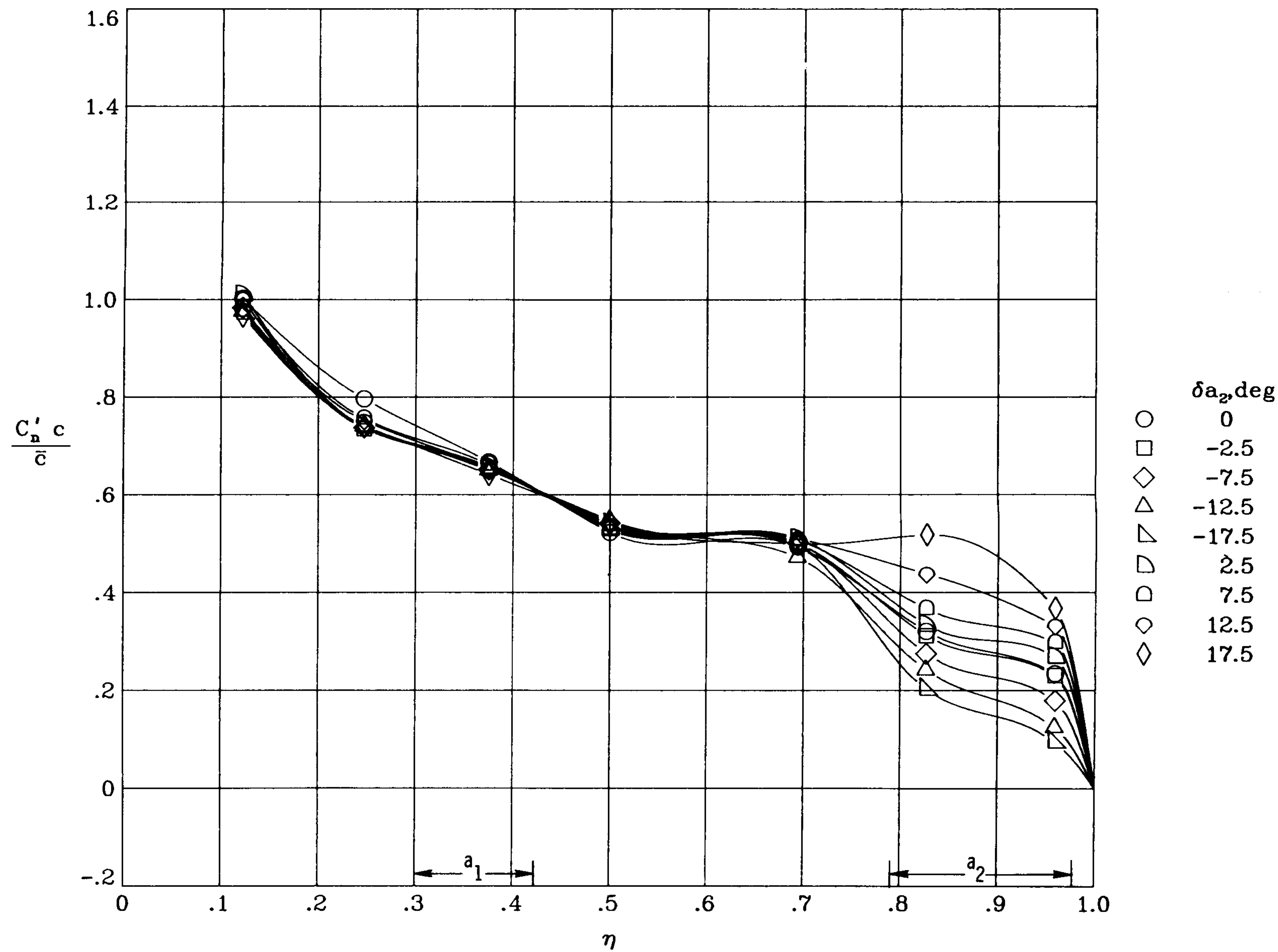

(d) $M_\infty = 0.90$; $\alpha = 4°$.

Figure 60.- Continued.

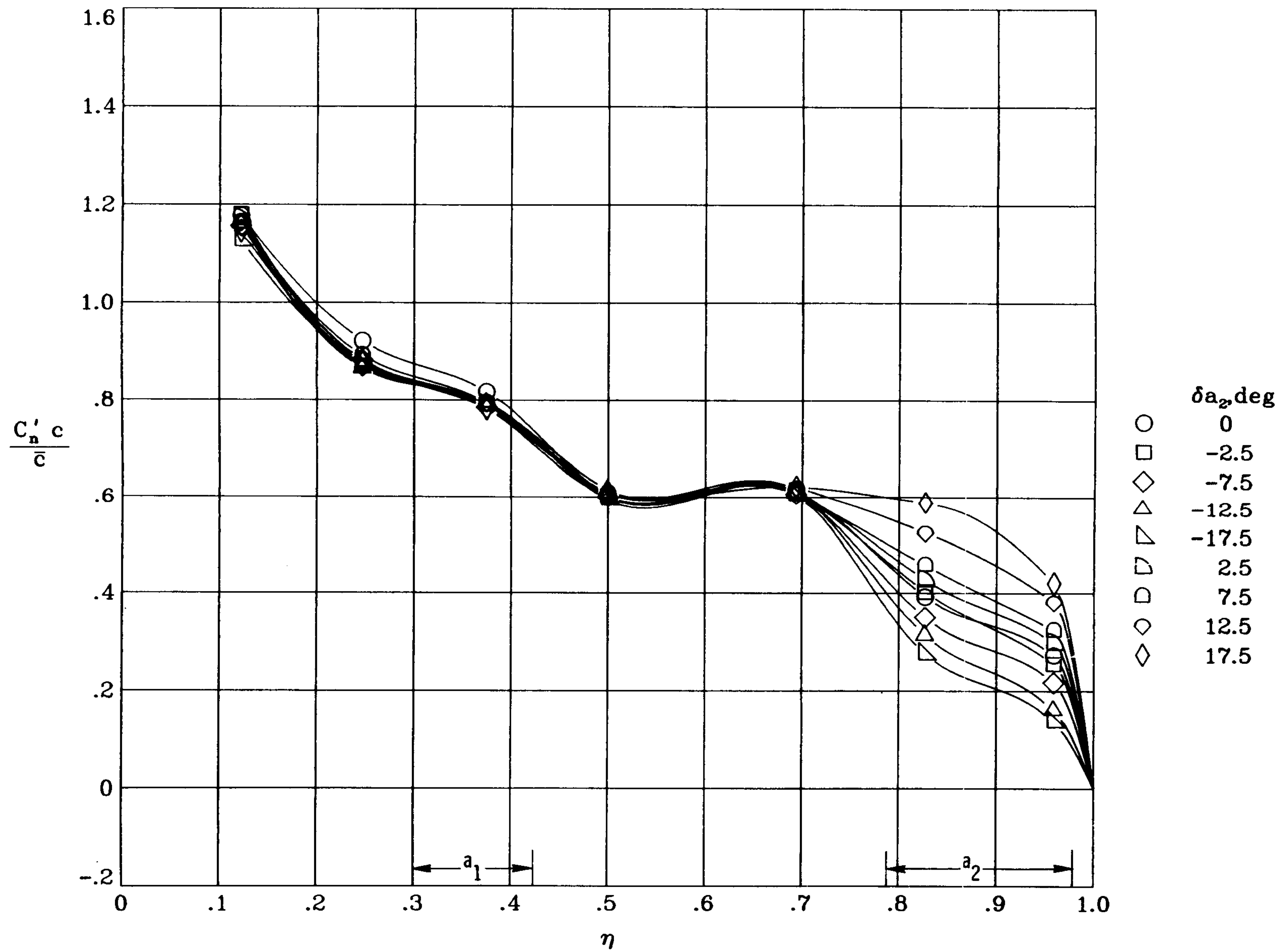

(e) $M_\infty = 0.90$; $\alpha = 5°$.

Figure 60.- Concluded.

1. Report No.	2. Government Accession No.	3. Recipient's Catalog No.
NASA TP-2478		

4. Title and Subtitle	5. Report Date
Effect of Aileron Deflections on the Aerodynamic Characteristics of a Semispan Model of a Subsonic Energy-Efficient Transport	October 1985
	6. Performing Organization Code 505-31-23-07
7. Author(s) Peter F. Jacobs	8. Performing Organization Report No. L-15934
	10. Work Unit No.
9. Performing Organization Name and Address NASA Langley Research Center Hampton, VA 23665	11. Contract or Grant No.
	13. Type of Report and Period Covered Technical Paper
12. Sponsoring Agency Name and Address National Aeronautics and Space Administration Washington, DC 20546	14. Sponsoring Agency Code

15. Supplementary Notes

16. Abstract

An investigation was conducted in the Langley 8-Foot Transonic Pressure Tunnel to determine the effect of aileron deflections on the aerodynamic characteristics of a subsonic energy-efficient transport (EET) model. The semispan model had an aspect-ratio-10 supercritical wing and was configured with a conventionally located set of ailerons (i.e., a high-speed aileron located inboard and a low-speed aileron located outboard). Data for the model were taken over a Mach number (M_∞) range from 0.30 to 0.90 and an angle of attack range from approximately -2° to 10°. The Reynolds number was 2.5×10^6 per foot for $M_\infty = 0.30$ and 4.0×10^6 per foot for the other Mach numbers. Model force and moment data, aileron-effectiveness parameters, aileron hinge-moment data, chordwise pressure distributions, and spanwise load data are presented.

17. Key Words (Suggested by Author(s))	18. Distribution Statement
Ailerons Control effectiveness Supercritical wing Lateral stability	Unclassified - Unlimited Subject Category 02

19. Security Classif. (of this report)	20. Security Classif. (of this page)	21. No. of Pages	22. Price
Unclassified	Unclassified	342	A15

N-305

For sale by the National Technical Information Service, Springfield, Virginia 22161

☆U.S. GOVERNMENT PRINTING OFFICE:1985 -537 -086/ 20013